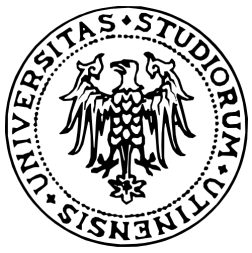

Università degli Studi Di Udine

PhD thesis

For the title of

Dottore di Ricerca dell'Università degli Studi di Udine
and
Docteur de l'Université de Grenoble

Dipartimento di Ingegneria Elettrica, Gestionale e Meccanica
Corso di Dottorato Internazionale in Ingegneria Industriale e dell'Informazione
XXVII ciclo

Institut de Microélectronique, Electromagnétisme et Photonique
Ecole Doctorale Électronique, Électrotechnique, Automatique, Télécomunications, Signal (EEATS)

Federico PITTINO

Udine, 21/05/2015

Prospects of nanoelectronic biosensing with high-frequency impedance spectroscopy

PhD jury
Prof. Paolo GARDONIO, President
Prof. Muhammad Ashraful ALAM, Reviewer
Prof. Danilo DE MARCHI, Reviewer
Prof. Clemens HEITZINGER, Reviewer
Dr. Thomas ERNST, Tutor (Fr)
Prof. Luca SELMI, Tutor (It)

Research work partially funded by UIF/UFI via the "Vinci" program

UNIVERSITÉ FRANCO ITALIENNE | UNIVERSITÀ ITALO FRANCESE

Contents

Summary **1**

Sommario **2**

Résumé **3**

Acknowledgements **4**

1 Introduction **5**
1.1 Biosensors . . . 5
1.1.1 Transducers . . . 6
1.1.1.1 Optical techniques . . . 7
1.1.1.2 Mass-sensitive techniques . . . 8
1.1.1.3 Electrochemical and electrical techniques . . . 9
1.1.2 Applications . . . 9
1.2 Sensors . . . 10
1.3 Capacitive biosensors . . . 11
1.4 Summary of the work and author's publications . . . 12

2 Physical models **14**
2.1 DC models . . . 14
2.1.1 Poisson equation . . . 14
2.1.1.1 Surface charges . . . 15
2.1.2 Current equations . . . 18
2.1.3 Boundary conditions . . . 20
2.2 AC models . . . 21
2.2.1 Poisson equation . . . 22
2.2.1.1 Surface charges . . . 22
2.2.2 Current equations . . . 24
2.2.3 Boundary conditions . . . 24
2.3 Electrolyte models . . . 24
2.3.1 Electrolyte permittivity . . . 25
2.3.2 Steric effects . . . 25
2.3.2.1 Stern layer . . . 26
2.3.2.2 Modified Poisson-Boltzmann equation . . . 28
2.4 Summary . . . 30

3 Analytical models for reference systems **31**
3.1 1D AC cartesian electrode-electrolyte system . . . 31
3.1.1 Electrolyte only . . . 31

3.1.1.1 Equivalent formulation . . . 37
3.1.1.2 Double layer admittance . . . 40
3.1.1.3 Cut off frequencies . . . 43
3.1.1.4 Electric field . . . 44
3.1.2 Dielectric layer and electrolyte . . . 46
3.1.3 Small-signal / differential capacitance . . . 48
3.1.3.1 System energy . . . 53
3.2 1D AC cartesian electrode-electrolyte with DC bias . . . 55
3.3 AC spherical electrode-electrolyte system . . . 57
3.3.1 1st order model - electrolyte only . . . 60
3.3.2 1st order model with particle . . . 64
3.3.3 0th order model - electrolyte only . . . 66
3.3.4 0th order model with particle . . . 69
3.3.5 Admittance and sensor response . . . 69
3.3.6 General model for the admittance change due to particles . . . 74
3.4 1D semiconductor resistor . . . 77
3.4.1 Resistor in AC small signal regime . . . 78
3.4.2 Capacitor in AC small signal regime . . . 79
3.5 1D AC Electrolyte/Insulator/Semiconductor system . . . 79
3.6 Switching capacitance . . . 84
3.7 Summary . . . 87
3.A Appendices . . . 89
3.A.1 1D cartesian model with electrolyte only - integration constants . . . 89
3.A.2 1D cartesian model with electrolyte only - derivation of the equivalent formulation . . . 90
3.A.3 1D cartesian model with a dielectric region inside the electrolyte . . . 91
3.A.3.1 Equivalent formulation . . . 93
3.A.4 1D cartesian model with dielectric layer, electrolyte and dielectric region inside . . . 93
3.A.5 1D cartesian model with DC bias (only electrolyte) - alternative derivation . . . 95
3.A.6 Spherical 1st order model with only electrolyte - integration constants 97
3.A.7 Spherical 1st order model with particle - integration constants . . . 98
3.A.8 Spherical 0th order model with only electrolyte - integration constants 101
3.A.9 Spherical 0th order model with particle - integration constants . . . 102
3.A.10 Derivation of the analytical model for the admittance change . . . 103
3.A.11 1D semiconductor resistor - integration constants . . . 106
3.A.12 Switching capacitance model parameters . . . 107

4 Numerical methods 108
4.1 Weak formulations . . . 108
4.1.1 DC models . . . 109
4.1.2 AC models . . . 110
4.2 CVFEM discretization of model equations . . . 110
4.2.1 CVFEM discretization of the DC equations . . . 112
4.2.1.1 Poisson equation . . . 112
4.2.1.2 Current equations . . . 114
4.2.1.3 Global conservation . . . 115
4.2.2 CVFEM discretization of the AC equations . . . 116

4.2.2.1 Poisson and current equations . . . 116
4.2.2.2 Global conservation . . . 118
4.2.2.3 Contact admittance . . . 119
4.2.3 Volume integrals . . . 119
4.2.4 Surface integrals . . . 122
4.3 1D CVFEM simulator . . . 124
4.3.1 DC model . . . 124
4.3.2 AC model . . . 127
4.4 Numerical implementation . . . 128
4.4.1 DC problem . . . 129
4.4.2 AC problem . . . 129
4.4.2.1 Generalized electrodes . . . 129
4.4.3 Simple example . . . 130
4.5 Model validation and comparisons with GFEM . . . 133
4.5.1 1D system CVFEM/GFEM comparison . . . 133
4.5.2 Nanoelectrode array . . . 136
4.5.3 Site-binding model . . . 136
4.6 Use of commercial TCAD . . . 138
4.6.1 Equivalent 1:1 electrolyte . . . 139
4.7 Summary . . . 141
4.A Appendices . . . 142
4.A.1 Jacobians for DC equations . . . 142
4.A.2 On the equivalence of CVFEM and GFEM . . . 143
4.A.3 Discretized AC GFEM coefficients . . . 144
4.A.4 Volume integrals . . . 145
4.A.5 Internal surface integrals . . . 146
4.A.6 Boundary surface integrals . . . 146
4.A.7 Geometric elements . . . 147
4.A.8 1D CVFEM coefficients . . . 148

5 Nanoelectrode array biosensors 150
5.1 Model validation . . . 151
5.2 Nanoelectrode array biosensor . . . 152
5.3 Detection of dielectric and conductive beads . . . 153
5.3.1 Simulation results . . . 154
5.3.2 Comparison to experiments . . . 158
5.3.3 Considerations on cell detection . . . 163
5.4 Model for the admittance change due to spherical particles . . . 165
5.4.1 Numerical reference model . . . 166
5.4.2 Verification . . . 169
5.4.2.1 Volume dependence . . . 170
5.4.2.2 Field dependence . . . 170
5.4.2.3 Concentration dependence . . . 173
5.4.3 Range of model validity . . . 174
5.5 Simulations with lumped double layer admittance . . . 174
5.5.1 Methodology . . . 176
5.5.2 Results . . . 179
5.6 ΔY for small spherical particles in constant field . . . 182
5.6.1 Physical effects on the admittance response . . . 183

5.6.2 Response due to a neutral spherical biomolecule . . . 185
5.6.3 Response due to a charged spherical biomolecule . . . 186
5.7 Nanoelectrode response to small spherical particles . . . 187
5.8 Detection of DNA strands and hybridization . . . 188
5.8.1 DNA / PNA model . . . 189
5.8.2 Simulations . . . 191
5.8.2.1 ΔC due to dsXNA and hybridization . . . 191
5.8.2.2 ΔC position effects . . . 192
5.8.2.3 ΔC orientation effects . . . 194
5.9 Summary . . . 195

6 Nanowire pH-sensors and bio-sensors 197
6.1 Nanowire pH sensors . . . 197
6.1.1 Measurements of pH ladders . . . 199
6.1.1.1 $n^+/n/n^+$ resistor . . . 200
6.1.1.2 pMOSFET . . . 203
6.1.2 Experimental admittance spectra versus salt concentration . . . 206
6.1.2.1 pMOSFET . . . 206
6.1.2.2 $n^+/n/n^+$ resistor . . . 206
6.2 Comparison with simulations . . . 213
6.2.1 Lumped element circuit for nanowire in electrolyte . . . 213
6.2.1.1 Extraction of circuit elements . . . 216
6.2.2 Parasitics and simulation comparisons . . . 218
6.3 Nanowire biosensors . . . 225
6.3.1 Models and devices . . . 225
6.3.2 Numerical simulations of nanowires . . . 226
6.4 Summary . . . 235

7 Conclusions and outlook 236

Bibliography 241

Summary

In recent years the possibility to combine nanoelectronics and biosensing has opened a very wide and promising field of research, which holds the potential to revolutionize analytical biology and to enable pervasive diagnostics and personalized medicine. Integrated nanoelectronic biosensor platforms based on established CMOS technology can provide compensation and calibration hardware, programmable firmware, improved sensitivity due to the very small dimensions, high parallelism, remarkable cost and size reduction and, ultimately, the vast markets needed by the semiconductor industry. As is the case for all integrated nanoelectronic sensors, reliable and affordable design is possible only if accurate models are available to elucidate and quantitatively predict the signal transduction process. However, with the exception of a few efforts, calibrated analytical and numerical models to accurately describe the response are often still lacking for most biosensor concepts.

Animated by the will to bridge this gap, in this work we develop compact analytical models and complex numerical simulation tools for the study of the transduction chain in impedimetric nanoelectronic biosensors. In particular, the 3D simulator ENBIOS, entirely developed and validated during this thesis, is a general-purpose tool that can be easily expanded to include new physical effects or more sophisticated descriptions of electrolytes and analytes coupled to semiconductor devices. The models point out the existence of two relevant cut-off frequencies governing the biosensor impedimetric response, they reveal the dependencies of biosensor response to the analyte and environmental conditions and they disclose the existence of well-defined signatures in the impedance signal.

The analytical and numerical tools are carefully verified and then used to examine several case studies. The first one we consider is an impedimetric nanoelectrode array biosensor. In collaboration with Twente University, we study its response to conductive and dielectric micro-particles under well controlled experimental conditions. We show that the simulation results are in very good agreement with the measurements and we provide insight on optimum detection conditions. By studying the biosensor response to small particles, like proteins, viruses or DNA, we then confirm by simulation the advantages of high frequency impedance spectroscopy, in particular the ability of AC signals at frequency above electrolyte's dielectric relaxation cut-off frequency to overcome the Debye screening and to probe the electrolyte volume with sensitivity almost independent of the particle position and charge and of salt concentration.

As a second notable example we consider the case of a Silicon Nanowire (SiNW) biosensor. We perform measurements and simulations on SiNWs in AC regime in collaboration with the CEA/LETI and EPFL/CLSE laboratories. We demonstrate the operation of SiNWs in AC in particular for pH sensing applications. We finally confirm potential advantage of a SiNW biosensor working at high frequency, in order to increase the response with respect to the DC operation.

Sommario

Negli ultimi anni la possibilità di combinare nanoelettronica e biosensoristica ha aperto un campo di ricerca molto vasto e promettente, che ha il potenziale di rivoluzionare la biologia analitica e di consentire diagnostica pervasiva e medicina personalizzata. Le piattaforme di biosensori nanoelettronici integrati sono potenzialmente in grado di fornire compensazioni e calibrazioni hardware, firmware programmabili, una maggiore sensibilità a causa delle ridotte dimensioni, elevato parallelismo, riduzione notevole dei costi e delle dimensioni e i vasti mercati necessari per il settore dei semiconduttori. Come nel caso di tutti i sensori nanoelettronici integrati, un progetto affidabile e conveniente è possibile solo se sono disponibili modelli accurati per comprendere e prevedere quantitativamente il processo di trasduzione del segnale. Tuttavia, con l'eccezione di alcuni pionieristici sforzi, mancano ancora spesso modelli analitici e numerici calibrati per descrivere accuratamente la risposta della maggior parte dei concept di biosensori.

Animati dalla volontà di colmare questa lacuna, in questo lavoro sviluppiamo modelli analitici compatti e complessi strumenti di simulazione numerica per lo studio della catena di trasduzione in biosensori nanoelettronici impedimetrici. In particolare, il simulatore 3D ENBIOS, interamente sviluppato e convalidato durante questa tesi, è uno strumento generale che può essere facilmente ampliato per includere nuovi effetti fisici o descrizioni più sofisticate di elettroliti e analiti accoppiati ai dispositivi a semiconduttore. I modelli rilevano l'esistenza di due frequenze di taglio rilevanti che regolano la risposta impedimetrica del biosensore, rivelano le dipendenze della risposta del biosensore all'analita e alle condizioni ambientali e l'esistenza di firme ben definite nel segnale di impedenza.

Gli strumenti analitici e numerici sono attentamente verificati e poi utilizzati per esaminare diversi casi di studio. Il primo che consideriamo è un biosensore impedimetrico a matrice di nanoelettrodi. In collaborazione con l'Università di Twente, studiamo la sua risposta a micro-particelle conduttive e dielettriche in condizioni sperimentali ben controllate. I risultati della simulazione sono in ottimo accordo con le misure e ci forniscono informazioni sulle condizioni di rilevamento ottimali. Studiando la risposta del biosensore a piccole particelle, come proteine, virus o DNA, confermiamo quindi tramite simulazioni i vantaggi della spettroscopia di impedenza ad alta frequenza, in particolare la capacità dei segnali in AC a frequenza superiore alla frequenza di taglio di rilassamento dielettrico dell'elettrolita di superare lo screening di Debye e di sondare il volume dell'elettrolita con una sensibilità quasi indipendente da posizione e carica della particella e dalla concentrazione salina.

Come secondo esempio notevole consideriamo il caso di un biosensore a Nanofilo di Silicio (SiNW). Eseguiamo misure e simulazioni su SiNWs in regime AC in collaborazione con i laboratori CEA / LETI ed EPFL / CLSE. Dimostriamo il funzionamento dei SiNWs in AC, in particolare per applicazioni di misura del pH. Infine, confermiamo i vantaggi potenziali di un biosensore a SiNW operante in alta frequenza, al fine di aumentare l'intensità della risposta rispetto al caso di funzionamento in DC.

Résumé

Au cours des dernières années, la possibilité de combiner la nanoélectronique et les biocapteurs a ouvert un champ très large et prometteur de la recherche, qui a le potentiel de révolutionner la biologie analytique et pour permettre le diagnostic envahissants et la médecine personnalisée. Plates-formes intégrées de biocapteurs nanoélectroniques peuvent fournir une compensation et l'étalonnage du matériel et des logiciels, une sensibilité améliorée en raison des très petites dimensions, parallélisme élevé, le coût remarquable et la réduction de la taille et les vastes marchés nécessaires à l'industrie des semi-conducteurs. Comme dans le cas de tous les capteurs intégrés nanoélectroniques, la conception fiable et abordable est possible que si des modèles précis sont disponibles pour élucider et quantitativement prédisent le processus de transduction du signal. Cependant, malgré les nombreux efforts, calibré modèles analytiques et numériques pour décrire avec précision la réponse du biocapteur sont encore souvent défaut.

Animé par la volonté de combler cette lacune, dans ce travail, nous développons des modèles analytiques compacts et des outils complexes de simulation numérique pour l'étude de la chaîne de transduction dans des biocapteurs nanoélectroniques impédimétriques. En particulier, les ENBIOS simulateur 3D, entièrement développées et validées au cours de cette thèse, est un outil polyvalent qui peut être facilement étendu pour inclure de nouveaux effets physiques ou des descriptions plus sophistiqués d'électrolytes et analytes couplés à des dispositifs semi-conducteurs. Les modèles soulignent l'existence de deux fréquences de coupure pertinentes régissant le biocapteur réponse impédimétriques, ils révèlent les dépendances de la réponse du biocapteur à l'analyte et des conditions environnementales et ils révèlent la présence de signatures bien définis dans le signal d'impédance.

Les outils analytiques et numériques sont soigneusement vérifiées et ensuite utilisés pour examiner plusieurs études de cas. La première que nous considérons est un réseau de impédimétriques nanoélectrode biocapteur. En collaboration avec l'Université de Twente, nous étudions sa réponse aux micro-particules conductrices et diélectriques dans des conditions expérimentales bien contrôlées. Nous montrons que les résultats de simulation sont en très bon accord avec les mesures et nous donnent un aperçu des conditions optimales de détection. En étudiant la réponse du biocapteur à de petites particules, comme des protéines, des virus ou de l'ADN, nous confirmons ensuite par simulation les avantages de la spectroscopie d'impédance à haute fréquence, en particulier la capacité des signaux de courant alternatif à une fréquence au-dessus de relaxation diélectrique de la fréquence de coupure de l'électrolyte pour surmonter la Debye criblage et de sonder le volume de l'électrolyte avec une sensibilité presque indépendante de la position et de la charge des particules et de concentration en sel.

Dans un deuxième exemple notable nous considérons le cas d'une Silicon Nanowire (SiNW) biocapteur. Nous effectuons les mesures et simulations sur SiNWs dans le régime AC en collaboration avec le CEA / LETI et laboratoires de l'EPFL / CLSE. Nous démontrons le fonctionnement de SiNWs AC en particulier pour les applications de détection pH. Nous confirmons enfin avantage potentiel d'un biocapteur SiNW travailler à haute fréquence, afin d'augmenter la réponse à l'égard de l'opération DC.

Acknowledgements

The wide range of activities during this thesis would have not been possible outside an extensive network of international collaborations, which mainly included:

- CEA/LETI (Dr. Thomas Ernst), who acted as cotutor of this PhD thesis and provided nanowire samples. At CEA/LETI I got in contact with my first nanowire sensor platform;
- NXP Semiconductors (in particular Dr. Frans Widdershoven), who has been a constant reference for stimulating suggestions, and triggered our interest for biosensor platforms and impedimetric nanoelectrode arrays;
- University of Twente (Prof. Serge Lemay, Cecilia Laborde), who developed the micro-particle experimental techniques and provided the corresponding measurements;
- EPFL/CLSE (Prof. Carlotta Guiducci, Enrico Accastelli), where I could develop the experimental setup for AC nanowire characterization and perform the measurements.

In addition, I want to acknowledge the useful and fruitful discussion with researchers and professors in my institution and abroad. In particular I thank Prof. Pierpaolo Palestri and Prof. David Esseni (University of Udine), Dr. Ruben Specogna (University of Udine), Prof. Rossana Vermiglio (University of Udine), Prof. Marco Tartagni (University of Bologna), Dr. Enrico Stalio (University of Modena and Reggio-Emilia) and all the others that lent me their hand when I needed their help. I also thank Dr. Harrie Verhoeven and Dr. Maarten Jongsma (Wageningen University) for their measurements on cell detection. Thanks also to Dr. Quentin Rafhay (IMEP) for his help with administrative procedures in Grenoble.

Special thanks go to all students that collaborated with me on these topics, and in particular to Paolo Scarbolo. His work has been precious in many aspects and I wish him a nice and fruitful continuation of his PhD on these topics. I also thank my colleagues for their help and for being able altogether to create a stimulating yet smooth working environment.

In addition, I would also like to thank prof. Luca Selmi, who has always been a constant and stimulating presence. It was thanks to him that we could open this topic on biosensors at the University of Udine with great success and with a wide range of prospects for the future. I've also had a wide range of opportunities during my PhD, both on the scientific and on the experience point of view. I could participate to outstanding international conferences and I could benefit from the collaborations and all international contacts which he could provide.

Last but not least I want to thank my family and my friends. In particular I want to dedicate this thesis to my nieces Iris and Ambra, hoping that they will find their own satisfaction being able to work on the topics that they find stimulating.

In the end one more thank, to G.M., for existing and being always by my side.

Chapter 1

Introduction

This work is focused on the study, modelling, simulation and characterization of nano-electronic impedimetric biosensors. To introduce the topic, we first present an overview of the main properties of sensors, then we focus on biosensors and finally we discuss novel biosensor concepts that take advantage of micro- and nano-electronic technologies.

In recent years, many new applications for sensors have emerged in addition to traditional ones, for instance in the drug and food industry, in the field of security and hazard prevention and for personalized medicine. Given the broad and still widening spectrum of possible applications, there is the tendency, if not the need, to develop general purpose sensor platforms, that can be easily functionalized, reconfigured or adapted to specific applications. As demonstrated in many diversified fields by the recent developments of semiconductor industry, the demand of general purpose reconfigurable platforms can be satisfied on a large scale only by means of microelectronics, which in turn enables increase of the sensitivity, miniaturization, massively parallelization and cost reduction.

Miniaturized sensors are indeed attracting increasing interest also in the scope of the "Internet of Things" paradigm [15], as powerful enablers on the one hand of extended sensor networks in the every-day environment, on the other hand of a plethora of new applications and services to augment our life experience, monitor processes and make them smarter. Example of applications for simple and cheap sensors could include the measurement of temperature, humidity, gas toxicity or human parameters (such as blood pressure, glucose level, temperature, etc.).

1.1 Biosensors

We now focus on biosensors, i.e. devices for the analysis of bio-material samples in order to gain an understanding of their bio-composition, structure and function by converting a biological response into an electrical or optical signal. Common biological sensors include sensors for whole cells, viruses, bacteria and other micro-organisms, DNA, proteins, small molecules and ions [16]. Examples of small molecules include glucose, lactate (a common by-product of anaerobic metabolism), H^+ ions (pH sensing), urea or neurotransmitters such as dopamine. Although, during the past more than 50 years, numerous new sensor designs with better and better specifications have been published and commercialized, the need for decreasing size and cost, while still improving sensitivity, detection limit, specificity and stability still challenges today's scientists and engineers [17]. As an example of successful biosensors who made it to the market, we recall miniaturized, fast, cheap, easy-to-use and reliable glucose biosensors that already make the life more comfortable and safe for those, who are suffering from diabetes [18]. Another very successful example

are the IonTorrent [19] or the DNA electronics Ltd. [20] technologies for massively parallel DNA sequencing.

The bio-sensing is invariably accomplished in the following three steps, which are summarized below:

1. The binding of one unit of a specific target species (the *analyte*) to one unit of a complementary capture species (the *receptor*) changes the analog state of a mechanical, optical or electrical variable. Because of this binding, these biosensors are usually called "affinity based", in the sense that the detection principle relies on the binding between two species that are affine to each other. The target species can be labeled with a molecular tag or fluorescence marker to facilitate optical detection when the binding event occurs; or it can be labeled with a magnetic bead to facilitate electrical detection when the binding event occurs. Certain forms of sensing do not require the use of such labels and are therefore termed *label free*. Label-free sensing is more convenient than labeled sensing but performance and cost are key determinants in measuring the pros and cons of one sensing scheme versus another.

2. The change in the mechanical, optical or electrical state is passively transduced to yet another domain, e.g., a mechanical state change is passively transduced to an electrical state change, or a mechanical state change is passively transduced to an optical state change. This is accomplished in the so-called *transducer* device.

3. The transduced signal is then actively amplified, usually in the electrical or optical domain, digitalized and elaborated to eliminate parasitic effects and noise.

The detection of species with high specificity (meaning that only the target species triggers detection) and high sensitivity (a few molecules or units of the target species are detectable), in a short time (a second), at physiological salt concentration ($\approx$ 100 mM), over a wide dynamic range in analyte concentration (e.g., fM to 0.1M) and with low-cost hardware is overwhelmingly challenging.

Miniaturization is beneficial also in this case since, if the biosensors dimension are comparable to those of the analytes, the interaction possibilities are increased. The interface with bio-materials is however interesting not only for sensing, but also for actuation (e.g., bidirectional interaction with neurons [21]).
The marriage between micro- and nanoelectronics and biosensors offers new opportunities that are already common in standard semiconductor industry such as: high parallelism and throughput, smartness, error correction, calibration and noise suppression.

1.1.1 Transducers

As outlined above, we can divide the transducers into three major classes [22], based on the physical mechanism that is involved:

- optical detection methods;
- mass detection methods;
- electrochemical and electrical detection methods.

1.1.1.1 Optical techniques

In optical sensors the information is gathered by the measurement of photons, more specifically based on the measurement of absorbance, reflectance, or fluorescence emissions that occur in the ultraviolet (UV), visible, or near-infrared (NIR) [23]. They are immune to electro-magnetic interference, capable of performing remote sensing, and can provide multiplexed detection within a single device by attaching different fluorescent probes to different types of target molecules.

Generally, there are two detection protocols that can be implemented in optical biosensing: *fluorescence-based detection* and *label-free detection* [24] (see Fig. 1.1). In fluorescence-based detection, either target molecules or biorecognition molecules are labeled with fluorescent tags, such as dyes; the intensity of the fluorescence indicates the presence of the target molecules and the interaction strength between target and biorecognition molecules [24]. Fluorescence-based detection is extremely sensitive, with a detection limit at the single molecule level. Besides this remarkable advantage, unfortunately, fluorescence based detection suffers from numerous drawbacks compared to label-free techniques [17]. Firstly, the chemical procedure of labeling is rather expensive, time and labor intensive. The number of fluorophores on the molecules cannot be controlled precisely, which leads to a fluorescence signal spread. Furthermore, the presence of these anchored tags could have a not-negligible effect on the molecules, affecting their dynamics or the way they react to the environment;hence, ultimately on the experimental results, as well.

In contrast, in label-free detection, target molecules are not labeled or altered, and are detected in their natural forms [24]. This type of detection is relatively easy and cheap to perform, and allows for quantitative and kinetic measurement of molecular interac-

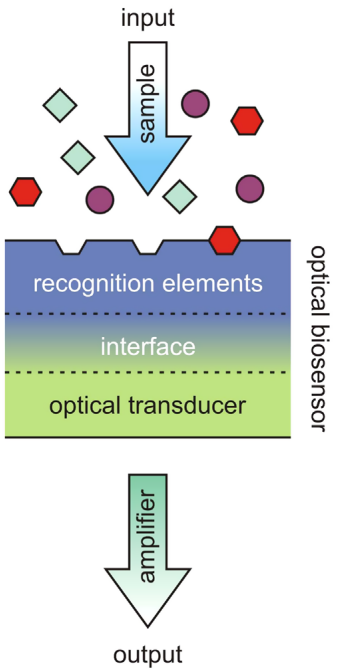

Fig 1.1: Schematic working principle of label-free optical biosensors taken from [17]. Surface immobilized recognition elements specifically bind the sample of interest; commonly one or several target molecules within a complex sample. The resulting mass adsorption and displacement of the surrounding medium results in a change of the local refractive index at the sensor surface. This variation has a direct effect on the physical properties of the interrogating electromagnetic wave, which can be amplified by the optical transducer.

tion. Additionally, some label-free detection mechanisms measure refractive index (RI) change induced by molecular interactions, which is related to the sample concentration or surface density, instead of total sample mass. As a result, the detection signal does not scale down with the sample volume. This characteristic is particularly attractive when ultrasmall (femtoliter to nanoliter) detection volume is involved and is advantageous over fluorescence-based detection whose signal usually depends on the total number of analytes in the detection volume or on the detection surface. Despite all these differences between fluorescence-based and label-free detection, both protocols are being widely used in optical sensors and provide vital and complementary information regarding interactions among biomolecules, which makes optical sensors more versatile than other types of sensing technologies where only label-free detection can be implemented. By immobilizing recognition elements and by mounting a flow-cell onto a label-free sensor chip, quantitative, in situ and real time detection of the target molecules or kinetic measurements of molecular interactions is possible with optical methods [17].
Under the cathegory of label-free optical detection, there exist a number of detection methods, including RI detection, optical absorption detection, and Raman spectroscopic detection. RI and absorption are the real and imaginary part of the more general complex RI constant and are related to each other via the Kronig-Kramers relations [24]. Raman detection is unique in that, on one hand, like RI and absorption detection, target molecules are not labeled; on the other hand, emitted Raman light is used for sensing, similar to fluorescence-based detection.

Regarding the competition of label-free signal transducers such as mass-sensitive, temperature-sensitive, electrochemical and optical biosensors, the optical methods are dominating both the research literature and the market. The reason is mainly that optical methods are merging the advantages of other label-free techniques in a cost-effective way [17]. The binding of the target analytes is detected in their natural form using low-power electric field in or close to the visible range with neither destructive nor considerable manipulative effect on the experiment. The sampling rate and the detection limit of surface mass density changes are outstandingly good, which allows a very efficient real-time monitoring. In most cases, performing parallel measurements is straightforward due to their ability of multiplexing for multi-parameter analysis. The technological demands for the fabrication of these transducers are relatively low and by batch manufacturing the optical elements in a more cost-effective and more compact way, their ongoing miniaturization leads to novel possibilities towards even lower reagent consumption, shorter analysis time and consequently towards point-of-care applications.

1.1.1.2 Mass-sensitive techniques

Another form of transduction that has been used for biosensors is the measurement of small changes in mass, for instance with MEMS [25]. This has been shown to capable of very sensitive measurements [25]. The principle means of mass analysis relies on the use of piezoelectric crystals. These crystals can be made to resonate with an electrical signal of specific frequency. The frequency of oscillation is therefore dependent on the electrical signal applied to the crystal as well as the crystal's mass. Therefore, when the mass increases due to binding of chemicals, the oscillation frequency changes and the resulting change can be accurately measured by electrical means (e.g., with a PLL) and be used to determine the additional mass of the crystal [25].

1.1.1.3 Electrochemical and electrical techniques

Electrochemical and electrical techniques rely on the measurement of electrical properties, such as a current, a voltage drop or a capacitance between electrodes placed in contact with a solution. This family of biosensors is very vast and the biosensor concepts that we study in this thesis fall in it. In this section we will outline the electrochemical techniques and the ones based on FET devices, leaving to Sec. 1.3 a more detailed discussion on the capacitive biosensors, which will be one of the major topics of this thesis.

Electrochemical detection is one possible mean of transduction that has been used in biosensors [26]. This technique is very complementary to optical detection methods such as fluorescence, the most sensitive of the optical techniques. Since many analytes of interest are not strongly fluorescent and tagging a molecule with a fluorescent label is often labor intensive, electrochemical transduction can be very useful. By combining the sensitivity of electrochemical measurements with the selectivity provided by bioreception, detection limits comparable to fluorescence biosensors are often achievable.
Electrochemical biosensors are normally based on enzymatic catalysis of a reaction that produces or consumes electrons (such enzymes are rightly called redox enzymes) [26]. Other biosensors rely on potentiometric measurements without any redox reaction implied.

A different concept relies on FET devices, as for instance the Ion Sensitive FET (ISFET) [27] or BioFETs [28]. The transduction mechanism relies on the variation of the FET DC conductance due to the presence of the analyte: it is therefore a charge sensing principle. However, Debye screening (which will be thoroughly discussed throughout this thesis) is well known to severely hamper the sensitivity [28]. So far, it has been overcome only by lowering the salt content of the solution [29, 30]. This is however neither desirable nor even possible in some applications, like DNA detection, since a high salt concentration is necessary for the biomolecules to bind correctly and maintain their shape.

1.1.2 Applications

There are many potential applications of biosensors of various types [16]. The main requirements for a biosensor approach to be valuable in terms of research and commercial applications are the identification of a target molecule, availability of a suitable biological recognition element, and the potential for disposable portable detection systems to be preferred to sensitive laboratory-based techniques in some situations. Some examples are given below:

1. Glucose monitoring in diabetes patients has been one of the historical market driver and is now an established technology [18]

2. DNA detection and sequencing, with possible applications in DNA computing [19]

3. Environmental applications e.g. the detection of pesticides and water contaminants

4. Detection of pathogens, phage and their competitive interaction

5. Drug discovery and evaluation of biological activity of new compounds

6. Protein engineering and fabrication

Another important emerging application for biosensors is the possibility to use them to create so called neuro-electronic interfaces, i.e. a direct communication between neural networks and electronic circuits, for instance, for deep brain stimulation. The development

of such a technology gave rise to the field of neuroprosthetics and is capable of revolutionize human-computer interfaces in the next decades, not to mention the very promising results in alleviating the most detrimental consequences of a few age diseases (e.g., Parkinson).

1.2 Sensors

A few performance metrics are of general interest to any kind of sensor [31]. These could be further subdivided into fundamental vs. practical metrics. In particular the most relevant fundamental figures of merit are:

- *settling time,* t_s: it is the average time that is required for the sensor to detect a defined value of the quantity of interest with known accuracy;

- *sensitivity,* S: it is the magnitude of the sensor response due to a defined value of the analyte; it also defines the minimum variation of the analyte that can be measured;

- *dynamic range*: it is the ratio between the maximum and minimum analyte quantity that can be measured;

- *selectivity*: it is the capacity of the sensor to respond selectively to the analyte and not to other parameters variation; it determines the expectation value of false positive and false negative events.

Additionally, the most relevant practical metrics are:

- *dimension*: the physical dimension of the sensor can be important when designing sensor networks or devices for operation in constricted environment (e.g. sensors implanted in the human body);

- *robustness*: it is the capacity to operate for a long time, possibly in aggressive environments (e.g. automotive applications, human body);

- *power consumption*: it is particularly important if the sensor is deployed in remote environments with not-easily accessible power sources (e.g.. geological surveys, human body) or if it is powered by harvesters;

- *cost*: it is especially important for dense sensor networks or for disposable sensors.

For a successful sensor design all these characteristics need to be properly modelled, studied and predicted. This makes nanoelectronic sensor design a very challenging and multidisciplinary task.

In this thesis we focus on the study of biosensors sensitivity. This is justified by the fact that, at present, this is on one hand the major driving force towards miniaturized biosensors and on the other hand the area which needs the most intensive studies to be able to fully understand the transduction mechanism, predict biosensors response to given analytes and ultimately support the quantitative extraction of the analyte characteristics from measurements.

1.3 Capacitive biosensors

A new kind of biosensor has received increasing attention in recent years: it's the so called capacitive biosensor [32]. Unlike the electrochemical biosensors described above, this sensor usually operates with an AC voltage between two electrodes at frequency sufficiently above the electrolyte's dielectric relaxation cut-off frequency. The absence of electrochemical reactions on the electrodes surface enables the possibility for a longer operating life and to use standard CMOS techniques and materials for manufacturing. To allow for particle detection with adequate selectivity, a recognition layer has to be employed: in this way a capacitive affinity biosensor can be constructed. This layer is usually referred to as Self Assembled Monolayer (SAM).
Capacitive biosensors have a significant advantage with respect to the conventional biosensors: they are label-free, i.e. no or very little sample preparation is needed prior to the measurement. A problem, though, associated with non-labeled biosensors is non-specific binding, as there is no descrimination between the measured signal from specific and non-specific interactions. It is therefore important to design the SAM surface in such a way that it ensures higher specific than non-specific binding.

Capacitive biosensors can be constructed by immobilizing recognition elements arranged in thin layers on an electrode or between two electrodes and measuring changes in the dielectric properties when the analyte binds to the surface. Changes in capacitance may also be induced when a large receptor molecule is displaced by a smaller analyte. If a protein on a surface changes its conformation after binding of an analyte it might also be detected by capacitance measurements.
Two approaches have been proposed for capacitance measurements. Either by measuring the change in the capacitance between two metal conductors in close proximity to each other with the recognition element immobilized between them (interdigitated electrodes), or by measuring the capacitance at an electrode/solution interface with the recognition elements on the surface of the working electrode.

These types of biosensors are generally built in two different ways:

- with large-area electrodes, for example using interdigitated electrodes (see for instance [32, 30]), to detect collective signals of large ensembles of biomolecules: this is the traditional approach;

- with arrays of nanoelectrodes: this innovative approach has been first presented in [33]. In principle it enables both single or few particle detection and spatial profiling of large objects on the same platform.

One important reason for using arrays of nanoelectrodes is that large-area sensing elements suffer from defects and imperfections in the sensing elements, including but not limited to leakage paths in the functionalization layers. Segmenting the electrodes into many nanoelectrodes enables identification and pruning of damaged nanoelectrodes by statistical data analysis. Another important advantage of nanoelectrode arrays realized with standard CMOS techniques is that the technology scaling (due to Moore's law) naturally pushes the array to a more-than-optical resolution. In optical biosensors, in contrast, it is not straightforward to increase the resolution by decreasing the wavelength, since if this becomes too small, for instance in the UV range, the photons might become too energetic and damage the biological material under study. We will discuss in more detail the nanoelectrode implementation [33] in Chap. 5.

Another distinction between different types of capacitive biosensors can be made considering the frequency range of measurements:

- low frequency, lower than the cut-off frequency of the electrolyte f_c (see Sec. 3.1.1.3), this is the traditional approach;
- high frequency, preferentially much greater than the cut-off frequency f_c: this is the approach that will be thoroughly investigated in this thesis.

A strong motivation in favour of using high modulation frequencies is that at low frequencies the signal due to particle induced admittance change is usually overwhelmed by variations in spurious signals arising from electrochemically active species like redox-active biomolecules, imperfect self-assembled monolayers (SAMs), etc. Therefore the usage of high frequencies where admittance changes become purely capacitive and independent of the electrolyte conductivity seems a promising way to overcome these undesidered effects.

1.4 Summary of the work and author's publications

Quantitatively accurate interpretation of the signal transduction mechanisms of nanoelectronic biosensors could disclose a wealth of useful information for many fields of biology and medicine. This endeavour is not inconceivable at the state of the art, but demands accurate and reliable models of the whole sensor signal acquisition chain, including in particular the less known sections where distributed alterations of potentials and fields are converted into well defined voltage (current) changes at circuit nodes (branches) respectively. At present, predictive models have started to appear in the literature (for instance [31, 34]), but modeling activities have to face a widespread scepticisms in fields historically relying almost exclusively on experiments and empiricism. Early works focused on DC operation. Impedimetric (capacitive) biosensors gain increasing attention on a daily basis, but general and non-empirical models for impedance spectroscopy are still rare and not generally accepted.

It is the purpose of this thesis work to advance the state of the art in the field by developing numerical and analytical DC and AC models and simulators of the response of nanoelectronic biosensors to analytes. The models and simulations are instrumental to investigate the electrostatics and the small signal response of biosensor systems to a variety of stimuli and physical conditions. This is a very complex puzzle and my work attempted to reveal at least some elements of the overall landscape.
We point out that in this work we do not address the problem of the diffusion of the particles or biomolecules towards the sensor. This important aspect of biosensor response has been thoroughly investigated in [31] and shown to be the bottleneck to achieve short settling time. Instead we investigate in detail the effect on the response of the sensor to the biomolecules, which we assume to have already come close to the sensor.

In particular, during my PhD thesis, I focused on the following aspects of the problem (the corresponding references and chapters in this document are linked):

1. development of simple analytical models for the AC response of nanoelectronic biosensors to guide intuition, set out simple design of experiment guidelines and provide exact reference solutions for verification purposes (Ref. [1], Chap. 3) and the extensive verification of a specific analytical model for the response of nanoelectrode biosensors to spherical particles (Ref. [2], Chap. 5);

2. development, validation and use of a simplified 2D numerical solver for nanoelectrode capacitive biosensors in DC and AC conditions to be used as an exploratory tool to understand the physics of nanoelectrode/electrolyte system and issue with the numerical solution of the model equations (Refs. [3, 1], Chap. 5);

3. development of a full 3D, general purpose solver of the Poisson-Boltzmann and Poisson-Nernst-Planck equations (ENBIOS) suited to calculate precisely the tiny admittance changes resulting from single biomolecule/sensor interactions for nanoelectronic biosensors (Ref. [4], Chap. 4);

4. tailoring of a commercial TCAD tool (Sentaurus Device [35]) for the simulation of nanoelectronic biosensors, and identification of the inherent limitations of such a simplified approach to describe BioFETs (Ref. [5, 6, 7], Chap. 4);

5. development of a general purpose procedure for the efficient simulation of impedimetric nanoelectrode array biosensors by replacing the double layer admittance with lumped elements (Ref. [8], Chap. 5);

6. theoretical investigation of some aspects of DNA detection (Refs. [9, 10], Chap. 5) and of single biomolecules detection (proteins, viruses, Refs. [3, 1, 11, 4, 2], Chap. 5) by means of impedimetric measurements with nanoelectrode biosensors;

7. theoretical and experimental investigation of micro-particle detection mechanisms and experimental proof that high frequency impedance spectroscopy with nanoelectrode biosensors makes possible to overcome static Debye screening limits (Ref. [12], Chap. 5);

8. theoretical and experimental investigation of the use of Silicon Nanowire pH sensors and biosensors operated in AC conditions (partly in [13, 14], Chap. 6).

As made apparent by the above list, the thesis work spanned from theoretical to modeling and numerical implementation issues and from simulation to calibration and experimental verification aspects. This wide range of activities would have not been possible outside a network of collaborations, which included:

- CEA/LETI (Dr. Thomas Ernst), who acted as cotutor of this PhD thesis and provided nanowire samples. At CEA/LETI I got in contact with my first nanowire sensor platform;

- NXP Semiconductors (in particular Dr. Frans Widdershoven), who has been a constant reference for stimulating suggestions, and triggered our interest for biosensor platforms and impedimetric nanoelectrode arrays;

- University of Twente (Prof. Serge Lemay, Cecilia Laborde), who developed the micro-particle experimental techniques and provided the corresponding measurements;

- EPFL/CLSE (Prof. Carlotta Guiducci, Enrico Accastelli), where I could develop the experimental setup for AC nanowire characterization and perform the measurements.

Chapter 2

Physical models

In this chapter we present DC and AC physical models, essentially based on existing literature, to describe three types of materials routinely used in the fabrication of nano-electronic biosensors: electrolytes, semiconductors and non-ideal dielectrics (with charges and losses). Most of these models have been implemented in the numerical solver ENBIOS, which constitutes an important part of this thesis work and will be described in Chapter 4.

Sections 2.1-2.2 report the model equations describing the basic physics. Section 2.3 describes a few second order physical effects that might occur in real systems, that were quantitatively evaluated in order to assess the validity limits of our models.

2.1 DC models

We begin describing the models for DC conditions. In this section all the quantities with subscript "0" will indicate DC variables. The domain of interest is denoted Ω and on its boundary Γ we set the boundary conditions.
The boundary surfaces where we use Dirichlet boundary condition for the electric potential are called electrodes. These can be directly related to the electrodes present in the real system. We assume that there exists two types of electrodes:

- ideally polarizable (or floating) electrodes, where there is no DC charge transfer (which should be provided by electrochemical reactions in the case of electrodes in contact with the electrolyte), so that they can not sustain any DC current flow;
- Faradaic (or Ohmic) electrodes, where both charge transfer and a DC current flow are possible.

Gold electrodes are in most instances good approximations of ideally polarizable electrodes, while typical Ag/AgCl electrodes behave essentially as Faradaic electrodes [36].
We will always assume that the electrolyte is in contact only with ideally polarizable electrodes and with one Faradaic electrode, which is called reference electrode.

2.1.1 Poisson equation

Poisson equation is the fundamental relation between electric potential and charges. For isotropic media it takes the usual form:

$$\boxed{\nabla \cdot (\varepsilon \nabla V_0) = -\rho_0 = -(\rho_f + \rho_{nl})} \tag{2.1}$$

where V_0 is the DC electrostatic potential, ρ_0 the DC volume charge density and ε the scalar material dielectric permittivity. Denoting Γ_D and Γ_N respectively the surfaces on which Dirichlet and Neumann boundary conditions are imposed, we can express the boundary conditions as:

$$\begin{cases} V_0 - V_D = 0 & \text{on } \Gamma_D \\ \varepsilon \nabla V_0 \cdot \hat{n} = 0 & \text{on } \Gamma_N \end{cases} \tag{2.2}$$

where $\hat{n}$ is the outward pointing unit normal on the boundary surface Γ. The charge density is expressed as $\rho_0 = \rho_f + \rho_{nl}$, where ρ_f is a fixed volume charge density and ρ_{nl} denotes the mobile charge, that in general is a non linear function of the potential V_0. An example of fixed charge in the semiconductor is given by the doping, i.e. $\rho_f = q(N_D - N_A)$ where N_D and N_A are the volume densities of donor and acceptor atoms respectively. For both electrolyte and semiconductor we can write:

$$\boxed{\rho_{nl} = \sum_{m=1}^{N_{sp}} Z_m q n_{0m}} \tag{2.3}$$

where N_{sp} is the number of charged species (ions in the electrolyte, electrons and holes in the semiconductor), q the absolute value of the electron charge, Z_m and n_{0m} the valence and DC concentration of species m respectively. Under quasi-equilibrium conditions and neglecting steric effects (see Sec. 2.3.2), the concentrations can be expressed as:

$$\boxed{n_m = n_m^{\infty} \exp\left(\frac{Z_m q}{k_B T}\left(\phi_m - V\right)\right)} \tag{2.4}$$

where n_m^{∞} is the bulk concentration in equilibrium and ϕ_m the quasi-potential of species m, k_B the Boltzmann's constant and T the absolute temperature. For a suitable choice of the reference potential we have $n_m^{\infty} = n_i$, i.e., the intrinsic concentration in the semiconductor. Note that Eq. 2.4 is always valid, not only in DC conditions, because it is a definition of the quasi-potential. Therefore we have dropped the subscript "0".

Since in the electrolyte only one Faradaic electrode is present (the reference electrode), there is no DC current flow, so that we set a constant $\phi_{0m} = V_{ref}$ for all ion species. Here V_{ref} is the potential at the reference electrode. This choice leads to recover the well known Poisson-Boltzmann (PB) equation [36] in DC, which explicitly reads:

$$\boxed{\nabla \cdot (\varepsilon \nabla V_0) = -\left(\rho_f + \sum_{m=1}^{N_{sp}} Z_m q n_m^{\infty} \exp\left(\frac{Z_m q}{k_B T}\left(\phi_{0m} - V_0\right)\right)\right)} \tag{2.5}$$

The PB equation is indeed a widely accepted modeling framework for the simulation of biosensors [31, 37, 38] and of biological systems in DC conditions [39, 40].

A simple way to model conductors in DC is to describe them as media with infinite (in practice very high) permittivity [41]. This approach will be followed in this thesis as well.

2.1.1.1 Surface charges

Surface charges can play an important role in determining the impedimetric response of biosensors. Therefore, they have been included in the model, as described in Sec. 4.2.1.1.

An important source of surface charges are the protonation or depronotation reactions of amphoteric surface sites at oxide surfaces immersed in water, which lead to the build-up of a pH dependent surface charge density σ_{sb} [C/m^2]. The charge density is described by the site-binding model [42] which in the case of SiO_2 and similar oxides (featuring only one type of surface sites) is based on the elementary reactions:

$$\mathrm{MOH} \overset{K'_a}{\rightleftharpoons} \mathrm{MO^-} + \mathrm{H^+} \tag{2.6a}$$

$$\mathrm{MOH_2^+} \overset{K'_b}{\rightleftharpoons} \mathrm{MOH} + \mathrm{H^+} \tag{2.6b}$$

where M is the metal or semiconductor of the dielectric (e.g. Si, Ta, Al or Hf). The equilibrium constants K'_a and K'_b are defined as:

$$K'_a = \frac{\nu_{0MO}\, n_{0H}}{\nu_{0MOH}}, \quad K'_b = \frac{\nu_{0MOH}\, n_{0H}}{\nu_{0MOH_2}} \tag{2.7}$$

where we have ignored the fact that activities should be used in place of concentrations. Note that the H^+ concentration n_{0H} is a volume density [m^{-3}], while all the ν_{0x} terms correspond to surface densities [m^{-2}].
The surface sites concentrations in DC are:

$$\begin{cases} \nu_{0MO} = \dfrac{\nu_{0MOH}}{n_{0Hs}} K'_a \\ \nu_{0MOH_2} = \dfrac{\nu_{0MOH}\, n_{0Hs}}{K'_b} \\ N_S = \nu_{0MOH} + \nu_{0MO} + \nu_{0MOH_2} \end{cases} \quad \Longrightarrow \quad \begin{cases} \nu_{0MO} = N_S \dfrac{K'_a K'_b}{n_{0Hs}^2 + n_{0Hs} K'_b + K'_a K'_b} \\ \nu_{0MOH_2} = N_S \dfrac{n_{0Hs}^2}{n_{0Hs}^2 + n_{0Hs} K'_b + K'_a K'_b} \\ \nu_{0MOH} = N_S \dfrac{n_{0Hs} K'_b}{n_{0Hs}^2 + n_{0Hs} K'_b + K'_a K'_b} \end{cases} \tag{2.8}$$

where N_S is the total surface sites density and n_{0Hs} the DC H^+ concentration at the surface.
The surface charge $\sigma_{sb} = q(\nu_{0MOH_2} - \nu_{0MO})$ then reads:

$$\boxed{\sigma_{sb} = qN_S \frac{n_{0Hs}^2 - K'_a K'_b}{n_{0Hs}^2 + K'_b n_{0Hs} + K'_a K'_b}} \tag{2.9}$$

where σ_{sb} is the site-binding surface charge [C/m^2]. In the case of Si_3N_4 two types of surface sites are present; assuming they are independent, the site-binding model reads [43]:

$$\sigma_{sb}^{Si_3N_4} = qN_S \frac{n_{0Hs}^2 - K'_a K'_b}{n_{0Hs}^2 + K'_b n_{0Hs} + K'_a K'_b} + qN_{nit} \frac{n_{0Hs}}{n_{0Hs} + K'_n}\,. \tag{2.10}$$

The expressions derived here look different from the ones in [42, 43] since we have chosen all SI measurement units. To obtain the classical expressions we remind that the pH is defined as:

$$pH = -\log_{10} a_H = -\log_{10}\left(\gamma_H \frac{n_H}{n_{ref}}\right)$$

where a_H is the hydrogen activity, γ_H the activity coefficient, n_H the hydrogen ion concentration and n_{ref} a reference concentration. Since we always use m^{-3} as a unit of

measurement for the ion concentrations and the reference concentration is usually taken as 1 M, we have that $n_{ref} = 10^3 N_A$, where N_A is Avogadro's number. We will always assume $\gamma_H = 1$; so, we can write:

$$n_H = 10^{-pH+3} N_A \quad \Longrightarrow \quad 10^{-pH} = 10^{-3} \frac{n_H}{N_A}$$

Defining then $K'_a = K_a 10^{-3} N_A$, $K'_b = K_b 10^{-3} N_A$ and $K'_n = K_n 10^{-3} N_A$ we obtain the classical expressions:

$$\sigma_{sb} = qN_S \frac{10^{-2pH_s} - K_a K_b}{10^{-2pH_s} + K_b 10^{-pH_s} + K_a K_b}$$
$$\sigma_{sb}^{Si_3N_4} = qN_S \frac{10^{-2pH_s} - K_a K_b}{10^{-2pH_s} + K_b 10^{-pH_s} + K_a K_b} + qN_{nit} \frac{10^{-pH_s}}{10^{-pH_s} + K_n} .$$

We also know that:

$$n_{0Hs} = n_H^\infty \exp\left(\frac{V_{ref} - V_{0S}}{V_{th}}\right),$$

where V_{0S} is the DC surface potential and $V_{th} = k_B T/q$. We can thus transform Eqs. 2.9-2.10 in the expressions:

$$\sigma_{sb} = qN_S \frac{(n_H^\infty)^2 e^{2\frac{V_{ref}-V_{0S}}{V_{th}}} - K'_a K'_b}{(n_H^\infty)^2 e^{2\frac{V_{ref}-V_{0S}}{V_{th}}} + K'_b n_H^\infty e^{\frac{V_{ref}-V_{0S}}{V_{th}}} + K'_a K'_b} \tag{2.11}$$

$$\sigma_{sb}^{Si_3N_4} = qN_S \frac{(n_H^\infty)^2 e^{2\frac{V_{ref}-V_{0S}}{V_{th}}} - K'_a K'_b}{(n_H^\infty)^2 e^{2\frac{V_{ref}-V_{0S}}{V_{th}}} + K'_b n_H^\infty e^{\frac{V_{ref}-V_{0S}}{V_{th}}} + K'_a K'_b} + qN_{nit} \frac{n_H^\infty e^{\frac{V_{ref}-V_{0S}}{V_{th}}}}{n_H^\infty e^{\frac{V_{ref}-V_{0S}}{V_{th}}} + K'_n} \tag{2.12}$$

These transformations are needed in order to obtain parameters always expressed in SI units, and to have a direct dependence of the surface charge on the electrostatic potential suitable for solution with Poisson equation.

High salt concentration effects As pointed out in [44], the site-binding theory in the form previously discussed becomes inaccurate at high salt concentration. This discrepancy is clearly visible in Fig. 2.1 that compares the surface potential predicted by the conventional site-binding model to the experimental data from [44]. The discrepancy has been attributed to surface complexation reactions with the electrolyte chlorine ions of the form

$$\mathrm{MOH_2^+} + \mathrm{Cl_s^-} \overset{K_c}{\rightleftharpoons} \mathrm{MOHCl^-} + \mathrm{H_B^+} \tag{2.13}$$

where $\mathrm{Cl_s^-}$ denotes the chlorine ions at the surface and $\mathrm{H_B^+}$ the hydrogen ions in the bulk. Following [44], we should thus describe the dielectric/electrolyte interface of SiO_2, HfO_2, Al_2O_3 and Ta_2O_5 with three coupled chemical reactions, whose dissociation constants are given by Eqs. 2.7 and by:

$$K_c = \frac{\nu_{MOHCl}\, n_H^\infty}{\nu_{MOH_2}\, n_{0Cls}} \tag{2.14}$$

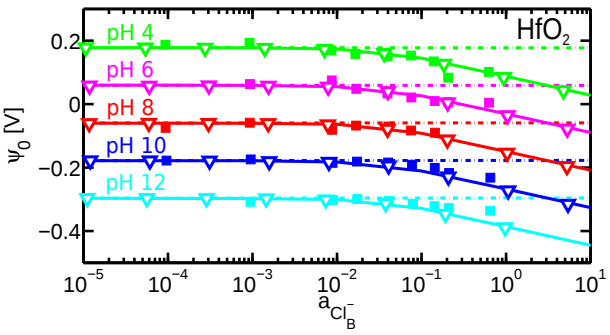

Fig 2.1: Surface potential experimental data in [44] (squares) compared to the site-binding model (dash-dotted lines), the model of [44] (open triangles) and our TCAD implementation (solid lines) reported in [7]. Following ref. [44], we compute $\psi_0 = V_{T,PZC} - V_T$, where $V_{T,PZC}$ is the V_T for the pH of zero charge ($pH_{PZC} = -0.5 \ln K_a \cdot K_b$) at very low electrolyte concentration (10μM). K_a=K_b=10^{-7}, K_c=3.3·10^{-6}.

where n_{0Cls} is the chlorine free-ions concentration at the surface and ν_{MOHCl^-} is the density of the negatively charged surface groups. The surface charge density is then given by:

$$\sigma_{sb} = q\left(\nu_{MOH_2} - \nu_{MO} - \nu_{MOHCl}\right) \quad . \tag{2.15}$$

Substitution of Eqs. 2.7-2.14 into Eq. 2.15 and the expression:

$$N_S = \nu_{MO} + \nu_{MOH} + \nu_{MOH_2} + \nu_{MOHCl} \quad , \tag{2.16}$$

allows us to derive:

$$\sigma_{sb} = qN_S \left(\frac{n_{0Hs}^2 n_H^\infty - K_a' K_b' n_H^\infty - K_c n_{0Cls} n_{0Hs}^2}{n_{0Hs}^2 n_H^\infty + K_a' K_b' n_H^\infty + K_c n_{0Cls} n_{0Hs}^2 + K_b' n_{0Cls} n_H^\infty} \right) \quad . \tag{2.17}$$

The term n_{0Cls} is, as usual (see Eq.
refeq:boltzmann):

$$n_{0Cls} = n_{Cl}^\infty \exp\left(\frac{V_{0S} - V_{ref}}{V_{th}}\right) \quad . \tag{2.18}$$

2.1.2 Current equations

As we assume no DC current flow in the electrolyte, the equations for the DC electrical current must be written only in the semiconductor. This can be described, at first order, by the well-known drift-diffusion equations (also known as Nernst-Planck equations in electro-chemistry [36]):

$$\frac{\partial n_m}{\partial t} + U = -\frac{1}{Z_m q} \nabla \cdot \vec{J}_m \tag{2.19a}$$

$$\vec{J}_m = -Z_m q \left(Z_m q \mu_m n_m \nabla V + D_m \nabla n_m\right) \tag{2.19b}$$

where U is the generation-recombination rate, $\vec{J}_m$ is the current density, μ_m the mobility (in [m/Ns]) and D_m the diffusion coefficient of species m, respectively. We will always assume that the Einstein relation holds, so that $D_m = k_B T \mu_m$.

The $\vec{J}_m$ expression we use looks different from the one normally employed in electro-chemistry and semiconductor physics (see, for instance, [36]) because we have chosen to

define the ion mobility as the ratio between the ion velocity and the applied force. This approach is consistent with classical physics and is justified noting that many semiconductor physics and electrochemistry equations describe phenomena that do not necessarily involve charge. An example is Einstein's relation between diffusivity and mobility, which can be derived imposing a thermodynamic equilibrium between mechanical force and diffusion of neutral species. However, assuming the semiconductor physics' definition of mobility, neutral atoms would have zero mobility, while still reacting to other forces. This dilemma is introduced in semiconductor physics, because it treats exclusively charged particles (electrons and holes) and the only source of force is the electric field. Therefore, the notation we use gives a broader and more general view on the real physical phenomena. Using Eq. 2.4, the expression of the current (Eq. 2.19b) becomes:

$$\vec{J}_m = -Z_m^2 q^2 \mu_m n_m \nabla \phi_m \tag{2.20}$$

We choose $n_m^\infty = n_i$ so that the ϕ_m are exactly the well-known quasi Fermi levels. Therefore, the drift-diffusion equations can be written as:

$$\boxed{\begin{aligned} U(\phi_m, V) + \left(\frac{\partial \phi_m}{\partial t} - \frac{\partial V}{\partial t}\right) n_i \frac{Z_m q}{k_B T} \exp\left(\frac{Z_m q}{k_B T}(\phi_m - V)\right) \\ = Z_m q \mu_m \nabla \cdot \left(n_i \exp\left(\frac{Z_m q}{k_B T}(\phi_m - V)\right) \nabla \phi_m\right) \end{aligned}} \tag{2.21}$$

We will call Eq. 2.21 as the first formulation of the current equations.

By expanding the second term as:

$$\begin{aligned} U(\phi_m, V) + \left(\frac{\partial \phi_m}{\partial t} - \frac{\partial V}{\partial t}\right) n_i \frac{Z_m q}{k_B T} \exp\left(\frac{Z_m q}{k_B T}(\phi_m - V)\right) \\ = Z_m q \mu_m n_i \exp\left(\frac{Z_m q}{k_B T}(\phi_m - V)\right) \left(\frac{Z_m q}{k_B T} \nabla \phi_m \cdot \nabla (\phi_m - V) + \nabla^2 \phi_m\right) \end{aligned}$$

a second formulation can be found, which reads:

$$\boxed{\hat{U}_m(\phi_m, V) + \left(\frac{\partial \phi_m}{\partial t} - \frac{\partial V}{\partial t}\right) \frac{\varepsilon}{\mu_m k_B T} = \varepsilon \left(\frac{Z_m q}{k_B T} \nabla \phi_m \cdot \nabla (\phi_m - V) + \nabla^2 \phi_m\right)} \tag{2.22}$$

where we have divided the equation by:

$$\frac{Z_m q\, \mu_m n_i}{\varepsilon} \exp\left(\frac{Z_m q}{k_B T}(\phi_m - V)\right)$$

in order to have the same measurements units as in Poisson equation, and:

$$\hat{U}_m(\phi_m, V) = \frac{U(\phi_m, V)}{n_i} \frac{\varepsilon}{Z_m q\, \mu_m} \frac{1}{\exp\left(\frac{Z_m q}{k_B T}(\phi_m - V)\right)}.$$

So far we have always used the general potentials V and ϕ_m, which may have both DC and time dependent components. The DC formulation can be easily found by substituting V and ϕ_m with V_0 and ϕ_{0m}, respectively, and recognizing that all time derivatives are equal

to zero. From now on, as a convention, we use $m = 1$ for the electrons and $m = 2$ for the holes. According to the Shockley-Read-Hall model for the generation-recombination rate:

$$\begin{aligned} U(\phi_m, V) &= \frac{np - n_i^2}{\tau_p\,(n + n_i) + \tau_n\,(p + n_i)} \\ &= n_i \frac{e^{\frac{q}{k_B T}(\phi_2 - \phi_1)} - 1}{\tau_2 \left(e^{-\frac{q}{k_B T}(\phi_1 - V)} + 1\right) + \tau_1 \left(e^{\frac{q}{k_B T}(\phi_2 - V)} + 1\right)} \end{aligned}$$

Hence, we can write:

$$\begin{aligned} \hat{U}_1(\phi_m, V) &= \frac{\varepsilon}{Z_1 q\,\mu_1} \frac{e^{\frac{Z_2 q}{k_B T}(\phi_2 - V)} - e^{-\frac{Z_1 q}{k_B T}(\phi_1 - V)}}{\tau_2 \left(e^{\frac{Z_1 q}{k_B T}(\phi_1 - V)} + 1\right) + \tau_1 \left(e^{\frac{Z_2 q}{k_B T}(\phi_2 - V)} + 1\right)} \\ \hat{U}_2(\phi_m, V) &= \frac{\varepsilon}{Z_2 q\,\mu_2} \frac{e^{\frac{Z_1 q}{k_B T}(\phi_1 - V)} - e^{-\frac{Z_2 q}{k_B T}(\phi_2 - V)}}{\tau_2 \left(e^{\frac{Z_1 q}{k_B T}(\phi_1 - V)} + 1\right) + \tau_1 \left(e^{\frac{Z_2 q}{k_B T}(\phi_2 - V)} + 1\right)}\,. \end{aligned}$$

As we expect modest recombination phenomena in our case studies, in the following we neglect the generation-recombination term. This term has not been implemented in the ENBIOS simulator described in Chap. 4.

2.1.3 Boundary conditions

We partition the surface Γ of the domain of interest Ω in two different ways:

$$\begin{aligned} \Gamma &= \Gamma_D^V \cup \Gamma_N^V \\ \Gamma &= \Gamma_D^\phi \cup \Gamma_N^\phi\,. \end{aligned}$$

Here Γ_D^V is the part of the boundary where we impose Dirichlet conditions on the potential, while on Γ_D^ϕ there are Dirichlet conditions for the quasi-potentials. Similarly for Neumann conditions on Γ_N^V and Γ_N^ϕ. This segmentation is necessary since, in general, there may be parts of the boundary where we want to impose only the electric potential (ideally polarizable electrodes), while on others (Faradaic electrodes) we want to set also the quasi-potential.

The boundary conditions can be written as:

$$\begin{cases} V_0 = V^D & \text{on } \Gamma_D^V \\ \phi_{0m} = \phi_m^D & \text{on } \Gamma_D^\phi \\ \varepsilon \nabla V_0 \cdot \hat{n} = 0 & \text{on } \Gamma_N^V \\ \nabla \phi_{0m} \cdot \hat{n} = 0 & \text{on } \Gamma_N^\phi \end{cases} \tag{2.23}$$

We can calculate explicitly ϕ_m^D for the electrodes that are in contact with the semiconductor. In fact, if we assume these to be Ohmic electrodes that fulfill charge neutrality and equilibrium conditions, then:

$$n_1^D - n_2^D = N_D - N_A, \quad n_1^D n_2^D = n_i^2$$

where we have used our convention that n_1 refers to electrons and n_2 to holes. In terms of quasi-potentials, these conditions imply that :

$$\phi_1^D = \phi_2^D = \phi_F$$

where ϕ_F is the Fermi potential at the contact, which equals V^D for non-resistive contacts. The potential on the semiconductor side of the electrode is:

$$V_{0I} = \phi_F + \frac{k_B T}{q} \text{asinh}\left(\frac{N_D - N_A}{2n_i}\right)$$

where the suffix I stands for "internal", denoting the first node inside the semiconductor domain.

Note that the existence and (local) uniqueness of solutions of the drift-diffusion-Poisson system (in the semiconductor) coupled with the Poisson-Boltzmann equation (in the electrolyte) and with interface conditions between the different regions was shown in [38].

2.2 AC models

Most of the work in this thesis is devoted to modeling and simulation of impedimetric nanobiosensors. It is thus important to develop model equations in the frequency domain using the small-signal approximation. To this purpose, we write the quasi-potentials, ϕ_m, and the electric potential, V, as:

$$\boxed{\begin{aligned} \phi_m &= \phi_{0m} + \Re\left[\tilde{\phi}_m \exp(j\omega t)\right] && \text{(2.24a)} \\ V &= V_0 + \Re\left[\tilde{V} \exp(j\omega t)\right] && \text{(2.24b)} \end{aligned}}$$

where $\tilde{V}$ and $\tilde{\phi}_m$ are the complex amplitudes of the AC potential and quasi-potentials. We remind that the small-signal approximation is valid if $|\tilde{\phi}_m|$, $|\tilde{V}| \ll k_B T/q$, i.e., the amplitude of the electric and quasi-potentials is small enough with respect to the thermal voltage ($\approx$ 25 mV at room temperature). Essentially, we are assuming that all signals are made of a DC component with in addition a small sinusoidal component. If the non-linearities of the system are small (for instance, in our case, because the AC signal is much lower than the thermal voltage $k_B T/q$), every arbitrary signal can be represented as a linear combination of sinusoids, as also shown in [45]. The amplitude of the AC signal should also be low enough to prevent self-heating effects (see [46]), which could locally increase the temperature. This is the case in all the biosensors implementation that we study in this thesis (for instance the modulation voltage at the electrodes of [33] is only a few times the thermal voltage), so that we will always neglect self-heating effects.
For the following calculations, it is useful to remind that we can always write $e^{j\omega t} = x + j\sqrt{1-x^2}$ with arbitrary $|x| \leq 1$, so that in general:

$$\Re\left[(a+jb)(x+j\sqrt{1-x^2})\right] = \Re\left[(c+jd)(x+j\sqrt{1-x^2})\right] \quad \Longleftrightarrow \quad a+jb = c+jd\,. \tag{2.25}$$

It is thus legitimate to solve the model equations in the domain of complex numbers $\tilde{V}$, $\tilde{\phi}_m$ only, because, thanks to the equivalence 2.25, this then entails the validity of the results for the quantities V and ϕ_m as given by Eq. 2.24.

In order to find general expressions for the small signal AC carrier concentrations, we start from Eq. 2.4 and we assume that $\left|\tilde{\phi}_m - \tilde{V}\right| \ll \dfrac{k_B T}{Z_m q}$. This condition is not always satisfied in real systems and notably for the nanocapacitor array described in Chap. 5. In the specific case, simple techniques have been devised to account for the not-always negligible harmonic content of the signals, as described in Sec. 3.6.

If we approximate the exponential with its Taylor expansion to the first order:

$$\exp\left(\frac{Z_m q}{k_B T}\left(\phi_m - V\right)\right) \simeq \exp\left(\frac{Z_m q}{k_B T}\left(\phi_{0m} - V_0\right)\right)\left[1 + \frac{Z_m q}{k_B T}\Re\left[\left(\tilde{\phi}_m - \tilde{V}\right)\exp(j\omega t)\right]\right] \tag{2.26}$$

then we can write the ion and carrier concentrations as:

$$n_m = n_{0m} + \Re\left[\tilde{n}_m \exp(j\omega t)\right] \tag{2.27}$$

where n_{0m} comes from Eq. 2.4 and the small-signal concentrations $\tilde{n}_m$ are:

$$\boxed{\tilde{n}_m = n_{0m}\frac{Z_m q}{k_B T}\left(\tilde{\phi}_m - \tilde{V}\right)} \tag{2.28}$$

Note that in the following we will always neglect the second and higher order terms in the small-signal components.

2.2.1 Poisson equation

To find the AC model we then start from Poisson equation:

$$\nabla \cdot (\varepsilon \nabla V) + \left[\rho_f + \sum_{m=1}^{N_{sp}} Z_m q n_m^{\infty} \exp\left(\frac{Z_m q}{k_B T}\left(\phi_m - V\right)\right)\right] = 0 \tag{2.29}$$

Using Eqs. 2.24-2.26 we then have:

$$\nabla \cdot \left[\varepsilon \nabla\left(V_0 + \Re\left(\tilde{V}\exp(j\omega t)\right)\right)\right] + \left[\rho_f + \sum_{m=1}^{N_{sp}} Z_m q n_m^{\infty} \exp\left(\frac{Z_m q}{k_B T}\left(\phi_{0m} - V_0\right)\right)\left(1 + \frac{Z_m q}{k_B T}\Re\left(\left(\tilde{\phi}_m - \tilde{V}\right)\exp(j\omega t)\right)\right)\right] = 0$$

Noting that the DC variables V_0 and ϕ_{0m} satisfy the Poisson-Boltzmann equation (Eq. 2.5), and using Eq. 2.25 we obtain the AC Poisson equation:

$$\boxed{\nabla \cdot \left(\varepsilon \nabla \tilde{V}\right) + \sum_{m=1}^{N_{sp}} \frac{Z_m^2 q^2}{k_B T} n_{0m}\left(\tilde{\phi}_m - \tilde{V}\right) = 0} \tag{2.30}$$

2.2.1.1 Surface charges

Fixed charges clearly do not contribute to the AC signals. The surface protonation/deprotonation and complexation reactions described in Sec. 2.1.1.1, instead, could affect the low frequency response in different ways. We therefore need a model to account for the site-binding surface charge and include it into the Poisson coefficients as done in Sec. 2.1.1.1 for the DC case.

To this purpose and following the approach presented in [47], we consider the surface reactions Eq. 2.6, assume them first order and write the reaction rates as:

$$\frac{dn_{SiO}}{dt} = -\frac{dn_{SiO_H}}{dt} = k_a^f n_{SiOH} - k_a^b n_{SiO} n_H \tag{2.31a}$$

$$\frac{dn_{SiOH_2}}{dt} = -k_b^f n_{SiOH_2} + k_b^b n_{SiOH} n_H \tag{2.31b}$$

where the "f" and "b" suffixes denote the left-to-right (forward, dissociation) and right-to-left (backwards, aggregation) reactions, respectively.
Recalling that $\sigma_{sb} = qN_S(n_{SiOH_2} - n_{SiO})$, we then find:

$$\frac{d\sigma_{sb}}{dt} = k_a^b n_{SiO} n_H - k_a^f n_{SiOH} - k_b^f n_{SiOH_2} + k_b^b n_{SiOH} n_H$$

Note also that, by definition, the equilibrium constants are:

$$K'_a = \frac{k_a^f}{k_a^b}, \quad K'_b = \frac{k_b^f}{k_b^b}$$

If we now write all the concentrations with the small-signal approximation Eq. 2.27 and we remind that the DC concentrations are in equilibrium (in the sense that they satisfy Eq. 2.31 with null time derivatives), we derive the AC formulation of Eq. 2.31:

$$\begin{aligned} j\omega\tilde{n}_{SiO} &= -k_a^b\left(\nu_{0MO}\tilde{n}_H + n_{0H}\tilde{n}_{SiO}\right) + k_a^f\tilde{n}_{SiOH} \\ j\omega\tilde{n}_{SiOH_2} &= -k_b^f\tilde{n}_{SiOH_2} + k_b^b\left(\nu_{0MOH}\tilde{n}_H + n_{0H}\tilde{n}_{SiOH}\right) . \end{aligned}$$

As a consequence:

$$\tilde{n}_{SiO} = \frac{-k_a^b\nu_{0MO}\tilde{n}_H + k_a^f\tilde{n}_{SiOH}}{k_a^b n_{0H} + j\omega} \tag{2.32a}$$

$$\tilde{n}_{SiOH_2} = \frac{k_b^b}{k_b^f + j\omega}\left(\nu_{0MOH}\tilde{n}_H + n_{0H}\tilde{n}_{SiOH}\right) . \tag{2.32b}$$

As $\tilde{n}_{SiOH} + \tilde{n}_{SiO} + \tilde{n}_{SiOH_2} = 0$, we can calculate the AC concentrations of SiO^-, SiOH and $SiOH_2^+$ from Eqs. 2.8-2.32:

$$\tilde{n}_{SiO} = -\frac{\tilde{n}_H(k_a^f k_b^b \nu_{0MOH} + k_a^b\nu_{0MO}(k_b^f + k_b^b n_{0H} + j\omega))}{k_a^f(k_b^f + j\omega) + (k_a^b n_{0H} + j\omega)(k_b^f + k_b^b n_{0H} + j\omega)}$$

$$\tilde{n}_{SiOH_2} = \frac{\tilde{n}_H(-k_b^b\nu_{0MOH}j\omega + k_a^b(-k_b^b n_{0H}\nu_{0MOH} + \nu_{0MO}(k_b^f + j\omega)))}{k_a^f(k_b^f + j\omega) + (k_a^b n_{0H} + j\omega)(k_b^f + k_b^b n_{0H} + j\omega)}$$

$$\tilde{n}_{SiOH} = \frac{k_b^b\tilde{n}_H(k_a^b n_{0H}(\nu_{0MO} + \nu_{0MOH}) + \nu_{0MOH}(k_a^f + j\omega))}{k_a^f(k_b^f + j\omega) + (k_a^b n_{0H} + j\omega)(k_b^f + k_b^b n_{0H} + j\omega)}$$

By combining expressions for the DC and AC concentrations:

$$n_{0H} = n_H^\infty \exp\left(-\frac{V_0 - V_{ref}}{V_{th}}\right)$$

$$\tilde{n}_H = n_{0H}\frac{\tilde{\phi}_H - \tilde{V}}{V_{th}}$$

where $\phi_H = V_{ref} + \Re\left\{\tilde{\phi}_H e^{j\omega t}\right\}$, being ϕ_H the quasi-potential of the hydrogen ions, we can finally calculate the AC site-binding charge $\tilde{\sigma}_{sb} = q\left(\tilde{n}_{SiOH_2} - \tilde{n}_{SiO}\right)$:

$$\boxed{\tilde{\sigma}_{sb} = qN_S\frac{K'_b(k_b^b n_{0H}(k_a^b n_{0H} + j\omega) + K'_a k_a^b(K'_b k_b^b + 4k_b^b n_{0H} + j\omega))}{(K'_a K'_b + n_{0H}(K'_b + n_{0H}))(K'_a k_a^b(K'_b k_b^b + j\omega) + (k_a^b n_{0H} + j\omega)(k_b^b(K'_b + n_{0H}) + j\omega))}\tilde{n}_H} \tag{2.33}$$

where we used the expressions $K'_a k_a^b = k_a^f$, $K'_b k_b^b = k_b^f$ to eliminate the forward reaction rates.

2.2.2 Current equations

The transport model is given by the drift-diffusion equations (Eq. 2.21), for both the electrolyte and the semiconductor. Using Eqs. 2.24-2.26 we obtain:

$$\Re\left(j\omega\left(\tilde{\phi}_m-\tilde{V}\right)e^{j\omega t}\right)n_i\frac{Z_mq}{k_BT}\exp\left(\frac{Z_mq}{k_BT}\left(\phi_{0m}-V_0\right)\right)\left[1+\frac{Z_mq}{k_BT}\Re\left(\left(\tilde{\phi}_m-\tilde{V}\right)e^{j\omega t}\right)\right]$$
$$=Z_mq\mu_m\nabla\cdot\left(n_i\exp\left(\frac{Z_mq}{k_BT}\left(\phi_{0m}-V_0\right)\right)\left[1+\frac{Z_mq}{k_BT}\Re\left(\left(\tilde{\phi}_m-\tilde{V}\right)e^{j\omega t}\right)\right]\left(\nabla\phi_{0m}+\Re\left(\nabla\tilde{\phi}_me^{j\omega t}\right)\right)\right).$$

By eliminating the DC components and neglecting the second order terms we find the small-signal drift-diffusion equation:

$$Z_mq\mu_m\nabla\cdot\left(n_{0m}\left(\frac{Z_mq}{k_BT}\left(\tilde{\phi}_m-\tilde{V}\right)\nabla\phi_{0m}+\nabla\tilde{\phi}_m\right)\right)-j\omega n_{0m}\frac{Z_mq}{k_BT}\left(\tilde{\phi}_m-\tilde{V}\right)=0 \quad (2.34)$$

We can simplify this equation in the electrolyte by noting that $\phi_{0m}=V_{ref}$, so that $\nabla\phi_{0m}=0$. Hence:

$$\boxed{Z_mq\mu_m\nabla\cdot\left(n_{0m}\nabla\tilde{\phi}_m\right)-j\omega n_{0m}\frac{Z_mq}{k_BT}\left(\tilde{\phi}_m-\tilde{V}\right)=0} \quad (2.35)$$

2.2.3 Boundary conditions

In order to define the boundary conditions we have first to calculate the AC current density:

$$\boxed{\vec{\tilde{J}}=\vec{\tilde{J}}_D+\sum_{m=1}^{N_{sp}}\vec{\tilde{J}}_m} \quad (2.36)$$

where the displacement and conduction contributions are:

$$\boxed{\begin{aligned}\vec{\tilde{J}}_D&=-j\omega\varepsilon\nabla\tilde{V} &(2.37a)\\ \vec{\tilde{J}}_m&=-Z_m^2q^2\mu_mn_{0m}\left(\frac{Z_mq}{k_BT}\left(\tilde{\phi}_m-\tilde{V}\right)\nabla\phi_{0m}+\nabla\tilde{\phi}_m\right) &(2.37b)\end{aligned}}$$

As for the boundary conditions, we use partitions of Γ similar, but not necessarily equal, to those defined in Sec. 2.1.2. The AC boundary conditions are:

$$\begin{cases}\tilde{V}=\tilde{V}^D & \text{on } \tilde{\Gamma}_D^V\\ \tilde{\phi}_m=\tilde{\phi}_m^D & \text{on } \tilde{\Gamma}_D^\phi\\ \varepsilon\nabla\tilde{V}\cdot\hat{n}=0 & \text{on } \tilde{\Gamma}_N^V\\ \vec{\tilde{J}}_m\cdot\hat{n}=0 & \text{on } \tilde{\Gamma}_N^\phi\end{cases} \quad (2.38)$$

where $\Gamma=\tilde{\Gamma}_D^V\cup\tilde{\Gamma}_N^V=\tilde{\Gamma}_D^\phi\cup\tilde{\Gamma}_N^\phi$. Note also that $\tilde{\Gamma}_N^\phi$ includes ideally polarizable electrodes in the electrolyte and floating electrodes in the semiconductor.

2.3 Electrolyte models

In this section we discuss a few physical effects and corrections to the basic electrolyte model, aimed at improving the description of the analyte/sensor interaction.

2.3.1 Electrolyte permittivity

At the high frequency of interest for this work (up to the GHz range) the dependency of the water permittivity ε_{el} on the frequency becomes not negligible. An accurate model of the dependency of ε_{el} on frequency and salt concentration useful for our purposes has been derived in [48]. The resulting expression for ε_{el} takes the form of the widely known double time constant Debye model [48]:

$$\varepsilon_{el} = \varepsilon_0 \left(\varepsilon_\infty + \frac{\varepsilon_s - \varepsilon_1}{1 + j\omega\tau_{e1}} + \frac{\varepsilon_1 - \varepsilon_\infty}{1 + j\omega\tau_{e2}} \right) \tag{2.39}$$

where ε_0 is the vacuum permittivity. The time constants τ_{e1} and τ_{e2} reflect relaxation processes of the water molecules. As discussed in [49], the first relaxation τ_{e1} comes directly from a Debye relaxation, which is the dielectric relaxation response of an ideal, noninteracting population of dipoles to an alternating external electric field. In contrast, the existence of τ_{e2} has been so far justified only as an experimental fit [49].
Deviating from [48], however, we have not included explicitly the term with the ionic conductivity because it is already taken into account by the Nernst-Planck equations (see also [50]). To account for the salt concentration in the electrolyte, the parameters in Eq. 2.39 are computed as a function of the so called practical salinity S and the temperature T. Thus, $\varepsilon_{el} = \varepsilon_{el}(S, T, \omega)$. The practical salinity S is defined with respect to a standard reference KCl solution. The concentration of KCl in the standard solution can be calculated from its mass fraction $w = 32.4356 \cdot 10^{-3}$ as $n_{stand} = w\rho / M_{KCl} = 0.43508$ M where $M_{KCl} = 0.001(39.0983 + 35.453)$ kg/mol is KCl molar mass and $\rho = 1$ kg/L is water's density. We can then calculate the DC conductivity of both the solution and the reference KCl solution as $\sigma = \sum_m Z_m^2 q^2 \mu_m n_{0m}$, and then calculate the ratio between conductivity and standard conductivity at 15°C $K_{15} = \sigma / \sigma_{stand}$. The salinity is then calculated using the expression $S = f(K_{15})$ [51]:

$$S = 0.008 - 0.1692K_{15}^{\frac{1}{2}} + 25.3851K_{15} + 14.0941K_{15}^{\frac{3}{2}} - 7.0261K_{15}^2 + 2.7081K_{15}^{\frac{5}{2}}$$

Fig. 2.2 shows ε_{el} calculated with Eq. 2.39 varying temperature, salt concentration and frequency. We have used a KCl salt, where the mobilities have been taken from [52] (see for instance Tab. 5.4).

2.3.2 Steric effects

The Poisson-Boltzmann equation (Eq. 2.4) supposes the ions are point-like non-interacting charges. When the ion concentrations become very large two so-called steric effects occur, which are due to the finite ionic radius r_i: 1) r_i becomes comparable to the width of the surface diffused layer and 2) the surface ion concentration is limited by r_i. These steric effects prevent the surface ion concentration to attain high values.

Two approaches are commonly used in the literature to describe these phenomena: the first one introduces a thin dielectric layer at the interface (called Stern layer in the classical model of the double layer) [36], while the second one modifies directly the Poisson-Boltzmann equation [53]. In the following both approaches will be quantitatively evaluated and compared to each other. Since our calculations showed that surface carrier concentrations are limited by steric effects only at the highest salt concentrations, just the simplest of these approaches (i.e., the dielectric layer) will be used throughout the remaining part of the thesis.

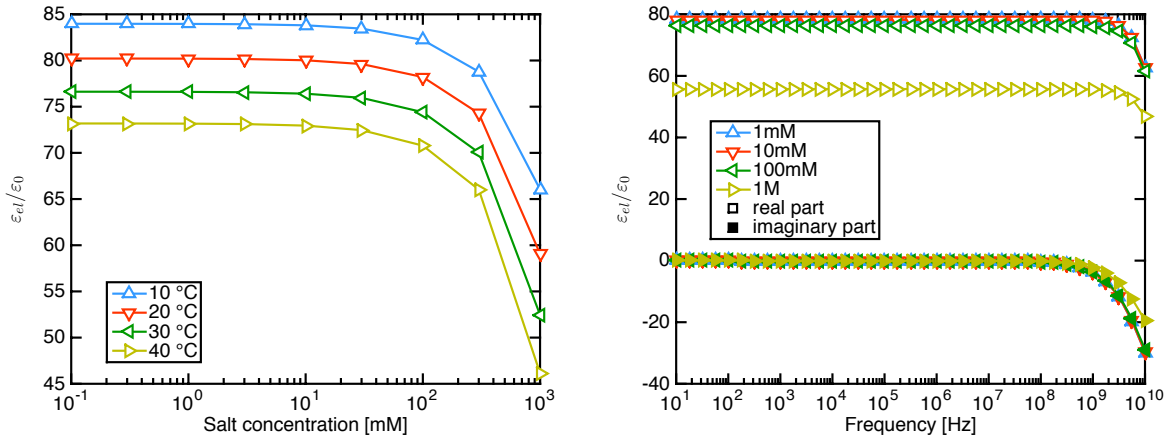

(a) in DC **(b)** at $T = 25°C$

Fig 2.2: Relative electrolyte permittivity calculated with Eq. 2.39 either in DC (left) or at a fixed temperature of 25°C (right) with a KCl salt.

2.3.2.1 Stern layer

We start considering the first approach to take into account steric effects, i.e. the introduction of a thin dielectric compact layer of counterions next to charged interfaces with electrolytes (Stern layer). Due to its nanoscale thickness and the high field therein, the Stern layer has a difficult to define permittivity, which is not equal to the bulk electrolyte permittivity. In fact, it is well known that the high electric field at the interface gives rise to a preferential polarization of the water molecules, so that the local permittivity is remarkably reduced [54]. There have been many attempts to describe this effect with analyticals model, and Ref. [54] provides a comprehensive description of their physical background. Among these, perhaps the most comprehensive is the original model, where the relative permittivity is expressed as [54]:

$$\varepsilon_r = n^2 + n_{0w} n_s \frac{p_0}{\varepsilon_0} \frac{2+n^2}{3} \frac{(\coth(u) - 1/u)\sinh(u)/u}{2n_0 E \cosh\left(\frac{qV_0}{k_B T}\right) + n_{0w} \frac{k_B T}{p_0 \gamma} \sinh(u)} \tag{2.40}$$

where $u = \frac{p_0 \gamma}{k_B T} E$, $\gamma = \frac{3}{2}\frac{2+n^2}{3}$, n is the refractive index of water, $n_{0w} = 55$ mol/L at 300 K, $n_s = 2n_0 + n_{0w}$, p_0 the magnitude of the dipole moment of a single water molecule in the electrolyte solution (eventually a fitting parameter) and E the magnitude of the electric field. Eq. 2.40 takes into account the orientation ordering of water molecules, the excluded volume effect due to the finite size of the ions and the cavity field.

To investigate the importance of these preferential polarization effects, we have implemented both a non self-consistent and a self-consistent solution of Eq. 2.40 assuming a piece-wise constant permittivity profile in the simulation domain. In particular, we consider a simple case with only two regions (see the sketch in Fig. 2.3): the first one is the thin dielectric compact layer on top of the electrode, the second one is the bulk electrolyte. In this second region the dielectric constant is obviously equal to the bulk electrolyte permittivity, while in the compact layer the permittivity is calculated using the following procedure.

Firstly, since the compact layer is dielectric and the system is one dimensional with no fixed charge accumulated, the potential in the layer is a linear function of position $V_0 = \alpha x + \beta$, where x is the direction perpendicular to the electrode: consequently the magnitude of the

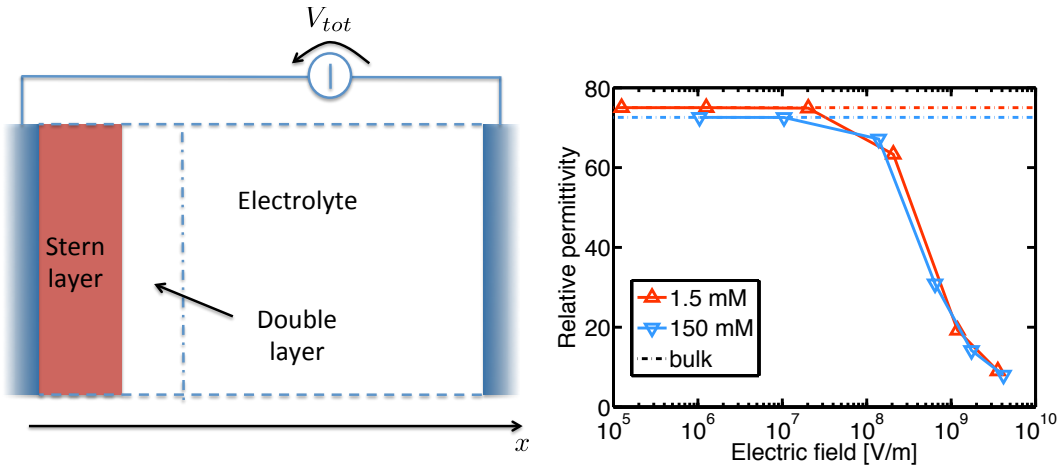

Fig 2.3: Sketch of the system (left) and effective relative permittivity of the surface compact layer as a function of the electric field (right) for two different bulk ion concentrations calculated solving self-consistently Eqs. 2.40-2.41 for the one-dimensional system sketched in the inset of Fig. 2.5. The electric field corresponds to applied voltages V_{tot} from 1mV to 1V. The horizontal lines show the salinity dependent bulk electrolyte permittivity calculated with the model of [54].

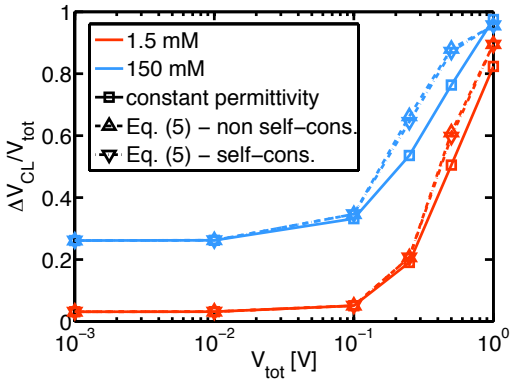

Fig 2.4: Potential difference across the compact layer ΔV_{CL} relative to the applied voltage ,V_{tot}, in the 1D structure sketched in the inset of Fig. 2.5 for different salt concentrations. The permittivity in the compact layer can be constant and equal to the bulk electrolyte permittivity or come either from a self-consistent or a non self-consistent solution of Eqs. 2.40-2.41.

electric field is constant $E = |\alpha|$. We then estimate the effective potential V_{eff} (referred to coordinate x_{eff}) which satisfies the condition:

$$\frac{1}{\cosh\left(\frac{qV_{eff}}{k_BT}\right) + \frac{n_{0w}}{2n_{0u}}\sinh(u)} = \frac{1}{a}\int_0^a \frac{1}{\cosh\left(\frac{qV_0(x)}{k_BT}\right) + \frac{n_{0w}}{2n_{0u}}\sinh(u)}dx \tag{2.41}$$

where a is empirically set equal to the ionic radius. The average permittivity $\varepsilon_{r,eff}$ is then calculated by using V_{eff} and the constant field $|\alpha|$ from Eq. 2.41 in Eq. 2.40 instead of V_0 and E. With this approach we derive then an average permittivity inside the Stern layer. Fig. 2.3 shows that the effect of the water molecule preferential ordering can lead to a remarkable decrease of the permittivity in the compact layer with respect to the bulk value, but only for very large field values.

To investigate the practical consequences of the decrease of the surface permittivity, Fig. 2.4 shows the potential difference across the compact layer ΔV_{CL} relative to the total voltage drop applied between the electrode and the bulk V_{tot} (see inset of Fig. 2.5) computed assuming either the constant bulk electrolyte permittivity or a piecewise constant

permittivity. At high applied voltage most of the potential drops across the compact layer ($\Delta V_{CL}/V_{tot}$ tends to 1) regardless of the permittivity model. Direct comparison of the solutions with constant permittivity (squares) to the ones calculated with Eqs. 2.40-2.41 (triangles) suggests that the value of $\varepsilon_{r,eff}$ in the compact layer has a very limited effect on ΔV_{CL}, especially at low salt concentration. Moreover, we observe that there is no appreciable difference between the self-consistent solution and the non self-consistent one where the corrected potential profile is a-priori given by a solution with a constant permittivity equal to the bulk value. The reason resides in the fact that, as we have already noted, at high applied voltage most of the potential drop occurs anyway in the compact layer which has always a permittivity which is much smaller than the electrolyte. This in turn means that the exact value of this permittivity does not change appreciably the potential profile, and therefore the non-self consistent solution is adequate enough.
The adequacy of a non self-consistent solution in describing the potential profile near the electrode suggests the possibility to first estimate the electric field profile from a first order simulation with a compact layer of thickness equal to the ionic radius and with a constant permittivity equal to that of the bulk electrolyte and then refine the results by calculating a new solution where the compact layer permittivity is given by Eqs. 2.40-2.41.

As a final remark, we note that the value of the permittivity calculated with this method is in agreement with the standard value of capacitance per unit area of the compact layer used in the literature of $\approx 20\ \mu\mathrm{F/cm^2}$ [55]. In particular, assuming a compact layer thickness of 0.25 nm, the compact layer capacitance translates to a permittivity $\varepsilon_{r,eff} = 5.6\varepsilon_0$.

2.3.2.2 Modified Poisson-Boltzmann equation

We now move to the second approach to account for steric effects. Following [53], we have modified the equation for the DC equilibrium concentration (Eq. 2.4), resulting in a Modified Poisson-Boltzmann (MPB) equation. Considering a symmetric Z:Z electrolyte and assuming that the ions can be treated as hard spheres with radius a, the DC concentrations are given by [53]:

$$n_0^{\pm} = \frac{n_0^{\infty} \exp\left(\mp \dfrac{Zq(V_0 - V_{ref})}{k_B T}\right)}{1 - 2n_0^{\infty}a^3 + 2n_0^{\infty}a^3 \cosh\left(\dfrac{Zq(V_0 - V_{ref})}{k_B T}\right)}\,. \tag{2.42}$$

As evident comparing the following results to those from previous section, the implementation of steric effects via a MPB for generic non-symmetric electrolytes causes significant complications of the equation without appreciably increasing the accuracy of the calculations compared to the use of Stern layers.
A method to include steric effects in AC calculations is presented in [56]. However, since the saturation of the carrier concentration at the interface implies the existence of a thin surface layer where $\tilde{n}_m = 0$, which is easily mimicked in AC simulations by introducing the Stern layer, steric effects have been neglected in AC calculations.

To investigate steric effects, we have used the full-custom PB and MPB simulator presented in [1] to determine reference solutions for the concentration and potential profiles of a simple one-dimensional system where one ideally polarizable electrode is in contact with the electrolyte and the opposite Faradaic electrode is located at a distance much larger than the Debye length and acts as a fluid gate (see the sketch in Fig. 2.3). As discussed in the previous section, a thin dielectric layer on top of the electrode is introduced

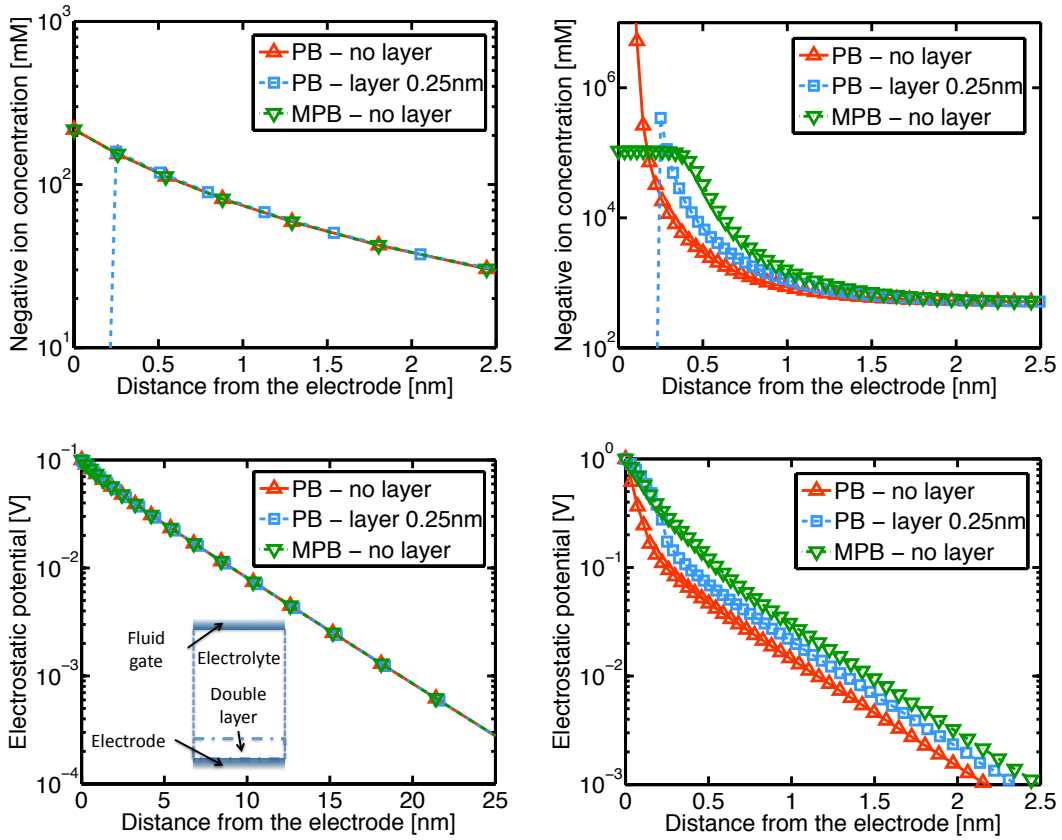

Fig 2.5: Ion concentration (top) and potential profiles (bottom) in a 1D structure consisting of an electrolyte with an electrode on the bottom ($y = 0$) and a fluid gate on the top (see inset). The solution of the Poisson-Boltzmann equation (using the TCAD) with and without an insulating layer with the thickness of the typical Na^+ or Cl^- ion radius ($a = 0.25$nm) is compared to the numerical solution of Eq. 2.42. Left plots: $n_0 = 5$ mM, $V_{el} = 100$ mV; right plots $n_0 = 500$ mM, $V_{el} = 1$ V.

to mimic the Stern layer [57] when solving the PB equation. Since we have just shown that the permittivity of the Stern layer does not have a strong impact on the solution, it is initially taken equal to the bulk electrolyte permittivity.

Fig. 2.5 compares the PB solution (triangles upward and rectangles) with Eq. 2.42 (triangles downward) in terms of ion concentration (top) and electrostatic potential (bottom). Indeed it shows that the steric effects are very important at high ion concentrations and high applied voltages (where $\frac{4}{3}\pi a^3 n_0^{\pm} \gg 1$) and that the PB theory gives unphysical results in this regime. However, we also see that the insertion of a dielectric "compact" layer somewhat mimics the steric effects when the PB equation is used, avoiding excessively large surface concentrations. The discrepancy between calculations with the PB equation without compact layer and the other two models is especially large in close proximity of the electrode. Since many impedance based biosensors operate by measuring the capacitance between electrodes in a liquid, this aspect has to be taken in great consideration in order to simulate correctly the current density at the electrodes, which gives the capacitance. The adoption of corrective measures as the thin compact layer proposed in this work improves appreciably the accuracy of the calculations. The plots on the left, derived for a low concentration and a low voltage, demonstrate that in these conditions the conventional PB theory is still appropriate without any dielectric layer and that the insertion of the layer does not appreciably alter the solution.

2.4 Summary

This chapter provides a general overview of the model equations to describe multi-ion electrolyte, insulator and semiconductor materials in the DC and AC small regime. These equations will be used extensively throughout this thesis as the starting point for the derivation of a few analytical and numerical models.
In particular, in DC conditions (Sec. 2.1) the models are:

- dielectrics: linear Poisson equation;
- electrolyte: Poisson-Boltzmann equation;
- semiconductor: Poisson-Nernst-Planck (PNP, also known as Poisson-drift-diffusion) equations.

In AC conditions (Sec. 2.2) the models are:

- dielectrics: linear AC Poisson equation;
- electrolyte and semiconductor: linearized Poisson-Nernst-Planck (also known as Poisson-drift-diffusion) equations.

In both the DC and AC regimes we impose a combination of Neumann (zero outer flux) and Dirichlet boundary conditions. The surfaces with Dirichlet boundary conditions are called electrodes and can be of two types:

- ideally polarizable (or floating) electrodes, where there is no DC and/or AC current flow;
- Faradaic (or Ohmic) electrodes, where a DC and/or AC current flow is possible.

For generality, we have let for instance ideally polarizable electrodes in DC to be Faradaic in AC and viceversa.

We have also investigated a few physical mechanisms possibly responsible of localized or global deviations of the electrolyte electrical properties from the relatively simple behaviour described by the PNP model equations. Among these, the electrolyte permittivity dependence on temperature, salt concentration and frequency (Sec. 2.3.1) and the so called steric effects (i.e., the compact layer of ions that forms at charged interfaces, Sec. 2.3.2). Careful implementation of refined model equations allowed us to identify the range of conditions where these effects become important and to conclude that, in many instances relevant for biosensor simulation, a simple but effective way to correct the simple PNP equations and to alleviate substantially the impact of model inaccuracy is to introduce a thin dielectric layer on the interfaces with the electrolyte mimicking the compact Stern layer. We have also shown that there is no need of employing a complex electric-field dependent model for the Stern layer permittivity, which could be easily estimated *a priori*.

Chapter 3

Analytical models for reference systems

In this chapter we derive a few analytical models which have been used to obtain reference solutions for the validation of a preliminary 2D numerical simulator of nanoelectrode sensors in cylindrical coordinates [1], and of the full 3D numerical solver ENBIOS [4]. Furthermore, these solutions provide useful physical insight on the phenomena involved in the signal transduction chain of simple systems.

3.1 1D AC cartesian electrode-electrolyte system

We start considering the 1D system sketched in Fig. 3.1, where variations occur along the cartesian direction x only. It is composed of one electrode at $x = 0$ and one at $x = L$, where either both electrodes are ideally polarizable, (i.e., no DC current flows through them) or just the rightmost electrode is Faradaic (i.e. it sustains a DC ionic current via electrochemical surface reactions). An electrolyte, a dielectric layer (for example the Stern layer as discussed in Sec. 2.3.2 or a Self Assembled Monolayer, SAM) and a particle or biomolecule can be optionally present between the electrodes. We typically assume that the electrolyte is symmetric with two ion species ($N_{sp} = 2$) of unitary valence. Under suitable approximations, realistic multi-ion electrolytes can be modelled with reasonable accuracy as 1:1 electrolytes as discussed in Sec. 4.6.1. The SAM and the biomolecule are modelled as ideal dielectric layers. Furthermore, we always assume that the electrodes are both DC biased at the reference voltage $V_{ref} = 0$ V; therefore, no DC bias is applied between them, which entails $V_0 = 0$ V and $n_{0m} = n_m^{\infty}$ everywhere in the domain. Depending upon the bias conditions and the AC signal, electrical double layers can form at the interface. We will study this system in the AC small signal regime.

3.1.1 Electrolyte only

If the entire system is composed only of electrolyte, the Poisson-Nernst-Planck system of equations (Eqs. 2.30-2.35) can be written as:

$$\begin{cases} -\dfrac{\varepsilon_{el}}{q}\dfrac{d^2\tilde{V}}{dx^2} = Z_1\tilde{n}_1 + Z_2\tilde{n}_2 \\ j\omega\tilde{n}_1 = Z_1 q\mu_1 n_{01}\dfrac{d^2\tilde{V}}{dx^2} + D_1\dfrac{d^2\tilde{n}_1}{dx^2} \\ j\omega\tilde{n}_2 = Z_2 q\mu_2 n_{02}\dfrac{d^2\tilde{V}}{dx^2} + D_2\dfrac{d^2\tilde{n}_2}{dx^2} \end{cases} \tag{3.1}$$

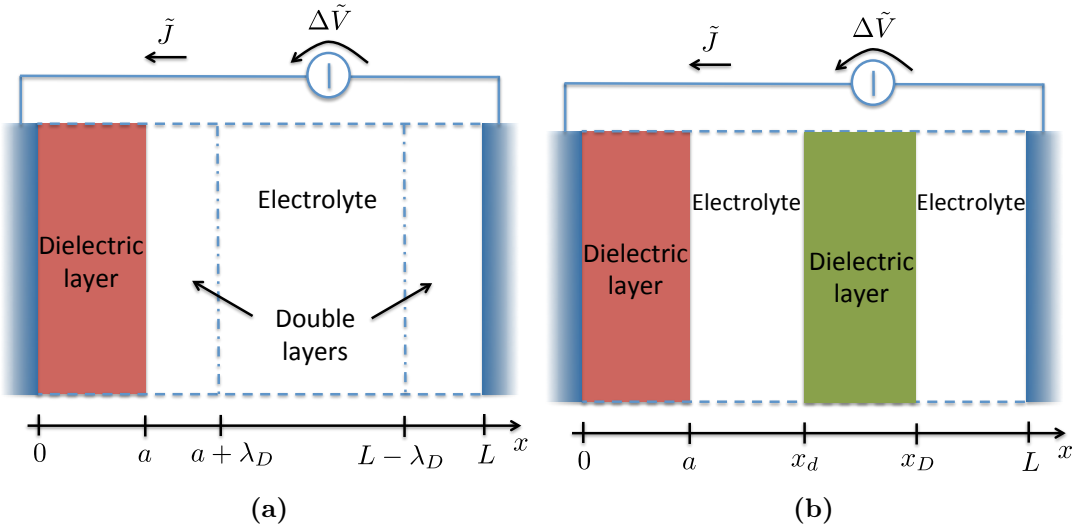

Fig 3.1: Sketch of the cartesian 1D models with and without a dielectric region between the electrodes. The red dielectric stands for a compact layer or a SAM. The green dielectric mimics a biomolecule floating in the electrolyte.

where $\tilde{V}$, $\tilde{n}_1$ and $\tilde{n}_2$ represent the complex small signal AC potential and ion concentrations respectively. Substituting the first equation into the others and isolating the term with the second derivatives we get:

$$\begin{cases} D_1 \dfrac{d^2\tilde{n}_1}{dx^2} = \left(\dfrac{Z_1^2 q^2}{\varepsilon_{el}} \mu_1 n_{01} + j\omega \right) \tilde{n}_1 + \dfrac{Z_1 Z_2 q^2}{\varepsilon_{el}} \mu_1 n_{01} \tilde{n}_2 \\ D_2 \dfrac{d^2\tilde{n}_2}{dx^2} = \left(\dfrac{Z_2^2 q^2}{\varepsilon_{el}} \mu_2 n_{02} + j\omega \right) \tilde{n}_2 + \dfrac{Z_1 Z_2 q^2}{\varepsilon_{el}} \mu_2 n_{02} \tilde{n}_1 \end{cases} . \tag{3.2}$$

We can define a 2×2 matrix $\mathbf{B}$ and cast the system of equations in the form:

$$\frac{d^2\tilde{\mathbf{n}}}{dx^2} = \mathbf{B}\,\tilde{\mathbf{n}} \quad \Longleftrightarrow \quad \frac{d^2}{dx^2} \begin{bmatrix} \tilde{n}_1 \\ \tilde{n}_2 \end{bmatrix} = \begin{bmatrix} a_1 & a_2 \\ b_1 & b_2 \end{bmatrix} \begin{bmatrix} \tilde{n}_1 \\ \tilde{n}_2 \end{bmatrix} \tag{3.3}$$

where:

$$\begin{cases} a_1 = \dfrac{1}{D_1} \left(\dfrac{Z_1^2 q^2}{\varepsilon_{el}} \mu_1 n_{01} + j\omega \right) \\ a_2 = \dfrac{Z_1 Z_2 q^2}{\varepsilon_{el}} \dfrac{1}{D_1} \mu_1 n_{01} \\ b_1 = \dfrac{Z_1 Z_2 q^2}{\varepsilon_{el}} \dfrac{1}{D_2} \mu_2 n_{02} \\ b_2 = \dfrac{1}{D_2} \left(\dfrac{Z_2^2 q^2}{\varepsilon_{el}} \mu_2 n_{02} + j\omega \right) \end{cases} . \tag{3.4}$$

To solve Eq. 3.3 we first need to decouple the two equations. To this end, we calculate the eigenvalues λ_1 and λ_2 of $\mathbf{B}$ from the characteristic equation:

$$(\lambda - a_1)(\lambda - b_2) - a_2 b_1 = \lambda^2 - (a_1 + b_2)\lambda + a_1 b_2 - a_2 b_1$$

$$\Delta = (a_1 + b_2)^2 - 4a_1 b_2 + 4a_2 b_1 = (a_1 - b_2)^2 + 4a_2 b_1 \tag{3.5}$$

$$\lambda_1 = \frac{a_1 + b_2 + \sqrt{\Delta}}{2}, \quad \lambda_2 = \frac{a_1 + b_2 - \sqrt{\Delta}}{2} . \tag{3.6}$$

The eigenvectors $\mathbf{T}_l$ are obtained as:

$$\mathbf{B}\mathbf{T}_l = \lambda_l \mathbf{T}_l \quad \Longrightarrow \quad \mathbf{T}_1 = \begin{bmatrix} 1 \\ \frac{\lambda_1 - a_1}{a_2} \end{bmatrix}, \; \mathbf{T}_2 = \begin{bmatrix} 1 \\ \frac{\lambda_2 - a_1}{a_2} \end{bmatrix}.$$

The system is then diagonalized defining the matrices $\mathbf{T}$, $\mathbf{\Lambda}$, $\mathbf{y}$:

$$\mathbf{T} = \begin{bmatrix} 1 & 1 \\ \frac{\lambda_1 - a_1}{a_2} & \frac{\lambda_2 - a_1}{a_2} \end{bmatrix}, \; \mathbf{\Lambda} = \begin{bmatrix} \lambda_1 & 0 \\ 0 & \lambda_2 \end{bmatrix}, \; \mathbf{y} = \mathbf{T}^{-1}\tilde{\mathbf{n}}\,. \tag{3.7}$$

We get then:

$$\frac{d^2\tilde{\mathbf{n}}}{dx^2} = \mathbf{B}\,\tilde{\mathbf{n}} \quad \Longleftrightarrow \quad \frac{d^2\tilde{\mathbf{n}}}{dx^2} = \mathbf{T}\,\mathbf{\Lambda}\,\mathbf{T}^{-1}\tilde{\mathbf{n}} \quad \Longleftrightarrow \quad \frac{d^2\mathbf{y}}{dx^2} = \mathbf{\Lambda}\,\mathbf{y}\,. \tag{3.8}$$

The solution for y is now straigthforward:

$$\begin{cases} \dfrac{d^2 y_1}{dx^2} = \lambda_1 y_1 \\ \dfrac{d^2 y_2}{dx^2} = \lambda_2 y_2 \end{cases} \quad \Longrightarrow \quad \begin{cases} y_1 = c_1 \exp(-\kappa_1 x) + d_1 \exp(\kappa_1 x) \\ y_2 = c_2 \exp(-\kappa_2 x) + d_2 \exp(\kappa_2 x) \end{cases} \tag{3.9}$$

where we have defined $\kappa_1^2 = \lambda_1$ and $\kappa_2^2 = \lambda_2$. The expressions for $\tilde{\mathbf{n}}$ are:

$$\tilde{\mathbf{n}} = \mathbf{T}\,\mathbf{y} = \begin{bmatrix} 1 & 1 \\ \frac{\kappa_1^2 - a_1}{a_2} & \frac{\kappa_2^2 - a_1}{a_2} \end{bmatrix} \begin{bmatrix} y_1 \\ y_2 \end{bmatrix} = \begin{bmatrix} y_1 + y_2 \\ \frac{\kappa_1^2 - a_1}{a_2} y_1 + \frac{\kappa_2^2 - a_1}{a_2} y_2 \end{bmatrix}$$

which is expanded as:

$$\begin{cases} \tilde{n}_1 = c_1 \exp(-\kappa_1 x) + d_1 \exp(\kappa_1 x) + c_2 \exp(-\kappa_2 x) + d_2 \exp(\kappa_2 x) \\ \tilde{n}_2 = \dfrac{\kappa_1^2 - a_1}{a_2} \left(c_1 \exp(-\kappa_1 x) + d_1 \exp(\kappa_1 x)\right) + \dfrac{\kappa_2^2 - a_1}{a_2} \left(c_2 \exp(-\kappa_2 x) + d_2 \exp(\kappa_2 x)\right) \end{cases}. \tag{3.10}$$

Substitution of these expressions for $\tilde{n}_1$ and $\tilde{n}_2$ into Eq. 3.1 yields:

$$\begin{aligned} -\frac{\varepsilon_{el}}{q}\frac{d^2\tilde{V}}{dx^2} = {} & Z_1 \left[c_1 \exp(-\kappa_1 x) + d_1 \exp(\kappa_1 x) + c_2 \exp(-\kappa_2 x) + d_2 \exp(\kappa_2 x)\right] \\ & + Z_2 \left[\frac{\kappa_1^2 - a_1}{a_2} \left(c_1 \exp(-\kappa_1 x) + d_1 \exp(\kappa_1 x)\right)\right. \\ & \left. + \frac{\kappa_2^2 - a_1}{a_2} \left(c_2 \exp(-\kappa_2 x) + d_2 \exp(\kappa_2 x)\right)\right] \end{aligned} \tag{3.11}$$

and eventually allows us to write the general form of the solution $\tilde{V}(x)$ as:

$$\begin{aligned} -\frac{\varepsilon_{el}}{q}\tilde{V} = {} & \frac{1}{\kappa_1^2}\left(Z_1 + Z_2\frac{\kappa_1^2 - a_1}{a_2}\right)\left(c_1 \exp(-\kappa_1 x) + d_1 \exp(\kappa_1 x)\right) \\ & + \frac{1}{\kappa_2^2}\left(Z_1 + Z_2\frac{\kappa_2^2 - a_1}{a_2}\right)\left(c_2 \exp(-\kappa_2 x) + d_2 \exp(\kappa_2 x)\right) + l_1 x + l_2\,. \end{aligned} \tag{3.12}$$

We note that, in addition to exponentially decaying terms with two different decay lengths $1/\kappa_1$ and $1/\kappa_2$, Eq. 3.12 contains terms that are linear in x. As we will see in Sec. 3.1.1.3, these terms play an important role especially at high frequency.

Boundary conditions To calculate the integration constants c_1, c_2, d_1, d_2, l_1 and l_2 we impose the boundary conditions $\tilde{J}_1(0) = \tilde{J}_2(0) = 0$, $\tilde{J}_1(L) = \tilde{J}_2(L) = 0$ (where $\tilde{J}_m(x)$ denotes the AC current of ion m at point x) corresponding to zero ionic current density at the ideally polarizable electrodes and $\tilde{V}(0) = \tilde{V}_B$, $\tilde{V}(L) = \tilde{V}_T$. Remembering the small signal ionic current expression (see Eq. 2.37b) written in terms of electric potential $\tilde{V}$ and concentrations $\tilde{n}_m$:

$$\tilde{J}_m = -Z_m^2 q^2 \mu_m n_{0m} \frac{d\tilde{V}}{dx} - Z_m q D_m \frac{d\tilde{n}_m}{dx} \tag{3.13}$$

We can then write:

$$\begin{cases} -Z_1 q \mu_1 n_{01} \dfrac{d\tilde{V}}{dx}\Big|_0 - D_1 \dfrac{d\tilde{n}_1}{dx}\Big|_0 = 0 \\ -Z_2 q \mu_2 n_{02} \dfrac{d\tilde{V}}{dx}\Big|_0 - D_2 \dfrac{d\tilde{n}_2}{dx}\Big|_0 = 0 \\ -Z_1 q \mu_1 n_{01} \dfrac{d\tilde{V}}{dx}\Big|_L - D_1 \dfrac{d\tilde{n}_1}{dx}\Big|_L = 0 \\ -Z_2 q \mu_2 n_{02} \dfrac{d\tilde{V}}{dx}\Big|_L - D_2 \dfrac{d\tilde{n}_2}{dx}\Big|_L = 0 \\ \tilde{V}(0) = \tilde{V}_B \\ \tilde{V}(L) = \tilde{V}_T \end{cases} \tag{3.14}$$

where

$$\begin{aligned} \frac{d\tilde{V}}{dx} = &-\frac{q}{\varepsilon_{el}} \left[\frac{1}{\kappa_1} \left(Z_1 + Z_2 \frac{\kappa_1^2 - a_1}{a_2} \right) \left(-c_1 \exp\left(-\kappa_1 x\right) + d_1 \exp\left(\kappa_1 x\right) \right) \right. \\ &\left. + \frac{1}{\kappa_2} \left(Z_1 + Z_2 \frac{\kappa_2^2 - a_1}{a_2} \right) \left(-c_2 \exp\left(-\kappa_2 x\right) + d_2 \exp\left(\kappa_2 x\right) \right) + l_1 \right] \end{aligned} \tag{3.15}$$

$$\frac{d\tilde{n}_1}{dx} = \kappa_1 \left(-c_1 \exp\left(-\kappa_1 x\right) + d_1 \exp\left(\kappa_1 x\right) \right) + \kappa_2 \left(-c_2 \exp\left(-\kappa_2 x\right) + d_2 \exp\left(\kappa_2 x\right) \right) \tag{3.16}$$

$$\begin{aligned} \frac{d\tilde{n}_2}{dx} = &\frac{\kappa_1^2 - a_1}{a_2} \kappa_1 \left(-c_1 \exp\left(-\kappa_1 x\right) + d_1 \exp\left(\kappa_1 x\right) \right) \\ &+ \frac{\kappa_2^2 - a_1}{a_2} \kappa_2 \left(-c_2 \exp\left(-\kappa_2 x\right) + d_2 \exp\left(\kappa_2 x\right) \right) \end{aligned} \tag{3.17}$$

Symmetrical electrolyte In order to reduce the complexity, we simplify the above equations assuming that the electrolyte is 1:1 and symmetrical, that is, with equal ion mobilities, and that, as usual, Einstein relation holds. This means $Z_1 = -Z_2 = 1$, $D_1 = D_2$, $\mu_1 = \mu_2$, $n_{01} = n_{02}$. In this section we will always make use of these assumptions. As a consequence the elements of the **B** matrix in Eq. 3.7 are:

$$\begin{cases} a_1 = \dfrac{1}{D} \left(\dfrac{q^2}{\varepsilon_{el}} \mu n_0 + j\omega \right) \\ a_2 = -\dfrac{q^2}{\varepsilon_{el}} \dfrac{1}{D} \mu n_0 \\ b_1 = a_2 \\ b_2 = a_1 \end{cases} .$$

Denoting $\Delta = 4a_2^2 = \frac{q^4}{\varepsilon_{el}^2}\frac{4}{D^2}\mu^2 n_0^2$, we then obtain:

$$\begin{cases} \kappa_1^2 = a_1 + \dfrac{\sqrt{\Delta}}{2} = a_1 + |a_2| \\ \kappa_2^2 = a_1 - \dfrac{\sqrt{\Delta}}{2} = a_1 - |a_2| \end{cases} \implies \begin{cases} \dfrac{\kappa_1^2 - a_1}{a_2} = \dfrac{|a_2|}{a_2} = -1 \\ \dfrac{\kappa_2^2 - a_1}{a_2} = \dfrac{-|a_2|}{a_2} = 1 \end{cases}, \ \mathbf{T} = \begin{bmatrix} 1 & 1 \\ -1 & 1 \end{bmatrix}$$

The expressions for the solutions become:

$$\tilde{V} = -\frac{q}{\varepsilon_{el}}\left[\frac{2}{\kappa_1^2}\left(c_1\exp\left(-\kappa_1 x\right) + d_1\exp\left(\kappa_1 x\right)\right) + l_1 z + l_2\right] \tag{3.18a}$$

$$\tilde{n}_1 = c_1\exp\left(-\kappa_1 x\right) + d_1\exp\left(\kappa_1 x\right) + c_2\exp\left(-\kappa_2 x\right) + d_2\exp\left(\kappa_2 x\right) \tag{3.18b}$$

$$\tilde{n}_2 = -\left(c_1\exp\left(-\kappa_1 x\right) + d_1\exp\left(\kappa_1 x\right)\right) + \left(c_2\exp\left(-\kappa_2 x\right) + d_2\exp\left(\kappa_2 x\right)\right) \tag{3.18c}$$

.

Straightforward but lengthy calculations (see Sec. 3.A.1 in the chapter appendix) eventually lead to the conclusion that $c_2 = d_2 = 0$, so that the only eigenvalue left is $\kappa = \kappa_1$. The solutions are then expressed as:

$$\begin{cases} \tilde{V} = -\dfrac{q}{\varepsilon_{el}}\left[\dfrac{2}{\kappa^2}\dfrac{\tilde{V}_T - \tilde{V}_B}{\beta - \delta - (\beta+\delta)\alpha}\left(e^{-\kappa x} - \alpha e^{\kappa x}\right) + l_1 x + l_2\right] \\ \tilde{n}_1 = \dfrac{\tilde{V}_T - \tilde{V}_B}{\beta - \delta - (\beta+\delta)\alpha}\left(e^{-\kappa x} - \alpha e^{\kappa x}\right) \\ \tilde{n}_2 = -\dfrac{\tilde{V}_T - \tilde{V}_B}{\beta - \delta - (\beta+\delta)\alpha}\left(e^{-\kappa x} - \alpha e^{\kappa x}\right) = -\tilde{n}_1 \end{cases} \tag{3.19}$$

with the parameters:

$$\begin{cases} \kappa^2 = 2\dfrac{q}{k_B T}\dfrac{q}{\varepsilon_{el}}n_0 + j\dfrac{\omega}{D} \\ \alpha = e^{-\kappa L} \\ \beta = \dfrac{q}{\varepsilon_{el}}\dfrac{4}{\kappa^2} \\ \delta = \dfrac{L}{q\mu n_0}v_d \\ v_d = q\mu n_0\dfrac{q}{\varepsilon_{el}}\dfrac{2}{\kappa} - D\kappa \\ l_1 = \dfrac{\varepsilon_{el}}{q}\dfrac{1}{q\mu n_0}v_d\left(\tilde{V}_T - \tilde{V}_B\right)\dfrac{\alpha+1}{\beta - \delta - (\beta+\delta)\alpha} \\ l_2 = \dfrac{2}{\kappa^2}\left(\tilde{V}_T - \tilde{V}_B\right)\dfrac{\alpha - 1}{\beta - \delta - (\beta+\delta)\alpha} - \dfrac{\varepsilon_{el}}{q}\tilde{V}_B \end{cases} . \tag{3.20}$$

The total current density can then be calculated knowing that:

$$\tilde{J}(x) = \frac{\partial \vec{D}}{\partial t} + \sum_{m=1}^{N_{ions}}\vec{\tilde{J}}_m = -j\omega\varepsilon_{el}\frac{d\tilde{V}}{dx} + \sum_{m=1}^{N_{ions}}\tilde{J}_m \tag{3.21}$$

where:

$$\tilde{J}_m = -Z_m^2 q^2 \mu_m n_{0m} \frac{d\tilde{V}}{dx} - Z_m q D_m \frac{d\tilde{n}_m}{dx} \tag{3.22}$$

$$\frac{d\tilde{V}}{dx} = \frac{\tilde{V}_T - \tilde{V}_B}{\beta - \delta - (\beta+\delta)\alpha} \left[\frac{q}{\varepsilon_{el}} \frac{2}{\kappa} \left(e^{-\kappa x} + \alpha e^{\kappa x} \right) - \left(\frac{q}{\varepsilon_{el}} \frac{2}{\kappa} - \frac{D\kappa}{q\mu n_0} \right) (\alpha + 1) \right] \tag{3.23}$$

$$\frac{d\tilde{n}_1}{dx} = -\kappa \frac{\tilde{V}_T - \tilde{V}_B}{\beta - \delta - (\beta+\delta)\alpha} \left(e^{-\kappa x} + \alpha e^{\kappa x} \right) \tag{3.24}$$

$$\frac{d\tilde{n}_2}{dx} = \kappa \frac{\tilde{V}_T - \tilde{V}_B}{\beta - \delta - (\beta+\delta)\alpha} \left(e^{-\kappa x} + \alpha e^{\kappa x} \right) . \tag{3.25}$$

Note that, with this definition, the current is taken positive when flowing in the x direction, that is from the left to the right electrode in Fig. 3.1. As expected since Eqs. 3.1 are conservation equations, the currents at the electrodes are equal ($\tilde{J}_1 = \tilde{J}_2$), so that at any position x Eq. 3.21 becomes:

$$\begin{aligned}
\tilde{J}(x) &= -j\omega\varepsilon_{el} \frac{d\tilde{V}}{dx} - 2q^2 \mu n_0 \frac{d\tilde{V}}{dx} + 2qD\kappa \frac{\tilde{V}_T - \tilde{V}_B}{\beta - \delta - (\beta+\delta)\alpha} \left(e^{-\kappa x} + \alpha e^{\kappa x} \right) \\
&= \frac{\Delta\tilde{V}}{\beta - \delta - (\beta+\delta)\alpha} \Bigg[\left(2q^2 \mu n_0 + j\omega\varepsilon_{el} \right) \left(\frac{q}{\varepsilon_{el}} \frac{2}{\kappa} \left(e^{-\kappa x} + \alpha e^{\kappa x} \right) - \left(\frac{q}{\varepsilon_{el}} \frac{2}{\kappa} - \frac{D\kappa}{q\mu n_0} \right) (\alpha + 1) \right) \\
&\quad - 2qD\kappa \left(e^{-\kappa x} + \alpha e^{\kappa x} \right) \Bigg] \\
&= \frac{\Delta\tilde{V}}{\beta - \delta - (\beta+\delta)\alpha} \Bigg[\left(e^{-\kappa x} + \alpha e^{\kappa x} \right) \left(q^2 \mu n_0 \frac{q}{\varepsilon_{el}} \frac{4}{\kappa} + j\omega q \frac{2}{\kappa} - 2qD\kappa \right) \\
&\quad - \left(2q^2 \mu n_0 + j\omega\varepsilon_{el} \right) \left(\frac{q}{\varepsilon_{el}} \frac{2}{\kappa} - \frac{D\kappa}{q\mu n_0} \right) (\alpha + 1) \Bigg]
\end{aligned}$$

where $\Delta\tilde{V} = \tilde{V}_B - \tilde{V}_T$. We can easily see that:

$$\begin{aligned}
\left(q^2 \mu n_0 \frac{q}{\varepsilon_{el}} \frac{4}{\kappa} + j\omega\varepsilon_{el} \frac{q}{\varepsilon_{el}} \frac{2}{\kappa} - 2qD\kappa \right) &= \frac{1}{\kappa} \left(4q^2 \mu n_0 \frac{q}{\varepsilon_{el}} + 2j\omega q - 2qD\kappa^2 \right) \\
&= \frac{1}{\kappa} \left(4q^2 \mu n_0 \frac{q}{\varepsilon_{el}} + 2j\omega q - 4qD \frac{q}{k_B T} \frac{q}{\varepsilon_{el}} n_0 - 2qDj \frac{\omega}{D} \right) = 0
\end{aligned}$$

This means that:

$$\begin{aligned}
\tilde{J}(x) &= -\frac{\Delta\tilde{V}}{\beta - \delta - (\beta+\delta)\alpha} \left(2q^2 \mu n_0 + j\omega\varepsilon_{el} \right) \left(\frac{q}{\varepsilon_{el}} \frac{2}{\kappa} - \frac{D\kappa}{q\mu n_0} \right) (\alpha + 1) \\
&= j\omega\varepsilon_{el} \frac{\alpha + 1}{\beta - \delta - (\beta+\delta)\alpha} \frac{D\kappa}{q\mu n_0} \Delta\tilde{V}
\end{aligned} \tag{3.26}$$

This equation provides an explicit expression of the AC admittance per unit area $y_{tot} = \tilde{J}/\Delta\tilde{V}$ of a slab of electrolyte. We use the symbol y and not the usual Y for the admittance in order to point out that, in this section, we are always referring to admittances per unit area. Since the parameters' definition (Eq. 3.20) are rather obscure, we now first derive an equivalent formulation of this model and then show some results obtained with it.

3.1.1.1 Equivalent formulation

We derive an equivalent formulation of the former model, which is useful to get a physical understanding of the phenomena. As a first step we make the substitution:

$$\boxed{\xi := 2\pi f_c := \frac{2q^2\mu n_0}{\varepsilon_{el}} = \frac{2q^2 D n_0}{\varepsilon_{el} k_B T}}. \tag{3.27}$$

Since the electrolyte conductivity is $\sigma_{el} = 2q^2\mu n_0$, we immediately note that ξ is the electrolyte dielectric's relaxation angular cut-off frequency $\sigma_{el}/\varepsilon_{el}$. Note that ξ, hence the corresponding cut-off frequency $f_c = \xi/2\pi$, is directly proportional to the salt concentration n_0. It follows:

$$\kappa^2 = \frac{\xi + j\omega}{D}, \qquad \kappa = \pm\frac{\xi + \sqrt{\xi^2+\omega^2} + j\omega}{\sqrt{2D}\sqrt{\xi + \sqrt{\xi^2+\omega^2}}}. \tag{3.28}$$

As expected, the decay length $1/\kappa$ at $\omega = 0$ is exactly the well-known Debye length [36] λ_D:

$$\boxed{\lambda_D = \frac{1}{\kappa(\omega=0)} = \sqrt{\frac{D}{\xi}} = \sqrt{\frac{\varepsilon_{el} k_B T}{2q^2 n_0}}}. \tag{3.29}$$

We can then write an alternative expression for κ by calling $\tau = \varepsilon_{el}/\sigma$ the electrolyte's relaxation time:

$$\kappa^2 = \frac{1 + j\omega\tau}{\lambda_D^2}. \tag{3.30}$$

Once again, lengthy but straightforward calculations (see Sec. 3.A.2) lead us to the solution:

$$\tilde{V} = \tilde{V}_B - \frac{-\xi\left(e^{-\kappa x} - \alpha e^{\kappa x}\right) + j\omega\kappa\left(1+\alpha\right)x + \xi\left(1-\alpha\right)}{2\xi\left(1-\alpha\right) + j\omega\kappa L\left(1+\alpha\right)}\Delta\tilde{V} \tag{3.31a}$$

$$\tilde{n}_1 = -q\mu n_0\kappa^2 \frac{\Delta\tilde{V}}{2\xi\left(1-\alpha\right) + j\omega\kappa L\left(1+\alpha\right)}\left(e^{-\kappa x} - \alpha e^{\kappa x}\right) \tag{3.31b}$$

$$\tilde{n}_2 = -\tilde{n}_1 \tag{3.31c}$$

$$\tilde{J} = j\omega\varepsilon_{el}\frac{D\kappa^3\left(\alpha+1\right)}{2\xi\left(1-\alpha\right) + j\omega\kappa L\left(1+\alpha\right)}\Delta\tilde{V}. \tag{3.31d}$$

Eqs. 3.31 represent an exact analytical model of the response of the electrolyte to AC small signal stimuli. In particular, Eq. 3.31d is an exact alternative formulation of Eq. 3.26.

We now rewrite the term $\alpha = \rho e^{j\theta}$ using the cartesian representation:

$$\begin{aligned}\alpha = e^{-\kappa L} &= \pm\frac{\rho}{\sqrt{1-\tan(\theta)^2}}\left(1 + j\tan(\theta)\right) \\ &= \pm\frac{\exp\left(-L\sqrt{\frac{\xi+\sqrt{\xi^2+\omega^2}}{2D}}\right)}{\sqrt{1-\tan\left(L\frac{j\omega}{\sqrt{2D}\sqrt{\xi+\sqrt{\xi^2+\omega^2}}}\right)^2}}\left[1 + j\tan\left(L\frac{j\omega}{\sqrt{2D}\sqrt{\xi+\sqrt{\xi^2+\omega^2}}}\right)\right]\end{aligned}$$

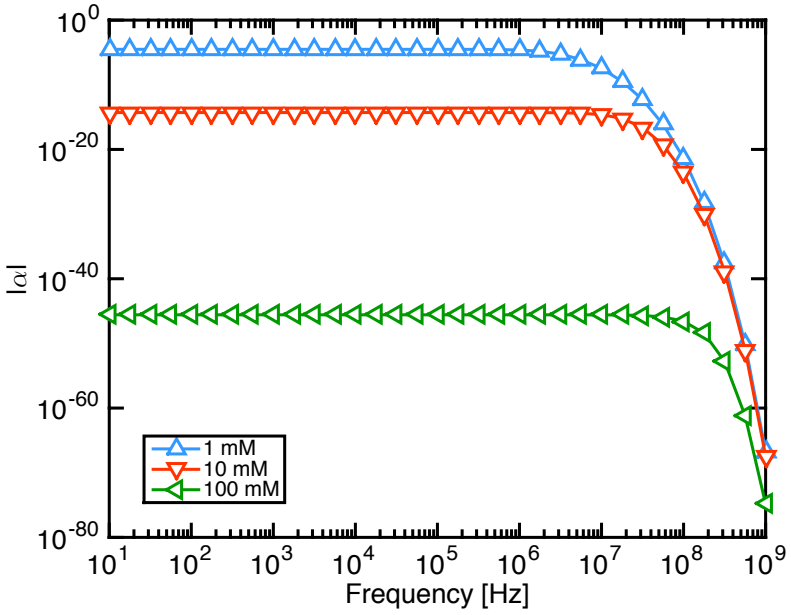

Fig 3.2: Frequency spectra of $|\alpha|$ at different salt concentrations for $L = 100$ nm, ion mobility $\mu = 3.24 \times 10^{11}$ m/Ns, temperature $T = 298$ K and electrolyte permittivity calculated via Eq. 2.39.

From this expression and its representation in Fig. 3.2, we immediately note that the modulus of $\alpha = \exp(-\kappa L)$, that is $|\rho|$, is much smaller than 1 at all frequencies and in practice very close to zero, both at high and low frequency, since the distance L is in practical cases always much larger than the Debye length $\lambda_D = \sqrt{D/\xi}$ (see Fig. 3.2). Assuming then a large domain compared to the Debye length λ_D, i.e. $L/\lambda_D \gg 1$, Eq. 3.31d simplifies to:

$$\tilde{J} \simeq j\omega\varepsilon_{el}\frac{\kappa}{2\xi + j\omega\kappa L}(\xi + j\omega)\,\Delta\tilde{V} \tag{3.32}$$

which provides a compact approximate expression of the bulk electrolyte admittance per unit area $y = \tilde{J}/\Delta\tilde{V}$. The expression assumes two non-Faradaic contacts and accounts for two AC electrical double layers. Current density spectra calculated with Eq. 3.31d are shown in Sec. 4.5.1, when discussing the validation of the numerical solver ENBIOS (in particular Fig. 4.7).

Results We now show some results obtained with the model of Eqs. 3.31. The parameters are given in Tab. 3.1, if not differently specified. The relevant parameter to describe the build-up of space charge regions at the electrodes and the screening is the real part of κ, which gives the attenuation of the AC concentrations in the electrolyte. We define the real part of κ as the inverse AC screening length and denote it with $1/L_S$. Recalling Eq. 3.30, its expression is:

$$\frac{1}{L_S} = \Re(\kappa) = \frac{1}{\lambda_D}\sqrt{\frac{1+\sqrt{1+\omega^2\tau^2}}{2}}\,. \tag{3.33}$$

Let us now go back to the more general case of a non-symmetric but still 1:1 electrolyte, therefore letting $\mu_1 \neq \mu_2$. Since the mobility is the only parameter that changed from the

Parameter	Symbol	Value	Units
System length	L	200	[nm]
Mobility of Na^+	μ_1	$3.242 \cdot 10^{11}$	[m/Ns]
Mobility of Cl^-	μ_2	$4.937 \cdot 10^{11}$	[m/Ns]
Temperature	T	307.66	[K]

Table 3.1: Parameters used in the calculations with the 1D analytical model.

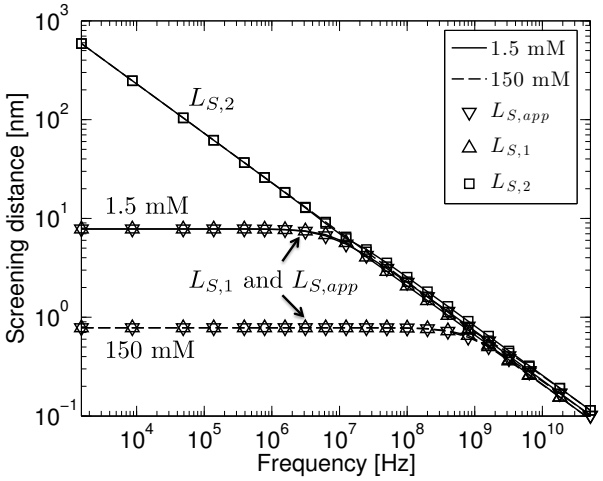

Fig 3.3: Characteristic screening length for a NaCl-water electrolyte, calculated using either Eq. 3.33 or the exact expression Eq. 3.34 for different salt concentrations. The electrolyte parameters are reported in Tab. 3.1 and the diffusion coefficients are calculated via the Einstein relation.

previous case, the Debye length remains unaffected. As seen at the beginning of Sec. 3.1, there are now two characteristic parameters κ_1 and κ_2:

$$\kappa_{1,2}^2 = \lambda_D^{-2} \frac{1 + j\omega(\tau_1 + \tau_2) \pm \sqrt{1 - \omega^2(\tau_1 - \tau_2)^2}}{2} \tag{3.34}$$

where the + sign is used for κ_1, the − for κ_2, $\tau_1 = 1/\lambda_D^2 D_1$ and $\tau_2 = 1/\lambda_D^2 D_2$. Thus, it is not possible to derive simple analytical expressions for the screening lengths as in the simplified case. We note, however, that κ_1 has a similar expression as κ in Eq. 3.30, but with an effective diffusivity $2/D_{eff} = 1/D_1 + 1/D_2$ and a small correction factor $1 - \sqrt{1 - \omega^2(\tau_1 - \tau_2)^2}$. We can also observe that κ_2 is almost purely imaginary if the diffusion coefficients are similar. A simple, approximated, expression for the first screening length ($\Re(1/\kappa_1)$) can be found introducing in Eq. 3.33 the effective diffusivity D_{eff} defined above. We denote this approximated screening length $L_{S,app}$ and the exact ones $L_{S,1} = 1/\Re(\kappa_1)$, $L_{S,2} = 1/\Re(\kappa_2)$. Fig. 3.3 shows $L_{S,1}$ and $L_{S,2}$ for an electrolyte made of NaCl in water as a function of the frequency and for different salt molar concentrations (as usual in electrochemistry).
It is interesting to note that Eq. 3.33 approximates very accurately $L_{S,1}$, and that $L_{S,1}$ is always shorter than $L_{S,2}$. This means that the limiting screening effect for detection is governed by $L_{S,1}$. If we now remember the definition of the electrolyte cut-off frequency $f_c = \xi/2\pi = 1/2\pi\tau$, then we note that $L_{S,1}$ decreases for $f > f_c$, meaning that the AC double-layer thickness becomes infinitesimal.

Having understood that the electrolyte asymmetry is not so relevant, we then go back to the case of a symmetric electrolyte. Fig. 3.4 shows the AC concentration profile near one of the electrodes of a system as in Fig. 3.1 for a 10 mM electrolyte at two different

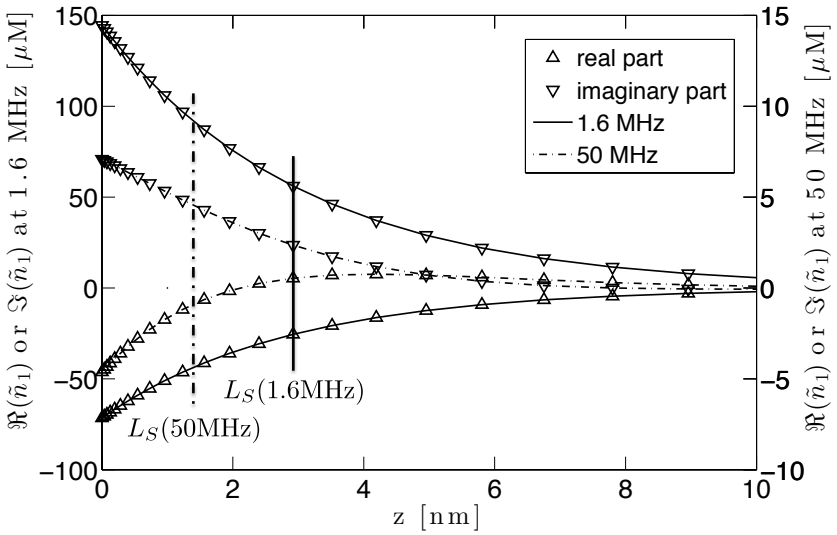

Fig 3.4: Real and imaginary part of the AC concentration of positive ions $\tilde{n}_1$ at 1.6 MHz (left axis) and 50 MHz (right axis). The ion concentration is 10 mM and the mobility is $3.242 \cdot 10^{11}$ m/Ns. $\Re(\tilde{n}_1) < 0$ because the electrode AC potential is positive.

frequencies together with the corresponding values of L_S. The low frequency (1.6 MHz) is in the range where $L_S \approx \lambda_D$ while the high frequency (50 MHz) is chosen to make $\omega\tau$ sufficiently greater than 1. We can then equivalently say that the low frequency is chosen to be sufficiently lower than $f_c = 23$ MHz and the high frequency to be sufficiently higher than f_c.
The screening parameter L_S plays for AC signals the same role as the static Debye length in DC conditions. In fact, as the frequency increases, L_S becomes shorter and the small-signal concentrations become smaller. Consequently, the AC electric double layer becomes thinner and the AC field penetrates into the electrolyte. This means that for increasing frequency the concentration variations become smaller and occupy a progressively thinner surface layer, until they become negligible, while the AC potential exhibits a linear dependence on the space due to the linear and constant terms in Eq. 3.31 (see Fig. 3.5). This in turn means that the electrolyte screening effect becomes negligible, therefore not limiting the detection sensitivity anymore.

3.1.1.2 Double layer admittance

In this section we derive lumped element circuit models for the admittance per unit area between the electrodes $y_{tot} = \tilde{J}/\Delta\tilde{V}$, where $\tilde{J}$ is calculated with Eq. 3.32, that assumes $L \gg \lambda_D$. Consistently with the 1D nature of the model, we will always use admittances, y, capacitances, c, and conductances, g, per unit area and denote them with lower case letters.

Parallel model The total admittance between the two ideally polarizable electrodes can be modelled by the parallel of the bulk electrolyte capacitance ($c_E = \varepsilon_{el}/L$) and the series of the bulk electrolyte conductance ($g_E = \xi\varepsilon_{el}/L$) with the double layer admittances at the two electrodes (y^P_{DL}, Fig. 3.6, left) as:

$$y_{tot} = \frac{g_E y^P_{DL}}{2g_E + y^P_{DL}} + j\omega c_E \tag{3.35}$$

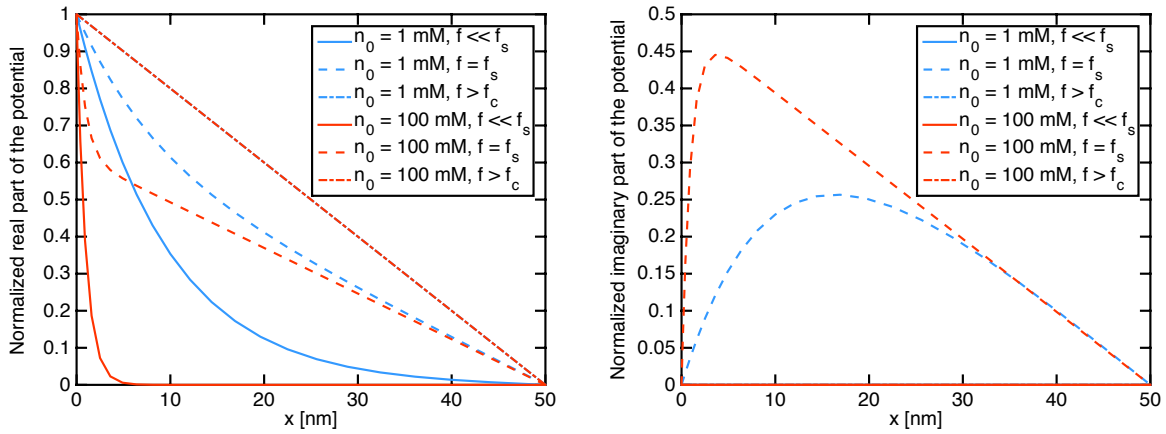

(a) real part **(b)** imaginary part

Fig 3.5: Real and imaginary parts of the normalized potential profile $\tilde{V}/\Delta\tilde{V}$ near the electrode with $L = 100$ nm at three different frequencies, that is, below f_s, at f_s and above f_c, where f_s is defined in Sec. 3.9. Note the penetration of the field at high frequency.

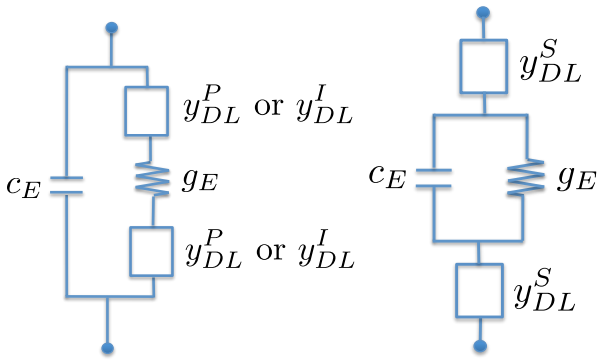

Fig 3.6: Sketch of the equivalent circuit models for the double layer admittance: parallel and integral models (left), series model (right).

By assuming again $L \gg \lambda_D$, we derive from Eq. 3.32:

$$y^P_{DL} = j\omega\varepsilon_{el}\frac{\kappa L - 2}{L}\frac{\xi}{\xi + j\omega} \simeq j\omega\varepsilon_{el}\kappa\frac{\xi}{\xi + j\omega} \tag{3.36}$$

Note that, as expected, the limit of y^P_{DL} for $\omega = 0$ yields the well-know linearized double layer capacitance [36] $c_{DL} = \varepsilon_{el}/\lambda_D$.

Series model Denoting now the high frequency admittance $y_H = g_E + j\omega c_E$, an alternative model is composed by the series of y_H and of the double layer admittance at the two electrodes (y^S_{DL}), Fig. 3.6:

$$\frac{1}{y_{tot}} = \frac{2}{y^S_{DL}} + \frac{1}{y_H} \tag{3.37}$$

We then derive:

$$y^S_{DL} = j\omega\varepsilon_{el}\kappa\frac{\xi + j\omega}{\xi} \tag{3.38}$$

Note that again, as expected, the limit of y^S_{DL} for $\omega = 0$ is the double layer capacitance $c_{DL} = \varepsilon_{el}/\lambda_D$.

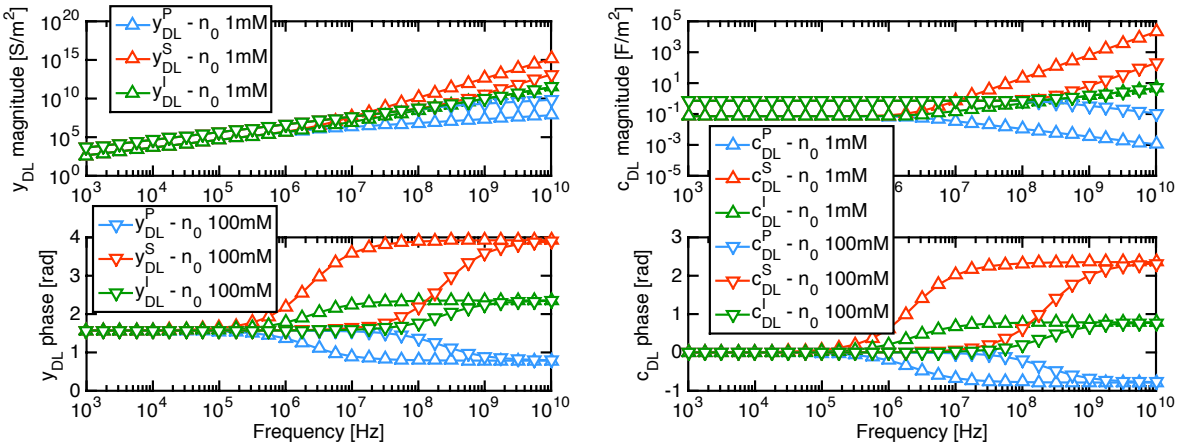

Fig 3.7: Double layer admittance spectra and corresponding generalized double layer capacitance $c_{DL} = y_{DL}/j\omega$ calculated according to the three models in Fig. 3.6 and for a few salt concentrations.

Integral model We also derive a third model of the double layer admittance (y^I_{DL}) calculated by direct integration of the AC charge. Since the system contains two symmetrical double layers, we compute the AC EDL charge per unit area at one electrode $\tilde{\sigma}_{DL}$ integrating the mobile charge in the bottom half domain, using Eq. 3.31:

$$\begin{aligned}\tilde{\sigma}_{DL} &= \int_0^{L/2} q(\tilde{n}_1 - \tilde{n}_2)dx = 2q\int_0^{L/2} \tilde{n}_1 dx \\ &= -2q^2\mu n_0\kappa^2 \frac{\Delta\tilde{V}}{2\xi\,(1-\alpha) + j\omega\kappa L\,(1+\alpha)} \int_0^{L/2} \left(e^{-\kappa x} - \alpha e^{\kappa x}\right) dx \\ &\simeq -\varepsilon_{el}\kappa \frac{\xi}{2\xi + j\omega\kappa L}\Delta\tilde{V} \end{aligned} \tag{3.39}$$

where we have assumed again $L \gg \lambda_D$. The calculated admittance is then:

$$y_I = -j\omega\frac{d\tilde{\sigma}_{DL}}{d\Delta\tilde{V}} = j\omega\varepsilon_{el}\kappa\frac{\xi}{2\xi + j\omega\kappa L} \tag{3.40}$$

Note that if we assume that the bulk electrolyte capacitance is in parallel with y_I, as we did for the parallel model, we get:

$$y_I + j\omega c_E = j\omega\varepsilon_{el}\frac{\xi\kappa L + 2\xi + j\omega\kappa L}{(2\xi + j\omega\kappa L)\,L} \simeq j\omega\varepsilon_{el}\kappa\frac{\xi + j\omega}{2\xi + j\omega\kappa L} = y_{tot}$$

i.e., we find the admittance y_{tot}, as expected.
To find the double layer admittance we assume that y_I is composed by the series of two y^I_{DL} and the bulk electrolyte conductance g_E. We obtain:

$$y^I_{DL} = -2\frac{g_E y_I}{y_I - g_E} = j\omega\varepsilon_{el}\kappa \tag{3.41}$$

Once again the limit of y^I_{DL} for $\omega = 0$ is the double layer capacitance c_{DL}.

Fig. 3.7 compares the three different models for the double layer admittance and capacitance c_{DL} with the equivalent circuits of Fig. 3.6. The models are all equivalent to each other at low frequency, as expected, where c_{DL} increases considerably with salt

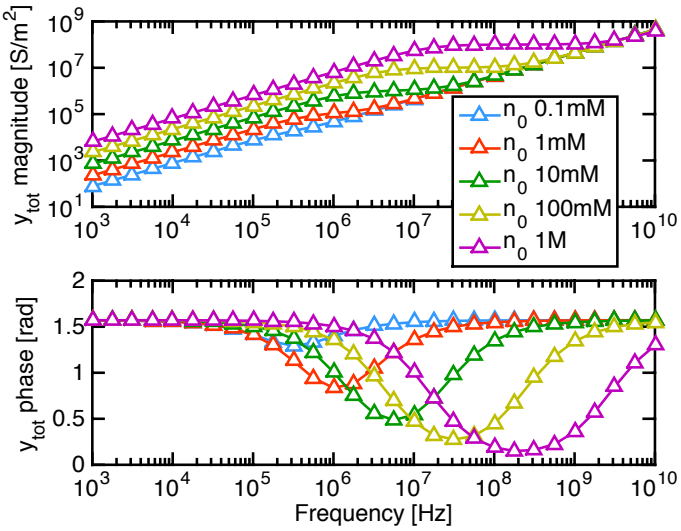

Fig 3.8: Admittance spectra between the electrodes y_{tot} as a function of salt concentration with $L = 100$ nm.

concentration. In contrast, the models tend to diverge for $f > f_c$, where they provide a negligible contribution to y_{tot}.
As a final remark, we note that the expressions 3.36 ,3.38, 3.41 for y_{DL} are different from each other, pointing out fact that the choice of equivalent circuits for the electrolyte region is not unique. The existence of different models is consistent with the approximation $L \gg \lambda_D$, which entails that the exact behaviour of Y_{DL} for $\omega > \xi$ is not so important and leaves freedom for different choices. All the proposed models comprise at least one element with anomalous (not rational) frequency dependence. For instance in the model of Eq. 3.36 at high frequency the dependence of y_{DL} is on $\omega^{\frac{1}{2}}$, while for Eq. 3.38 it is on $\omega^{\frac{5}{2}}$ and for Eq. 3.41 on $\omega^{\frac{3}{2}}$. This means that they cannot be represented by equivalent circuits made of conventional linear resistors or capacitors.

3.1.1.3 Cut off frequencies

Having discussed the double layer admittance models, we can now come back to understand the total admittance y_{tot} between the electrodes calculated using Eq. 3.31. The ion mobility in this section is $\mu = 3.24 \times 10^{11}$ m/Ns, which is representative of common monovalent ions like Na^+, K^+ and Cl^- [52]. The results presented here are therefore representative also of a real 1:1 electrolyte, as for instance KCl.

Fig. 3.8 shows the spectra of y_{tot} varying the salt concentration with $L = 100$ nm. We immediately see that, despite the complicated dependencies on ω in Eq. 3.31, the curves in Fig. 3.8 seem fairly simple, all exhibiting two zeros (one in the origin) and one pole.

The identification of these critical frequencies is fairly simple. In fact, as evident from Eq. 3.31, the second zero frequency is just the dielectric relaxation's cut-off frequency $f_c = \xi/2\pi$. The pole frequency f_s is, instead:

$$\boxed{f_s = \frac{1}{2\pi}\frac{2\xi}{\kappa L} \simeq \frac{\xi}{\pi}\frac{\lambda_D}{L}} \tag{3.42}$$

where we have used the fact that, since $f_s < f_c$, $\kappa \simeq \lambda_D$. Note that we would have arrived to the same result if we had used for instance the series model for the double layer

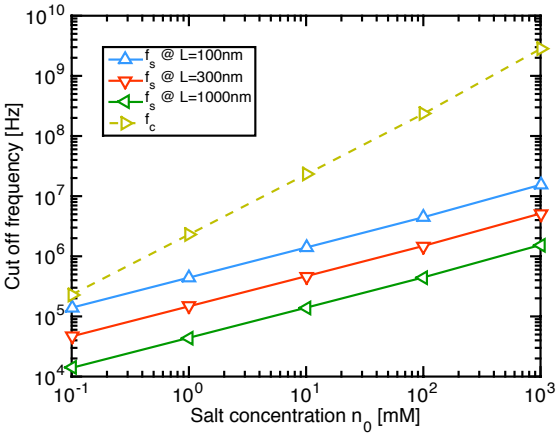

Fig 3.9: Cut off frequencies calculated with Eqs. 3.27 (f_c) and 3.42 (f_s) and ion mobility $\mu = 3.24 \times 10^{11}$ m/Ns.

admittance in Fig. 3.6b, approximating $y^S_{DL} \simeq c_{DL} = \varepsilon_{el}/\lambda_D$ and calculating:

$$f_s = \frac{1}{2\pi}\frac{c_{DL}/2 + c_E}{g_E}, \qquad f_c = \frac{1}{2\pi}\frac{c_E}{g_E}. \tag{3.43}$$

This fact proves the usefulness and validity of the circuit models for the double layer admittance developed above.

Fig. 3.9 shows the cut off frequencies f_s and f_c calculated with Eqs. 3.27-3.42. We immediately note the different dependence on salt concentration between f_s and f_c. Indeed while $f_c \propto n_0$, $f_s \propto \sqrt{n_o}$, but as we will see in the following (for instance in Sec. 3.1.2) this is a general property for f_c but not for f_s. In addition, we recognize that f_s is geometry dependent and it decreases if L increases.

Looking again at Fig. 3.8, we then easily see that for $f < f_s$ the double layer screening is dominant and y_{tot} is essentially given by the double layer capacitance c_{DL}. This means that anything that happens in the bulk electrolyte is not visible in this regime. The admittance only reflects perturbations at the surface of the electrode. Increasing the frequency in the range $f_s < f < f_c$ we overcome the screening and begin to probe the bulk electrolyte properties. However, we are still sensitive to the double layers and to the electrolyte conductivity. As we will see in Chap. 5, we are also very sensitive to free charges and in general to everything that can change the electrical properties of the space between the electrodes. Finally, for $f > f_c$ the screening is completely overcome, the electrical double layers disappear and we sense only the dielectric properties of the bulk electrolyte.

3.1.1.4 Electric field

As predicted in Sec. 3.3.6 and demonstrated in Sec. 5.4, under suitable approximations the response of a nanoelectrode biosensor is proportional to $\left(\tilde{E}_0(x)/\Delta\tilde{V}_0\right)^2$, where x is the position of the analyte, $\tilde{E}_0(x)$ the unperturbed electric field in the absence of the analyte and $\Delta\tilde{V}$ the applied potential at the electrodes. In fact, introduction of analytes in the domain perturbs the electric field and the corresponding electrostatic energy spatial density. We are thus interested in deriving an explicit expression of the electric field. From

Eq. 3.31 we get:

$$\tilde{E}_0 = -\frac{\partial \tilde{V}}{\partial x} = \kappa \frac{\xi\left(e^{-\kappa z} + \alpha e^{\kappa x}\right) + j\omega\left(1+\alpha\right)}{2\xi\left(1-\alpha\right) + j\omega\kappa L\left(1+\alpha\right)} \Delta\tilde{V}\,.$$

Therefore:

$$\left(\frac{\tilde{E}_0(x)}{\Delta\tilde{V}}\right)^2 = \left(\frac{\xi\left(e^{-\kappa x} + \alpha e^{\kappa x}\right) + j\omega\left(1+\alpha\right)}{2\xi\left(1-\alpha\right) + j\omega\kappa L\left(1+\alpha\right)}\right)^2 \kappa^2$$

Assuming again $L/\lambda_D \gg 1$, so that $\alpha \simeq 0$, we can then safely make the approximation:

$$\left(\frac{\tilde{E}_0(x)}{\Delta\tilde{V}}\right)^2 \simeq \left(\frac{\xi\left(e^{-\kappa x} + e^{\kappa(x-L)}\right) + j\omega}{2\xi + j\omega\kappa L}\right)^2 \kappa^2$$

where we have also substituted the expression for α. Similar considerations as above lead us to say that provided the point x we are looking at is far enough from the electrodes, we can approximate $\left(\tilde{E}_0(x)/\Delta\tilde{V}_0\right)^2$ as:

$$\begin{aligned}
\left(\frac{\tilde{E}_0}{\Delta\tilde{V}}\right)^2\Bigg|_{x=\infty} &\simeq \left(\frac{j\omega}{2\xi + j\omega\kappa L}\right)^2 \kappa^2 = -\frac{\omega^2}{4\xi^2 - \omega^2\kappa^2 L^2 + j4\xi\omega\kappa L}\kappa^2 \\
&= -\frac{\omega^2}{4\xi^2 - \omega^2\dfrac{\xi + j\omega}{D}L^2 + j4\xi\omega\dfrac{\eta + j\omega}{\sqrt{2D}\sqrt{\eta}}L}\frac{\xi + j\omega}{D} \\
&= -\frac{\omega^2\left(\xi + j\omega\right)\left(\xi\left(4D\xi - \omega^2L^2 - 4\omega^2\sqrt{\dfrac{D}{2\eta}}L\right) - j\omega L\left(-\omega^2 L + 4\xi\eta\sqrt{\dfrac{D}{2\eta}}\right)\right)}{\xi^2\left(4D\xi - \omega^2L^2 - 4\omega^2\sqrt{\dfrac{D}{2\eta}}L\right)^2 + \omega^2L^2\left(-\omega^2L + 4\xi\eta\sqrt{\dfrac{D}{2\eta}}\right)^2} \\
&= -\omega^2\Bigg[\xi^2\left(4D\xi - \omega^2L^2 - 4\omega^2\sqrt{\frac{D}{2\eta}}L\right) + \omega^2L\left(-\omega^2L + 4\xi\eta\sqrt{\frac{D}{2\eta}}\right) \\
&\quad - j4\omega\xi\left(-D\xi + \sqrt{\frac{D}{2\eta}}L\left(\omega^2 + \xi\eta\right)\right)\Bigg] \\
&\quad \Big/\left[\xi^2\left(4D\xi - \omega^2L^2 - 4\omega^2\sqrt{\frac{D}{2\eta}}L\right)^2 + \omega^2L^2\left(-\omega^2L + 4\xi\eta\sqrt{\frac{D}{2\eta}}\right)^2\right]
\end{aligned}$$

where the notation $x = \infty$ reminds that this expression is valid far from the electrodes and, for a compact expression, we have made the substitution:

$$\eta := \xi + \sqrt{\xi^2 + \omega^2} \tag{3.44}$$

As we will demonstrate in Sec. 5.4, the capacitive component of the biosensor response to particles far enough from the electrodes is proportional to the factor:

$$\begin{aligned}
\chi(\omega)|_{x=\infty} &= -\left\{\Re\left[\left(\frac{\tilde{E}_0}{\Delta\tilde{V}}\right)^2\Bigg|_{x=\infty}\right] + \frac{\xi}{\omega}\Im\left[\left(\frac{\tilde{E}_0}{\Delta\tilde{V}}\right)^2\Bigg|_{x=\infty}\right]\right\} \\
&\simeq \omega^2\frac{8D\xi^3 - \omega^2L^2\left(\xi^2 + \omega^2\right) - 4\xi\sqrt{\dfrac{D}{2\eta}}L\left(2\xi\omega^2 + \eta\left(\xi^2 - \omega^2\right)\right)}{\xi^2\left(4D\xi - \omega^2L^2 - 4\omega^2\sqrt{\dfrac{D}{2\eta}}L\right)^2 + \omega^2L^2\left(-\omega^2L + 4\xi\eta\sqrt{\dfrac{D}{2\eta}}\right)^2}
\end{aligned} \tag{3.45}$$

where we have used the fact that the DC conductivity of the electrolyte is $\sigma_{el} = \xi\varepsilon_{el}$. We note also that the Debye length is $\lambda_D = \sqrt{D/\xi}$, which means that $\sqrt{D/\eta} \leq \lambda_D$ for every ω. In particular we then see that $\sqrt{D/2\eta} \ll L$, so we can neglect terms in $\sqrt{D/2\eta}$ in Eq. 3.45 and obtain:

$$\chi(\omega)|_{x=\infty} \simeq \omega^2 \frac{8D\xi^3 - \omega^2 L^2\left(\xi^2+\omega^2\right)}{\xi^2\left(4D\xi - \omega^2L^2\right)^2 + \omega^6L^4}\,.$$

We attempt to identify optimum frequencies for maximum or minimum response from the condition:

$$\left.\frac{d\chi}{d\omega}\right|_{x=\infty} \simeq 32D^2\xi^4\omega \frac{8D\xi^3 - 2\xi^2L^2\omega^2 - 3L^2\omega^4}{\left(\xi^2\left(4D\xi - \omega^2L^2\right)^2 + \omega^6L^4\right)^2} = 0 \tag{3.46}$$

which gives as solutions: $\omega_1 = 0$, $\omega_2 = \infty$, and the non-trivial expression:

$$\omega_3 = \sqrt{\frac{1}{3}\left(-\xi^2 + \xi\sqrt{\xi^2 + 24D\frac{\xi}{L^2}}\right)} = \xi\sqrt{\frac{1}{3}\left(-1 + \sqrt{1 + 24\frac{\lambda_D^2}{L^2}}\right)}\,. \tag{3.47}$$

ω_3 is the solution that corresponds to the peak of the response. The corresponding value of the peak is:

$$\chi(\omega_3)|_{x=\infty} \simeq \frac{L^4 + 24\lambda_D^2L\sqrt{(24\lambda_D^2 + L^2)} + L^2\left(28\lambda_D^2 + L\sqrt{(24\lambda_D^2 + L^2)}\right)}{8\lambda_D^2L^2\left(27\lambda_D^2 + L^2\right)}\,.$$

Recall that the existence of a peak in the factor χ is derived assuming to be at a point x distant from the electrodes.

We now note that, in the 1D system under study, at very high frequency:

$$\left.\left(\frac{\tilde{E}_0}{\Delta\tilde{V}}\right)^2\right|_{\omega=\infty} = \frac{1}{L^2}$$

independent of x, so that we attempt to generalize the expression for the frequency of maximum response in a generic system with non uniform field distribution $\tilde{E}_0$:

$$\boxed{\omega_P = \xi\sqrt{\frac{1}{3}\left(-1 + \sqrt{1 + 24\lambda_D^2\left.\left(\frac{\tilde{E}_0}{\Delta\tilde{V}}\right)^2\right|_{\omega=\infty}}\right)}} \tag{3.48}$$

where $\tilde{E}_0$ is the unperturbed AC field at the particle position. Eq. 3.48 provides a compact expression for the frequency of peak capacitive response (which corresponds to the optimum signal), as will be illustrated in more detail in Sec. 5.4.

3.1.2 Dielectric layer and electrolyte

Let us now consider the presence of an ideal charge-free dielectric layer of thickness a (for instance a SAM or a compact layer) on the bottom electrode as shown in Fig. 3.1. Laplace's equation holds in the dielectric:

$$\frac{d^2\tilde{V}}{dx^2} = 0 \tag{3.49}$$

The solution therein takes the form:

$$\tilde{V} = f_1 x + f_2 \tag{3.50}$$

The solution in the electrolyte is exactly the same obtained in Sec. 3.1.1, except that $\tilde{V}_B$ is replaced by $\tilde{V}_I$, namely, the potential at the interface between dielectric and electrolyte. We also suppose that the electrolyte lies in the region between a and L. We immediately see that:

$$\begin{cases} \tilde{V} = \dfrac{\tilde{V}_I - \tilde{V}_B}{a} x + \tilde{V}_B & x \in [0, a] \\ \tilde{V} = -\dfrac{q}{\varepsilon_{el}} \left[\dfrac{2}{\kappa^2} \dfrac{\tilde{V}_T - \tilde{V}_I}{\beta - \delta - (\beta + \delta)\alpha} \left(e^{-\kappa(x-a)} - \alpha e^{\kappa(x-a)} \right) + l_1 (x - a) + l_2 \right] & x \in [a, L] \end{cases} \tag{3.51}$$

where the parameters are given by Eq. 3.20 upon substitution of L with $L - a$.
To calculate $\tilde{V}_I$ we impose the continuity of the normal component of the electric induction through the interface:

$$\varepsilon_s \left. \frac{d\tilde{V}}{dx} \right|_{a^-} = \varepsilon_{el} \left. \frac{d\tilde{V}}{dx} \right|_{a^+}$$

$$\implies \quad \varepsilon_s \frac{\tilde{V}_I - \tilde{V}_B}{a} = -\varepsilon_{el} \frac{q}{\varepsilon_{el}} \left(\tilde{V}_T - \tilde{V}_I \right) \frac{\alpha + 1}{\beta - \delta - (\beta + \delta)\alpha} \left[-\frac{2}{\kappa} + \frac{\varepsilon_{el}}{q} \frac{1}{q\mu n_0} v_d \right]$$

where ε_s is the dielectric layer permittivity. Rearranging this equation we get:

$$\tilde{V}_I = \frac{\tilde{V}_B + \tilde{V}_T \dfrac{\alpha + 1}{\beta - \delta - (\beta + \delta)\alpha} \dfrac{\varepsilon_{el}}{\varepsilon_s} a \dfrac{D\kappa}{q\mu n_0}}{1 + \dfrac{\alpha + 1}{\beta - \delta - (\beta + \delta)\alpha} \dfrac{\varepsilon_{el}}{\varepsilon_s} a \dfrac{D\kappa}{q\mu n_0}} \tag{3.52}$$

The current is constant in each section, and we can easily calculate it in the dielectric region:

$$\tilde{J} = -j\omega\varepsilon_s \frac{\tilde{V}_I - \tilde{V}_B}{a} = j\omega \frac{\Delta\tilde{V}}{\dfrac{\beta - \delta - (\beta + \delta)\alpha}{\alpha + 1} \dfrac{1}{\varepsilon_{el}} \dfrac{qn_0}{k_B T \kappa} + \dfrac{a}{\varepsilon_s}} \tag{3.53}$$

where again $\Delta\tilde{V} = \tilde{V}_B - \tilde{V}_T$. We immediately note that, as expected, the admittance y_{tot} is the series connection of the dielectric layer admittance $(j\omega\varepsilon_s/a)$ with the electrolyte admittance y_{tot} given by Eq. 3.32.
Fig. 3.10 shows the admittance y_{tot} with two different dielectric layers, either resemblant of a Stern layer (a) or of a SAM (b). We see that qualitatively the curves are very similar to the case with no dielectric layer (Fig. 3.8), but the first cut-off frequency f_s does not show a simple dependence on salt concentration as in Sec. 3.1.1.3. We will analyze this aspect in more detail in the following.

The electric field in the electrolyte is given by:

$$\tilde{E} = -\frac{d\tilde{V}}{dx} = -\frac{\tilde{V}_T - \tilde{V}_I}{\beta - \delta - (\beta + \delta)\alpha} \left[\frac{q}{\varepsilon_{el}} \frac{2}{\kappa} \left(e^{-\kappa(x-a)} + \alpha e^{\kappa(x-a)} \right) - \frac{\alpha + 1}{q\mu n_0} v_d \right] \tag{3.54}$$

Appendices 3.A.3 - 3.A.4 report similar derivations for cases where the dielectric region lies inside the electrolyte, which can represent the situation where a dielectric biomolecule floats in the liquid, with or without the SAM or compact layer on top of the electrode. These models, although simply 1D, constitute useful reference solutions to test the accuracy of numerical simulations and understand nanocapacitor response to biomolecules.

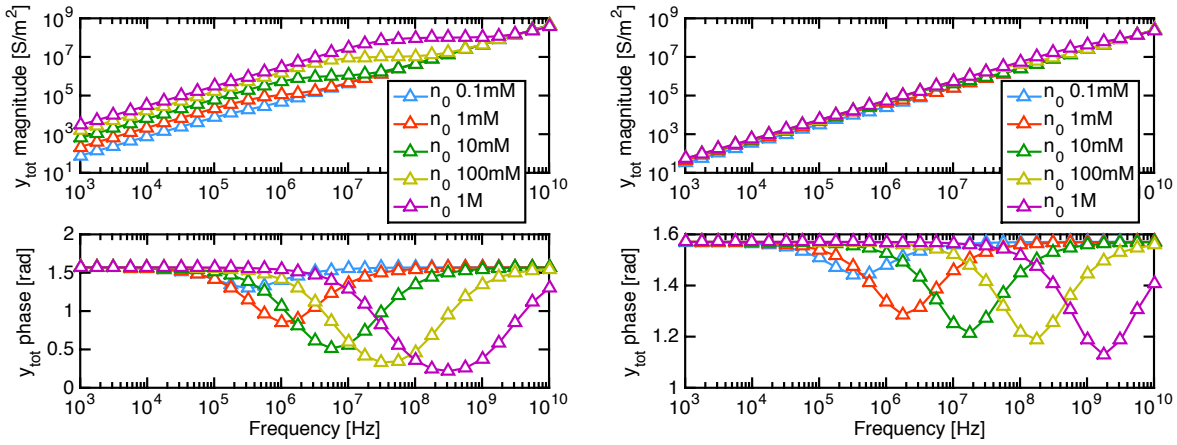

(a) $a = 0.25$ nm, $\varepsilon_s = 25\varepsilon_0$ **(b)** $a = 2.5$ nm, $\varepsilon_s = 2.5\varepsilon_0$

Fig 3.10: Admittance spectra between the electrodes y_{tot} as a function of salt concentration with $L - a = 100$ nm and a dielectric layer on the left electrode either resemblent of a Stern layer (a) or of a SAM (b).

Long system We now assume again that $L - a \gg \lambda_D$, so that $\alpha \simeq 0$ and we can write explicitly the system admittance per unit area y_{tot} from Eq. 3.53:

$$y_{tot} \simeq j\omega\varepsilon_s\varepsilon_{el}\kappa \frac{\xi + j\omega}{\xi\left(\varepsilon_{el}\kappa a + 2\varepsilon_s\right) + j\omega\kappa\left(\varepsilon_{el}a + \varepsilon_s(L-a)\right)} \tag{3.55}$$

We immediately see that the second cut-off frequency is again f_c. From the denominator of this expression, instead, we calculate the first cut-off frequency f_s in this case as:

$$f_s = \frac{\xi}{2\pi} \frac{\varepsilon_{el}a + 2\varepsilon_s/\kappa}{\varepsilon_{el}a + \varepsilon_s(L-a)} \tag{3.56}$$

From Fig. 3.10 we immediately see that in all cases $f_s \ll f_c$, so that we can again write $\kappa \simeq 1/\lambda_D$ and simplify the above expression as:

$$f_s \simeq \frac{\xi}{2\pi} \frac{\varepsilon_{el}a + 2\varepsilon_s\lambda_D}{\varepsilon_{el}a + \varepsilon_s(L-a)} \tag{3.57}$$

As noted also in Fig. 3.10, it is now evident that, when the dielectric layer is very thin and with high permittivity (for instance if it resembles a Stern layer) y_{tot} in this case is very similar to the one derived from Eq. 3.32 and $f_s \propto \sqrt{n_0}$ as in Sec. 3.1.1.3. On the other hand, if the dielectric layer is thicker and with lower permittivity (for instance if it resembles a SAM), the double layer admittance contribution almost vanishes, since it is in series with the dielectric layer admittance, and $f_s \propto n_0$. These observations are confirmed in Fig. 3.11, which also shows that at low frequency and especially at high salt concentration most of the potential drop occurs in the dielectric layer.

3.1.3 Small-signal / differential capacitance

A technique that is well established in the characterization of MOSFETs involves the measurement of the differential capacitance at the gate as a function of the applied bias. In this section, we will then investigate the differential capacitance in DC for the electrode/electrolyte system and compare it to the small signal AC capacitance.

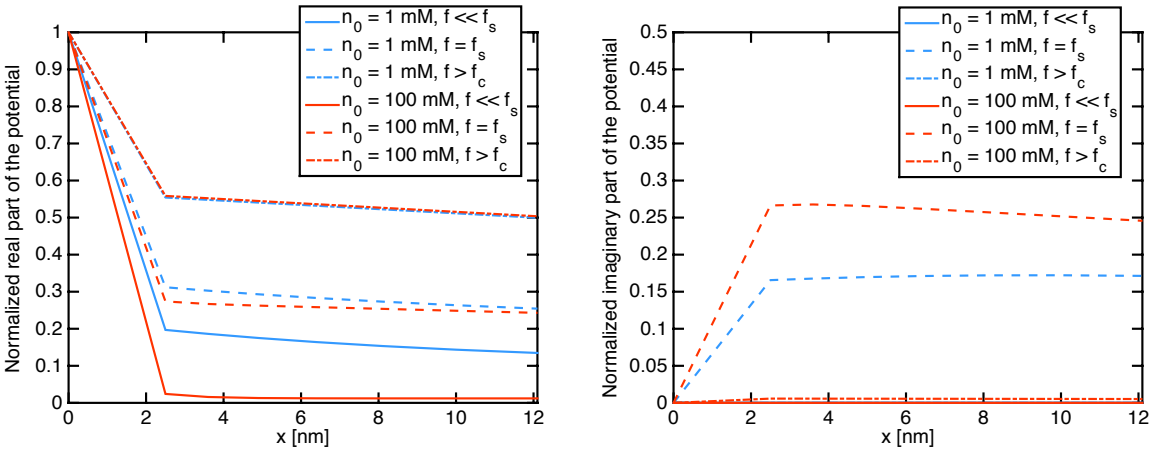

(a) real part **(b)** imaginary part

Fig 3.11: Real and imaginary parts of the normalized potential profile $\tilde{V}/\Delta\tilde{V}$ near the electrode with $L = 100$ nm, $a = 2.5$ nm and $\varepsilon_s = 2.5\varepsilon_0$ at three different frequencies, that is, below f_s, at f_s and above f_c. Note the penetration of the field at high frequency and that at low frequency most of the potential drop occurs in the dielectric layer.

We consider again the case made in Sec. 3.1.2 (Fig. 3.1), where a dielectric layer lies on top of the left electrode. The Gouy-Chapman theory for a Z:Z electrolyte predicts that the DC potential between the dielectric surface and the bulk of the electrolyte can be expressed as [36]:

$$V_0(x) = \frac{2k_BT}{Zq}\ln\left(\frac{\alpha\, e^{\frac{x-a}{\lambda_D}}+1}{\alpha\, e^{\frac{x-a}{\lambda_D}}-1}\right) = \frac{4k_BT}{Zq}\,\mathrm{atanh}\left(\tanh\left(\frac{ZqV_I}{4k_BT}\right)e^{-\frac{x-a}{\lambda_D}}\right) \tag{3.58}$$

where $\tanh u = \dfrac{e^{2u}-1}{e^{2u}+1}$, $\lambda_D = \sqrt{\dfrac{\varepsilon_{el}k_BT}{2n_\infty Z^2q^2}}$ is the Debye length, V_I is the potential at the dielectric/electrolyte interface and:

$$\alpha = \frac{e^{\frac{ZqV_I}{2k_BT}}+1}{e^{\frac{ZqV_I}{2k_BT}}-1}\,. \tag{3.59}$$

Note that, differently from our previous calculations and Fig. 3.1, in the Gouy-Chapman model the right most electrode is Faradaic and biased at the constant reference voltage $V_T = V_{ref}$; therefore, it does not have any double layer. An alternative expression for $V_0(x)$ can be derived noting that $\tanh u = \dfrac{e^{2u}-1}{e^{2u}+1}$. The potential profile across the dielectric is:

$$V_0(x) = V_B + \frac{V_I - V_B}{a}x\,. \tag{3.60}$$

Therefore:

$$\frac{dV_0}{dx} = \begin{cases} -\sqrt{\dfrac{8k_BTn_\infty}{\varepsilon_{el}}}\sinh\left(\dfrac{ZqV_0}{2k_BT}\right) & \text{in the electrolyte} \\ \dfrac{V_I - V_B}{a} & \text{in the dielectric} \end{cases}.$$

The continuity of the dielectric displacement at the dielectric/electrolyte interface:

$$-\varepsilon_{el}\sqrt{\frac{8k_BTn_\infty}{\varepsilon_{el}}}\sinh\left(\frac{ZqV_I}{2k_BT}\right)=\varepsilon_s\frac{V_I-V_B}{a} \tag{3.61}$$

provides us an expression that, if solved numerically, allows us to calculate V_I. The ion concentrations are then easily found reminding that $n_{0\pm}=n^\infty\exp\left(\mp\frac{Zq}{k_BT}V_0\right)$, which yields:

$$n_{0+}=n_\infty\left(\frac{\alpha\, e^{\frac{z-a}{\lambda_D}}-1}{\alpha\, e^{\frac{z-a}{\lambda_D}}+1}\right)^2 \tag{3.62a}$$

$$n_{0-}=n_\infty\left(\frac{\alpha\, e^{\frac{z-a}{\lambda_D}}+1}{\alpha\, e^{\frac{z-a}{\lambda_D}}-1}\right)^2=\frac{(n^\infty)^2}{n_{0+}} \tag{3.62b}$$

We can then calculate the static differential capacitance (per unit area) of the dielectric/electrolyte system according to the Gouy-Chapman theory as [36]:

$$\boxed{c_{DC}=\frac{d\sigma_{el}}{dV_0}=\left(\frac{a}{\varepsilon_s}+\frac{\lambda_D}{\varepsilon_{el}\cosh\left(\frac{ZqV_I}{2k_BT}\right)}\right)^{-1}}. \tag{3.63}$$

For the simple case $V_I=0$ we have:

$$c_{DC}=\left(\frac{a}{\varepsilon_s}+\frac{\lambda_D}{\varepsilon_{el}}\right)^{-1}. \tag{3.64}$$

Differential capacitance at low frequency In order to compare Eq. 3.63 with the AC small-signal capacitance in the limit $\omega\to 0$ we have to do some calculations first. We calculate the capacitance per unit area ($c_{AC}=y_{tot}/j\omega$) at zero frequency from Eq. 3.53 and remininding that $\kappa=1/\lambda_D$, $\beta=2\dfrac{k_BT}{qn_0}$ and $\delta=0$ we obtain:

$$c_{AC}(\omega=0)=\frac{1}{\frac{\beta-\delta-(\beta+\delta)\alpha}{\alpha+1}\frac{1}{\varepsilon_{el}}\frac{qn_0}{k_BT\kappa}+\frac{a}{\varepsilon_s}}=\left(\frac{a}{\varepsilon_s}+2\frac{\lambda_D}{\varepsilon_{el}}\frac{1-e^{-\frac{L-a}{\lambda_D}}}{1+e^{-\frac{L-a}{\lambda_D}}}\right)^{-1}. \tag{3.65}$$

Since Eq. 3.63 is derived assuming that the reference electrode is at infinite distance, we have to take the limit of c_{AC} in Eq. 3.65 for $L\to\infty$, i.e. c_{AC}^∞. We obtain:

$$c_{AC}^\infty(0)=\lim_{L\to+\infty}c_{AC}(0)=\left(\frac{a}{\varepsilon_s}+2\frac{\lambda_D}{\varepsilon_{el}}\right)^{-1} \tag{3.66}$$

To compare this expression with Eq. 3.64 we remind that, since the potential difference between the reference electrode and the counter electrode is zero in DC, only one double-layer if formed on the SAM/electrolyte interface. On the contrary, in the AC case a double layer on the top electrode is also present. Therefore, we define c_{AC}^{eq} the AC admittance in the case with no double layer on the top electrode, which is calculated as:

$$c_{AC}^{eq}=2\left(\frac{1}{c_{AC}^\infty(0)}+\frac{a}{\varepsilon_s}\right)^{-1}=\left(\frac{a}{\varepsilon_s}+\frac{\lambda_D}{\varepsilon_{el}}\right)^{-1} \tag{3.67}$$

Eq. 3.67 proves that $c_{AC}^{eq} = c_{DC}(V_B = 0)$, that is, the small signal model for $\omega \to 0$ is perfectly equivalent to the DC differential theory at $V_B = 0$, as expected.

Fig. 3.12 shows the simulated AC small signal capacitance at low frequency, the simulated DC differential capacitance and the DC differential capacitance according to the Gouy-Chapman theory (Eq. 3.63) as a function of the applied DC voltage and of the ion concentration. A thin dielectric Stern layer, with thickness 0.25 nm and permittivity equal to the bulk electrolyte permittivity ($\varepsilon_{el} \simeq 80\varepsilon_0$) is attached to the left electrode. The Gouy-Chapman theory (dashed lines) is very well reproduced by the DC numerical simulations (triangles up). The capacitance increases for increasing bias because the excess charge piles up in a progressively thinner layer at the interface as demonstrated in Fig. 3.12. As expected the small signal and the DC differential capacitances match very closely in all regimes, except for the case at low salt concentration and large DC bias, likely due to small residual numerical errors or meshing problems. It has to be emphasized in fact that, however simple it may appear, the result in Fig. 3.12 is definitely non trivial, given the huge variation of concentrations over such a wide bias range.
As a matter of fact, it was by meas of curves and comparisons such as those in Fig. 3.12 that we became aware of subtle issues (and sometimes implementation errors) in the accurate calculation of small signal currents in finite difference and finite element models. More details at this regard are given in Sec. 4.2.1.3. This proves once more, if at all necessary, the importance of exact analytical reference models.

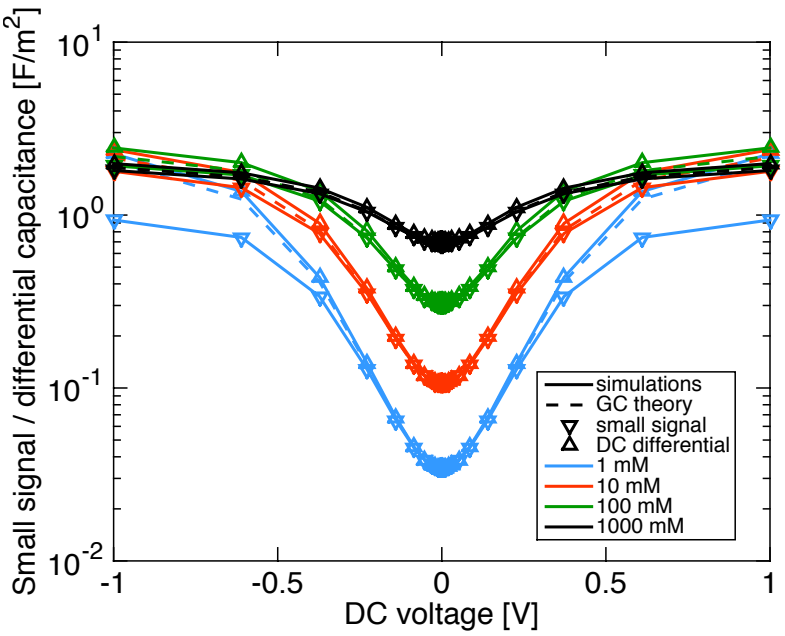

Fig 3.12: Comparison between simulations (solid lines) of the DC differential capacitance (triangles up) and the AC small-signal capacitance at very low frequency (triangles down, calculated using the transformation 3.67) and the Gouy-Chapman model of the DC differential capacitance (dashed lines) for a system as the one in Fig. 3.1.

Two compact layers Let us consider also the case where a SAM and two compact layers (one per electrode, both having dielectric constant ε_{CL}) are present (Fig. 3.13). This is obviously the case when the top electrode is not Faradaic. The electrostatic

potential in the dielectrics is then given by:

$$V_0 = \begin{cases} \dfrac{V_s - V_B}{x_s} z + V_B & z \in [0, x_s] \\ \dfrac{V_{IB} - V_s}{x_{clB} - x_s} z + V_s & z \in [x_s, x_{clB}] \\ \dfrac{V_T - V_{IT}}{L - x_{clT}} z + V_{IT} & z \in [x_{clT}, L] \end{cases}$$

The electric field in the electrolyte is:

$$\frac{dV_0}{dx} = \begin{cases} -\sqrt{\dfrac{8k_BTn_\infty}{\varepsilon_{el}}} \sinh\left(\dfrac{Zq(V_0 - V_{ref})}{2k_BT}\right) & \text{bottom region of the electrolyte} \\ \sqrt{\dfrac{8k_BTn_\infty}{\varepsilon_{el}}} \sinh\left(\dfrac{Zq(V_0 - V_{ref})}{2k_BT}\right) & \text{top region of the electrolyte} \end{cases}$$

since in the bottom region $V_0 - V_{ref} > 0$, while in the top region $V_0 - V_{ref} < 0$. The continuity of the dielectric displacement yields:

$$\begin{cases} \varepsilon_s \dfrac{V_s - V_B}{x_s} = \varepsilon_{CL} \dfrac{V_{IB} - V_s}{x_{clB} - x_s} \\ \varepsilon_{CL} \dfrac{V_{IB} - V_s}{x_{clB} - x_s} = -\varepsilon_{el} \sqrt{\dfrac{8k_BTn_\infty}{\varepsilon_{el}}} \sinh\left(\dfrac{Zq(V_{IB} - V_{ref})}{2k_BT}\right) \\ \varepsilon_{el} \sqrt{\dfrac{8k_BTn_\infty}{\varepsilon_{el}}} \sinh\left(\dfrac{Zq(V_{IT} - V_{ref})}{2k_BT}\right) = \varepsilon_{CL} \dfrac{V_T - V_{IT}}{L - x_{clT}} \end{cases}$$

Using the first of these three equations and enforcing the symmetry of the electrolyte double layers (that is, $V_{ref} = (V_{IB} + V_{IT})/2$) we obtain:

$$\begin{cases} \varepsilon_s \dfrac{V_s - V_B}{x_s} = -\varepsilon_{el} \sqrt{\dfrac{8k_BTn_\infty}{\varepsilon_{el}}} \sinh\left(\dfrac{Zq(V_{IB} - V_{IT})}{4k_BT}\right) \\ -\varepsilon_{el} \sqrt{\dfrac{8k_BTn_\infty}{\varepsilon_{el}}} \sinh\left(\dfrac{Zq(V_{IB} - V_{IT})}{4k_BT}\right) = \varepsilon_{CL} \dfrac{V_T - V_{IT}}{L - x_{clT}} \end{cases} \tag{3.68}$$

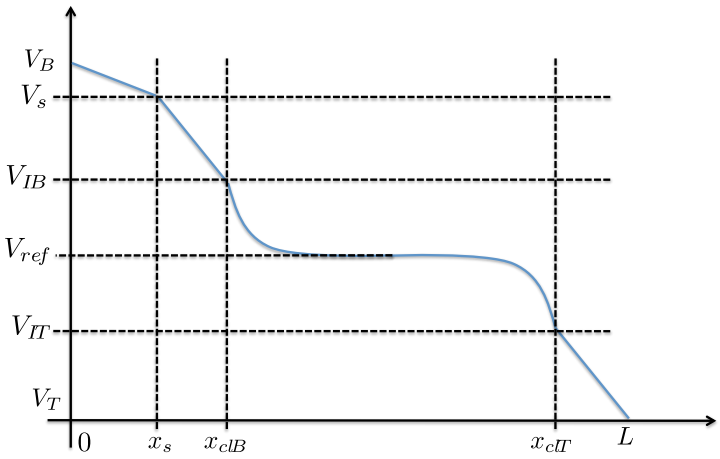

Fig 3.13: Sketch of the electric potential across a dielectric/electrolyte system with compact layers at the bottom and top interfaces and SAM at the bottom interface.

The SAM surface potential is given by:

$$V_s = V_B + \frac{\varepsilon_{CL}}{\varepsilon_s}\frac{x_s}{L - x_{cl\Gamma}}\left(V_T - V_{I\Gamma}\right) .$$

From the system of equations we also get:

$$\begin{aligned}
\frac{\varepsilon_s}{x_s}\left(\frac{\varepsilon_{CL}}{\varepsilon_s}\frac{x_s}{L - x_{cl\Gamma}}\left(V_T - V_{I\Gamma}\right)\right) &= \frac{\varepsilon_{CL}}{x_{clB} - x_s}\left(V_{IB} - V_B - \frac{\varepsilon_{CL}}{\varepsilon_s}\frac{x_s}{L - x_{cl\Gamma}}\left(V_T - V_{I\Gamma}\right)\right) \\
\Rightarrow \quad \left(V_T - V_{I\Gamma}\right) &= \frac{1}{x_{clB} - x_s}\left(\left(L - x_{cl\Gamma}\right)\left(V_{IB} - V_B\right) - \frac{\varepsilon_{CL}}{\varepsilon_s}x_s\left(V_T - V_{I\Gamma}\right)\right) \\
\Rightarrow \quad V_{IB} &= V_B + \left(V_T - V_{I\Gamma}\right)\frac{\left(x_{clB} - x_s\right)\varepsilon_s + x_s\varepsilon_{CL}}{\left(L - x_{cl\Gamma}\right)\varepsilon_s} .
\end{aligned} \tag{3.69}$$

Substituting this expression for V_{IB} into the second equation in Eq. 3.68, we solve for $V_{I\Gamma}$ to obtain:

$$-\varepsilon_{el}\sqrt{\frac{8k_BTn_\infty}{\varepsilon_{el}}}\sinh\left(\frac{Zq(V_{IB} - V_{I\Gamma})}{4k_BT}\right) = \varepsilon_{CL}\frac{V_T - V_{I\Gamma}}{L - x_{cl\Gamma}}$$

Alternatively, we can derive a second formulation by writing:

$$V_{I\Gamma} = V_{cel} + \left(V_{el} - V_{IB}\right)\frac{\left(L - x_{cl\Gamma}\right)\varepsilon_s}{\left(x_{clB} - x_s\right)\varepsilon_s + x_s\varepsilon_{CL}}$$

and solve for V_{IB} the equation:

$$\varepsilon_{CL}\frac{V_{IB} - V_s}{x_{clB} - x_s} = -\varepsilon_{el}\sqrt{\frac{8k_BTn_\infty}{\varepsilon_{el}}}\sinh\left(\frac{Zq(V_{IB} - V_{I\Gamma})}{4k_BT}\right)$$

This second formulation is useful when there is no compact layer at the top (e.g., because the contact to the fluid gate is assumed perfectly Faradaic), so that $V_{I\Gamma} = V_T$. Eq. 3.68 then becomes:

$$\begin{cases}
\varepsilon_{CL}\dfrac{V_{IB} - V_s}{x_{clB} - x_s} = -\varepsilon_{el}\sqrt{\dfrac{8k_BTn_\infty}{\varepsilon_{el}}}\sinh\left(\dfrac{Zq(V_{IB} - V_T)}{4k_BT}\right) \\
V_s = \dfrac{\varepsilon_s\left(x_{clB} - x_s\right)V_B + \varepsilon_{CL}x_sV_{IB}}{\varepsilon_s\left(x_{clB} - x_s\right) + \varepsilon_{CL}x_s}
\end{cases}$$

3.1.3.1 System energy

In this section we will calculate the energy in the system. Such a calculation can be useful to estimate at which distance from the electrode the biomolecule would preferentially be. A more sophisticated analysis for the case of nanowire FET biosensors is reported in [58]. In the following we assume again that a particle is placed inside the system. An important information in this case will then be if it exists a preferential position for the particle, stemming from energetic considerations. It is thus useful at this stage to calculate the total energy U in the system. The general expression for the energy given V and n_m is [59]:

$$U = \int_\Omega \left[k_BT\sum_{m=1}^{N_{ions}} n_m \log\frac{n_m}{n_{0m}^\infty} + \frac{1}{2}\left(\rho_{0f} + \sum_{m=1}^{N_{ions}} Z_mqn_m\right)V\right]d\Omega \tag{3.70}$$

where Ω is the domain. The Poisson-Boltzmann equation (Eq. 2.5) holds in DC regime, so that for $V_{ref} = 0$ the energy is given by:

$$\begin{aligned} U_0 &= \int \left[k_B T \sum_{m=1}^{N_{ions}} n_{0m} \log \frac{n_{0m}}{n_{0m}^{\infty}} + \frac{1}{2} \left(\rho_{0f} + \sum_{m=1}^{N_{ions}} Z_m q n_{0m} \right) V_0 \right] d\vec{x} \\ &= \int \sum_{m=1}^{N_{ions}} n_{0m} \left[k_B T \log \frac{n_{0m}}{n_{0m}^{\infty}} + \frac{1}{2} Z_m q V_0 \right] d\vec{x} \\ &= - \int \sum_{m=1}^{N_{ions}} Z_m q n_{0m}^{\infty} \exp\left(-\frac{Z_m q V_0}{k_B T} \right) \frac{V_0}{2} d\vec{x} \end{aligned} \tag{3.71}$$

In the small-signal AC case with no DC bias applied and $V_{ref} = 0$ the V and n_m to use in Eq. 3.70 are:

$$V = \Re\left(\tilde{V} \exp(j\omega t) \right), \quad n_m = n_{0m}^{\infty} \left[1 + \frac{Z_m q}{k_B T} \Re\left(\left(\tilde{\phi}_m - \tilde{V} \right) \exp(j\omega t) \right) \right]$$

Because of the small signal approximation we can write that:

$$\log \frac{n_m}{n_{0m}^{\infty}} \simeq \frac{Z_m q}{k_B T} \Re\left(\left(\tilde{\phi}_m - \tilde{V} \right) \exp(j\omega t) \right) .$$

Substitution in Eq. 3.70 yields:

$$\begin{aligned} \tilde{U} &= \int \sum_{m=1}^{N_{ions}} n_m \left[k_B T \log \frac{n_m}{n_{0m}^{\infty}} + \frac{1}{2} Z_m q V \right] d\vec{x} \\ &\simeq \int \sum_{m=1}^{N_{ions}} Z_m q n_{0m}^{\infty} \left[1 + \frac{Z_m q}{k_B T} \Re\left(\left(\tilde{\phi}_m - \tilde{V} \right) e^{j\omega t} \right) \right] \left[\Re\left(\left(\tilde{\phi}_m - \tilde{V} \right) e^{j\omega t} \right) + \frac{1}{2} \Re\left(\tilde{V} e^{j\omega t} \right) \right] d\vec{x} \end{aligned}$$

We now use the fact that we have a symmetric 1:1 electrolyte, so $\phi_1 = \phi_2 = \phi$ and:

$$\begin{aligned} &\sum_{m=1}^{N_{ions}} Z_m q n_{0m}^{\infty} \left[\Re\left(\left(\tilde{\phi}_m - \tilde{V} \right) e^{j\omega t} \right) + \frac{1}{2} \Re\left(\tilde{V} e^{j\omega t} \right) \right] \\ &\qquad = q n_0 \Re\left[\left(\tilde{\phi} - \frac{1}{2} \tilde{V} \right) e^{j\omega t} \right] (Z_1 + Z_2) = 0 \end{aligned}$$

This means that:

$$\begin{aligned} \tilde{U} &= \int \sum_{m=1}^{2} \frac{Z_m^2 q^2}{k_B T} n_0 \Re\left(\left(\tilde{\phi} - \tilde{V} \right) e^{j\omega t} \right) \Re\left[\left(\tilde{\phi} - \frac{1}{2} \tilde{V} \right) e^{j\omega t} \right] d\vec{x} \\ &= 2 \frac{q^2}{k_B T} n_0 \int \Re\left[\left(\tilde{\phi} - \tilde{V} \right) e^{j\omega t} \right] \Re\left[\left(\tilde{\phi} - \frac{1}{2} \tilde{V} \right) e^{j\omega t} \right] d\vec{x} \end{aligned} \tag{3.72}$$

Eqs. 3.71-3.72 are in principle useful to estimate which is the position that a biomolecule would preferentially occupy under given DC and AC excitation. Since we always work in the AC small signal regime, in the following we concentrate on the DC energy U_0, assuming that it gives the dominant effect. Fig. 3.14 shows the energy in a 1D cartesian system without SAM, varying the distance between the particle and the electrode for two salt concentrations. We immediately note that there is a minimum of the energy, indicating that, in absence of other forces (for instance, chemical adhesion forces) and of Brownian motion, the particle would preferentially lie at a certain distance from the electrode, which is a fraction of the Debye length (10 nm at 1 mM, 3 nm at 10 mM).

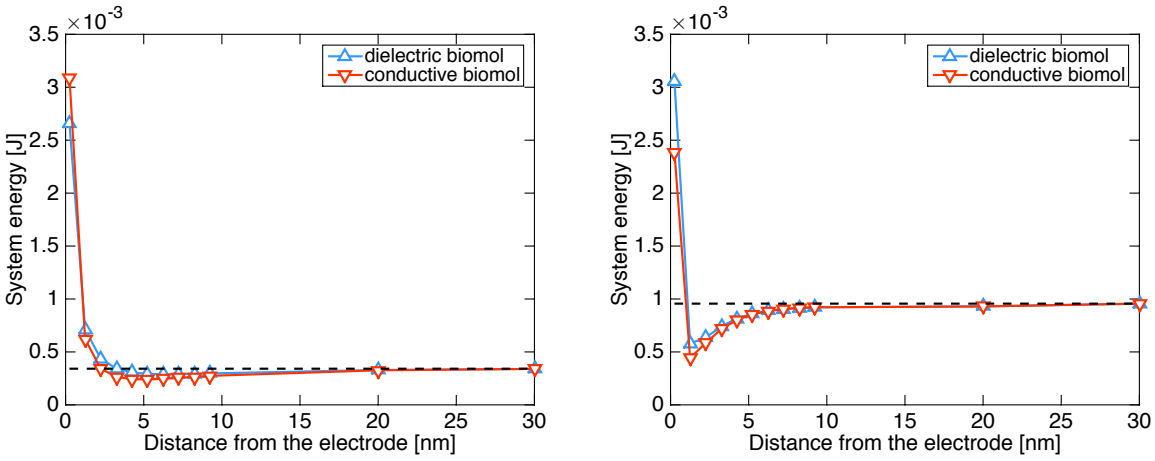

(a) 1 mM **(b)** 10 mM

Fig 3.14: Plots of the DC energy (Eq. 3.71) in a 1D cartesian system without SAM, varying the distance between the particle and the electrode. The dashed horizontal lines represent the value of the energy when the particle is very far from the electrodes. The particle has thickness 4.5 μm, can be either dielectric with relative permittivity 2.3 or conductive and does not have a surface charge. The DC potential at the electrode is 100 mV.

3.2 1D AC cartesian electrode-electrolyte with DC bias

Until now we have assumed zero DC bias between the top and bottom electrodes. In the following we attempt to derive an analytical model which extends previous calculations by considering the possible presence of a DC bias. All the other assumptions remain the same.

As will be apparent in the following, this effort has unfortunately remained incomplete due to insurmountable technical difficulties, which prevented us to obtain a reference analytical solution for this important case. Fortunately, we will see in Chaps. 5 - 6 that the simple model derived in Sec. 3.1 is adequate to interpret the results of our case studies, despite the fact that in some conditions a small DC bias is applied to the system electrodes.

To develop the calculation, we now use the Poisson-Nernst-Planck formulation with quasi-potentials. The equations are:

$$\varepsilon\frac{d^2\tilde{V}}{dx^2}+\frac{Z^2q^2}{k_BT}\left(n_{0+}\left(\tilde{\phi}_+-\tilde{V}\right)+n_{0-}\left(\tilde{\phi}_--\tilde{V}\right)\right)=0$$

$$Zq\mu\frac{d}{dx}\left(n_{0+}\frac{d\tilde{\phi}_+}{dx}\right)-j\omega n_{0+}\frac{Zq}{k_BT}\left(\tilde{\phi}_+-\tilde{V}\right)=0$$

$$Zq\mu\frac{d}{dx}\left(n_{0-}\frac{d\tilde{\phi}_-}{dx}\right)-j\omega n_{0-}\frac{Zq}{k_BT}\left(\tilde{\phi}_--\tilde{V}\right)=0$$

where the suffix $+$ and $-$ refer to the two symmetric ionic species. We can rewrite these equations as:

$$\varepsilon\frac{d^2\tilde{V}}{dx^2}+\frac{Z^2q^2}{k_BT}\left(n_{0+}\left(\tilde{\phi}_+-\tilde{V}\right)+\frac{n_\infty^2}{n_{0+}}\left(\tilde{\phi}_--\tilde{V}\right)\right)=0$$

$$Zq\mu\frac{d}{dx}\left(n_{0+}\frac{d\tilde{\phi}_+}{dx}\right)-j\omega n_{0+}\frac{Zq}{k_BT}\left(\tilde{\phi}_+-\tilde{V}\right)=0$$

$$Zq\mu\frac{d}{dx}\left(\frac{n_\infty^2}{n_{0+}}\frac{d\tilde{\phi}_-}{dx}\right)-j\omega\frac{n_\infty^2}{n_{0+}}\frac{Zq}{k_BT}\left(\tilde{\phi}_--\tilde{V}\right)=0$$

where $n_{0+}=n_\infty\left[\left(\alpha\,e^{\frac{x-a}{\lambda_D}}-1\right)/\left(\alpha\,e^{\frac{x-a}{\lambda_D}}+1\right)\right]^2$. We rewrite the system in compact form as:

$$\frac{d^2\tilde{V}}{dx^2}+\frac{\kappa_D^2}{2}\left(\delta(x)\left(\tilde{\phi}_+-\tilde{V}\right)+\frac{1}{\delta(x)}\left(\tilde{\phi}_--\tilde{V}\right)\right)=0 \tag{3.73a}$$

$$\frac{d}{dx}\left(\delta(x)\frac{d\tilde{\phi}_+}{dx}\right)-\kappa_\omega^2\delta(x)\left(\tilde{\phi}_+-\tilde{V}\right)=0 \tag{3.73b}$$

$$\frac{d}{dx}\left(\frac{1}{\delta(x)}\frac{d\tilde{\phi}_-}{dx}\right)-\kappa_\omega^2\frac{1}{\delta(x)}\left(\tilde{\phi}_--\tilde{V}\right)=0 \tag{3.73c}$$

where $\kappa_D^2=\dfrac{1}{\lambda_D^2}=\dfrac{2n_\infty Z^2q^2}{\varepsilon k_BT}$, $\kappa_\omega^2=j\dfrac{\omega}{\mu k_BT}=j\dfrac{\omega}{D}$ and $\delta(x)=\left[\left(\alpha\,e^{\frac{x-a}{\lambda_D}}-1\right)/\left(\alpha\,e^{\frac{x-a}{\lambda_D}}+1\right)\right]^2$.

A possible way of solving this system of equations is reported in Sec. 3.A.5. A different solution method, which could give results easier to analyze, is to expand the unknown functions into spatial harmonics of the form $\tilde{u}=\int\tilde{u}_\kappa\exp(\kappa x)\,d\kappa$ where $\tilde{u}\in\left[\tilde{V},\tilde{\phi}_+,\tilde{\phi}_-\right]$ and we used the notation $\tilde{u}_\kappa$ for the unknown function $\tilde{u}$ in the κ-space (which is then a function of κ and not x). We can then rewrite Eqs. 3.73 as:

$$\kappa^2\tilde{V}_\kappa+\frac{\kappa_D^2}{2}\left(\delta(x)\left(\tilde{\phi}_{\kappa,+}-\tilde{V}_\kappa\right)+\frac{1}{\delta(x)}\left(\tilde{\phi}_{\kappa,-}-\tilde{V}_\kappa\right)\right)=0 \tag{3.74a}$$

$$\kappa^2\tilde{\phi}_{\kappa,+}+\kappa\,\eta(x)\tilde{\phi}_{\kappa,+}-\kappa_\omega^2\left(\tilde{\phi}_{\kappa,+}-\tilde{V}_\kappa\right)=0 \tag{3.74b}$$

$$\kappa^2\tilde{\phi}_{\kappa,-}-\kappa\,\eta(x)\tilde{\phi}_{\kappa,-}-\kappa_\omega^2\left(\tilde{\phi}_{\kappa,-}-\tilde{V}_\kappa\right)=0 \tag{3.74c}$$

where we have now defined:

$$\eta(x)=\frac{1}{\delta(x)}\frac{d\delta(x)}{dx}=\frac{4\alpha}{\lambda_D}\frac{e^{\frac{x-a}{\lambda_D}}}{\left(\alpha\,e^{\frac{x-a}{\lambda_D}}+1\right)\left(\alpha\,e^{\frac{x-a}{\lambda_D}}-1\right)}$$

The matrix form of Eq. 3.74 is $\mathbf{Au}=0$, where:

$$\mathbf{u}=\begin{bmatrix}\tilde{V}\\ \tilde{\phi}_+\\ \tilde{\phi}_-\end{bmatrix},\qquad \mathbf{A}=\begin{bmatrix}\kappa^2-\dfrac{\kappa_D^2}{2}\left(\delta(x)+\dfrac{1}{\delta(x)}\right) & \dfrac{\kappa_D^2}{2}\,\delta(x) & \dfrac{\kappa_D^2}{2\delta(x)}\\ \kappa_\omega^2 & \kappa^2+\kappa\,\eta(x)-\kappa_\omega^2 & 0\\ \kappa_\omega^2 & 0 & \kappa^2-\kappa\,\eta(x)-\kappa_\omega^2\end{bmatrix}$$

Non-zero solutions of this system exist for $\det(\mathbf{A})=0$, so that we get the characteristic equation:

$$\kappa\left[\kappa^5-\left(2\kappa_\omega^2+\frac{\kappa_D^2}{2}\left(\delta+\frac{1}{\delta}\right)+\eta^2\right)\kappa^3+\frac{\kappa_\omega^4\delta+\dfrac{\kappa_D^2}{2}\left(1+\delta^2\right)\left(\kappa_\omega^2+\eta^2\right)}{\delta}\kappa+\frac{\dfrac{\kappa_D^2}{2}\kappa_\omega^2\left(\delta^2-1\right)\eta}{\delta}\right]=0$$

This equation has in general 6 solutions which we denote κ_l, $l\in[1,..,6]$. The only one that can be easily calculated is $\kappa_1=0$. In general, all the other solutions are functions of

x, i.e. $\kappa_l = \kappa_l(x)$. Because the admissible values for κ are only 6 at each x, the spatial harmonics have to be defined as:

$$\tilde{u} = \sum_{l=1}^{6} \tilde{u}_l \exp\left(\kappa_l(x)x\right)$$

where we have simplified the notation defining $\tilde{u}_l \triangleq \tilde{u}_{\kappa_l}$. To find the constants $\tilde{u}_l$ we can first make use of Eqs. 3.74b - 3.74c and write:

$$\tilde{\phi}_{l,+} = -\frac{\kappa_\omega^2}{\kappa_l^2 + \kappa_l\eta - \kappa_\omega^2}\tilde{V}_l \tag{3.75}$$

$$\tilde{\phi}_{l,-} = -\frac{\kappa_\omega^2}{\kappa_l^2 - \kappa_l\eta - \kappa_\omega^2}\tilde{V}_l \tag{3.76}$$

The boundary conditions:

$$\begin{bmatrix} \tilde{V} \\ \dfrac{d\tilde{\phi}_+}{dx} \\ \dfrac{d\tilde{\phi}_-}{dx} \end{bmatrix}_0 = \begin{bmatrix} \tilde{V}_B \\ 0 \\ 0 \end{bmatrix} \qquad \text{and} \qquad \begin{bmatrix} \tilde{V} \\ \dfrac{d\tilde{\phi}_+}{dx} \\ \dfrac{d\tilde{\phi}_-}{dx} \end{bmatrix}_L = \begin{bmatrix} \tilde{V}_T \\ 0 \\ 0 \end{bmatrix}$$

provide us the equations to close the system and to find the constants $\tilde{u}_l$. More explicitly, if we assume the constants $\tilde{V}_l$ to be independent of x, we have:

$$\begin{aligned}
\frac{d\tilde{\phi}_+}{dx} &= \frac{d}{dx}\left(\sum_{l=1}^{6} \tilde{\phi}_{l,+} e^{\kappa_l(x)x}\right) = \sum_{l=1}^{6}\left(\frac{d\tilde{\phi}_{l,+}}{dx}e^{\kappa_l x} + \tilde{\phi}_{l,+}\left(\kappa_l + \frac{d\kappa_l}{dx}x\right)e^{\kappa_l x}\right) \\
&= \sum_{l=1}^{6} \frac{\kappa_\omega^2 V_l}{\kappa_l^2 + \kappa_l\eta - \kappa_\omega^2}\left(\frac{1}{\kappa_l^2 + \kappa_l\eta - \kappa_\omega^2}\left(\left(\kappa_l + \eta\right)\frac{d\kappa_l}{dx} + \kappa_l\frac{d\eta}{dx}\right) - \left(\kappa_l + \frac{d\kappa_l}{dx}x\right)\right)e^{\kappa_l x} \\
\frac{d\tilde{\phi}_-}{dx} &= \sum_{l=1}^{6} \frac{\kappa_\omega^2 V_l}{\kappa_l^2 - \kappa_l\eta - \kappa_\omega^2}\left(\frac{1}{\kappa_l^2 - \kappa_l\eta - \kappa_\omega^2}\left(\left(\kappa_l - \eta\right)\frac{d\kappa_l}{dx} - \kappa_l\frac{d\eta}{dx}\right) - \left(\kappa_l + \frac{d\kappa_l}{dx}x\right)\right)e^{\kappa_l x}
\end{aligned}$$

where the boundary conditions entail:

$$\begin{cases} \displaystyle\sum_{l=1}^{6} \tilde{V}_l = \tilde{V}_B \\ \displaystyle\sum_{l=1}^{6} \tilde{V}_l \exp\left(\kappa_l(L)L\right) = \tilde{V}_T \end{cases} .$$

3.3 AC spherical electrode-electrolyte system

1D cartesian models are extremely useful to understand the fundamentals of high frequency sensor response. In particular, they allowed us to clarify the behaviour of AC double layers and to identify the existence of two cut-off frequencies relevant to sensor operation.
However, analytes have complex three dimensional shapes that are difficult to grasp in cartesian coordinates. In this section we develop equations in spherical coordinates which

describe the model systems depicted in Fig. 3.15. Such systems provide rough approximations to the capacitive nanoelectrode biosensor for the detection of spherical biomolecules, which is the main objective of this dissertation. As we will see and discuss in more detail in Chap. 5, spherical particles are a good approximation of a wide range of biologically-relevant entities, such as cells, viruses and globular proteins. We will also show that the inclusion of surface charges on the particle provides only quantitative but not qualitative deviations to the predictions of simple analytical models (see for instance Sec. 5.4).
In particular, the first system we consider (Fig. 3.15a) is meant to mimic detection in a constant electric field, therefore the approximation is more suited to the case when the biomolecules are much smaller than the electrodes. This is the most relevant case in a biosensor and, as we will see, this model represents a situation which is closer to the nanoelectrode array. For all these reasons we will consider this model first and denote it as 1st order model.
On the other hand, the second system (Fig. 3.15b) mimics more accurately the detection of very large particles. Due to the approximations of the model, however, the results obtained in this case are of less general applicability. We will denote it as 0th order model. At the end of this section we show and compare results obtained with the different models developed hereby.

We start again with a symmetrical 1:1 electrolyte, no DC bias and ideally polarizable electrodes (as in Sec. 3.1), and solve the equations in spherical coordinates, with different assumptions on the excitation in order to derive both a 1D in the radial coordinate and a 2D in radial and angular coordinates model. The model equations are (see also Eqs. 3.1):

$$\begin{cases} -\dfrac{\varepsilon_{el}}{q}\nabla^2\tilde{V} = Z_1\tilde{n}_1 + Z_2\tilde{n}_2 \\ j\omega\tilde{n}_1 = Z_1 q\mu_1 n_{01}\nabla^2\tilde{V} + D_1\nabla^2\tilde{n}_1 \\ j\omega\tilde{n}_2 = Z_2 q\mu_2 n_{02}\nabla^2\tilde{V} + D_2\nabla^2\tilde{n}_2 \end{cases} \tag{3.77}$$

Following the same procedure of Sec. 3.1 we can substitute the first equation in the other ones to obtain:

$$\begin{cases} \nabla^2\tilde{V} = -\dfrac{q}{\varepsilon_{el}}\left(Z_1\tilde{n}_1 + Z_2\tilde{n}_2\right) \\ D_1\nabla^2\tilde{n}_1 = Z_1 q\mu_1 n_{01}\dfrac{q}{\varepsilon_{el}}\left(Z_1\tilde{n}_1 + Z_2\tilde{n}_2\right) + j\omega\tilde{n}_1 \\ D_2\nabla^2\tilde{n}_2 = Z_2 q\mu_2 n_{02}\dfrac{q}{\varepsilon_{el}}\left(Z_1\tilde{n}_1 + Z_2\tilde{n}_2\right) + j\omega\tilde{n}_2 \end{cases}$$

We decouple the equations, as previously in Sec. 3.1.1:

$$\begin{cases} \nabla^2 v_1 = \kappa_1^2 v_1 \\ \nabla^2 v_2 = \kappa_2^2 v_2 \end{cases}, \qquad \begin{cases} \kappa_1^2 = \dfrac{a_1 + b_2 + \sqrt{(a_1 - b_2)^2 + 4a_2 b_1}}{2} \\ \kappa_2^2 = \dfrac{a_1 + b_2 - \sqrt{(a_1 - b_2)^2 + 4a_2 b_1}}{2} \end{cases}$$

where:

$$\begin{cases} a_1 = \dfrac{1}{D_1}\left(\dfrac{Z_1^2 q^2}{\varepsilon_{el}}\mu_1 n_{01} + j\omega\right) = \dfrac{\xi_1 + j\omega}{D_1} \\ a_2 = \dfrac{Z_1 Z_2 q^2}{\varepsilon_{el}}\dfrac{1}{D_1}\mu_1 n_{01} = \dfrac{\xi_{12}}{D_1} \\ b_1 = \dfrac{Z_1 Z_2 q^2}{\varepsilon_{el}}\dfrac{1}{D_2}\mu_2 n_{02} = \dfrac{\xi_{21}}{D_2} \\ b_2 = \dfrac{1}{D_2}\left(\dfrac{Z_2^2 q^2}{\varepsilon_{el}}\mu_2 n_{02} + j\omega\right) = \dfrac{\xi_2 + j\omega}{D_2} \end{cases}$$

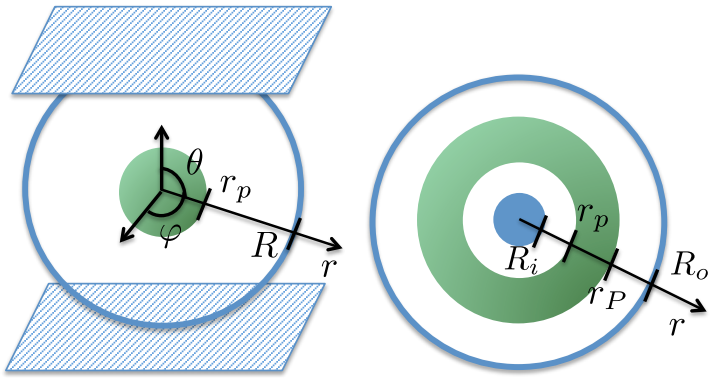

(a) 1st order **(b)** 0th order

Fig 3.15: Sketches of the 1st and 0th order spherical models. In the 1st order model the approximation of two plane parallel electrodes at $R \gg r_p$ is highlighted.

If we assume a symmetric electrolyte with $Z_1 = -Z_2 = 1$, $D_1 = D_2 = D$, $\mu_1 = \mu_2 = \mu$, $n_{01} = n_{02} = n_0$ we find:

$$\begin{cases} a_1 = \dfrac{\xi_1 + j\omega}{D} \\ a_2 = -\dfrac{\xi_1}{D} \\ b_1 = a_2 \\ b_2 = a_1 \end{cases} \quad \Longrightarrow \quad \begin{cases} \kappa_1^2 = a_1 + |a_2| = \dfrac{\xi + j\omega}{D} \\ \kappa_2^2 = a_1 - |a_2| = \dfrac{j\omega}{D} \end{cases}$$

with the usual definition where $\xi = 2q^2\mu n_0/\varepsilon_{el} = \sigma_{el}/\varepsilon_{el}$ is the electrolyte's dielectric relaxation cut-off frequency.

Alternatively, and consistently with Eqs. 2.30-2.35, we can start from Eqs. 3.77 in the potential and quasi-potentials and, using the same parameters as before, we obtain:

$$\begin{cases} \nabla^2\tilde{V} = -\left(\dfrac{\xi_1}{D_1}\left(\tilde{\phi}_1 - \tilde{V}\right) + \dfrac{\xi_2}{D_2}\left(\tilde{\phi}_2 - \tilde{V}\right)\right) \\ \nabla^2\tilde{\phi}_1 = \dfrac{j\omega}{D_1}\left(\tilde{\phi}_1 - \tilde{V}\right) \\ \nabla^2\tilde{\phi}_2 = \dfrac{j\omega}{D_2}\left(\tilde{\phi}_2 - \tilde{V}\right) \end{cases} \tag{3.78}$$

We can then write the system as:

$$\nabla^2\tilde{\mathbf{U}} = \mathbf{B}\,\tilde{\mathbf{U}} \quad \Longleftrightarrow \quad \nabla^2 \begin{bmatrix} \tilde{V} \\ \tilde{\phi}_1 \\ \tilde{\phi}_2 \end{bmatrix} = \begin{bmatrix} \dfrac{\xi_1}{D_1} + \dfrac{\xi_2}{D_2} & -\dfrac{\xi_1}{D_1} & -\dfrac{\xi_2}{D_2} \\ -\dfrac{j\omega}{D_1} & \dfrac{j\omega}{D_1} & 0 \\ -\dfrac{j\omega}{D_2} & 0 & \dfrac{j\omega}{D_2} \end{bmatrix} \begin{bmatrix} \tilde{V} \\ \tilde{\phi}_1 \\ \tilde{\phi}_2 \end{bmatrix} \tag{3.79}$$

As in Sec. 3.1, in order to diagonalize this equation we have to find the transformation $\mathbf{T}$, which is the matrix of the eigenvectors, such that $\tilde{\mathbf{U}} = \mathbf{T}\mathbf{v}$, where $\mathbf{v}$ are the diagonalized unknown functions. The eigenvalues κ^2 are the solution of the characteristic equation:

$$\begin{aligned} &\left(\kappa^2 - \frac{\xi_1}{D_1} - \frac{\xi_2}{D_2}\right)\left(\kappa^2 - \frac{j\omega}{D_1}\right)\left(\kappa^2 - \frac{j\omega}{D_2}\right) \\ &\quad - \left(\frac{\xi_1}{D_1}\right)\frac{j\omega}{D_1}\left(\kappa^2 - \frac{j\omega}{D_2}\right) - \left(\frac{\xi_2}{D_2}\right)\left(\kappa^2 - \frac{j\omega}{D_1}\right)\frac{j\omega}{D_2} = 0 \end{aligned} \tag{3.80}$$

For the symmetric electrolyte this yields:

$$\kappa_1^2 = \frac{\xi + j\omega}{D}, \quad \kappa_2^2 = \frac{j\omega}{D}, \quad \kappa_3^2 = 0 \tag{3.81}$$

or, being $\tau = 1/\xi$ the electrolyte relaxation time and λ_D the Debye length:

$$\kappa_1^2 = \frac{1 + j\omega\tau}{\lambda_D^2}, \quad \kappa_2^2 = \frac{j\omega\tau}{\lambda_D^2}, \quad \kappa_3^2 = 0 \tag{3.82}$$

with the eigenvectors $\mathbf{T}_l$:

$$\mathbf{B}\mathbf{T}_l = \kappa_l^2 \mathbf{T}_l \quad \Longrightarrow \quad \mathbf{T}_1 = \begin{bmatrix} -\dfrac{\xi}{j\omega} \\ 1 \\ 1 \end{bmatrix}, \mathbf{T}_2 = \begin{bmatrix} 0 \\ -1 \\ 1 \end{bmatrix}, \mathbf{T}_3 = \begin{bmatrix} 1 \\ 1 \\ 1 \end{bmatrix}$$

The system is then diagonalized by defining the matrices:

$$\mathbf{T} = \begin{bmatrix} -\dfrac{\xi}{j\omega} & 0 & 1 \\ 1 & -1 & 1 \\ 1 & 1 & 1 \end{bmatrix}, \mathbf{\Lambda} = \begin{bmatrix} \kappa_1^2 & 0 & 0 \\ 0 & \kappa_2^2 & 0 \\ 0 & 0 & \kappa_3^2 \end{bmatrix}. \tag{3.83}$$

We finally have to solve the decoupled equations:

$$\nabla^2 v_l = \kappa_l^2 v_l \tag{3.84}$$

where the v_l are the components of vector $\mathbf{v}$.

This second formulation is more convenient for the solution of the system of equations, so we will use it throughout this section.

3.3.1 1st order model - electrolyte only

Assuming no variation along the angular component φ (the planar one, see Fig. 3.15b), we have:

$$\nabla^2 = \frac{1}{r^2}\frac{\partial}{\partial r}\left(r^2 \frac{\partial}{\partial r}\right) + \frac{1}{r^2 \sin\theta}\frac{\partial}{\partial \theta}\left(\sin\theta \frac{\partial}{\partial \theta}\right) = \frac{\partial^2}{\partial r^2} + \frac{2}{r}\frac{\partial}{\partial r} + \frac{1}{r^2}\frac{\partial^2}{\partial \theta^2} + \frac{1}{r^2 \tan\theta}\frac{\partial}{\partial \theta}.$$

Eq. 3.84 takes the form:

$$\frac{1}{r^2}\frac{\partial}{\partial r}\left(r^2 \frac{\partial v_l}{\partial r}\right) + \frac{1}{r^2 \sin\theta}\frac{\partial}{\partial \theta}\left(\sin\theta \frac{\partial v_l}{\partial \theta}\right) = \kappa_l^2 v_l$$

where the κ_l ($l = 1..3$) come from Eq. 3.81. Using the separation of variables $v_l(r,\theta) = R_l(r)\Theta_l(\theta)$, dividing by $R_l\Theta_l$ and multiplying by r^2 we obtain:

$$\begin{cases} r^2 \dfrac{\partial^2 R_l}{\partial r^2} + 2r\dfrac{\partial R_l}{\partial r} - \kappa_l^2 r^2 R_l = \alpha_l^2 R_l \\ \dfrac{\partial^2 \Theta_l}{\partial \theta^2} + \dfrac{1}{\tan\theta}\dfrac{\partial \Theta_l}{\partial \theta} = -\alpha_l^2 \Theta_l \end{cases}$$

where α_l is an integration parameter. The solution is given in terms of spherical Bessel functions (j_n, y_n) and Legendre polynomials (P_n, Q_n) of order n:

$$\begin{cases} R_l = c_l' \, \mathrm{y}_{\left(-1-\sqrt{1+4\alpha_l^2}\right)/2}(-j\kappa_l r) + d_l' \, \mathrm{j}_{\left(-1-\sqrt{1+4\alpha_l^2}\right)/2}(-j\kappa_l r) \\ \Theta_l = e_l P_{\left(-1+\sqrt{1+4\alpha_l^2}\right)/2}(\cos\theta) + f_l Q_{\left(-1+\sqrt{1+4\alpha_l^2}\right)/2}(\cos\theta) \end{cases}$$

where c_l', d_l', e_l and f_l are integration constants. We assume in the following that the angular part is given by $\Theta_l = \cos\theta$, which means that $\alpha_l^2 = 2$ and $f_l = 0$. This is the lowest order choice which gives a non-trivial solution. In particular, the potential distribution around $r = 0$ resembles the one due to two infinite parallel conducting plates. Thus, we have:

$$\begin{aligned} v_l &= \left(c_l' \, \mathrm{y}_{-2}(-j\kappa_l r) + d_l' \, \mathrm{j}_{-2}(-j\kappa_l r)\right)\cos\theta \\ &= \left(c_l \exp(\kappa_l r)\left(\frac{1}{\kappa_l r} - \frac{1}{\kappa_l^2 r^2}\right) + d_l \exp(-\kappa_l r)\left(\frac{1}{\kappa_l r} + \frac{1}{\kappa_l^2 r^2}\right)\right)\cos\theta \end{aligned}$$

where $c_l = (jc_l' - d_l')/2$, $d_l = (jc_l' + d_l')/2$ and we substituted the explicit expression of $\mathrm{y}_{-2}(-j\kappa_l r)$ and $\mathrm{j}_{-2}(-j\kappa_l r)$. Since $r = 0$ is part of the domain of interest, we have to set $d_l' = 0$ or equivalently $c_l = d_l$ for a non-diverging solution. In the end:

$$y_l = c_l' \, \mathrm{y}_{-2}(-j\kappa_l r)\cos\theta = c_l\left(\exp(\kappa_l r)\left(\frac{1}{\kappa_l r} - \frac{1}{\kappa_l^2 r^2}\right) + \exp(-\kappa_l r)\left(\frac{1}{\kappa_l r} + \frac{1}{\kappa_l^2 r^2}\right)\right)\cos\theta$$

Note that for $\kappa_3 = 0$:

$$y_3 = \left(c_3 r^{\frac{j}{2}\left(j-\sqrt{-1-4\alpha^2}\right)} + d_3 r^{\frac{j}{2}\left(j+\sqrt{-1-4\alpha^2}\right)}\right)\cos\theta = \left(c_3 r + \frac{d_3}{r^2}\right)\cos\theta$$

Since $r = 0$ is part of the domain of interest, we deduce $d_3 = 0$. As in the 1D cartesian model (Sec. 3.1), the eigenvalue κ_3 corresponds to the solution of the linear Laplace equation, as would be the case if the system was made of a dielectric instead of the electrolyte. This represents a long-range solution in the absence of electrical double layers or, equivalently, the solution in the high frequency limit.
Using Eq. 3.83, we can then write the solution as:

$$\tilde{V}(r,\theta) = \left(-\frac{\xi}{j\omega}c_1' \, \mathrm{y}_{-2}(-j\kappa_1 r) + c_3 r\right)\cos\theta \tag{3.85a}$$

$$\tilde{\phi}_1(r,\theta) = \left(c_1' \, \mathrm{y}_{-2}(-j\kappa_1 r) - c_2' \, \mathrm{y}_{-2}(-j\kappa_2 r) + c_3 r\right)\cos\theta \tag{3.85b}$$

$$\tilde{\phi}_2(r,\theta) = \left(c_1' \, \mathrm{y}_{-2}(-j\kappa_1 r) + c_2' \, \mathrm{y}_{-2}(-j\kappa_2 r) + c_3 r\right)\cos\theta \tag{3.85c}$$

Boundary conditions We assume Neumann boundary conditions on the current on the entire border, because of the ideally polarizable electrodes, and to have a Dirichlet boundary condition on the voltage $\tilde{V}(R,\theta) = \tilde{V}_0\cos\theta$ where R is the radius of the domain. Considering Fig. 3.15 again, it is clear that such boundary condition mimics for $r \ll R$ the presence of two equipotential plates above and below the spherical domain. Remembering the ionic current expression 2.37b:

$$\vec{\tilde{J}}_m = -Z_m^2 q^2 \mu_m n_{0m} \nabla\tilde{\phi}_m \tag{3.86}$$

we can then write:

$$\begin{cases} -Z_1^2 q^2 \mu_1 n_{01} \nabla \tilde{\phi}_1 \Big|_{R,\theta} \cdot \hat{r} = 0 \\ -Z_2^2 q^2 \mu_2 n_{02} \nabla \tilde{\phi}_2 \Big|_{R,\theta} \cdot \hat{r} = 0 \\ \tilde{V}(R,\theta) = \tilde{V}_0 \cos\theta \end{cases} . \tag{3.87}$$

The calculations of the integration constants are reported in Sec. 3.A.6 in the chapter appendix. Since the constant c_2' vanishes, we define $\kappa = \kappa_1$. So in the end we obtain:

$$\tilde{V}(r,\theta) = \left(\frac{2\xi}{\omega} c_1' \, \mathrm{y}_{-2}(-j\kappa r) + c_3 r \right) \cos\theta \tag{3.88a}$$

$$\tilde{\phi}_1(r,\theta) = \left(\frac{2}{j} c_1' \, \mathrm{y}_{-2}(-j\kappa r) + c_3 r \right) \cos\theta \tag{3.88b}$$

$$\tilde{\phi}_2(r,\theta) = \left(\frac{2}{j} c_1' \, \mathrm{y}_{-2}(-j\kappa r) + c_3 r \right) \cos\theta = \tilde{\phi}_1 \tag{3.88c}$$

which can be alternatively put in the form:

$$\boxed{\begin{aligned} \tilde{V}(r,\theta) &= \left(-\frac{\xi c_1}{j\omega} \left(\exp(\kappa r) \left(\frac{1}{\kappa r} - \frac{1}{\kappa^2 r^2} \right) + \exp(-\kappa r) \left(\frac{1}{\kappa r} + \frac{1}{\kappa^2 r^2} \right) \right) + c_3 r \right) \cos\theta && \text{(3.89a)} \\ \tilde{\phi}_1(r,\theta) &= \left(c_1 \left(\exp(\kappa r) \left(\frac{1}{\kappa r} - \frac{1}{\kappa^2 r^2} \right) + \exp(-\kappa r) \left(\frac{1}{\kappa r} + \frac{1}{\kappa^2 r^2} \right) \right) + c_3 r \right) \cos\theta && \text{(3.89b)} \\ \tilde{\phi}_2(r,\theta) &= \tilde{\phi}_1 && \text{(3.89c)} \end{aligned}}$$

The potential profiles computed according to Eq. 3.89 are reported in Fig. 3.16. We immediately see that the potential profiles are very similar to the ones reported in Fig. 3.5 for the cartesian system and that a linear term in r independent of κ exists also in this case.
The electric field is:

$$\begin{aligned} \vec{\tilde{E}}(r,\theta) = -\nabla \tilde{V} &= -\left(\frac{2\xi}{\omega} c_1 \frac{\partial \mathrm{y}_{-2}(-j\kappa r)}{\partial r} + c_3 \right) \cos\theta \, \hat{r} + \left(\frac{2\xi}{\omega} c_1 \, \mathrm{y}_{-2}(-j\kappa r) + c_3 r \right) \frac{\sin\theta}{r} \hat{\theta} \\ &= \left(\frac{2\xi}{j\omega} c_1 \frac{-2\kappa r \cosh(\kappa r) + (2+\kappa^2 r^2)\sinh(\kappa r)}{\kappa^2 r^3} - c_3 \right) \cos\theta \, \hat{r} \\ &\quad - \left(\frac{2\xi}{j\omega} c_1 \frac{\kappa r \cosh(\kappa r) - \sinh(\kappa r)}{\kappa^2 r^3} - c_3 \right) \sin\theta \, \hat{\theta} \end{aligned}$$

whereas current density is given by:

$$\vec{\tilde{J}} = j\omega \varepsilon_{el} \vec{\tilde{E}} - \sum_{m=1}^{N_{ions}} Z_m^2 q^2 \mu_m n_{0m} \nabla \tilde{\phi}_m \, . \tag{3.90}$$

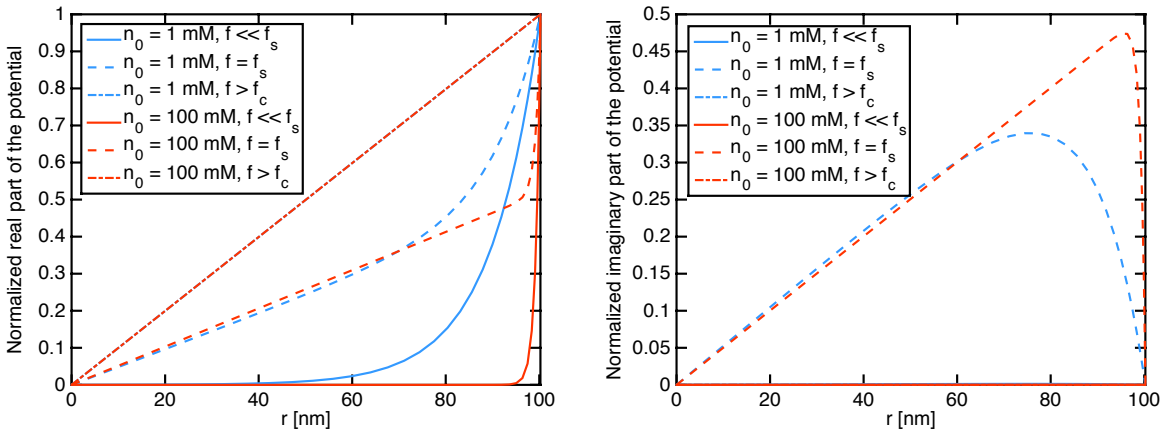

(a) real part **(b)** imaginary part

Fig 3.16: Real and imaginary parts of the normalized potential profile $\tilde{V}/\tilde{V}_0$ computed by means of Eq. 3.89 along r with $\theta = 0$ and $R = 100$ nm at three different frequencies, that is, below f_s, at f_s and above f_c. Note the penetration of the field at high frequency. The potential profiles are very similar to the ones in Fig. 3.5.

Because of the boundary conditions, we know that the ionic current density on the border is zero; therefore, the contact current is given only by displacement current:

$$\begin{aligned}
\tilde{I} &= -\int \vec{\tilde{J}}(R,\theta)\cdot\hat{r}dS_r = -j\omega\varepsilon_{el}\int \vec{\tilde{E}}\cdot\hat{r}\,dS_r = -j\omega\varepsilon_{el}\int_0^{2\pi}d\phi\int_0^{\pi/2}d\theta\vec{\tilde{E}}(R,\theta)\cdot\hat{r}\,R^2\sin\theta \\
&= -2\pi R^2 j\omega\varepsilon_{el}\left(\frac{2\xi}{j\omega}c_1\frac{-2\kappa R\cosh(\kappa R)+(2+\kappa^2R^2)\sinh(\kappa R)}{\kappa^2R^3}-c_3\right)\int_0^{\pi/2}\cos\theta\sin\theta\,d\theta \\
&= -\pi R^2 j\omega\varepsilon_{el}\left(\frac{2\xi}{j\omega}c_1\frac{-2\kappa R\cosh(\kappa R)+(2+\kappa^2R^2)\sinh(\kappa R)}{\kappa^2R^3}-c_3\right) \\
&= \pi R j\omega\varepsilon_{el}\frac{-2\kappa R\cosh(\kappa R)+(2+\kappa^2R^2)\sinh(\kappa R)}{\kappa R(\xi-2j\omega)\cosh(\kappa R)+(-\xi+(2+\kappa^2R^2)\,j\omega)\sinh(\kappa R)}(\xi+j\omega)\,\tilde{V}_0
\end{aligned}$$

where dS_r denotes the surface element in direction $\hat{r}$ and we have integrated on the half bottom sphere to have the current on one contact. Note also that we added a $-$ sign, which is necessary to have an inner orientation for the current on the electrode. This expression can be rewritten in terms of exponential functions by multiplying numerator and denominator by $\exp(-\rho_0)$ where $\rho_0 = \kappa R$:

$$\boxed{\tilde{I} = \pi R j\omega\varepsilon_{el}\frac{-2\rho_0\,(1+\exp(-2\rho_0))+\left(2+\rho_0^2\right)(1-\exp(-2\rho_0))}{\rho_0(\xi-2j\omega)\,(1+\exp(-2\rho_0))+\left(-\xi+\left(2+\rho_0^2\right)j\omega\right)(1-\exp(-2\rho_0))}(\xi+j\omega)\,\tilde{V}_0} \tag{3.91}$$

The current $\tilde{I}$ will be shown in Sec. 3.3.5. Eq. 3.91 provides an explicit expression for the admittance $Y = \tilde{I}/\tilde{V}_0$ of the system.

Case $|\kappa R| \gg 1$ Since, as usual, the screening length $1/\kappa$ is typically much thinner than the typical dimension of the system, we can approximate Eq. 3.91 for $|\kappa R| = |\rho_0| \gg 1$,

and then write:

$$c_1' \simeq -2\omega \exp(-\rho_0)\frac{\rho_0}{\xi+\rho_0 j\omega}\tilde{V}_0$$
$$c_3 \simeq \frac{j\omega}{R}\frac{\rho_0}{\xi+\rho_0 j\omega}\tilde{V}_0$$

In this way:

$$\begin{aligned}\tilde{V} &\simeq \left(-j2\xi\exp(-\rho_0)\mathrm{y}_{-2}(-j\rho)+\frac{j\omega}{R}r\right)\frac{\rho_0}{\xi+\rho_0 j\omega}\tilde{V}_0\cos\theta\\ &= \left(\xi\left(\exp(\rho-\rho_0)\left(\frac{1}{\kappa r}-\frac{1}{\kappa^2r^2}\right)+\exp(-\rho-\rho_0)\left(\frac{1}{\kappa r}+\frac{1}{\kappa^2r^2}\right)\right)+c_3 r\right)\cos\theta\\ \tilde{\phi}_1=\tilde{\phi}_2 &\simeq \left(-2\omega\exp(-\rho_0)\mathrm{y}_{-2}(-j\rho)+\frac{j\omega}{R}r\right)\frac{\rho_0}{\xi+\rho_0 j\omega}\tilde{V}_0\cos\theta\\ &= \left(c_1\left(\exp(\kappa r)\left(\frac{1}{\kappa r}-\frac{1}{\kappa^2r^2}\right)+\exp(-\kappa r)\left(\frac{1}{\kappa r}+\frac{1}{\kappa^2r^2}\right)\right)+c_3 r\right)\cos\theta\end{aligned}$$

The current is then:

$$\boxed{\begin{aligned}\tilde{I} &\simeq \pi R j\omega\varepsilon_{el}\frac{-2\rho_0+2+\rho_0^2}{\rho_0(\xi-2j\omega)-\xi+(2+\rho_0^2)\,j\omega}\left(\xi+j\omega\right)\tilde{V}_0\\ &\simeq \pi R j\omega\varepsilon_{el}\frac{\rho_0}{\xi+\rho_0 j\omega}\left(\xi+j\omega\right)\tilde{V}_0\end{aligned}} \tag{3.92}$$

3.3.2 1st order model with particle

We now assume that the region $0 < r < r_p$ is dielectric with complex permittivity $\epsilon_p = \varepsilon_p - j\sigma_p/\omega$: this region represents a particle or biomolecule. Now we cannot disregard the solution with j_{-2} in the electrolyte, since the point $r = 0$ is not part of the domain and therefore the solution cannot diverge. Since we use the complex permittivity, it can be either dielectric or conductive or of intermediate physical properties. As a result:

$$\begin{aligned}y_l &= \left(c_l'\,\mathrm{y}_{-2}(-j\kappa_l r)+d_l'\,\mathrm{j}_{-2}(-j\kappa_l r)\right)\cos\theta\\ &= \left(c_l\exp(\kappa_l r)\left(\frac{1}{\kappa_l r}-\frac{1}{\kappa_l^2r^2}\right)+d_l\exp(-\kappa_l r)\left(\frac{1}{\kappa_l r}+\frac{1}{\kappa_l^2r^2}\right)\right)\cos\theta\end{aligned}$$

This means that the solution in the electrolyte is:

$$\tilde{V} = \left(-\frac{\xi}{j\omega}\left(c_1\exp(\kappa_1 r)\left(\frac{1}{\kappa_1 r}-\frac{1}{\kappa_1^2r^2}\right)+d_1\exp(-\kappa_1 r)\left(\frac{1}{\kappa_1 r}+\frac{1}{\kappa_1^2r^2}\right)\right)+c_3 r+\frac{d_3}{r^2}\right)\cos\theta \tag{3.93a}$$

$$\begin{aligned}\tilde{\phi}_1 = \Bigg(&c_1\exp(\kappa_1 r)\left(\frac{1}{\kappa_1 r}-\frac{1}{\kappa_1^2r^2}\right)+d_1\exp(-\kappa_1 r)\left(\frac{1}{\kappa_1 r}+\frac{1}{\kappa_1^2r^2}\right)\\ &-c_2\exp(\kappa_2 r)\left(\frac{1}{\kappa_2 r}-\frac{1}{\kappa_2^2r^2}\right)-d_2\exp(-\kappa_2 r)\left(\frac{1}{\kappa_2 r}+\frac{1}{\kappa_2^2r^2}\right)+c_3 r+\frac{d_3}{r^2}\Bigg)\cos\theta\end{aligned} \tag{3.93b}$$

$$\begin{aligned}\tilde{\phi}_2 = \Bigg(&c_1\exp(\kappa_1 r)\left(\frac{1}{\kappa_1 r}-\frac{1}{\kappa_1^2r^2}\right)+d_1\exp(-\kappa_1 r)\left(\frac{1}{\kappa_1 r}+\frac{1}{\kappa_1^2r^2}\right)\\ &+c_2\exp(\kappa_2 r)\left(\frac{1}{\kappa_2 r}-\frac{1}{\kappa_2^2r^2}\right)+d_2\exp(-\kappa_2 r)\left(\frac{1}{\kappa_2 r}+\frac{1}{\kappa_2^2r^2}\right)+c_3 r+\frac{d_3}{r^2}\Bigg)\cos\theta\end{aligned} \tag{3.93c}$$

whereas inside the particle the solution is:

$$\tilde{V} = \left(e_1 r + \frac{f_1}{r^2}\right)\cos\theta = e_1 r\cos\theta \tag{3.94}$$

because the point $r = 0$ is part of the domain, and thus $f_1 = 0$. The gradients of the quasi potentials are:

$$\begin{aligned}\nabla\tilde{\phi}_1\cdot\hat{r} = \Bigg(& c_1\exp(\kappa_1 r)\frac{2+\kappa_1 r(-2+\kappa_1 r)}{\kappa_1^2 r^3} + d_1\exp(-\kappa_1 r)\frac{-2-\kappa_1 r(2+\kappa_1 r)}{\kappa_1^2 r^3}\\ & - c_2\exp(\kappa_2 r)\frac{2+\kappa_2 r(-2+\kappa_2 r)}{\kappa_2^2 r^3} - d_2\exp(-\kappa_2 r)\frac{-2-\kappa_2 r(2+\kappa_2 r)}{\kappa_2^2 r^3} + c_3 - 2\frac{d_3}{r^3}\Bigg)\cos\theta\\ \nabla\tilde{\phi}_2\cdot\hat{r} = \Bigg(& c_1\exp(\kappa_1 r)\frac{2+\kappa_1 r(-2+\kappa_1 r)}{\kappa_1^2 r^3} + d_1\exp(-\kappa_1 r)\frac{-2-\kappa_1 r(2+\kappa_1 r)}{\kappa_1^2 r^3}\\ & + c_2\exp(\kappa_2 r)\frac{2+\kappa_2 r(-2+\kappa_2 r)}{\kappa_2^2 r^3} + d_2\exp(-\kappa_2 r)\frac{-2-\kappa_2 r(2+\kappa_2 r)}{\kappa_2^2 r^3} + c_3 - 2\frac{d_3}{r^3}\Bigg)\cos\theta\end{aligned}$$

and the boundary conditions are:

$$\begin{cases} -Z_1^2 q^2 \mu_1 n_{01}\nabla\tilde{\phi}_1\Big|_{R,\theta}\cdot\hat{r} = 0\\ -Z_2^2 q^2 \mu_2 n_{02}\nabla\tilde{\phi}_2\Big|_{R,\theta}\cdot\hat{r} = 0\\ \tilde{V}(R,\theta) = \tilde{V}_0\cos\theta\end{cases} \tag{3.95}$$

Subtracting the first two equations immediately tells us that $c_2 = d_2 = 0$. The system of equations is closed by adding the continuity conditions:

$$\begin{cases}\tilde{V}(r_p^+,\theta) = \tilde{V}(r_p^-,\theta)\\ \varepsilon_{el}\left.\dfrac{d\tilde{V}}{dr}\right|_{r_p^+} = \epsilon_p\left.\dfrac{d\tilde{V}}{dr}\right|_{r_p^-}\\ -Z_1^2 q^2\mu_1 n_{01}\nabla\tilde{\phi}_1\Big|_{r_p,\theta}\cdot\hat{r} = 0\end{cases}$$

where we used the fact that $\tilde{\phi}_1 = \tilde{\phi}_2$, so that the additional equation for $\tilde{\phi}_2$ would be redundant. By solving these equations we derive the constants, as reported in Sec. 3.A.7.

The electric field in the electrolyte is:

$$\begin{aligned}\vec{\tilde{E}} &= -\nabla\tilde{V} = -\nabla\left(-\frac{\xi}{j\omega}\left(c_1\exp(\kappa r)\left(\frac{1}{\kappa r}-\frac{1}{\kappa^2 r^2}\right) + d_1\exp(-\kappa r)\left(\frac{1}{\kappa r}+\frac{1}{\kappa^2 r^2}\right)\right) + c_3 r + \frac{d_3}{r^2}\right)\cos\theta\\ &= \left(c_1\frac{\xi}{j\omega}\exp(\kappa_1 r)\frac{2+\kappa_1 r(-2+\kappa_1 r)}{\kappa_1^2 r^3} + d_1\frac{\xi}{j\omega}\exp(-\kappa_1 r)\frac{-2-\kappa_1 r(2+\kappa_1 r)}{\kappa_1^2 r^3} - c_3 + 2\frac{d_3}{r^3}\right)\cos\theta\,\hat{r}\\ &+ \left(\frac{\xi}{j\omega}\left(c_1\exp(\kappa_1 r)\left(\frac{1}{\kappa_1 r}-\frac{1}{\kappa_1^2 r^2}\right) + d_1\exp(-\kappa_1 r)\left(\frac{1}{\kappa_1 r}+\frac{1}{\kappa_1^2 r^2}\right)\right) - c_3 r - \frac{d_3}{r^2}\right)\sin\theta\,\hat{\theta}\,.\end{aligned}$$

The current on the half bottom sphere is equal to:

$$\begin{aligned}\tilde{I} &= -\int\vec{\tilde{J}}(R,\theta)\cdot\,\hat{r}dS_r = -j\omega\varepsilon_{el}\int\vec{\tilde{E}}\cdot\hat{r}\,dS_r = -j\omega\varepsilon_{el}\int_0^{2\pi}d\phi\int_0^{\pi/2}d\theta\vec{\tilde{E}}(R,\theta)\cdot\hat{r}\,R^2\sin\theta\\ &= -\pi R^2 j\omega\varepsilon_{el}\left(c_1\frac{\xi}{j\omega}\exp(\kappa R)\frac{2+\kappa R(-2+\kappa R)}{\kappa^2 R^3} + d_1\frac{\xi}{j\omega}\exp(-\kappa R)\frac{-2-\kappa R(2+\kappa R)}{\kappa^2 R^3} - c_3 + 2\frac{d_3}{R^3}\right)\end{aligned}$$

By setting $\rho = \kappa r$, so that $\rho_p = \kappa r_p$ and $\rho_0 = \kappa R$ and assuming that the system dimensions are large on the scale of $1/\kappa$ (so that $|\rho_0| \gg 1$) we obtain:

$$\begin{aligned}\tilde{I} &= -\pi R\varepsilon_{el}\left(c_1\xi\exp(\rho_0)\frac{2+\rho_0(-2+\rho_0)}{\rho_0^2} + d_1\xi\exp(-\rho_0)\frac{-2-\rho_0(2+\rho_0)}{\rho_0^2} - c_3 j\omega R + 2j\omega\frac{d_3}{R^2}\right)\\ &\simeq -\pi R\varepsilon_{el}\left(c_1\xi\exp(\rho_0) - d_1\xi\exp(-\rho_0) - c_3 j\omega R + 2j\omega\frac{d_3}{R^2}\right)\end{aligned} \tag{3.96}$$

Large particle We assume now that also the particle or biomolecule is very large on the scale of $1/\kappa$, so that $|\rho_p| \gg 1$. The constants take the form reported in Sec. 3.A.7.

If we further assume that $\rho_0 \approx \rho_p$, which implies $c_1\exp(\rho_0) \to 0$ and that the particle is at large distance from the electrodes, we can then simplify the expression of the current (see Sec. 3.A.7). Morevoer, if we also assume that the domain is much larger than the particle's volume then $R^3 \gg r_p^3$ and:

$$\boxed{\tilde{I} \simeq \pi R\omega^2\varepsilon_{el}\frac{\rho_0}{\xi+\rho_0 j\omega}\rho_p\frac{2(\epsilon_p+\varepsilon_{el})\xi + (\epsilon_p+2\varepsilon_{el})j\omega}{(\epsilon_p+2\varepsilon_{el})\rho_p j\omega + 2(\epsilon_p+\varepsilon_{el}\rho_p)\xi}\tilde{V}_0} \tag{3.97}$$

We can now consider two limiting cases. In the first one, representative of dielectric particles, $|\epsilon_p| \ll \varepsilon_{el}$, so that:

$$\tilde{I} \simeq \pi R\omega^2\varepsilon_{el}\frac{\rho_0}{\xi+\rho_0 j\omega}\rho_p\frac{\xi+j\omega}{\rho_p j\omega + (\epsilon_p/\varepsilon_{el}+\rho_p)\xi}\tilde{V}_0 \tag{3.98}$$

The second one, representative of conductive particles, $|\epsilon_p| \simeq \sigma_p/\omega \gg \varepsilon_{el}$, so that:

$$\tilde{I} \simeq \pi R\omega^2\varepsilon_{el}\frac{\rho_0}{\xi+\rho_0 j\omega}\rho_p\frac{2\xi+j\omega}{\rho_p j\omega + 2\xi}\tilde{V}_0 \tag{3.99}$$

The admittance $Y = \tilde{I}/\tilde{V}_0$ calculated according to the above equations is shown in Sec. 3.3.5. By subtracting Eq. 3.92 to Eq. 3.97 we can then derive the admittance (hence, the capacitance) change due to the introduction of a biomolecule in the system. $\Im[\Delta Y/\omega]$ represents the useful signal of nanoelectrode biosensors as those described in Chap. 5.

3.3.3 0th order model - electrolyte only

The system considered so far has the advantage of describing in a simple but realistic way the response of a capacitive biosensor to particles that are much smaller than the device dimensions. However, if the particle dimensions are larger than the electrodes, this model may be inadequate, since by construction it assumes that the entire surface of the particle interacts with the electrodes.

For this reason, in this section we derive an alternative model with spherical symmetry but for a slightly different geometry, as shown in Fig. 3.15b. It consists of an electrode of (large) radius R_o and a smaller electrode of radius R_i, both ideally polarizable and with the centers at $r = 0$, and an electrolyte in between. This configuration resembles the physical system studied in cartesian coordinates in Sec. 3.1.

The solution is given by Eqs. 3.84 above, namely:

$$\begin{cases} R_l = c_l' \mathrm{y}_{\left(-1-\sqrt{1+4\alpha^2}\right)/2}(-j\kappa_i r) + d_l' \mathrm{j}_{\left(-1-\sqrt{1+4\alpha^2}\right)/2}(-j\kappa_i r) \\ \Theta_l = e_l P_{\left(-1+\sqrt{1+4\alpha^2}\right)/2}(\cos\theta) + f_l Q_{\left(-1+\sqrt{1+4\alpha^2}\right)/2}(\cos\theta) \end{cases}$$

Differently from the previous section, here we assume invariance with respect to θ, so that $\alpha = 0$. The solutions represent a 0-th order model, preserve perfectly the radial symmetry and read:

$$v_l = c_l' \, \mathrm{y}_{-1}(-j\kappa_l r) + d_i' \, \mathrm{j}_{-1}(-j\kappa_l r) = \frac{c_l \exp(\kappa_l r) + d_l \exp(-\kappa_l r)}{\kappa_l r}, \qquad \kappa_l \neq 0$$
$$v_3 = c_3 + \frac{d_3}{r}, \qquad \kappa_3 = 0$$

where $c_l = (jd_l' + c_l')/2$, $d_l = (jd_l' - c_l')/2$. The potential and ion quasi-potentials are:

$$\tilde{V} = -\frac{\xi}{j\omega} v_1 + v_3 = -\frac{\xi}{j\omega} \frac{c_1 \exp(\kappa_1 r) + d_1 \exp(-\kappa_1 r)}{\kappa_1 r} + c_3 + \frac{d_3}{r}$$
$$\tilde{\phi}_1 = v_1 - v_2 + v_3 = \frac{c_1 \exp(\kappa_1 r) + d_1 \exp(-\kappa_1 r)}{\kappa_1 r} - \frac{c_2 \exp(\kappa_2 r) + d_2 \exp(-\kappa_2 r)}{\kappa_2 r} + c_3 + \frac{d_3}{r}$$
$$\tilde{\phi}_2 = v_1 + v_2 + v_3 = \frac{c_1 \exp(\kappa_1 r) + d_1 \exp(-\kappa_1 r)}{\kappa_1 r} + \frac{c_2 \exp(\kappa_2 r) + d_2 \exp(-\kappa_2 r)}{\kappa_2 r} + c_3 + \frac{d_3}{r}$$

Note that the solution includes terms exponentially decaying with r and terms with lower spatial decay as $1/r$.
The gradients are then:

$$\nabla \tilde{V} = \left[-\frac{\xi}{j\omega} \left(c_1 \exp(\kappa_1 r) \frac{\kappa_1 r - 1}{\kappa_1 r^2} - d_1 \exp(-\kappa_1 r) \frac{\kappa_1 r + 1}{\kappa_1 r^2} \right) - \frac{d_3}{r^2} \right] \hat{r}$$
$$\nabla \tilde{\phi}_1 = \left[c_1 \exp(\kappa_1 r) \frac{\kappa_1 r - 1}{\kappa_1 r^2} - d_1 \exp(-\kappa_1 r) \frac{\kappa_1 r + 1}{\kappa_1 r^2} - c_2 \exp(\kappa_2 r) \frac{\kappa_2 r - 1}{\kappa_2 r^2} \right.$$
$$\left. + d_2 \exp(-\kappa_2 r) \frac{\kappa_2 r + 1}{\kappa_2 r^2} - \frac{d_3}{r^2} \right] \hat{r}$$
$$\nabla \tilde{\phi}_2 = \left[c_1 \exp(\kappa_1 r) \frac{\kappa_1 r - 1}{\kappa_1 r^2} - d_1 \exp(-\kappa_1 r) \frac{\kappa_1 r + 1}{\kappa_1 r^2} + c_2 \exp(\kappa_2 r) \frac{\kappa_2 r - 1}{\kappa_2 r^2} \right.$$
$$\left. - d_2 \exp(-\kappa_2 r) \frac{\kappa_2 r + 1}{\kappa_2 r^2} - \frac{d_3}{r^2} \right] \hat{r} \, .$$

The boundary conditions are:

$$\begin{cases} -Z_1^2 q^2 \mu_1 n_{01} \nabla \tilde{\phi}_1 \Big|_{R_i,\theta} \cdot \hat{r} = 0 \\ -Z_2^2 q^2 \mu_2 n_{02} \nabla \tilde{\phi}_2 \Big|_{R_i,\theta} \cdot \hat{r} = 0 \\ -Z_1^2 q^2 \mu_1 n_{01} \nabla \tilde{\phi}_1 \Big|_{R_o,\theta} \cdot \hat{r} = 0 \\ -Z_2^2 q^2 \mu_2 n_{02} \nabla \tilde{\phi}_2 \Big|_{R_o,\theta} \cdot \hat{r} = 0 \\ \tilde{V}(R_i) = \tilde{V}_0 \\ \tilde{V}(R_o) = 0 \end{cases} \tag{3.100}$$

Solving this system of equations yields the coefficients, which are reported in Sec. 3.A.8. Because of the boundary conditions, we know that the ionic current density on the border

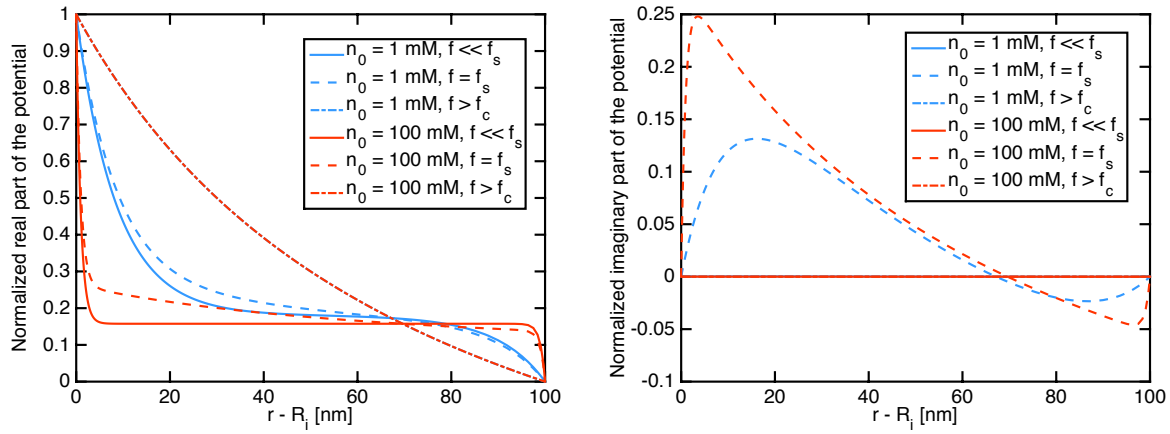

(a) real part **(b)** imaginary part

Fig 3.17: Real and imaginary parts of the normalized potential profile $\tilde{V}/\tilde{V}_0$ along r with $R_i = 75$ nm and $R_o = R_i + 100$ nm at three different frequencies, that is, below f_s, at f_s and above f_c. Note the penetration of the field at high frequency. The potential profiles are qualitatively similar to the ones in Figs. 3.5 - 3.16.

is zero; therefore, the contact current is given only by displacement current:

$$\begin{aligned}
\tilde{I} &= \int \vec{\tilde{J}}(R_i,\theta)\cdot\hat{r}dS_r = j\omega\varepsilon_{el}\int \vec{\tilde{E}}\cdot\hat{r}\,dS_r = j\omega\varepsilon_{el}\int_0^{2\pi}d\phi\int_0^{\pi}d\theta\vec{\tilde{E}}(R_i,\theta)\cdot\hat{r}\,R_i^2\sin\theta \\
&= -2\pi R_i^2 j\omega\varepsilon_{el}\left[-\frac{\xi}{j\omega}\left(c_1\exp(\kappa R_i)\frac{\kappa R_i-1}{\kappa R_i^2} - d_1\exp(-\kappa R_i)\frac{\kappa R_i+1}{\kappa R_i^2}\right) - \frac{d_3}{R_i^2}\right] \\
&= \Big(2\pi R_i R_o\tilde{V}_0\epsilon_{el}\left(-(1+\rho_i)(-1+\rho_o)+\alpha^2(-1+\rho_i)(1+\rho_o)\right)j\omega(\xi+j\omega)\Big)\Big/ \\
&\quad\Big(R_i\xi\left(1+\alpha^2(-1+\rho_i)+\rho_i-4\alpha\rho_o\right)+R_o\left(-1+\rho_o+\alpha^2(1+\rho_o)\right)(\xi+j\omega) \\
&\quad + R_i\left(1+\rho_i-(2+\rho_i)\rho_o+\rho_o^2+\alpha^2(-1+\rho_i-\rho_o)(1+\rho_o)\right)j\omega\Big)
\end{aligned}$$

where we have defined $\rho_i = \kappa R_i$, $\rho_o = \kappa R_o$ and $\alpha = \exp(\rho_i - \rho_o)$.

The potential profiles in the system are reported in Fig. 3.17 with $R_i = 75$ nm and $R_o = R_i + 100$ nm. We note similar behaviours as in Figs. 3.5 - 3.16, but in this case the high frequency profile is dependent on $1/r$ and not on r.

Large radius inner electrode If the inner electrode has a large radius ($\rho_i = \kappa R_i \gg 1$), but still much smaller than the outer electrode ($\rho_i \ll \rho_o$, $\alpha \to 0$), then we can further simplify the solution as shown in Sec. 3.A.8.
The current is then expressed as:

$$\begin{aligned}
\tilde{I} &= 2\pi R_i^2 j\omega\varepsilon_{el}\left[-\frac{\xi}{j\omega}\left(c_1\exp(\kappa R_i)\frac{\kappa R_i-1}{\kappa R_i^2} - d_1\exp(-\kappa R_i)\frac{\kappa R_i+1}{\kappa R_i^2}\right) - \frac{d_3}{R_i^2}\right] \\
&\simeq 2\pi R_i^2 j\omega\varepsilon_{el}\left[-\frac{\xi}{j\omega}\left(\rho_o j\omega\left(e^{-\rho_o}\rho_i - e^{-2\rho_o}\rho_o\right) - \rho_o j\omega\left(e^{-\rho_o}\rho_i-\rho_o\right)\right) + \frac{R_o j\omega\left(-\rho_i\rho_o + e^{-2\rho_o}\rho_i\rho_o\right)}{R_i}\right]\frac{\tilde{V}_0}{\eta} \\
&\simeq -2\pi R_i^2 j\omega\varepsilon_{el}\left[\xi\rho_o^2 + \frac{R_o\rho_i\rho_o}{R_i}j\omega\right]\frac{\tilde{V}_0}{\eta} = -2\pi R_i j\omega\varepsilon_{el}\frac{\rho_i}{\xi+\rho_i j\omega}(\xi+j\omega)\tilde{V}_0 \qquad (3.101)
\end{aligned}$$

3.3.4 0th order model with particle

We now assume that the region $r_p < r < r_P$ is dielectric with complex permittivity $\epsilon_p = \varepsilon_p - j\sigma_p/\omega$, as depicted in Fig. 3.15. This approximation mimics a physical system where the dimension of the particle are larger than the electrodes dimensions. To some extent this is the case we will examine experimentally in Sec. 5.3, where we show the response of a 75 nm radius electrode to a particle with diameter ≥ 5 μm. Following this approximation, we can say that in the electrolyte regions it still holds that:

$$\tilde{V} = -\frac{\xi}{j\omega}\frac{c_{1i}\exp(\kappa r) + d_{1i}\exp(-\kappa r)}{\kappa r} + c_{3i} + \frac{d_{3i}}{r} \tag{3.102}$$

$$\tilde{\phi} = \frac{c_{1i}\exp(\kappa r) + d_{1i}\exp(-\kappa r)}{\kappa r} + c_{3i} + \frac{d_{3i}}{r} \tag{3.103}$$

where the subscript i indicates that the constants refer to the inner electrolyte region. The potential inside the region occupied by the particle is:

$$\tilde{V} = e + \frac{f}{r}\,. \tag{3.104}$$

The boundary and continuity conditions are:

$$\begin{cases} \nabla\tilde{\phi}\Big|_{R_i}\cdot\hat{r} = 0 \\ \nabla\tilde{\phi}\Big|_{R_o}\cdot\hat{r} = 0 \\ \nabla\tilde{\phi}\Big|_{r_p}\cdot\hat{r} = 0 \\ \nabla\tilde{\phi}\Big|_{r_P}\cdot\hat{r} = 0 \\ \tilde{V}(R_i) = \tilde{V}_0 \\ \tilde{V}(R_o) = 0 \end{cases} \quad , \quad \begin{cases} \tilde{V}(r_p^+) = \tilde{V}(r_p^-) \\ \tilde{V}(r_P^+) = \tilde{V}(r_P^-) \\ \epsilon_p \left.\dfrac{d\tilde{V}}{dr}\right|_{r_p^+} = \varepsilon_{el} \left.\dfrac{d\tilde{V}}{dr}\right|_{r_p^-} \\ \varepsilon_{el} \left.\dfrac{d\tilde{V}}{dr}\right|_{r_P^+} = \epsilon_p \left.\dfrac{d\tilde{V}}{dr}\right|_{r_P^-} \end{cases} \tag{3.105}$$

The above equations allow us to compute the constants, which are reported in Sec. 3.A.9 of the chapter appendix.

The current is then:

$$\begin{aligned} \tilde{I} &= \int \vec{\tilde{J}}(R_i,\theta)\cdot\hat{r}dS_r = j\omega\varepsilon\int\vec{\tilde{E}}\cdot\hat{r}\,dS_r = j\omega\varepsilon\int_0^{2\pi}d\phi\int_0^{\pi}d\theta\vec{\tilde{E}}(R_i,\theta)\cdot\hat{r}\,R_i^2\sin\theta \\ &= 2\pi r_p r_P R_o\varepsilon_p\epsilon_{el}j\omega(\xi+j\omega)^2\left((-1+\rho_p)(1+\rho_i) - (1+\rho_p)(-1+\rho_i)\alpha_i^2\right) \\ &\quad \left((1+\rho_P)(-1+\rho_o) - (-1+\rho_P)(1+\rho_o)\alpha_o^2\right)\tilde{V}_0/\eta \end{aligned} \tag{3.106}$$

where η is defined in Sec. 3.A.9.

3.3.5 Admittance and sensor response

Based on the potential profile versus distance as a function of frequency and salt concentration, we now elucidate the operating principle behind high-frequency impedance spectroscopy. To this purpose, Fig. 3.18 (left plot) reports the magnitude of the small signal potential as a function of distance from the electrode for two cases:

1. No particle (blue curves).
2. One dielectric particle (red curves) located beyond the Debye screening length (50 nm distance from the electrode, which corresponds to 17 Debye lengths at 10 mM).

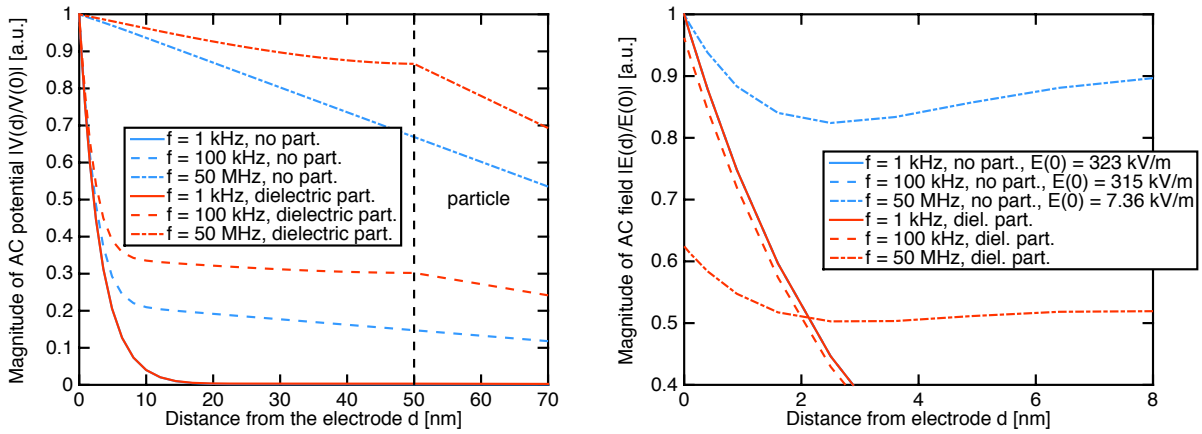

Fig 3.18: Magnitude of the AC potential (left) and electric field (right) in absence (blue) and presence (red) of the dielectric particle normalized to their value at the electrode in absence of the particle as a function of the radial distance from the electrode d and at different frequency. The particle has $r_p = 100$ nm; the salt concentration is 10 mM.

The plot shows the potential along the vertical line (symmetry axis) of the particle, taking the electrode as origin. Three frequencies are considered: below f_s (solid lines), between f_s and f_c (dashed lines), and above f_c (dash-dotted lines).
We see the following:

1. At low frequency, the AC potential decays rapidly with distance from the electrode, the decay length being essentially the same Debye length that rules the space dependence of the total DC potential. The particle lies in a quasi-neutral region of essentially zero AC electric field and its presence has no influence on the AC field at the electrode, which is proportional to the slope of the AC potential versus distance curve at zero distance. In particular, the AC electric field is independent of whether or not a particle is present (solid blue and red lines are indistinguishable).

2. At 100 kHz the AC potential is perturbed but the AC electric field at the surface, hence the AC charge on the electrode, stays essentially the same. Therefore the presence of the particle will still be not measurable at the electrode.

3. At high frequency the AC potential varies more slowly with distance, and the perturbation introduced by the particle propagates back to the electrode surface. The surface AC electric field and the charge on the electrode are therefore affected. Since the sensor measures this charge, the particle becomes visible at this frequency.

These graphs elucidate the basic operating principle of AC detection. Experimental evidence of this interpretation is provided in Sec. 5.3. To complete the physical picture and relate it to the expected signal amplitude, the right plot of Fig. 3.18 shows the magnitude of the AC electric field normalized to the surface value in the unperturbed case $E(0)$ for all cases above. Each curve for the perturbed case is normalized to the corresponding unperturbed surface field value. So the difference between perturbed and unperturbed cases is representative of the relative amplitude of the measured signal. The legend reports the normalization values $E(0)$. We see that the surface AC field is much larger at low or intermediate frequency but the relative change due to the particle is larger at high frequency than at low frequency (almost 0% at 1 kHz, 4% at 100 kHz, 40% at 50 MHz).

Those results point out that a large relative signal is obtained in the neighbourhood of a smaller AC field (hence surface charge) value.

In this section we compare the admittance $Y = \tilde{I}/\tilde{V}_0$ and the admittance variations due to the introduction of a particle ΔY for the AC spherical models presented in Secs. 3.3.1 - 3.3.4.
Assuming large electrodes, the expression of Y in the absence of particle is, in the two models (see Eqs. 3.92-3.101):

$$Y_0 = 2\pi R_i j\omega\varepsilon_{el}\frac{\rho_i}{\xi + \rho_i j\omega}(\xi + j\omega) \qquad \text{0th order model} \tag{3.107}$$

$$Y_1 = \frac{\pi}{2}Rj\omega\varepsilon_{el}\frac{\rho_0}{\xi + \rho_0 j\omega}(\xi + j\omega) \qquad \text{1st order model}\,. \tag{3.108}$$

The two expressions are very similar, except for the pre-factor and the substitution of R_i with R. Viewing the admittance as a transfer function between voltage and current, we usually observe the behaviour shown in Fig. 3.19. Consistently with Sec. 3.1.1.3, we then conclude that the admittance transfer function has 2 zeros and 1 pole. The zeros are easily found and they are, as in Sec. 3.1.1.3:

$$\omega_{z1} = 0, \quad \omega_{z2} = \xi$$

As in Sec. 3.1.1.3, we assume that the pole frequency $f_s \ll \xi/2\pi$ and we can write that:

$$f_{s0} = \frac{1}{2\pi}\frac{\lambda_D}{R_i}, \quad f_{s1} = \frac{1}{2\pi}\frac{\lambda_D}{R}\,.$$

These expressions are conceptually similar but underline the geometry dependence of f_s. If we use a parallel model for the admittance we can write that $Y = G + j\omega C$, so that the effective capacitance is $C = \Im\{Y\}/\omega$:

$$C_0 = 2\pi R_i\varepsilon_{el}\,\Re\left\{\frac{\rho_i}{\xi + \rho_i j\omega}(\xi + j\omega)\right\} \tag{3.109}$$

$$C_1 = \frac{\pi}{2}R\varepsilon_{el}\,\Re\left\{\frac{\rho_0}{\xi + \rho_0 j\omega}(\xi + j\omega)\right\} \tag{3.110}$$

In nanoelectrode biosensors, as we discuss in more detail in Sec. 3.6 and Chap. 5, the capacitance is typically measured via a charge pump cycle, i.e. repeatedly charging and discharging the nanoelectrode. In these conditions the imaginary part of the admittance can be rather inaccurate in representing the measured capacitance. Since in the real detector the capacitance is extracted from the integral of the total charge, it appears legitimate to calculate an effective capacitance $C_{eff} = |Y|/\omega$ from the modulus of the charge at the electrode, thus accounting for both the real and imaginary part of the current. We thus obtain:

$$C_0^{eff} = 2\pi R_i\varepsilon_{el}\left|\frac{\rho_i}{\xi + \rho_i j\omega}(\xi + j\omega)\right| \tag{3.111}$$

$$C_1^{eff} = \frac{\pi}{2}R\varepsilon_{el}\left|\frac{\rho_0}{\xi + \rho_0 j\omega}(\xi + j\omega)\right| \tag{3.112}$$

Fig. 3.20 shows the capacitance calculated for the two models starting from the same data of Fig. 3.19 and with the parameters given in Tab. 3.2. Note that the capacitance is not constant in frequency, and therefore cannot be modelled by a unique linear capacitor.

Moreover, the frequency of the zero is equal to ξ in the case of C_{eff}, while it is always lower than ξ in the case of C and it has a weaker dependence on salt concentration. These markable differences represent clear signatures of the two models that should be easier to identify experimentally than a quantitative difference in the absolute capacitance value.

Parameter	**Symbol**	**Value**	**Units**
Inner electrode radius (0th order)	R_i	75	[nm]
Outer electrode radius (0th order)	R_o	$r_P + 500$	[nm]
Particle radius (1st order)	r_p	4.5	[μm]
Ion mobility	μ_1	$3.242 \cdot 10^{11}$	[m/Ns]
Temperature	T	298	[K]
Electrolyte permittivity	ε_{el}	Eq. 2.39	[F/m]
Particle permittivity (dielectric)	ε_p	$2.6\varepsilon_0$	[F/m]
Particle permittivity (conductive)	ε_p	$6.9\varepsilon_0$	[F/m]
Particle conductivity (conductive)	σ_p	6.3×10^7	[S/m]

Table 3.2: Parameters used in the calculation of the admittance in the AC spherical models (unless otherwise stated).

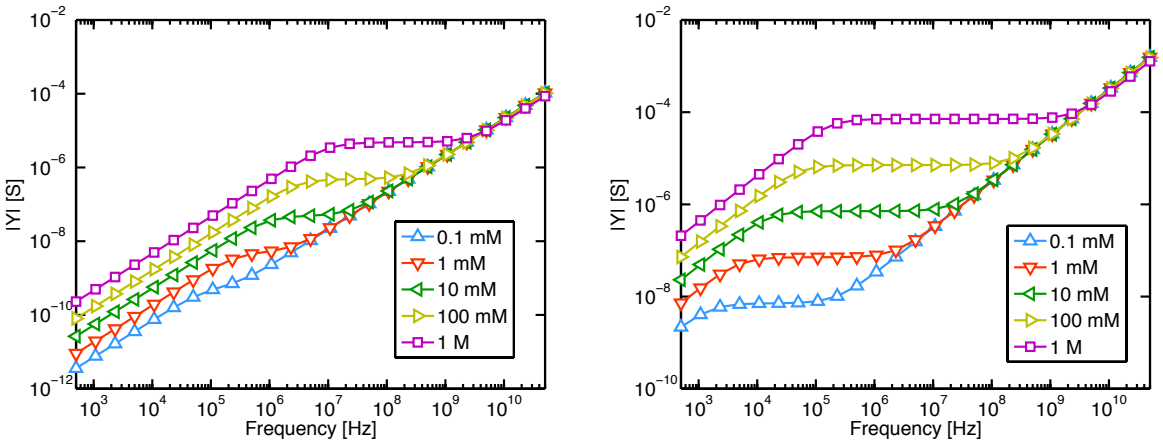

(a) 0th order model **(b)** 1st order model, $R = 4510$ nm

Fig 3.19: Magnitude of the electrode admittance according to the two spherical models.

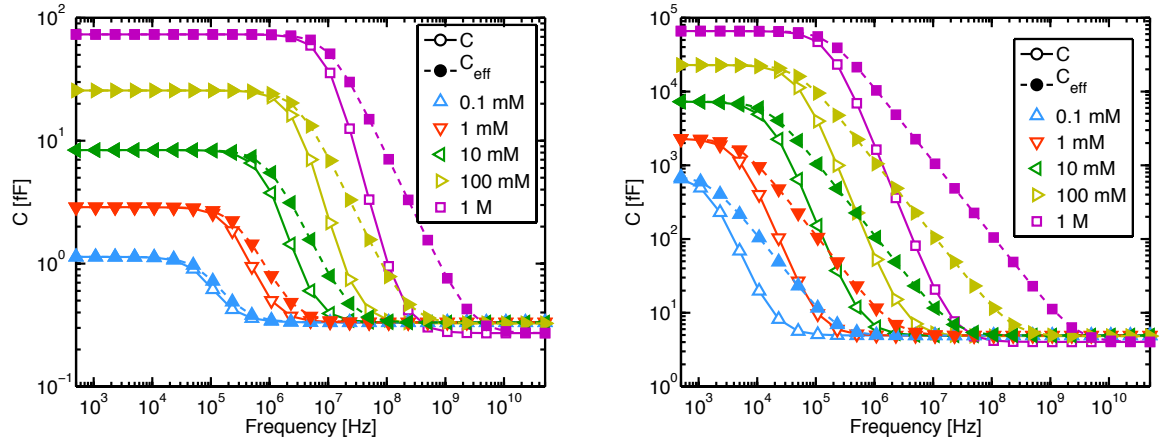

(a) 0th order model **(b)** 1st order model, $R = 4510$ nm

Fig 3.20: Small signal and effective capacitance in the two spherical models in absence of particles. Note the differenct concentration of the C and C_{eff} upper zero frequency.

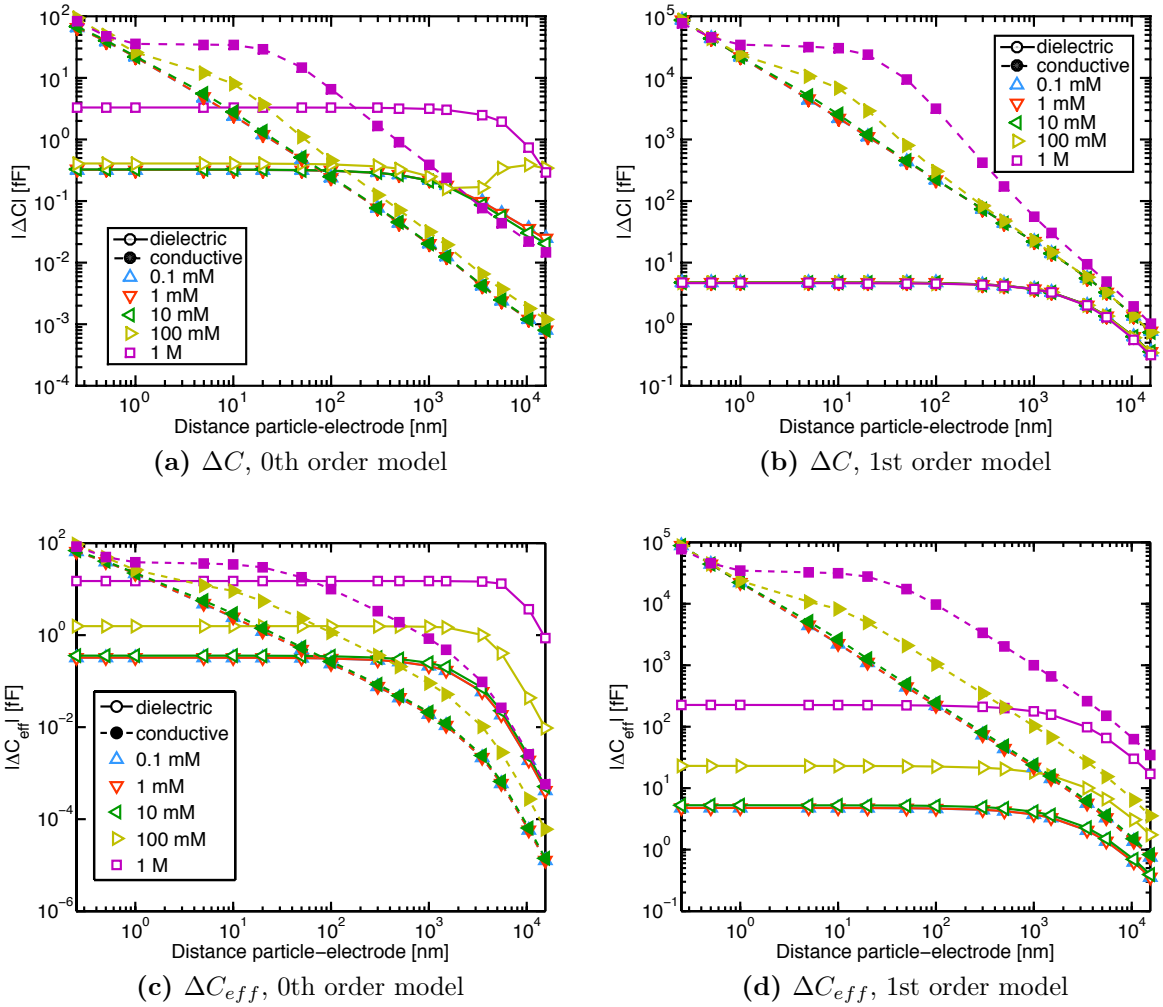

(a) ΔC, 0th order model

(b) ΔC, 1st order model

(c) ΔC_{eff}, 0th order model

(d) ΔC_{eff}, 1st order model

Fig 3.21: Change in capacitance due to a particle at 50 MHz. In the 0th order model the distance is $r_p - R_i$, while in the 1st order model it is $\Delta r = R - r_p$.

We always calculate the change in capacitance as the difference between the case without particles and the case with it: $\Delta C = C_0 - C_p$. For the sake of comparison, we have chosen a spherical particle of 4.5 μm radius for the 1st order model, and a spherical shell particle with this same volume for the 0th order model. Figs. 3.21 and 3.22 show that the ΔC predicted by the two models are fairly different and feature quite different dependencies on the particle distance from the electrode defined as $r_p - R_i$ in the 0th order model and $R - r_p$ in the 1st order one. It is interesting to note that the ΔC and ΔC_{eff} for conductive particles exhibit sharp dips that reflect a sign change. The frequency where the dip occurs is different for ΔC and ΔC_{eff}.

In order to understand the physical origin of the sign changes in Fig. 3.22 we make use of the 1st order model. Fig. 3.23 shows the real part of the electric field lines in absence (a-c) or presence either of a dielectric (d-f) or conductive (g-i) particle. The perturbed path of the field lines around the particle surface denotes the formation of an electrical double layer with limited thickness at 10 mM (plots b, e, h). The borders of the EDLs are easily recognizable by looking at the points where the electric field lines are sharply deviated. If the concentration is reduced at constant low frequency, the EDL of the particle interacts with that of the outer electrode (plots a, d, g) whereas if the frequency is increased at constant concentration (plots c, f, i) all EDLs disappear and we retain the

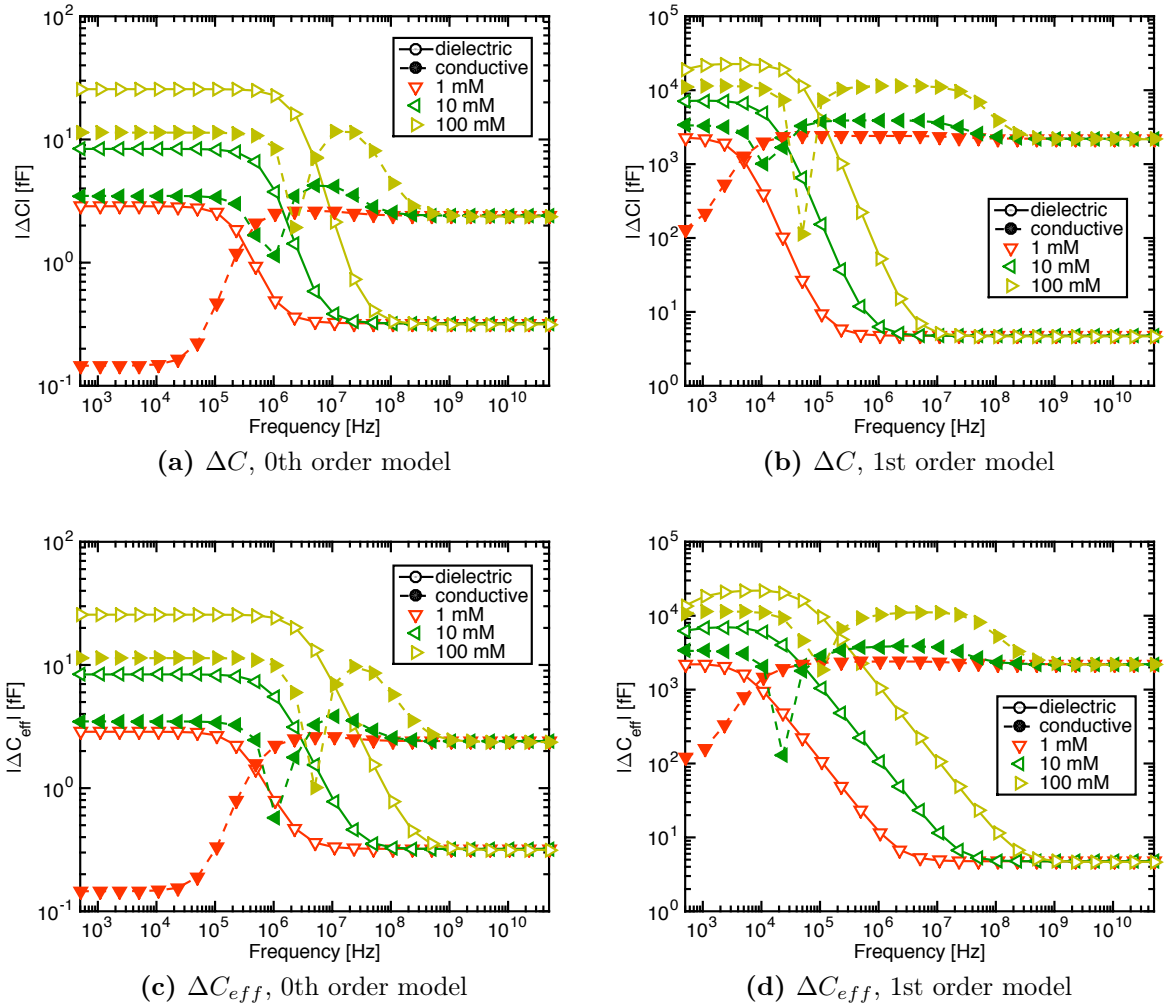

(a) ΔC, 0th order model

(b) ΔC, 1st order model

(c) ΔC_{eff}, 0th order model

(d) ΔC_{eff}, 1st order model

Fig 3.22: Change in capacitance due to the introduction of a particle at different distances from the electrode. In the 0th order model $r_p - R_i = 10$ nm, while in the 1st order one $\Delta r = 10$ nm.

electrostatic limit, as expected. We immediately see that, since the dielectric particle has a lower permittivity with respect to the electrolyte, it always repels the field lines, both at low and high frequency.
On the contrary, the conductive particle shows a more complicated behaviour. In particular, when the double layer on the electrode and on the particle do not overlap (Fig. 3.23h, the Debye length $\simeq 3$ nm is much smaller than $R - r_p$), the electric field lines are repelled similarly to the case of the dielectric particle. On the other hand, at high frequency the field lines are attracted by the particle. This explains why there is no sign change in ΔC for dielectric particles in Fig. 3.22 and why instead sign changes appear in ΔC for conductive particles. It can be shown that the sign change unavoidably shows up in multi-domain media where materials with variable or different complex conductivity, EDLs or SAM are present.

3.3.6 General model for the admittance change due to particles

We now present the derivation and verification of an improved version of the analytical model presented in [33] for the admittance change (ΔY) induced by spherical dielectric (colloidal) particles at ideally polarizable electrodes that explicitly takes into account ionic

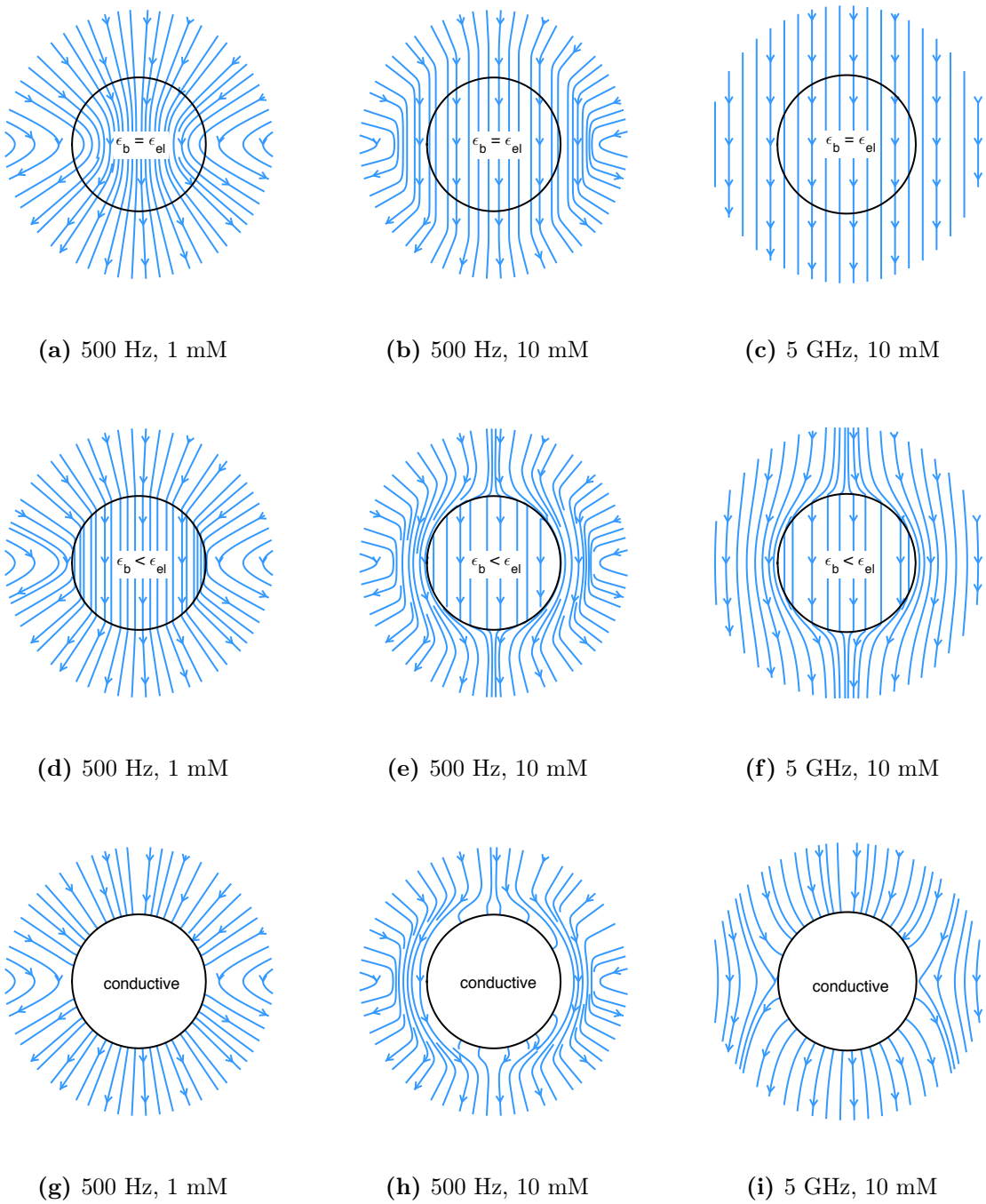

(a) 500 Hz, 1 mM **(b)** 500 Hz, 10 mM **(c)** 5 GHz, 10 mM

(d) 500 Hz, 1 mM **(e)** 500 Hz, 10 mM **(f)** 5 GHz, 10 mM

(g) 500 Hz, 1 mM **(h)** 500 Hz, 10 mM **(i)** 5 GHz, 10 mM

Fig 3.23: Real part of the electric field lines calculated with the 1st order spherical model in absence (a-c) or presence either of a dielectric (d-f) or conductive (g-i) particle. $R = 200$ nm, $r_p = 100$ nm. ε_b denotes the permittivity in the particle volume.

diffusion currents.
In order to derive the model we start considering again the system of Sec. 3.3.1 (Fig. 3.15), i.e. an empty electrolyte region and a spherical coordinate system with no variation along the planar angular component φ and a dependence on the vertical angular component of the type $\cos\theta$. However, differently from Sec. 3.3.1, we now assume that the outer shell is made of a Faradaic electrode which is kept at a potential equal to $\tilde{V}_b \cos\theta$ and where $\tilde{\phi}_1(R) = \tilde{\phi}_2(R) = \tilde{V}(R)$, and the region is filled with a symmetric electrolyte. As shown

in Sec. 3.A.10, the derived solution is given again by Eqs. 3.89 but with the constants:

$$c_3 = \frac{\tilde{V}_b}{R}, \qquad c_1 = 0, \qquad d_1 = 0 \tag{3.113}$$

We then consider a case similar to the one of Sec. 3.3.2, where a dielectric particle with permittivity ϵ_p (i.e., an ion-free spherical inner region of radius r_p) is introduced in the electrolyte and therefore is surrounded by a concentric outer region of radius $R \gg r_p$, while the outer shell is again a Faradaic electrode. In general the dielectric constants can be complex, where the imaginary parts account for possible electronic conduction and/or relaxation losses in the materials, as necessary to describe conducting particles like gold nanoparticles. The solutions are given by Eqs. 3.93-3.94. In these conditions and in absence of the particle, the radial component of the complex electric field $\tilde{E}_0$ is constant over the region which will be occupied by the particle ($\tilde{E}_0 = -\tilde{V}_b/R$). Since the field is uniform, we can express the change in the conjugate complex power induced by the introduction of the particle in the system as:

$$\Delta S^* = S^*_{with} - S^*_{w/out} = f(\omega)(\sigma_{el} + j\omega\varepsilon_{el})\Omega_p|\tilde{E}_0|^2 \tag{3.114}$$

where $\sigma_{el} = 2q^2\mu n_0$ is the electrolyte conductivity, $\Omega_p = 4\pi r_p^3/3$ the particle volume and

$$f(\omega) = -\frac{3}{2}\frac{\frac{1+\kappa r_p}{2+2\kappa r_p+\kappa^2 r_p^2} + \frac{\varepsilon_{el}}{\epsilon_p} + j\omega\tau_{el}(\frac{\varepsilon_{el}}{\epsilon_p} - 1)}{\frac{1+\kappa r_p}{2+2\kappa r_p+\kappa^2 r_p^2} + \frac{\varepsilon_{el}}{\epsilon_p} + j\omega\tau_{el}(\frac{\varepsilon_{el}}{\epsilon_p} + \frac{1}{2})} \tag{3.115}$$

is a complex function of frequency that depends slightly on the particle radius r_p and the electrolyte and particle conductivities and permittivities. In the expression above $\kappa = (1 + j\omega\tau_{el})^{1/2}/\lambda_D$, $\tau_{el} = 1/\xi_{el} = \varepsilon_{el}/\sigma_{el}$. The complete derivation of this expression is shown in Sec. 3.A.10. We can then interpret the change in conjugate complex power as due to a change in the nanoelectrode admittance. By defining $\tilde{V}_0$ the total voltage drop between the electrodes ($\tilde{V}_0$=$2\tilde{V}_b$ in this case) we have: $\Delta S^* = \tilde{V}_0^*\Delta I = \Delta Y|\tilde{V}_0|^2$, so that ΔY would be proportional to $|\tilde{E}_0|^2/|\tilde{V}_0|^2$.

For generalization to non-uniform fields generated, for instance, by multi-domain regions (e.g. a working electrode covered with the electrical double layer, Stern layer or a self-assembled monolayer) the $|\tilde{E}_0|^2$ factor in Eq. 3.114 is replaced by the square of the (in general complex) unperturbed electric field at the particle position $\tilde{E}_0^{\,2}$. In this general case, the admittance variation due to the insertion of a nanoparticle in the electrolyte can thus be expressed as:

$$\boxed{\Delta Y = \Delta G + j\omega\Delta C = f(\omega)\,(\sigma_{el} + j\omega\varepsilon_{el})\Omega_p\left(\frac{\tilde{E}_0}{\tilde{V}_0}\right)^2} \tag{3.116}$$

which represents the analytical model we were looking for. Eq. 3.116 generalizes a similar expression presented in [33] but extends it considerably by accounting for the ionic diffusion currents, which were instead neglected in [33]. Eq. 3.116 predicts that for small particles ($r_p \ll R$) the nanoelectrode response should be proportional to the electrolyte complex conductivity, to the particle volume, and to the squared unperturbed electric field at the particle location. In Sec. 5.4 we will validate Eq. 3.116 by means of extensive two-dimensional numerical simulations.

3.4 1D semiconductor resistor

The 3D simulator ENBIOS (see Chap. 4) has been designed as a general purpose platform for the analysis of electrolyte/insulator/semiconductor (EIS) systems. It is therefore useful to examine simple solutions also for the semiconductor regions. In particular, here we assume a 1D semiconductor resistor where both the DC electrostatic potential and the DC electron and hole quasi-potentials are linear, so that the carrier concentrations are constant throughout the system. The equations for the small signal AC regime are:

$$\varepsilon\frac{d^2\tilde{V}}{dx^2}+\sum_{m=1}^{N_{sp}}\frac{Z_m^2q^2}{k_BT}n_{0m}\left(\tilde{\phi}_m-\tilde{V}\right)=0$$
$$Z_mq\mu_m\frac{d}{dx}\left(n_{0m}\left(\frac{Z_mq}{k_BT}\left(\tilde{\phi}_m-\tilde{V}\right)\frac{d\phi_{0m}}{dx}+\frac{d\tilde{\phi}_m}{dx}\right)\right)-j\omega n_{0m}\frac{Z_mq}{k_BT}\left(\tilde{\phi}_m-\tilde{V}\right)=0$$

where m now denotes the free carriers (electrons and holes). Using the fact that $d\phi_{0m}/dx = V_0/L$ (where V_0 is the DC bias and L the resistor length) and that the concentrations are constant (we call n_{0n} the electron and n_{0p} the DC hole concentration), we can then write:

$$\varepsilon\frac{d^2\tilde{V}}{dx^2}+\frac{q^2}{k_BT}\left(n_{0n}\left(\tilde{\phi}_n-\tilde{V}\right)+n_{0p}\left(\tilde{\phi}_p-\tilde{V}\right)\right)=0$$
$$-q\mu_nn_{0n}\frac{d}{dx}\left(-\frac{q}{k_BT}\left(\tilde{\phi}_n-\tilde{V}\right)\frac{V_0}{L}+\frac{d\tilde{\phi}_n}{dx}\right)+j\omega n_{0n}\frac{q}{k_BT}\left(\tilde{\phi}_n-\tilde{V}\right)=0$$
$$q\mu_pn_{0p}\frac{d}{dx}\left(\frac{q}{k_BT}\left(\tilde{\phi}_p-\tilde{V}\right)\frac{V_0}{L}+\frac{d\tilde{\phi}_p}{dx}\right)-j\omega n_{0p}\frac{q}{k_BT}\left(\tilde{\phi}_p-\tilde{V}\right)=0$$

So finally:

$$\frac{d^2\tilde{V}}{dx^2}+\frac{q^2}{\varepsilon k_BT}\left(n_{0n}\left(\tilde{\phi}_n-\tilde{V}\right)+n_{0p}\left(\tilde{\phi}_p-\tilde{V}\right)\right)=0$$
$$\frac{d^2\tilde{\phi}_n}{dx^2}-\frac{V_0}{L}\frac{q}{k_BT}\left(\frac{d\tilde{\phi}_n}{dx}-\frac{d\tilde{V}}{dx}\right)-\frac{j\omega}{\mu_nk_BT}\left(\tilde{\phi}_n-\tilde{V}\right)=0$$
$$\frac{d^2\tilde{\phi}_p}{dx^2}+\frac{V_0}{L}\frac{q}{k_BT}\left(\frac{d\tilde{\phi}_p}{dx}-\frac{d\tilde{V}}{dx}\right)-\frac{j\omega}{\mu_pk_BT}\left(\tilde{\phi}_p-\tilde{V}\right)=0$$

In practice, however, it will always be true that either $n_{0n} \gg n_{0p}$ or $n_{0n} \ll n_{0p}$, so that we can neglect the contribution of the minority carrier. We then denote n_0 the DC majority carrier concentration, Z its valence and μ its mobility.
We also define the symbols $\kappa_D^2 = Z^2q^2n_0/\varepsilon k_BT$, $\kappa_\omega^2 = j\omega/\mu k_BT$, $V_{th} = k_BT/Zq$ and $v_0 = V_0/V_{th}$.

We choose here to deal with this system of equations by expanding the unknowns into spatial harmonics $\tilde{u} = \int \tilde{u}_\kappa \exp(\kappa x)\, d\kappa$, as in Sec. 3.2. In this way we get the system of equations:

$$\begin{cases}\kappa^2\tilde{V}_\kappa+\kappa_D^2\left(\tilde{\phi}_\kappa-\tilde{V}_\kappa\right)=0\\ \kappa^2\tilde{\phi}_\kappa+2\kappa_L\kappa\left(\tilde{\phi}_\kappa-\tilde{V}_\kappa\right)-\kappa_\omega^2\left(\tilde{\phi}_\kappa-\tilde{V}_\kappa\right)=0\end{cases} \tag{3.117}$$

where $\kappa_L = v_0/2L$. We can write Eqs. 3.117 in a matrix form as $\mathbf{Au} = 0$, where:

$$\mathbf{u} = \begin{bmatrix} \tilde{V}_\kappa \\ \tilde{\phi}_\kappa \end{bmatrix}, \qquad \mathbf{A} = \begin{bmatrix} \kappa^2 - \kappa_D^2 & \kappa_D^2 \\ -2\kappa_L\kappa + \kappa_\omega^2 & \kappa^2 + 2\kappa_L\kappa - \kappa_\omega^2 \end{bmatrix}$$

In order to find non-zero solutions we have to set $\det(\mathbf{A}) = 0$, a condition that gives us the characteristic equation:

$$\kappa^2 \left(\kappa^2 + 2\kappa_L\kappa - \kappa_D^2 - \kappa_\omega^2\right) = 0$$

The 4 solutions, which we denote κ_l, are:

$$\kappa_{1,2} = 0, \qquad \kappa_3 = -\kappa_L + \kappa_s, \qquad \kappa_4 = -\kappa_L - \kappa_s$$

where $\kappa_s = \sqrt{\kappa_L^2 + \kappa_D^2 + \kappa_\omega^2}$. The general solution is then:

$$\tilde{u} = \tilde{u}_1 + \tilde{u}_2 x + \sum_{l=3}^{4} \tilde{u}_l \exp\left(\kappa_l x\right)$$

where once again we use the simplified the notation where $\tilde{u}_l \triangleq \tilde{u}_{\kappa_l}$. To find the $\tilde{V}_l$ and $\tilde{\phi}_l$ we have to substitute the eigenvalues in Eq. 3.117a, so that:

$$\kappa_D^2 \left(\tilde{\phi}_{1,2} - \tilde{V}_{1,2}\right) = 0 \quad \Longleftrightarrow \quad \tilde{\phi}_{1,2} = \tilde{V}_{1,2}$$

$$\kappa_3^2 \tilde{V}_3 + \kappa_D^2 \left(\tilde{\phi}_3 - \tilde{V}_3\right) = 0 \quad \Longleftrightarrow \quad \tilde{\phi}_3 = -\frac{\kappa_\omega^2 + 2\kappa_L\left(\kappa_L - \kappa_s\right)}{\kappa_D^2}\tilde{V}_3$$

$$\kappa_4^2 \tilde{V}_4 + \kappa_D^2 \left(\tilde{\phi}_4 - \tilde{V}_4\right) = 0 \quad \Longleftrightarrow \quad \tilde{\phi}_4 = -\frac{\kappa_\omega^2 + 2\kappa_L\left(\kappa_L + \kappa_s\right)}{\kappa_D^2}\tilde{V}_4$$

We now calculate the integration constants applying two different systems of boundary conditions. In the first case we assume that the contacts are ohmic both in DC and AC, so that we retrieve the simple 1D semiconductor resistor. In the second case we assume that the contacts are ideally polarizable in AC, so that AC double layers on the electrodes are formed. This latter case does not describe a physical situation in real semiconductors, but it provides a useful reference calculation for the validation of the numerical solver.
Remembering that the carrier current density $\tilde{J}_c$ is given by Eq. 2.37b, we can write (neglecting the minority carrier contribution):

$$\tilde{J}_c = -Z^2 q^2 \mu n_0 \left(\frac{Zq}{k_B T}\frac{V_0}{L}\left(\tilde{\phi} - \tilde{V}\right) + \nabla\tilde{\phi}\right) \tag{3.118}$$

3.4.1 Resistor in AC small signal regime

The boundary conditions for the resistor case are:

$$\tilde{V}(0) = \tilde{\phi}(0) = 0, \qquad \tilde{V}(L) = \tilde{\phi}(L) = \tilde{V}_0$$

The calculation of the integration constants is reported in Sec. 3.A.11 in the chapter appendix. The potential and quasi-potentials are then, as expected:

$$\tilde{V} = \tilde{\phi} = \frac{\tilde{V}_0}{L}x\,. \tag{3.119}$$

We can also calculate the current density in the resistor:

$$\tilde{J} = -j\omega\varepsilon\frac{d\tilde{V}}{dx} + \tilde{J}_c = -\frac{\tilde{V}_0}{L}\left(q^2\mu n_0 + j\omega\varepsilon\right) \tag{3.120}$$

3.4.2 Capacitor in AC small signal regime

The boundary conditions are:

$$\tilde{V}(0) = 0, \qquad \tilde{V}(L) = \tilde{V}_0, \qquad \tilde{J}_c(0) = 0, \qquad \tilde{J}_c(L) = 0$$

where the last two equations correspond to the hypothesis of ideally polarizable electrodes. The integration constants for this case are reported in Sec. 3.A.11.
The current density is easily calculated as:

$$\begin{aligned}\tilde{J} &= -j\omega\varepsilon\frac{d\tilde{V}}{dx} + \tilde{J}_c = -\left(Z^2q^2\mu n_0 + j\omega\varepsilon\right)\tilde{V}_2 \\ &= -\frac{e^{\frac{ZqV_0}{2k_BT}}}{\eta}\left(-1 + e^{\sqrt{\frac{Z^2q^2\left(4k_BTn_0L^2+V_0^2\varepsilon\right)\mu+4k_BTL^2\varepsilon j\omega}{k_B^2T^2\varepsilon\mu}}}\right)\frac{(j\omega)^2}{k_B^3T^3\varepsilon\mu^3}\left(Z^2q^2\mu n_0 + j\omega\varepsilon\right)^2\tilde{V}_0\end{aligned} \tag{3.121}$$

3.5 1D AC Electrolyte/Insulator/Semiconductor system

We will now study the system sketched in Fig. 3.24 which is often referred to as the EIS system. We assume a flat-band condition in DC, i.e. $V_0 = 0$ everywhere, so that the ion and carrier concentrations n_{0m} are constant. We apply an AC small-signal potential $\tilde{V}_B$ at the semiconductor electrode while the contact to the electrolyte is grounded and, furthermore, it acts as an AC reference electrode (i.e., it is a Faradaic contact). We consider the symmetric 1:1 electrolyte, with the parameters $\xi_{el} = 2q^2\mu_{el}n_{0el}/\varepsilon_{el}$ and $\kappa_{el}^2 = (\xi_{el} + j\omega)/D_{el}$ (compare with Eqs. 3.31 in Sec. 3.1.1). The equations are then:

$$\text{electrolyte:} \begin{cases} \dfrac{d^2\tilde{V}}{dx^2} = -\dfrac{\xi_{el}}{2D_{el}}\left(\tilde{\phi}_1 + \tilde{\phi}_2 - 2\tilde{V}\right) \\ \dfrac{d^2\tilde{\phi}_1}{dx^2} = \dfrac{j\omega}{D_{el}}\left(\tilde{\phi}_1 - \tilde{V}\right) \\ \dfrac{d^2\tilde{\phi}_2}{dx^2} = \dfrac{j\omega}{D_{el}}\left(\tilde{\phi}_2 - \tilde{V}\right) \end{cases}$$

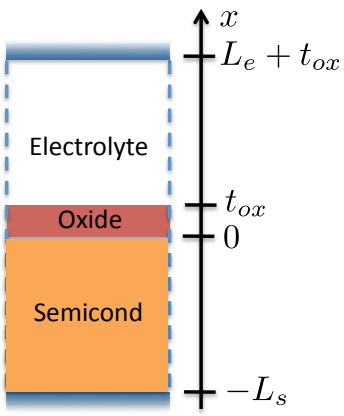

Fig 3.24: Sketch of the domain.

$$\text{oxide: } \frac{d^2\tilde{V}}{dx^2} = 0$$

$$\text{semiconductor: } \begin{cases} \dfrac{d^2\tilde{V}}{dx^2} + \dfrac{q^2}{\varepsilon_s k_B T}\left(n_{0n}\left(\tilde{\phi}_n - \tilde{V}\right) + n_{0p}\left(\tilde{\phi}_p - \tilde{V}\right)\right) = 0 \\ \dfrac{d^2\tilde{\phi}_n}{dx^2} - \dfrac{d\phi_{0n}}{dx}\dfrac{q}{k_B T}\left(\dfrac{d\tilde{\phi}_n}{dx} - \dfrac{d\tilde{V}}{dx}\right) - \dfrac{j\omega}{\mu_n k_B T}\left(\tilde{\phi}_n - \tilde{V}\right) = 0 \\ \dfrac{d^2\tilde{\phi}_p}{dx^2} + \dfrac{d\phi_{0p}}{dx}\dfrac{q}{k_B T}\left(\dfrac{d\tilde{\phi}_p}{dx} - \dfrac{d\tilde{V}}{dx}\right) - \dfrac{j\omega}{\mu_p k_B T}\left(\tilde{\phi}_p - \tilde{V}\right) = 0 \end{cases}$$

We immediately note that, as in all previous case studies, $\tilde{\phi}_1 = \tilde{\phi}_2 = \tilde{\phi}$ in the electrolyte. We also assume that the semiconductor is n-type with doping N_D, so that we can write (because of the zero DC bias condition) $n_{0n} = N_D$, $n_{0p} = n_i^2/N_D \simeq 0$ and neglect the minority carrier contribution in Poisson equation. The zero DC bias condition also implies that $\dfrac{d\phi_{0n}}{dx} = \dfrac{d\phi_{0p}}{dx} = 0$ and we do not need to calculate the equations for $\tilde{\phi}_p$, so we can simplify the notation by dropping the suffix "n" and obtain the simplified equations as follows:

$$\text{electrolyte: } \begin{cases} \dfrac{d^2\tilde{V}}{dx^2} = -\dfrac{\xi_{el}}{D_{el}}\left(\tilde{\phi} - \tilde{V}\right) \\ \dfrac{d^2\tilde{\phi}}{dx^2} = \dfrac{j\omega}{D_{el}}\left(\tilde{\phi} - \tilde{V}\right) \end{cases} \tag{3.122a}$$

$$\text{oxide: } \frac{d^2\tilde{V}}{dx^2} = 0 \tag{3.122b}$$

$$\text{semiconductor: } \begin{cases} \dfrac{d^2\tilde{V}}{dx^2} = -\dfrac{\xi_n}{D_n}\left(\tilde{\phi} - \tilde{V}\right) \\ \dfrac{d^2\tilde{\phi}}{dx^2} = \dfrac{j\omega}{D_n}\left(\tilde{\phi} - \tilde{V}\right) \end{cases} \tag{3.122c}$$

where the semiconductor cut-off frequency is $\xi_n = q^2\mu_n N_D/\varepsilon_s$. We immediately see that the equations in the electrolyte and in the semiconductor are formally equivalent, so that the general solution of this former case applies to the latter as well.
The general solution (Eqs. 3.18a-3.18b) is not expressed in terms of quasi-potentials, but we can easily derive it in the form of the unknown vector $\begin{bmatrix}\tilde{V} & \tilde{\phi}\end{bmatrix}^T$. Based on Eq. 3.122c, the system matrix and the eigenvalues are:

$$\mathbf{A} = \begin{bmatrix} \dfrac{\xi}{D} & -\dfrac{\xi}{D} \\ -\dfrac{j\omega}{D} & \dfrac{j\omega}{D} \end{bmatrix} \quad \Longrightarrow \quad \det\left(\kappa^2\mathbf{I} - \mathbf{A}\right) = 0 \Leftrightarrow \left(\kappa^2 - \frac{\xi}{D}\right)\left(\kappa^2 - \frac{j\omega}{D}\right) - \frac{j\omega\xi}{D^2} = 0$$

which provides the usual solutions, $\kappa^2 = 0$ and $\kappa^2 = (\xi + j\omega)/D$. We will simply denote the latter as κ^2 in the following. The transformation matrix $\mathbf{T}$ is:

$$\mathbf{T} = \begin{bmatrix} 1 & 1 \\ 1 & -\dfrac{j\omega}{\xi} \end{bmatrix}$$

and the general solution is:

$$\tilde{V} = l_1 x + l_2 + c_1 \exp(-\kappa x) + d_1 \exp(\kappa x) \tag{3.123a}$$

$$\tilde{\phi} = l_1 x + l_2 - \frac{j\omega}{\xi}\left(c_1 \exp(-\kappa x) + d_1 \exp(\kappa x)\right) \tag{3.123b}$$

where l_1, l_2, c_2, d_1 are constants. In the end, we can then write the general solutions in the three regions as:

$$\text{electrolyte: } \begin{cases} \tilde{V} = l_{1e}x + l_{2e} + c_{1e}\exp\left(-\kappa_{el}x\right) + d_{1e}\exp\left(\kappa_{el}x\right) \\ \tilde{\phi} = l_{1e}x + l_{2e} - \dfrac{j\omega}{\xi_{el}}\left(c_{1e}\exp\left(-\kappa_{el}x\right) + d_{1e}\exp\left(\kappa_{el}x\right)\right) \end{cases} \tag{3.124a}$$

$$\text{oxide: } \tilde{V} = l_{1o}x + l_{2o} \tag{3.124b}$$

$$\text{semiconductor: } \begin{cases} \tilde{V} = l_{1s}x + l_{2s} + c_{1s}\exp\left(-\kappa_{n}x\right) + d_{1s}\exp\left(\kappa_{n}x\right) \\ \tilde{\phi} = l_{1s}x + l_{2s} - \dfrac{j\omega}{\xi_{n}}\left(c_{1s}\exp\left(-\kappa_{n}x\right) + d_{1s}\exp\left(\kappa_{n}x\right)\right) \end{cases} \tag{3.124c}$$

We now need to set the boundary conditions. To this purpose, we denote $\tilde{V}_{os}$ the potential at $x = 0$ (the oxide/semiconductor interface) and $\tilde{V}_{eo}$ the potential at $x = t_{ox}$ (the electrolyte/oxide interface). The boundary conditions are:

$$\text{electrolyte: } \begin{cases} \tilde{V}(L_{el} + t_{ox}) = 0 \\ \tilde{\phi}(L_{el} + t_{ox}) = 0 \\ \tilde{V}(t_{ox}) = \tilde{V}_{eo} \\ \tilde{J}_m^{\perp}\Big|_{t_{ox}} = 0 \end{cases}, \qquad \text{semiconductor: } \begin{cases} \tilde{V}(0) = \tilde{V}_{os} \\ \tilde{J}_m^{\perp}\Big|_{0} = 0 \\ \tilde{V}(-L_s) = \tilde{V}_B \\ \tilde{\phi}(-L_s) = \tilde{V}_B \end{cases} \tag{3.125}$$

We remind that the ionic and electronic currents are proportional to $\nabla\tilde{\phi}$ to say that:

$$\tilde{J}_m^{\perp} = 0 \quad \Longleftrightarrow \quad \frac{d\tilde{\phi}}{dx} = 0$$

In the electrolyte then, the following system of equations holds:

$$\begin{cases} l_{1e}(L_{el} + t_{ox}) + l_{2e} + c_{1e}\exp\left(-\kappa_{el}(L_{el} + t_{ox})\right) + d_{1e}\exp\left(\kappa_{el}(L_{el} + t_{ox})\right) = 0 \\ l_{1e}(L_{el} + t_{ox}) + l_{2e} - \dfrac{j\omega}{\xi_{el}}\left(c_{1e}\exp\left(-\kappa_{el}(L_{el} + t_{ox})\right) + d_{1e}\exp\left(\kappa_{el}(L_{el} + t_{ox})\right)\right) = 0 \\ l_{1e}t_{ox} + l_{2e} + c_{1e}\exp\left(-\kappa_{el}t_{ox}\right) + d_{1e}\exp\left(\kappa_{el}t_{ox}\right) = \tilde{V}_{eo} \\ l_{1e} - \dfrac{j\omega}{\xi_{el}}\kappa_{el}\left(-c_{1e}\exp\left(-\kappa_{el}t_{ox}\right) + d_{1e}\exp\left(\kappa_{el}t_{ox}\right)\right) = 0 \end{cases}$$

The solution of this system with boundary conditions (3.125) is:

$$\tilde{V} = \frac{\kappa_{el}\left(1 + \alpha_{el}\right)j\omega\left(L_{el} + t_{ox} - x\right) + \xi_{el}\left(e^{\kappa_{el}(t_{ox}-x)} - e^{\kappa_{el}(x-(2L_{el}+t_{ox}))}\right)}{\left(1 - \alpha_{el}\right)\xi_{el} + \kappa_{el}L_{el}\left(1 + \alpha_{el}\right)j\omega}\tilde{V}_{eo} \tag{3.126a}$$

$$\tilde{\phi} = \frac{\kappa_{el}\left(1 + \alpha_{el}\right)j\omega\left(L_{el} + t_{ox} - x\right) - j\omega\left(e^{\kappa_{el}(t_{ox}-x)} - e^{\kappa_{el}(x-(2L_{el}+t_{ox}))}\right)}{\left(1 - \alpha_{el}\right)\xi_{el} + \kappa_{el}L_{el}\left(1 + \alpha_{el}\right)j\omega}\tilde{V}_{eo} \tag{3.126b}$$

where $\alpha_{el} = \exp\left(-2\kappa_{el}L_{el}\right)$.
The solution in the oxide is straightforward:

$$\tilde{V} = \frac{\tilde{V}_{eo} - \tilde{V}_{os}}{t_{ox}}x + \tilde{V}_{os} \tag{3.127}$$

whereas in the semiconductor we have:

$$\begin{cases} l_{2s} + c_{1s} + d_{1s} = \tilde{V}_{os} \\ l_{1s} - \dfrac{j\omega}{\xi_n}\kappa_n\left(-c_{1s} + d_{1s}\right) = 0 \\ -l_{1s}L_s + l_{2s} + c_{1s}\exp\left(\kappa_n L_s\right) + d_{1s}\exp\left(-\kappa_n L_s\right) = \tilde{V}_B \\ -l_{1s}L_s + l_{2s} - \dfrac{j\omega}{\xi_n}\left(c_{1s}\exp\left(\kappa_n L_s\right) + d_{1s}\exp\left(-\kappa_n L_s\right)\right) = \tilde{V}_B \end{cases}$$

which yields ($\alpha_n = \exp(-2\kappa_n L_s)$):

$$\tilde{V} = \frac{\tilde{V}_B(1-\alpha_n)\xi_n + \kappa_n(-\tilde{V}_B x + \tilde{V}_{os}(L_s+x))(1+\alpha_n)j\omega - \xi_n\left(e^{\kappa_n x} - e^{-\kappa_n(2L_s+x)}\right)\left(\tilde{V}_B - \tilde{V}_{os}\right)}{(1-\alpha_n)\xi_n + \kappa_n L_s(1+\alpha_n)j\omega} \tag{3.128a}$$

$$\tilde{\phi} = \frac{\tilde{V}_B(1-\alpha_n)\xi_n + \kappa_n(-\tilde{V}_B x + \tilde{V}_{os}(L_s+x))(1+\alpha_n)j\omega + j\omega\left(e^{\kappa_n x} - e^{-\kappa_n(2L_s+x)}\right)\left(\tilde{V}_B - \tilde{V}_{os}\right)}{(1-\alpha_n)\xi_n + \kappa_n L_s(1+\alpha_n)j\omega}\,. \tag{3.128b}$$

To complete the model, we need to find the values of $\tilde{V}_{eo}$ and $\tilde{V}_{os}$. This is achieved by imposing the continuity of the dielectric displacement on the electrolyte/oxide and oxide/semiconductor interfaces:

$$\begin{cases} \varepsilon_{el}\left.\dfrac{d\tilde{V}}{dx}\right|_{t_{ox}^+} = \varepsilon_{ox}\left.\dfrac{d\tilde{V}}{dx}\right|_{t_{ox}^-} \\ \varepsilon_{ox}\left.\dfrac{d\tilde{V}}{dx}\right|_{0^+} = \varepsilon_{s}\left.\dfrac{d\tilde{V}}{dx}\right|_{0^-} \end{cases}$$

Solving explicitly this system of equations yields:

$$\tilde{V}_{eo} = -\frac{c_{ox}c_s}{c_{ox}^2 - (c_{ox}+c_{el})(c_{ox}+c_s)}\tilde{V}_B$$
$$\tilde{V}_{os} = -\frac{c_s(c_{ox}+c_{el})}{c_{ox}^2 - (c_{ox}+c_{el})(c_{ox}+c_s)}\tilde{V}_B$$

where:

$$y_{ox} = j\omega\frac{\varepsilon_{ox}}{t_{ox}} \tag{3.129a}$$

$$y_{el} = j\omega\varepsilon_{el}\frac{\kappa_{el}(1+\alpha_{el})(\xi_{el}+j\omega)}{(1-\alpha_{el})\xi_{el} + \kappa_{el}L_{el}(1+\alpha_{el})j\omega} \tag{3.129b}$$

$$y_s = j\omega\varepsilon_s\frac{\kappa_n(1+\alpha_n)(\xi_n+j\omega)}{(1-\alpha_n)\xi_n + \kappa_n L_s(1+\alpha_n)j\omega} \tag{3.129c}$$

As we will shortly see, y_s and y_{el} are the admittances per unit area of the semiconductor and the electrolyte respectively. The total admittance is then, as expected:

$$y_{tot} = j\omega\frac{\varepsilon_{ox}}{\tilde{V}_B}\left.\frac{d\tilde{V}}{dx}\right|_{ox} = j\omega\varepsilon_{ox}\frac{\tilde{V}_{eo}-\tilde{V}_{os}}{t_{ox}\tilde{V}_{el}} = -y_{ox}\frac{y_s y_{el}}{y_{ox}^2 - (y_{ox}+y_{el})(y_{ox}+y_s)}$$
$$= \left[\frac{1}{y_{ox}} + \frac{1}{y_s} + \frac{1}{y_{el}}\right]^{-1} \tag{3.130}$$

Alternatively we can write:

$$\tilde{V}_{eo} = \frac{y_{tot}}{y_{el}}\tilde{V}_B, \quad \tilde{V}_{os} = y_{tot}\left(\frac{1}{y_{el}} + \frac{1}{y_{ox}}\right)\tilde{V}_B\,.$$

This expression emphasizes once more the fact that, as expected, the admittance of the EIS system is calculated as the series connection of the admittances of the three regions.

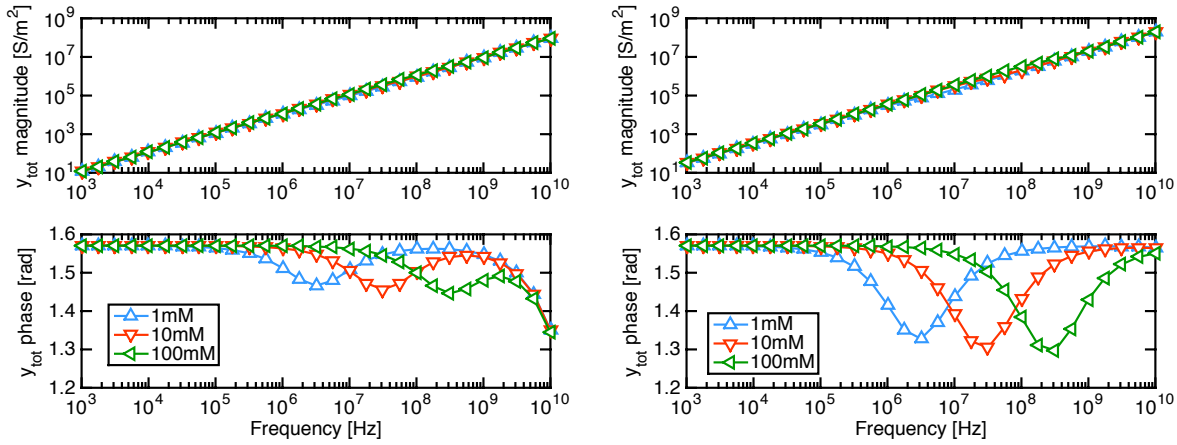

(a) $n = 10^{22}$ m^{-3} **(b)** $n = 10^{24}$ m^{-3}

Fig 3.25: Admittance per unit area y_{tot} in the EIS model varying doping and salt concentration with $t_{ox} = 5$ nm.

The similarity with the simple electrolyte system suggests that both the semiconductor and electrolyte regions should be described by equivalent anomalous circuits as those in Fig. 3.6.

Fig. 3.25 shows the admittance y_{tot} spectra varying the doping concentration and with the parameters in Tab. 3.3. We immediately note that, even in the case with the lower doping concentration, y_{tot} exhibits a very similar behaviour to the case in Sec. 3.1.2. Neglecting the cut-off frequencies due to relaxation processes in the semiconductor, we can then find again two cut-off frequencies f_s and f_c, which both depend linearly on the salt concentration (as evident looking at the phase plots in Fig. 3.25). In the following we will find an approximate way to calculate these frequencies.

Long system If the dimensions of the system satisfy the conditions $L_{el} \gg 1/\Re(\kappa_{el})$ and $L_s \gg 1/\Re(\kappa_n)$, we can assume that $\alpha_{el} \simeq \alpha_n \simeq 0$, as in Sec. 3.1.1.1. We can then simplify the expressions (3.126-3.128b) as:

$$\text{electrolyte:} \begin{cases} \tilde{V} = \dfrac{\kappa_{el} j\omega \left(L_{el} + t_{ox} - x\right) + \xi_{el} \left(e^{\kappa_{el}(t_{ox}-x)} - e^{\kappa_{el}(x-(2L_{el}+t_{ox}))}\right)}{\xi_{el} + \kappa_{el} L_{el} j\omega} \tilde{V}_{eo} \\ \tilde{\phi} = \dfrac{\kappa_{el} j\omega \left(L_{el} + t_{ox} - x\right) - j\omega \left(e^{\kappa_{el}(t_{ox}-x)} - e^{\kappa_{el}(x-(2L_{el}+t_{ox}))}\right)}{\xi_{el} + \kappa_{el} L_{el} j\omega} \tilde{V}_{eo} \end{cases}$$

Parameter	Symbol	Value	Units
Semiconductor length	L_s	600	[nm]
Insulator thickness	t_{ox}	5	[nm]
Electrolyte length	L_e	$t_{ox} - 100$	[nm]
Electron mobility	μ_n	$8.73 \cdot 10^{17}$	[m/Ns]
Ion mobility	μ_{el}	$4.75 \cdot 10^{11}$	[m/Ns]
Temperature	T	298	[K]
Semiconductor permittivity	ε_s	$12.4\varepsilon_0$	[F/m]
Insulator permittivity	ε_p	$3.9\varepsilon_0$	[F/m]
Electrolyte permittivity	ε_{el}	Eq. 2.39	[F/m]

Table 3.3: Parameters used in the calculations of the EIS model (unless otherwise stated).

$$\text{oxide: } \tilde{V} = \frac{\tilde{V}_{eo} - \tilde{V}_{os}}{t_{ox}} x + \tilde{V}_{os}$$

$$\text{semiconductor: } \begin{cases} \tilde{V} = \dfrac{\tilde{V}_B \xi_n + \kappa_n(-\tilde{V}_B x + \tilde{V}_{os}(L_s + x))j\omega - \xi_n \left(e^{\kappa_n x} - e^{-\kappa_n(2L_s+x)}\right)\left(\tilde{V}_B - \tilde{V}_{os}\right)}{\xi_n + \kappa_n L_s j\omega} \\ \tilde{\phi} = \dfrac{\tilde{V}_B \xi_n + \kappa_n(-\tilde{V}_B x + \tilde{V}_{os}(L_s + x))j\omega + j\omega \left(e^{\kappa_n x} - e^{-\kappa_n(2L_s+x)}\right)\left(\tilde{V}_B - \tilde{V}_{os}\right)}{\xi_n + \kappa_n L_s j\omega} \end{cases}$$

The parameters are:

$$y_{el} = j\omega\varepsilon_{el}\frac{\kappa_{el}(\xi_{el} + j\omega)}{\xi_{el} + \kappa_{el}L_{el}j\omega}, \quad y_s = j\omega\varepsilon_s\frac{\kappa_n(\xi_n + j\omega)}{\xi_n + \kappa_n L_s j\omega}.$$

We can therefore find an explicit expression for y_{tot}, using Eq. 3.130:

$$y_{tot} = \frac{j\omega\varepsilon_{ox}\varepsilon_{el}\varepsilon_s\kappa_{el}\kappa_n(\xi_{el} + j\omega)(\xi_n + j\omega)}{\varepsilon_s\kappa_n(\xi_n + j\omega)\left(\varepsilon_{el}\kappa_{el}t_{ox}(\xi_{el} + j\omega) + \varepsilon_{ox}(\xi_{el} + \kappa_{el}L_{el}j\omega)\right) + \varepsilon_{ox}\varepsilon_{el}\kappa_{el}(\xi_{el} + j\omega)(\xi_n + \kappa_n L_s j\omega)} \tag{3.131}$$

From this expression we can immediately see that the second cut-off frequency is again $f_c = \xi_{el}/2\pi$, as in all the models presented in this chapter. We can then conclude that f_c in capacitive biosensors is indeed a physical property of the electrolyte and does not depend on the geometry or on other materials. On the other hand, f_s is heavily dependent on geometry, and in this case it comes from the denominator of Eq. 3.131. As evident from Fig. 3.25, it depends linearly on the salt concentration. This is an important difference with the results from Sec. 3.1.1.3, where f_s was found to depend on $\sqrt{n_0}$.
Fig. 3.26 shows the potential profiles in the system near the insulator interfaces. We immediately note that at low frequency there is little potential drop in the electrolyte, especially at high salt concentration. When the frequency increases, also the potential drop in the electrolyte increases.

We can also calculate the ion and carrier concentrations, noting that:

$$\tilde{n} = \frac{Zq}{k_B T} N_D \left(\tilde{\phi} - \tilde{V}\right)$$

Therefore, the electron concentration in the semiconductor is:

$$\tilde{n}_n = -\frac{q}{k_B T} N_D \left(e^{\kappa_n x} - e^{-\kappa_n(2L_s+x)}\right) \frac{y_{tot}}{j\omega\varepsilon_s\kappa_n}\tilde{V}_B \tag{3.132}$$

3.6 Switching capacitance

In all the calculations we have made so far, and also in the ones we will do using the numerical solver ENBIOS, the AC problem is solved in the small signal approximation. Accurate capacitance measurements most often rely on CBCM digital techniques, where the capacitance is extracted by the average charge/discharge current per cycle and square waveforms are used [60]. This is indeed the case for the biosensor in [33]. Therefore, if we want to apply our results to the system presented in [33], some further considerations need to be made. Since in [33] the capacitance is measured via a charge-pump circuit, the capacitance calculated in the harmonic domain with a small signal approximation may not be adequate. To address this problem, we then need to estimate a switching capacitance C_{sw}, as the one measured by the actual device. The material in this section

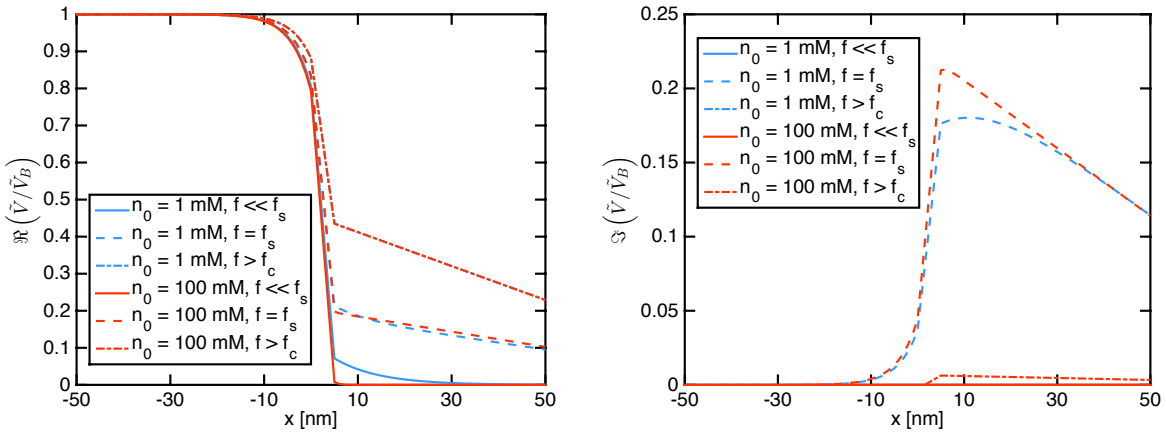

Fig 3.26: Potential profiles in the EIS model with $t_{ox} = 5$ nm and doping concentration $n = 10^{24}$ m^{-3}.

is derived from a personal communication of Frans Widdershoven.
To this purpose, we assume that the reading circuit is made of two ideal switches S_U and S_D (see Fig. 3.27) and that the nanoelectrode is modelled by a parasitic capacitance in parallel with a circuit model for the electrolyte that resembles the series model for the double layer admittance developed in Sec. 3.1.1.2. We however assume that the series capacitance C_s, which comprises the double layer capacitance and the optional contribution due to surface dielectric layers (such as a SAM), is a regular constant capacitance. The resulting charge pumped from the charge node at potential V_{DD} to the discharge node at potential 0 is then a measure for the capacitance C_{sw} free of anomalous frequency dependencies as those highlighted in Sec. 3.1.1.2 or of non-linear effects. If the nanoelectrode was a pure capacitor with capacitance C_s, it could be determined by measuring the average charge pumping current I flowing into the charge node:

$$I = f_p \left(C_s + C_p\right) V_{DD} \tag{3.133}$$

where $f_p = 1/T$ is the switching frequency, T the switching period and V_{DD} the supply voltage. To avoid a short circuit path between the charge and discharge nodes the switches

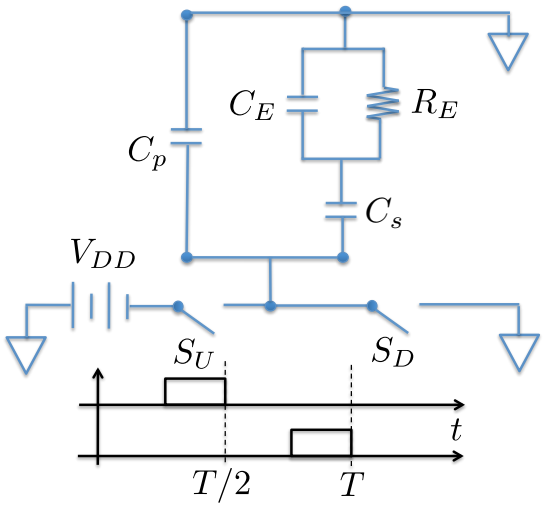

Fig 3.27: Circuit model for the calculation of the switching capacitance C_{sw}.

should never be on simultaneously. We then define as duty-cycle the ratio d between the time when S_U is on (which is assumed equal to the time when S_D is on) divided by the period T. In the case of Fig. 3.27, where the switches are open for $T/4$ each, $d = 25\%$. Assuming for the nanoelectrode the model in Fig. 3.27, we can then calculate the charge Q_p transferred from the charge node to the discharge node during one period T (see Sec. 3.A.12). We then define the charge pump efficiency factor γ as:

$$\begin{aligned}\gamma &= \frac{Q_p}{(C_s + C_p) V_{DD}} \\ &= 1 - p_b p_a \frac{e_1 (1 - e_3 (e_4 + (1 - e_4) p_b p_a)) + e_3 (1 - e_1 (e_2 + (1 - e_2) p_b p_a))}{1 - e_3 (e_4 + (1 - e_4) p_b p_a) e_1 (e_2 + (1 - e_2) p_b p_a)}\end{aligned} \tag{3.134}$$

The switching capacitance is then calculated as:

$$C_{sw} = \gamma(C_s + C_p) \tag{3.135}$$

Assuming a 50% duty cycle we obtain:

$$\begin{aligned}C_{sw} &= \left(1 - p_b p_a \frac{2e_1}{1 + e_1}\right)(C_s + C_p) \\ e_1 &= \exp\left(-\frac{1}{2\tau_a f_p}\right), \quad p_a = \frac{C_s}{C_s + C_E}\end{aligned} \tag{3.136}$$

With a 25% duty cycle instead:

$$\begin{aligned}C_{sw} &= \left(1 - p_b p_a \frac{2e_1}{1 + e_1 (e_2 + (1 - e_2) p_b p_a)}\right)(C_s + C_p) \\ p_a &= \frac{C_s}{C_s + C_E} \qquad p_b = \frac{C_s}{C_s + C_p} \\ \tau_a &= R_E (C_s + C_E) \qquad \tau_b = R_E \left(\frac{C_s C_p}{C_s + C_p} + C_E\right) \\ e_1 &= e_3 = \exp\left(-\frac{1}{4\tau_a f_p}\right) \qquad e_2 = e_4 = \exp\left(-\frac{1}{4\tau_b f_p}\right)\end{aligned} \tag{3.137}$$

A thorough comparison of C_{eff} and C_{sw} in the case study of the nanoelectrode array of [33] is presented in Sec. 5.3. We anticipate here that, in all cases considered, the difference between the predictions obtained considering C_{eff} or C_{sw} are very small. This means that, although C_{eff} is easily determined from simple AC small signal calculations, it is an accurate metric for the purpose of comparison with the experiments as will be done in Sec. 5.3.

Note that both C_{eff} and C_{sw} stem from a linear model of the system, which neglects non linearities, possible existing because of excessively large signals. It also neglects dielectric heating in water, which may be a relevant effect and was studied in [46]. We believe that in our system the non-linearities and heating effects would be not so relevant since the modulation voltage of the nanoelectrode platform [33] that will be discussed in this thesis is on the order of 100 mV, which is just a few times the thermal voltage $k_B T/q$. In addition, the nanoelectrodes size is much smaller than the size of the heaters in [46], so that only a very small current (and therefore power consumption) flows into the electrolyte. Such a small localized heating can be easily and quickly compensated by the big thermal bath made of the electrolyte solution.

Parameter	Symbol	Expression
Debye screening length	λ_D	$= \sqrt{\frac{\varepsilon_{el} k_B T}{2q^2 n_0}}$
Angular cut-off frequency	ξ	$= \frac{2q^2 \mu n_0}{\varepsilon_{el}} = \frac{\sigma_{el}}{\varepsilon_{el}} = \frac{1}{\tau} = 2\pi f_c$
First cut-off frequency (1D cartesian)	f_s	$\simeq \frac{\xi}{\pi} \frac{\lambda_D}{L}$
AC inverse screening length	κ	$= \sqrt{\frac{\xi + j\omega}{D}} = \frac{1}{\lambda_D}\sqrt{1 + j\omega\tau}$
Double layer admittance	y_{DL}	$\propto j\omega\varepsilon_{el}\kappa$

Table 3.4: Summary of the most relevant electrolyte parameters derived in the AC models of Secs. 3.1-3.3.

3.7 Summary

The first part of this chapter reports the derivation of original analytical models for the AC small signal regime in electrode/dielectric/electrolyte systems either in 1D cartesian (3.1) or 1D and 2D spherical (3.3) coordinates. The electrodes are always assumed ideally polarizable, which is a desirable property for impedimetric sensors sometimes difficult to achieve in real systems. In all cases we have shown the formation of the Electrical Double Layer (EDL) at the electrodes at low frequency. The EDL prevents the electric field to penetrate into the bulk of the system, thus hampering the ability of the electrode to probe analytes at large distance. We have also shown that a first cut-off frequency f_s exists, above which the electric field begins to penetrate into the electrolyte, and that above a second cut-off frequency f_c the EDLs disappear and the response of the system is purely dielectric. We have noted that f_s is geometry dependent, while f_c is not since it solely depends on the electrolyte conductive and dielectric properties.
As we will show in the following chapters, despite the simplifications made in the derivation of these models, some relevant parameters (summarized in Tab. 3.4) have a general applicability regardless of the system geometry (cartesian or 1D or 2D spherical). Among these, the most important ones are the AC screening length κ, the first cut off frequency f_s, the angular dielectric's relaxation cut-off frequency $\xi = 2\pi f_c$ and the double layer admittance y_{DL}.

Having in mind our general objective to develop a complete simulation platform for miniaturized integrated biosensors, we have also derived models for both DC and AC regimes in a 1D semiconductor uniform resistor (Sec. 3.4). These will be useful for the validation of the full 3D numerical biosensor simulator ENBIOS, whose realization constitutes an important part of this thesis work (see Chap. 4).

We also derived an AC model for an Electrolyte/Oxide/Semiconductor (EOS) capacitor, see Sec. 3.5 and verified that, as expected, the model for the semiconductor admittance is very similar to the electrolyte admittance.

Comparing the predictions from all the models above, we have concluded that the electrolyte dielectric relaxation cut-off frequency f_c is a general property of all the considered systems, regardless of geometry and properties of the electrodes surface. In contrast, we have seen that the first cut-off frequency f_s is heavily dependent not only on the geometry but also on the physical details of the electrodes surface compared to the electrolyte properties. In real biosensor systems this could be an issue, since on the electrodes surface electrochemical phenomena and deviations from simple theory may occur, leading to a

not well-controlled behaviour in the frequency range between f_s and f_c.

Finally, in Sec. 3.6 we have examined the relation between the admittance calculated in the AC small signal regime and the capacitance measured with a switching capacitor circuit. As we will see in Sec. 5.3, this is relevant for the comparison with experiments performed on the nanoelectrode array system described in Sec. 5.2.

3.A Appendices

3.A.1 1D cartesian model with electrolyte only - integration constants

Starting from Eqs. 3.18, we can rewrite the system of boundary conditions:

$$\begin{cases} \frac{q^2}{\varepsilon_{el}}\mu n_0\left[\frac{2}{\kappa_1}\left(-c_1+d_1\right)+l_1\right]-D\kappa_1\left(-c_1+d_1\right)-D\kappa_2\left(-c_2+d_2\right)=0 \\ -\frac{q^2}{\varepsilon_{el}}\mu n_0\left[\frac{2}{\kappa_1}\left(-c_1+d_1\right)+l_1\right]-D\kappa_1\left(c_1-d_1\right)-D\kappa_2\left(-c_2+d_2\right)=0 \\ \frac{q^2}{\varepsilon_{el}}\mu n_0\left[\frac{2}{\kappa_1}\left(-c_1\exp\left(-\kappa_1 L\right)+d_1\exp\left(\kappa_1 L\right)\right)+l_1\right]-D\kappa_1\left(-c_1\exp\left(-\kappa_1 L\right)\right. \\ \qquad \left.+d_1\exp\left(\kappa_1 L\right)\right)-D\kappa_2\left(-c_2\exp\left(-\kappa_2 L\right)+d_2\exp\left(\kappa_2 L\right)\right)=0 \\ -\frac{q^2}{\varepsilon_{el}}\mu n_0\left[\frac{2}{\kappa_1}\left(-c_1\exp\left(-\kappa_1 L\right)+d_1\exp\left(\kappa_1 L\right)\right)+l_1\right]-D\kappa_1\left(c_1\exp\left(-\kappa_1 L\right)\right. \\ \qquad \left.-d_1\exp\left(\kappa_1 L\right)\right)-D\kappa_2\left(-c_2\exp\left(-\kappa_2 L\right)+d_2\exp\left(\kappa_2 L\right)\right)=0 \\ -\frac{q}{\varepsilon_{el}}\left[\frac{2}{\kappa_1^2}\left(c_1+d_1\right)+l_2\right]=\tilde{V}_B \\ -\frac{q}{\varepsilon_{el}}\left[\frac{2}{\kappa_1^2}\left(c_1\exp\left(-\kappa_1 L\right)+d_1\exp\left(\kappa_1 L\right)\right)+l_1 L+l_2\right]=\tilde{V}_T \end{cases}$$

Summing the first and the second equation we get:

$$-2D\kappa_2\left(-c_2+d_2\right)=0 \quad \Longrightarrow \quad c_2=d_2 \tag{3.138}$$

Then, summing the third and the fourth equation and using the above equation:

$$-2D\kappa_2\left(-\exp\left(-\kappa_2 L\right)+\exp\left(\kappa_2 L\right)\right)c_2=0 \quad \Longrightarrow \quad c_2=d_2=0 \tag{3.139}$$

We see that κ_2 does not show up in the equations, so that we can denote $\kappa_1=\kappa$. The system then simplifies to:

$$\begin{cases} \frac{q^2}{\varepsilon_{el}}\mu n_0\left[\frac{2}{\kappa}\left(-c_1+d_1\right)+l_1\right]+D\kappa\left(c_1-d_1\right)=0 \\ \frac{q^2}{\varepsilon_{el}}\mu n_0\left[\frac{2}{\kappa}\left(-c_1\exp\left(-\kappa L\right)+d_1\exp\left(\kappa L\right)\right)+l_1\right] \\ \qquad +D\kappa\left(c_1\exp\left(-\kappa L\right)-d_1\exp\left(\kappa L\right)\right)=0 \\ -\frac{q}{\varepsilon_{el}}\left[\frac{2}{\kappa^2}\left(c_1+d_1\right)+l_2\right]=\tilde{V}_B \\ -\frac{q}{\varepsilon_{el}}\left[\frac{2}{\kappa^2}\left(c_1\exp\left(-\kappa L\right)+d_1\exp\left(\kappa L\right)\right)+l_1 L+l_2\right]=\tilde{V}_T \end{cases} \tag{3.140}$$

Subtracting the first from the second expression yields to:

$$\begin{aligned} &\left(1-\exp\left(-\kappa L\right)\right)\left(\frac{q^2}{\varepsilon_{el}}\mu n_0\frac{2}{\kappa}-D\kappa\right)c_1 \\ &\qquad +\left(\exp\left(\kappa L\right)-1\right)\left(\frac{q^2}{\varepsilon_{el}}\mu n_0\frac{2}{\kappa}-D\kappa\right)d_1=0 \end{aligned} \tag{3.141}$$

$$\Longrightarrow \quad c_1=-\frac{d_1}{\alpha}, \;\; \alpha=\frac{1-\exp\left(-\kappa L\right)}{\exp\left(\kappa L\right)-1}=\exp\left(-\kappa L\right) \tag{3.142}$$

Then from the first equation of system 3.140:

$$\left(\frac{1}{\alpha}+1\right)\left(\frac{q^2}{\varepsilon_{el}}\mu n_0\frac{2}{\kappa}-D\kappa\right)d_1+\frac{q^2}{\varepsilon_{el}}\mu n_0 l_1=0$$
$$\implies \quad l_1=-\frac{1}{\frac{q^2}{\varepsilon_{el}}\mu n_0}v_d\left(\frac{1}{\alpha}+1\right)d_1,\ \ v_d=\frac{q^2}{\varepsilon_{el}}\mu n_0\frac{2}{\kappa}-D\kappa\,. \tag{3.143}$$

Subtracting the third from the fourth equation of system 3.140:

$$-\left[\frac{q}{\varepsilon_{el}}\frac{2}{\kappa^2}\left(-\frac{1}{\alpha}\left(\exp\left(-\kappa L\right)-1\right)+\left(\exp\left(\kappa L\right)-1\right)\right)-\frac{L}{q\mu n_0}v_d\left(\frac{1}{\alpha}+1\right)\right]d_1=\tilde{V}_T-\tilde{V}_B$$
$$\implies d_1=-\alpha\frac{\tilde{V}_T-\tilde{V}_B}{\beta-\delta-(\beta+\delta)\,\alpha},\ \ \beta=\frac{q}{\varepsilon_{el}}\frac{4}{\kappa^2},\ \ \delta=\frac{L}{q\mu n_0}v_d \tag{3.144}$$

Finally from the third equation of 3.140 we get:

$$-\frac{q}{\varepsilon_{el}}\left[\frac{2}{\kappa^2}\frac{\tilde{V}_T-\tilde{V}_B}{\beta-\delta-(\beta+\delta)\,\alpha}\left(1-\alpha\right)+l_2\right]=\tilde{V}_B \tag{3.145}$$
$$\implies \quad l_2=\frac{2}{\kappa^2}(\alpha-1)\frac{\tilde{V}_T-\tilde{V}_B}{\beta-\delta-(\beta+\delta)\,\alpha}-\frac{\varepsilon_{el}}{q}\tilde{V}_B$$

3.A.2 1D cartesian model with electrolyte only - derivation of the equivalent formulation

Starting from Eqs. 3.20 - 3.27, we see that:

$$v_d=q\mu n_0\frac{q}{\varepsilon_{el}}\frac{\xi}{\kappa}-D\kappa=\frac{\xi}{\kappa}-D\kappa$$
$$q\mu n_0\beta=q\mu n_0\frac{q}{\varepsilon_{el}}\frac{4}{\kappa^2}=2\frac{\xi}{\kappa^2}$$
$$q\mu n_0\delta=q\mu n_0\frac{L}{q\mu n_0}v_d=L\left(\frac{\xi}{\kappa}-D\kappa\right),$$

which implies that:

$$q\mu n_0\left(\beta-\delta-(\beta+\delta)\,\alpha\right)=2\frac{\xi}{\kappa^2}-L\left(\frac{\xi}{\kappa}-D\kappa\right)-\left(2\frac{\xi}{\kappa^2}+L\left(\frac{\xi}{\kappa}-D\kappa\right)\right)\alpha$$
$$=2\frac{\xi}{\kappa^2}\left(1-\alpha\right)-L\left(\frac{\xi}{\kappa}-D\kappa\right)\left(1+\alpha\right).$$

We can then rewrite the expression for the potential as:

$$\tilde{V}=\frac{q}{\varepsilon_{el}}\frac{2}{\kappa^2}\frac{\Delta\tilde{V}}{\beta-\delta-(\beta+\delta)\alpha}\left(e^{-\kappa x}-\alpha e^{\kappa x}\right)+\frac{v_d}{q\mu n_0}\Delta\tilde{V}\frac{1+\alpha}{\beta-\delta-(\beta+\delta)\alpha}x$$
$$-\frac{q}{\varepsilon_{el}}\frac{2}{\kappa^2}\Delta\tilde{V}\frac{1-\alpha}{\beta-\delta-(\beta+\delta)\alpha}+\tilde{V}_B$$
$$=\xi\frac{\Delta\tilde{V}}{2\xi\left(1-\alpha\right)-L\left(\xi\kappa-D\kappa^3\right)\left(1+\alpha\right)}\left(e^{-\kappa x}-\alpha e^{\kappa x}\right)$$

$$
\begin{aligned}
&+ \left(\xi\kappa - D\kappa^3\right)\Delta\tilde{V}\frac{1+\alpha}{2\xi\left(1-\alpha\right) - L\left(\xi\kappa - D\kappa^3\right)\left(1+\alpha\right)}x \\
&- \xi\Delta\tilde{V}\frac{1-\alpha}{2\xi\left(1-\alpha\right) - L\left(\xi\kappa - D\kappa^3\right)\left(1+\alpha\right)} + \tilde{V}_B \\
&= \xi\frac{\Delta\tilde{V}}{2\xi\left(1-\alpha\right) + j\omega\kappa L\left(1+\alpha\right)}\left(e^{-\kappa x} - \alpha e^{\kappa x}\right) \\
&- j\omega\kappa\Delta\tilde{V}\frac{1+\alpha}{2\xi\left(1-\alpha\right) + j\omega\kappa L\left(1+\alpha\right)}x \\
&- \xi\Delta\tilde{V}\frac{1-\alpha}{2\xi\left(1-\alpha\right) + j\omega\kappa L\left(1+\alpha\right)} + \tilde{V}_B\,.
\end{aligned}
$$

3.A.3 1D cartesian model with a dielectric region inside the electrolyte

Let us now focus on the case where a dielectric region of permittivity ε_d (which can represent for instance a biomolecule) is introduced inside the electrolyte region. We solution in the system where the dielectric region lies inside the interval $[x_d,\, x_D]$, which is a subdomain of the region $[0,\, L]$, that is $0 \leq x_d \leq x_D \leq L$.
We denote $\tilde{V}_d = \tilde{V}(x_d)$, $\tilde{V}_D = \tilde{V}(x_D)$ and see from Eq. 3.51 that the potential has the expression:

$$
\tilde{V} = \begin{cases}
-\dfrac{q}{\varepsilon_{el}}\left[\dfrac{2}{\kappa^2}\dfrac{\tilde{V}_d - \tilde{V}_B}{\beta - \delta_B - (\beta+\delta_B)\alpha_B}\left(e^{-\kappa x} - \alpha_B e^{\kappa x}\right) + l_{1B}x + l_{2B}\right] & x \in [0, x_d] \\
\dfrac{\tilde{V}_D - \tilde{V}_d}{x_D - x_d}\left(x - x_d\right) + \tilde{V}_d & x \in [x_d, x_D] \\
-\dfrac{q}{\varepsilon_{el}}\left[\dfrac{2}{\kappa^2}\dfrac{\tilde{V}_T - \tilde{V}_D}{\beta - \delta_T - (\beta+\delta_T)\alpha_T}\left(e^{-\kappa(x-x_D)} - \alpha_T e^{\kappa(x-x_D)}\right) + l_{1T}\left(x - x_D\right) + l_{2T}\right] & x \in [x_D, L]
\end{cases}
\tag{3.146}
$$

where:

$$
\begin{cases}
\alpha_B = e^{-\kappa x_d} \\
\alpha_T = e^{-\kappa(L - x_D)} \\
\delta_B = \dfrac{x_d}{q\mu n_0}v_d \\
\delta_T = \dfrac{L - x_D}{q\mu n_0}v_d \\
l_{1B} = \dfrac{\varepsilon_{el}}{q}\dfrac{1}{q\mu n_0}v_d\left(\tilde{V}_d - \tilde{V}_B\right)\dfrac{\alpha_B + 1}{\beta - \delta_B - (\beta+\delta_B)\alpha_B} \\
l_{1T} = \dfrac{\varepsilon_{el}}{q}\dfrac{1}{q\mu n_0}v_d\left(\tilde{V}_T - \tilde{V}_D\right)\dfrac{\alpha_T + 1}{\beta - \delta_T - (\beta+\delta_T)\alpha_T} \\
l_{2B} = \dfrac{2}{\kappa^2}\left(\tilde{V}_d - \tilde{V}_B\right)\dfrac{\alpha_B - 1}{\beta - \delta_B - (\beta+\delta_B)\alpha_B} - \dfrac{\varepsilon_{el}}{q}\tilde{V}_B \\
l_{2T} = \dfrac{2}{\kappa^2}\left(\tilde{V}_T - \tilde{V}_D\right)\dfrac{\alpha_T - 1}{\beta - \delta_T - (\beta+\delta_T)\alpha_T} - \dfrac{\varepsilon_{el}}{q}\tilde{V}_D
\end{cases}
$$

The continuity of the normal component of the electric induction through the interface provides the following boundary conditions:

$$\varepsilon_{el}\left.\frac{d\tilde{V}}{dx}\right|_{x_d^-} = \varepsilon_d\left.\frac{d\tilde{V}}{dx}\right|_{x_d^+} \quad \text{and} \quad \varepsilon_d\left.\frac{d\tilde{V}}{dx}\right|_{x_D^-} = \varepsilon_{el}\left.\frac{d\tilde{V}}{dx}\right|_{x_D^+}$$

From the first equation we get:

$$-q\left[-\frac{2}{\kappa}\frac{\tilde{V}_d-\tilde{V}_B}{\beta-\delta_B-(\beta+\delta_B)\alpha_B}\left(\alpha_B+1\right)+l_{1B}\right]=\varepsilon_d\frac{\tilde{V}_D-\tilde{V}_d}{x_D-x_d}$$

$$\implies \quad \frac{\alpha_B+1}{\beta-\delta_B-(\beta+\delta_B)\alpha_B}\left(\tilde{V}_d-\tilde{V}_B\right)\frac{\varepsilon_{el}}{q\mu n_0}D\kappa=\varepsilon_d\frac{\tilde{V}_D-\tilde{V}_d}{x_D-x_d}\,, \tag{3.147}$$

and from the second:

$$\varepsilon_d\frac{\tilde{V}_D-\tilde{V}_d}{x_D-x_d}=-q\left[-\frac{2}{\kappa}\frac{\tilde{V}_T-\tilde{V}_D}{\beta-\delta_T-(\beta+\delta_T)\alpha_T}\left(1+\alpha_T\right)+l_{1T}\right]$$

$$\implies \quad \varepsilon_d\frac{\tilde{V}_D-\tilde{V}_d}{x_D-x_d}=\frac{\alpha_T+1}{\beta-\delta_T-(\beta+\delta_T)\alpha_T}\left(\tilde{V}_T-\tilde{V}_D\right)\frac{\varepsilon_{el}}{q\mu n_0}D\kappa\,. \tag{3.148}$$

Substituting Eq. 3.147 into Eq. 3.148, we obtain:

$$\frac{\alpha_B+1}{\beta-\delta_B-(\beta+\delta_B)\alpha_B}\left(\tilde{V}_d-\tilde{V}_B\right)\frac{\varepsilon_{el}}{q\mu n_0}D\kappa=\frac{\alpha_T+1}{\beta-\delta_T-(\beta+\delta_T)\alpha_T}\left(\tilde{V}_T-\tilde{V}_D\right)\frac{\varepsilon_{el}}{q\mu n_0}D\kappa$$

$$\implies \quad \tilde{V}_d=\tilde{V}_B+\frac{\alpha_T+1}{\alpha_B+1}\frac{\beta-\delta_B-(\beta+\delta_B)\alpha_B}{\beta-\delta_T-(\beta+\delta_T)\alpha_T}\left(\tilde{V}_T-\tilde{V}_D\right),$$

and using again the second continuity condition:

$$\varepsilon_d\frac{\tilde{V}_D-\tilde{V}_B-\dfrac{\alpha_T+1}{\alpha_B+1}\dfrac{\beta-\delta_B-(\beta+\delta_B)\alpha_B}{\beta-\delta_T-(\beta+\delta_T)\alpha_T}\left(\tilde{V}_T-\tilde{V}_D\right)}{x_D-x_d}=\frac{\alpha_T+1}{\beta-\delta_T-(\beta+\delta_T)\alpha_T}\left(\tilde{V}_T-\tilde{V}_D\right)\frac{\varepsilon_{el}}{q\mu n_0}D\kappa$$

$$\implies \quad \tilde{V}_D=\frac{\dfrac{\varepsilon_d}{x_D-x_d}\left(\tilde{V}_B+\tilde{V}_T\dfrac{\alpha_T+1}{\alpha_B+1}\dfrac{\beta-\delta_B-(\beta+\delta_B)\alpha_B}{\beta-\delta_T-(\beta+\delta_T)\alpha_T}\right)+\tilde{V}_T\dfrac{\alpha_T+1}{\beta-\delta_T-(\beta+\delta_T)\alpha_T}\dfrac{\varepsilon_{el}}{q\mu n_0}D\kappa}{\dfrac{\varepsilon_d}{x_D-x_d}\left(1+\dfrac{\alpha_T+1}{\alpha_B+1}\dfrac{\beta-\delta_B-(\beta+\delta_B)\alpha_B}{\beta-\delta_T-(\beta+\delta_T)\alpha_T}\right)+\dfrac{\alpha_T+1}{\beta-\delta_T-(\beta+\delta_T)\alpha_T}\dfrac{\varepsilon_{el}}{q\mu n_0}D\kappa}\,.$$

Then denoting:

$$\gamma=\frac{\alpha_T+1}{\alpha_B+1}\frac{\beta-\delta_B-(\beta+\delta_B)\alpha_B}{\beta-\delta_T-(\beta+\delta_T)\alpha_T} \tag{3.149}$$

we finally get:

$$\begin{cases}\tilde{V}_D=\dfrac{\tilde{V}_B+\tilde{V}_T\left(\gamma+\dfrac{\alpha_T+1}{\beta-\delta_T-(\beta+\delta_T)\alpha_T}\dfrac{\varepsilon_{el}}{\varepsilon_d}\left(x_D-x_d\right)\dfrac{D\kappa}{q\mu n_0}\right)}{1+\gamma+\dfrac{\alpha_T+1}{\beta-\delta_T-(\beta+\delta_T)\alpha_T}\dfrac{\varepsilon_{el}}{\varepsilon_d}\left(x_D-x_d\right)\dfrac{D\kappa}{q\mu n_0}}\\ \tilde{V}_d=\dfrac{\tilde{V}_T\gamma+\tilde{V}_B\left(1+\dfrac{\alpha_T+1}{\beta-\delta_T-(\beta+\delta_T)\alpha_T}\dfrac{\varepsilon_{el}}{\varepsilon_d}\left(x_D-x_d\right)\dfrac{D\kappa}{q\mu n_0}\right)}{1+\gamma+\dfrac{\alpha_T+1}{\beta-\delta_T-(\beta+\delta_T)\alpha_T}\dfrac{\varepsilon_{el}}{\varepsilon_d}\left(x_D-x_d\right)\dfrac{D\kappa}{q\mu n_0}}\end{cases}. \tag{3.150}$$

Because the current is the same in each section, we compute it as displacement current in the dielectric:

$$\tilde{J} = -j\omega\varepsilon_d \frac{\tilde{V}_D - \tilde{V}_d}{x_D - x_d} = -\frac{j\omega\varepsilon_d \left(\tilde{V}_T - \tilde{V}_B\right) \dfrac{\alpha_T + 1}{\beta - \delta_T - (\beta + \delta_T)\alpha_T} \dfrac{\varepsilon_{el}}{\varepsilon_d} \dfrac{D\kappa}{q\mu n_0}}{1 + \gamma + \dfrac{\alpha_T + 1}{\beta - \delta_T - (\beta + \delta_T)\alpha_T} \dfrac{\varepsilon_{el}}{\varepsilon_d} (x_D - x_d) \dfrac{D\kappa}{q\mu n_0}}$$

$$= j\omega \frac{\Delta\tilde{V}}{(1+\gamma) \dfrac{\beta - \delta_T - (\beta + \delta_T)\alpha_T}{\alpha_T + 1} \dfrac{1}{\varepsilon_{el}} \dfrac{qn_0}{k_B T\kappa} + \dfrac{x_D - x_d}{\varepsilon_d}} \,. \tag{3.151}$$

3.A.3.1 Equivalent formulation

According to the equivalent formulation developed in Sec. 3.1.1.1, we have:

$$q\mu n_0 \kappa^2 \left(\beta - \delta - (\beta + \delta)\,\alpha\right) = 2\xi\,(1 - \alpha) + j\omega\kappa L\,(1 + \alpha) \,.$$

This means that:

$$\gamma = \frac{\alpha_T + 1}{\alpha_B + 1} \frac{2\xi\,(1 - \alpha_B) + j\omega\kappa\Delta x_B\,(1 + \alpha_B)}{2\xi\,(1 - \alpha_T) + j\omega\kappa\Delta x_T\,(1 + \alpha_T)}$$

where $\Delta x_B = x_d$ and $\Delta x_T = L - x_D$. We obtain then:

$$\tilde{J} = j\omega \frac{\Delta\tilde{V}}{(1+\gamma) \dfrac{2\xi\,(1 - \alpha_T) + j\omega\kappa\Delta z_T\,(1 + \alpha_T)}{1 + \alpha_T} \dfrac{1}{\varepsilon_{el} D\kappa^3} + \dfrac{h_d}{\varepsilon_d - j\sigma_d/\omega}} \tag{3.152}$$

where we have also included a finite conductivity σ_d in the dielectric region representing the biomolecule and $h_d = x_D - x_d$. If we now assume that $|\alpha_T| \ll 1$ and $|\alpha_B| \ll 1$, we can approximate the former equation as:

$$\tilde{J} \simeq j\omega \frac{\Delta\tilde{V}}{(1+\gamma) \dfrac{2\xi + j\omega\kappa\Delta z_T}{\varepsilon_{el} D\kappa^3} + \dfrac{h_d}{\varepsilon_d - j\sigma_d/\omega}} \tag{3.153}$$

$$= j\omega \frac{\Delta\tilde{V}}{\dfrac{4\xi + j\omega\kappa h_d}{\varepsilon_{el} D\kappa^3} + \dfrac{h_d}{\varepsilon_d - j\sigma_d/\omega}} \tag{3.154}$$

As expected, also in this case the admittance y_{tot} is the series connection of the dielectric region and the electrolyte region admittances.

3.A.4 1D cartesian model with dielectric layer, electrolyte and dielectric region inside

We consider the possibility of having at the same time a dielectric layer in the region [0, a] and another dielectric layer in the region [x_d, x_D] which are distinct subdomains of the region [0, L].
We denote $\tilde{V}_I = \tilde{V}(a)$, $\tilde{V}_d = \tilde{V}(x_d)$ and $\tilde{V}_D = \tilde{V}(x_D)$ and, using the results in Sec. 3.1.2,

write the potential in the overall domain as:

$$\tilde{V} = \begin{cases} \dfrac{\tilde{V}_I - \tilde{V}_B}{a} x + \tilde{V}_B & x \in [0, a] \\ -\dfrac{q}{\varepsilon_{el}} \left[\dfrac{2}{\kappa^2} \dfrac{\tilde{V}_d - \tilde{V}_I}{\beta - \delta_B - (\beta + \delta_B)\alpha_B} \left(e^{-\kappa(x-a)} - \alpha_B e^{\kappa(x-a)} \right) \right. & \\ \qquad \left. + l_{1B} (x - a) + l_{2B} \right] & x \in [a, x_d] \\ \dfrac{\tilde{V}_D - \tilde{V}_d}{x_D - x_d} (x - x_d) + \tilde{V}_d & x \in [x_d, x_D] \\ -\dfrac{q}{\varepsilon_{el}} \left[\dfrac{2}{\kappa^2} \dfrac{\tilde{V}_T - \tilde{V}_D}{\beta - \delta_T - (\beta + \delta_T)\alpha_T} \left(e^{-\kappa(x-x_D)} - \alpha_T e^{\kappa(x-x_D)} \right) \right. & \\ \qquad \left. + l_{1T} (x - x_D) + l_{2T} \right] & x \in [x_D, L] \end{cases} \tag{3.155}$$

Imposing the continuity of the normal component of the dielectric induction through the interfaces yields:

$$\begin{cases} \varepsilon_s \dfrac{\tilde{V}_I - \tilde{V}_B}{a} = \dfrac{\alpha_B + 1}{\beta - \delta_B - (\beta + \delta_B)\alpha_B} \left(\tilde{V}_d - \tilde{V}_I \right) \dfrac{\varepsilon_{el}}{q\mu n_0} D\kappa \\ \dfrac{\alpha_B + 1}{\beta - \delta_B - (\beta + \delta_B)\alpha_B} \left(\tilde{V}_d - \tilde{V}_I \right) \dfrac{\varepsilon_{el}}{q\mu n_0} D\kappa = \varepsilon_d \dfrac{\tilde{V}_D - \tilde{V}_d}{x_D - x_d} \\ \varepsilon_d \dfrac{\tilde{V}_D - \tilde{V}_d}{x_D - x_d} = \dfrac{\alpha_T + 1}{\beta - \delta_T - (\beta + \delta_T)\alpha_T} \left(\tilde{V}_T - \tilde{V}_D \right) \dfrac{\varepsilon_{el}}{q\mu n_0} D\kappa \end{cases}$$

From the first and the second equation:

$$\varepsilon_s \frac{\tilde{V}_I - \tilde{V}_B}{a} = \varepsilon_d \frac{\tilde{V}_D - \tilde{V}_d}{x_D - x_d} \quad \Longrightarrow \quad \tilde{V}_I = \tilde{V}_B + \frac{\varepsilon_d}{\varepsilon_s} \frac{a}{x_D - x_d} \left(\tilde{V}_D - \tilde{V}_d \right)$$

Eq. 3.150 still holds substituting $\tilde{V}_B$ with $\tilde{V}_I$, so that we get:

$$\begin{aligned} \tilde{V}_I &= \tilde{V}_B + \frac{\varepsilon_d}{\varepsilon_s} \frac{a}{x_D - x_d} \left(\tilde{V}_T - \tilde{V}_I \right) \frac{\dfrac{\alpha_T + 1}{\beta - \delta_T - (\beta + \delta_T)\alpha_T} \dfrac{\varepsilon_{el}}{\varepsilon_d} (x_D - x_d) \dfrac{D\kappa}{q\mu n_0}}{1 + \gamma + \dfrac{\alpha_T + 1}{\beta - \delta_T - (\beta + \delta_T)\alpha_T} \dfrac{\varepsilon_{el}}{\varepsilon_d} (x_D - x_d) \dfrac{D\kappa}{q\mu n_0}} \\ &= \tilde{V}_B + \frac{a}{\varepsilon_s} \frac{\tilde{V}_T - \tilde{V}_I}{(1 + \gamma) \dfrac{\beta - \delta_T - (\beta + \delta_T)\alpha_T}{\alpha_T + 1} \dfrac{1}{\varepsilon_{el}} \dfrac{qn_0}{k_B T \kappa} + \dfrac{x_D - x_d}{\varepsilon_d}} \end{aligned}$$

If we now call:

$$\begin{aligned} \eta &= (1 + \gamma) \frac{\beta - \delta_T - (\beta + \delta_T)\alpha_T}{\alpha_T + 1} \frac{1}{\varepsilon_{el}} \frac{qn_0}{k_B T \kappa} + \frac{x_D - x_d}{\varepsilon_d} \\ &= \left(\frac{\beta - \delta_T - (\beta + \delta_T)\alpha_T}{\alpha_T + 1} + \frac{\beta - \delta_B - (\beta + \delta_B)\alpha_B}{\alpha_B + 1} \right) \frac{1}{\varepsilon_{el}} \frac{qn_0}{k_B T \kappa} + \frac{x_D - x_d}{\varepsilon_d} \end{aligned}$$

We have:

$$\begin{cases} \tilde{V}_I = \dfrac{\tilde{V}_B \varepsilon_s \eta + \tilde{V}_T a}{\varepsilon_s \eta + a} \\ \tilde{V}_D = \dfrac{\tilde{V}_I + \tilde{V}_T \left(\gamma + \dfrac{\alpha_T + 1}{\beta - \delta_T - (\beta + \delta_T)\alpha_T} \dfrac{\varepsilon_{el}}{\varepsilon_d} (x_D - x_d) \dfrac{D\kappa}{q\mu n_0} \right)}{1 + \gamma + \dfrac{\alpha_T + 1}{\beta - \delta_T - (\beta + \delta_T)\alpha_T} \dfrac{\varepsilon_{el}}{\varepsilon_d} (x_D - x_d) \dfrac{D\kappa}{q\mu n_0}} \\ \tilde{V}_d = \dfrac{\tilde{V}_T \gamma + \tilde{V}_I \left(1 + \dfrac{\alpha_T + 1}{\beta - \delta_T - (\beta + \delta_T)\alpha_T} \dfrac{\varepsilon_{el}}{\varepsilon_d} (x_D - x_d) \dfrac{D\kappa}{q\mu n_0} \right)}{1 + \gamma + \dfrac{\alpha_T + 1}{\beta - \delta_T - (\beta + \delta_T)\alpha_T} \dfrac{\varepsilon_{el}}{\varepsilon_d} (x_D - x_d) \dfrac{D\kappa}{q\mu n_0}} \end{cases} \tag{3.156}$$

The current then is:

$$\tilde{J} = -j\omega\varepsilon_s \frac{\tilde{V}_I - \tilde{V}_B}{a} = j\omega \frac{\Delta\tilde{V}}{\eta + \dfrac{a}{\varepsilon_s}}$$

3.A.5 1D cartesian model with DC bias (only electrolyte) - alternative derivation

We can write Eq. 3.73 in a matrix form $\dfrac{d\mathbf{u}}{dx} = \mathbf{A}\mathbf{u}$, where:

$$\mathbf{u} = \begin{bmatrix} \tilde{V} \\ \tilde{\phi}_+ \\ \tilde{\phi}_- \\ \dfrac{d\tilde{V}}{dx} \\ \dfrac{d\tilde{\phi}_+}{dx} \\ \dfrac{d\tilde{\phi}_-}{dx} \end{bmatrix}, \quad \mathbf{A} = \begin{bmatrix} 0 & 0 & 0 & 1 & 0 & 0 \\ 0 & 0 & 0 & 0 & 1 & 0 \\ 0 & 0 & 0 & 0 & 0 & 1 \\ \dfrac{\kappa_D^2}{2}\left(\delta(x) + \dfrac{1}{\delta(x)}\right) & -\dfrac{\kappa_D^2}{2}\delta(x) & -\dfrac{\kappa_D^2}{2\delta(x)} & 0 & 0 & 0 \\ -\kappa_\omega^2 & \kappa_\omega^2 & 0 & 0 & -\dfrac{1}{\delta(x)}\dfrac{d\delta(x)}{dx} & 0 \\ -\kappa_\omega^2 & 0 & \kappa_\omega^2 & 0 & 0 & \dfrac{1}{\delta(x)}\dfrac{d\delta(x)}{dx} \end{bmatrix}$$

We calculate the eigenvalues (κ) by solving the characteristic equation:

$$\det(\kappa\mathbf{I} - \mathbf{A}) = \det \begin{bmatrix} \kappa & 0 & 0 & -1 & 0 & 0 \\ 0 & \kappa & 0 & 0 & -1 & 0 \\ 0 & 0 & \kappa & 0 & 0 & -1 \\ -\dfrac{\kappa_D^2}{2}\left(\delta(x) + \dfrac{1}{\delta(x)}\right) & \dfrac{\kappa_D^2}{2}\delta(x) & \dfrac{\kappa_D^2}{2\delta(x)} & \kappa & 0 & 0 \\ \kappa_\omega^2 & -\kappa_\omega^2 & 0 & 0 & \kappa + \eta(x) & 0 \\ \kappa_\omega^2 & 0 & -\kappa_\omega^2 & 0 & 0 & \kappa - \eta(x) \end{bmatrix}$$

$$= \kappa \left[\kappa^5 - \left(2\kappa_\omega^2 + \frac{\kappa_D^2}{2}\left(\delta + \frac{1}{\delta}\right) + \eta^2 \right)\kappa^3 + \frac{\kappa_\omega^4\delta + \dfrac{\kappa_D^2}{2}\left(1 + \delta^2\right)\left(\kappa_\omega^2 + \eta^2\right)}{\delta}\kappa + \frac{\dfrac{\kappa_D^2}{2}\kappa_\omega^2\left(\delta^2 - 1\right)\eta}{\delta} \right]$$

where we have defined:

$$\eta(x) = \frac{1}{\delta(x)}\frac{d\delta(x)}{dx} = \frac{4\alpha}{\lambda_D} \frac{e^{\frac{x-a}{\lambda_D}}}{\left(\alpha\, e^{\frac{x-a}{\lambda_D}} + 1\right)\left(\alpha\, e^{\frac{x-a}{\lambda_D}} - 1\right)}.$$

The only eigenvalue that can be immediately found is $\kappa_1 = 0$; the other ones have to be computed numerically. We then find the matrix transformation $\mathbf{T}(x)$ such that $\mathbf{A} = \mathbf{T}\mathbf{\Lambda}\mathbf{T}^{-1}$ where $\mathbf{\Lambda}$ is the diagonal matrix of the eigenvalues. The system is then diagonalized as:

$$\frac{d\mathbf{u}}{dx} = \mathbf{A}\,\mathbf{u} \quad \Longleftrightarrow \quad \frac{d\mathbf{u}}{dx} = \mathbf{T}\,\mathbf{\Lambda}\,\mathbf{T}^{-1}\mathbf{u} \quad \Longleftrightarrow \quad \frac{d\mathbf{y}}{dx} = \mathbf{\Lambda}\,\mathbf{y} \tag{3.157}$$

where $\mathbf{y} = \mathbf{T}^{-1}\mathbf{u}$. The solution of the diagonalized system is:

$$y_l(x) = C_l \exp\left(\int_{x_0}^{x} \kappa_l(\zeta)d\zeta\right) = s_l \exp\left(\int_{x_0}^{x} \kappa_l(\zeta)d\zeta + c_l\right)$$

where $l = 1..6$ is the eigenvalue index, x_0 is the lower boundary of the domain, in our case then $x_0 = 0$, and we have chosen to include the constant inside the exponential, adding the sign s_l.
The boundary conditions are:

$$\begin{bmatrix} \tilde{V} \\ \dfrac{d\tilde{\phi}_+}{dx} \\ \dfrac{d\tilde{\phi}_-}{dx} \end{bmatrix}_0 = \begin{bmatrix} \tilde{V}_B \\ 0 \\ 0 \end{bmatrix} \qquad \text{and} \qquad \begin{bmatrix} \tilde{V} \\ \dfrac{d\tilde{\phi}_+}{dx} \\ \dfrac{d\tilde{\phi}_-}{dx} \end{bmatrix}_L = \begin{bmatrix} \tilde{V}_T \\ 0 \\ 0 \end{bmatrix}$$

As we know that the actual solution is $\mathbf{u} = \mathbf{T}\mathbf{y}$, we can write:

$$\begin{bmatrix} \mathbf{T}_1\mathbf{y} \\ \mathbf{T}_5\mathbf{y} \\ \mathbf{T}_6\mathbf{y} \end{bmatrix}_0 = \begin{bmatrix} \tilde{V}_B \\ 0 \\ 0 \end{bmatrix} \qquad \text{and} \qquad \begin{bmatrix} \mathbf{T}_1\mathbf{y} \\ \mathbf{T}_5\mathbf{y} \\ \mathbf{T}_6\mathbf{y} \end{bmatrix}_L = \begin{bmatrix} \tilde{V}_T \\ 0 \\ 0 \end{bmatrix}$$

where $\mathbf{T}_k$ denotes the k-th row of $\mathbf{T}$. Because one row of $\mathbf{T}$ is arbitrary, we can set $\mathbf{T}_1 = \begin{bmatrix} 1 & 1 & 1 & 1 & 1 & 1 \end{bmatrix}$. Solving this system of equations we obtain the constants c_l. The matrix $\mathbf{T}$ can be easily calculated noting that the columns $\mathbf{T}^l$ are:

$$\mathbf{T}^l = \begin{bmatrix} 1 \\ -\dfrac{\kappa_\omega^2}{\kappa_l^2 + \kappa_l\eta - \kappa_\omega^2} \\ -\dfrac{\kappa_\omega^2}{\kappa_l^2 - \kappa_l\eta - \kappa_\omega^2} \\ \dfrac{\kappa_D^2}{2\kappa_l}\left(\left(\delta + \dfrac{1}{\delta}\right) + \delta\dfrac{\kappa_\omega^2}{\kappa_l^2 + \kappa_l\eta - \kappa_\omega^2} + \dfrac{1}{\delta}\dfrac{\kappa_\omega^2}{\kappa_l^2 - \kappa_l\eta - \kappa_\omega^2}\right) \\ -\kappa_l\dfrac{\kappa_\omega^2}{\kappa_l^2 + \kappa_l\eta - \kappa_\omega^2} \\ -\kappa_l\dfrac{\kappa_\omega^2}{\kappa_l^2 - \kappa_l\eta - \kappa_\omega^2} \end{bmatrix}$$

and the column corresponding to $\kappa_l = 0$ is $\mathbf{T}^l = \begin{bmatrix} 1 & 1 & 1 & 0 & 0 & 0 \end{bmatrix}^T$. In this way we can write explicitly the system of boundary conditions (denoting with $l = 1$ the eigenvalue

$\kappa_l = 0$, as previously done):

$$\begin{cases} \sum_{l=1}^{6} s_l e^{c_l} = \tilde{V}_B \\ \sum_{l=2}^{6} s_l e^{c_l} \kappa_l(0) \dfrac{\kappa_\omega^2}{\kappa_l(0)^2 + \kappa_l(0)\eta(0) - \kappa_\omega^2} = 0 \\ \sum_{l=2}^{6} s_l e^{c_l} \kappa_l(0) \dfrac{\kappa_\omega^2}{\kappa_l(0)^2 - \kappa_l(0)\eta(0) - \kappa_\omega^2} = 0 \\ \sum_{l=1}^{6} s_l e^{c_l} \exp\left(\int_0^L \kappa_l(\zeta) d\zeta\right) = \tilde{V}_T \\ \sum_{l=2}^{6} s_l e^{c_l} \kappa_l(L) \dfrac{\kappa_\omega^2}{\kappa_l(L)^2 + \kappa_l(L)\eta(L) - \kappa_\omega^2} \exp\left(\int_0^L \kappa_l(\zeta) d\zeta\right) = 0 \\ \sum_{l=2}^{6} s_l e^{c_l} \kappa_l(L) \dfrac{\kappa_\omega^2}{\kappa_l(L)^2 - \kappa_l(L)\eta(L) - \kappa_\omega^2} \exp\left(\int_0^L \kappa_l(\zeta) d\zeta\right) = 0 \end{cases}$$

3.A.6 Spherical 1st order model with only electrolyte - integration constants

To calculate the integration constants in Eqs. 3.85, first we note that:

$$\frac{\partial \mathrm{y}_{-2}(-j\kappa_i r)}{\partial r} = j \frac{(-2\kappa_l r \cosh(\kappa_l r) + (2 + \kappa_l^2 r^2) \sinh(\kappa_l r))}{\kappa_l^2 r^3}.$$

The expressions for the gradients are:

$$\nabla\tilde{\phi}_1 \cdot \hat{r} = \frac{\partial\tilde{\phi}_1}{\partial r} = \left(c_1' \frac{\partial \mathrm{y}_{-2}(-j\kappa_1 r)}{\partial r} - c_2' \frac{\partial \mathrm{y}_{-2}(-j\kappa_2 r)}{\partial r} + c_3\right) \cos\theta$$
$$\nabla\tilde{\phi}_2 \cdot \hat{r} = \frac{\partial\tilde{\phi}_2}{\partial r} = \left(c_1' \frac{\partial \mathrm{y}_{-2}(-j\kappa_1 r)}{\partial r} + c_2' \frac{\partial \mathrm{y}_{-2}(-j\kappa_2 r)}{\partial r} + c_3\right) \cos\theta$$

Therefore, we need to solve the system:

$$\begin{cases} c_1' \dfrac{\partial \mathrm{y}_{-2}(-j\kappa_1 r)}{\partial r}\Big|_R - c_2' \dfrac{\partial \mathrm{y}_{-2}(-j\kappa_2 r)}{\partial r}\Big|_R + c_3 = 0 \\ c_1' \dfrac{\partial \mathrm{y}_{-2}(-j\kappa_1 r)}{\partial r}\Big|_R + c_2' \dfrac{\partial \mathrm{y}_{-2}(-j\kappa_2 r)}{\partial r}\Big|_R + c_3 = 0 \\ -\dfrac{\xi}{j\omega} c_1' \, \mathrm{y}_{-2}(-j\kappa_1 R) + c_3 R = \tilde{V}_0 \end{cases} . \tag{3.158}$$

Subtracting the first equation from the second immediately tells that $c_2' = c_2 = 0$. The other constants are (with the substitution $\rho_0 = \kappa R$):

$$\begin{aligned} c_1 = \frac{j}{2} c_1' &= -\frac{j\omega}{2} \frac{\kappa^2 R^2}{\kappa R(\xi - 2j\omega)\cosh(\kappa R) + (-\xi + (2 + \kappa^2 R^2)\, j\omega)\sinh(\kappa R)} \tilde{V}_0 \\ &= -j\omega \frac{\rho_0^2 \exp(-\rho_0)}{\rho_0(\xi - 2j\omega)\,(1 + \exp(-2\rho_0)) + (-\xi + (2 + \rho_0^2)\, j\omega)\,(1 - \exp(-2\rho_0))} \tilde{V}_0 \end{aligned}$$

$$c_3 = \frac{j\omega}{R}\frac{-2\kappa R\cosh(\kappa R) + (2+\kappa^2R^2)\sinh(\kappa R)}{\kappa R(\xi-2j\omega)\cosh(\kappa R) + (-\xi+(2+\kappa^2R^2)\,j\omega)\sinh(\kappa R)}\tilde{V}_0$$
$$= \frac{j\omega}{R}\frac{-2\rho_0\,(1+\exp(-2\rho_0)) + (2+\rho_0^2)\,(1-\exp(-2\rho_0))}{\rho_0(\xi-2j\omega)\,(1+\exp(-2\rho_0)) + (-\xi+(2+\rho_0^2)\,j\omega)\,(1-\exp(-2\rho_0))}\tilde{V}_0$$

3.A.7 Spherical 1st order model with particle - integration constants

The expressions of the integration constants in Eq. 3.93 are:

$$\begin{aligned}
c_1 &= 3R^5V_0\kappa^2 j\omega\Big[-3e^{\rho_p}r_p^3\epsilon_p(2+\rho_0(2+\rho_0))j\omega \\
&\quad + e^{\rho_0}\Big(\left(R^3-r_p^3\right)(\epsilon_p(1+\rho_p)+\varepsilon_{el}(2+\rho_p(2+\rho_p)))2\xi \\
&\quad + \left(2r_p^3(\epsilon_p-\varepsilon_{el})+R^3(\epsilon_p+2\varepsilon_{el})\right)(2+\rho_p(2+\rho_p))j\omega\Big)\Big]/\eta \\
d_1 &= e^{\rho_0+\rho_p}3R^5V_0\kappa^2 j\omega\Big[-3e^{\rho_0}r_p^3\epsilon_p(2+\rho_0(-2+\rho_0))j\omega \\
&\quad + e^{\rho_p}\Big(\left(R^3-r_p^3\right)(\epsilon_p(1-\rho_p)+\varepsilon_{el}(2+\rho_p(-2+\rho_p)))2\xi \\
&\quad + \left(2r_p^3(\epsilon_p-\varepsilon_{el})+R^3(\epsilon_p+2\varepsilon_{el})\right)(2+\rho_p(-2+\rho_p))j\omega\Big)\Big]/\eta \\
c_3 &= 3R^5V_0 j\omega\Big[e^{2\rho_p}(2+\rho_0(2+\rho_0))\Big((\epsilon_p(1-\rho_p)+\varepsilon_{el}(2+\rho_p(-2+\rho_p)))2\xi \\
&\quad + (\epsilon_p+2\varepsilon_{el})(2+\rho_p(-2+\rho_p))j\omega\Big) \\
&\quad - e^{2\rho_0}(2+\rho_0(-2+\rho_0))\Big((\epsilon_p(1+\rho_p)+\varepsilon_{el}(2+\rho_p(2+\rho_p)))2\xi \\
&\quad + (\epsilon_p+2\varepsilon_{el})(2+\rho_p(2+\rho_p))j\omega\Big) + 4e^{\rho_0+\rho_p}\epsilon_p\rho_p^3\xi\Big]/\eta \\
d_3 &= 3R^5r_p^3V_0 j\omega\Big[e^{2\rho_p}(2+\rho_0(2+\rho_0))\Big((\epsilon_p(1-\rho_p)+\varepsilon_{el}(2+\rho_p(-2+\rho_p)))\xi \\
&\quad + j(-\epsilon_p+\varepsilon_{el})(2+\rho_p(-2+\rho_p))\omega\Big) \\
&\quad - e^{2\rho_0}(2+\rho_0(-2+\rho_0))\Big((\epsilon_p(1+\rho_p)+\varepsilon_{el}(2+\rho_p(2+\rho_p)))\xi \\
&\quad + j(-\epsilon_p+\varepsilon_{el})(2+\rho_p(2+\rho_p))\omega\Big) + 2e^{\rho_0+\rho_p}\epsilon_p\rho_0^3\xi\Big]/\eta \\
e_1 &= 3R^5V_0\varepsilon_{el}(\xi+j\omega)\Big[-4e^{\rho_0+\rho_p}\left(R^3-r_p^3\right)\kappa^3\xi \\
&\quad + 3je^{2\rho_p}(2+\rho_0(2+\rho_0))(2+\rho_p(-2+\rho_p))\omega \\
&\quad - 3je^{2\rho_0}(2+\rho_0(-2+\rho_0))(2+\rho_p(2+\rho_p))\omega\Big]/\eta \\
\eta &= -\Big(3je^{\rho_p}R^3(\epsilon_p(-1+\rho_p)-\varepsilon_{el}(2+\rho_p(-2+\rho_p)))\xi \\
&\quad + e^{\rho_0}\big(-j\left(2r_p^3(\epsilon_p-\varepsilon_{el})+R^3(\epsilon_p+2\varepsilon_{el})\right)(-1+\rho_0)\xi \\
&\quad + \left(r_p^3(-\epsilon_p+\varepsilon_{el})+R^3(\epsilon_p+2\varepsilon_{el})\right)(2+\rho_0(-2+\rho_0))\omega\big)\Big) \\
&\quad \Big(-3e^{\rho_0}R^3(2+\rho_p(2+\rho_p))\omega + e^{\rho_p}\left(2j\left(R^3-r_p^3\right)(1+\rho_0)\xi + \left(2R^3+r_p^3\right)(2+\rho_0(2+\rho_0))\omega\right)\Big) \\
&\quad + \Big(-3e^{\rho_p}R^3(2+\rho_p(-2+\rho_p))\omega \\
&\quad + e^{\rho_0}\left(-2j\left(R^3-r_p^3\right)(-1+\rho_0)\xi + \left(2R^3+r_p^3\right)(2+\rho_0(-2+\rho_0))\omega\right)\Big)
\end{aligned}$$

$$\Big(-3je^{\rho_0}R^3(\epsilon_p(1+\rho_p)+\varepsilon_{el}(2+\rho_p(2+\rho_p)))\xi$$
$$+ e^{\rho_p}\Big(j\left(2r_p^3(\epsilon_p-\varepsilon_{el})+R^3(\epsilon_p+2\varepsilon_{el})\right)(1+\rho_0)\xi$$
$$+ \left(r_p^3(-\epsilon_p+\varepsilon_{el})+R^3(\epsilon_p+2\varepsilon_{el})\right)(2+\rho_0(2+\rho_0))\omega\Big)\Big)$$

where we have set again $\rho=\kappa r$, so that $\rho_p=\kappa r_p$ and $\rho_0=\kappa R$. We also can assume that $\rho_0 \gg 1$. The constants then are:

$$c_1 = 3R^5V_0\kappa^2 j\omega\Big[-3e^{\rho_p}r_p^3\epsilon_p\rho_0^2 j\omega + e^{\rho_0}\Big(\left(R^3-r_p^3\right)(\epsilon_p(1+\rho_p)+\varepsilon_{el}(2+\rho_p(2+\rho_p)))2\xi$$
$$+ \left(2r_p^3(\epsilon_p-\varepsilon_{el})+R^3(\epsilon_p+2\varepsilon_{el})\right)(2+\rho_p(2+\rho_p))j\omega\Big)\Big]/\eta$$
$$d_1 = e^{\rho_0+\rho_p}3R^5V_0\kappa^2 j\omega\Big[-3e^{\rho_0}r_p^3\epsilon_p\rho_0^2 j\omega + e^{\rho_p}\Big(\left(R^3-r_p^3\right)(\epsilon_p(1-\rho_p)+\varepsilon_{el}(2+\rho_p(-2+\rho_p)))2\xi$$
$$+ \left(2r_p^3(\epsilon_p-\varepsilon_{el})+R^3(\epsilon_p+2\varepsilon_{el})\right)(2+\rho_p(-2+\rho_p))j\omega\Big)\Big]/\eta$$
$$c_3 = 3R^5V_0 j\omega\Big[e^{2\rho_p}\rho_0^2\Big((\epsilon_p(1-\rho_p)+\varepsilon_{el}(2+\rho_p(-2+\rho_p)))2\xi+(\epsilon_p+2\varepsilon_{el})(2+\rho_p(-2+\rho_p))j\omega\Big)$$
$$- e^{2\rho_0}\rho_0^2\Big((\epsilon_p(1+\rho_p)+\varepsilon_{el}(2+\rho_p(2+\rho_p)))2\xi+(\epsilon_p+2\varepsilon_{el})(2+\rho_p(2+\rho_p))j\omega\Big)+4e^{\rho_0+\rho_p}\rho_p^3\epsilon_p\xi\Big]/\eta$$
$$d_3 = 3R^5r_p^3V_0 j\omega\Big[e^{2\rho_p}\rho_0^2\Big((\epsilon_p(1-\rho_p)+\varepsilon_{el}(2+\rho_p(-2+\rho_p)))\xi+j(-\epsilon_p+\varepsilon_{el})(2+\rho_p(-2+\rho_p))\omega\Big)$$
$$- e^{2\rho_0}\rho_0^2\Big((\epsilon_p(1+\rho_p)+\varepsilon_{el}(2+\rho_p(2+\rho_p)))\xi+j(-\epsilon_p+\varepsilon_{el})(2+\rho_p(2+\rho_p))\omega\Big)+2e^{\rho_0+\rho_p}\rho_0^3\epsilon_p\xi\Big]/\eta$$
$$e_1 = 3R^5V_0\varepsilon_{el}(\xi+j\omega)\Big[-4e^{\rho_0+\rho_p}\left(\rho_0^3-\rho_p^3\right)\xi$$
$$+ 3je^{2\rho_p}\rho_0^2(2+\rho_p(-2+\rho_p))\omega - 3je^{2\rho_0}\rho_0^2(2+\rho_p(2+\rho_p))\omega\Big]/\eta$$
$$\eta = -\Big(3je^{\rho_p}R^3(\epsilon_p(-1+\rho_p)-\varepsilon_{el}(2+\rho_p(-2+\rho_p)))\xi$$
$$+ e^{\rho_0}\left(-j\left(2r_p^3(\epsilon_p-\varepsilon_{el})+R^3(\epsilon_p+2\varepsilon_{el})\right)\rho_0\xi+\left(r_p^3(-\epsilon_p+\varepsilon_{el})+R^3(\epsilon_p+2\varepsilon_{el})\right)\rho_0^2\omega\right)\Big)$$
$$\Big(-3e^{\rho_0}R^3(2+\rho_p(2+\rho_p))\omega + e^{\rho_p}\left(2j\left(R^3-r_p^3\right)\rho_0\xi+\left(2R^3+r_p^3\right)\rho_0^2\omega\right)\Big)$$
$$+\Big(-3e^{\rho_p}R^3(2+\rho_p(-2+\rho_p))\omega + e^{\rho_0}\left(-2j\left(R^3-r_p^3\right)\rho_0\xi+\left(2R^3+r_p^3\right)\rho_0^2\omega\right)\Big)$$
$$\Big(-3je^{\rho_0}R^3(\epsilon_p(1+\rho_p)+\varepsilon_{el}(2+\rho_p(2+\rho_p)))\xi$$
$$+ e^{\rho_p}\Big(j\left(2r_p^3(\epsilon_p-\varepsilon_{el})+R^3(\epsilon_p+2\varepsilon_{el})\right)\rho_0\xi+\left(r_p^3(-\epsilon_p+\varepsilon_{el})+R^3(\epsilon_p+2\varepsilon_{el})\right)\rho_0^2\omega\Big)\Big)$$

Large particle Assuming $|\rho_p| \gg 1$, the constants are:

$$c_1 = 3R^5V_0\kappa^2 j\omega\Big[-3e^{\rho_p-2\rho_0}r_p^3\epsilon_p\rho_0^2 j\omega + e^{-\rho_0}\Big(\left(R^3-r_p^3\right)(\epsilon_p\rho_p+\varepsilon_{el}\rho_p^2)2\xi$$
$$+ \left(2r_p^3(\epsilon_p-\varepsilon_{el})+R^3(\epsilon_p+2\varepsilon_{el})\right)\rho_p^2 j\omega\Big)\Big]/\eta$$
$$d_1 = e^{\rho_p}3R^5V_0\kappa^2 j\omega\Big[-3r_p^3\epsilon_p\rho_0^2 j\omega + e^{\rho_p-\rho_0}\Big(\left(R^3-r_p^3\right)(-\epsilon_p\rho_p+\varepsilon_{el}\rho_p^2)2\xi$$
$$+ \left(2r_p^3(\epsilon_p-\varepsilon_{el})+R^3(\epsilon_p+2\varepsilon_{el})\right)\rho_p^2 j\omega\Big)\Big]/\eta$$
$$c_3 = 3R^5V_0 j\omega\Big[e^{2\rho_p-2\rho_0}\rho_0^2\Big((-\epsilon_p\rho_p+\varepsilon_{el}\rho_p^2)2\xi+(\epsilon_p+2\varepsilon_{el})\rho_p^2 j\omega\Big)$$

$$
\begin{aligned}
&- \rho_0^2\Big((\epsilon_p\rho_p + \varepsilon_{el}\rho_p^2)2\xi + (\epsilon_p + 2\varepsilon_{el})\rho_p^2 j\omega\Big) + 4e^{\rho_p-\rho_0}\rho_p^3\epsilon_p\xi\Big]/\eta \\
d_3 &= 3R^5 r_p^3 V_0 j\omega\Big[e^{2\rho_p-2\rho_0}\rho_0^2\Big((-\epsilon_p\rho_p + \varepsilon_{el}\rho_p^2)\xi + (-\epsilon_p + \varepsilon_{el})\rho_p^2 j\omega\Big) \\
&- \rho_0^2\Big((\epsilon_p\rho_p + \varepsilon_{el}\rho_p^2)\xi + (-\epsilon_p + \varepsilon_{el})\rho_p^2 j\omega\Big) + 2e^{\rho_p-\rho_0}\rho_0^3\epsilon_p\xi\Big]/\eta \\
e_1 &= 3R^5 V_0\varepsilon_{el}(\xi + j\omega)\Big[- 4e^{\rho_p-\rho_0}\left(\rho_0^3 - \rho_p^3\right)\xi + 3je^{2\rho_p-2\rho_0}\rho_0^2\rho_p^2\omega - 3j\rho_0^2\rho_p^2\omega\Big]/\eta \\
\eta &= -\Big(3je^{\rho_p-\rho_0}R^3(\epsilon_p\rho_p - \varepsilon_{el}\rho_p^2)\xi \\
&\quad - j\left(2r_p^3(\epsilon_p - \varepsilon_{el}) + R^3(\epsilon_p + 2\varepsilon_{el})\right)\rho_0\xi + \left(r_p^3(-\epsilon_p + \varepsilon_{el}) + R^3(\epsilon_p + 2\varepsilon_{el})\right)\rho_0^2\omega\Big) \\
&\Big(- 3R^3\rho_p^2\omega + e^{\rho_p-\rho_0}\left(2j\left(R^3 - r_p^3\right)\rho_0\xi + \left(2R^3 + r_p^3\right)\rho_0^2\omega\right)\Big) \\
&+ \Big(- 3e^{\rho_p-\rho_0}R^3\rho_p^2\omega - 2j\left(R^3 - r_p^3\right)\rho_0\xi + \left(2R^3 + r_p^3\right)\rho_0^2\omega\Big) \\
&\Big(- 3jR^3(\epsilon_p\rho_p + \varepsilon_{el}\rho_p^2)\xi \\
&\quad + e^{\rho_p-\rho_0}\Big(j\left(2r_p^3(\epsilon_p - \varepsilon_{el}) + R^3(\epsilon_p + 2\varepsilon_{el})\right)\rho_0\xi + \left(r_p^3(-\epsilon_p + \varepsilon_{el}) + R^3(\epsilon_p + 2\varepsilon_{el})\right)\rho_0^2\omega\Big)\Big)
\end{aligned}
$$

where we have also multiplied nominator and denominator by $\exp(-2\rho_0)$.

If we now assume that $\rho_0 \gg \rho_p$ the constants simplify to:

$$
\begin{aligned}
c_1 &= e^{-\rho_0}3R^5V_0\kappa^2 j\omega\Big(\left(R^3 - r_p^3\right)(\epsilon_p\rho_p + \varepsilon_{el}\rho_p^2)2\xi \\
&\quad + \left(2r_p^3(\epsilon_p - \varepsilon_{el}) + R^3(\epsilon_p + 2\varepsilon_{el})\right)\rho_p^2 j\omega\Big)/\eta \\
d_1 &= -e^{\rho_p}9R^5V_0\kappa^2 j\omega r_p^3\epsilon_p\rho_0^2 j\omega/\eta \\
c_3 &= -3R^5V_0 j\omega\rho_0^2\Big((\epsilon_p\rho_p + \varepsilon_{el}\rho_p^2)2\xi + (\epsilon_p + 2\varepsilon_{el})\rho_p^2 j\omega\Big)/\eta \\
d_3 &= -3R^5 r_p^3 V_0 j\omega\rho_0^2\Big((\epsilon_p\rho_p + \varepsilon_{el}\rho_p^2)\xi + (-\epsilon_p + \varepsilon_{el})\rho_p^2 j\omega\Big)/\eta \\
e_1 &= -9R^5V_0\varepsilon_{el}(\xi + j\omega)\rho_0^2\rho_p^2 j\omega/\eta \\
\eta &= -3R^3\rho_p^2 j\omega\Big(\left(2r_p^3(\epsilon_p - \varepsilon_{el}) + R^3(\epsilon_p + 2\varepsilon_{el})\right)\rho_0\xi - \left(r_p^3(-\epsilon_p + \varepsilon_{el}) + R^3(\epsilon_p + 2\varepsilon_{el})\right)\rho_0^2 j\omega\Big) \\
&\quad + 3R^3(\epsilon_p\rho_p + \varepsilon_{el}\rho_p^2)\xi\Big(- 2\left(R^3 - r_p^3\right)\rho_0\xi + \left(2R^3 + r_p^3\right)\rho_0^2 j\omega\Big)
\end{aligned}
$$

If we instead assume that $\rho_0 \approx \rho_p$, which implies $c_1\exp(\rho_0) \to 0$, we can simplify the expression of the current as follows:

$$
\begin{aligned}
\tilde{I} &\simeq \pi R\varepsilon_{el}\Big(- d_1\xi\exp(-\rho_0) - c_3 j\omega R + 2j\omega\frac{d_3}{R^2}\Big) \\
&\simeq 3\pi R^4\tilde{V}_0 j\omega\varepsilon_{el}\Big[2R^2\left(R^3 - r_p^3\right)\alpha\kappa^2\xi^2\rho_p(\epsilon_p - \alpha\epsilon_p + (1+\alpha)\varepsilon_{el}\rho_p) \\
&\quad + \xi\Big(r_p^3\alpha\epsilon_p\rho_0^2\left(-3R^2(1+\alpha)\kappa^2 + 4\rho_0\right) + 2\left(R^3 - r_p^3\right)\left(1+\alpha^2\right)\epsilon_p\rho_0^2\rho_p \\
&\quad + (1+\alpha)\left(R^2\alpha\left(2r_p^3(\epsilon_p - \varepsilon_{el}) + R^3(\epsilon_p + 2\varepsilon_{el})\right)\kappa^2 - 2\left(R^3 - r_p^3\right)(-1+\alpha)\varepsilon_{el}\rho_0^2\right)\rho_p^2 \\
&\quad - 4R^3\alpha\epsilon_p\rho_p^3\Big)j\omega + \left(-1+\alpha^2\right)\left(2r_p^3(\epsilon_p - \varepsilon_{el}) + R^3(\epsilon_p + 2\varepsilon_{el})\right)\rho_0^2\rho_p^2\omega^2\Big]/\eta
\end{aligned}
$$

where we have written $\alpha = \exp(\rho_p - \rho_0)$.

If we now assume that the particle is at large distance from the electrodes, then $\alpha \simeq 0$

and:

$$\begin{aligned}
\tilde{I} \simeq & -3\pi R^4 \tilde{V}_0 j\omega\varepsilon_{el}\Big[\xi\Big(2\left(R^3-r_p^3\right)\epsilon_p\rho_0^2\rho_p+\left(2\left(R^3-r_p^3\right)\varepsilon_{el}\rho_0^2\right)\rho_p^2\Big)j\omega \\
& -\left(2r_p^3(\epsilon_p-\varepsilon_{el})+R^3(\epsilon_p+2\varepsilon_{el})\right)\rho_0^2\rho_p^2\omega^2\Big]/ \\
& \Big[\Big(\left(2r_p^3(\epsilon_p-\varepsilon_{el})+R^3(\epsilon_p+2\varepsilon_{el})\right)\rho_0\xi+\left(r_p^3(-\epsilon_p+\varepsilon_{el})+R^3(\epsilon_p+2\varepsilon_{el})\right)\rho_0^2 j\omega\Big) \\
& \Big(3R^3\rho_p^2 j\omega\Big) \\
& +\Big(2\left(R^3-r_p^3\right)\rho_0\xi+\left(2R^3+r_p^3\right)\rho_0^2 j\omega\Big)\Big(3R^3(\epsilon_p\rho_p+\varepsilon_{el}\rho_p^2)\xi\Big)\Big] \\
= & \,\pi R\tilde{V}_0\omega^2\varepsilon_{el}\rho_0\rho_p\Big[2\left(R^3-r_p^3\right)(\epsilon_p+\varepsilon_{el})\,\xi+\left(2r_p^3(\epsilon_p-\varepsilon_{el})+R^3(\epsilon_p+2\varepsilon_{el})\right)j\omega\Big]/ \\
& \Big[\Big(\left(2r_p^3(\epsilon_p-\varepsilon_{el})+R^3(\epsilon_p+2\varepsilon_{el})\right)\xi+\left(r_p^3(-\epsilon_p+\varepsilon_{el})+R^3(\epsilon_p+2\varepsilon_{el})\right)\rho_0 j\omega\Big)\rho_p j\omega \\
& +\Big(2\left(R^3-r_p^3\right)\xi+\left(2R^3+r_p^3\right)\rho_0 j\omega\Big)(\epsilon_p+\varepsilon_{el}\rho_p)\xi\Big]
\end{aligned}$$

3.A.8 Spherical 0th order model with only electrolyte - integration constants

As before, subtracting the first two equations from Eq. 3.100 tells us immediately that $c_2 = d_2 = 0$ and $\tilde{\phi}_1 = \tilde{\phi}_2 = \tilde{\phi}$. Eq. 3.100 transforms then to:

$$\begin{cases}
c_1\exp(\kappa R_i)\dfrac{\kappa R_i-1}{\kappa R_i^2}-d_1\exp(-\kappa R_i)\dfrac{\kappa R_i+1}{\kappa R_i^2}-\dfrac{d_3}{R_i^2}=0 \\
c_1\exp(\kappa R_o)\dfrac{\kappa R_o-1}{\kappa R_o^2}-d_1\exp(-\kappa R_o)\dfrac{\kappa R_o+1}{\kappa R_o^2}-\dfrac{d_3}{R_o^2}=0 \\
-\dfrac{\xi}{j\omega}\dfrac{c_1\exp(\kappa R_i)+d_1\exp(-\kappa R_i)}{\kappa R_i}+c_3+\dfrac{d_3}{R_i}=\tilde{V}_0 \\
-\dfrac{\xi}{j\omega}\dfrac{c_1\exp(\kappa R_o)+d_1\exp(-\kappa R_o)}{\kappa R_o}+c_3+\dfrac{d_3}{R_o}=0
\end{cases}$$

The solution is:

$$\begin{aligned}
c_1 &= R_iR_o\kappa j\omega\left(e^{-\rho_o}(1+\rho_i)-e^{\rho_i-2\rho_o}(1+\rho_o)\right)\tilde{V}_0/\eta \\
d_1 &= R_iR_o\kappa j\omega\left(-e^{2\rho_i-\rho_o}(1-\rho_i)+e^{\rho_i}(1-\rho_o)\right)\tilde{V}_0/\eta \\
c_3 &= R_i\left(-2e^{\rho_i-\rho_o}\rho_o\xi+(1+\rho_i)(\xi+j\omega(1-\rho_o))-e^{2\rho_i-2\rho_o}(1-\rho_i)(\xi+j\omega(1+\rho_o))\right)\tilde{V}_0/\eta \\
d_3 &= -R_iR_oj\omega\left((1+\rho_i)(1-\rho_o)-e^{2\rho_i-2\rho_o}(1-\rho_i)(1+\rho_o)\right)\tilde{V}_0/\eta \\
\eta &= -4e^{\rho_i-\rho_o}R_iR_o\kappa\xi-\left((R_o(1-\rho_o)-R_i(1+\rho_i))\xi+(R_o-R_i)(1+\rho_i)(1-\rho_o)j\omega\right) \\
&\quad +e^{2\rho_i-2\rho_o}\left((R_o(1+\rho_o)-R_i(1-\rho_i))\xi+(R_o-R_i)(1-\rho_i)(1+\rho_o)j\omega\right)
\end{aligned}$$

where $\rho_i = \kappa R_i$ and $\rho_o = \kappa R_o$.
We now define $\alpha = \exp(\rho_i - \rho_o)$. We can safely assume that the outer electrode has a

wide radius, so that $\rho_o = \kappa R_o \gg 1$. In this way the constants simplify to:

$$\begin{aligned}
c_1 &= e^{-\rho_o} R_i R_o \kappa j\omega \left((1+\rho_i) - \alpha\rho_o\right) \tilde{V}_0/\eta \\
d_1 &= e^{\rho_i} R_i R_o \kappa j\omega \left(-\alpha\left(1-\rho_i\right) - \rho_o\right) \tilde{V}_0/\eta \\
c_3 &= R_i \left(-2\alpha\rho_o\xi + \left(1+\rho_i\right)\left(\xi - j\omega\right) - \alpha^2\left(1-\rho_i\right)\left(\xi + j\omega\right)\right) \tilde{V}_0/\eta \\
d_3 &= -R_i R_o j\omega \left(-\left(1+\rho_i\right)\rho_o - \alpha^2\left(1-\rho_i\right)\rho_o\right) \tilde{V}_0/\eta \\
\eta &= -4\alpha R_i R_o \kappa\xi - \left(\left(-R_o\rho_o - R_i\left(1+\rho_i\right)\right)\xi + \left(R_o - R_i\right)\left(1+\rho_i\right)\rho_o j\omega\right) \\
&\quad + \alpha^2\left(\left(R_o\rho_o - R_i\left(1-\rho_i\right)\right)\xi + \left(R_o - R_i\right)\left(1-\rho_i\right)\rho_o j\omega\right)
\end{aligned}$$

Large radius inner electrode If the inner electrode has a large radius ($\rho_i = \kappa R_i \gg 1$), but still much smaller than the outer electrode ($\rho_i \ll \rho_o$, $\alpha \to 0$), then we can further simplify the solution:

$$\begin{aligned}
c_1 &= e^{-\rho_o} R_i R_o \kappa j\omega \left(1+\rho_i\right) \tilde{V}_0/\eta \\
d_1 &= -e^{\rho_i} R_i R_o \kappa j\omega\rho_o \tilde{V}_0/\eta \\
c_3 &= R_i \left(1+\rho_i\right)\left(\xi - j\omega\right) \tilde{V}_0/\eta \\
d_3 &= R_i R_o j\omega \left(1+\rho_i\right)\rho_o \tilde{V}_0/\eta \\
\eta &= -\left(\left(-R_o\rho_o - R_i\left(1+\rho_i\right)\right)\xi + \left(R_o - R_i\right)\left(1+\rho_i\right)\rho_o j\omega\right)
\end{aligned}$$

3.A.9 Spherical 0th order model with particle - integration constants

Defining $\alpha_i = \exp(\rho_i - \rho_p)$ and $\alpha_o = \exp(\rho_P - \rho_o)$ the constants in Eqs. 3.103 - 3.104 are:

$$\begin{aligned}
c_{1i} &= r_p r_P R_o \tilde{V}_0 \epsilon_p \kappa \left(-e^{\rho_i}(1+\rho_p) + e^{\rho_p}(1+\rho_i)\right) \\
&\quad \left(e^{2\rho_o}(1+\rho_P)(-1+\rho_o) - e^{2\rho_P}(-1+\rho_P)(1+\rho_o)\right) j\omega(\xi + j\omega)/\eta \\
d_{1i} &= e^{(r_p+R_i)\kappa} r_p r_P R_o \tilde{V}_0 \epsilon_p \kappa \left(e^{\rho_p}(-1+\rho_p) + e^{\rho_i}(1-\rho_i)\right) \\
&\quad \left(-e^{2\rho_o}(1+\rho_P)(-1+\rho_o) + e^{2\rho_P}(-1+\rho_P)(1+\rho_o)\right) j\omega(\xi + j\omega)/\eta \\
c_{3i} &= \frac{1}{R_i} r_p r_P R_o \tilde{V}_0 \epsilon_p \left(e^{2\rho_o}(1+\rho_P)(-1+\rho_o) - e^{2\rho_P}(-1+\rho_P)(1+\rho_o)\right)\left(\xi + j\omega\right) \\
&\quad \left(2e^{(r_p+R_i)\kappa}\rho_i\xi - e^{2\rho_i}(1+\rho_p)(\xi + j\omega - \rho_i j\omega) - e^{2\rho_p}(-1+\rho_p)(\xi + j\omega + \rho_i j\omega)\right)/\eta + \tilde{V}_0 \\
d_{3i} &= r_p r_P R_o \tilde{V}_0 \epsilon_p \left(-e^{2\rho_i}(1+\rho_p)(-1+\rho_i) + e^{2\rho_p}(-1+\rho_p)(1+\rho_i)\right) \\
&\quad \left(e^{2\rho_o}(1+\rho_P)(-1+\rho_o) - e^{2\rho_P}(-1+\rho_P)(1+\rho_o)\right) j\omega(\xi + j\omega)/\eta \\
c_{1o} &= r_p r_P R_o \tilde{V}_0 \epsilon_p \kappa \left(-e^{2\rho_i}(1+\rho_p)(-1+\rho_i) + e^{2\rho_p}(-1+\rho_p)(1+\rho_i)\right) \\
&\quad \left(e^{\rho_o}(1+\rho_P) - e^{\rho_P}(1+\rho_o)\right) j\omega(\xi + j\omega)/\eta \\
d_{1o} &= e^{(r_P+R_o)\kappa} r_p r_P R_o \tilde{V}_0 \epsilon_p \kappa \left(-e^{2\rho_i}(1+\rho_p)(-1+\rho_i) + e^{2\rho_p}(-1+\rho_p)(1+\rho_i)\right) \\
&\quad \left(e^{\rho_P}(-1+\rho_P) + e^{\rho_o}(1-\rho_o)\right) j\omega(\xi + j\omega)/\eta \\
c_{3o} &= -\frac{r_p r_P \tilde{V}_0 \epsilon_p}{-e^{2\rho_o}(1+\rho_P)(-1+\rho_o) + e^{2\rho_P}(-1+\rho_P)(1+\rho_o)} \\
&\quad \left(-e^{2\rho_i}(1+\rho_p)(-1+\rho_i) + e^{2\rho_p}(-1+\rho_p)(1+\rho_i)\right) \\
&\quad \left(e^{2\rho_o}(1+\rho_P)(-1+\rho_o) - e^{2\rho_P}(-1+\rho_P)(1+\rho_o)\right)\left(\xi + j\omega\right) \\
&\quad \left(-2e^{(r_P+R_o)\kappa}\rho_o\xi + e^{2\rho_o}(1+\rho_P)(\xi + j\omega - \rho_o j\omega) + e^{2\rho_P}(-1+\rho_P)(\xi + j\omega + \rho_o j\omega)\right)/\eta \\
d_{3o} &= r_p r_P R_o \tilde{V}_0 \epsilon_p \left(-e^{2\rho_i}(1+\rho_p)(-1+\rho_i) + e^{2\rho_p}(-1+\rho_p)(1+\rho_i)\right)
\end{aligned}$$

$$
\begin{aligned}
&\left(e^{2\rho_o}(1+\rho_P)(-1+\rho_o) - e^{2\rho_P}(-1+\rho_P)(1+\rho_o)\right) j\omega(\xi+j\omega)/\eta \\
e = &\frac{r_P R_o \tilde{V}_0}{R_i\left(e^{\rho_i}(1+\rho_p) - e^{\rho_p}(1+\rho_i)\right)}\left(-e^{\rho_i}(1+\rho_p) + e^{\rho_p}(1+\rho_i)\right) \\
&\left(e^{2\rho_o}(1+\rho_P)(-1+\rho_o) - e^{2\rho_P}(-1+\rho_P)(1+\rho_o)\right)(\xi+j\omega) \\
&\Big(-4e^{(r_p+R_i)\kappa} r_p R_i \epsilon_p \kappa\xi + e^{2\rho_i}\big(R_i(\epsilon_p-\varepsilon_{el})(-1+\rho_i)(\xi+j\omega) \\
&+ r_p^2\epsilon_p\kappa(\xi+j\omega-\rho_i j\omega) + r_p\left(-R_i\varepsilon_{el}\kappa(-1+\rho_i)(\xi+j\omega) + \epsilon_p\left(\xi+(-1+\rho_i)^2 j\omega\right)\right)\big) \\
&+ e^{2\rho_p}\big(R_i(\epsilon_p-\varepsilon_{el})(1+\rho_i)(\xi+j\omega) + r_p^2\epsilon_p\kappa(\xi+j\omega+\rho_i j\omega) \\
&+ r_p\left(R_i\varepsilon_{el}\kappa(1+\rho_i)(\xi+j\omega) - \epsilon_p\left(\xi+(1+\rho_i)^2 j\omega\right)\right)\big)\Big)/\eta + \tilde{V}_0 \\
f = &\, r_p r_P R_o \tilde{V}_0 \varepsilon_{el}\left(-e^{2\rho_i}(1+\rho_p)(-1+\rho_i) + e^{2\rho_p}(-1+\rho_p)(1+\rho_i)\right) \\
&\left(e^{2\rho_o}(1+\rho_P)(-1+\rho_o) - e^{2\rho_P}(-1+\rho_P)(1+\rho_o)\right)(\xi+j\omega)^2/\eta \\
\eta = &\frac{1}{R_i} e^{-2(\rho_p+\rho_o)}(\xi+j\omega)\Big[-2e^{\rho_p+\rho_i+2\rho_o} r_P R_o \epsilon_p \xi(1+\rho_P)(R_i\rho_p + r_p\rho_i)(-1+\rho_o) \\
&+ 4e^{\rho_P+2\rho_i+\rho_o} r_p r_P R_i \epsilon_p \xi(1+\rho_p)(-1+\rho_i)\rho_o - 4e^{2\rho_p+\rho_P+\rho_o} r_p r_P R_i \epsilon_p \xi(-1+\rho_p)(1+\rho_i)\rho_o \\
&+ 2e^{\rho_p+2\rho_P+\rho_i} r_P R_o \epsilon_p \xi(-1+\rho_P)(R_i\rho_p + r_p\rho_i)(1+\rho_o) \\
&+ e^{2(\rho_i+\rho_o)}(r_P R_i R_o(1+\rho_P)(-1+\rho_i)(-1+\rho_o)(-\varepsilon_{el}(1+\rho_p)(\xi+j\omega) + \epsilon_p(\xi+j\omega+\rho_p j\omega)) \\
&\quad - r_p(1+\rho_p)(R_i R_o(-1+\rho_i)(-1+\rho_o)(\epsilon_p(\xi+j\omega) - \varepsilon_{el}(\xi+\xi\rho_P+j\omega)) \\
&\quad + r_P(-R_o\epsilon_p(1+\rho_P)(-1+\rho_o)(\xi+j\omega-\rho_i j\omega) \\
&\quad + R_i(-1+\rho_i)(-\varepsilon_{el}(-1+\rho_o)\rho_o j\omega + \epsilon_p(\xi(1+\rho_P) - (1+\rho_P-\rho_o)(-1+\rho_o)j\omega))))) \\
&+ e^{2(\rho_p+\rho_o)}(r_P R_i R_o(1+\rho_P)(1+\rho_i)(-1+\rho_o)(\varepsilon_{el}(-1+\rho_p)(\xi+j\omega) + \epsilon_p(\xi+j\omega-\rho_p j\omega)) \\
&\quad + r_p(-1+\rho_p)(R_i R_o(1+\rho_i)(-1+\rho_o)(\epsilon_p(\xi+j\omega) - \varepsilon_{el}(\xi+\xi\rho_P+j\omega)) \\
&\quad + r_P(R_o\epsilon_p(1+\rho_P)(-1+\rho_o)(\xi+j\omega+\rho_i j\omega) + R_i(1+\rho_i)(-\varepsilon_{el}(-1+\rho_o)\rho_o j\omega \\
&\quad + \epsilon_p(\xi(1+\rho_P) - (1+\rho_P-\rho_o)(-1+\rho_o)j\omega))))) \\
&+ e^{2(\rho_P+\rho_i)}(-r_P R_i R_o(-1+\rho_P)(-1+\rho_i)(1+\rho_o)(-\varepsilon_{el}(1+\rho_p)(\xi+j\omega) + \epsilon_p(\xi+j\omega+\rho_p j\omega)) \\
&\quad - r_p(1+\rho_p)(R_i R_o(-1+\rho_i)(1+\rho_o)(\varepsilon_{el}(\xi(-1+\rho_P) - j\omega) + \epsilon_p(\xi+j\omega)) \\
&\quad + r_P(R_o\epsilon_p(-1+\rho_P)(1+\rho_o)(\xi+j\omega-\rho_i j\omega) + R_i(-1+\rho_i)(\varepsilon_{el}\rho_o(1+\rho_o)j\omega \\
&\quad + \epsilon_p(\xi(-1+\rho_P) + (-1+\rho_P-\rho_o)(1+\rho_o)j\omega))))) \\
&+ e^{2(\rho_p+\rho_P)}(-r_P R_i R_o(-1+\rho_P)(1+\rho_i)(1+\rho_o)(\varepsilon_{el}(-1+\rho_p)(\xi+j\omega) + \epsilon_p(\xi+j\omega-\rho_p j\omega)) \\
&\quad + r_p(-1+\rho_p)(R_i R_o(1+\rho_i)(1+\rho_o)(\varepsilon_{el}(\xi(-1+\rho_P) - j\omega) + \epsilon_p(\xi+j\omega)) \\
&\quad + r_P(-R_o\epsilon_p(-1+\rho_P)(1+\rho_o)(\xi+j\omega+\rho_i j\omega) + R_i(1+\rho_i)(\varepsilon_{el}\rho_o(1+\rho_o)j\omega \\
&\quad + \epsilon_p(\xi(-1+\rho_P) + (-1+\rho_P-\rho_o)(1+\rho_o)j\omega)))))\Big]
\end{aligned}
$$

3.A.10 Derivation of the analytical model for the admittance change

As a first step we note that again the solution in the particle is simply given by:

$$\tilde{V}(r,\theta) = e_1 r\cos\theta \tag{3.159}$$

The solution in the electrolyte is given again by Eq. 3.93 with $c_2 = d_2 = 0$.
From now on we concentrate on the dependence on r, since the dependence on $\cos\theta$ does not show up in the calculation of the integration constants. This happens because for the continuity of the dielectric displacement we need to calculate the derivative of the

potential with respect to the direction normal to the surface, which is simply $\hat{r}$. Setting explicitly the boundary conditions gives then the following equations:

$$c_3 R + \frac{d_3}{R^2} - \frac{1}{j\omega\tau}\left[c_1\left(\frac{1}{\kappa R} - \frac{1}{\kappa^2 R^2}\right)\exp(\kappa R) + d_1\left(\frac{1}{\kappa R} + \frac{1}{\kappa^2 R^2}\right)\exp(-\kappa R)\right] = \tilde{V}_b \quad (3.160a)$$

$$c_3 R + \frac{d_3}{R^2} + c_1\left(\frac{1}{\kappa R} - \frac{1}{\kappa^2 R^2}\right)\exp(\kappa R) + d_1\left(\frac{1}{\kappa R} + \frac{1}{\kappa^2 R^2}\right)\exp(-\kappa R) = \tilde{V}_b \quad (3.160b)$$

$$c_3 r_p + \frac{d_3}{r_p^2} - \frac{1}{j\omega\tau}\left[c_1\left(\frac{1}{\kappa r_p} - \frac{1}{\kappa^2 r_p^2}\right)\exp(\kappa r_p) + d_1\left(\frac{1}{\kappa r_p} + \frac{1}{\kappa^2 r_p^2}\right)\exp(-\kappa r_p)\right] = e_3 r_p \quad (3.160c)$$

$$c_3 - 2\frac{d_3}{r_p^3} + c_1\left(\frac{1}{r} - \frac{2}{\kappa r^2} + \frac{2}{\kappa^2 r^3}\right)\exp(\kappa r) - d_1\left(\frac{1}{r} + \frac{2}{\kappa r^2} + \frac{2}{\kappa^2 r^3}\right)\exp(-\kappa r) = 0 \quad (3.160d)$$

$$\varepsilon_{el}\left[c_3 - 2\frac{d_3}{r_p^3} - \frac{c_1}{j\omega\tau}\left(\frac{1}{r} - \frac{2}{\kappa r^2} + \frac{2}{\kappa^2 r^3}\right)\exp(\kappa r) + \frac{d_1}{j\omega\tau}\left(\frac{1}{r} + \frac{2}{\kappa r^2} + \frac{2}{\kappa^2 r^3}\right)\exp(-\kappa r)\right] = \epsilon_p e_3 \quad (3.160e)$$

Solving this system of equations gives:

$$\begin{aligned}
c_3 &= R^2\Big((R\kappa-1)\left(\epsilon_p\left(r_p^2\kappa^2 j\omega\tau + 2r_p(\kappa j\omega\tau+\kappa) + 2j\omega\tau + 2\right) + 2\varepsilon_{el}\left(2 + 2\kappa r_p + \kappa^2 r_p^2\right)(1+j\omega\tau)\right)\\
&\quad + e^{2\kappa(r_p-R)}(R\kappa+1)\left(\epsilon_p\left(r_p^2\kappa^2 j\omega\tau - 2r_p(\kappa j\omega\tau+\kappa) + 2j\omega\tau + 2\right) + 2\varepsilon_{el}\left(r_p^2\kappa^2 - 2r_p\kappa + 2\right)(1+j\omega\tau)\right)\Big)\tilde{V}_b/\eta\\
d_3 &= -r_p^3 R^2\Big((R\kappa-1)\left(\epsilon_p\left(r_p^2\kappa^2 j\omega\tau + r_p\kappa(2j\omega\tau-1) + 2j\omega\tau - 1\right) - \varepsilon_{el}\left(2 + 2\kappa r_p + \kappa^2 r_p^2\right)(1+j\omega\tau)\right)\\
&\quad + e^{2\kappa(r_p-R)}(R\kappa+1)\left(\epsilon_p\left(r_p^2\kappa^2 j\omega\tau + r_p(\kappa - 2\kappa j\omega\tau) + 2j\omega\tau - 1\right) - \varepsilon_{el}\left(r_p^2\kappa^2 - 2r_p\kappa + 2\right)(1+j\omega\tau)\right)\Big)\tilde{V}_b/\eta\\
c_1 &= -3j\omega\tau r_p^3 R^2\kappa^2\epsilon_p e^{\kappa(r_p-2b)}(R\kappa+1)\tilde{V}_b/\eta\\
d_1 &= 3j\omega\tau r_p^3 R^2\kappa^2\epsilon_p(R\kappa-1)e^{\kappa r_p}\tilde{V}_b/\eta\\
e_3 &= 3R^2\varepsilon_{el}(1+j\omega\tau)\left(\left(2 + 2\kappa r_p + \kappa^2 r_p^2\right)(R\kappa-1) + e^{2\kappa(r_p-R)}\left(r_p^2\kappa^2 - 2r_p\kappa + 2\right)(R\kappa+1)\right)\tilde{V}_b/\eta\\
\eta &= (R\kappa-1)\Big(\left(r_p^3 + 2R^3\right)\left(r_p\kappa\epsilon_p + \varepsilon_{el}(2 + 2\kappa r_p + \kappa^2 r_p^2) + \epsilon_p\right) - j\omega\tau(2 + 2\kappa r_p + \kappa^2 r_p^2)\\
&\quad \left(r_p^3(\epsilon_p - \varepsilon_{el}) - R^3(\epsilon_p + 2\varepsilon_{el})\right)\Big) + e^{2\kappa(r_p-R)}(R\kappa+1)\Big(\left(r_p^3 + 2R^3\right)\left(\epsilon_p(1 - r_p\kappa) + \varepsilon_{el}(r_p\kappa(r_p\kappa-2)+2)\right)\\
&\quad - j\omega\tau(r_p\kappa(r_p\kappa-2)+2)\left(r_p^3(\epsilon_p - \varepsilon_{el}) - R^3(\epsilon_p + 2\varepsilon_{el})\right)\Big)
\end{aligned}$$

If we assume that $R - r_p \gg |1/\kappa|$, this implies $|e^{\kappa(r_p-R)}| \to 0$. It is then natural to assume also $R \gg |1/\kappa|$. We can then simplify the constants:

$$\begin{aligned}
c_3 &= R^3\kappa\left(\epsilon_p\left(r_p^2\kappa^2 j\omega\tau + 2r_p(\kappa j\omega\tau+\kappa) + 2j\omega\tau + 2\right) + 2\varepsilon_{el}\left(2 + 2\kappa r_p + \kappa^2 r_p^2\right)(1+j\omega\tau)\right)\tilde{V}_b/\eta\\
d_3 &= -r_p^3 R^3\kappa\left(\epsilon_p\left(r_p^2\kappa^2 j\omega\tau + r_p\kappa(2j\omega\tau-1) + 2j\omega\tau - 1\right) - \varepsilon_{el}\left(2 + 2\kappa r_p + \kappa^2 r_p^2\right)(1+j\omega\tau)\right)\tilde{V}_b/\eta\\
c_1 &\simeq 0\\
d_1 &= 3j\omega\tau r_p^3 R^3\kappa^3\epsilon_p e^{\kappa r_p}\tilde{V}_b/\eta\\
e_3 &= 3R^3\kappa\varepsilon_{el}(1+j\omega\tau)\left(2 + 2\kappa r_p + \kappa^2 r_p^2\right)\tilde{V}_b/\eta\\
\eta &= \kappa R\Big(\left(r_p^3 + 2R^3\right)\left(r_p\kappa\epsilon_p + \varepsilon_{el}(2 + 2\kappa r_p + \kappa^2 r_p^2) + \epsilon_p\right) - j\omega\tau(2 + 2\kappa r_p + \kappa^2 r_p^2)\\
&\quad \left(r_p^3(\epsilon_p - \varepsilon_{el}) - R^3(\epsilon_p + 2\varepsilon_{el})\right)\Big)
\end{aligned}$$

If we further assume that, not only $R - r_p \gg |1/\kappa|$, but also $R \gg r_p$, we can further

simplify the constants:

$$c_3 \simeq \frac{1}{R}\frac{\epsilon_p\left(2+2\kappa r_p+j\omega\tau(2+2\kappa r_p+\kappa^2 r_p^2)\right)+2\varepsilon_{el}\left(2+2\kappa r_p+\kappa^2 r_p^2\right)(1+j\omega\tau)}{2(\epsilon_p(1+\kappa r_p)+\varepsilon_{el}(2+2\kappa r_p+\kappa^2 r_p^2))+j\omega\tau(2+2\kappa r_p+\kappa^2 r_p^2)(\epsilon_p+2\varepsilon_{el})}\tilde{V}_b$$
$$= \frac{\tilde{V}_b}{R} \tag{3.161a}$$

$$d_3 \simeq \frac{r_p^3}{R}\frac{\epsilon_p\left(1+\kappa r_p-j\omega\tau(2+2\kappa r_p+\kappa^2 r_p^2)\right)+\varepsilon_{el}\left(2+2\kappa r_p+\kappa^2 r_p^2\right)(1+j\omega\tau)}{2(\epsilon_p(1+\kappa r_p)+\varepsilon_{el}(2+2\kappa r_p+\kappa^2 r_p^2))+j\omega\tau(2+2\kappa r_p+\kappa^2 r_p^2)(\epsilon_p+2\varepsilon_{el})}\tilde{V}_b \tag{3.161b}$$

$$c_1 \simeq 0 \tag{3.161c}$$

$$d_1 \simeq 3j\omega\tau\frac{r_p^3}{R}\kappa^2\frac{\epsilon_p e^{\kappa r_p}}{2(\epsilon_p(1+\kappa r_p)+\varepsilon_{el}(2+2\kappa r_p+\kappa^2 r_p^2))+j\omega\tau(2+2\kappa r_p+\kappa^2 r_p^2)(\epsilon_p+2\varepsilon_{el})}\tilde{V}_b \tag{3.161d}$$

$$e_3 \simeq 3\frac{1}{R}\frac{\varepsilon_{el}(1+j\omega\tau)\left(2+2\kappa r_p+\kappa^2 r_p^2\right)}{2(\epsilon_p(1+\kappa r_p)+\varepsilon_{el}(2+2\kappa r_p+\kappa^2 r_p^2))+j\omega\tau(2+2\kappa r_p+\kappa^2 r_p^2)(\epsilon_p+2\varepsilon_{el})}\tilde{V}_0 \tag{3.161e}$$

Since, as we show in the following, the calculation of ΔS entails subtracting α and $\tilde{V}_b/R$, the approximation $\alpha \simeq \tilde{V}_b/R$ is not accurate enough, and we have to retain at least the second order term in r_p^3. This approximation should work only near $r = R$, where in any case $\gamma^- \simeq 0$ with our assumptions. Using Eq. 3.160a we can then immediately write:

$$c_3 = \frac{\tilde{V}_b}{R} - \frac{d_3}{R^3} \tag{3.162}$$

The solution in absence of the particle can be immediately found letting $r_p \to 0$, leading to the constants:

$$c_3^0 = \frac{\tilde{V}_b}{R}, \qquad c_1^0 = 0, \qquad d_1^0 = 0$$

Using the usual definition, we now compute the complex conjugate of complex power through outer interface of region b:

$$S^* = -\int_0^\pi \tilde{V}^*(R,\theta)\tilde{J}_r(R,\theta)2\pi R^2\sin\theta d\theta \tag{3.163}$$

where the $*$ denotes the conjugate operation and $\tilde{J}_r$ is the total current density in the r direction:

$$\tilde{J}_r = -j\omega\varepsilon\frac{d\tilde{V}}{dr} - 2q^2\mu n_0\frac{d\tilde{\phi}}{dr} \tag{3.164}$$

Note also the minus sign in Eq. 3.163 which is necessary to have an inner orientation for the current on the electrode. Since we have assumed that $R - r_p \gg |1/\kappa|$, we can make the approximation:

$$\left.\frac{d\tilde{V}}{dr}\right|_{r=R} \simeq \left.\frac{d\tilde{\phi}}{dr}\right|_{r=R} \simeq \left(c_3 - 2\frac{d_3}{R^3}\right)\cos\theta \tag{3.165}$$

The complex power in presence of the particle is then:

$$\begin{aligned} S_p^* &= \int_0^\pi \tilde{V}_b^* \cos\theta \left(\sigma_b + j\omega\varepsilon_{el}\right) \left(c_3 - 2\frac{d_3}{R^3}\right) \cos\theta 2\pi R^2 \sin\theta d\theta \\ &= \frac{4\pi}{3} R^2 \left(\sigma_b + j\omega\varepsilon_{el}\right) \tilde{V}_b^* \left(c_3 - 2\frac{d_3}{R^3}\right) \end{aligned} \tag{3.166}$$

where $\sigma_b = 2q^2\mu n_0$ is the electrolyte conductivity.
The complex power in absence of the particle is similarly expressed as:

$$S_0^* = \frac{4\pi}{3} R^2 \left(\sigma_b + j\omega\varepsilon_{el}\right) \tilde{V}_b^* c_3^0 \tag{3.167}$$

The difference in complex conjugate power with and without particle is then:

$$\begin{aligned} \Delta S^* &= S_p^* - S_0^* = -\frac{4\pi}{3} \left(\sigma_b + j\omega\varepsilon_{el}\right) \tilde{V}_b^* 3\frac{d_3}{R} \\ &= -\frac{3}{2} \frac{\frac{1+\kappa r_p}{2+2\kappa r_p+\kappa^2 r_p^2} + \frac{\varepsilon_{el}}{\epsilon_p} + \jmath\omega\tau\left(\frac{\varepsilon_{el}}{\epsilon_p} - 1\right)}{\frac{1+\kappa r_p}{2+2\kappa r_p+\kappa^2 r_p^2} + \frac{\varepsilon_{el}}{\epsilon_p} + \jmath\omega\tau\left(\frac{\varepsilon_{el}}{\epsilon_p} + \frac{1}{2}\right)} \Omega_p \left(\sigma_b + j\omega\varepsilon_{el}\right) \left|\tilde{E}_0\right|^2 \end{aligned} \tag{3.168}$$

where we have used Eqs. 3.161b - 3.162, the value of the unperturbed electric field $\tilde{E}_0 = -\tilde{V}_b/R$ and the fact that the volume of the particle is:

$$\Omega_p = \frac{4\pi}{3} r_p^3 \tag{3.169}$$

This proves Eq. 3.114.

3.A.11 1D semiconductor resistor - integration constants

Resistor in AC small signal regime We have to solve:

$$\begin{aligned} &\tilde{V}_1 + \tilde{V}_3 + \tilde{V}_4 = 0 \\ &\tilde{V}_1 - \frac{1}{\kappa_D^2}\left(\left(\kappa_\omega^2 + 2\kappa_L\left(\kappa_L - \sqrt{\kappa_D^2 + \kappa_L^2 + \kappa_\omega^2}\right)\right)\tilde{V}_3 + \left(\kappa_\omega^2 + 2\kappa_L\left(\kappa_L + \sqrt{\kappa_D^2 + \kappa_L^2 + \kappa_\omega^2}\right)\right)\tilde{V}_4\right) = 0 \\ &\tilde{V}_1 + \tilde{V}_2 L + \tilde{V}_3 \exp\left(\kappa_3 L\right) + \tilde{V}_4 \exp\left(\kappa_4 L\right) = \tilde{V}_0 \\ &\tilde{V}_1 + \tilde{V}_2 L - \frac{1}{\kappa_D^2}\Bigg(\left(\kappa_\omega^2 + 2\kappa_L\left(\kappa_L - \sqrt{\kappa_D^2 + \kappa_L^2 + \kappa_\omega^2}\right)\right)\tilde{V}_3 \exp\left(\kappa_3 L\right) \\ &\qquad + \left(\kappa_\omega^2 + 2\kappa_L\left(\kappa_L + \sqrt{\kappa_D^2 + \kappa_L^2 + \kappa_\omega^2}\right)\right)\tilde{V}_4 \exp\left(\kappa_4 L\right)\Bigg) = \tilde{V}_0 \end{aligned}$$

The solution is simply given by:

$$\tilde{V}_1 = \tilde{V}_3 = \tilde{V}_4 = 0, \qquad \tilde{V}_2 = \frac{\tilde{V}_0}{L}$$

Capacitor in AC small signal regime The solution of the system of boundary conditions gives:

$$\tilde{V}_1 = \kappa_D^2 \Bigg(2\left(-e^{-2\kappa_s L}+1\right)\left(\kappa_D^2\kappa_L + 2\kappa_L^3\right) + \\ + \left(e^{-2\kappa_s L} + 1 - 2e^{(\kappa_L-\kappa_s)L}\right)\kappa_s\kappa_\omega^2 - \left(-e^{-2\kappa_s L}+1\right)\kappa_L\left(2\kappa_s^2-\kappa_\omega^2\right)\Bigg)\frac{\tilde{V}_0}{\eta}$$

$$\tilde{V}_2 = -\Big(4\kappa_L^2\left(\kappa_D^2+\kappa_L^2-\kappa_s^2\right)^2 + 4\kappa_L^2\left(\kappa_D^2+\kappa_L^2-\kappa_s^2\right)\kappa_\omega^2 + (\kappa_L-\kappa_s)(\kappa_L+\kappa_s)\kappa_\omega^4\Big)\times \\ \times\left(-e^{-2\kappa_s L}+1\right)\frac{\tilde{V}_0}{\eta}$$

$$\tilde{V}_3 = -\left(-e^{-2\kappa_s L} + e^{(\kappa_L-\kappa_s)L}\right)\kappa_D^2\left(2\kappa_D^2\kappa_L + (\kappa_L-\kappa_s)\left(2\kappa_L(\kappa_L+\kappa_s)+\kappa_\omega^2\right)\right)\frac{\tilde{V}_0}{\eta}$$

$$\tilde{V}_4 = \left(-1 + e^{(\kappa_L-\kappa_s)L}\right)\kappa_D^2\left(2\kappa_D^2\kappa_L + (\kappa_L+\kappa_s)\left(2\kappa_L(\kappa_L-\kappa_s)+\kappa_\omega^2\right)\right)\frac{\tilde{V}_0}{\eta}$$

$$\eta = -2e^{-(\kappa_L+\kappa_s)L}\kappa_D^2\kappa_s\kappa_\omega^2 - 2e^{(\kappa_L-\kappa_s)L}\kappa_D^2\kappa_s\kappa_\omega^2 + e^{-2\kappa_s L}\Big(4L\kappa_L^2\left(\kappa_D^2+\kappa_L^2-\kappa_s^2\right)^2 \\ + 2\left(\kappa_D^2\kappa_s + 2L\kappa_L^2\left(\kappa_D^2+\kappa_L^2-\kappa_s^2\right)\right)\kappa_\omega^2 + L(\kappa_L-\kappa_s)(\kappa_L+\kappa_s)\kappa_\omega^4\Big) + \\ + \Big(2\kappa_D^2\kappa_s\kappa_\omega^2 - L\Big(4\kappa_L^2\left(\kappa_D^2+\kappa_L^2-\kappa_s^2\right)^2 + 4\kappa_L^2\left(\kappa_D^2+\kappa_L^2-\kappa_s^2\right)\kappa_\omega^2 + (\kappa_L-\kappa_s)(\kappa_L+\kappa_s)\kappa_\omega^4\Big)\Big)$$

3.A.12 Switching capacitance model parameters

The contents of this section have been kindly provided by F. Widdershoven.
The charge transferred from the charge node to the discharge node during one switching period is:

$$Q_p = \left[(C_s+C_p) - C_s p_a \frac{e_1\left(1-e_3\left(e_4+(1-e_4)\,p_b p_a\right)\right) + e_3\left(1-e_1\left(e_2+(1-e_2)\,p_b p_a\right)\right)}{1-e_3\left(e_4+(1-e_4)\,p_b p_a\right)e_1\left(e_2+(1-e_2)\,p_b p_a\right)}\right]V_{DD} \tag{3.170}$$

with the parameters:

$$p_a = \frac{C_s}{C_s+C_E} \qquad p_b = \frac{C_s}{C_s+C_p} \tag{3.171a}$$

$$\tau_a = R_E\left(C_s+C_E\right) \qquad \tau_b = R_E\left(\frac{C_s C_p}{C_s+C_p}+C_E\right) \tag{3.171b}$$

$$e_1 = \exp\left(-\frac{t_1}{\tau_a}\right) \qquad e_2 = \exp\left(-\frac{t_2-t_1}{\tau_b}\right) \tag{3.171c}$$

$$e_3 = \exp\left(-\frac{t_3-t_2}{\tau_a}\right) \qquad e_4 = \exp\left(-\frac{t_4-t_3}{\tau_b}\right) \tag{3.171d}$$

Chapter 4

Numerical methods

This chapter describes the theory behind the development of a simulator based on the Control Volume Finite Element Method (CVFEM) for the DC and AC behaviour of nanoelectrode biosensors in three dimensions (3D).The choice to develop a custom, full 3D numerical solver maturated at the start of this thesis work, after having evaluated 1D and 2D models implemented with finite difference discretization schemes. In fact, it soon became clear that on the one hand only a full 3D code could address the complex geometrical problem of the interaction of an analyte with the biosensors. On the other hand, since the response due to a single biomolecule is typically very small, a very high accuracy is necessary to fully assess the biosensor response. The chosen CVFEM enables a very accurate calculation of the current at the contacts, and therefore of the change in admittance at the electrodes due to the presence of a small biomolecule.
The derivation of the CVFEM discretization of the PB and PNP equations with non linear (exponential) charge terms is an original contribution of this work and poses specific discretization and accuracy problems.
Commercial general purpose FEM solvers (e.g. Comsol [61]) in general do not provide the level of accuracy needed for our calculations. On the contrary simulation tools specifically dedicated to electronic devices (TCAD, e.g. Sentaurus Device [35]) always lack specific models to describe electrolytes and surface electrochemical phenomena specific of biosensors. At the end of this chapter (Sec. 4.6), however, we will show a possible strategy to overcome some of the issues of commercial TCAD.

4.1 Weak formulations

In order to use the Finite Element Methods (FEMs), we have to start from a weak formulation of the equations of interest. In a classical formulation, like the ones derived in Chap. 2, the solution is defined point-wise and all derivatives up to the derivatives in the equation are known to exist. Weak formulations are defined via integrals against certain "test functions". Therefore the solution is only unique up to a set of points of Lebesgue measure zero (i.e., not an interval).
In practice this procedure is performed starting from a residual formulation of the equations [62], so that we seek an unknown function $\mathbf{u}$ (for instance V or ϕ_m) such that it satisfies a set of differential equations $A_i(\mathbf{u})$ in the form:

$$\mathcal{A}(\mathbf{u}) = \begin{bmatrix} A_1(\mathbf{u}) \\ A_2(\mathbf{u}) \\ \vdots \end{bmatrix} = \mathbf{0} \tag{4.1}$$

in the domain Ω. The function $\mathbf{u}$ may be a scalar quantity or may represent a vector of several variables. Similarly, the differential equation $\mathcal{A}(\mathbf{u})$ may be a single one or a set of simultaneous possibly non-linear equations $A_i(\mathbf{u})$.

As the set of differential equations 4.1 has to be zero at each point of the domain Ω, it follows that we can use a weak formulation and write:

$$\int_\Omega \mathbf{v}^T \mathcal{A}(\mathbf{u}) d\Omega = 0\,, \tag{4.2}$$

where $\mathbf{v}^T = \begin{bmatrix} v_1 & v_2 & \dots \end{bmatrix}$ is a set of arbitrary test functions and the length of $\mathbf{v}$ is equal to the number of equations (or components of $\mathbf{u}$). We recall that the weak formulation means that the equation (Eq. 4.2) must hold for all test functions $\mathbf{v}$. We will not address in this thesis the question from which function space the test functions should be chosen, for which the reader can refer to specialized texts.
This formalism will be always the starting point for our analysis of FEMs. The different methods that lie in the FEM family differ on the choice of the functions $\mathbf{v}$. The specific ultimate goal is to develop an accurate, current conservative and efficient FEM on arbitrary tetrahedral grids.

4.1.1 DC models

Poisson equation The residual statement of Poisson equation (Eq. 2.1) is:

$$\mathcal{A}(V_0) = \nabla \cdot (\varepsilon \nabla V_0) + \rho_0 \tag{4.3}$$

where V_0 is the DC potential and ρ_0 the volume charge density. Using an arbitrary smooth scalar test function v we can then cast it into the weak formulation:

$$\int_\Omega v \mathcal{A}(V_0) d\Omega = \int_\Omega v \left(\nabla \cdot (\varepsilon \nabla V_0) + \rho_0\right) d\Omega = 0\,.$$

Integrating by parts we obtain:

$$\int_\Omega v \nabla \cdot \varepsilon \nabla V_0 d\Omega = -\int_\Omega \nabla v \cdot \varepsilon \nabla V_0 d\Omega + \oint_\Gamma v \varepsilon \nabla V_0 \cdot \hat{n}\, d\Gamma\,.$$

The weak formulation then is:

$$-\int_\Omega \nabla v \cdot \varepsilon \nabla V_0 d\Omega + \int_{\Gamma_D} v \varepsilon \nabla V_0 \cdot \hat{n}\, d\Gamma + \int_\Omega v \rho_0 d\Omega = 0 \tag{4.4}$$

for all test functions v, where we have also used the boundary conditions (Eq. 2.2).

Current equations Taking into account the boundary conditions, the DC weak form of the first formulation (Eq. 2.21) is:

$$\begin{aligned} -\int_\Omega Z_m q \mu_m \nabla v \cdot \left(n_i \exp\left(\frac{Z_m q}{k_B T}\left(\phi_{0m} - V_0\right)\right) \nabla \phi_{0m} \right) d\Omega \\ + \int_{\Gamma_D^\phi} v Z_m q \mu_m n_i \exp\left(\frac{Z_m q}{k_B T}\left(\phi_{0m} - V_0\right)\right) \nabla \phi_{0m} \cdot \hat{n}\, d\Gamma = 0 \end{aligned} \tag{4.5}$$

and for the second formulation (Eq. 2.22):

$$-\int_{\Omega}\varepsilon\nabla v\cdot\nabla\phi_m d\Omega+\int_{\Omega}v\varepsilon\frac{Z_m q}{k_B T}\nabla\phi_m\cdot\nabla\left(\phi_m-V\right)d\Omega+\int_{\Gamma_D^{\phi}}v\varepsilon\nabla\phi_m\cdot\hat{n}\,d\Gamma=0\,. \tag{4.6}$$

for all test functions v. In the following we will derive the discretized form for both formulations of the current equations.

4.1.2 AC models

Poisson equation Following the same methodology, we derive the weak formulation of Eq. 2.30:

$$-\int_{\Omega}\nabla v\cdot\varepsilon\nabla\tilde{V}d\Omega+\int_{\Gamma_D}v\varepsilon\nabla\tilde{V}\cdot\hat{n}\,d\Gamma+\int_{\Omega}v\sum_{m=1}^{N_{sp}}\frac{Z_m^2q^2}{k_BT}n_{0m}\left(\tilde{\phi}_m-\tilde{V}\right)d\Omega=0\,. \tag{4.7}$$

for all test functions v.

Current equations The weak formulation for the current equations (Eq. 2.34) is:

$$\begin{aligned}&-\int_{\Omega}Z_m q\mu_m\nabla v\cdot\left(n_{0m}\left(\frac{Z_m q}{k_BT}\left(\tilde{\phi}_m-\tilde{V}\right)\nabla\phi_{0m}+\nabla\tilde{\phi}_m\right)\right)d\Omega\\&+\int_{\Gamma_D^{\phi}}vZ_m q\mu_m\left(n_{0m}\left(\frac{Z_m q}{k_BT}\left(\tilde{\phi}_m-\tilde{V}\right)\nabla\phi_{0m}+\nabla\tilde{\phi}_m\right)\right)\cdot\hat{n}\,d\Gamma\\&-\int_{\Omega}vj\omega n_{0m}\frac{Z_m q}{k_BT}\left(\tilde{\phi}_m-\tilde{V}\right)d\Omega=0\,.\end{aligned} \tag{4.8}$$

for all test functions v.

4.2 CVFEM discretization of model equations

We look for the discretized formulation of the models equations 4.4-4.8 in the framework of the well-known finite element methods [62]. In particular, we use the common Galerkin Finite Element Method (GFEM [62]) as a reference to assess advantages and limitations of the Control Volume Finite Element Method (CVFEM [63]). In fact CVFEM has the potential to efficiently achieve high accuracy and current conservation. These methods differ only for the choice of the basis function, so that the general discretization procedure remains the same.

The first step in the discretization is to divide the domain Ω in a discrete set of nodes, edges, faces and volumes that, in our case, will always be elements of a 3D tetrahedral mesh. The second step is then to approximate the components of the unknown functions vector $\mathbf{u}$ (hereafter denoted u) by calculating their value u^j on the nodes and interpolating them in the mesh volumes using interpolation functions N^j [62]:

$$u\simeq\sum_{j=1}^{N_{nod}}N^j u^j\,. \tag{4.9}$$

The N^j are the basis functions for the finite-dimensional function space where the solution is calculated. In this work we will always use piece-wise linear interpolation functions, so that ∇N^j is constant inside each mesh volume, and we consider only the neighbour nodes for the interpolation, i.e. $N^j = 0$ in the mesh volumes that are not connected to node n^j. These particular functions are often called hat functions.
The weak formulations, due to their integral nature, allow an approximation to be made if, in place of any test function $\mathbf{v}$, we put a finite set of approximate functions [62]:

$$\mathbf{v} \simeq \sum_{j=1}^{N_{nod}} \mathbf{w}^j \delta\hat{\mathbf{u}}^j \tag{4.10}$$

where N_{nod} is the number of mesh nodes, $\mathbf{w}^j$ the basis functions associated to node j and the $\delta\hat{\mathbf{u}}^j$ are arbitrary (constant) parameters. Using the approximation 4.10, we can then transform the weak formulation (Eq. 4.2) to:

$$(\delta\hat{\mathbf{u}}^j)^T \int_\Omega \mathbf{w}^{j\mathrm{T}} \mathcal{A}(\mathbf{u}) d\Omega = \mathbf{0} = \begin{bmatrix} 0 \\ 0 \\ \dots \end{bmatrix}; \quad j = 1, ..., N_{nod}$$

for all $\delta\hat{\mathbf{u}}^j$, and since they are arbitrary and using Eq. 4.9 we have a set of equations which is sufficient to determine the parameters u^i:

$$\int_\Omega \mathbf{w}^{j\mathrm{T}} \mathcal{A}(\mathbf{u}) d\Omega = \mathbf{0}; \quad j = 1, ..., N_{nod}\,.$$

We also use the same basis functions for each variable in vector $\mathbf{u}$, i.e. $\mathbf{w}^j = w^j$.

The last step is the choice of basis functions w^j. In GFEM the choice is $w^j = N^j$ [62], whereas in CVFEM the choice is $w^j = \gamma^j$, where [63]:

$$\gamma^j = \begin{cases} 1 & \text{in } \Omega_c^j \in \Omega \\ 0 & \text{in the complement} \end{cases}$$

where Ω_c^j is the control volume around node n^j and $\Gamma^j = \partial\Omega_c^j$ its border. In our context the control volume borders are defined by connecting the baricenters of volumes, faces and edges as shown in Fig. 4.1. The basis function γ^j has the following properties [63]:

$$\int_\Omega \nabla\gamma^j \cdot \boldsymbol{\sigma} d\Omega = -\int_{\Gamma^j} \boldsymbol{\sigma} \cdot \hat{n}\, d\Gamma$$

$$\int_\Omega \nabla \cdot \left(\gamma^j \boldsymbol{\sigma}\right) d\Omega = 0$$

where $\boldsymbol{\sigma}$ is any smooth vector field.

In the following sections we explicitly derive the models' discretization for the CVFEM, since this method has never been applied before in our context. Moreover, we report the final results for GFEM and carry out a detailed comparison between the two methods. For convenience, Fig. 4.1 reports some useful definitions that are used in the derivations. Note that, as usual in Finite Element Methods, we will always choose $u^j = u^D$ (where u^D is the Dirichlet boundary condition for the unknown function u) for the nodes $n^j \in \Gamma_D$; consequently, neither we need to write the discretized equations for these nodes, nor we need to calculate the integrals on Γ_D. As we will see when discussing global conservation (Sec. 4.2.1.3), however, these integrals are necessary for a post processing computation of the current at the contacts.

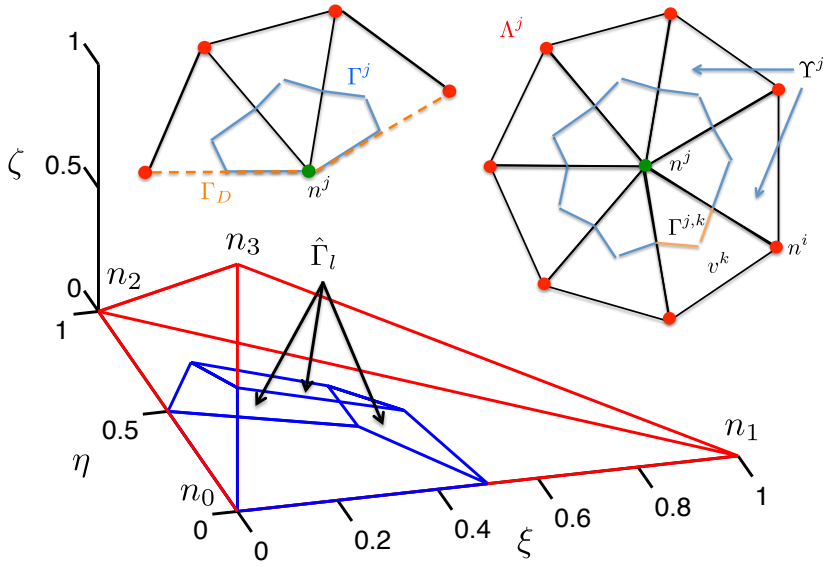

Fig 4.1: Unitary reference tetrahedron (red) and control volume $\hat{\Omega}_c$ around node n_0 (blue). In addition, 2D cuts (for clarity) with node n^j and its neighbour volumes and nodes are shown. The node is either on Dirichlet boundary (left) or in the bulk (right). The control volume is highlighted and the surfaces Γ_D, Γ^j and $\Gamma^{j,k}$ are marked.

4.2.1 CVFEM discretization of the DC equations

4.2.1.1 Poisson equation

The first step is to use the CVFEM basis functions in Eq. 4.4, which yields:

$$\int_{\Gamma^j} \varepsilon \nabla V_0 \cdot \hat{n}\, d\Gamma + \int_{\Omega_c^j} \rho_{0f} d\Omega + \sum_{m=1}^{N_{sp}} Z_m q \int_{\Omega_c^j} n_{0m} d\Omega = 0 \tag{4.11}$$

where, as already discussed, we discretize the equations only on the nodes $n^i \notin \Gamma_D$, so that the integrals on Γ_D can be dropped. To discretize Eq. 4.4 we then first use the approximation 4.9:

$$\sum_{i=1}^{N_{nod}} V_0^i \int_{\Gamma^j} \varepsilon \nabla N^i \cdot \hat{n}\, d\Gamma + \int_{\Omega_c^j} \rho_{0f} d\Omega + \sum_{m=1}^{N_{sp}} Z_m q \int_{\Omega_c^j} n_{0m} d\Omega = 0$$

Using the linear interpolation functions N^j defined above we can write:

$$\sum_{i=1}^{N_{nod}} V_0^i \int_{\Gamma^j} \varepsilon \nabla N^i \cdot \hat{n}\, d\Gamma = \sum_{i \in \Lambda_I^j} V_0^i \sum_{k \in \Upsilon^{i,j}} \int_{\Gamma^{j,k}} \varepsilon \nabla N^{i,k} \cdot \hat{n}\, d\Gamma + V_0^j \sum_{i \in \Lambda_I^j} \sum_{k \in \Upsilon^j} \int_{\Gamma^{j,k}} \varepsilon \nabla N^{j,k} \cdot \hat{n}\, d\Gamma$$

where Λ_I^j are the nodes connected to node n^j, Υ^j the tetrahedral volumes connected to node n^j and $\Upsilon^{i,j}$ the volumes connected to both node n^j and n^i. $\Gamma^{j,k}$, $N^{j,k}$ and $N^{i,k}$ are the portions of Γ^j, N^j and N^i that lie inside the primal volume v^k, respectively.
We can then write the discretized Poisson equation as:

$$\sum_{i \in \Lambda_I^j} a^{i,j} V_0^i + b^j V_0^j + \int_{\Omega_c^j} \rho_{0f} d\Omega + \sum_{m=1}^{N_{ions}} Z_m q \int_{\Omega_c^j} n_{0m} d\Omega = 0 \tag{4.12}$$

where ρ_{0f} is the constant volume charge density and:

$$a^{i,j} = \sum_{k \in \Upsilon^{i,j}} \int_{\Gamma^{j,k}} \varepsilon \nabla N^{i,k} \cdot \hat{n} \, d\Gamma \tag{4.13a}$$

$$b^j = \sum_{i \in \Lambda^j} \sum_{k \in \Upsilon^{i,j}} \int_{\Gamma^{j,k}} \varepsilon \nabla N^{j,k} \cdot \hat{n} \, d\Gamma = - \sum_{i \in \Lambda_I^j} a^{i,j} \tag{4.13b}$$

where we used the property that if the basis functions are linear, then:

$$\nabla N^{j,k} \cdot \boldsymbol{\sigma} = - \sum_{i \in \Lambda^{j,k}} \nabla N^{i,k} \cdot \boldsymbol{\sigma}$$

for any $\boldsymbol{\sigma}$ smooth vector field, where $\Lambda_I^{j,k}$ are the nodes connected to node n^j and to volume v^k. We can write more explicitly the non-linear term:

$$Q_{0el}^j = \int_{\Omega_c^j} \rho_{0el} d\Omega = \sum_{m=1}^{N_{ions}} Z_m q n_m^\infty \int_{\Omega_c^j} \exp\left(\frac{Z_m q}{k_B T} \sum_{i \in \Lambda^j} N^i \left(\phi_{0m}^i - V_0^i \right) \right) d\Omega \tag{4.14}$$

where Λ^j are the nodes connected to node n^j, with n^j included.
A surface charge density (σ_0) can be easily specified on the mesh surfaces by adding to the equation for node n^j a term:

$$Q_S^j = \int_{\Gamma_P^j} \sigma_0 d\Gamma$$

where Γ_P^j is the part of the primal surface that is included in the control volume Ω_c^j. In this expression σ_0 can be an arbitrary function of the potential V_0 as for instance the site-binding charge σ_{sb} (Eqs. 2.11-2.12).

The non-linear system made by Eq. 4.12 is then solved using a standard Newton-Raphson method, as we will see in Sec. 4.4. Therefore, for the solution of the system, we need also to compute the Jacobian; its non-linear part is derived in Sec. 4.A.1. More details on the solution algorithm are reported at the beginning of Section 4.4. Note that the non-linear system could be solved also using an iterative solver, without the need of computing the Jacobian, but we would expect the convergence to be significantly slower.

As we will show in Sec. 4.A.2, in our specific case where: 1) the control volume is defined using the faces and volumes centroids and 2) the basis functions are linear, then the a and b coefficients in Eq. 4.13 are exactly the same as the ones obtained for the GFEM. This is consistent with the findings of [64] for the box method. This means that an expression alternative to Eq. 4.13 is:

$$a^{i,j} = - \sum_{k \in \Upsilon^{i,j}} \int_{v^k} \nabla N^{j,k} \cdot \varepsilon \nabla N^{i,k} d\Omega = - \sum_{k \in \Upsilon^{i,j}} \varepsilon^k v^k \nabla N^{j,k} \cdot \nabla N^{i,k}$$

$$b^j = - \sum_{i \in \Lambda^j} \sum_{k \in \Upsilon^{i,j}} \int_{v^k} \nabla N^{j,k} \cdot \varepsilon \nabla N^{j,k} d\Omega = - \sum_{k \in \Upsilon^{i,j}} \varepsilon^k v^k \nabla N^{j,k} \cdot \nabla N^{j,k} = - \sum_{i \in \Lambda^{j,k}} a^{i,j}$$

In this way the GFEM formulation reads:

$$\sum_{i \in \Lambda^j} a^{i,j} V_0^i + b^j V_0^j + \int_{\Omega^j} N^j \rho_{0f} d\Omega + \sum_{m=1}^{N_{ions}} Z_m q \int_{\Omega^j} N^j n_{0m} d\Omega = 0 \tag{4.15}$$

where $\Omega^j = \cup_{k \in \Upsilon^j} v^k$ is the union of all tetrahedra connected to node n^j.

4.2.1.2 Current equations

First formulation The weak formulation with the CVFEM shape functions is:

$$Z_m q \mu_m \int_\Omega \gamma^j \nabla \cdot \left(n_m^\infty \exp\left(\frac{Z_m q}{k_B T} \left(\phi_{0m} - V_0 \right) \right) \nabla \phi_{0m} \right) d\Omega = 0 \,.$$

Integrating again by parts and using the properties of the shape functions we can directly write:

$$Z_m q \mu_m n_m^\infty \int_{\Gamma^j} \exp\left(\frac{Z_m q}{k_B T} \left(\phi_{0m} - V_0 \right) \right) \nabla \phi_{0m} \cdot \hat{n} \, d\Gamma = 0 \,.$$

Using also the approximations 4.9 we obtain:

$$Z_m q \mu_m n_m^\infty \sum_{i \in \Lambda^j} \phi_{0m}^i \sum_{k \in \Upsilon^{i,j}} \int_{\Gamma^{j,k}} \exp\left(\frac{Z_m q}{k_B T} \sum_{i \in \Lambda^{j,k}} N^{i,k} \left(\phi_{0m}^i - V_0^i \right) \right) \nabla N^{i,k} \cdot \hat{n} \, d\Gamma = 0$$

where Λ^j are the nodes connected to n^j (including n^j itself) while $\Lambda^{j,k}$ are those nodes in the Λ^j set that are also bound to the tetrahedron k.
In order to have the same units of measurement as for the Poisson equation, we multiply the equation by $(\varepsilon / Z_m q \mu_m n_m^\infty)$, so that we obtain:

$$\sum_{i \in \Lambda^j} \phi_{0m}^i \sum_{k \in \Upsilon^{i,j}} \varepsilon^k \int_{\Gamma^{j,k}} \exp\left(\frac{Z_m q}{k_B T} \sum_{i \in \Lambda^{j,k}} N^{i,k} \left(\phi_{0m}^i - V_0^i \right) \right) \nabla N^{i,k} \cdot \hat{n} \, d\Gamma = 0 \,. \tag{4.16}$$

Second formulation In this case the weak formulation with the CVFEM shape functions reads:

$$\int_\Omega \gamma^j \varepsilon \left(\frac{Z_m q}{k_B T} \nabla \phi_{0m} \cdot \nabla \left(\phi_{0m} - V_0 \right) + \nabla^2 \phi_{0m} \right) d\Omega = 0 \,.$$

Integrating again by parts and using the properties of the shape functions we can directly write:

$$\frac{Z_m q}{k_B T} \int_{\Omega_c^j} \varepsilon \nabla \phi_{0m} \cdot \nabla \left(\phi_{0m} - V_0 \right) d\Omega + \int_{\Gamma^j} \varepsilon \nabla \phi_{0m} \cdot \hat{n} \, d\Gamma = 0 \,.$$

Using also the approximations 4.9 we obtain:

$$\frac{Z_m q}{k_B T} \int_{\Omega_c^j} \varepsilon \nabla \left(\sum_{i=1}^{N_{nod}} N^i \phi_{0m}^i \right) \cdot \nabla \sum_{i=1}^{N_{nod}} N^i \left(\phi_{0m}^i - V_0^i \right) d\Omega + \int_{\Gamma^j} \varepsilon \nabla \left(\sum_{i=1}^{N_{nod}} N^i \phi_{0m}^i \right) \cdot \hat{n} \, d\Gamma = 0$$

and noting that $\nabla N^{i,k}$ is a constant inside each tetrahedron:

$$\begin{aligned} \frac{Z_m q}{k_B T} \sum_{k \in \Upsilon^j} \Omega_c^{j,k} \mathcal{V}_k \left(\sum_{i \in \Lambda^{j,k}} \phi_{0m}^i \nabla N^{i,k} \right) \cdot \left(\sum_{i \in \Lambda^{j,k}} \left(\phi_{0m}^i - V_0^i \right) \nabla N^{i,k} \right) \\ + \sum_{i \in \Lambda^j} \phi_{0m}^i \sum_{k \in \Upsilon^{i,j}} \mathcal{V}_k \Gamma^{j,k} \cdot \nabla N^{i,k} = 0 \end{aligned}$$

where $\mathcal{V}_k$ is the volume of tetrahedron v^k. We can write this equation in a more compact form by denoting:

$$a_S^{i,j} = \sum_{k \in \Upsilon^{i,j}} \varepsilon^k \Gamma^{j,k} \cdot \nabla N^{i,k}$$
$$b_S^j = \sum_{i \in \Lambda^j} \sum_{k \in \Upsilon^{i,j}} \varepsilon^k \Gamma^{j,k} \cdot \nabla N^{j,k} = -\sum_{i \in \Lambda^j} a_S^{i,j} .$$

The coefficients $a_S^{i,j}$ and b_S^j are exactly the same ones of the linear part of Poisson equation (Eq. 4.13), but only if the entire system is composed of semiconductor. In fact, since the current equations Eq. 2.22 are valid only in the semiconductor, the sums on the volumes in these coefficients range only on the volumes that lie in this material.

4.2.1.3 Global conservation

In typical nanoelectronic sensors, the output signal consists in the value of electrical quantities at the terminals (e.g., dielectric displacement flux, current, etc). For few particles' sensors the signal is given by a tiny change of these quantitites: current and flux conservation are thus key ingredients for an accurate sensor simulation. If global conservation is not verified, the calculation of these boundary quantities is not consistent and can be affected by excessively large errors for single molecule analysis purposes.

Since in CVFEM the fluxes are calculated on the control volume surfaces, the method has the so called telescoping property [65], which ensures that the fluxes are conserved when passing from one control volume to the adjacent ones. CVFEM is thus locally conservative with respect to these fluxes. To ensure the global conservation property, however, fluxes on the Dirichlet control volumes (DCV) have to be calculated with special care [63]. As usual in FEMs, we always assume that two adjacent but distinct electrodes are separated by at least two points. Following [63], we show below that global conservation is retained if the boundary quantities are carefully calculated by consistently post-processing the simulation data. In fact, in the DCVs the control volume equation is:

$$\int_{\Gamma_{int}^j} \varepsilon \nabla V_0 \cdot \hat{n}\, d\Gamma - \int_{\Gamma_D \cap \Gamma^j} D_\perp d\Gamma + \int_{\Omega_c^j} \rho_{0f} d\Omega + \int_{\Omega_c^j} \rho_{0el} d\Omega = 0$$

where the V_0^i are known because they come from the solution of the system and $D_\perp = -\varepsilon \nabla V_0 \cdot \hat{n}$ are the normal components of the dielectric displacements on the Dirichlet boundary. We divide the surface integral in the part on the Dirichlet boundary Γ_D and the part of the DCV surface outside Γ_D, that is $\Gamma_{int}^j = \Gamma^j - (\Gamma_D \cap \Gamma^j)$ (see the left sketch in Fig. 4.1). We represent $D_\perp$ in the same basis as the potential, $D_\perp = \sum_i N^i D_\perp^i$. This equation has to be discretized consistently with Eq. 4.12 to find a system of equations with $D_\perp^i$ as unknowns:

$$\sum_{i \in \Lambda_I^j} a^{i,j} V_0^i + b^j V_0^j - \sum_{i \in \Lambda_D^j} D_\perp^i e^{i,j} - D_\perp^j f^j + \int_{\Omega_c^j} \rho_{0f} d\Omega + \int_{\Omega_c^j} \rho_{0el} d\Omega = 0 \tag{4.17}$$

where $a^{i,j}$ and b^j are given by Eq. 4.13 and:

$$e^{i,j} = \int_{\Gamma_D \cap \Gamma^j \cap \Gamma^i} N^i d\Gamma, \qquad f^j = \int_{\Gamma_D \cap \Gamma^j} N^j d\Gamma \tag{4.18}$$

This procedure yields the dielectric displacement's fluxes on the Dirichlet boundary, i.e., the electrodes. According to Gauss's law, the flux can be used to calculate for instance the DC differential capacitance of the sensor.

Following similar steps we can write the current equations on the DCVs, making use of Eq. 2.20. In this case it is more convenient to use the first formulation, that is:

$$-\frac{1}{Z_m q}\int\limits_{\Gamma_D\cap\Gamma^j} J_{\perp,m}\,d\Gamma + Z_m q\mu_m n_m^\infty \int\limits_{\Gamma^j_{int}} \exp\left(\frac{Z_m q}{k_B T}\left(\phi_{0m}-V_0\right)\right)\nabla\phi_{0m}\cdot\hat{n}\,d\Gamma = 0$$

where we denote with $J_{\perp,m} = \vec{J}_m\cdot\hat{n}$ the normal component of the ionic or electronic current due to the species m flowing through the Dirichlet boundary. As we have done for the dielectric displacement, we represent $J_{\perp,m}$ in the same basis as the potential, $J_{\perp,m} = \sum_i N^i J^i_{\perp,m}$. This equation has to be discretized in the same way as for the dielectric displacement to find a system of equation with $J^i_{\perp,m}$ as unknowns:

$$\begin{aligned} Z_m q\mu_m n_m^\infty \sum_{k\in\Upsilon^j}\sum_{i\in\left(j,\Lambda^{j,k}\right)} \phi^i_{0m}\int\limits_{\Gamma^{j,k}_{int}} \exp\left(\frac{Z_m q}{k_B T}\sum_{i\in\left(j,\Lambda^{j,k}\right)} N^{i,k}\left(\phi^i_{0m}-V^i_0\right)\right)\nabla N^{i,k}\cdot\hat{n}\,d\Gamma \\ -\frac{1}{Z_m q}\left(\sum_{i\in\Lambda^j_D} J^i_{\perp,m}e^{i,j} + J^j_{\perp,m}f^j\right) = 0 \end{aligned} \tag{4.19}$$

where $e^{i,j}$ and f^j are exactly the same of Eq. 4.18.

For the purpose of comparing CVFEM and GFEM we observe that, in order for GFEM to be globally conservative, the same approach described here should be used, by substituting the appropriate GFEM expressions of the coefficients in Eq. 4.17.

4.2.2 CVFEM discretization of the AC equations

4.2.2.1 Poisson and current equations

Following the same CVFEM procedure described above, we can discretize the Poisson (Eq. 4.7) and the current (Eq. 4.8) equations. We thus obtain:

$$\text{Poisson:}\quad \sum_{i=1}^{N_{nod}}\tilde{V}^i\int\limits_{\Gamma^j}\varepsilon\nabla N^i\cdot\hat{n}\,d\Gamma + \sum_{m=1}^{N_{ions}}\frac{Z_m^2q^2}{k_BT}\sum_{i=1}^{N_{nod}}\left(\tilde{\phi}^i_m-\tilde{V}^i\right)\int\limits_{\Omega^j_c}N^i n_{0m}d\Omega = 0$$

$$\begin{aligned}\text{Current:}\quad & -jZ_m^2q^2\frac{\mu_m}{\omega}\left[\sum_{i=1}^{N_{nod}}\tilde{\phi}^i_m\int\limits_{\Gamma^j}n_{0m}\nabla N^i\cdot\hat{n}\,d\Gamma + \frac{Z_mq}{k_BT}\sum_{i=1}^{N_{nod}}\left(\tilde{\phi}^i_m-\tilde{V}^i\right)\int\limits_{\Gamma^j}n_{0m}N^i\sum_{l=1}^{N_{nod}}\phi^l_{0m}\nabla N^l\cdot\hat{n}\,d\Gamma\right] \\ & -\frac{Z_m^2q^2}{k_BT}\sum_{i=1}^{N_{nod}}\left(\tilde{\phi}^i_m-\tilde{V}^i\right)\int\limits_{\Omega^j_c}N^i n_{0m}d\Omega = 0\end{aligned}$$

where we also have multiplied the current equations by $Z_mq/j\omega$ in order to have the coefficients with the same unit of measurement (Farads) as in Poisson equation. Following the same discretization procedure described in Sec. 4.2.1.1, we can write Poisson equation as:

$$\sum_{i\in\Lambda^j}c^{i,j}\tilde{V}^i + d^j\tilde{V}^j + \sum_{m=1}^{N_{ions}}\left(\sum_{i\in\Lambda^j}s^{i,j}_m\tilde{\phi}^i_m + t^j_m\tilde{\phi}^j_m\right) = 0 \tag{4.20}$$

and the current equations as:

$$\sum_{i\in\Lambda^j}\left(s_m^{i,j}+g_m^{i,j}\right)\tilde{V}^i+\left(t_m^j+h_m^j\right)\tilde{V}^j+\sum_{i\in\Lambda^j}o_m^{i,j}\tilde{\phi}_m^i+p_m^j\tilde{\phi}_m^j=0 \tag{4.21}$$

The coefficients are:

$$s_m^{i,j}=\frac{Z_m^2q^2}{k_BT}\sum_{k\in\Upsilon^{i,j}}\int_{\Omega_c^{j,k}}N^{i,k}n_{0m}d\Omega \tag{4.22a}$$

$$t_m^j=\frac{Z_m^2q^2}{k_BT}\sum_{i\in\Lambda^j}\sum_{k\in\Upsilon^{i,j}}\int_{\Omega_c^{j,k}}N^{j,k}n_{0m}d\Omega \tag{4.22b}$$

$$c^{i,j}=a^{i,j}-\sum_{m=1}^{N_{ions}}s_m^{i,j} \tag{4.22c}$$

$$d^j=b^j-\sum_{m=1}^{N_{ions}}t_m^j \tag{4.22d}$$

$$g_m^{i,j}=j\frac{Z_m^3q^3}{k_BT}\frac{\mu_m}{\omega}\sum_{k\in\Upsilon^{i,j}}\sum_{l\in\Lambda^{j,k}}\phi_{0m}^l\int_{\Gamma^{j,k}}N^{i,k}n_{0m}\nabla N^{l,k}\cdot\hat{n}\,d\Gamma \tag{4.22e}$$

$$h_m^j=j\frac{Z_m^3q^3}{k_BT}\frac{\mu_m}{\omega}\sum_{i\in\Lambda^j}\sum_{k\in\Upsilon^{i,j}}\sum_{l\in\Lambda^{j,k}}\phi_{0m}^l\int_{\Gamma^{j,k}}N^{j,k}n_{0m}\nabla N^{l,k}\cdot\hat{n}\,d\Gamma \tag{4.22f}$$

$$o_m^{i,j}=-jZ_m^2q^2\frac{\mu_m}{\omega}\sum_{k\in\Upsilon^{i,j}}\int_{\Gamma^{j,k}}n_{0m}\nabla N^{i,k}\cdot\hat{n}\,d\Gamma-\left(s_m^{i,j}+g_m^{i,j}\right) \tag{4.22g}$$

$$p_m^j=-jZ_m^2q^2\frac{\mu_m}{\omega}\sum_{i\in\Lambda^j}\sum_{k\in\Upsilon^{i,j}}\int_{\Gamma^{j,k}}n_{0m}\nabla N^{j,k}\cdot\hat{n}\,d\Gamma-\left(t_m^j+h_m^j\right) \tag{4.22h}$$

Note that in the electrolyte $g_m^{i,j}=h_m^j=0$, since $\nabla\phi_{0m}=0$.

Site-binding charge The implementation of the site-binding model Eq. 2.33 gives additional contributions to Poisson equation:

$$\tilde{Q}_{sb}=q\int_{\Gamma_P^{j,k}}N_S\alpha_{sb}\frac{\tilde{\phi}_H-\tilde{V}}{V_{th}}d\Gamma$$

where $\Gamma_P^{j,k}$ is the part of the primal surface (i.e., the surfaces of the tetrahedra) that is included in control volume Ω_c^j and tetrahedron v^k:

$$\alpha_{sb}=\frac{K_b'(k_b^bn_{0H}(k_a^bn_{0H}+j\omega)+K_a'k_a^b(K_b'k_b^b+4k_b^bn_{0H}+j\omega))}{(K_a'K_b'+n_{0H}(K_b'+n_{0H}))(K_a'k_a^b(K_b'k_b^b+j\omega)+(k_a^bn_{0H}+j\omega)(k_b^b(K_b'+n_{0H})+j\omega))}$$

The additional coefficients are then:

$$s_{sb}^{i,j}=\frac{q}{V_{th}}\sum_{k\in\Upsilon^{i,j}}\int_{\Gamma_P^{j,k}}N^{i,k}N_S\alpha_{sb}d\Gamma \tag{4.23a}$$

$$t_{sb}^j=\frac{q}{V_{th}}\sum_{i\in\Lambda^j}\sum_{k\in\Upsilon^{i,j}}\int_{\Gamma_P^{j,k}}N^{j,k}N_S\alpha_{sb}d\Gamma \tag{4.23b}$$

So that the voltage coefficients for the Poisson equation are not the ones in Eq. 4.22 any more, but change to:

$$c^{i,j} = a^{i,j} - \sum_{m=1}^{N_{ions}} s_m^{i,j} - s_{sb}^{i,j} \tag{4.24a}$$

$$d^{j} = b^{j} - \sum_{m=1}^{N_{ions}} t_m^{j} - t_{sb}^{j} \tag{4.24b}$$

. The quasi-potential coefficients for the hydrogen become:

$$sp_H^{i,j} = s_H^{i,j} + s_{sb}^{i,j} \tag{4.25a}$$

$$tp_H^{j} = t_H^{j} + t_{sb}^{j} \tag{4.25b}$$

where we used the subscript H instead of the generic ion index m to indicate the hydrogen coefficients.

The corresponding AC coefficients using the GFEM are reported in the chapter appendix 4.A.3.

4.2.2.2 Global conservation

As in the DC case (Eq. 4.17), the electric displacement on the boundary has to be computed with care in order to ensure global conservation hence, a consistent calculation of the terminal currents. For the sake of finding generally applicable results, we avoid the assumption that the electrodes are ideally polarizable, so that the contact current density is:

$$\vec{\tilde{J}} = j\omega\vec{\tilde{D}} + \sum_m \vec{\tilde{J}}_m$$

Consistently with Sec. 4.2.1.3, we denote $\tilde{D}_\perp^j$ the normal component of the nodal dielectric displacement at node j, and $\tilde{J}_{\perp,m}^j$ the normal component of the nodal ionic current density of carrier species m at node j. Since we recall (Eq. 2.37b) that:

$$\vec{\tilde{J}}_m = -Z_m^2 q^2 \mu_m n_{0m} \left(\frac{Z_m q}{k_B T} \left(\tilde{\phi}_m - \tilde{V} \right) \nabla \phi_{0m} + \nabla \tilde{\phi}_m \right)$$

the equivalent of Eq. 4.17 at faradaic (ohmic) contacts is then:

$$\sum_{i\in\Lambda^j} c^{i,j}\tilde{V}^i + d^j\tilde{V}^j - \sum_{i\in\Lambda_D^j} \tilde{D}_\perp^i e^{i,j} - \tilde{D}_\perp^j f^j + \sum_{m=1}^{N_{ions}} \left(\sum_{i\in\Lambda^j} s_m^{i,j}\tilde{\phi}_m^i + t_m^j\tilde{\phi}_m^j \right) = 0 \tag{4.26a}$$

$$\sum_{i\in\Lambda^j} \left(s_m^{i,j} + g_m^{i,j}\right)\tilde{V}^i + \left(t_m^j + h_m^j\right)\tilde{V}^j + \sum_{i\in\Lambda^j} o_m^{i,j}\tilde{\phi}_m^i + p_m^j\tilde{\phi}_m^j - \sum_{i\in\Lambda_D^j} \tilde{J}_{\perp,m}^i e^{i,j}/j\omega - \tilde{J}_{\perp,m}^j f^j/j\omega = 0 \tag{4.26b}$$

where $e^{i,j}$ and f^j are the same as in the DC case (Eq. 4.18) and the other coefficients are given by Eq. 4.22. Note that the corresponding equations for ideally polarizable contacts are readily recovered by removing the equations for $\tilde{J}_{\perp,m}$.

4.2.2.3 Contact admittance

As we will discuss in Sec. 5.5, it is useful to foresee a more general case where the contacts (identified by integer index l) can have a lumped series admittance Y_l as sketched in Fig. 4.2. This implies that the current going out of the contact $\tilde{I}_l$ is given by:

$$\tilde{I}_l = -Y_l(\tilde{V}^l_{el} - \tilde{V}^l_{int})$$

where $\tilde{V}^l_{el}$ is the voltage imposed at the electrode and $\tilde{V}^l_{int}$ is the potential in the inner part of the electrode (see Fig. 4.2). The addition of external lumped elements to the simulation domain is well known in TCAD and obviously results in additional unknowns (the $\tilde{V}^l_{int}$) and equations. The equations to add are:

$$\sum_{i\in\Lambda^j} c^{i,j}\tilde{V}^i + d^j\tilde{V}^j - \sum_{i\in\Lambda^j_D} \tilde{D}^i_\perp e^{i,j} - \tilde{D}^j_\perp f^j + \sum_{m=1}^{N_{ions}} \left(\sum_{i\in\Lambda^j} s^{i,j}_m \tilde{\phi}^i_m + t^j_m \tilde{\phi}^j_m \right) = 0$$

$$\sum_{i\in\Lambda^j} \left(s^{i,j}_m + g^{i,j}_m\right)\tilde{V}^i + \left(t^j_m + h^j_m\right)\tilde{V}^j + \sum_{i\in\Lambda^j} o^{i,j}_m\tilde{\phi}^i_m + p^j_m\tilde{\phi}^j_m - \sum_{i\in\Lambda^j_D} \tilde{J}^i_{\perp,m} e^{i,j}/j\omega - \tilde{J}^j_{\perp,m} f^j/j\omega = 0$$

$$\sum_{j\in\Lambda^l_{el}} \left[\sum_{i\in\Lambda^j_D} \left(j\omega\tilde{D}^i_\perp + \sum_{m=1}^{N_{ions}} \tilde{J}^i_{\perp,m} \right) e^{i,j} + \left(j\omega\tilde{D}^j_\perp + \sum_{m=1}^{N_{ions}} \tilde{J}^j_{\perp,m} \right) f^j \right] = -Y_l(\tilde{V}^l_{el} - \tilde{V}^l_{int})$$

where Λ^l_{el} denotes the nodes connected to electrode l. In order to have the same units of measurements for all the unknowns, we use the variables $\tilde{V}^j_D = j\omega\tilde{D}^j_\perp/Y_l$ and $\tilde{V}^j_m = \tilde{J}^j_{\perp,m}/Y_l$ and thus alleviate possible ill-conditioning problems of the system of equations. The subscript l is not needed in the definition of $\tilde{V}^j_D$ and $\tilde{V}^j_m$ since each node n^j can lie only on one electrode l. In this way we can write:

$$\sum_{i\in\Lambda^j} c^{i,j}\tilde{V}^i + d^j\tilde{V}^j - \sum_{i\in\Lambda^j_D} \tilde{V}^i_D \frac{Y_l}{j\omega} e^{i,j} - \tilde{V}^j_D \frac{Y_l}{j\omega} f^j + \sum_{m=1}^{N_{ions}} \left(\sum_{i\in\Lambda^j} s^{i,j}_m \tilde{\phi}^i_m + t^j_m \tilde{\phi}^j_m \right) = 0$$

$$\sum_{i\in\Lambda^j} \left(s^{i,j}_m + g^{i,j}_m\right)\tilde{V}^i + \left(t^j_m + h^j_m\right)\tilde{V}^j + \sum_{i\in\Lambda^j} o^{i,j}_m\tilde{\phi}^i_m + p^j_m\tilde{\phi}^j_m - \sum_{i\in\Lambda^j_D} \tilde{V}^i_m \frac{Y_l}{j\omega} e^{i,j} - \tilde{V}^j_m \frac{Y_l}{j\omega} f^j = 0$$

$$\frac{Y_l}{j\omega} \sum_{j\in\Lambda^l_{el}} \left[\sum_{i\in\Lambda^j_D} \left(\tilde{V}^i_D + \sum_{m=1}^{N_{ions}} \tilde{V}^i_m \right) e^{i,j} + \left(\tilde{V}^j_D + \sum_{m=1}^{N_{ions}} \tilde{V}^j_m \right) f^j \right] = -\frac{Y_l}{j\omega}(\tilde{V}^l_{el} - \tilde{V}^l_{int})$$

As usual we have made the assumption that two adjacent but distinct electrodes are separated by at least two points.

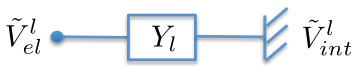

Fig 4.2: Sketch of a generic electrode (identified by the index l) with a lumped series admittance Y_l.

4.2.3 Volume integrals

As we have just seen, in order to calculate the discretized coefficients we need to compute volume and surface integrals. This computation is very expensive in terms of resources,

since it has to be done multiple times for each mesh node. In addition, the accuracy of this calculation is critical to determine the overall accuracy of the simulation method. These reasons justify the necessity to discuss in detail how the numerical integration is performed.

We start discussing the calculation of volume integrals. According to Eq. 4.12, given a tetrahedron identified by the index k, that has node n^j as one of the vertices, we have to calculate integrals $\mathcal{I}$ of the kind:

$$\mathcal{I} = \int\limits_{\Omega_c^{j,k}} f(\vec{x}) d\Omega \tag{4.27}$$

where $f(\vec{x})$ is an arbitrary continuos function, and for the sake of a lean notation we dropped the indices j and k. In the following we concentrate on the calculation of $\mathcal{I}$ in the CVFEM case; however, very similar considerations apply to the calculation of volume integrals in GFEM.

An important advantage of CVFEM over GFEM is that integrals of the kind in Eq. 4.27 are generally of lower order with respect to those of GFEM (compare for example the CVFEM and GFEM AC coefficients Eqs. 4.22-4.54). The higher is the integral order, the more integration points are needed to retain the same accuracy using a Gauss integration rule [66]; this fact highlights the need of accurate and efficient integration procedures.

Several approaches have been proposed to calculate Eq. 4.27. Perhaps the most common one [67] is to transform the coordinates from $\vec{x}$ to $\vec{\xi} = \begin{bmatrix} \xi & \eta & \zeta \end{bmatrix}^T$ by a transformation $\mathbf{T}$ such that $\vec{x} = \mathbf{T}\,\vec{\xi}$ and such that the calculation is appreciably simpler. Using $\mathbf{T}$ the integral becomes:

$$\mathcal{I} = \int\limits_{\Omega_c^{j,k}} f(\vec{x}) d\Omega = \int\limits_{\hat{\Omega}_c^{j,k}} f(\vec{\xi})\, |\det(\mathbf{J})|\, d\hat{\Omega}$$

where $\hat{\Omega}_c^{j,k}$ is the control volume in the transformed space and $\mathbf{J}$ is the Jacobian matrix of $\mathbf{T}$. In standard GFEM on a simplicial mesh, the transformation is chosen in a way that maps the k-th element into a reference unitary simplex (Fig. 4.1). The transformation is thus an affinity and $|\det(\mathbf{J})|$ is either equal to the length or to twice the area or to six times the volume of the simplex when working in one, two or three dimensions, respectively. In our case this implies that:

$$\mathcal{I} = 6\mathcal{V}_k \int\limits_{\hat{\Omega}_c} f(\vec{\xi}) d\hat{\Omega} = 6\mathcal{V}_k \hat{\mathcal{I}} \tag{4.28}$$

where $\hat{\Omega}_c$ is the control volume in the reference tetrahedron (the blue shape in Fig. 4.1) and $\mathcal{V}_k$ is the volume of the original tetrahedron v^k. Note that the integral in Eq. 4.28 does not depend on the specific tetrahedron but only on the integrand function f. An important difference of CVFEM with respect to GFEM is that in Eq. 4.28 the term $\hat{\mathcal{I}}$ is calculated only on the control volume $\hat{\Omega}_c$ and not on the entire tetrahedron. This implies that the well-known exact expressions for the integration coefficients of polynomial expressions using baricentric coordinates [67] can not be used in the CVFEM case and an alternative mean to compute $\hat{\mathcal{I}}$ has to be devised.

Another approach to compute $\hat{\mathcal{I}}$ is to use numeric integration with quadrature formulas, for instance using Gauss points [67]. However, since the region $\hat{\Omega}_c$ is not the unitary

reference cube, this approach requires to divide $\hat{\Omega}_c$ in elementary subvolumes and to carry out numerical integration on each of them.

Another possibility would be to use a transformation to directly map the control volume into a unitary reference cube and then calculate nodes and weights as tensor products of the Gauss's quadrature formulas from the 1-dimensional case [67]. The required transformation however is non-linear and complicates the overall calculation.

Yet another approach is presented in [68] for a quadrilateral or hexaedral mesh, but it requires to define the control volume boundaries on the Gauss-Legendre points instead of the much simpler centroids of faces and elements as done in this work. In addition, it is not straightforward to translate the approach of [68] from hexaedral to tetrahedral meshes.

For all these reasons, we have decided to calculate $\hat{\mathcal{I}}$ via direct symbolic integration. The integral $\hat{\mathcal{I}}$ is then computed as a sum of integrals $\hat{\mathcal{I}}_{lP}$ on elementary subvolumes included in the ξ domain in the interval $\xi \in [\xi_a, \xi_b]$, in the η domain from line l_a to line l_b and in the ζ domain from the $\xi\eta$ plane to the plane P.

As a first example of this procedure, we calculate the volume of $\hat{\Omega}_c$; that is, we set $f(\xi, \eta, \zeta) = 1$. We can simply prove by direct calculation or by geometrical considerations that $\text{Vol}\left(\hat{\Omega}_c\right) = 1/24$, that is, $1/4$ of the volume of the unitary tetrahedron. Similarly we can prove that:

$$\int_{\hat{\Omega}_c} N_0 d\hat{\Omega} = \frac{25}{1152}, \quad \int_{\hat{\Omega}_c} N_{1..3} d\hat{\Omega} = \frac{23}{3456} \tag{4.29}$$

where we have called $N_{0..3}$ the linear basis functions of nodes $n_{0..3}$ respectively in the unitary reference tetrahedron (see Eq. 4.59). The expressions of $N_{0..3}$ are reported in Sec. 4.A.7 in the chapter appendix.

We also need to calculate the integrals containing non linear functions of V_0, such as for instance Eq. 4.14. In the specific case of Eq. 4.14 the integrand becomes:

$$f(\vec{x}) = \exp\left[\frac{Z_m q}{k_B T}\left(V_{ref} - N^{j,k}V_0^j - \sum_{i \in \Lambda^{j,k}} N^{i,k}V_0^i\right)\right]. \tag{4.30}$$

To maintain a simple notation, we introduce a new variable v_l with $l = 0..3$ where:

$$v_0 = \frac{Z_m q}{k_B T}\left(V_{ref} - V_0^j\right), \quad v_{1..3} = \frac{Z_m q}{k_B T}\left(V_{ref} - V_0^i\right)$$

so that the integrand is:

$$f(\vec{x}) = \exp\left(v_0 N^{j,k} + \sum_{i \in \Lambda^{j,k}} v_i N^{i,k}\right) \tag{4.31}$$

where we have used the fact that $N^{j,k} + \sum_i N^{i,k} = 1$. The integral of $f(\vec{x})$ in Eq. 4.31 is given in Eq. 4.56 as a function of the terms $u_l = v_l - v_0$ where $l = 1..3$. The expression of the integral reveals that numerical issues could arise due to the limit forms $0/0$. This problem, however, can be easily overcome by using a Taylor expansion. For instance, an expansion at third order around $u_l = 0$ is given in the Sec. 4.A.4. Note that using a Taylor expansion is equivalent to employing a quadrature integration rule, but the advantage of our method is that the integral can also in principle be computed exactly (using Eq. 4.56)

and that there is no need to define integration points inside the tetrahedron for each integral that we need to calculate.

Another important advantage of the proposed method is the reduced calculation complexity at the same desired accuracy. In fact, using the quadrature integration and assuming that $\hat{\Omega}_c^{j,k}$ is mapped into the unitary reference cube via a non-linear transformation, 6 integration points would be necessary to have an approximation of order 3 [66]. This means that we need to evaluate the integrand function, in our case an exponential, 6 times. Because the exponential function is numerically implemented as a series and assuming to truncate it at the third order, then we need to sum 24 terms. On the other hand, using the exact expression of $\hat{\mathcal{I}}$ expanded in Taylor series at order 3 requires to evaluate a series of 20 terms plus one exponential function (4 additional terms if truncated at third order), which gives the same computational cost as the quadrature formula. Our approach, however, as already discussed, uses a linear transformation, which means that only the volume needs to be actually computed, while mapping $\hat{\Omega}_c^{j,k}$ into a cube would require to calculate also the non-linear transformation. In addition, the quadrature formula from [66] uses the values of the function on the faces baricenters, while we directly use the nodal values. The advantage of our method comes from the fact that, in the approximate calculation, we use the known expansion of the exponential function.

As a final remark we note that, in order to solve the non-linear system of equations (Eq. 4.12), we also need to calculate the Jacobian of the system (Eq. 4.51). These terms include integrals very similar to $\mathcal{I}$, so that the same considerations above apply to them as well. Also in this case we can overcome issues with $0/0$ forms by using a Taylor expansion. The Taylor forms are reported in Sec. 4.A.4 for the sake of an immediate use by the interested reader.

4.2.4 Surface integrals

In CVFEM integrals of the form:

$$\mathcal{I}_S = \int_{\Gamma^{j,k}} f(\vec{x}) \nabla_{\vec{x}}\, g(\vec{x}) \cdot \hat{n}\, d\Gamma \tag{4.32}$$

appear, where $f(\vec{x})$ and $g(\vec{x})$ are again continuous and differentiable functions. For instance these are found in Eq. 4.22. In all cases considered here $g(\vec{x})$ will be one of the linear basis functions. The surface $\Gamma^{j,k}$ can be divided into 3 planar surfaces, each one intersecting one of the edges that connect node j with the other 3 tetrahedron's nodes (see Fig. 4.1). We will call these surfaces $\Gamma_1^{j,k}$, $\Gamma_2^{j,k}$, $\Gamma_3^{j,k}$, where we choose $\Gamma_i^{j,k}$ as the surface that intersects the edge that connects nodes n^j and n^i. We can then write the surface integral as a sum of three terms $\mathcal{I}_S^l$:

$$\mathcal{I}_S = \sum_{l=1}^{3} \int_{\Gamma_l^{j,k}} f(\vec{x}) \nabla_{\vec{x}}\, g(\vec{x}) \cdot \hat{n}\, d\Gamma = \sum_{l=1}^{3} \mathcal{I}_S^l \tag{4.33}$$

We apply again the transformation to the unitary reference tetrahedron of Fig. 4.1 $\vec{x} = \mathbf{T}\,\vec{\xi}$ to each integral, so that:

$$\nabla_{\vec{x}}\, g(\vec{x}) = \mathbf{J}^{-T} \nabla_{\vec{\xi}}\, g(\vec{x}(\vec{\xi}))$$

where $\mathbf{J}^{-T}$ is the transposed inverse matrix of $\mathbf{J}$. The surface element is written explicitly:

$$\hat{n}\, d\Gamma = \frac{\partial \vec{r}_l}{\partial x} \times \frac{\partial \vec{r}_l}{\partial y} dy\, dx$$

where $\vec{r}_l = \begin{bmatrix} x & y & a_P^l + b_P^l x + c_P^l y \end{bmatrix}^T$ (i.e, the vector defining the surface (plane) $\Gamma_l^{j,k}$) can be described by the vector $\vec{\Gamma}_l^{j,k}$ whose norm is equal to the surface area and whose direction is orthogonal to the surface with outer orientation with respect to $\Omega_c^{j,k}$. When applying the transformation $\mathbf{T}$ we can prove that the following relations hold:

$$\left\| \vec{\Gamma}_l^{j,k} \right\| \frac{\dfrac{\partial \vec{r}_l}{\partial x} \times \dfrac{\partial \vec{r}_l}{\partial y}}{\left\| \dfrac{\partial \vec{r}_l}{\partial x} \times \dfrac{\partial \vec{r}_l}{\partial y} \right\|} = |\det(\mathbf{J})| \left\| \vec{\hat{\Gamma}}_l \right\| \mathbf{J}^{-T} \frac{\left(\dfrac{\partial \vec{\hat{r}}_l}{\partial \xi} \times \dfrac{\partial \vec{\hat{r}}_l}{\partial \eta} \right)}{\left\| \dfrac{\partial \vec{\hat{r}}_l}{\partial \xi} \times \dfrac{\partial \vec{\hat{r}}_l}{\partial \eta} \right\|}$$

$$\int\limits_{\Gamma_l^{j,k}} f(\vec{r}_l) \frac{\left\| \dfrac{\partial \vec{r}_l}{\partial x} \times \dfrac{\partial \vec{r}_l}{\partial y} \right\|}{\left\| \vec{\Gamma}_l^{j,k} \right\|} dy\, dx = \int\limits_{\hat{\Gamma}_l} f(\vec{\hat{r}}_l) \frac{\left\| \dfrac{\partial \vec{\hat{r}}_l}{\partial \xi} \times \dfrac{\partial \vec{\hat{r}}_l}{\partial \eta} \right\|}{\left\| \vec{\hat{\Gamma}}_l \right\|} d\eta\, d\xi$$

where $\vec{\hat{r}}_l = \begin{bmatrix} \xi & \eta & \alpha_P^l + \beta_P^l \xi + \gamma_P^l \eta \end{bmatrix}^T$ is the vector defining the surface (plane) $\hat{\Gamma}_l$ in the transformed space. We can then write the complete expression of the integral:

$$\mathcal{I}_S^l = \left(\mathbf{J}^{-T} \nabla_{\vec{\xi}}\, g(\vec{x}(\vec{\xi})) \right) \cdot \vec{\gamma}_l^{j,k} \int\limits_{\hat{\Gamma}_l} f(\vec{\hat{r}}_l) d\eta\, d\xi \tag{4.34}$$

where:

$$\vec{\gamma}_l^{j,k} = |\det(\mathbf{J})|\, \mathbf{J}^{-T} \left(\frac{\partial \vec{\hat{r}}_l}{\partial \xi} \times \frac{\partial \vec{\hat{r}}_l}{\partial \eta} \right)$$

Note that, since g and $\vec{\hat{r}}_l$ are linear functions, their derivatives have been taken out of the integral and that:

$$\vec{\Gamma}_l^{j,k} = \vec{\gamma}_l^{j,k} \frac{\left\| \vec{\hat{\Gamma}}_l \right\|}{\left\| \dfrac{\partial \vec{\hat{r}}_l}{\partial \xi} \times \dfrac{\partial \vec{\hat{r}}_l}{\partial \eta} \right\|} \tag{4.35}$$

The values of the integrals in Eq. 4.33 are reported in the appendix. Once again, in order to avoid issues with $0/0$ forms, we used a Taylor expansion of the integral.

Primal surface integrals In order to impose the global conservation we have to calculate integrals of the form (see Eq. 4.18):

$$\mathcal{I}_S = \int\limits_{\Gamma_P^{j,k}} f(\vec{x}) d\Gamma$$

where $\Gamma_P^{j,k}$ is the part of the primal surfaces of the tetrahedron comprised in the control volume $\Omega_c^{j,k}$ on which we set Dirichlet boundary conditions. In each volume $\Omega_c^{j,k}$, $\Gamma_P^{j,k}$ can

be made of a different number of surfaces, from 0 to 3. From now on we will assume that $\Gamma_P^{j,k}$ is made of all the facets on the 3 primal surfaces, i.e $\Gamma_P^{j,k} = \sum_l \Gamma_{Pl}^{j,k}$ with l ranging from 1 to 3. For each facet we can then write:

$$\mathcal{I}_S^l = 2\Gamma_{Pl} \int_{\hat{\Gamma}_{Pl}} f(\vec{\hat{r}}) d\Xi_2 \, d\Xi_1$$

where Γ_{Pl} is the area of the primary face opposite to node n_l in the original space and we have used the fact that the faces are planar surfaces, so that the surface element is constant and can be taken out of the integral. More explicitly then:

$$\Gamma_{Pl} = \frac{1}{2} |\det(\mathbf{J})| \left\| \mathbf{J}^{-T} \left(\frac{\partial \vec{\hat{r}}_{Pl}}{\partial \Xi_1} \times \frac{\partial \vec{\hat{r}}_{Pl}}{\partial \Xi_2} \right) \right\|$$

where $\vec{\hat{r}}_{Pl}$ is again the vector defining the face (similarly as $\vec{\hat{r}}_l$). We denote $\hat{\Gamma}_{Pl}$ the surface opposite to node n_l in the transformed space and we have also called Ξ_i the coordinates, because they have to be chosen differently according to the surface $\hat{\Gamma}_{Pl}$. In particular we have that:

$$(\Xi_1, \Xi_2) = \begin{cases} (\xi, \eta) & \text{if } l = 3 \\ (\xi, \zeta) & \text{if } l = 2 \\ (\eta, \zeta) & \text{if } l = 1 \end{cases}$$

The values of the integrals are explicitly reported in Sec. 4.A.6.

4.3 1D CVFEM simulator

The full 3D simulator is a very general purpose tool for sensor analysis whose capability will be demonstrated in Chaps. 5-6. However, it usually requires a large computational effort for the purpose of studying simple 1D systems, it is convenient to use a 1D model. In the following we will then present the development of a 1D CVFEM simulator for dielectric/electrolyte systems, that is derived from the general 3D expressions presented in this chapter. We therefore make the same assumptions as above, for instance the linearity of the basis functions N^j. We will therefore not include the model for the semiconductor material.

4.3.1 DC model

Let's assume a 1D system develops along x (see the sketch in Fig. 4.3). We use j as the node index and we do not need a different index for the volume (k in the 3D simulator), since in this simple 1D system the number of volumes is $N_{nod} - 1$, where N_{nod} is the number of nodes. In addition, each mesh node j is attached only to two volumes, so that we can use the same index j for both entities. With the help of Fig. 4.3, we denote then

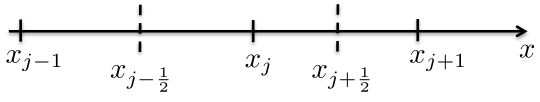

Fig 4.3: Sketch of a generic point x_j in the 1D mesh.

$N^{j,j}$ as the basis function around node x_j defined inside the volume between x_j and x_{j+1}. The basis functions become finally:

$$N^{j,j} = \frac{x_{j+1} - x}{x_{j+1} - x_j}, \qquad N^{j,j-1} = \frac{x - x_{j-1}}{x_j - x_{j-1}}$$

$$N^{j+1,j} = \frac{x - x_j}{x_{j+1} - x_j}, \qquad N^{j-1,j-1} = \frac{x_j - x}{x_j - x_{j-1}}.$$

Consistently with the previous section, we define the control volume by using the baricenters of the mesh volumes, which is denoted $x_{j+\frac{1}{2}} = (x_j + x_{j+1})/2$. We can then specialize Eq. 4.12 as:

$$a^{j+}V_0^{j+1} + a^{j-}V_0^{j-1} + b^jV_0^j + \int_{x_{j-\frac{1}{2}}}^{x_{j+\frac{1}{2}}} \rho_{0f}dx + \sum_{m=1}^{N_{ions}} Z_m q \int_{x_{j-\frac{1}{2}}}^{x_{j+\frac{1}{2}}} n_{0m}\left(\sum_{i=1}^{N_{nod}} N^iV_0^i\right)dx = 0 \tag{4.36}$$

The coefficients are:

$$a^{j+} = \frac{1}{A}\int_{\partial C_{j,j+1}} \varepsilon\nabla N^{j+1,k}\cdot\hat{n}\,d\Gamma = \frac{\varepsilon_j}{x_{j+1} - x_j} \tag{4.37a}$$

$$a^{j-} = \frac{1}{A}\int_{\partial C_{j,j-1}} \varepsilon\nabla N^{j-1,k}\cdot\hat{n}\,d\Gamma = \frac{\varepsilon_{j-1}}{x_j - x_{j-1}} \tag{4.37b}$$

$$b^j = \frac{1}{A}\left(\int_{\partial C_{j,j+1}} \varepsilon\nabla N^{j,k}\cdot\hat{n}\,d\Gamma + \int_{\partial C_{j,j-1}} \varepsilon\nabla N^{j,k}\cdot\hat{n}\,d\Gamma\right) = -(a^{j-} + a^{j+}) \tag{4.37c}$$

where ε_j is the permittivity in the mesh volume x_j, $\partial C_{j-1,j}$ and $\partial C_{j,j+1}$ the control volume surfaces (in the transversal y and z coordinates) at $x_{j-\frac{1}{2}}$ and $x_{j+\frac{1}{2}}$ respectively. The coefficients are calculated per unit transversal area A. The non-linear charge term is calculated as:

$$\begin{aligned}
\sum_{m=1}^{N_{ions}} Z_m q \int_{x_{j-\frac{1}{2}}}^{x_{j+\frac{1}{2}}} n_{0m}\left(\sum_{i=1}^{N_{nod}} N^iV_0^i\right)dx &= \sum_{m=1}^{N_{ions}} Z_m q \int_{x_{j-\frac{1}{2}}}^{x_{j+\frac{1}{2}}} n_{0m}\left(N^jV_0^j + \sum_{i\in\Lambda_I^j} N^iV_0^i\right)dx \\
&= \sum_{m=1}^{N_{ions}} Z_m q n_{0m}^{\infty} \int_{x_{j-\frac{1}{2}}}^{x_{j+\frac{1}{2}}} \exp\left(-\frac{Z_m q}{k_B T}\left(N^jV_0^j + \sum_{i\in\Lambda_I^j} N^iV_0^i - V_{ref}\right)\right)dx \\
&= \sum_{m=1}^{N_{ions}} Z_m q n_{0m}^{\infty}\left[\int_{x_{j-\frac{1}{2}}}^{x_j} e^{N_{eq}^{j-}}dx + \int_{x_j}^{x_{j+\frac{1}{2}}} e^{N_{eq}^{j+}}dx\right]
\end{aligned} \tag{4.38}$$

where:

$$N_{eq}^{j-} = \frac{Z_m q}{k_B T}\left(V_{ref} - N^{j,j-1}V_0^j - N^{j-1,j-1}V_0^{j-1}\right)$$

$$N_{eq}^{j+} = \frac{Z_m q}{k_B T}\left(V_{ref} - N^{j,j}V_0^j - N^{j+1,j}V_0^{j+1}\right)$$

We now define:

$$v_m^j = \frac{Z_m q}{k_B T}V_0^j, \quad u_{m-}^j = v_m^j - v_m^{j-1}, \quad u_{m+}^j = v_m^j - v_m^{j+1}$$

and we also call $l_{j-} = x_j - x_{j-1}$ and $l_{j+} = x_{j+1} - x_j$ the lengths of the cells around node x_j. We can finally calculate the integrals in Eq. 4.38:

$$Ie^j_{m-} = \int_{z^{j-\frac{1}{2}}}^{z^j} e^{N^{j-}_{eq}}\, dz = \exp\left(\frac{Z_m q}{k_B T}\left(V_{ref} - V_0^j\right)\right) \frac{\exp\left(u^j_{m-}/2\right) - 1}{u^j_{m-}} l_{j-} \tag{4.39a}$$

$$Ie^j_{m+} = \int_{z^j}^{z^{j+\frac{1}{2}}} e^{N^{j+}_{eq}}\, dz = \exp\left(\frac{Z_m q}{k_B T}\left(V_{ref} - V_0^j\right)\right) \frac{\exp\left(u^j_{m+}/2\right) - 1}{u^j_{m+}} l_{j+} \tag{4.39b}$$

Since we need to calculate other integrals (e.g., for the Jacobian computation), it would be useful to have a general procedure to compute integrals. We show in the following how a general procedure can be established.

For the implementation of the 1D CVFEM model, we need to calculate integrals of the type:

$$\int_{x_1}^{x_2} f\left(V(x)\right) dx$$

where $V(x) = N_1(x)V_1 + N_2(x)V_2$ is the interpolation in terms of the basis functions. Since we always use linear basis functions with the properties that $N_1(x_1) = 1$, $N_1(x_2) = 0$, $N_2(x_1) = 0$, $N_2(x_2) = 1$, we can immediately see that:

$$V(x) = \frac{x_2 - x}{x_2 - x_1} V_1 + \frac{x - x_1}{x_2 - x_1} V_2, \quad \frac{dV(x)}{dx} = \frac{V_2 - V_1}{x_2 - x_1}$$

We can then easily see that:

$$\begin{aligned}\int_{x_a}^{x_b} f\left(V(x)\right) dx &= \frac{x_2 - x_1}{V_2 - V_1} \int_{x_a}^{x_b} f\left(V(x)\right) \frac{dV(x)}{dx} dx \\ &= \frac{x_2 - x_1}{V_2 - V_1} \left(F(V(x_b)) - F(V(x_a))\right)\end{aligned}$$

where F is the primitive of f with respect to the variable x. We immediately notice that Eqs. 4.39 above are indeed in this form. This also tells us that for any function f the integrals depend on the geometry only through the length of the cell, provided that we use linear basis functions and that the extrema x_a and x_b are x_1 and x_2 (as in the FEM) or x_1 and $(x_1 + x_2)/2$ (as in the CVFEM).

The non-linear Jacobian coefficients are reported in Sec. 4.A.8 in the chapter appendix.

Global conservation We specialize Eq. 4.17 on the two boundaries of the 1D domain:

$$a^{1+}V_0^2 + b^1 V_0^1 - D^1_\perp + \int_{x_1}^{x_{1+\frac{1}{2}}} \rho_{0f} dx + \sum_{m=1}^{N_{ions}} Z_m q \int_{x_1}^{x_{1+\frac{1}{2}}} n_{0m} \left(\sum_{i=1}^{N_{nod}} N^i V_0^i\right) dx = 0$$

$$a^{N_{nod}-}V_0^{N_{nod}-1} + b^{N_{nod}} V_0^{N_{nod}} - D^{N_{nod}}_\perp + \int_{x_{N_{nod}-\frac{1}{2}}}^{x_{N_{nod}}} \rho_{0f} dx + \sum_{m=1}^{N_{ions}} Z_m q \int_{x_{N_{nod}-\frac{1}{2}}}^{x_{N_{nod}}} n_{0m} \left(\sum_{i=1}^{N_{nod}} N^i V_0^i\right) dx = 0$$

where we have used the fact that:

$$f^j = \frac{1}{A} \int\limits_{\Gamma_D \cap \Gamma^j} N^j d\Gamma = 1$$

4.3.2 AC model

To derive the 1D AC model we start from Eqs. 4.20 - 4.21:

$$\text{Poisson}: \quad c^{j+}\tilde{V}^{j+1} + c^{j-}\tilde{V}^{j-1} + d^{j}\tilde{V}^{j} + \sum_{m=1}^{N_{ions}} \left(s_m^{j+}\tilde{\phi}_m^{j+1} + s_m^{j-}\tilde{\phi}_m^{j-1} + t_m^{j}\tilde{\phi}_m^{j} \right) = 0 \quad (4.40)$$

$$\text{current}: \quad g_m^{j+}\tilde{V}^{j+1} + g_m^{j-}\tilde{V}^{j-1} + h_m^{j}\tilde{V}^{j} + o_m^{j+}\tilde{\phi}_m^{j+1} + o_m^{j-}\tilde{\phi}_m^{j-1} + p_m^{j}\tilde{\phi}_m^{j} = 0 \quad (4.41)$$

The coefficients are reported in Sec. 4.A.8.

Current through ideally polarizable electrodes In the following, we show how to compute the current at the bottom electrode ($x = 0$). The current at the other contact can be immediately calculated in a similar way but it should give exactly the same result, since in a 1D system the total current has to be conserved.
To compute the current density at the contacts, we impose the global conservation, so that we need to compute the dielectric displacements $\tilde{D}_\perp$, as in Sec. 4.2.2.2, solving as a post-processing step the following equations:

$$c^{j+}\tilde{V}^{j+1} + d^{j}\tilde{V}^{j} - \tilde{D}_\perp^{j} + \sum_{m=1}^{N_{ions}} \left(s_m^{j+}\tilde{\phi}_m^{j+1} + t_m^{j}\tilde{\phi}_m^{j} \right) = 0, \qquad \text{for } j = 1$$

$$c^{j-}\tilde{V}^{j-1} + d^{j}\tilde{V}^{j} - \tilde{D}_\perp^{j} + \sum_{m=1}^{N_{ions}} \left(s_m^{j-}\tilde{\phi}_m^{j-1} + t_m^{j}\tilde{\phi}_m^{j} \right) = 0, \qquad \text{for } j = N_{nod}$$

At ideally polarizable electrodes the total current is just a displacement current that reads:

$$\tilde{J}_{ex} = -j\omega\tilde{D}_\perp^1 = j\omega\tilde{D}_\perp^{N_{nod}} .$$

With this notation the current density in the system is positive when flowing along the x direction, that is from the bottom to the top electrode.

Current through Faradaic electrodes with admittance in series We assume now that the electrodes can be connected in series with admittances (per unit area) y_l, where consistently with Sec. 4.2.2.2, l is the electrode index. In the following we will always assume that $l = 1$ and $l = 2$ at the bottom and top electrodes respectively. We also suppose that the electrodes can have a Dirichlet boundary condition on the quasi-potentials, so that the contact current has also ionic contributions. This is clearly a very general case which goes beyond what is examined in the results section of this thesis. The contact current is then:

$$\tilde{J}(0) = -j\omega\tilde{D}_\perp^1 - \sum_m \tilde{J}_{\perp,m}^1$$
$$\tilde{J}(L) = j\omega\tilde{D}_\perp^{N_{nod}} + \sum_m \tilde{J}_{\perp,m}^{N_{nod}} .$$

The equation for the current at the electrodes is:

$$\tilde{J}(0) = y_1(\tilde{V}_{el}^1 - \tilde{V}^1) \quad (4.42a)$$
$$\tilde{J}(L) = -y_2(\tilde{V}_{el}^2 - \tilde{V}^{N_{nod}}) \quad (4.42b)$$

where $\tilde{V}^1_{el}$ and $\tilde{V}^2_{el}$ are the potential externally applied at the bottom and top electrodes. In the system matrix we then need to add $N_{ions}+3$ rows that represent the contact equations. If we choose to calculate the current at the bottom electrode (current conservation will enforce the same current at the top electrode), then the equations are given by Eq. 4.42a and the following four relations:

$$c^{1+}\tilde{V}^2 + d^1\tilde{V}^1 - \tilde{D}^1_\perp + \sum_{m=1}^{N_{ions}} \left(s^{1+}_m \tilde{\phi}^2_m + t^1_m \tilde{\phi}^1_m \right) = 0$$

$$g^{1+}_m \tilde{V}^2 + h^1_m \tilde{V}^1 + o^{1+}_m \tilde{\phi}^2_m - \tilde{J}^1_{\perp,m}/\omega + p^1_m \tilde{\phi}^1_m = 0$$

$$\tilde{D}^1_\perp + \sum_m \tilde{J}^1_{\perp,m}/j\omega = -y_1(\tilde{V}^1_{el} - \tilde{V}^1)/j\omega$$

$$\tilde{D}^1_\perp + \sum_m \tilde{J}^1_{\perp,m}/j\omega = y_2(\tilde{V}^2_{el} - \tilde{V}^{N_{nod}})/j\omega$$

As in the 3D solver, it is useful for numerical reasons to have the same units of measurements for all the unknowns. We then use the variables $\tilde{V}^1_D = j\omega\tilde{D}^1_\perp/y_1$ and $\tilde{V}^1_m = \tilde{J}^1_{\perp,m}/y_1$ (as in Sec. 4.2.2.2), so that we can write:

$$c^{1+}\tilde{V}^2 + d^1\tilde{V}^1 - \tilde{V}^1_D \frac{y_1}{j\omega} + \sum_{m=1}^{N_{ions}} \left(s^{1+}_m \tilde{\phi}^2_m + t^1_m \tilde{\phi}^1_m \right) = 0 \tag{4.43a}$$

$$g^{1+}_m \tilde{V}^2 + h^1_m \tilde{V}^1 + o^{1+}_m \tilde{\phi}^2_m - \tilde{V}^1_m \frac{y_1}{\omega} + p^1_m \tilde{\phi}^1_m = 0 \tag{4.43b}$$

$$\tilde{V}^1_D \frac{y_1}{j\omega} + \sum_m \tilde{V}^1_m \frac{y_1}{j\omega} = -\frac{y_1}{j\omega}(\tilde{V}^1_{el} - \tilde{V}^1) \tag{4.43c}$$

$$\tilde{V}^1_D \frac{y_1}{j\omega} + \sum_m \tilde{V}^1_m \frac{y_1}{j\omega} = \frac{y_2}{j\omega}(\tilde{V}^2_{el} - \tilde{V}^{N_{nod}}) \tag{4.43d}$$

The system of equations is then solved using the same techniques used for the DC solver. This will be the topic of the next section.

4.4 Numerical implementation

A full three dimensional CVFEM and GFEM simulator (hereafter denoted ENBIOS: Electronic NanoBIOsensor Simulator) has been implemented using MATLAB [69], based on *Netgen* general purpose tetrahedral meshes [70]. The non-linear DC system (Eqs. 4.12-4.16) has been solved using MATLAB's built-in routine *fsolve* through Levenberg-Marquardt's algorithm [71], which was the one that proved to be most robust and accurate among MATLAB's default choices. The convergence criterion was set to machine precision and corresponds to about 10^{-6} elementary charges for the quadratic norm of the $\mathbf{S}$ vector in Eq. 4.44. Typically convergence is obtained in five iterations starting from the initial guess given by the linear Poisson solution.
The AC problem is instead solved using *Matlab*'s built-in routine *mldivide* (the backslash operator), which uses different direct methods to find the solution of a linear system depending on the properties of the matrices. Since the system matrix is fairly large, it would appear that an iterative method could be advantageous. However, *mldivide* is usually so efficient that, unless there are memory issues or one can provide a very good estimate of the solution, the iterative solvers provided with *Matlab* are unlikely to offer a significant advantage.

We did not explore this point in more detail since the linear system's solution is usually not the bottleneck of our simulation code. We had neither memory issues nor lack of computational power, since we could use machines with up to 200 GB of RAM and 64 cores each.

4.4.1 DC problem

Boundary conditions for the DC problem are a mixture of Dirichlet and Neumann conditions. The Neumann borders don't need any special care (since as usual in FEMs [62], these are the natural boundary conditions for the method), while the voltages on the Dirichlet boundaries are known and therefore do not contribute to the variables vector. The overall system of equations can be put in the form:

$$\mathbf{S} = \mathbf{A}_0 \mathbf{V}_0 + \mathbf{C}_0 + \mathbf{Q}_{0f} + \mathbf{Q}_{0el} = 0 \tag{4.44}$$

where $\mathbf{A}_0$ is the matrix containing Poisson coefficients (Eq. 4.13), the voltage vector $\mathbf{V}_0$ has dimensions $N_{nodes} - N_{ext}$ where N_{ext} is the number of nodes on the Dirichlet boundaries and the vector $\mathbf{C}_0$ contains the coefficients related to the voltages on the Dirichlet boundary. The non-linear vector $\mathbf{Q}_{0el}$ contains the expression in Eq. 2.4 for the ion concentrations.

4.4.2 AC problem

Since the AC model equations are linearized, the resulting solution system is linear. It can then be written as:

$$\mathbf{A}\,\tilde{\mathbf{U}} + \mathbf{C} = 0 \tag{4.45}$$

where $\tilde{\mathbf{U}} = \begin{bmatrix}\tilde{\mathbf{V}} & \tilde{\boldsymbol{\phi}}_1 & \dots & \tilde{\boldsymbol{\phi}}_{N_{ions}}\end{bmatrix}^T$ is the vector of unknown variables, the voltage vector $\tilde{\mathbf{V}}$ has again dimensions $N_{nodes} - N_{ext}$ and the vector $\mathbf{C}$ contains the coefficients related to the voltages on the Dirichlet boundary, both for Poisson and for the ion current equations. If all the electrodes are ideally polarizable, the vectors $\tilde{\boldsymbol{\phi}}_m$ have dimensions N_{nodes}. The top left part of matrix $\mathbf{A}$, which encloses the Poisson coefficients for the voltage vector, has exactly the same structure of $\mathbf{A}_0$, since Poisson DC and AC equations have a very similar form.

4.4.2.1 Generalized electrodes

If we allow some electrodes to be Faradaic or to be connected in series with a lumped admittance, the vector of unknown variables is:

$$\tilde{\mathbf{U}} = \begin{bmatrix} \tilde{\mathbf{V}} \\ \tilde{\boldsymbol{\phi}}_1 \\ \dots \\ \tilde{\boldsymbol{\phi}}_{N_{ions}} \\ \tilde{\mathbf{V}}_D \\ \tilde{\mathbf{V}}_1 \\ \dots \\ \tilde{\mathbf{V}}_{N_{ions}} \\ \tilde{\mathbf{V}}_{int} \end{bmatrix}, \qquad \begin{cases} \tilde{\mathbf{V}} \to n_{int}^V : \text{points that are not on the electrodes} \\ \tilde{\boldsymbol{\phi}}_i \to n_{int}^\phi : \text{points that are not on the Faradaic electrodes} \\ \tilde{\mathbf{V}}_D \to n_{el}^V : \text{points that are on the electrodes with admittance} \\ \tilde{\mathbf{V}}_i \to n_{el}^\phi : \text{points that are on the Faradaic electrodes with admittance} \\ \tilde{\mathbf{V}}_{int} \to n_{el} : \text{electrodes with admittance} \end{cases}$$

where the dimensions of each subarray are also shown. The constant vector $\mathbf{C}$ contains the voltages applied on all the electrodes and the quasi-potentials on Faradaic electrodes.

4.4.3 Simple example

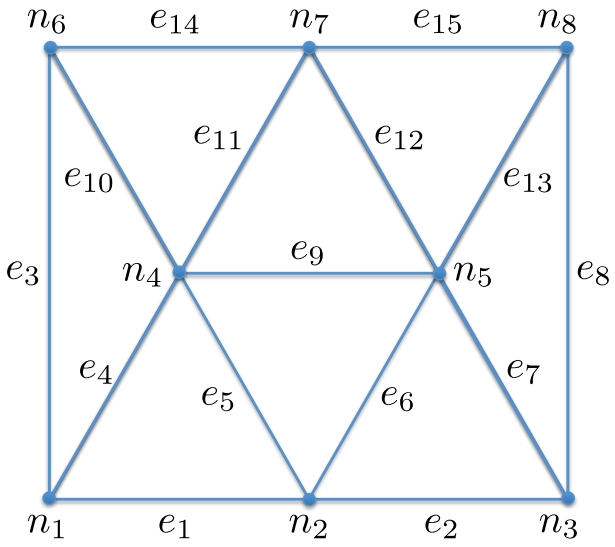

Fig 4.4: Simple 2D mesh.

In order to understand all implementation details, we consider as a simple 2D example the mesh shown in Fig. 4.4, where we suppose that the system is entirely composed of electrolyte. The mesh is composed of 15 edges and 8 nodes. We suppose Dirichlet boundary conditions on nodes n_1, n_2 and n_3. No external lumped component is considered. The 15×8 edges-nodes incidence matrix $\mathbf{G}$ of such a mesh is:

$$\mathbf{G} = \begin{bmatrix} 1 & -1 & 0 & 0 & 0 & 0 & 0 & 0 \\ 0 & 1 & -1 & 0 & 0 & 0 & 0 & 0 \\ 1 & 0 & 0 & 0 & 0 & -1 & 0 & 0 \\ 1 & 0 & 0 & -1 & 0 & 0 & 0 & 0 \\ 0 & 1 & 0 & -1 & 0 & 0 & 0 & 0 \\ 0 & 1 & 0 & 0 & -1 & 0 & 0 & 0 \\ 0 & 0 & 1 & 0 & -1 & 0 & 0 & 0 \\ 0 & 0 & 1 & 0 & 0 & 0 & 0 & -1 \\ 0 & 0 & 0 & 1 & -1 & 0 & 0 & 0 \\ 0 & 0 & 0 & 1 & 0 & -1 & 0 & 0 \\ 0 & 0 & 0 & 1 & 0 & 0 & -1 & 0 \\ 0 & 0 & 0 & 0 & 1 & 0 & -1 & 0 \\ 0 & 0 & 0 & 0 & 1 & 0 & 0 & -1 \\ 0 & 0 & 0 & 0 & 0 & 1 & -1 & 0 \\ 0 & 0 & 0 & 0 & 0 & 0 & 1 & -1 \end{bmatrix}$$

For each edge the matrix element value is -1 for the first node and $+1$ for the second. As a convention, the first node is the one with the lower index. Based on Eq. 4.12, the DC matrices are:

$$\mathbf{A}_0 = \begin{bmatrix} b^4 & -a^9 & -a^{10} & -a^{11} & 0 \\ -a^9 & b^5 & 0 & -a^{12} & -a^{13} \\ -a^{10} & 0 & b^6 & -a^{14} & 0 \\ -a^{11} & -a^{12} & -a^{14} & b^7 & -a^{15} \\ 0 & -a^{13} & 0 & -a^{15} & b^8 \end{bmatrix}, \quad \mathbf{C}_0 = \begin{bmatrix} -a^4 V_0^1 - a^5 V_0^2 \\ -a^6 V_0^2 - a^7 V_0^3 \\ -a^3 V_0^1 \\ 0 \\ -a^8 V_0^3 \end{bmatrix}, \quad \mathbf{V}_0 = \begin{bmatrix} V_0^4 \\ V_0^5 \\ V_0^6 \\ V_0^7 \\ V_0^8 \end{bmatrix}$$

where the coefficients are given by Eq. 4.13.
The AC matrices for a simple electrolyte with only two ion species are:

$$\begin{bmatrix} \tilde{\mathbf{V}} \\ \tilde{\boldsymbol{\phi}}_1 \\ \tilde{\boldsymbol{\phi}}_2 \end{bmatrix} = \begin{bmatrix} \tilde{V}^4 \\ \tilde{V}^5 \\ \tilde{V}^6 \\ \tilde{V}^7 \\ \tilde{V}^8 \\ \tilde{\phi}_1^1 \\ \tilde{\phi}_1^2 \\ \tilde{\phi}_1^3 \\ \tilde{\phi}_1^4 \\ \tilde{\phi}_1^5 \\ \tilde{\phi}_1^6 \\ \tilde{\phi}_1^7 \\ \tilde{\phi}_1^8 \\ \tilde{\phi}_2^1 \\ \tilde{\phi}_2^2 \\ \tilde{\phi}_2^3 \\ \tilde{\phi}_2^4 \\ \tilde{\phi}_2^5 \\ \tilde{\phi}_2^6 \\ \tilde{\phi}_2^7 \\ \tilde{\phi}_2^8 \end{bmatrix}, \qquad \mathbf{C} = \begin{bmatrix} -c^4\tilde{V}^1 - c^5\tilde{V}^2 \\ -c^6\tilde{V}^2 - c^7\tilde{V}^3 \\ -c^3\tilde{V}^1 \\ 0 \\ -c^8\tilde{V}^3 \\ h_1^1\tilde{V}^1 - g_1^1\tilde{V}^2 \\ h_1^2\tilde{V}^2 - g_1^1\tilde{V}^1 - g_1^2\tilde{V}^3 \\ h_1^3\tilde{V}^3 - g_1^2\tilde{V}^2 \\ -g_1^4\tilde{V}^1 - g_1^5\tilde{V}^2 \\ -g_1^6\tilde{V}^2 - g_1^7\tilde{V}^3 \\ -g_1^3\tilde{V}^1 \\ 0 \\ -g_1^8\tilde{V}^3 \\ h_2^1\tilde{V}^1 - g_2^1\tilde{V}^2 \\ h_2^2\tilde{V}^2 - g_2^1\tilde{V}^1 - g_2^2\tilde{V}^3 \\ h_2^3\tilde{V}^3 - g_2^2\tilde{V}^2 \\ -g_2^4\tilde{V}^1 - g_2^5\tilde{V}^2 \\ -g_2^6\tilde{V}^2 - g_2^7\tilde{V}^3 \\ -g_2^3\tilde{V}^1 \\ 0 \\ -g_2^8\tilde{V}^3 \end{bmatrix}$$

$$
\mathbf{A} = \left[\begin{array}{ccccc|cccccccc|cccccccc}
d^4 & -c^9 & -c^{10} & -c^{11} & 0 & s_1^{1,4} & s_1^{2,4} & 0 & t_1^4 & s_1^{5,4} & s_1^{6,4} & s_1^{7,4} & 0 & s_2^{1,4} & s_2^{2,4} & 0 & t_2^4 & s_2^{5,4} & s_2^{6,4} & s_2^{7,4} & 0 \\
-c^9 & d^5 & 0 & -c^{12} & -c^{13} & 0 & s_1^{2,5} & s_1^{3,5} & s_1^{4,5} & t_1^5 & 0 & s_1^{7,5} & s_1^{8,5} & 0 & s_2^{2,5} & s_2^{3,5} & s_2^{4,5} & t_2^5 & 0 & s_2^{7,5} & s_2^{8,5} \\
-c^{10} & 0 & d^6 & -c^{14} & 0 & s_1^{1,6} & 0 & 0 & s_1^{4,6} & 0 & t_1^6 & s_1^{7,6} & 0 & s_2^{1,6} & 0 & 0 & s_2^{4,6} & 0 & t_2^6 & s_2^{7,6} & 0 \\
-c^{11} & -c^{12} & -c^{14} & d^7 & -c^{15} & 0 & 0 & 0 & s_1^{4,7} & s_1^{5,7} & s_1^{6,7} & t_1^7 & s_1^{8,7} & 0 & 0 & 0 & s_2^{4,7} & s_2^{5,7} & s_2^{6,7} & t_2^7 & s_2^{8,7} \\
0 & -c^{13} & 0 & -c^{15} & d^8 & 0 & 0 & s_1^{3,8} & 0 & s_1^{5,8} & 0 & s_1^{7,8} & t_1^8 & 0 & 0 & s_2^{3,8} & 0 & s_2^{5,8} & 0 & s_2^{7,8} & t_2^8 \\
\hline
-g_1^4 & 0 & -g_1^3 & 0 & 0 & p_1^1 & o_1^1 & 0 & o_1^4 & 0 & o_1^3 & 0 & 0 & 0 & 0 & 0 & 0 & 0 & 0 & 0 & 0 \\
-g_1^5 & -g_1^6 & 0 & 0 & 0 & o_1^1 & p_1^2 & o_1^2 & o_1^5 & o_1^6 & 0 & 0 & 0 & 0 & 0 & 0 & 0 & 0 & 0 & 0 & 0 \\
0 & -g_1^7 & 0 & 0 & -g_1^8 & 0 & o_1^2 & p_1^3 & 0 & o_1^7 & 0 & 0 & o_1^8 & 0 & 0 & 0 & 0 & 0 & 0 & 0 & 0 \\
h_1^4 & -g_1^9 & -g_1^{10} & -g_1^{11} & 0 & o_1^4 & o_1^5 & 0 & p_1^4 & o_1^9 & o_1^{10} & o_1^{11} & 0 & 0 & 0 & 0 & 0 & 0 & 0 & 0 & 0 \\
-g_1^9 & h_1^5 & 0 & -g_1^{12} & -g_1^{13} & 0 & o_1^6 & o_1^7 & o_1^9 & p_1^5 & 0 & o_1^{12} & o_1^{13} & 0 & 0 & 0 & 0 & 0 & 0 & 0 & 0 \\
-g_1^{10} & 0 & h_1^6 & -g_1^{14} & 0 & o_1^3 & 0 & 0 & o_1^{10} & 0 & p_1^6 & o_1^{14} & 0 & 0 & 0 & 0 & 0 & 0 & 0 & 0 & 0 \\
-g_1^{11} & -g_1^{12} & -g_1^{14} & h_1^7 & -g_1^{15} & 0 & 0 & 0 & o_1^{11} & o_1^{12} & o_1^{14} & p_1^7 & o_1^{15} & 0 & 0 & 0 & 0 & 0 & 0 & 0 & 0 \\
0 & -g_1^{13} & 0 & -g_1^{15} & h_1^8 & 0 & 0 & o_1^8 & 0 & o_1^{13} & 0 & o_1^{15} & p_1^8 & 0 & 0 & 0 & 0 & 0 & 0 & 0 & 0 \\
\hline
-g_2^4 & 0 & -g_2^3 & 0 & 0 & 0 & 0 & 0 & 0 & 0 & 0 & 0 & 0 & p_2^1 & o_2^1 & 0 & o_2^4 & 0 & o_2^3 & 0 & 0 \\
-g_2^5 & -g_2^6 & 0 & 0 & 0 & 0 & 0 & 0 & 0 & 0 & 0 & 0 & 0 & o_2^1 & p_2^2 & o_2^2 & o_2^5 & o_2^6 & 0 & 0 & 0 \\
0 & -g_2^7 & 0 & 0 & -g_2^8 & 0 & 0 & 0 & 0 & 0 & 0 & 0 & 0 & 0 & o_2^2 & p_2^3 & 0 & o_2^7 & 0 & 0 & o_2^8 \\
h_2^4 & -g_2^9 & -g_2^{10} & -g_2^{11} & 0 & 0 & 0 & 0 & 0 & 0 & 0 & 0 & 0 & o_2^4 & o_2^5 & 0 & p_2^4 & o_2^9 & o_2^{10} & o_2^{11} & 0 \\
-g_2^9 & h_2^5 & 0 & -g_2^{12} & -g_2^{13} & 0 & 0 & 0 & 0 & 0 & 0 & 0 & 0 & 0 & o_2^6 & o_2^7 & o_2^9 & p_2^5 & 0 & o_2^{12} & o_2^{13} \\
-g_2^{10} & 0 & h_2^6 & -g_2^{14} & 0 & 0 & 0 & 0 & 0 & 0 & 0 & 0 & 0 & o_2^3 & 0 & 0 & o_2^{10} & 0 & p_2^6 & o_2^{14} & 0 \\
-g_2^{11} & -g_2^{12} & -g_2^{14} & h_2^7 & -g_2^{15} & 0 & 0 & 0 & 0 & 0 & 0 & 0 & 0 & 0 & 0 & 0 & o_2^{11} & o_2^{12} & o_2^{14} & p_2^7 & o_2^{15} \\
0 & -g_2^{13} & 0 & -g_2^{15} & h_2^8 & 0 & 0 & 0 & 0 & 0 & 0 & 0 & 0 & 0 & 0 & o_2^8 & 0 & o_2^{13} & 0 & o_2^{15} & p_2^8
\end{array}\right]
$$

4.5 Model validation and comparisons with GFEM

4.5.1 1D system CVFEM/GFEM comparison

Given the complexity of the endeavour, a structured verification strategy has been deployed to validate ENBIOS in a variety of simple cases and to compare it to the established GFEM approach. In particular, we will compare CVFEM and GFEM in a 3D rectangular prism domain which consists of a uniform region (100 nm long in the z direction) with a square cross section of 10 nm edge (Fig. 4.5). All the quantities are expect to depend only on z like in a 1D case. We point out that, although the system is by construction 1D, the mesh is fully 3D. The simple 1D model described in Sec. 3.1 has thus been used for verification. The maximum spacing is set uniform in the entire region and it is the same in all 3 spatial directions. The electrolyte is 1:1 symmetric with mobility of the two species equal to 3.24×10^{11} m/Ns. The permittivity is calculated as a function of the salt concentration according to [48], while its dependence on the frequency is neglected, since it will become important only over 1 GHz, i.e., frequencies not accessible by state of the art hardware [33]. The bottom electrode is always ideally polarizable, while the top electrode is Faradaic in DC and ideally polarizable in AC. The validation and comparison between CVFEM and GFEM will be first made for a DC problem, then we will move to an AC problem with no DC bias applied. For both these cases exact analytical solutions to compare with [36, 1] have been given in Secs. 3.1.3-3.1. Then we will compare CVFEM and GFEM on an AC problem with a DC bias applied. Since CVFEM falls in the family of the Finite Volume methods, we expect the convergence behaviour reported in the literature for the latter methods [64, 72] to be valid also for CVFEM.

DC problem Under DC bias conditions the reference analytical solution is given by the Gouy-Chapman model [36] (see also Sec. 3.1.3), which reads:

$$V_0 = \frac{4k_BT}{q}\tanh^{-1}\left(\tanh\left(\frac{q\left(V_B - V_{ref}\right)}{4k_BT}\right)e^{-\frac{z}{\lambda_D}}\right) \tag{4.46}$$

where $\lambda_D = \sqrt{\varepsilon k_B T/2n^\infty q^2}$ is the Debye length and V_B is the potential at the bottom electrode. The model assumes that the potential on the opposite electrode is equal to V_{ref}, so that the double layer is formed only at the bottom electrode, and that the electrodes are very far away from each other (in practice more than a few λ_D). In the following we will always assume $V_{ref} = 0$ V.
Fig. 4.6 shows the difference δV_0 between Eq. 4.46 and the simulations performed with the 3D code for a few V_B and bulk salt concentration n^∞. The solution is calculated on

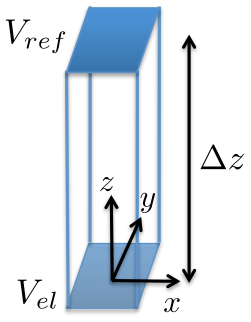

Fig 4.5: Sketch of the 1D system used to compare CVFEM and GFEM solvers. The domain is filled by a 1:1 symmetric electrolyte.

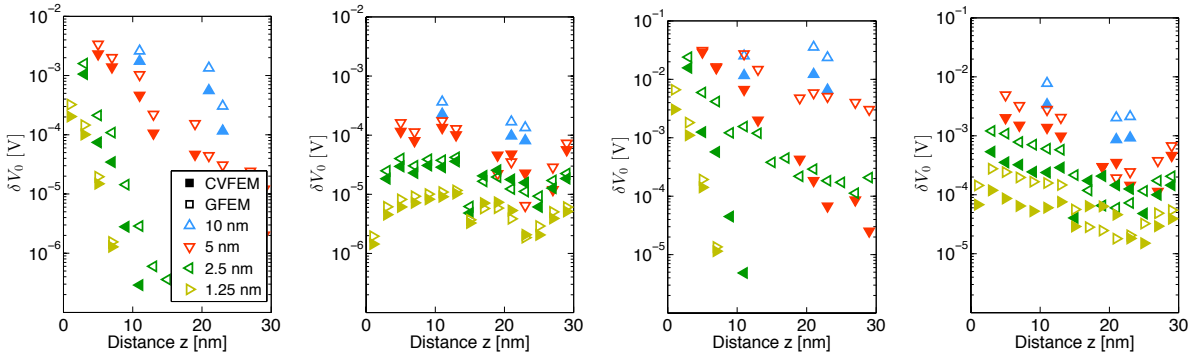

(a) 150 mM, 10 mV **(b)** 1.5 mM, 10 mV **(c)** 150 mM, 100 mV **(d)** 1.5 mM, 100 mV

Fig 4.6: Error δV_0 in the potential profile calculated using the CVFEM (filled symbols) or the GFEM (empty symbols) with respect to the analytical Gouy-Chapman solution [36] for the 1D system (Eq. 4.46) at different height above the bottom electrode and for four meshes with maximum spacing equal to 10, 5, 2.5, 1.25 nm. The calculations refer to different bulk salt concentration and the potential applied at one electrode.

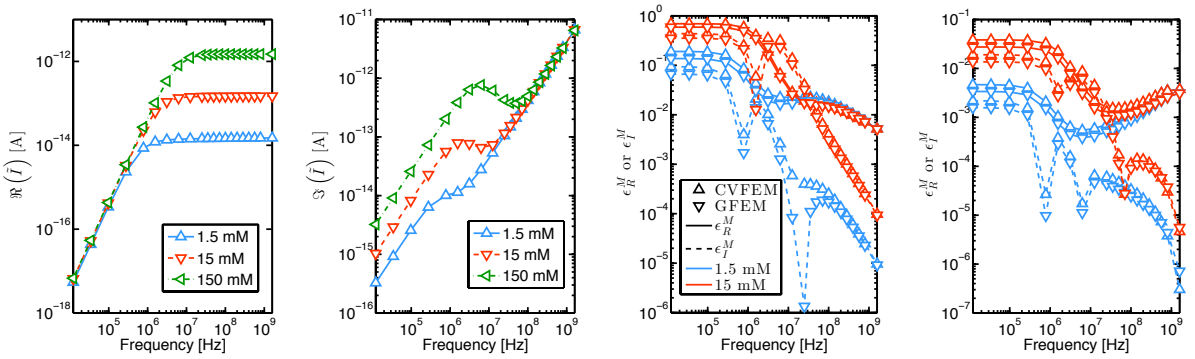

(c) 10 nm **(d)** 1.25 nm

Fig 4.7: Real and imaginary parts of the small signal current versus frequency (left) and relative difference between the real and imaginary parts of the simulated current and the analytical model of [1] for a 1D system of 100 nm length and 100 nm^2 area, with a maximum mesh node spacing of 10 nm (c) or 1.25 nm (d). No DC bias is applied.

4 different meshes, corresponding to decreasing mesh size. Noting that $\lambda_D = 8$ nm at 1.5 mM and $\lambda_D = 0.8$ nm at 150 mM, we see that CVFEM and GFEM solutions match very closely when the grid is sufficiently refined (b-d). This is consistent with the findings of [63] for linear problems, but in our case there is still a slight advantage of CVFEM. On the other hand, on coarse grids (a-c) CVFEM offers a greater advantage with respect to GFEM, especially when the non-linearity is stronger (c) because of a larger applied DC bias. This indicates also that the convergence of the non-linear solver in the GFEM case is more difficult than in the CVFEM case. Since the only coefficients that differ between CVFEM and GFEM are the ones in $\mathbf{Q}_{0el}$, we have to compare the non-linear integral calculations. To this purpose, a direct comparison of the 0th order and of the cubic terms in Eqs. 4.57-4.58 shows that CVFEM weights more the value v_0 than v_i with respect to GFEM, an observation that contributes to explain the slightly different results provided by the two methods.

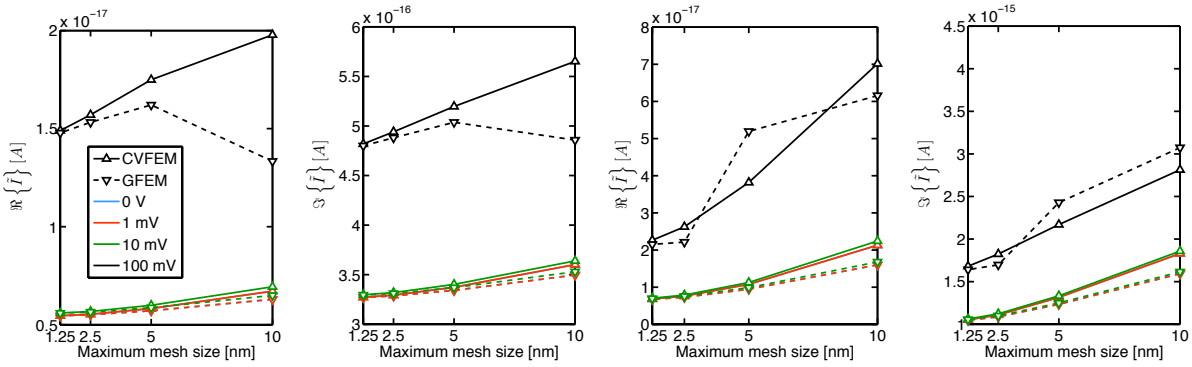

(a) 1.5 mM **(b)** 1.5 mM **(c)** 15 mM **(d)** 15 mM

Fig 4.8: Convergence of the real and imaginary parts of the current varying the maximum mesh spacing at two different bulk salt concentrations and for different potential applied at one electrode. The simulations are made at a frequency of 12 kHz. $\lambda_D = 8$ nm at 1.5 mM and 2.5 nm at 15 mM.

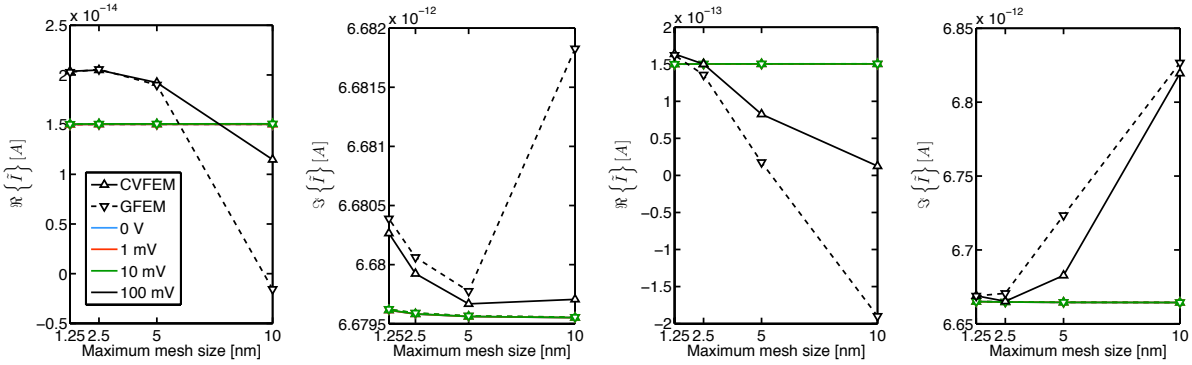

(a) 1.5 mM **(b)** 1.5 mM **(c)** 15 mM **(d)** 15 mM

Fig 4.9: Same as Fig. 4.8 but at a frequency of 1.6 GHz.

AC problem Since our simulation tool is designed to study impedimetric biosensors, and in particular nanoelectrode based capacitive biosensor, the first desired output of the simulation is the small-signal admittance Y_i at each contact electrode i, which is simply calculated from the contact current $\tilde{I}_i$:

$$Y_i \triangleq \frac{\tilde{I}_i}{\tilde{V}_{el}} = G_i + j\omega C_i$$

where all the contacts are either grounded or biased at the voltage $\tilde{V}_{el}$.
We assume here that no DC bias is applied, and we use as a benchmark the analytical solution of the model equations presented in [1]. Fig. 4.7 (two leftmost graphs) shows the real and imaginary parts of the current spectra at the contacts for three different salt concentrations. We define ϵ_R^M and ϵ_I^M as the relative difference between the analytical model [1] and the simulation of the real and imaginary parts of the current respectively. As we see from Fig. 4.7c, ϵ_R^M and ϵ_I^M are not negligible at low frequency, since in this case the maximum spacing is always greater than or at most comparable to the Debye length (8 nm at 1.5 mM and 2.5 nm at 15 mM). We point out, however, that at low frequency the current itself is very small and that the error decreases greatly when increasing the frequency, since the ions start to be not fast enough to follow the field oscillations. At high

frequency then ϵ_R^M tends to a constant and ϵ_I^M is very small because the solution tends to be that of a conventional Laplace equation, which is linear and therefore solved exactly (up to machine precision) by both methods. We also note that CVFEM and GFEM are very close to each other, while GFEM offers a modest advantage in terms of error with the analytical model. This is again consistent with the findings of [63]. If we now compare the AC coefficients of GFEM and CVFEM reported in Eqs. 4.22-4.54 at zero DC bias (hence constant n_{0m}) by using Eqs. 4.29-4.55, we see that CVFEM weights more the value of the potentials around node n^j than around the neighbor nodes with respect to GFEM, as previously observed for the DC case. Upon mesh refinement (Fig. 4.7d), provided the maximum mesh size h is always smaller than the Debye length, CVFEM and GFEM the errors at low frequency reduce with dependence $O(h^2)$, both in real and imaginary parts.

AC problem with DC bias We also simulated a case similar to the previous one, but we also apply a DC bias at the bottom electrode. In this case a reference analytical solution is not available. Figs. 4.8 - 4.9 show the convergence of the real and imaginary parts of the current at low (12 kHz) and high (1.6 Ghz) frequency as a function of the DC potential V_B applied at the electrode and of the bulk salt concentration n^∞. For reference the electrolyte cut-off frequency is 3.5 and 350 MHz for $n^\infty = 1$ and 100 mM. As we see (Fig. 4.8), at low frequency and at high DC bias the CVFEM converges more regularly with the mesh refinement than in the case of GFEM. The real and imaginary parts behave similarly between each other.
From Fig. 4.9 we see that, at high frequency, the convergence on the imaginary part of the current is very rapid, as shown also in the previous paragraph. Also the real part is converging well, except at high DC bias, where the GFEM can sometimes give incorrect results on coarse grids (change of sign of the current in Fig. 4.9a-c). Overall, the CVFEM proves also in this case to have a better convergence behaviour than the GFEM especially on coarse grids and with a DC bias.

4.5.2 Nanoelectrode array

We report in this section a comparison between ENBIOS and the results obtained with GFEM for a realistic biosensor. In particular, we consider the CMOS integrated nanoelectrode array presented in [33] (see the sketch in Fig. 5.3), where one row of electrodes is polarized at a potential V_{el} and the remaining ones are grounded, thus constituting a counter electrode. The current is measured individually at each electrode. First of all we consider a small array of 3×3 electrodes of 20nm radius with pitch 70nm and 80nm in the x and y directions respectively. Such dimensions are not representative of the real array [33], but are needed in order to keep the number of mesh points to a reasonable level and to test the convergence. In fact, we set a mesh maximum spacing of 10nm in the proximity of the electrodes, and we uniformly refine the entire mesh twice, therefore increasing each time by 8 the number of mesh points. Fig. 4.10 shows the convergence of the current at the central electrode as a function of the mesh size for different DC bias and salt concentrations. The results are very similar to the ones in Figs. 4.8-4.9.

4.5.3 Site-binding model

In this section we report the verification of the implementation of the DC site-binding surface charge model (Eq. 2.11). The AC site-binding model (Eq. 2.33) has not been implemented in the current version of the code yet.

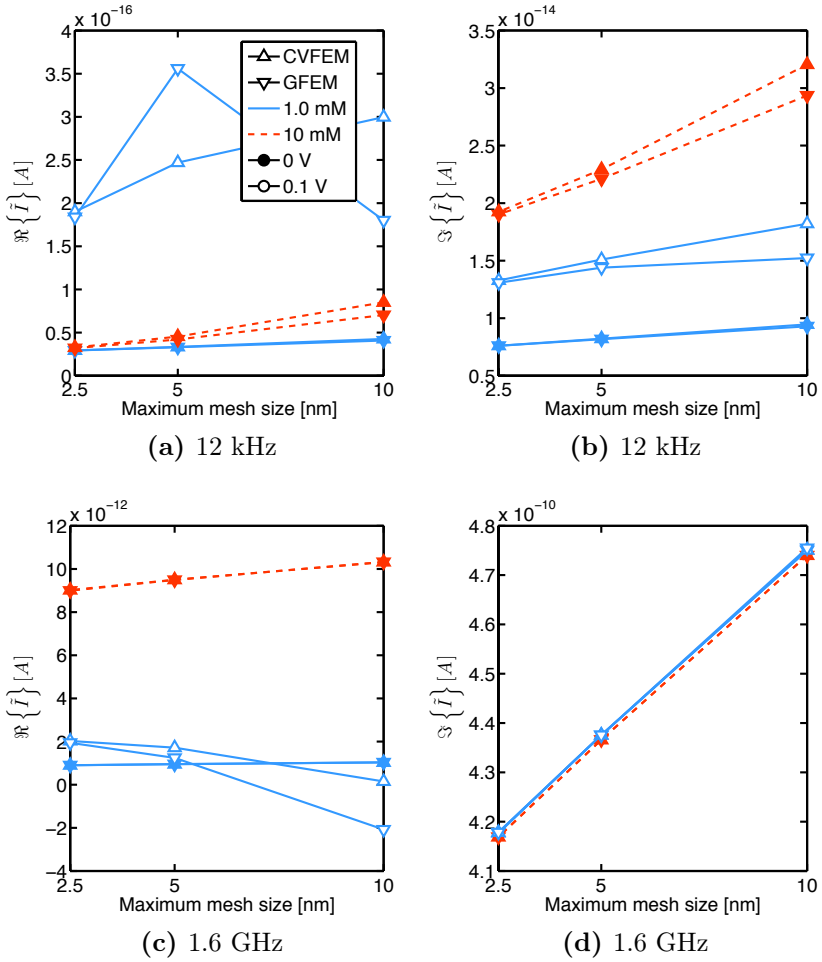

(a) 12 kHz **(b)** 12 kHz

(c) 1.6 GHz **(d)** 1.6 GHz

Fig 4.10: Nanoelectrode array - Convergence of the real and imaginary parts of the current at the central electrode varying the maximum mesh spacing in the electrodes proximity at two different bulk salt concentrations and for different potential applied at the central electrode row. The curves at very low DC bias are typically one on top of the other, so they are not visible. λ_D = 9.6 nm at 1 mM and 3 nm at 10 mM.

We then simulate a simple 1D system similar to that of Fig. 4.5, where an additional oxide with $t_{ox} = 3$ nm thickness and a compact layer (CL) with $t_{CL} = 0.25$ nm on top cover the bottom electrode. In these conditions an analytical model for the potential profile in the structure can be derived and used as reference to compare with simulations. We use again the Gouy-Chapman model (Eq. 4.46) and denote V_0 the potential at the CL/electrolyte interface, and V_{ox} the potential at the oxide/CL interface. In these conditions, by imposing the continuity of potential and dielectric displacement at the interfaces and the linearity of the potential profiles across the oxide and CL (both assumed as ideal dielectrics), besides the SB charge model of Eq. 2.11, we get the following system of equations:

$$\sigma_{SB}(V_{ox}) = \frac{\varepsilon_{ox}}{t_{ox}}(V_{ox} - V_{el}) - \frac{\varepsilon_{CL}}{t_{CL}}(V_0 - V_{ox}) \tag{4.47a}$$

$$0 = \frac{\varepsilon_{CL}}{t_{CL}}(V_0 - V_{ox}) + \sqrt{8k_BTn_0\varepsilon_{el}}\sinh\left(\frac{qV_{el}}{2k_BT}\right) \tag{4.47b}$$

This system of equations has to be solved numerically to calculate V_0 and V_{ox}. Note that we have decided to place the SB charge at the oxide/CL interface, consistently with the results in [55].

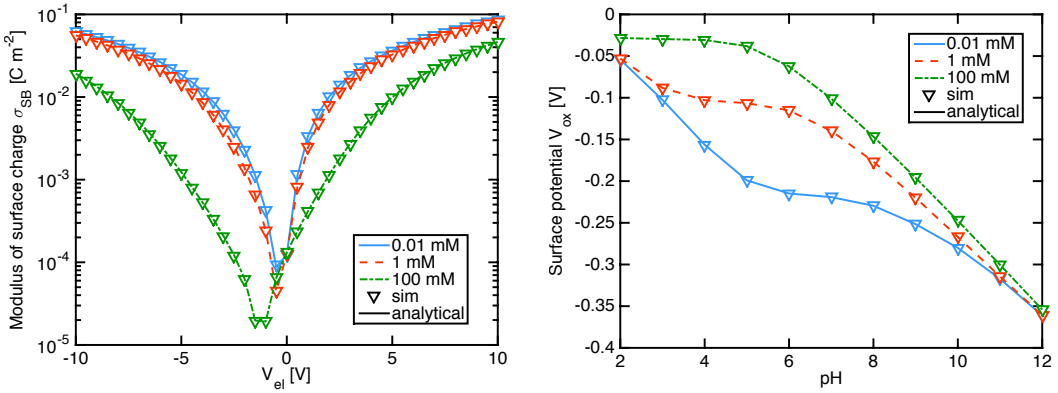

(a) pH = 3 **(b)** $V_{el} = 0$ V

Fig 4.11: Comparison between simulations (symbols) and the model of Eq. 4.47 (lines). The agreement is excellent in all conditions, demonstrating the correct and accurate implementation of SBC in ENBIOS.

Fig. 4.11 shows the comparison between the simulations versus V_{el} (a) and pH (b) and the model. In this case we decided not to simulate explicitly the pH, that is to sum the H^+ and OH^- concentrations to the K^+ and Cl^- concentrations, respectively, so that we could consider a 1:1 electrolyte with one cation and one anion species. The information about the pH is however necessary to correctly compute σ_{SB}.
We see that the agreement between simulations and the analytical model is excellent, both considering the value of σ_{SB} and of the surface potential V_{ox}, at all salt concentrations, pHs and DC bias.

4.6 Use of commercial TCAD

An alternative approach to the simulation of nanoelectronic biosensors, instead of the development of ad-hoc numerical models, would be the use of available TCAD tools such as, for instance, Sentaurus Device [35]. On the one hand, TCAD offers detailed and accurate models for the semiconductors and the capability to handle complex and arbitrary device geometries. However, at the time of writing this thesis, commercial TCAD is not equipped to model electrolytes or buffer solutions.
In order to expand the applicability of TCAD to biosensors, a simple technique has been developed to include an "electrolyte material" region into the commercial TCAD simulator Sentaurus Device [35]; this approach trades a simplified description of the electrolyte for the possibility to exploit the above mentioned pros of the TCAD. Most of the results reported in this section have been presented in [6]. We have obtained further results by implementing also the site-binding model in TCAD [7], but these are not shown here since the work has been mostly carried out by another student.

Our approach exploits the similarity between the equations describing positive and negative ions in the electrolyte and those for holes and electrons in a semiconductor. In this respect, a 1:1 electrolyte can be described in SDevice as a semiconductor (that we call "electrolyte material") with zero gap, a constant permittivity and an effective density of states in conduction and valence band:

$$N_C = N_V = N_A n_0 \times 10^{-3} \tag{4.48}$$

where N_A is Avogadro's number and n_0 the ion molar concentration (M=mol/l) in the bulk of the solution, defined as a region where we have the same concentration of positive and

negative ions, hence overall charge neutrality. Setting $E_G = 0$ implies $np = N_C N_V$. The electron and hole mobility in this "electrolyte material" is adjusted to the corresponding values of the ions [52]. Care should be paid to disable the default temperature dependence of the model parameters and to avoid the build-up of unphysical offsets in N_C, N_V, E_G and mobility whenever the temperature is different from the model reference value.

The proposed approach allows us to easily exploit all the features of the TCAD, such as: calibrated mobility models for silicon, multiple type of analysis and the handling of arbitrary geometries in 2D and in 3D. Clearly, there are limitations as well. First of all, only a single 1:1 ionic solution can be included, whereas electrolytes with many types of ions and diversified valence are used in experiments; this point will be discussed in the next section. In addition, only idealized interfaces without steric effects [53] and without surface reactions [42] can be treated. The control on the numerical error is also quite limited with respect to ad-hoc codes developed for the modelling of electrolyte screening, such as ENBIOS. The work presented in this dissertation goes well beyond the similar model in [73] by proposing strategies to account for steric effects, solutions with multi-ions, water molecule polarizability at the interfaces.

4.6.1 Equivalent 1:1 electrolyte

One of the basic assumptions behind the TCAD approach proposed is that the electrolyte must be symmetric with ion species of unit valence. In real world, however, most biosensors operate with multi-ion electrolytes and buffer solutions featuring several ion species of diverse valence. For instance, a commonly used Phosphate Buffered Saline (PBS) in biosensor research is composed of four salts: potassium dihydrogen phosphate (KH_2PO_4), disodium hydrogen phosphate (Na_2HPO_4), sodium chloride (NaCl) and potassium chloride (KCl). At the bulk concentration $n_0 = 248.4$ mM and the temperature $T = 300$ K, the dissociation leads to the following distribution of ion concentrations: $K^+ = 45$ mM, $H_2PO_4^- = 18$ mM, $Na^+ = 203.4$ mM, $HPO_4^{2-} = 101$ mM, $Cl^- = 28.4$ mM. The description of such a complex electrolyte would be time consuming in ad-hoc simulators as ENBIOS and actually impossible in state of the art TCAD tools , but it could be greatly simplified if we could introduce an *equivalent electrolyte* composed only of two monovalent ion species, one cation and one anion. To understand the accuracy limitations of such a simplification, we firstly note that in DC conditions, under the assumption of a dilute electrolyte with non-interacting ion species, the Gouy-Chapman theory predicts that the potential profile decays with characteristic length equal to the Debye length (λ_D) [74]:

$$\lambda_D = \sqrt{\frac{\varepsilon k_B T}{\sum_{m_a} (Z_m q)^2 n_{0m} + \sum_{m_c} (Z_m q)^2 n_{0m}}} \tag{4.49}$$

where we have separated the contributions of the anions, in number m_a, from that of the cations, in number m_c. The biosensor response is determined by the screening properties of the electrolyte and since the latter are defined by the Debye length (Eq. 4.49), then it makes sense to define the ion concentration of the equivalent electrolyte in such a way that its Debye length is the same as the one of the actual electrolyte. We will assume, in general, that the equivalent electrolyte has an unsigned valence Z_a for the anions and unsigned valence Z_c for the cations. Imposing the equivalence of the Debye lengths and the bulk charge neutrality for the equivalent electrolyte, we have the following system of equations:

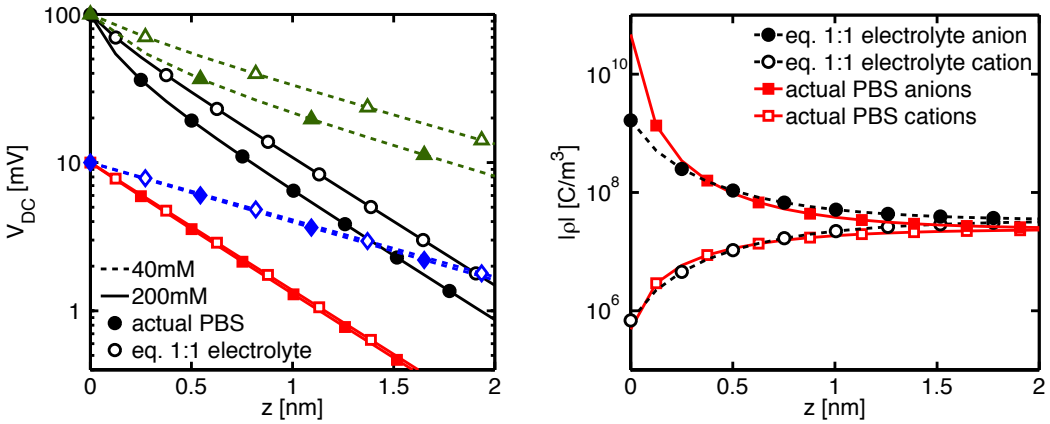

Fig 4.12: Comparison of potential profiles (left) and absolute charge density profiles of anions and cations (right) between the PBS solution with $F_a \neq F_c$ (filled symbols) and the equivalent electrolyte with unit valence (open symbols). The curves in the left plot correspond to $n_0 = 40$ mM (dashed lines) and 200 mM (solid lines) and $V_{DC} = 10$ mV and 100 mV, while in the right plot $V_0 = 100$ mV and $n_0 = 200$ mM. We verified explicitly that the mutual agreement at high V_{DC} is much improved if an equivalent electrolyte with $Z = 2$ is chosen (not shown). Unfortunately this is not possible in commercial TCAD.

$$\begin{cases} \sum_{m_a} Z_m^2 n_{0m} = Z_a^2 n_{0a} \\ \sum_{m_c} Z_m^2 n_{0m} = Z_c^2 n_{0c} \\ Z_a n_{0a} = Z_c n_{0c} \end{cases} \quad \Rightarrow \quad \begin{cases} n_{0a} = \frac{F_a}{Z_a^2} \\ n_{0c} = \frac{F_c}{Z_c^2} \\ Z_a = \frac{F_a}{F_c} Z_c \end{cases} \tag{4.50}$$

where $F_a = \sum_{m_a} Z_m^2 n_{0m}$ and $F_c = \sum_{m_c} Z_m^2 n_{0m}$. As expected the system is underdetermined and one free parameter (either Z_a or Z_c) remains. We also note that if an integer Z_c is chosen, then Z_a may not be an integer number, and that only if $F_a = F_c$ then the equivalent electrolyte has symmetric valence $Z{:}Z$ and concentrations $n_{0a} = n_{0c}$. Consequently, only in this case it is possible to assume unit valence and then also exactly represent the actual electrolyte with an equivalent one having $n_{0a} = F_a$ and $n_{0c} = F_c$ by setting the corresponding effective density of states according to Eq. 4.50. The PBS solution we introduced before fulfills the charge neutrality condition but it does not fulfil the condition $F_a = F_c$. Therefore, it cannot be modeled exactly with an equivalent electrolyte of unit valence. In this case we have decided to use a mean of F_a and F_c in Eq. 4.50, namely $F_M = (F_a + F_c)/2$.

To quantify the error induced in the solution, we report in the left plot of Fig. 4.12 the mean field electrostatic potential profiles across a simple electrolyte slab such as that in Fig. 4.5 for two values of n_0 and two values of V_0. The right plot shows the corresponding charge density profiles due to anions and cations at $V_0 = 100$ mV and $n_0 = 200$ mM. All the simulations were made using our full-custom Poisson-Boltzmann solver ENBIOS. As expected, the symmetric 1:1 electrolyte does not exactly mimic the real PBS, but in this case the maximum error on the potential is at most a fraction of $k_B T/q$. We also note that the charge profile of the real electrolyte is squeezed toward the interface more than that of the equivalent electrolyte. This is because the solution has a large component, both in cations and in anions, of ions with valence modulus 2, hence it has a shorter Debye length.

To understand in detail the derivations above, we simulated an hypothetical buffer solution with composition: $K^+ = 45$ mM, $H_2PO_4^- = 18$ mM, $Ca^{2+} = 101.4$ mM, $HPO_4^{2-} = 101.4$ mM, $Na^+ = 1.4$ mM, $Cl^- = 28.4$ mM, where we have replaced some Na^+ with Ca^{2+}

in order satisfy the condition $F_a = F_c$. The equivalent electrolyte was chosen to be 1:1 symmetric, as the one simulated by the TCAD. In this case the agreement between simulations with the actual and the equivalent electrolyte is improved but there is still a small error. If we then use a valence of 2 instead of 1 in the equivalent electrolyte, in particular if the valence of the symmetric species of the equivalent electrolyte is chosen to be equal to the one of the ion species dominating the composition of the buffer, we can obtain an almost perfect agreement between simulations with the actual and the equivalent electrolyte. Unfortunately, it is not possible in TCAD to change the electron and hole charges so as to mimic valence values different from 1. Therefore the accuracy of TCAD simulations is inherently limited by the small errors exemplified in Fig. 4.12.

4.7 Summary

In this chapter we have developed and validated a numerical simulator ENBIOS for nanoelectronic biosensors. ENBIOS relies on the models described in Chap. 2, which have been solved on general 3D unstructured tetrahedral grids using for the first time the Control Volume Finite Element Method. Particular care has been given to calculate accurately the currents at the electrodes in order to retain the method's global conservation, hence the accuracy on current calculations, that is needed to compute the tiny admittance changes due to the introduction of small molecules in the domain. We have also discussed in detail the methods for the calculations of surface and volume integrals, with respect to accuracy and computational speed. In fact, the presence of highly non linear (exponential) terms poses unique and delicate accuracy problems in the evaluation of these integrals.
The implementation has been validated against the analytical models described in Chap. 3. A comparison with the standard Galerkin Finite Element Method is also discussed, showing that CVFEM offers an advantage, especially for coarse grids. This in turn entails the possibility to use CVFEM with less refined grids than GFEM.

Finally, we have shown a procedure to use a commercial TCAD for semiconductor devices (Sentaurus Device, which does not natively support the electrolyte environment, Sec. 4.6) to describe electrolytes. Despite the successful results, the inherent limitations of TCAD prevent this approach to be widely applicable to all classes of biosensors. This further justifies our need of developing an ad-hoc instrument like ENBIOS.

4.A Appendices

4.A.1 Jacobians for DC equations

The non-linear Jacobian components of Poisson equation $J_P^{j,V_0^j} = \partial Q_{0el}^j/\partial V_0^i$, $J_P^{j,V_0^l} = \partial Q_{0el}^j/\partial V_0^j$, $J_P^{j,\phi_{0m}^j} = \partial Q_{0el}^j/\partial \phi_{0m}^i$ and $J_P^{j,\phi_{0m}^l} = \partial Q_{0el}^j/\partial \phi_{0m}^j$ are calculated as:

$$J_P^{j,V_0^j} = -\sum_{m=1}^{N_{sp}} \frac{Z_m^2 q^2}{k_B T} n_m^\infty \sum_{k\in\Upsilon^j} \int_{\Omega_c^{j,k}} N^{j,k} \exp\left(\frac{Z_m q}{k_B T}\left(N^j\left(\phi_{0m}^j - V_0^j\right) + \sum_{i\in\Lambda^j} N^i\left(\phi_{0m}^i - V_0^i\right)\right)\right) d\Omega \tag{4.51a}$$

$$J_P^{j,V_0^l} = -\sum_{m=1}^{N_{sp}} \frac{Z_m^2 q^2}{k_B T} n_m^\infty \sum_{k\in\Upsilon^{j,l}} \int_{\Omega_c^{j,k}} N^{l,k} \exp\left(\frac{Z_m q}{k_B T}\left(N^j\left(\phi_{0m}^j - V_0^j\right) + \sum_{i\in\Lambda^j} N^i\left(\phi_{0m}^i - V_0^i\right)\right)\right) d\Omega \tag{4.51b}$$

$$J_P^{j,\phi_{0m}^j} = \frac{Z_m^2 q^2}{k_B T} n_m^\infty \sum_{k\in\Upsilon^j} \int_{\Omega_c^{j,k}} N^{j,k} \exp\left(\frac{Z_m q}{k_B T}\left(N^j\left(\phi_{0m}^j - V_0^j\right) + \sum_{i\in\Lambda^j} N^i\left(\phi_{0m}^i - V_0^i\right)\right)\right) d\Omega \tag{4.51c}$$

$$J_P^{j,\phi_{0m}^l} = \frac{Z_m^2 q^2}{k_B T} n_m^\infty \sum_{k\in\Upsilon^{j,l}} \int_{\Omega_c^{j,k}} N^{l,k} \exp\left(\frac{Z_m q}{k_B T}\left(N^j\left(\phi_{0m}^j - V_0^j\right) + \sum_{i\in\Lambda^j} N^i\left(\phi_{0m}^i - V_0^i\right)\right)\right) d\Omega \tag{4.51d}$$

Note that for the nodes in the electrolyte ϕ_{0m} is not a variable because it is equal to V_{ref}, therefore we do not need to calculate J_P^{j,ϕ_{0m}^j} and J_P^{j,ϕ_{0m}^l}.

The Jacobians of the current equation in the first formulation are:

$$J_{Cm}^{j,V_0^j} = -\frac{Z_m q}{k_B T} \sum_{i\in\Lambda^j} \phi_{0m}^i \sum_{k\in\Upsilon^{i,j}} \varepsilon^k \int_{\Gamma^{j,k}} N^{j,k} \exp\left(\frac{Z_m q}{k_B T} \sum_{i\in\Lambda^{j,k}} N^{i,k}\left(\phi_{0m}^i - V_0^i\right)\right) \nabla N^{i,k}\cdot\hat{n}\, d\Gamma \tag{4.52a}$$

$$J_{Cm}^{j,V_0^l} = -\frac{Z_m q}{k_B T} \sum_{i\in\Lambda^{j,l}} \phi_{0m}^i \sum_{k\in\Upsilon^{i,j,l}} \varepsilon^k \int_{\Gamma^{j,k}} N^{l,k} \exp\left(\frac{Z_m q}{k_B T} \sum_{i\in\Lambda^{j,k}} N^{i,k}\left(\phi_{0m}^i - V_0^i\right)\right) \nabla N^{i,k}\cdot\hat{n}\, d\Gamma \tag{4.52b}$$

$$\begin{aligned} J_{Cm}^{j,\phi_{0m}^j} = &\sum_{k\in\Upsilon^j} \varepsilon^k \int_{\Gamma^{j,k}} \exp\left(\frac{Z_m q}{k_B T} \sum_{i\in\Lambda^{j,k}} N^{i,k}\left(\phi_{0m}^i - V_0^i\right)\right) \nabla N^{j,k}\cdot\hat{n}\, d\Gamma \\ &+ \frac{Z_m q}{k_B T} \sum_{i\in\Lambda^j} \phi_{0m}^i \sum_{k\in\Upsilon^{i,j}} \varepsilon^k \int_{\Gamma^{j,k}} N^{j,k} \exp\left(\frac{Z_m q}{k_B T} \sum_{i\in\Lambda^{j,k}} N^{i,k}\left(\phi_{0m}^i - V_0^i\right)\right) \nabla N^{i,k}\cdot\hat{n}\, d\Gamma \end{aligned} \tag{4.52c}$$

$$J_{Cm}^{j,\phi_{0m}^l} = \sum_{k\in\Upsilon^{j,l}} \varepsilon^k \int_{\Gamma^{j,k}} \exp\left(\frac{Z_m q}{k_B T} \sum_{i\in\Lambda^{j,k}} N^{i,k}\left(\phi_{0m}^i - V_0^i\right)\right) \nabla N^{l,k}\cdot\hat{n}\, d\Gamma$$

$$+\frac{Z_m q}{k_B T}\sum_{i\in\Lambda^{j,l}}\phi^i_{0m}\sum_{k\in\Upsilon^{i,j,l}}\varepsilon^k\int_{\Gamma^{j,k}}N^{l,k}\exp\left(\frac{Z_m q}{k_B T}\sum_{i\in\Lambda^{j,k}}N^{i,k}\left(\phi^i_{0m}-V^i_0\right)\right)\nabla N^{i,k}\cdot\hat{n}\,d\Gamma \tag{4.52d}$$

The Jacobians of the current equation according to the second formulation are:

$$J^{j,V^j_0}_{Cm}=-\frac{Z_m q}{k_B T}\sum_{k\in\Upsilon^j}\varepsilon^k\Omega^{j,k}_c\left(\sum_{i\in\Lambda^{j,k}}\phi^i_{0m}\nabla N^{i,k}\right)\cdot\nabla N^{j,k} \tag{4.53a}$$

$$J^{j,V^l_0}_{Cm}=-\frac{Z_m q}{k_B T}\sum_{k\in\Upsilon^{j,l}}\varepsilon^k\Omega^{j,k}_c\left(\sum_{i\in\Lambda^{j,k}}\phi^i_{0m}\nabla N^{i,k}\right)\cdot\nabla N^{l,k} \tag{4.53b}$$

$$J^{j,\phi^j_{0m}}_{Cm}=\frac{Z_m q}{k_B T}\sum_{k\in\Upsilon^j}\varepsilon^k\Omega^{j,k}_c\nabla N^{j,k}\cdot\left(\sum_{i\in\Lambda^{j,k}}\left(2\phi^i_{0m}-V^i_0\right)\nabla N^{i,k}\right)+\sum_{k\in\Upsilon^j}\varepsilon^k\Gamma^{j,k}\cdot\nabla N^{j,k} \tag{4.53c}$$

$$J^{j,\phi^l_{0m}}_{Cm}=\frac{Z_m q}{k_B T}\sum_{k\in\Upsilon^{j,l}}\varepsilon^k\Omega^{j,k}_c\nabla N^{l,k}\cdot\left(\sum_{i\in\Lambda^{j,k}}\left(2\phi^i_{0m}-V^i_0\right)\nabla N^{i,k}\right)+\sum_{k\in\Upsilon^{j,l}}\varepsilon^k\Gamma^{j,k}\cdot\nabla N^{l,k} \tag{4.53d}$$

4.A.2 On the equivalence of CVFEM and GFEM

Here we prove that, in our specific case where the control volumes are defined with reference to the centroids of the edges and faces, and the basis functions are linear, discretized Poisson coefficients are exactly equal in GFEM and CVFEM. Similar conclusions have been found in [64] for the Box method. Starting from:

$$\begin{aligned}\int_{v^k}\nabla N^{j,k}\cdot\nabla N^{i,k}d\Omega&=\int_{\Gamma^k}N^{j,k}\nabla N^{i,k}\cdot\hat{n}\,d\Gamma-\int_{v^k}N^{j,k}\nabla\cdot\nabla N^{i,k}d\Omega\\&=\int_{\Gamma^k}N^{j,k}\nabla N^{i,k}\cdot\hat{n}\,d\Gamma\quad,\end{aligned}$$

where Γ^k is the surface of the tetrahedron k, we need to prove that:

$$\sum_{l=1}^{3}\int_{\Gamma^{j,k}_l}\nabla N^{i,k}\cdot\hat{n}\,d\Gamma=-\sum_{l=0}^{3}\int_{\Gamma^k_l}\nabla N^{i,k}\cdot\hat{n}\,N^{j,k}d\Gamma$$

that is:

$$\begin{aligned}&|\det(\mathbf{J})|\,\nabla N^{i,k}\cdot\mathbf{J}^{-T}\sum_{l=1}^{3}\left(\frac{\partial\vec{\hat{r}}_l}{\partial\xi}\times\frac{\partial\vec{\hat{r}}_l}{\partial\eta}\right)\int_{\hat{\Gamma}_l}d\eta\,d\xi=\\&-|\det(\mathbf{J})|\,\nabla N^{i,k}\cdot\mathbf{J}^{-T}\sum_{l=0}^{3}\left(\frac{\partial\vec{\hat{r}}_{Pl}}{\partial\Xi_1}\times\frac{\partial\vec{\hat{r}}_{Pl}}{\partial\Xi_2}\right)\int_{\hat{\Gamma}_{Pl}}N_0(\vec{\hat{r}}_{Pl})d\Xi_1\,d\Xi_2\end{aligned}$$

where $\Gamma^{j,k}_l$ are the three facets that compose $\Gamma^{j,k}$ and Γ^k_l are the four faces of the tetrahedron. Here the convention is the one already defined; namely: $\Gamma^{j,k}_l$ is the facet between node n_0 and n_l and Γ^k_l is the face opposite to node n_l. The term $|\det(\mathbf{J})|\,\nabla N^{i,k}\cdot\mathbf{J}^{-T}$ is

the same at both sides of the expression.
We can proceed further by combining Eqs.B.5e-g with Eqs.B.5h-j to get:

$$\left(\frac{\partial\vec{\hat{r}}_l}{\partial\xi}\times\frac{\partial\vec{\hat{r}}_l}{\partial\eta}\right)\int\limits_{\hat{\Gamma}_l} d\eta\, d\xi = \vec{\hat{\Gamma}}_l \qquad .$$

In addition, from Eqs.B.5a we compute:

$$\int\limits_{\hat{\Gamma}_{P0}} N_0(\vec{\hat{r}}_{P0}) d\xi\, d\eta = 0$$

and taking into consideration also Eqs.B.5k-m we obtain:

$$\int\limits_{\hat{\Gamma}_{Pl}} N_0(\vec{\hat{r}}_{Pl}) d\Xi_1\, d\Xi_2 = \frac{1}{6}, \quad l = 1..3$$

where the definition of Ξ_1 and Ξ_2 implies an outer orientation to the surface $\hat{\Gamma}_{Pl}$. Then, we conclude that:

$$\begin{aligned} &-\sum_{l=0}^{3}\left(\frac{\partial\vec{\hat{r}}_{Pl}}{\partial\Xi_1}\times\frac{\partial\vec{\hat{r}}_{Pl}}{\partial\Xi_2}\right)\int\limits_{\hat{\Gamma}_{Pl}} N_0(\vec{\hat{r}}_{Pl}) d\Xi_1\, d\Xi_2 \\ &=\sum_{l=1}^{3}\left(\frac{\partial\vec{\hat{r}}_l}{\partial\xi}\times\frac{\partial\vec{\hat{r}}_l}{\partial\eta}\right)\int\limits_{\hat{\Gamma}_l} d\eta\, d\xi = \frac{1}{6}\,[1,1,1] \end{aligned}$$

which is the desired result.

4.A.3 Discretized AC GFEM coefficients

In the GFEM case the coefficients are very similar to Eq. 4.22 and read:

$$s_m^{i,j} = \frac{Z_m^2 q^2}{k_B T}\sum_{k\in\Upsilon^{i,j}}\int\limits_{v^k} N^{j,k}N^{i,k}n_{0m}d\Omega \tag{4.54a}$$

$$t_m^{j} = \frac{Z_m^2 q^2}{k_B T}\sum_{i\in\Lambda^j}\sum_{k\in\Upsilon^{i,j}}\int\limits_{v^k} \left(N^{j,k}\right)^2 n_{0m}d\Omega \tag{4.54b}$$

$$c^{i,j} = a^{i,j} - \sum_{m=1}^{N_{ions}} s_m^{i,j} \tag{4.54c}$$

$$d^{j} = b^{j} - \sum_{m=1}^{N_{ions}} t_m^{j} \tag{4.54d}$$

$$o_m^{i,j} = jZ_m^2 q^2\frac{\mu_m}{\omega}\sum_{k\in\Upsilon^{i,j}}\int\limits_{v^k} n_{0m}\nabla N^{j,k}\cdot\nabla N^{i,k}d\Omega - s_m^{i,j} \tag{4.54e}$$

$$p_m^{j} = jZ_m^2 q^2\frac{\mu_m}{\omega}\sum_{i\in\Lambda^j}\sum_{k\in\Upsilon^{i,j}}\int\limits_{v^k} n_{0m}\nabla N^{j,k}\cdot\nabla N^{j,k}d\Omega - t_m^{j} \tag{4.54f}$$

For simplicity, we have written here only the coefficients for the electrolyte, not for the semiconductor case. Note also that:

$$\int_{\hat{\Omega}} N_0^2 d\Omega = \frac{1}{60}, \quad \int_{\hat{\Omega}} N_0 N_i d\Omega = \frac{1}{120} \tag{4.55}$$

4.A.4 Volume integrals

Denoting $u_l = v_l - v_0$, the non-linear volume integral is:

$$\begin{aligned}
\mathcal{I} &= \int_{\Omega_c^{j,k}} \exp\left(N^{j,k} v_0 + \sum_{i \in \Lambda^{j,k}} N^{i,k} v_i\right) d\Omega \\
&= 6\mathcal{V}_k\, e^{v_0} \Bigg(\frac{4\left(e^{\frac{u_1}{2}} - e^{\frac{1}{3}(u_1+u_3)}\right)}{u_1\,(u_1-2u_2)\,(u_1-2u_3)} - \frac{9\left(e^{\frac{1}{3}(u_1+u_2)} - e^{\frac{1}{4}(u_1+u_2+u_3)}\right)}{(2u_1^2-5u_1u_2+2u_2^2)\,(u_1+u_2-3u_3)} \\
&- \frac{4\left(e^{\frac{u_2}{2}} - e^{\frac{1}{3}(u_2+u_3)}\right)}{(2u_1-u_2)\,u_2\,(u_2-2u_3)} + \frac{-1+e^{\frac{u_3}{2}}}{u_1u_2u_3} + \frac{e^{\frac{u_3}{2}} - e^{\frac{1}{3}(u_1+u_3)}}{u_1\,(u_1-u_2)\,(-2u_1+u_3)} \\
&+ \frac{-e^{\frac{1}{3}(u_1+u_3)} + e^{\frac{1}{4}(u_1+u_2+u_3)}}{(u_1^2-3u_1u_2+2u_2^2)\,(u_1-3u_2+u_3)} + \frac{-e^{\frac{u_3}{2}} + e^{\frac{1}{3}(u_2+u_3)}}{(u_1-u_2)\,u_2\,(-2u_2+u_3)} \\
&+ \frac{-e^{\frac{1}{3}(u_2+u_3)} + e^{\frac{1}{4}(u_1+u_2+u_3)}}{(u_1-u_2)\,(2u_1-u_2)\,(-3u_1+u_2+u_3)}\Bigg)
\end{aligned} \tag{4.56}$$

Its Taylor expansion at third order around $u_i = 0$ gives:

$$\begin{aligned}
\mathcal{I} \simeq \frac{\mathcal{V}_k\, e^{v_0}}{2488320} \big(&622080 + 1067u_1^3 + 1067u_2^3 + 3u_2^2\,(3864+491u_3) + 3u_1^2\,(3864+491u_2+491u_3) \\
&+ 3u_2\,(33120 + u_3\,(4656+491u_3)) + 3u_1\big(33120 + 491u_2^2 + 582u_2\,(8+u_3) + u_3\,(4656+491u_3)\big) \\
&+ u_3\,(99360 + u_3\,(11592+1067u_3))\big)
\end{aligned} \tag{4.57}$$

The Taylor expansions of the Jacobian terms are:

$$\begin{aligned}
\frac{\partial \mathcal{I}}{\partial v_0} \simeq \frac{\mathcal{V}_k\, e^{v_0}}{52254720} \big(&10364u_1^3 + 10364u_2^3 + 15120\,(450 + 67u_2 + 67u_3) + 6u_2u_3\,(22155 + 2258u_3) \\
&+ 3u_2^2\,(38115 + 4516u_3) + 3u_1^2\,(38115 + 4516u_2 + 4516u_3) + u_3^2\,(114345 + 10364u_3) \\
&+ 6u_1\big(168840 + 2258u_2^2 + 3u_2\,(7385 + 864u_3) + u_3\,(22155 + 2258u_3)\big)\big)
\end{aligned}$$

$$\begin{aligned}
\frac{\partial \mathcal{I}}{\partial v_1} \simeq \frac{\mathcal{V}_k\, e^{v_0}}{52254720} \big(&6833u_1^3 + 2605u_2^3 + 3024\,(690 + 97u_2 + 97u_3) + 9u_2^2\,(3437 + 391u_3) \\
&+ 9u_2u_3\,(4074 + 391u_3) + u_3^2\,(30933 + 2605u_3) + u_1^2\,(67221 + 7815u_2 + 7815u_3) \\
&+ u_1\big(486864 + 6051u_2^2 + 61866u_3 + 6051u_3^2 + 18u_2\,(3437 + 391u_3)\big)\big)
\end{aligned}$$

Due to symmetry, in order to find $\partial\mathcal{I}/\partial v_2$ and $\partial\mathcal{I}/\partial v_3$ we start from $\partial\mathcal{I}/\partial v_1$ and make the substitutions $(u_1, u_2) \to (u_2, u_1)$ and $(u_1, u_3) \to (u_3, u_1)$ respectively.

As an example, we report also the Taylor expansion for $\mathcal{I}$ in the GFEM case:

$$\begin{aligned}
\mathcal{I} &= \int_{v^k} N^{j,k} \exp\left(N^{j,k} v_0 + \sum_{i \in \Lambda^{j,k}} N^{i,k} v_i\right) d\Omega \\
&\simeq \frac{\mathcal{V}_k}{840}\Big(u_1^3 + u_2^3 + u_2^2(7+u_3) + u_2u_3(7+u_3) + u_3^2(7+u_3) + 42(5+u_2+u_3) \\
&+ u_1^2(7+u_2+u_3) + u_1\left(42 + u_2^2 + u_2(7+u_3) + u_3(7+u_3)\right)\Big)
\end{aligned} \tag{4.58}$$

4.A.5 Internal surface integrals

We denote with $\mathcal{I}^l_{Sf}$ the integrals calculated in the transformed space:

$$\mathcal{I}^l_{Sf} = \int_{\hat{\Gamma}_l} f(\vec{\hat{r}}_l) d\eta \, d\xi$$

The explicit expressions for $\mathcal{I}^l_{Sf}$ when f is given by Eq. 4.30 are:

$$\begin{aligned}
\mathcal{I}^1_{Sf} = \frac{e^{v_0}}{u_1 - 2u_2} \Bigg(& - \frac{3\left(e^{\frac{1}{3}(u_1+u_2)} - e^{\frac{1}{4}(u_1+u_2+u_3)}\right)}{u_1 + u_2 - 3u_3} \\
& + \frac{2\left(e^{\frac{u_1}{2}} - e^{\frac{1}{3}(u_1+u_3)}\right)}{u_1 - 2u_3} + \frac{-e^{\frac{1}{3}(u_1+u_3)} + e^{\frac{1}{4}(u_1+u_2+u_3)}}{u_1 - 3u_2 + u_3} \Bigg) \\
\mathcal{I}^2_{Sf} = \frac{e^{v_0}}{2u_1 - u_2} \Bigg(& \frac{3\left(e^{\frac{1}{3}(u_1+u_2)} - e^{\frac{1}{4}(u_1+u_2+u_3)}\right)}{u_1 + u_2 - 3u_3} \\
& - \frac{2\left(e^{\frac{u_2}{2}} - e^{\frac{1}{3}(u_2+u_3)}\right)}{u_2 - 2u_3} + \frac{e^{\frac{1}{3}(u_2+u_3)} - e^{\frac{1}{4}(u_1+u_2+u_3)}}{-3u_1 + u_2 + u_3} \Bigg) \\
\mathcal{I}^3_{Sf} = \frac{2\, e^{v_0}}{u_1 - u_2} \Bigg(& \frac{e^{\frac{u_3}{2}} - e^{\frac{1}{3}(u_1+u_3)}}{-2u_1 + u_3} + \frac{e^{\frac{1}{3}(u_1+u_3)} - e^{\frac{1}{4}(u_1+u_2+u_3)}}{u_1 - 3u_2 + u_3} \\
& + \frac{-e^{\frac{u_3}{2}} + e^{\frac{1}{3}(u_2+u_3)}}{-2u_2 + u_3} + \frac{-e^{\frac{1}{3}(u_2+u_3)} + e^{\frac{1}{4}(u_1+u_2+u_3)}}{-3u_1 + u_2 + u_3} \Bigg)
\end{aligned}$$

Also in this case, to avoid potential $0/0$ limit forms, we can take a Taylor expansion around $u_i = 0$.

4.A.6 Boundary surface integrals

The integrals calculated in the transformed space on the boundary facets that we need for the global conservation are:

$$\begin{aligned}
\int_{\hat{\Gamma}_{Pl}} N_0 d\Xi_2 \, d\Xi_1 &= \frac{11}{108} \\
\int_{\hat{\Gamma}_{Pl}} N_i d\Xi_2 \, d\Xi_1 &= \frac{7}{216} (1 - \delta_{il})
\end{aligned}$$

where δ_{il} is the Kronecker's delta and we have chosen to call $\hat{\Gamma}_{Pl}$ the surface opposite to node n_l.

4.A.7 Geometric elements

If we consider the unitary reference tetrahedron of Fig. 4.1, we can calculate all the geometric elements that we need in the integrals:

$$N_0 = 1 - \xi - \eta - \zeta \tag{4.59a}$$
$$N_1 = \xi \tag{4.59b}$$
$$N_2 = \eta \tag{4.59c}$$
$$N_3 = \zeta \tag{4.59d}$$
$$\frac{\partial \vec{\hat{r}}_1}{\partial \xi} \times \frac{\partial \vec{\hat{r}}_1}{\partial \eta} = \begin{bmatrix} 2 & 1 & 1 \end{bmatrix} \tag{4.59e}$$
$$\frac{\partial \vec{\hat{r}}_2}{\partial \xi} \times \frac{\partial \vec{\hat{r}}_2}{\partial \eta} = \begin{bmatrix} 1 & 2 & 1 \end{bmatrix} \tag{4.59f}$$
$$\frac{\partial \vec{\hat{r}}_3}{\partial \xi} \times \frac{\partial \vec{\hat{r}}_3}{\partial \eta} = \frac{1}{2} \begin{bmatrix} 1 & 1 & 2 \end{bmatrix} \tag{4.59g}$$
$$\vec{\hat{\Gamma}}_1 = \frac{1}{24} \frac{\partial \vec{\hat{r}}_1}{\partial \xi} \times \frac{\partial \vec{\hat{r}}_1}{\partial \eta} \tag{4.59h}$$
$$\vec{\hat{\Gamma}}_2 = \frac{1}{24} \frac{\partial \vec{\hat{r}}_2}{\partial \xi} \times \frac{\partial \vec{\hat{r}}_2}{\partial \eta} \tag{4.59i}$$
$$\vec{\hat{\Gamma}}_3 = \frac{1}{12} \frac{\partial \vec{\hat{r}}_3}{\partial \xi} \times \frac{\partial \vec{\hat{r}}_3}{\partial \eta} \tag{4.59j}$$
$$\frac{\partial \vec{\hat{r}}_{P1}}{\partial \eta} \times \frac{\partial \vec{\hat{r}}_{P1}}{\partial \zeta} = \begin{bmatrix} 1 & 0 & 0 \end{bmatrix} \tag{4.59k}$$
$$\frac{\partial \vec{\hat{r}}_{P2}}{\partial \zeta} \times \frac{\partial \vec{\hat{r}}_{P2}}{\partial \xi} = \begin{bmatrix} 0 & 1 & 0 \end{bmatrix} \tag{4.59l}$$
$$\frac{\partial \vec{\hat{r}}_{P3}}{\partial \xi} \times \frac{\partial \vec{\hat{r}}_{P3}}{\partial \eta} = \begin{bmatrix} 0 & 0 & 1 \end{bmatrix} \tag{4.59m}$$

We have chosen to call n_1, n_2 and n_3 the nodes on the ξ, η and ζ axes respectively. The transformation $\vec{x} = \mathbf{T}\,\vec{\xi}$ is given by:

$$\mathbf{T} = \begin{bmatrix} x_1 & x_2 & x_3 \\ y_1 & y_2 & y_3 \\ z_1 & z_2 & z_3 \end{bmatrix}$$

where $[x_i, y_i, z_i]$ are the coordinates of the node n_i of the original tetrahedron in a system of coordinates where node $n^{j,k}$ is in the origin. Because the transformation $\mathbf{T}$ is linear, $\mathbf{J} = \mathbf{T}$. In the original tetrahedron we have also that:

$$\mathcal{V}_k = \frac{|\det(\mathbf{J})|}{6}$$
$$\vec{\Gamma}_l^{j,k} = |\det(\mathbf{J})| \frac{\left\| \vec{\hat{\Gamma}}_l \right\|}{\left\| \frac{\partial \vec{\hat{r}}_l}{\partial \xi} \times \frac{\partial \vec{\hat{r}}_l}{\partial \eta} \right\|} \left(\frac{\partial \vec{\hat{r}}_l}{\partial \xi} \times \frac{\partial \vec{\hat{r}}_l}{\partial \eta} \right) \mathbf{J}^{-1}$$

4.A.8 1D CVFEM coefficients

Useful definitions that we will use in the following are:

$$\delta_{eq}^{-} = -\frac{u_{m-}^{j}}{l_{j-}}, \quad \delta_{eq}^{+} = \frac{u_{m+}^{j}}{l_{j+}}$$

The non linear part of the Jacobian is:

$$J^{j} = \frac{\partial}{\partial V_0^{j}} \int_{x_{j-\frac{1}{2}}}^{x_{j+\frac{1}{2}}} \rho_{0el} dx = -\sum_{m=1}^{N_{ions}} \frac{Z_m^2 q^2}{k_B T} n_{0m}^{\infty} \int_{x_{j-\frac{1}{2}}}^{x_{j+\frac{1}{2}}} N^{j} e^{N_{eq}^{j}} dx$$

$$J^{j-} = \frac{\partial}{\partial V_0^{j-1}} \int_{x_{j-\frac{1}{2}}}^{x_{j+\frac{1}{2}}} \rho_{0el} dx = -\sum_{m=1}^{N_{ions}} \frac{Z_m^2 q^2}{k_B T} n_{0m}^{\infty} \int_{x_{j-\frac{1}{2}}}^{x_{j}} N^{j-1,j-1} e^{N_{eq}^{j-}} dx$$

$$J^{j+} = \frac{\partial}{\partial V_0^{j+1}} \int_{x_{j-\frac{1}{2}}}^{x_{j+\frac{1}{2}}} \rho_{0el} dx = -\sum_{m=1}^{N_{ions}} \frac{Z_m^2 q^2}{k_B T} n_{0m}^{\infty} \int_{x_{j}}^{x_{j+\frac{1}{2}}} N^{j+1,j} e^{N_{eq}^{j+}} dx$$

The integrals in the Jacobian coefficients are easily calculated:

$$\begin{aligned}
IJ_{-}^{j,j} &= \int_{x_{j-\frac{1}{2}}}^{x_j} N^{j,j-1} e^{N_{eq}^{j-}} dx \\
&= \frac{e^{N_{eq}^{j-}(x_j)} \left(-1 + \delta_{eq}^{-} \left(x_j - x_{j-1}\right)\right) + e^{N_{eq}^{j-}(x_{j-\frac{1}{2}})} \left(1 + \delta_{eq}^{-} \left(x_{j-1} - x_{j-\frac{1}{2}}\right)\right)}{\left(x_j - x_{j-1}\right) \left(\delta_{eq}^{-}\right)^2} \\
IJ_{+}^{j,j} &= \int_{x_j}^{x_{j+\frac{1}{2}}} N^{j,j} e^{N_{eq}^{j+}} dx \\
&= \frac{e^{N_{eq}^{j+}(z^{j+\frac{1}{2}})} \left(-1 + \delta_{eq}^{+} \left(x_{j+\frac{1}{2}} - x_{j+1}\right)\right) + e^{N_{eq}^{j+}(x_j)} \left(1 + \delta_{eq}^{+} \left(x_{j+1} - x_j\right)\right)}{\left(x_j - x_{j+1}\right) \left(\delta_{eq}^{+}\right)^2} \\
IJ_{-}^{j,j-1} &= \int_{x_{j-\frac{1}{2}}}^{x_j} N^{j-1,j-1} e^{N_{eq}^{j-}} dx \\
&= \frac{e^{N_{eq}^{j-}(x_j)} - e^{N_{eq}^{j-}(x_{j-\frac{1}{2}})} \left(1 + \delta_{eq}^{-} \left(x_j - x_{j-\frac{1}{2}}\right)\right)}{\left(x_j - x_{j-1}\right) \left(\delta_{eq}^{-}\right)^2} \\
IJ_{+}^{j,j+1} &= \int_{x_j}^{x_{j+\frac{1}{2}}} N^{j+1,j} e^{N_{eq}^{j+}} dx \\
&= -\frac{e^{N_{eq}^{j+}(x_j)} - e^{N_{eq}^{j+}(z^{j+\frac{1}{2}})} \left(1 + \delta_{eq}^{+} \left(x_j - x_{j+\frac{1}{2}}\right)\right)}{\left(x_j - x_{j+1}\right) \left(\delta_{eq}^{+}\right)^2}
\end{aligned}$$

When the potential is constant, $\delta_{eq}^{-} = 0$ and $\delta_{eq}^{+} = 0$. For numerical reasons it is more convenient to treat this case separately, deriving that:

$$IJ_{-}^{j,j} = e^{\alpha_{eq}^{-}} \frac{\left(x_j - x_{j-\frac{1}{2}}\right) \left(x_j + x_{j-\frac{1}{2}} - 2x_{j-1}\right)}{2\left(x_j - x_{j-1}\right)}$$

$$IJ_{+}^{j,j} = -e^{\alpha_{eq}^{+}} \frac{\left(x_j - x_{j+\frac{1}{2}}\right) \left(x_j + x_{j+\frac{1}{2}} - 2x_{j+1}\right)}{2\left(x_j - x_{j+1}\right)}$$

$$IJ_{-}^{j,j-1} = e^{\alpha_{eq}^{-}} \frac{\left(x_j - x_{j-\frac{1}{2}}\right)^2}{2\left(x_j - x_{j-1}\right)}$$

$$IJ_{+}^{j,j+1} = -e^{\alpha_{eq}^{+}} \frac{\left(x_j - x_{j+\frac{1}{2}}\right)^2}{2\left(x_j - x_{j+1}\right)}$$

The AC coefficients are:

$$s_m^{j-} = \frac{Z_m^2 q^2}{k_B T} \int_{x_{j-\frac{1}{2}}}^{x_j} N^{j-1,j-1} n_{0m} dx$$

$$s_m^{j+} = \frac{Z_m^2 q^2}{k_B T} \int_{x_j}^{x_{j+\frac{1}{2}}} N^{j+1,j} n_{0m} dx$$

$$t_m^j = \frac{Z_m^2 q^2}{k_B T} \left(\int_{x_{j-\frac{1}{2}}}^{x_j} N^{j,j-1} n_{0m} dx + \int_{x_j}^{x_{j+\frac{1}{2}}} N^{j,j} n_{0m} dx \right)$$

$$c^{j-} = a^{j-} - \sum_{m=1}^{N_{ions}} s_m^{j-}$$

$$c^{j+} = a^{j+} - \sum_{m=1}^{N_{ions}} s_m^{j+}$$

$$d^j = b^j - \sum_{m=1}^{N_{ions}} t_m^j$$

$$g_m^{j-} = j \frac{Z_m^2 q^2}{k_B T} \int_{x_{j-\frac{1}{2}}}^{x_j} N^{j-1,j-1} n_{0m} dx = j s_m^{j-}$$

$$g_m^{j+} = j \frac{Z_m^2 q^2}{k_B T} \int_{x_j}^{x_{j+\frac{1}{2}}} N^{j+1,j} n_{0m} dx = j s_m^{j-}$$

$$h_m^j = j \frac{Z_m^2 q^2}{k_B T} \left(\int_{x_{j-\frac{1}{2}}}^{x_j} N^{j,j-1} n_{0m} dx + \int_{x_j}^{x_{j+\frac{1}{2}}} N^{j,j} n_{0m} dx \right) = j t_m^j$$

$$o_m^{j-} = Z_m^2 q^2 \frac{\mu_m}{\omega} n_{0m} \Big|_{x_{j-\frac{1}{2}}} \frac{1}{x_j - z^{j-1}} - g_m^{j-}$$

$$o_m^{j+} = Z_m^2 q^2 \frac{\mu_m}{\omega} n_{0m} \Big|_{x_{j+\frac{1}{2}}} \frac{1}{x_{j+1} - x_j} - g_m^{j+}$$

$$p_m^j = -Z_m^2 q^2 \frac{\mu_m}{\omega} \left(n_{0m} \Big|_{x_{j-\frac{1}{2}}} \frac{1}{x_j - x_{j-1}} + n_{0m} \Big|_{x_{j+\frac{1}{2}}} \frac{1}{x_{j+1} - x_j} \right) - h_m^j$$

Chapter 5

Nanoelectrode array biosensors

This chapter reports the analysis and simulation of nanoelectrode array biosensors. The reference system considered in the study is the one presented in [33], but we emphasize that several papers reported on similar integrated systems in the recent literature [75, 76, 77, 76]. From the standpoint of physics, as outlined in previous chapters, we always assume that the electrodes are ideally polarizable, so that no electrochemical reaction is possible on them, and therefore no DC current flows. This is a reasonable approximation if the electrodes are coated with gold, as in [33, 75]. Simulations will always be in the frequency domain, and we will use a circuit model (see Sec. 3.6) to translate the so-calculated admittance into a capacitance value representative of a real switching biosensor like [33]. For the simulations, we use either a full-custom 2D finite difference / finite volume solver, which we reported earlier [1], or the 3D simulator ENBIOS presented in the previous chapter.

We start showing the validation of ENBIOS with experimental results for capacitive biosensors reported in the literature. We then describe simulations and experiments on microparticles detection, where the experimental part was mostly carried out by the University of Twente, project partner. The study has led to a direct experimental verification of the theory as well as some interesting conclusions about capacitive biosensors. We then present and verify a model for the nanoelectrode response to spherical particles, which could not be experimentally tested yet. Since the simulation of a large array entails a heavy computational burden, we developed an original technique to reduce calculation time which is described in Sec. 5.5. Finally we discuss in Sec. 5.8 a few case studies more relevant for biological application, that is, the detection of small biomolecules such as proteins and DNA.

In all our simulations we will use simplified models for the microparticles and biomolecules, such as spheres and cylinders. The microparticles we used [12] were manufactured in a spherical shape, so our approximation is fully appropriate. For the case of biomolecules, however, one may be concerned about our approximation with spheres and cylinders. This concern can be answered noting that for a few biomolecules, e.g. short DNA strans, cylindrical models have been reported in the literature to be very accurate [40]. Spherical models can resemble very closely the shape of viruses and globular proteins, and therefore we expect these to be relatively as well. Since the detection is made possible by the change of the electric energy due to replacement of the electrolyte with a particle, in the high-frequency limit we expect a response proportional to the volume (Eq. 5.4) and not much sensitive to the particle shape as long as the field is roughly constant. In order to improve the model accuracy, we also included charges on the biomolecules' surface, with values extracted from experimental results or from higher accuracy models in the

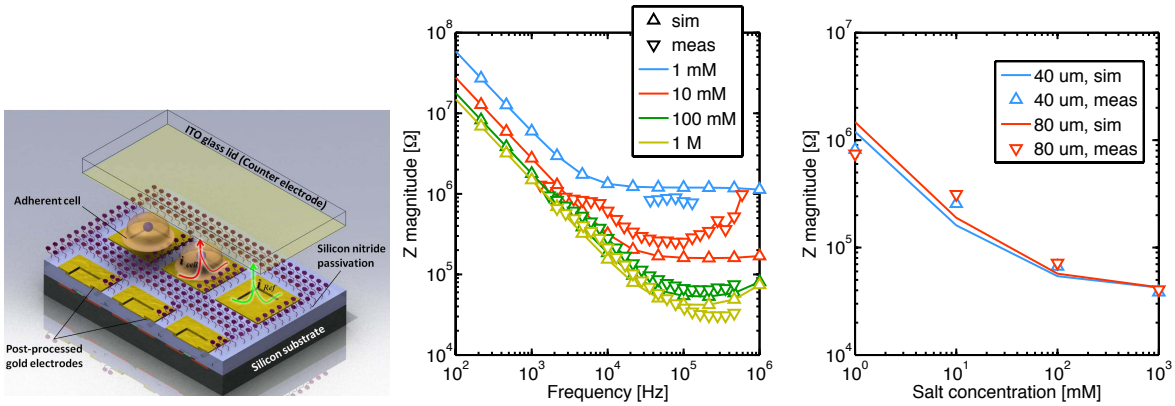

(a) (b) (c)

Fig 5.1: Sketch of the system of [76] reproduced from the original paper and comparison of simulated impedance spectra with the measurements in Fig. 6b (b) and 6c (c) of ref. [76]. Resistive and inductive series parasitics, likely present in the real system because of the off-chip measurement setup, have been introduced in the simulations to match the experiments.

literature. Finally, we note that ENBIOS allows to describe arbitrary geometries, the only practical limitation being the mesh size and the corresponding calculation time.
We also point out that, at this phase, we are aiming only to give qualitative explanations and highlight possible advantages in the operation of nanoelectrode biosensors. Despite these approximations, as we will show in this chapter, our simplified models can provide a very good physical insight.

5.1 Model validation

To the best of our knowledge, there is very limited experimental data available yet for high frequency impedance spectroscopy detection of small individual biomolecules beyond $\xi = \sigma_{el}/\varepsilon_{el}$. This is even more true if we focus on the case study system of [33]. Some results have been published only very recently for interdigitated capacitors detecting entire cells. The salt concentration had to be reduced orders of magnitude below the physiological limit to reduce the cut-off frequency and probe above f_c in spite of the large fringing capacitance. Existing demonstrators of micro-electrode arrays operate at relatively small frequency ($\leq$ 1 MHz, [75, 76, 77]) and perform measurements partly off chip, hence with non negligible parasitics.

We attempted a preliminary validation of the sensor model using the results in [76], where an ideally polarizable electrode of 22×22 μm^2 size is at a 40 or 80 μm distance from a Faradaic electrode of 100×100 μm^2 size. As in this case the electrodes are very large compared to the Debye length, we resorted to the numerical technique described in Sec. 5.5 to shorten the simulation time and make simulations manageable.
The left graph in Fig. 5.1 reports the comparison of the baseline capacitance in the absence of functionalization or biomolecules for different salt concentrations. The simulations show a respectable agreement with experiments in the explored frequency range, but we had to assume that large resistive and inductive series parasitics are present. These are very likely present in the real system because of the off-chip measurement setup, and we will show in Sec. 6.2.1 that are very important to take into account in non-integrated realizations (as also pointed out in [78]). The weak dependence of the impedance on chamber height shown in [76] is also captured by our simulations (graph on the right).

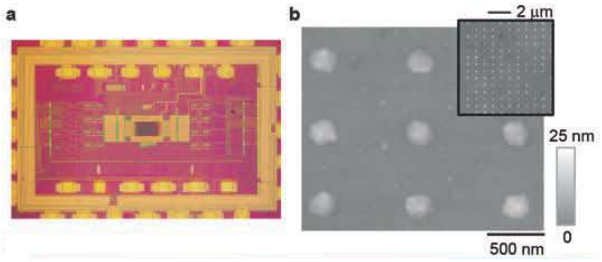

Fig 5.2: **a**, Optical image of the CMOS chip showing the nanoelectrode array (dark rectangle) and readout circuitry (yellow and green). **b**, AFM topographic images of the nanoelectrodes.

The experimental curves are affected by noise, parasitics and possibly the result are of not so stable experiments, therefore the verification has not so compelling validity.

In the following section we will show a more thorough validation, performed by comparing our simulations to very well controlled experiments done at Twente University (Prof. Serge Lemay, Cecilia Laborde) using the system of [33].

5.2 Nanoelectrode array biosensor

The sensing platform presented in [33] consists of a 90 nm CMOS chip (Fig. 5.2a) with a 256×256 nanoelectrode array (90 nm radius polished Au islands on a 0.6×0.89 μm^2 grid; Fig. 5.2b) and integrated readout circuitry. The nanoelectrodes are row-wise selectable and column-wise individually readable. When immersed in fluid they form metal/liquid nanocapacitors. A selected row of nanocapacitors is repetitively charged/discharged at 50 MHz with a modulation voltage step $V_{MOD} = 245$ mV via two individual MOS transistors using all unselected nanoelectrodes in parallel as counter electrode. The charge/discharge current of a selected nanocapacitor is integrated over multiple cycles and read out via on-chip analog/digital converters. In this way high-frequency operation with attofarad resolution is achieved. We express the measured response signal as an equivalent switching capacitance C_{exp}, defined as the integrated charge per charge/discharge cycle divided by the modulation voltage step. This approach takes simultaneously advantage of three strengths of integrated circuits: high frequencies, miniaturization and large-scale integration. Although other promising concepts have been reported [79, 80, 81, 76, 29], this biosensor platform has unique features, enabling real time, massively parallel high-frequency impedance measurements and imaging with attofarad resolution on the submicron scale.
Individual chips are placed in a custom-built test socket (CSP/μBGA Test & Burn socket - Aries Electronics, Inc.) mounted on a readout printed circuit board. A PDMS gasket is used to create a solution reservoir (volume $\sim$ 50 nl) directly on top of the nanoelectrode array. Two 500 μm holes fitted with tubing (PEEK, ID 125 μm, OD 510 μm) provide fluidic access to the measurement volume. The potential of a complete row of electrodes is switched simultaneously and the capacitive responses of the individual electrodes C_{exp} are measured and discretized with 8 on-chip A/D converters. The remaining 255 rows of the array act as a pseudo-reference electrode. Typically, 1350 charge-discharge cycles are employed per measurement of C_{exp} and 9 subsequent measurements per row were averaged on-chip, resulting in a complete array scan rate of 4.76 frames/second. Real time imaging is thus enabled by the platform.

5.3 Detection of dielectric and conductive beads

In search for accurate validations of our simulations we have started a collaboration with Twente University, where a nanoelectrode array sensing platform is available from NXP Semiconductors (the developer of the system in [33], see Sec. 5.2) to the electro-chemists group of Prof. Serge Lemay. Several experiments were carried out concerning the baseline and the response to fairly large dielectric and conductive spherical beads. In fact, the use

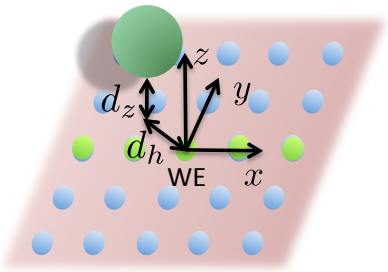

Fig 5.3: Sketch of the nanoelectrode array, where the central row (green) is biased while the other ones remain grounded and the current is measured independently at each biased electrode (WE) in the active row.

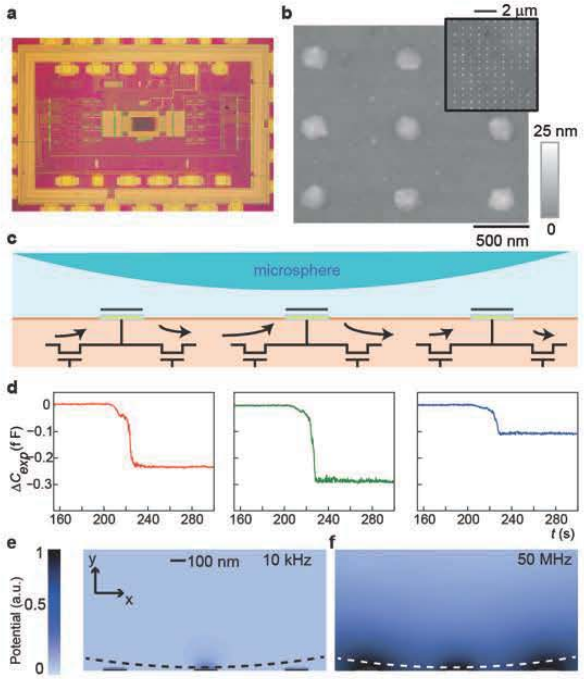

Fig 5.4: **a**, Optical image of the CMOS chip showing the nanoelectrode array (dark rectangle) and readout circuitry (yellow and green). **b**, AFM topographic images of the nanoelectrodes. **c-d**, Each electrode is alternately charged and discharged at 50 MHz with two MOS transistors, producing a detectable average electrical measured current (black arrows). A 4.4 μm radius microsphere landing on the array perturbs the electric field generated by each electrode, inducing a position-dependent change in the current (expressed as a change in capacitance ΔC_{exp}) of three neighboring electrodes. **e**, Theoretical spatial distribution of AC potential at low frequency in 150 mM salt. The electric field only penetrates a few Debye screening lengths into the solution except for the central electrode, which is positioned within a Debye length of the particle. The dashed line indicates the microsphere position. **f**, AC potential amplitude at 50 MHz in 150 mM salt, where the potential extends deep into the solution.

Parameter	Symbol	Value	Units
Electrode radius	r_{el}	75	[nm]
Electrode x-pitch	p_x	600	[nm]
Electrode y-pitch	p_y	890	[nm]
Particle radius	r_b	2.5 or 4.5	[μm]
Mobility of K^+	μ_1	$4.75 \cdot 10^{11}$	[m/Ns]
Mobility of Cl^-	μ_2	$5.05 \cdot 10^{11}$	[m/Ns]
Temperature	T	298.16	[K]
Electrolyte permittivity	ε_{el}	Eq. 2.39	[F/m]
Particle permittivity (dielectric)	ε_p	$2.6\varepsilon_0$	[F/m]
Particle permittivity (conductive)	ε_p	$6.9\varepsilon_0$	[F/m]
Particle conductivity (conductive)	σ_p	6.3×10^7	[S/m]

Table 5.1: Parameters used in the simulations.

of small particles is presently made difficult by the absence of a reliable protocol to attach the beads on the sensor surface, thus it leaves excessive uncertainty on the particle height above the electrodes. The sedimentation is instead very efficient with large particles. We then compare our results to these experiments performed at Twente University on the system of [33].

In the experiments, dielectric microspheres of $8.7 \pm 0.7\mu$m and $5 \pm 0.7\mu$m diameter aldehyde/sulfate latex beads from Life Technologies with dielectric constant $\varepsilon_{bead} = (2.49 \div 2.55)\varepsilon_0$ between 1 kHz and 1 GHz, and conducting microspheres ($8.75 \pm 0.13\mu$m and $5 \pm 0.7\mu$m diameter Au-coated polystyrene beads from microParticles GmbH) were suspended in 6.6 pH PBS (0.1 mM H_3PO_4, 0.1mM KOH). The salt concentration of the buffer solution was further adjusted by adding KCl. The bead-containing solution was injected in the detection chamber, replacing the bead-free buffer, and the sedimentation process was monitored in real time. No Brownian motion of the microparticles was observed following sedimentation. The measurements are a courtesy of C. Laborde and S. Lemay, University of Twente [12], the author of this thesis participated to one measurement session.

In the simulations, the particle is spherical with either 9 or 5 μm diameter, the electrolyte is made of KCl with appropriate salt concentration. The complete set of simulation parameters is summarized in Tab. 5.1. Fig. 5.3 shows a sketch of a part of the simulated nanoelectrode array (see Sec. 5.2). The complete array features 256×256 nanoelectrodes with 0.6×0.89 μm spacing.

Figs. 5.4a-b show in more detail the nanoelectrode array biosensor [33], which has been used for the experiments. The detection principle, outlined in Sec. 3.6, is also depicted in Figs. 5.4c-d. As evident from all the discussions throughout this thesis, we expect the biosensors to be able to detect the presence of the particles at low frequency only if they are very close to the electrode, while they should be visible from a larger distance at high frequency (compare Figs. 5.4e-f).

5.3.1 Simulation results

Since the particle is large compared to the electrode pitch (5 μm versus 0.6 or 0.89 μm, if not otherwise specified), we have to simulate a large portion of the nanoelectrode array in order not to introduce numerical truncation errors. We then simulate a subset of 13×17 nanoelectrodes, but the domain size is set to even larger dimensions (a cube with edge

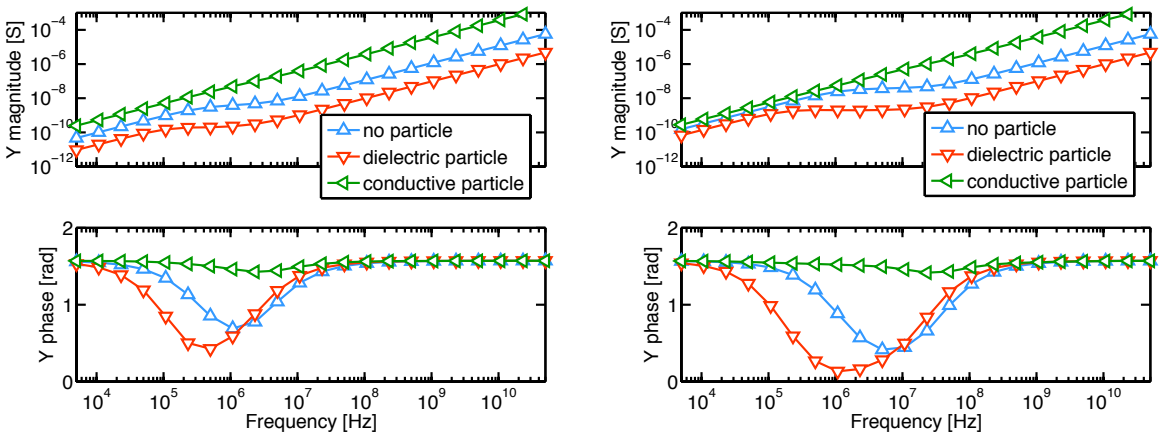

(a) 1 mM **(b)** 10 mM

Fig 5.5: Total admittance at the central electrode with particle height $d_z = 1$ nm over the central electrode and centered on its top. Note that both the pole and the zero frequencies change with salt concentration as in the model of Sec. 3.1.1.3.

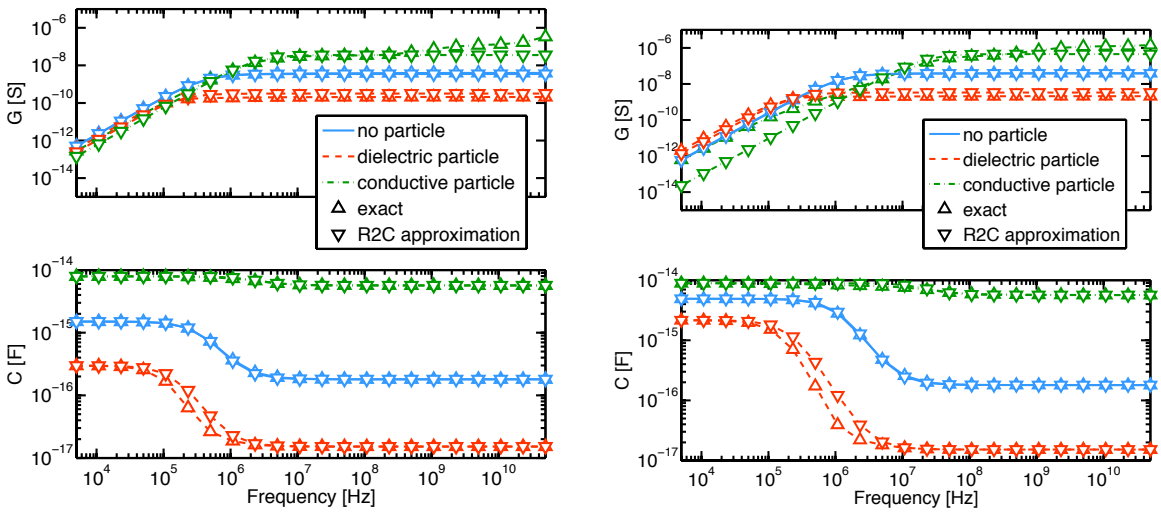

(a) 1 mM **(b)** 10 mM

Fig 5.6: Total admittance at the central electrode (split in conductance and capacitance) and corresponding fit with an equivalent circuit composed of the series of one capacitor C_s and the parallel of a resistor G_E and a capacitor C_E (R2C model, see Fig. 3.27). The particle is located at $d_z = 1$ nm over the electrode and is centered on its top. Note that the fit is very good and that the large error on G with the conductive particle at high frequency is ininfluential since it has a small impact on the total Y.

50 μm). As the number of electrodes is so large, the minimum mesh spacing in their proximity can be set to a value appropriate for simulations up to about 10 mM (2 nm $\simeq \lambda_D$ at 10 mM) at most, and it is too coarse at higher salt concentrations. Therefore, the simulations at 100 mM which we performed to compare with measurements may be affected by relatively larger errors at low frequency.

Since we apply no DC bias at the electrodes, we do not include a Stern layer in the simulations. In addition, as in the experiments, no SAM is present on top of the electrodes.

Fig. 5.5 shows the admittance at the central electrode in absence or presence of a

n_0 [mM]	Particle	C_s [fF]	C_E [fF]	G_E [nS]
1	None	1.51	0.205	4.48
	Dielectric	0.297	0.016	0.35
	Conductive	7.94	20.0	435
10	None	4.90	0.187	40.9
	Dielectric	2.16	0.015	3.35
	Conductive	8.91	15.6	3410

Table 5.2: Table of the lumped circuit elements for the R2C model used in Fig. 5.6.

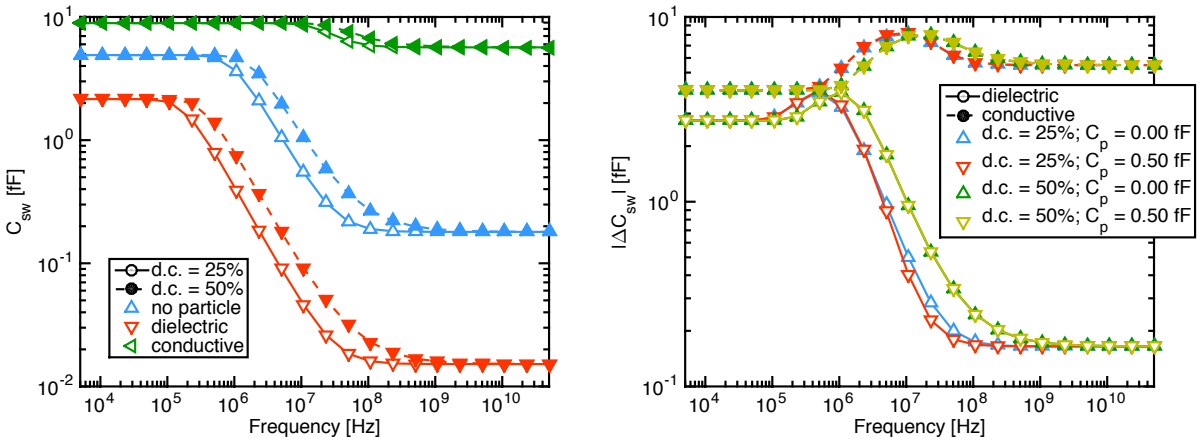

(a) C_p 0 fF

Fig 5.7: Switching capacitance C_{sw} at the central electrode with salt concentration 10 mM, varying the model parameters for the switching capacitance (duty-cycle and parasitic capacitance C_p). The particle has $d_z = 1$ nm over the electrode and is centered on its top. There are interesting peaks in the response.

particle centered on its top at a distance $d_z = 1$ nm. We immediately note that, depending on the particle's material, the admittance may decrease or increase with respect to the reference case without particle. This is easily understood considering that, in one case, part of the electrolyte volume is replaced with a lower dielectric constant material, while in the other case the field lines are grouped and focused by the metallic particle. We also see that the admittance spectra are relatively simple to interpret, since they show with evidence only two zeros and one pole. This is also apparent in Fig. 5.6, where the admittance is now represented as $Y = G + j\omega C$ and accurately fitted to a lumped elements circuit model (R2C) with one resistor and two capacitors like the one in Fig. 3.27. The lumped element values are reported in Tab. 5.2.
Consistently with Sec. 3.1.1.3, we define the first cut-off frequency f_s as the frequency of the pole, while the second zero is the electrolyte's dielectric relaxation cut-off frequency f_c. f_s defines the frequency above which the static Debye screening starts to be overcome, while above f_c the response depends only on the bulk dielectric properties of the materials that lie between the electrodes and not on the AC EDLs, which have disappeared.

To compare AC small signal simulations with measurements, as outlined in Sec. 3.6, we have to first calculate an approximation of the measured capacitance C_{exp}. In fact, C_{exp} is measured with CBCM techniques [33] from the average value of the discharge current under pulsed excitation.
One possibility is to consider the switching capacitance C_{sw} was calculated as explained

in Sec. 3.6 by using the R2C model of Fig. 3.27 with parameter values as in Tab. 5.2. Fig. 5.7 shows C_{sw} at the central electrode for a few duty cycle (d) and parasitic capacitance (C_p) values. We immediately see that C_{sw} is generally sensitive to the duty cycle only in the small frequency interval between f_s and f_c. Furthermore, outside this interval, the change in capacitance $\Delta C = C_{wp} - C_{w/op}$ between the cases with and without particle is insensitive to C_p, as expected. Based on the device architecture of [33], a realistic duty cycle is $d.c. \simeq 25\%$ and an average $C_p \simeq 0.5$ fF was estimated; we will always use these values in the following calculations.
An alternative way to estimate the measured capacitance is to calculate the modulus of the charge at the nanoelectrode, leading to an effective capacitance $C_{eff} = |Y/j\omega|$. This definition of C_{eff} is justified based on the observation that the detector responds to both the real and imaginary parts of the admittance in a way that is not easily predictable a-priori and that the total charge, roughly proportional to the modulus of Y, should contribute. Fig. 5.8 compares C_{eff} and C_{sw} for an extensive set of cases, showing that the two approximations for ΔC are very close to each other, except in the intermediate region between the cut-off frequencies. In the following we will therefore use both approximations to compare with measurements. Note that zeros and sign changes are not visible in these cases essentially due to the very non-uniform field distribution and to the fact that the particle is close to the electrode and therefore interacts with its EDL.

Fig. 5.9 shows the simulated profile of ΔC along the central row of electrodes at 50 MHz, while the particle is located above the center of the central electrode. Since we are in the high-frequency limit (f_c(10mM) $\simeq$ 20 MHz), the response is independent of the salt concentration, except for the weak modulation of the electrolyte permittivity (see Eq. 2.39). We also note that ΔC depends weakly on the exact distance between the particle and the electrode d_z, except at the central electrode for conductive particles. This is because a conductive particle attached to the electrode effectively acts as a protrusion, extending the electrode inside the electrolyte and thus remarkably increasing the electrode surface. Fig. 5.9 also shows that, as expected, not only the central electrode, which is the only one within one Debye length to the particle, but also the adjacent electrodes are able to detect the analyte. We also note that there are peaks in the response. We will analyze this interesting aspect in more detail in Sec. 5.4.
To gain further insight on the results above, Fig. 5.10 shows the real part of the potential $\tilde{V}$ at $x = y = 0$ in the z direction, that is perpendicularly to the electrodes. The particle is neutral with 5 μm radius and located at distance d_z from the electrode. We immediately recognize the Debye screening layer at low frequency. We also note that, at high frequency, the potential of the conductive particle is not at the bulk value (i.e. the value at infinite distance), while at low frequency it is always very close to that value even at a distance (1 nm) much smaller than the Debye length (10 nm). This effect is due to the large size of the particle with respect to the nanoelectrodes dimensions. Fig. 5.11 shows the modulus of the electric field $|\tilde{E}|$ at high frequency (50 MHz) in the nanoelectrode plane. As expected, $|\tilde{E}|$ is larger on the nanoelectrode's edge.

Since, as we have seen, the electric field at high frequency decays slowly for increasing distance from the electrodes, we have also tested the influence of the system's dimensions on the simulated response. Fig. 5.12 reports the baseline C_{eff}, that is, the effective capacitance at one electrode in absence of the particle, varying the medium (air, IPA and an electrolyte with various concentrations of KCl), the frequency and the size of the domain. Air and IPA have been simulated as dielectric materials with relative permittivities of 1 and 18 respectively. In particular we simulated a small array of 5×5 nanoelectrodes and a large array of 13×17 nanoelectrodes. We immediately see that, in all cases considered

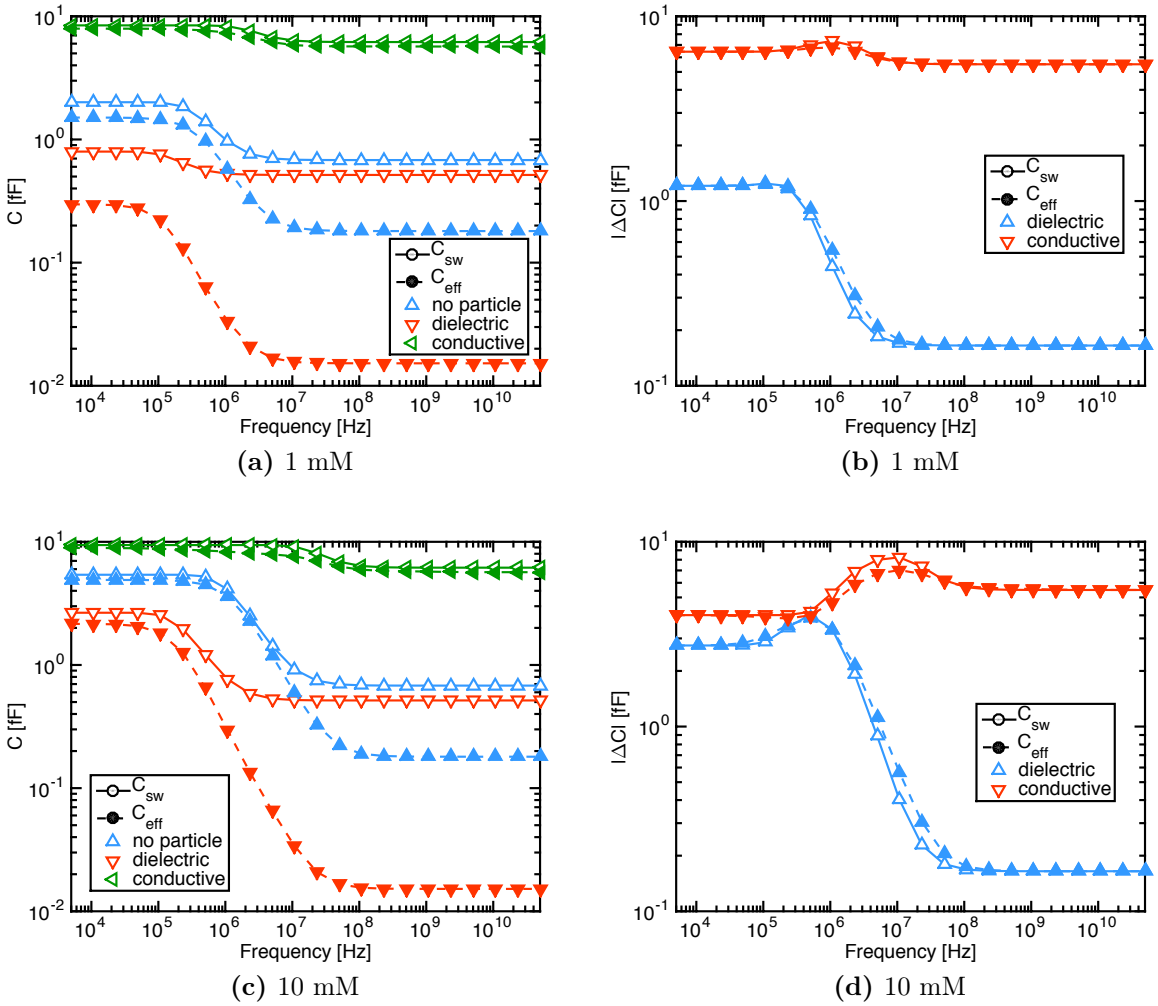

(a) 1 mM **(b)** 1 mM

(c) 10 mM **(d)** 10 mM

Fig 5.8: Left: effective and switching capacitance at the central electrode. The particle has $d_z =$ 1 nm over the electrode and is centered on its top. Right: corresponding change in capacitance for dielectric and conductive particles. Note that, although C_{sw} and C_{eff} are different from each other, due to the introduction of C_p in the model for C_{sw}, the ΔC in presence of the particle are essentially very similar between the models.

here, the domain size does not have an appreciable impact on the results, thus providing reassuring indications on the validity of the adopted model.

5.3.2 Comparison to experiments

Fig. 5.13 shows the comparison between the measured baseline capacitance (i.e., without particles) and the corresponding simulated switching capacitance, calculated for duty-cycle $d = 25\%$ and parasitic capacitance $C_p = 0.5$ fF, varying the salt concentration, as for the indications in Sec. 3.6. We observe that the agreement between simulations and measurements is very good, despite the use of a single calibration parameter (C_p). Fig. 5.14a shows similar baseline measurements varying the operation frequency and for various media (i.e., air, IPA, milliQ water and various solutions of KCl in water). We note once again the large spread in the measurements, which is due to a spread in parasitic capacitance at the electrodes. In Fig. 5.14b we compare these measurement to the simulation data, and find once again that the agreement is excellent, both on the absolute

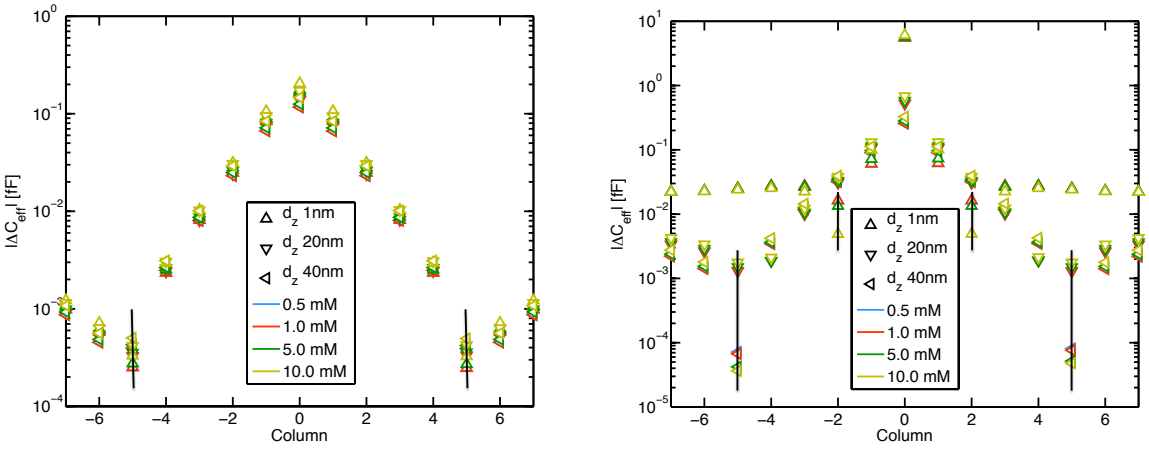

(a) dielectric particle **(b)** conductive particle

Fig 5.9: Change in effective capacitance on the central row. The particle of radius 5 μm has varying d_z over the electrode and is centered on its top, frequency 50 MHz. The vertical lines mark sign changes. Note that the response id independent of salt concentration at high frequency.

value and on the location of the transition frequencies. In the simulations a compact layer of 0.25 nm thickness and relative permittivity 7 is present on the electrodes, since at high salt concentration we expect the CL to give an important contribution to the total capacitance. Also in this case there is a larger error in the comparison at high salt concentration, probably due on the one hand to an uncertainty on the CL's properties and on the other hand to a not yet accurate array calibration in all conditions. However we point out that the transition frequency is correctly reproduced by simulations also in this case.

Fig. 5.15a shows two-dimensional maps of the measured response ΔC_{exp} of the nanoelectrode array to sedimented dielectric microspheres for three different frequencies. Below the first cut-off frequency f_s (1.6 MHz) the microspheres are undetectable except when they sediment directly on one electrode (red circle), as expected. Upon increasing the frequency to 7.1 MHz and 50 MHz the particles become visible over an increasingly large area of the array, demonstrating that screening by the double layer is being overcome. *This result is a remarkable confirmation of the theoretical predictions and explanations given in Sec. 3.3.5.*

To make this conclusion more quantitative, we define the effective size of the particles σ, defined as:

$$\sigma^2 = \frac{\sum_i \sum_j \left[(p_x i - r_{0x})^2 + (p_y j - r_{0y})^2\right] \Delta C_{exp}(i,j)}{\sum_i \sum_j \Delta C_{exp}(i,j)} \tag{5.1}$$

where p_x and p_y are the electrode pitches in the x and y directions, r_{0x} and r_{0y} are the coordinates of the center of mass of the distribution and $\Delta C_{exp}(i,j)$ is the change in capacitance for electrode (i,j) after sedimentation of the particles. The same expression was used to compute σ in simulations, except that ΔC_{exp} was replaced by ΔC_{th}, where C_{th} is the simulated capacitance and can stand either for C_{eff} or C_{sw}.
Fig. 5.15b shows capacitance maps of individual particles for salt concentrations ranging from 1 mM (typical in field-effect detection experiments [82, 83]) to 100 mM (near physiological conditions). The measured apparent radius σ_{exp} of the microparticles ($\sigma_{exp} \simeq 2.5$ μm, comparable to their physical radius) is orders of magnitude larger than the Debye

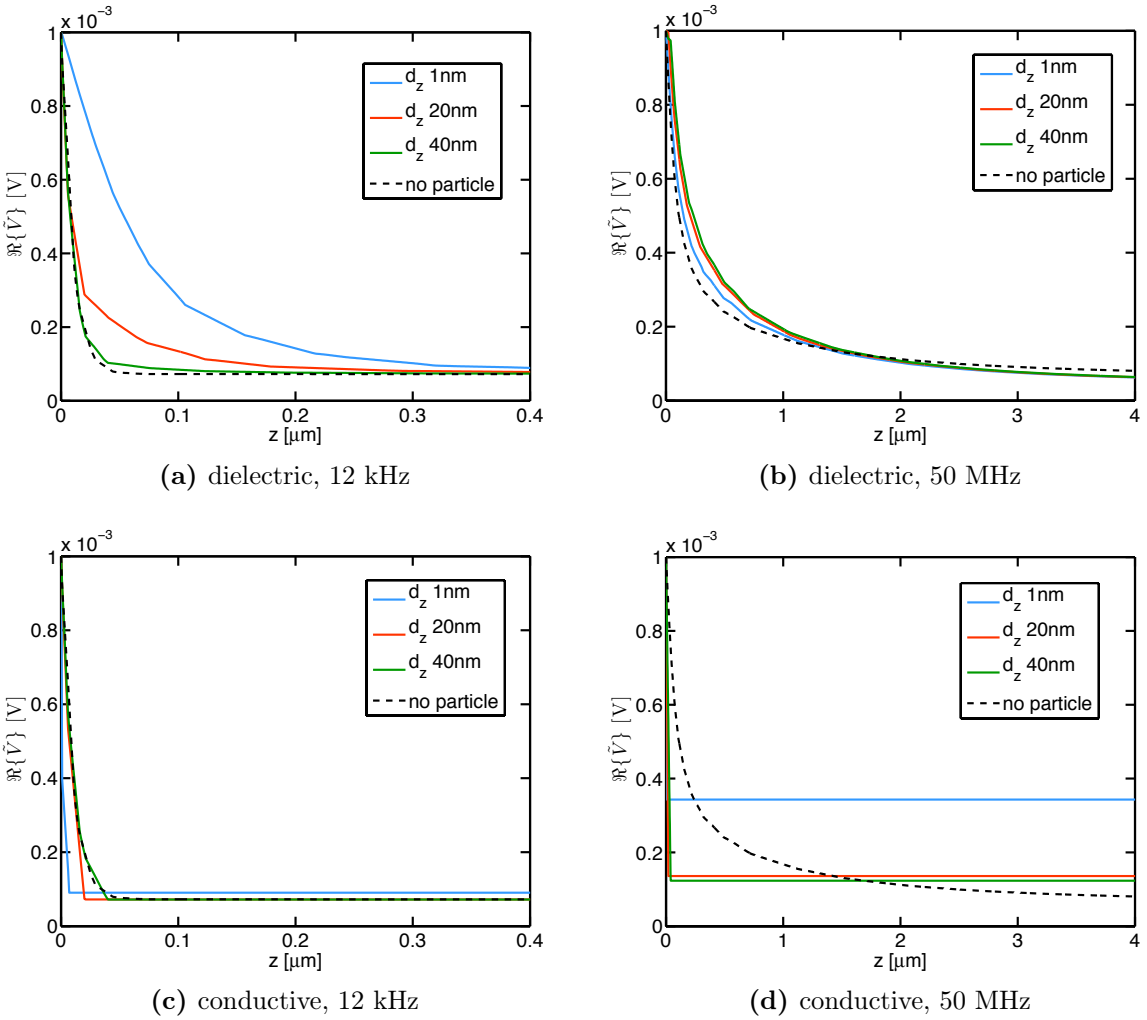

(a) dielectric, 12 kHz

(b) dielectric, 50 MHz

(c) conductive, 12 kHz

(d) conductive, 50 MHz

Fig 5.10: Real part of the electric potential in the vertical (z) direction above the center of the central electrode ($x = y = 0$), with salt concentration 1 mM and applied voltage 1 mV. Note that, at high frequency, the conductive particle potential is not at the bulk value (i.e. the value at infinite distance), while at low frequency it is always very close to it even at a distance (1 nm) much smaller than the Debye length (10 nm).

length λ_D and independent of salt concentration. Fig. 5.15c shows the corresponding simulated responses that are in excellent quantitative agreement with experimental results. This *ab-initio* predictability is remarkable considering that most impedance spectroscopy data obtained with macroelectrodes can only be interpreted qualitatively by fitting to empirical models [84, 85]. Fig. 5.15d further demonstrates theoretically and experimentally that particles of different diameters can be distinguished, illustrating that the spatial resolution is determined by solution-side processes and is not introduced by the measurement electronics. These observations represent a direct illustration that double layer screening is effectively mitigated by high-frequency operation of the nanoelectrode array.

As shown in the previous section by means of simulations (Fig. 5.8), dielectric spheres replace high-permittivity electrolyte by a medium with much lower permittivity, repelling the electric field lines and causing C_{exp} to decrease ($\Delta C_{exp} < 0$). Conducting spheres, on the other hand, attract electric field lines, causing C_{exp} to increase ($\Delta C_{exp} > 0$). This effect can be used for discriminating between different particles. Fig. 5.16a and 5.16b show experimental ΔC_{exp} maps of a mixture of dielectric (latex) and conducting (gold-coated

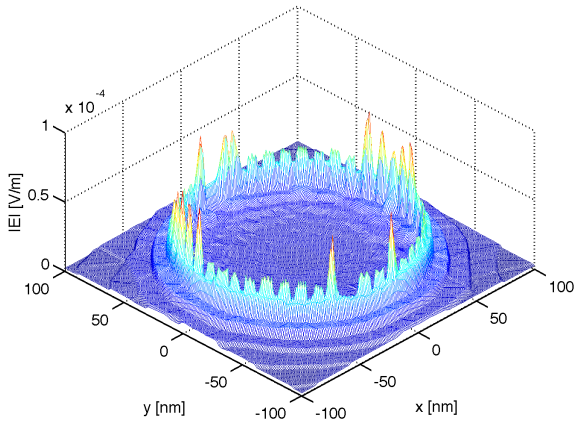

Fig 5.11: Vector modulus of the amplitude of the electric field near the central electrode in the electrode plane ($z = 0$) with no particles. Frequency 50MHz and salt concentration 1 mM. Numerical noise affects the field values at the edge of the electrode.

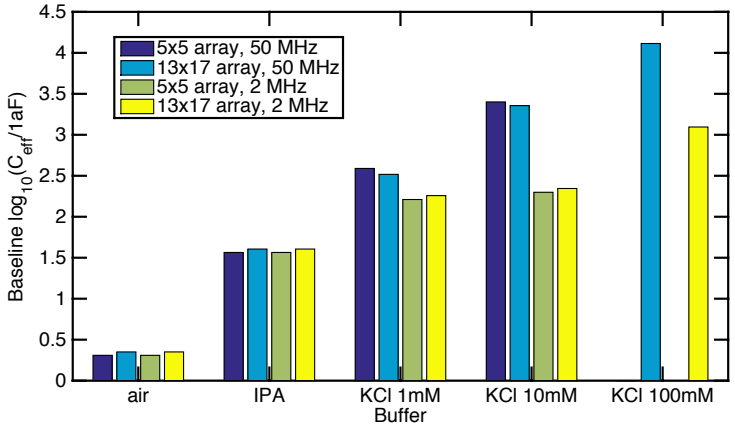

Fig 5.12: Simulated baseline effective capacitance C_{eff} in absence of the particle for various media and frequencies and changing the dimensions of the array. We immediately see that there is no appreciable change in C_{eff} between the small (5×5) and large (13×17) array.

polystyrene) particles with the same 2.5 μm radius. While the apparent particle radius is similar for both cases ($\sigma \simeq 1.7$ μm), the conductive microparticles show an increase in capacitance ($\Delta C_{exp} > 0$) instead of a decrease. Once again the experimental response, in particular the sign change, confirms the predictions by simulations (Fig. 5.16c), thus proving the ability of the physical model to capture the main features of the experiment. This capability of discriminating between particles purely based on their intrinsic electrical properties is unique to high-frequency spectroscopy, as presented here.

We now look at these data under a different perspective, and use simulations to better understand the measurements. Fig. 5.17 shows again the measured ΔC profiles along the central row, and the corresponding simulations, for a few particle distances from the electrode. We see that, as expected from previous results in Fig. 5.16, the simulations match very well the experiments both in the prediction of the peak values and of the decay law of ΔC with the electrode position. The discrepancy at high distance may be due to the noise and, in the case of simulations, to numerical errors. Looking at simulations data in Fig. 5.17b, we can estimate a particle's distance from the electrode about 20 nm.
Finally, Fig. 5.18 shows similar data, normalized to the peak value at the central electrode

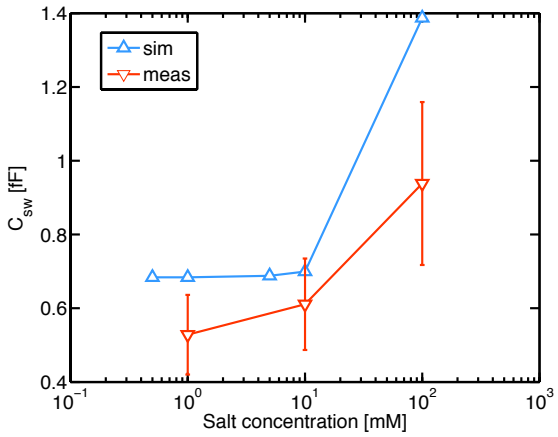

Fig 5.13: Comparison between the measured and the switching capacitance C_{sw} calculated with the model in Sec. 3.6 at 50 MHz with duty-cycle $d = 25\%$ and parasitic capacitance $C_p = 0.5$ fF. The measurements are a courtesy of C. Laborde and S. Lemay, University of Twente [12].

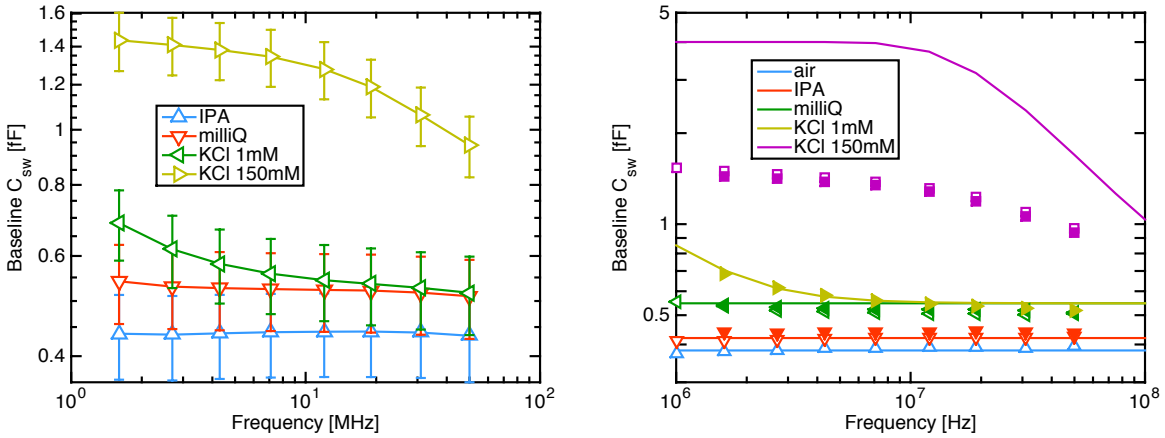

Fig 5.14: Measured capacitance (a) varying the frequency and the medium on top of the array and comparison (b) between the measured and the switching capacitance C_{sw} calculated with the model in Sec. 3.6 with duty-cycle $d = 25\%$ and parasitic capacitance $C_p = 0.37$ fF, that is equal to the measured capacitance in air. In (b) the solid lines are the simulation data, the filled symbols are the means of the measurement in (a) and the empty symbols are the means on similar measurements on another chip. In the simulations a compact layer of 0.25 nm thickness and relative permittivity 7 is present on the electrodes. The measurements are a courtesy of C. Laborde and S. Lemay, University of Twente [12].

for different particle's size. We note that again the simulations can reproduce very accurately the measured response, in all conditions. We also see that the decay of the response with distance depends on the particle's dimensions, which gives a further indication on the imaging capabilities of this biosensor platform.

Regarding the broad shoulder that is visible in measured data in Fig. 5.17a, we should note that its value is $\Delta C \approx 5aF$, which is about 1% of the total capacitance at the electrodes (see Fig. 5.13). A possible explanation for this effect (that is not visible in all experiments, see for instance Fig. 5.18 comparing 5 μm and 9 μm beads), may reside in small differences between the permittivity of the PBS electrolyte used when measuring in absence of the beads and the one where the beads are dispersed, due to contaminations.

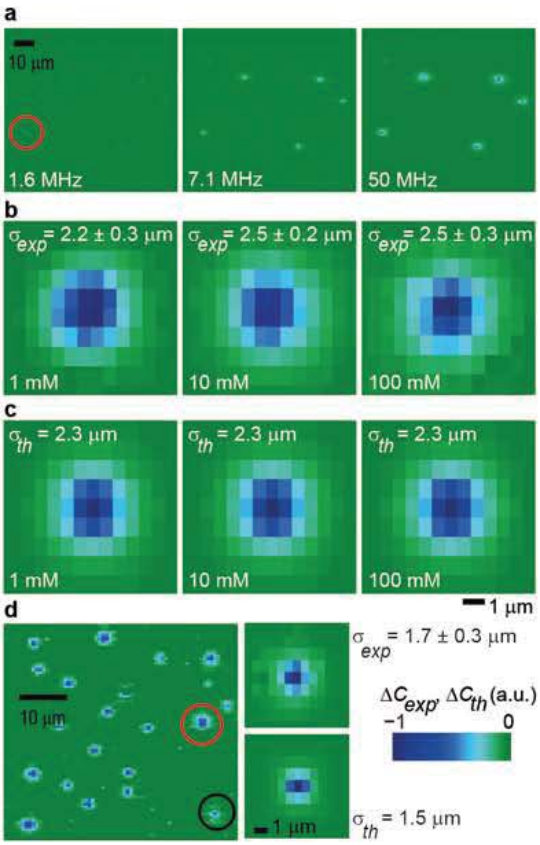

Fig 5.15: **a**, Spatial map of the measured capacitance change (ΔC_{exp}) induced by the sedimentation of insulating 4.4 μm radius particles for frequencies of 1.6 MHz, 7.1 MHz and 50 MHz. Each pixel represents a nanoelectrode. The sensitivity to the presence of microparticles increases with the frequency. **b**, Response to a single particle at salt concentrations of 1 mM, 10 mM and 100 mM and a frequency of 50 MHz. The rectangular shape corresponds to the asymmetry in the pitch of the array. The apparent particle size σ is independent of ionic strength over two orders of magnitude. Each map was normalized to the maximum value of $|\Delta C_{exp}|$. **c**, Theoretical predictions (ΔC_{th}) for the same conditions as in b. **d**, Map of the array's experimental response to a mixture of two sizes of microparticles, radius 4.4 μm (red circle) and 2.5 μm (black circle) at 100 mM salt concentration. The insets show the experimental (top) and theoretical (bottom) maps for a single 2.5 μm particle. The measurements are a courtesy of C. Laborde and S. Lemay, University of Twente [12].

5.3.3 Considerations on cell detection

An important application for biosensors is stimulation and sensing of biological cells. In this section we provide an outline about why moving to very high frequency is advantageous also in this case.

Using ENBIOS, we have run numerical simulations of a model system where either a model cell of cylindrical shape (radius 5 μm, height 4.86 μm, membrane thickness 5 nm, roughly representative of the dimensions of an eukaryotic cell) or a homogeneous dielectric particle with the same dimensions lies on top of the nanoelectrode array. The cell is described as an outer dielectric shell with relative dielectric constant equal to 2.6 (see the top sketch in Fig. 5.19). The internal cytoplasm is described as an aqueous medium with the same properties as the outer electrolyte (100 mM KCl salt concentration, i.e. approximately physiological conditions). The bead dielectric constant is the same as the

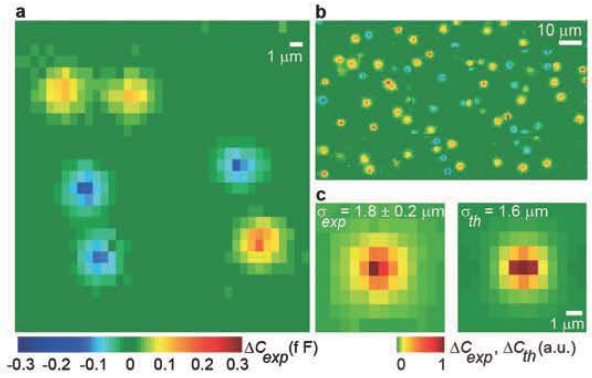

Fig 5.16: **a**, Response of the array to a mixture of dielectric and conducting 2.5 μm radius spheres. The signals have opposite polarities, demonstrating the ability to discriminate between two types of particles at high frequencies. **b**, Zoomed out view of figure a, comprising 30% of the nanoelectrode array surface. **c**, Comparison of experimental (left) and theoretical (right) capacitance maps of a conducting particle at 50 MHz and 100 mM salt. The measurements are a courtesy of C. Laborde and S. Lemay, University of Twente [12].

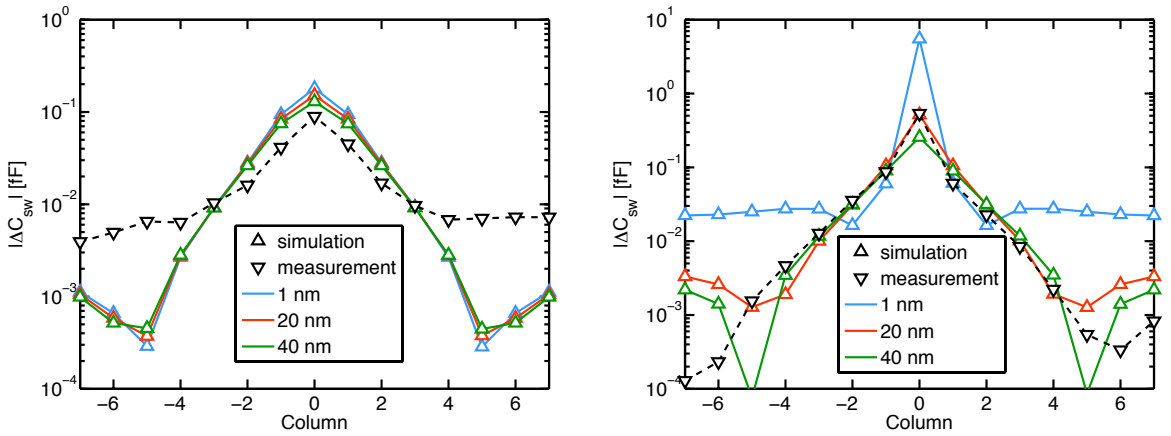

(a) dielectric, 10 mM **(b)** conductive, 1 mM

Fig 5.17: Change in switching capacitance at the central electrode, compared with measurements. In the simulations the particle is centered on the central electrode, the salt concentration is 1 mM (conductive particle) or 10 mM (dielectric particle) and the frequency 50 MHz. The measurements are a courtesy of C. Laborde and S. Lemay, University of Twente [12].

one of the cell wall (bottom sketch in Fig. 5.19). The elevation of the bead and the cell above the electrodes is chosen equal to 50 nm, as a first order approximation of typical conditions in experiments. The electrode dimensions are the same as in the real system (Tab. 5.1).

Fig. 5.19 shows the effective capacitance change induced by the bead and the model cell over a wide frequency range. We observe that up to $f = 1$ MHz the cell and the bead provide essentially the same frequency response, demonstrating that below approximately 1 MHz the AC probe field used for impedance measurements does not penetrate the wall of the cell. Only above about 10 MHz the two spectra start to diverge considerably, pointing out the penetration of the field inside the cytoplasm. These results clearly point out that only by reaching high frequencies in the 10 MHz range it is possible to probe the inner portion of the cells. In this way also the inner cell structures may become accessible

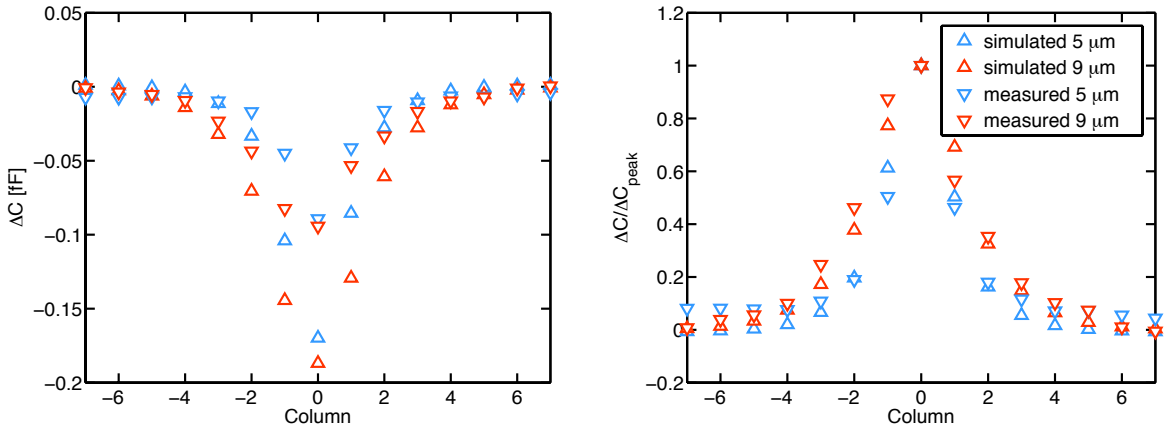

Fig 5.18: Change in effective capacitance at the central electrode for a dielectric particle of either 5 μm or 9 μm diameter, compared with measurements. In the simulations the particle has $d_z = 20$ nm and it is centered on the electrode edge at an angle $\pi/4$ with respect to the x axis. Salt concentration 10 mM. The measurements are a courtesy of C. Laborde and S. Lemay, University of Twente [12].

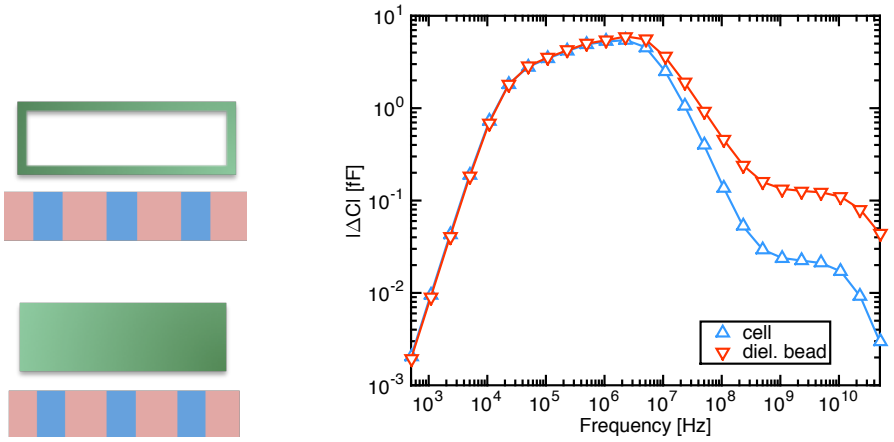

Fig 5.19: Change in effective capacitance at the central electrode for either a homogeneous cylindrical dielectric particle (radius 5 μm, height 4.86 μm) or a model cell with the same size but filled with electrolyte except for the 5 nm outer membrane (which is made of the same material of the dielectric particle). In the simulations the particle and the cell have $d_z = 50$ nm and they are centered on the electrode center. Salt concentration 100 mM.

to the sensor, both on the detection and on the stimulus point of view. Conventional impedance spectroscopy, on the other hand, is not able to penetrate the cell membrane due to lower applied frequencies.

5.4 Model for the admittance change due to spherical particles

The numerical models introduced in Chap. 4 offer many advantages; among them: flexibility in the definition of the sensor and particle geometrical and physical parameters, and accuracy of the solution. Unfortunately, as seen in Chap. 3, significantly different spatial

scales characterize the solution of the PB and PNP equations in biosensors, because of the extremely small value of the static Debye length compared to the sensor dimensions. The inherently multiscale nature of the solution is most often addressed via an aggressive grid refinement, which in turn implies lengthy calculations, severe memory requirements and sometimes convergence problems, especially at high electrolyte salt concentration and with applied DC bias, cannot be excluded.
For all these reasons the derivation of analytical compact models to highlight the main dependencies of the biosensor response is highly desirable. In this spirit, analytical models were derived in Chap. 3. Also, in Sec. 5.5 we will see an alternative to mesh refinement which, although very accurate and powerful, can not be applied to all cases of interest. Analytical compact models of, for instance, ISFET based pH sensors, have been proposed in the past [86, 87], but rarely verified extensively against numerical simulations or experiments.

In this context, we now present the verification of the model of Sec. 3.3.6 for the admittance change (ΔY) induced by spherical dielectric (colloidal) particles at nanoelectrodes. We demonstrate that, in spite of the approximations made, the compact model for ΔY expressed by Eq. 3.116 nicely captures the dependence of the nanoelectrode admittance change upon frequency (f), particle volume (Ω_a) and complex permittivity of the media, over a wide range of sensor and particle physical and geometrical parameters. The model implicitly assumes that the particle is small compared to the electrodes and located at some distance from them. Therefore, it is not directly applicable to the measurements in the previous section. Our results support the possibility to use the analytical model for interpreting the nanoelectrode response, especially in the high frequency limit.
An experimental confirmation of this capability has been obtained by the group of Maarten Jongsma and Harrie Verhoeven via measurements on live and dead cells. The results have been reported in [12].

5.4.1 Numerical reference model

In order to validate the analytical model of Eq. 3.116 we used as reference the two-dimensional numerical finite-difference solver for the Poisson-Boltzmann (Eq. 2.1) and Poisson-Nernst-Planck equations (Eqs. 2.30-2.35) described in [1, 9]. This simulator has been the test bench for the modeling activities that led to the development of ENBIOS during the thesis. Given the good results obtained by the verification and the good agreement between calculations with ENBIOS full 3D models and 2D models with ring shaped electrodes (not shown here), it was felt that entirely repeating the analysis with the full 3D code was not worth the effort.
Compared to the early results of [1], more accurate description of a typical nanoelectrode array geometry was achieved adding the possibility to define more than just one electrode on the same plane at the bottom of the simulation domain (Fig. 5.20b). This planar arrangement of the electrodes closely resembles that of fabricated biosensors (Fig. 5.20c) and, compared to Fig. 5.20a, generates a highly non uniform distribution of the electric field in the electrolyte. By an appropriate choice of the electrode dimensions and particle radius, the electric field over the extension of the particle can be made highly non uniform, especially at low frequency up to approximately the electrolyte dielectric's relaxation cut-off frequency f_c. Therefore, differently from [1, 9] where electrodes were located one in front of the other, the improved simulation code used in this section can be used to test if the assumption of field uniformity made in the derivation of Eq. 3.116 has an appreciable impact on the accuracy of the results. We will use electrodes with radius of 75 nm and

pitch (defined as the distance between the electrodes centers) of 660 nm, which is of the same order as the interelectrode distance in the array of [33]. The difference between the inner and the outer radii of the counter electrodes CE1, CE2 (see Fig. 5.20b) is 150 nm.

In all simulations, the DC bias on the electrodes and the net charge on the particle are both zero. The particle permittivity is taken equal to $2.3\varepsilon_0$ and its radius ranges from 5 nm (which may represent a large protein [88]) to 500 nm (a virus or a colloidal particle [89]). A thin dielectric layer with permittivity ε=$75\varepsilon_0$ and thickness 0.25 nm, mimicking the Stern compact layer (Sec. 2.3.2 and [90]) was considered on the bottom surface. Note that in the Stern layer the permittivity should be lower than in the electrolyte, as discussed in Sec. 2.3.2, but, because in all the simulations no DC bias is applied, as we have seen the exact value of the compact layer permittivity has a modest quantitative impact on the results, thus justifying the assumptions made.

The system geometry is sketched in Fig. 5.20. One active electrode and two counter electrodes are included in the simulation domain and we explicitly verified that the addition of more electrodes would not change the results in the range of particle radii considered. For the sake of simplicity the electrolyte dielectric constant is independent of ion-concentration and frequency [48, 50]. This approximation has a small quantitative impact but no qualitative practical consequence on the results) as also illustrated in Sec. 2.3.1).

Fig. 5.21 compares the change in conductance (ΔG, top) and capacitance (ΔC, bottom) obtained by means of 2D numerical simulations with the predictions of Eq. 3.116 for particles of different radius (from 40 nm to 500 nm, left) suspended 200 nm above the bottom electrode and for a particle with fixed 40 nm radius suspended at different height above the electrode (right). The analytical model (open symbols) nicely reproduces all features in the simulated nanoelectrode admittance response, and shows very good quantitative agreement for particles smaller than the electrode radius placed at least a few Debye lengths above the electrode surface. In most cases, ΔG and ΔC increase for increasing frequency and tend to a constant value for $f \gg f_c = \sigma_{el}/(2\pi\varepsilon_{el})$, being as usual f_c the electrolyte dielectric relaxation cut-off frequency. A peak in ΔC is sometimes observed, which will be discussed in more detail in Sec. 5.4.2. The dips in ΔG are caused by sign changes. It can be shown analytically that these sign changes appear in multi-domain media with spacially dependent complex conductivity that entail sign changes of the frequency dependent real part of $(\tilde{E}_0/\tilde{V}_0)^2$ (see also left graph in Fig. 5.26).

Actual biomolecules often carry a pH dependent surface charge when dispersed in electrolyte environment. To exemplify the impact of this charge on the admittance response,

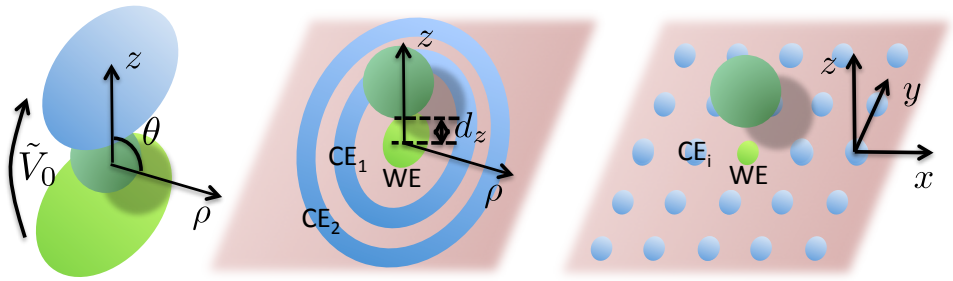

(**a**) uniform field (**b**) 2D approximation (**c**) real array

Fig 5.20: Sketch of the uniform field system where the analytical model is derived (a), of the 2D approximation with cylindrical symmetry of the nanoelectrode array (b) and of the real array (c). The DC and AC potential is applied to the working electrode (WE, green). Its neighbours (counter electrodes CE, blue) are grounded. Moving to cylindrical coordinates, the 8 nearest CEs in (c) become the CE1 electrode in (b), the next 16 become the CE2 and so on.

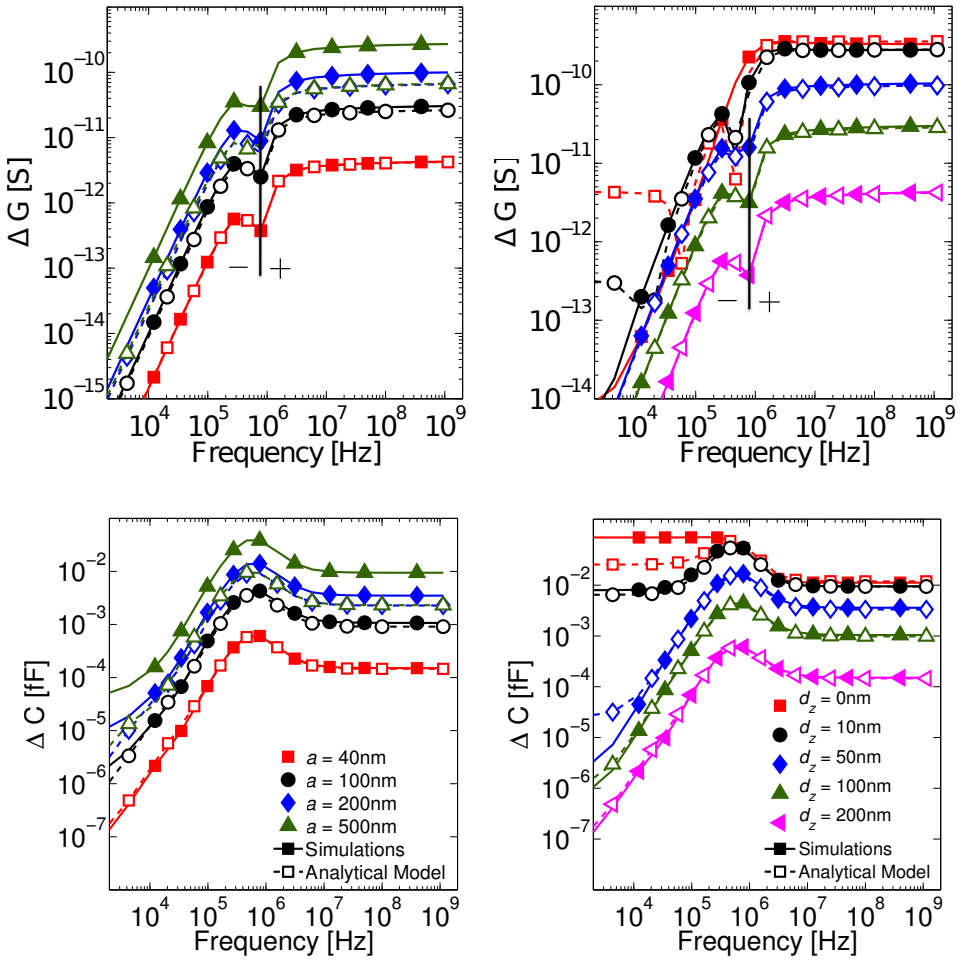

Fig 5.21: Comparison between the change in conductance (ΔG, top) and capacitance (ΔC, bottom) obtained by means of 2D numerical simulations and the predictions of the proposed analytical model for particles of different radius suspended 200 nm above the bottom electrode (left) and for a particle with fixed $r_p = 40$ nm suspended at different height above the electrode (right). Sign changes on ΔG are marked .Bulk ion concentration n^∞=1.5 mM.

Fig. 5.22 shows ΔG and ΔC for neutral and positively charged biomolecules ($\sigma_q \approx 5$ mC/m^2, see e.g., [88]). As can be seen, consistently with previous results [1, 10], the charge affects mostly the low frequencies below the peak frequency, but does not upset the qualitative features of the spectrum, which still exhibits a maximum and two cut-off frequencies. Similar results were obtained upon application of a DC bias up to about 100-200 mV between the electrodes. These simulations suggest that, although derived for neutral biomolecules at zero DC voltage, the model of Eq. 3.116 retains its ability to provide qualitative insight even in these more general conditions.

In order to understand in more detail the role played by the environment and the system parameters on the nanoelectrode response and the applicability of the analytical model to a wide range of physical conditions we will separately examine in the following all the main dependencies of ΔY=$\Delta G + j\omega\Delta C$. In particular, we focus on the change in capacitance ΔC at high frequency because tiny capacitance changes can be accurately measured on integrated circuits [91] and because the high frequency regime hols the promise for accurate and sensitive detection of analytes.

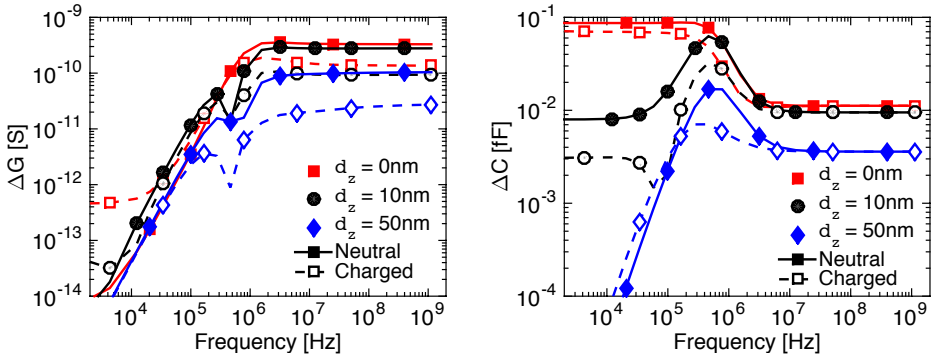

Fig 5.22: *Change in conductance ΔG and capacitance ΔC due to a particle with fixed $a = 40$ nm suspended at different height above the electrode. Filled symbols: neutral particles. Open symbols: charged particles with surface charge σ_q=5 mC/m^2.*

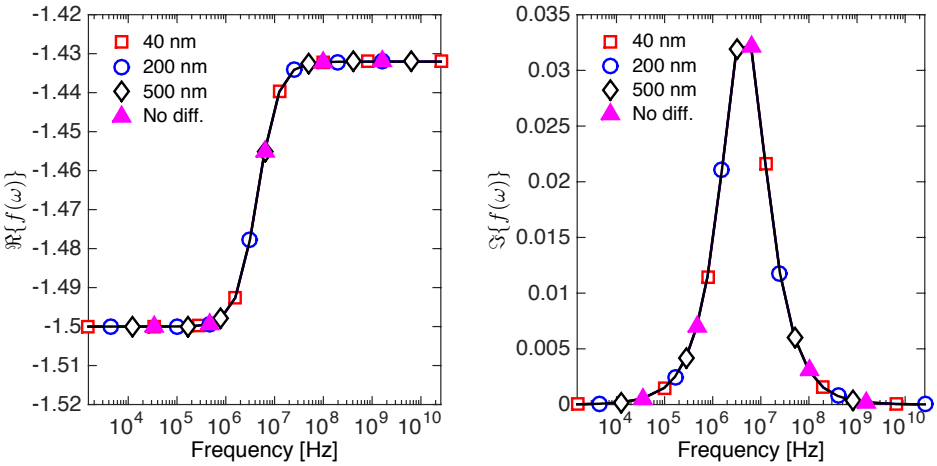

Fig 5.23: Real (left) and Imaginary (right) part of $f(\omega)$ of Eq. 3.115 for particles of different radius. Note that $|\Re\{f(\omega)\}| \gg |\Im\{f(\omega)\}|$. Bulk ion concentration n^{∞}=1.5 mM. Filled symbols show simulations without AC diffusion currents. These are not so important for the considered dielectric particles but instead extremely relevant for conductive particles.

5.4.2 Verification

As a first step we examine the term $f(\omega)$. Fig. 5.23 reports its real (left) and imaginary (right) parts over a wide frequency range for particles of $r_p = 40$, 200 and 500 nm radius. Clearly, $f(\omega)$ has a negligibly small imaginary part (compared to the real part) and, as expected from Eq. 3.115, tends to $-3/2$ for $\omega \to 0$. For insulating particles, which are the scope of this section, the inclusion of diffusion AC currents is not so important (compare filled and open symbols in Fig. 5.23) and furthermore, $f(\omega)$ exhibits a very modest variation over the entire frequency range and a negligible dependence on the particle size. For conducting particles instead (not shown), $f(\omega)$ is strongly affected by diffusion AC currents, it is remarkably frequency dependent and even changes sign around f_c. However, a detailed analysis of this effect goes beyond the scope of this section. Therefore, for all practical cases of dielectric particles $f(\omega)$ does not affect the expected proportionality between ΔY and Ω_p, $(\tilde{E}_0/\tilde{V}_0)^2$ and the complex permittivity of the electrolyte $\sigma_{el} + j\omega\varepsilon_{el}$. Consequently, in the following we will consider $f(\omega)$ a real constant.

5.4.2.1 Volume dependence

Next we examine the proportionality of ΔY to the particle volume Ω_p. To test the model prediction we run 2D numerical simulations for particles of increasing radius located at fixed height above the electrode. Fig. 5.24 shows the high frequency ΔG and ΔC ($f \gg f_c$) as a function of particle volume and clearly demonstrates that proportionality to Ω_p is verified as long as the particle is located sufficiently above the electrode, and the particle radius is not too large. Similar results (not shown) were obtained also at lower frequencies $f \approx f_c$ and $f \ll f_c$. Meaningful discrepancies with respect to the model predictions could be found only for relatively large particles at very small distance from or in contact with the electrode.

In this context a particle can be smaller than an electrode and still too close to it to be described with a bulk model, as that of Eq. 3.116. Alternatively, it can be a few 100 nm above the working electrode but its radius can be comparable to the inner radius of CE1. In that case it will experience a highly nonuniform electric field. Both these cases lead to deviations from the model of Eq. 3.116, as seen in Fig. 5.24. In the first case deviations from the model occur if the particle/electrode separation is:

1. less than a few Debye lengths;

2. comparable or less than the particle radius (but still considerably larger than the Debye length).

5.4.2.2 Field dependence

Since very sensitive and accurate capacitance measurements are possible with integrated circuitry in CMOS technology [33, 92], in the following we will restrict our attention on the change in capacitance ΔC due to insertion of particles in the nanoelectrode sensor. As we will see, especially at high frequency particle detection based on high frequency ΔC offers several advantages that justify this choice. To this purpose, starting from Eq.

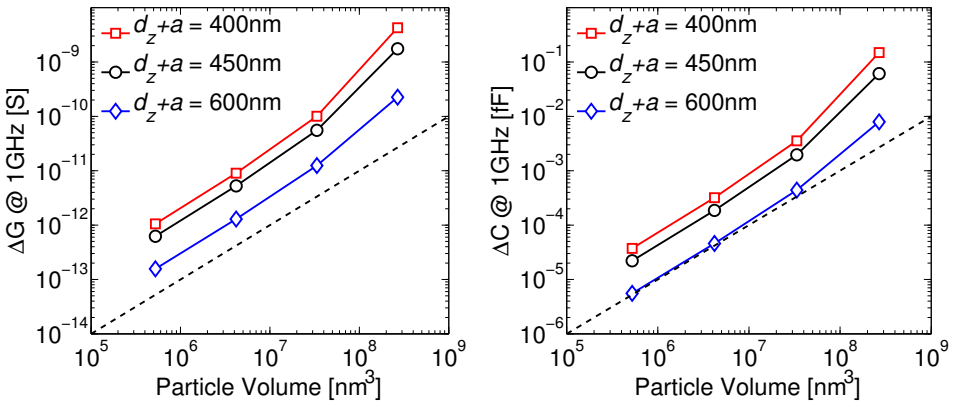

Fig 5.24: ΔG (left plot) and ΔC (right plot) at high frequency versus particle volume ($\propto r_p^3$) and d_z. r_p = 50, 100, 200 and 400 nm. We note the linearity of the curves when the particle bottom surface is not too close to the electrode (the straight dashed curve is a guide for the eye with unitary slope). Bulk ion concentration n^∞=1.5 mM.

3.116 and reminding that $f(\omega)$ is essentially a real term, we can express ΔC as:

$$\Delta C = f(\omega)\Omega_p \varepsilon_{el}\, \chi \tag{5.2}$$

$$\chi = \Re\left\{\left[\frac{\tilde{E}_0}{\tilde{V}_0}\right]^2\right\} + \frac{1}{\omega\tau_{el}}\Im\left\{\left[\frac{\tilde{E}_0}{\tilde{V}_0}\right]^2\right\} \tag{5.3}$$

ΔC is the sum of two contributions, respectively proportional to the imaginary part of $(\tilde{E}_0/\tilde{V}_0)^2$ multiplied by the electrolyte conductivity $\sigma_{el} = \varepsilon_{el}/\tau_{el}$ and the real part of $(\tilde{E}_0/\tilde{V}_0)^2$ multiplied by the electrolyte permittivity.

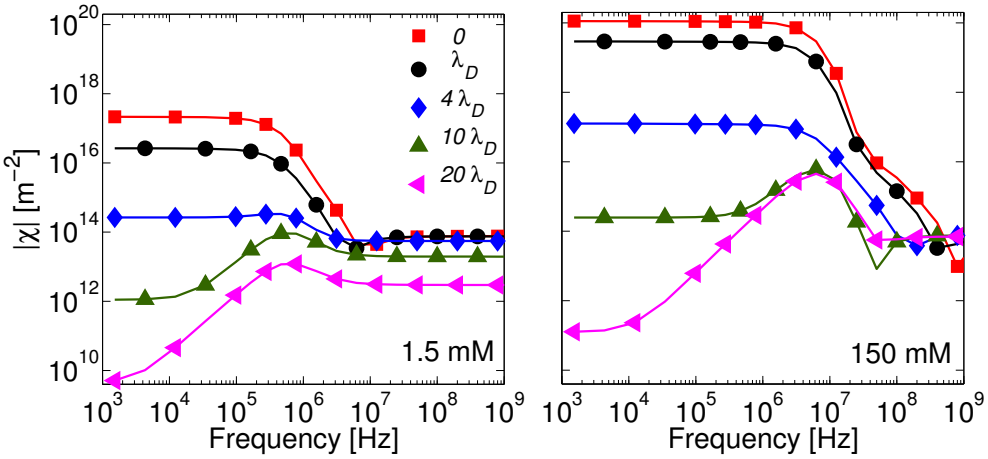

Fig 5.25: Frequency dependence of $|\chi|$ at a few locations above the electrode center. The data refers to electrolyte molar concentrations $n^\infty = 1.5$ mM (left) and 150 mM (right).

In order to test and understand the dependence of ΔC on the field intensity contained in the χ parameter (Eq. 5.3), we run 2D simulations for a variety of physical conditions. In fact, the analytical model has been derived under the assumption of a small particle suspended much above the electrode in a spherically symmetric field configuration while in reality the electrodes are lying adjacent to one another on the chip surface, so that the accuracy of the expression for χ cannot be given for granted. On the other hand, since the field configuration and intensity at the location where the particle stands can be engineered to some extent via a suitable sensor design, insight in the field dependence of the nanoelectrode response clearly bears extremely useful practical information.

Fig. 5.25 shows the frequency dependence of $|\chi(\omega)|$ computed numerically at a few locations above the electrode center. We note that if $|\chi(\omega)|$ is calculated at a distance from the electrodes larger than a few Debye lengths λ_D, then a peak appears in the spectrum.

As shown in Fig. 5.26 this peak is due to the second term in the expression of χ (see Eq. 5.3), that is, to the frequency dependence of the imaginary part of $(\tilde{E}_0/\tilde{V}_0)^2$. The presence of such a peak is also visible in Fig. 5.21 and was previously observed in [1]. Using the simple 1D analytical model of Sec. 3.1.1, we can derive an approximate analytical expression for the peak frequency assuming the particle is not too close to the electrode . In particular, following the calculations in Sec. 3.1.1.4, the expression reads (see also Eq. 3.48):

$$f_p^2 = \frac{f_c^2}{3}\left(-1 + \sqrt{1 + 24\lambda_D^2\left(\frac{\tilde{E}_0}{\tilde{V}_0}\right)^2\Big|_{\omega=\infty}}\right) \tag{5.4}$$

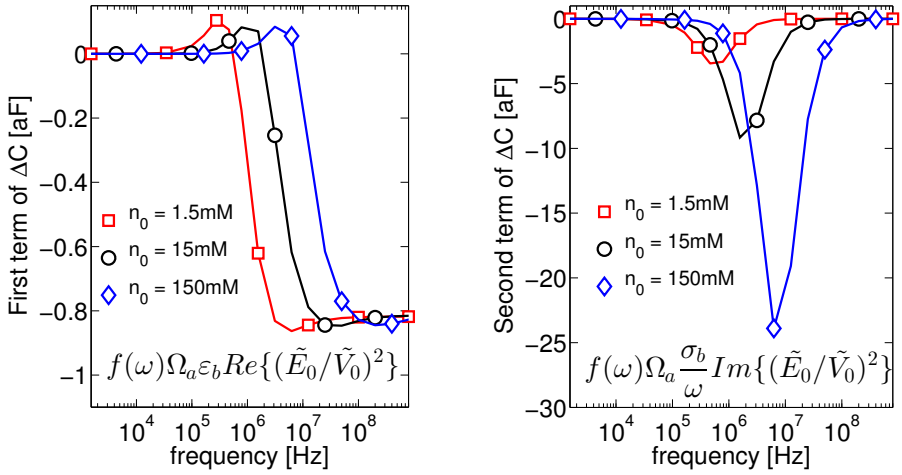

Fig 5.26: Comparison between the two terms contributing to ΔC in Eq. 5.3 as a function of frequency and for a few bulk electrolyte concentrations n^∞. The sum of these terms gives the analytic ΔC.

n^∞ [mM]	f_c [MHz]	d_z	f_p [MHz]	f_p^{sim} [MHz]
1.5	5.22	$10\lambda_D$	0.60	0.61
		$20\lambda_D$	0.58	0.61
150	543	$10\lambda_D$	6.08	6.25
		$20\lambda_D$	5.86	6.25

Table 5.3: Table of the peak frequencies calculated with Eq. 5.4 (f_p) and extracted from Fig. 5.25 (f_p^{sim}), for different salt concentrations and heights above the centre of the electrode. The electrolyte dielectric relaxation's cut-off frequency f_c is also shown.

where $f_c = 1/2\pi\tau_{el} = \sigma_{el}/2\pi\varepsilon_{el}$ is again the electrolyte's dielectric relaxation cut-off frequency and the term $\tilde{E}_0/\tilde{V}_0$ is calculated in the limit of high (infinite) frequency, where it is a real number. Note that, because $\tilde{E}_0/\tilde{V}_0$ is a function of the position, so is f_p. In Tab. 5.3 we show that this approximate expression can reproduce very well the peak frequencies extracted from Fig. 5.25. In this case the electric field $\tilde{E}_0$ has been directly calculated in the simulations. Since in practical cases it is always true that $\lambda_D^2(\tilde{E}_0/\tilde{V}_0)|_{\omega=\infty} \ll 1$, we expand the square root in Eq. 5.4 and note that f_p is proportional to λ_D, i.e. it is roughly proportional to the square root of n^∞, while f_c is directly proportional to n^∞ via the σ_{el} term. This observation is consistent with the data reported in Tab. 5.3.

Large particles located in proximity of the electrode tend to average out the electric field; therefore the peak will smear out and possibly disappear from the capacitive response of large particles, as visible in Fig. 5.8. Furthermore, the peak is expected to disappear for small particles nearly attached to the electrode as in Fig. 5.46, since in this case the influence of the AC double layer becomes important. Unfortunately, at the time of writing, these predictions could not be verified experimentally yet because the software of [33] is not ready to perform calibrated frequency sweeps.

Fig. 5.27 reports ΔC at the frequency of peak response (open symbols) and ΔC at high frequency (1 GHz, filled symbols) versus $|\chi|$ over a wide range of molar concentration, particle radius and height above the electrode. In many of these conditions the model assumption of a large R/r_p ratio and consequently an essentially constant AC electric field in the region occupied by the particle is not well satisfied. Nevertheless we see that the capacitance change is approximately linear in $|\chi|$, as expected based on the compact

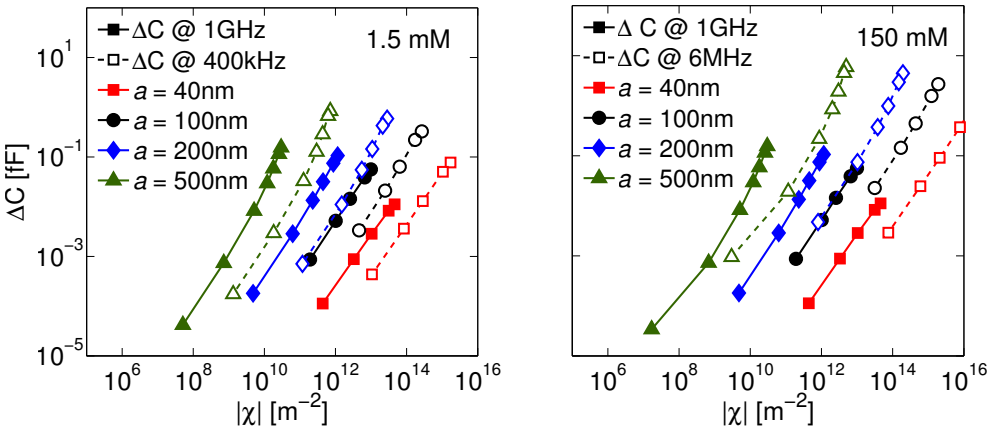

Fig 5.27: Nanoelectrode response ΔC to the introduction of a particle in the electrolyte as a function of $|\chi|$, where χ is the term in square brackets in Eq. 5.3 and $\tilde{E}_0$ is the unperturbed electric field at the position of the center of the particle. The data refers to electrolyte molar concentrations of 1.5 mM (left) and 150 mM (right), at $f = f_c$ and $f \gg f_c$, particle height above the electrode between 0 and 1000 nm.

analytical model, except when the particle is large and its elevation above the electrode very small, as discussed in Sec. 5.4.2.1. These results further confirm the validity of the analytical model.

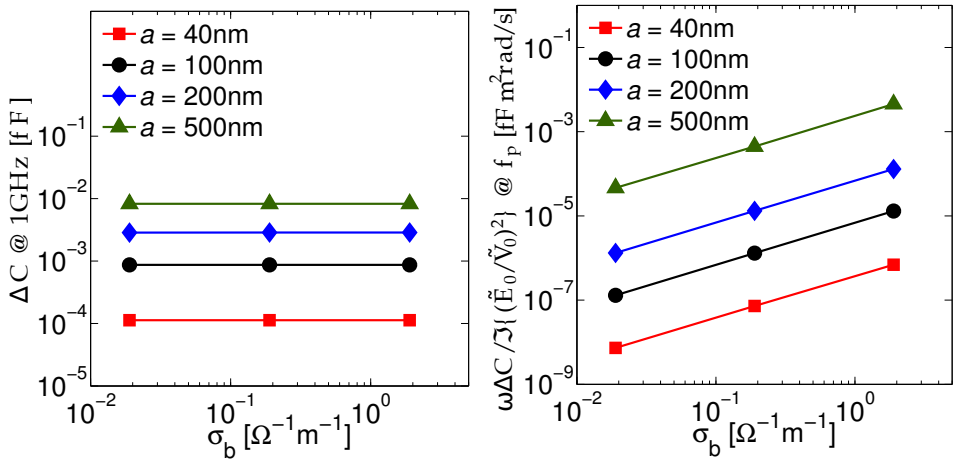

Fig 5.28: Simulated ΔC at 1 GHz (left) and $\omega \Delta C / \Im\{(\tilde{E}_0/\tilde{V}_0)^2\}$ at the frequency of the peak response (right) as a function of electrolyte bulk conductivity for a few particle sizes. The elevation above the electrode is $d_z = 200$ nm.

5.4.2.3 Concentration dependence

The results in Fig. 5.26 show that the imaginary part of $(\tilde{E}_0/\tilde{V}_0)^2$ divided by ω (second term in Eq. 5.3) is vanishingly small for both low and high ω while the first term containing the real part of $(\tilde{E}_0/\tilde{V}_0)^2$ is small below f_c and tends to a constant value for $f \to \infty$. Therefore, since σ_{el} is proportional to the electrolyte molar concentration while ε_{el} is very weakly affected by it, based on the analytical model we expect ΔC at high frequency to

be dominated by the first term in Eq. 5.3 and to be essentially independent of frequency and salt concentration regardless of details such as the particle dimensions.

To prove this point, Fig. 5.28 (left) reports the simulated ΔC at high frequency (1 GHz) as a function of the electrolyte conductivity σ_{el}. We see that the predictions of the analytical model are fully confirmed over a wide range of parameter values and the high frequency ΔC is as expected independent of salinity. In fact, such a behaviour has been observed previously in simulations [1, 3, 9].

In general, however, both terms contributing to χ may be relevant. We can then write that:

$$\frac{\omega\chi}{\Im\left\{(\tilde{E}_0/\tilde{V}_0)^2\right\}} = \omega\frac{\Re\left\{(\tilde{E}_0/\tilde{V}_0)^2\right\}}{\Im\left\{(\tilde{E}_0/\tilde{V}_0)^2\right\}} + \frac{\sigma_{el}}{\varepsilon_{el}} = \omega\frac{\Re\left\{(\tilde{E}_0/\tilde{V}_0)^2\right\}}{\Im\left\{(\tilde{E}_0/\tilde{V}_0)^2\right\}} + 2\pi f_c$$

From this expression we immediately note that, if the real and imaginary parts of $(\tilde{E}_0/\tilde{V}_0)^2$ are of comparable magnitude and the frequency is much smaller than f_c, the second term should be dominant and directly proportional to σ_{el}. This condition is indeed fulfilled at the frequency of the peak as evident from the numerical simulations shown in Fig. 5.28 (right). These results confirm the concentration dependence predictions of the analytical model.

5.4.3 Range of model validity

Having characterized the main model dependencies in Section 5.4.2, we then tested the high frequency analytical model predictions for many different parameter sets. In fact high frequency operation, although more difficult to implement in hardware, is very promising. Figure 5.29 shows the high frequency ΔC calculated for five different particles located at three different heights above the nanoelectrode (0 nm, 10 nm and 100 nm). The particle radius is 5, 30, 50, 100 and 300 nm. For curves with circles, the term $\tilde{E}_0$ is computed from the 2D simulations as the electric field at the location of the particle center in absence of the particle. As we can see, the analytical model captures very well the sensor response for small particles but the discrepancy with the numerical model increases for particle radii comparable to electrode dimensions, and decreasing distance from the electrode. Figure 5.30 shows similar results, but now, the radius is fixed and the height is changed. Similar results were obtained for the high frequency ΔC for an electrolyte concentration of 150 mM. This is expected, because at frequency above the electrolyte cut-off AC screening becomes ineffective and the capacitance change is independent of the ion concentration (as demonstrated in Fig. 5.28 left).

Note that if the electric field at the position of the particle center is replaced by the average field over the particle volume the model accuracy is remarkably improved, especially for large particles and small elevation values. This observation entails that there is no real advantage in making the field non uniform over the particle volume, but it is advantageous if the particle occupies a region with high average unperturbed electric field. Moreover, it suggests the possibility to reliably use the model predictions well beyond the strict domain of validity of the approximations used.

5.5 Simulations with lumped double layer admittance

Since, as already pointed out, at high molarity the electrolyte Debye screening length (λ_D) is much shorter than typical sensor dimensions, challenging multiscale-multiphysics

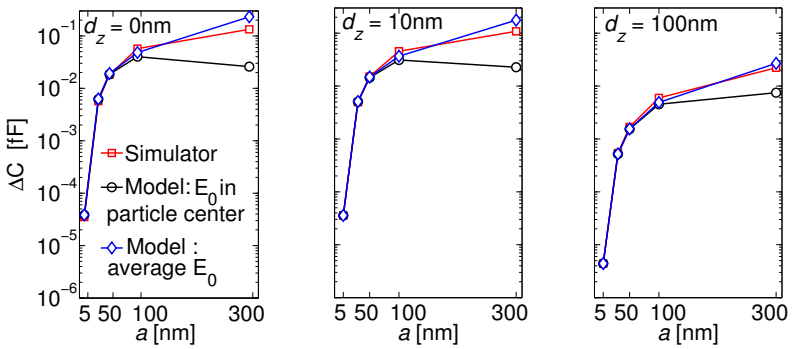

Fig 5.29: High frequency capacitance change ΔC due to biomolecules of 5 different radii (5, 30, 50, 100 and 300 nm). Biomolecule attached on the electrode (left), biomolecule detached by 10 nm (center) and biomolecule detached by 100 nm (right). Ion concentration 1.5 mM, $\lambda_D \simeq$ 10 nm.

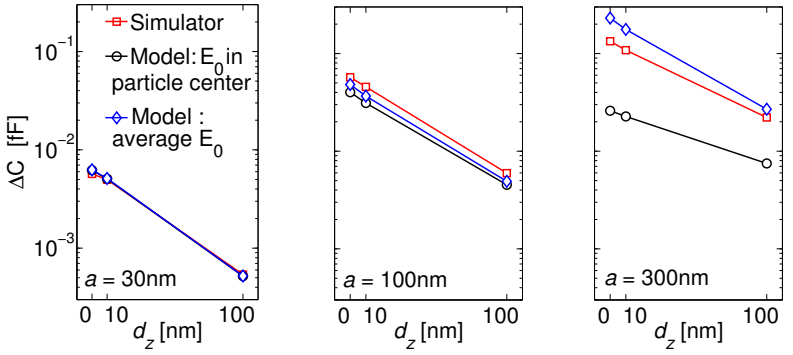

Fig 5.30: High frequency capacitance change ΔC due to biomolecules with 3 different positions (0, 10 and 100 nm from the electrode surface). Biomolecule radius r_p = 30 nm (left), 100 nm (center) and 300 nm (right). Ion concentration 1.5 mM.

simulation problems arise. Issues are especially severe for impedimetric sensor arrays as the one described in Sec. 5.2 [33, 76] because every electrode has on top a thin electrical double layer (EDL) with rapidly changing ion concentrations (n_m) and potential (V) [36] which in turn demand either a fine mesh or special purpose boundary conditions [93]. To make things even worse, very accurate calculations are necessary because the useful signal is a small change of the electrode admittance with respect to a reference condition ($\Delta Y = Y - Y_0$) due to changes of the analyte configuration (e.g. introduction of a biomolecule, drift of a biomolecule's position with respect to the electrode, etc.).

In this section we propose a technique to efficiently account for the EDLs in computing the small signal AC response of impedimetric sensors [33, 76]. The technique significantly reduces the need of fine meshing the EDLs, thus enabling fast simulation of many analyte configurations.
This technique can be useful also in the scope of a domain decomposition (which has been applied to biosensors for instance in [93]), although we will not use it for this purpose. Instead, we will apply the technique only on the external boundary of the domain.

5.5.1 Methodology

We illustrate the method with reference to the nanoelectrode array biosensor presented in Sec. 5.2 [33] (Fig. 5.31), and we use the 3D numerical model ENBIOS to prove the effectiveness of the proposed approach. The array behaves as a multi-terminal device (Fig. 5.32a), and due to the small λ_D accurate simulations require a very fine mesh next to each electrode, especially at low frequency.

To gain a first insight into the problem, we make use of the analytical 1D model of Sec. 3.1.1 (see Fig. 3.1, left), and use the series model for the admittance double layer (Eq. 3.38), which is reported here for convenience:

$$y_{DL} = j\omega\varepsilon_{el}\kappa\frac{\xi + j\omega}{\xi} \tag{5.5}$$

where $\kappa^2 = (\xi + j\omega)/D$ is the squared inverse screening length, $\xi = 2q^2\mu n_0/\varepsilon_{el}$ the electrolyte cut-off angular frequency, μ the ion mobility (in m/Ns), $D{=}\mu kT$ the diffusivity, n_0 the DC bulk ion concentration.
Eq. 3.38 shows that y_{DL} is inversely proportional to the scale length $1/\kappa$ which provides an estimate of the thickness of the EDL. The double layer capacitance $c_{DL} = \Im\left(y_{DL}\right)/\omega$ has a $\omega^{3/2}$ dependence and tends to infinity at high frequency, whereas y_H tends to a constant capacitance per unit area $c_H = \varepsilon_{el}/L$. These observations suggest to represent the EDL as a lumped admittance in series to an electrode in direct contact to the bulk electrolyte. This representation can be generalized to a multiterminal nanoelectrode array as described in the following.

Firstly, we group the array electrodes as follows (Fig. 5.31 and Fig. 5.32): the grounded ones are connected to terminal C. Among the remaining N electrodes (which we assume all biased at the same DC and AC voltage, as in [33]), we group in terminal P those whose EDL is affected by changes in the analyte configuration, while the others are grouped in terminal A. Detailed knowledge of the ion concentrations n_m and potential ϕ in the EDL for all analyte configurations is thus necessary only for electrodes which belong to set P; not for those of set A. In fact, by definition, the EDLs of electrodes in C and A stay the same for all configurations. Note that if the analytes are smaller than the electrode pitch, and with a proper definition of the configuration space, P cointains only one electrode, whereas the A set groups many of them. We now denote M the terminal where the AC current, hence, the admittance is measured.

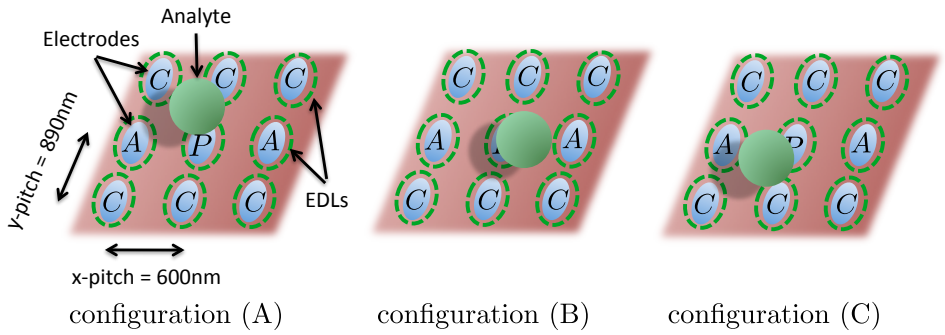

Fig 5.31: Nanoelectrode array sensor with the definition of the different families of electrodes. Electrode radius $r_{el}{=}75$ nm [33]. Each configuration corresponds for instance to a different location of the particle.

***M* and *P* are coincident** We start assuming that $M = P$. We will then discuss the case when M is in group A. The definitions above allow us to model the device as a 2-port with admittance matrix:

$$\mathbf{Y}_2 = \begin{bmatrix} Y_{PP} & Y_{PA} \\ Y_{AP} & Y_{AA} \end{bmatrix} = \begin{bmatrix} \sum_{j\in P}\sum_{l\in P} Y_{jl} & \sum_{j\in P}\sum_{l\in A} Y_{jl} \\ \sum_{j\in A}\sum_{l\in P} Y_{jl} & \sum_{j\in A}\sum_{l\in A} Y_{jl} \end{bmatrix}$$

where the Y_{jl} are the elements of the device N-port $\mathbf{Y}$ matrix.

As suggested in Sec. 3.1.1.2, we write the k-th electrode admittance, Y_k ($k \in P$), as the series connection of the EDL admittance, Y_{DLk}, given by the rapidly space-varying field near the electrode, and the bulk admittance, Y_{bk}, given by the field that deeply penetrates into the electrolyte:

$$\frac{1}{Y_k} = \frac{1}{Y_{DLk}} + \frac{1}{Y_{bk}} \quad . \tag{5.6}$$

The Y_{DLk}s can be computed once for all analyte configurations.

The next step is to transform the 2-port into a new 2-port with admittance matrix $\mathbf{Y}_{2i}$ connected to the admittances Y_{DLC}, Y_{DLA} (Fig. 5.32c), respectively representing the EDLs of the electrodes in groups C and A. Clearly, only $\mathbf{Y}_{2i}$ is affected by changes in the analyte configuration, whereas Y_{DLA} and Y_{DLC} are not.

If ports $M = P$ and A are both biased at V_H, the admittance between port M and ground is $Y = Y_{PP} + Y_{PA}$. To identify the unknown admittances Y_{DLC} and Y_{DLA} and then calculate Y for all configurations of interest, we can thus proceed as sketched in Fig. 5.33; namely:

1. we extract the k-th terminal double layer admittance Y_{DLk} in the reference configuration using Eq. 5.6 where $1/Y_{bk}$ is the admittance obtained when the EDL is

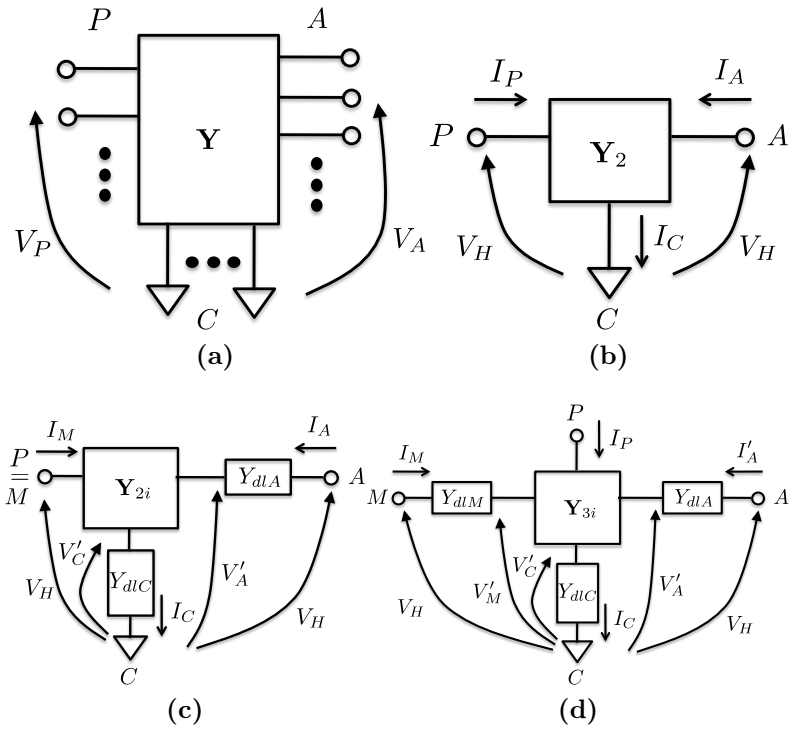

Fig 5.32: AC small signal representations of the nanoelectrode array: (a) multi-terminal; (b) 2-port; (c) 2-port with external lumped elements ($M = P$); (d) 3-port with external lumped elements ($M \neq P$).

eliminated by setting Dirichlet boundary conditions (DBCs). If the electrodes are all identical (as is typically the case in regular arrays [33, 76]), we can then easily calculate Y_{DLA} and Y_{DLC} as the parallel connection of an appropriate number of Y_{dlk};

2. we set DBCs at all terminals except M (which eliminates the corresponding EDLs and the need for a fine mesh next to the electrodes) and compute the intrinsic $\mathbf{Y}_{2i}$;

3. according to the model of Fig. 5.32c, and denoting Δ the determinant of $\mathbf{Y}_{2i}$, $Y_{iP} = Y_{iPP} + Y_{iPA}$ and $Y_{iA} = Y_{iAP} + Y_{iAA}$, we compute the admittance at M as:

$$Y \approx Y' = Y_{DLC} \frac{\Delta + Y_{iP}\, Y_{DLA}}{\Delta + Y_{iAA}\, Y_{DLC} + Y_{DLA}\,(Y_{iA} + Y_{iP} + Y_{DLC})} \tag{5.7}$$

4. we change analyte configuration, go back to steps (2)-(3), where meshing of only one EDL is necessary, and efficiently recompute Y' for the new configuration.

Since the EDLs vanish at small distance from the electrodes, simulations at step (1) can be run (with remarkable time saving) on a small subset of the array and imposing DBC on all electrodes other than k.
We emphasize that DC bias, Stern layers [36] and self-assembled monolayers (SAMs, assuming that they are much thinner than the separation between the electrodes) should be included in the simulations used to calculate Y_{DLA} and Y_{DLC}. We also underline that the method assumes that the EDL thickness is much smaller than the dimensions of the system. In this way when DBCs are imposed and Y_{bk} is identified including the region previously occupied by the EDL only a negligible error is introduced.

***M* and *P* are not coincident** Let us now consider the case where M is one of the electrodes in A and it is therefore distinct from P. A 3-port model is now mandatory (Fig. 5.32d). The system matrix is:

$$\mathbf{Y}_3 = \begin{bmatrix} Y_{MM} & Y_{MP} & Y_{MA} \\ Y_{PM} & Y_{PP} & Y_{PA} \\ Y_{AM} & Y_{AP} & Y_{AA} \end{bmatrix}$$

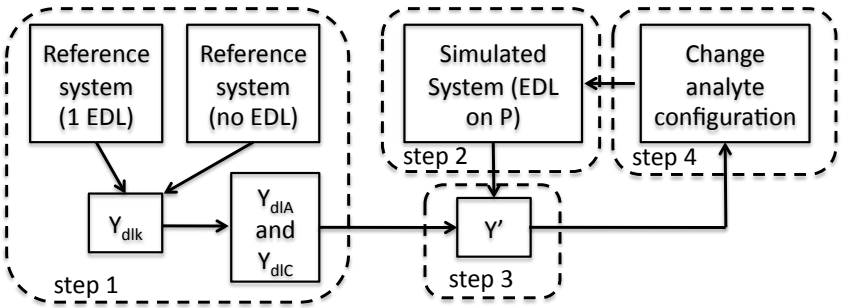

Fig 5.33: Flowchart of the procedure to calculate Y' when M=P. The outer loop on the right (steps 2-4) is repeated for each analyte configuration, while Y_{DLA} and Y_{DLC} are retained. Step 1 is executed only once. Similar procedures are used to calculate Y'' and Y''' (see text).

and the expression for the admittance at M is now:

$$Y \simeq Y''' = (Y_{DLC}Y_{dlM}(Y_{DLA}Y_{iM} + \Delta_{21} + \Delta_{22})) \Big/ \Big(\Delta + Y_{DLC}\Delta_{22} + Y_{dlM}(Y_{iAA}Y_{DLC} + Y_{DLA}(Y_{iA} + Y_{DLC} + Y_{iP} + Y_{iM}) + \Delta_{11} + \Delta_{12} + \Delta_{21} + \Delta_{22}) + Y_{DLA}(Y_{DLC}Y_{iMM} + \Delta_{22} + \Delta_{23} + \Delta_{32} + \Delta_{33})\Big) \quad (5.8)$$

where Δ is the determinant of $\mathbf{Y}_{3i}$, Δ_{ij} is the determinant of the matrix obtained eliminating row i and column j from the matrix $\mathbf{Y}_{3i}$, $Y_{iM} = Y_{iMM} + Y_{iMP} + Y_{iMA}$, $Y_{iP} = Y_{iPM} + Y_{iPP} + Y_{iPA}$ and $Y_{iA} = Y_{iAM} + Y_{iAP} + Y_{iAA}$. The steps to compute the unknowns in Eq. 5.8 and the Y_{DLA}, Y_{dlM} and Y_{DLC} are the same explained for the two-port case (see also Fig. 5.33).The method and Eqs.5.7-5.8 can be further generalized to cases where the EDLs of more than one active electrode have to be meshed and resolved or when $V_M \neq V_A$, but the computational advantage becomes progressively less pronounced.

An alternative method, inspired to the mixed device circuits simulation approach [94], would be to solve the intrinsic system (i.e., with no EDLs on both A and C) simultaneously with the equations that give the potential drop on the Y_{dlk}s. The mixed mode approach is fully general and requires to run only one simulation for each analyte configuration (compared to 2 in the 2-port procedure), but it greatly complicates the algorithm implementation and it may introduce numerical issues, because the values of the matrix elements in the rows that correspond to the Y_{dlk} are of very different magnitude with respect to those in the rows corresponding to the intrinsic part of the system under study. This is evident seeing at the explanation of Sec. 4.2.2.3.

5.5.2 Results

We tested accuracy and numerical efficiency of the method by investigating the response of the nanoelectrode array in [33] to neutral spherical particles representative of various biomolecules: large proteins ($r_p = 10$nm) [88], viruses ($r_p = 500$ nm) [95], and cylindrical DNA strands ($r_p = 1.25$ nm, h=13.2 nm corresponding to 40 basis) [40]. We typically simulate a subset of 5×5 electrodes or less depending on particle size. The molecule is

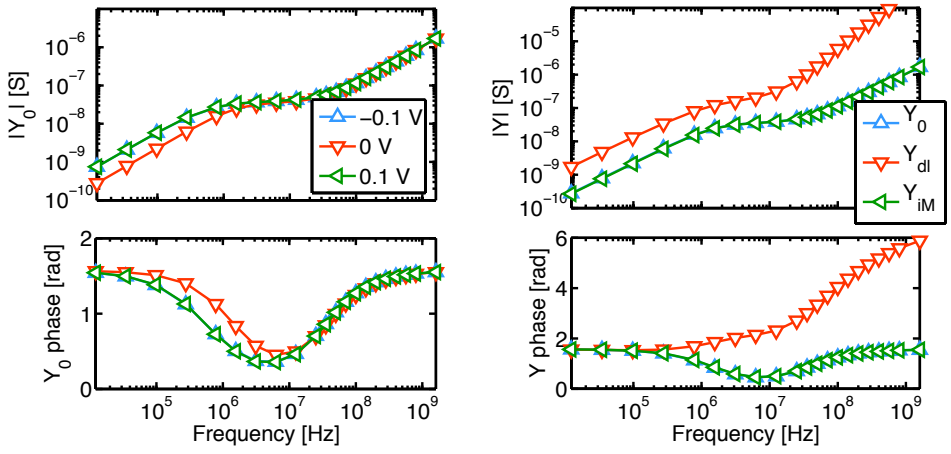

Fig 5.34: Left: exact total admittance at port M=P in the absence of molecules (Y_0, reference configuration) for a few DC bias voltages. Note the symmetric response for positive and negative bias voltages. Right: total admittance at port M (Y_0), one-electrode EDL admittance (Y_{dl}), and intrinsic admittance at port M (Y_{iM}). DC bias V_{DC}=0 V; NaCl bulk electrolyte concentration n^{∞}=10 mM.

located next to the center electrode (P) and no SAM is present unless otherwise specified. The absence of dielectric layers, hence of site binding charge, entails a symmetric response for positive and negative bias voltages.

Fig. 5.34 reports the P-electrode admittance in the absence of molecules (Y_0, reference configuration) calculated with the exact 3D reference model (i.e., with all EDLs included, left, [4]), the intrinsic Y_i (EDL on P only) and the one-electrode EDL admittance Y_{DL} (right). Y_{DL} is comparable to Y at low frequency, whereas $|Y_{DL}| \gg |Y| \simeq |Y_i|$ at high frequency. Fig. 5.35 shows the change in admittance and in capacitance $\Delta C = \Im(\Delta Y)/\omega$ due to dielectric or metallic particles calculated with the exact 3D model and with the proposed lumped element approximation of the EDLs ($\Delta Y'$). The excellent agreement observed at all frequencies between ΔY and $\Delta Y'$ demonstrates the accuracy of the proposed method.

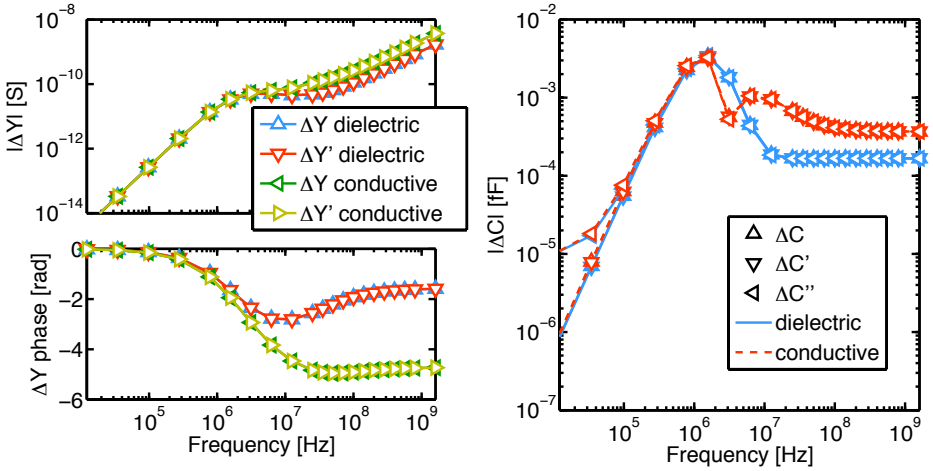

Fig 5.35: Change in admittance (left) and corresponding change in capacitance (right) due to the introduction of a spherical dielectric or conductive particle (r_p= 10 nm) on the center electrode of the array calculated at M=P with exact 3D simulations (ΔY, ΔC; all EDLs included), with the proposed method ($\Delta Y'$, $\Delta C'$; lumped elements at $k \notin M$) and neglecting EDLs for $k \notin M$ ($\Delta C''$). $\Delta Y'$ and $\Delta C'$ are excellent approximations to ΔY, ΔC at all frequencies. $\Delta Y''$ and $\Delta C''$, instead, deviate at low frequency. Particle height d_z = 20 nm; V_{DC}=0 V; n^{∞}=10 mM.

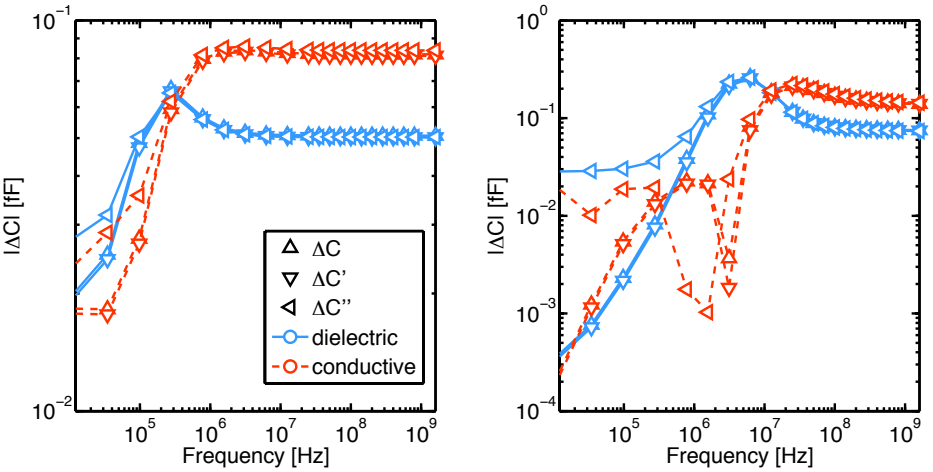

(a) d_z = 20 nm, 0.1 mM, DC 0 V **(b)** d_z = 1 nm, 10 mM, DC 0.1 V

Fig 5.36: Change in capacitance due to a spherical dielectric or conductive particle (r_p = 500nm) at the center electrode M=P of the array calculated with the reference full 3D simulations (ΔC) and the lumped element model of Fig. 5.32c ($\Delta C'$ and $\Delta C''$). $\Delta Y'$ and $\Delta C'$ are excellent approximations of ΔY and ΔC at all frequencies; $\Delta Y''$ and $\Delta C''$ only at high frequency. SAM thickness 2.5nm.

Since at high frequency Y_{DLA} and Y_{DLC} are often much larger than Y, we also computed Y''=lim$_{Y_{DLA},Y_{DLC}\to\infty} Y'$. We see from Fig. 5.34 that $Y'' \simeq Y'$ at high frequency, which suggests the possibility to further simplify the simulations by neglecting the EDLs on all counterelectrodes except P whenever Y_{dl} is very large, i.e. at large salt concentration and high frequency. The inclusion of Y_{DLA} and Y_{DLC} in the model is instead mandatory for accurate results at low frequency.
Similar conclusions were obtained for any particle height, d_z, and radius, r_p, provided the analyte interacts only with electrode P. This is demonstrated in Fig. 5.36, which reports ΔC due to the r_p=500 nm particle in presence of a 2.5nm thick SAM and for varying position, DC bias and salt concentration. Needless to say, all these considerations depend on the actual system geometry, the frequency range of and the salt concentration. It is therefore recommended that the use of this technique is guided by experience and common sense to avoid naive errors.

Fig. 5.37 shows the results when $M \neq P$ and the 3-port model is used (triangles left). The comparison with the results obtained with a 2-port approximation (where we included the electrodes P in set A, and calculated Y_{DLA} as the parallel of only those Y_{DL}s that are not in series with P) demonstrates the need of a 3-port representation when $M \neq P$. In fact, the 2-port approximation under- or overestimates ΔC especially at high frequency.

Fig. 5.38 shows the simulated change in admittance ΔY=$Y_{ss}-Y_{ds}$ and capacitance ΔC when a single strand DNA attached to a 2.5 nm SAM on top of the electrode is hybridized with a complementary sequence, thus forming a double strand (ds). The agreement with the reference full 3D simulations is again excellent if the calculation is carried out with the proposed method. More results on the response of the array to DNA strand hybridization is found in Sec. 5.8.

Last but definitely not the least, Fig. 5.39 shows the relative speedup provided by our method with respect to calculations where all EDLs are explicitly meshed. All cases discussed above are reported. A remarkable speedup factor of about a factor of 3 to 30 is observed, roughly proportional to the square of the ratio between the number of mesh-points in the systems without and with the lumped elements.

Besides the insight on the role of EDLs in the array response, the proposed technique is thus very advantageous, accurate and easy to implement.

As a final note, see that there are sign changes in ΔC in Figs. 5.36 - 5.37, which

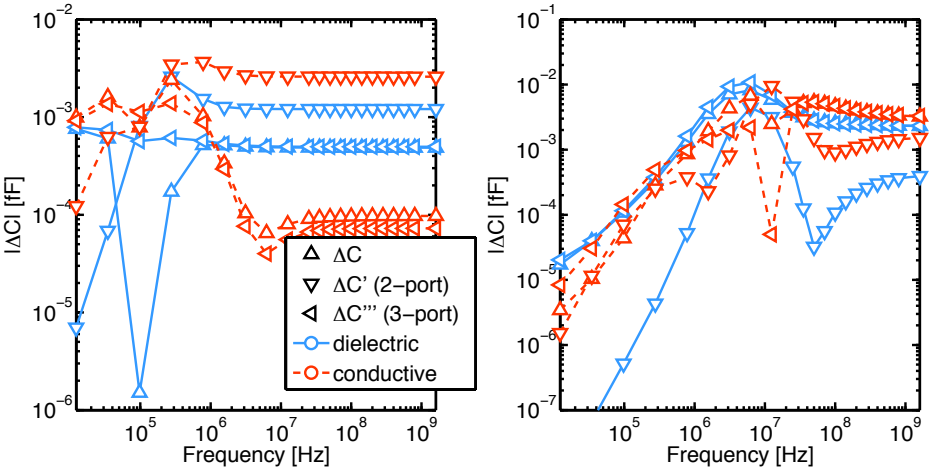

(a) $d_z = 20$ nm, 0.1 mM, DC 0 V **(b)** $d_z = 1$ nm, 10 mM, DC 0.1 V

Fig 5.37: Same as in Fig. 5.36, but calculating ΔC at the first neighbour from the central electrode ($M \neq P$). The results given by the 2-port and 3-port models ($\Delta C'$ and $\Delta C'''$) are shown. Note that $\Delta C'''$ is a good approximation of ΔC at all frequencies while $\Delta C'$ is not.

correspond to the sharp dips. As illustrated already in Sec. 3.3.5, the sign changes are due to the balance between diffusion forces on the one hand and ohmic transport on the other hand. This effect is more evident when the double layers are more pronounced, i.e., in the cases with conductive particles and applied DC bias.

5.6 ΔY for small spherical particles in constant field

We now analyse the biosensor response due to the same spherical dielectric particle of 10 nm radius (representative of a big protein [88], $\varepsilon = 2.6\varepsilon_0$). In order to easily understand the physical phenomena, like the frequency dependence of the electrolyte permittivity, steric effects, biomolecule charge and AC diffusion currents, and to more easily compare to the study in Sec. 5.4, we take a step back and analyse a slightly simpler 2D system with cylindrical symmetry (Fig. 5.40). In absence of particles this is a 1D system, like the one solved in Sec. 3.1. We simulate the change in admittance ΔY between the electrodes due to the introduction of a small spherical particle. The simulation parameters are reported

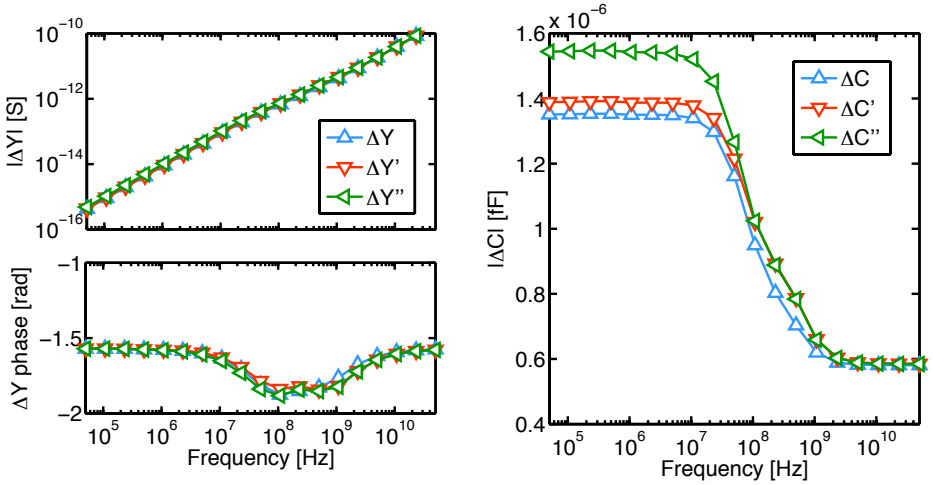

Fig 5.38: Change in admittance (left) and capacitance (right) due to DNA hybridization. The single (ss) and double (ds) DNA strands are modeled as in [9]. Calculations are done with exact 3D simulations explicitly accounting for all EDLs (ΔY=Y_{ss}-Y_{ds}, ΔC=$\Im(\Delta Y)/\omega$), with the proposed procedure based on lumped elements ($\Delta Y'$, $\Delta C'$) and neglecting all EDLs except the one on M=P ($\Delta Y''$, $\Delta C''$). The DNA is attached to a 2.5 nm SAM and stands upright from the electrode center; n^{∞}=150 mM. $\Delta Y'$ and $\Delta C'$ are excellent approximations to ΔY, ΔC at all frequencies. $\Delta Y''$ and $\Delta C''$ only at high frequency.

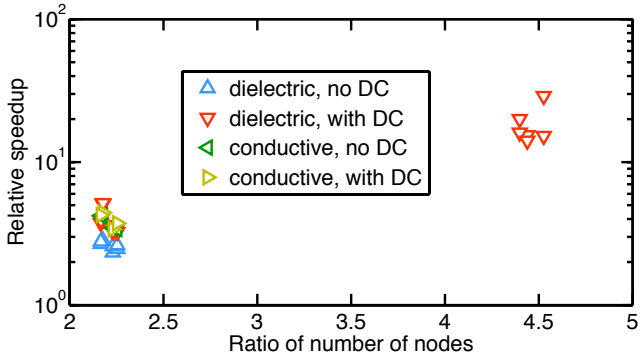

Fig 5.39: Simulation speedup between the proposed method ($\Delta Y'$, i.e. EDL only on M and lumped elements for $k \notin M$) and the case where all EDLs are explicitly meshed and accounted for (ΔY) versus the ratio of the number of mesh points in the grids. M=P. $|V_{DC}|$=0.1 V. The speedup is a factor of 2/3 smaller when $M \neq P$ because one extra simulation is required for each analyte configuration.

Parameter	Symbol	Value	Units
Bottom electr. DC pot.	V_{0B}	0.05	[V]
Top electr. DC pot.	V_{0T}	0	[V]
Bulk potential	V_{ref}	0	[V]
System radius	ρ_{max}	91	[nm]
System height	z_{max}	200	[nm]
SAM thickness	h_{SAM}	2.5	[nm]
Mobility of Na^+	μ_1	$3.242 \cdot 10^{11}$	[m/Ns]
Mobility of Cl^-	μ_2	$4.937 \cdot 10^{11}$	[m/Ns]
Temperature	T	307.66	[K]
SAM permittivity	ε_{SAM}	$2.3\varepsilon_0$	[F/m]
Biomolecule permittivity	ε_{biomol}	$2.3\varepsilon_0$	[F/m]

Table 5.4: Parameters used in the simulations.

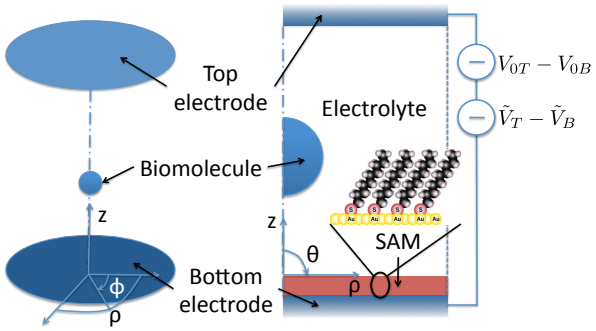

Fig 5.40: Sketch of the 2D system with cylindrical symmetry used to study the impact of AC diffusion currents, SAM and particle position on the response of a nanoelectrode to the introduction of biomolecules.

in Tab. 5.4 and for the simulation we use the solver presented in [1].

5.6.1 Physical effects on the admittance response

In the previous version of our solver, reported in [3], we did not take into account neither the AC diffusion currents nor the electrolyte permittivity dispersion nor the steric effects. To assess the impact of these additional terms on the total admittance Y_0, we have decided to study them one at a time. The considered model system is shown in Fig. 5.40, where a SAM is present on top of the bottom electrode.
Fig. 5.41 compares the admittance between the electrodes in absence of particles Y_0 calculated using the old solver (upward triangles), adding the AC diffusion terms to the equations (downward triangles) and accounting also for the electrolyte permittivity dispersion through Eq. 2.39, where $G_0 = \Re(Y_0)$ and $C_0 = \Im(Y_0/\omega)$. The parameters used in this section are reported in Tab. 5.4. If not otherwise specified, the electrolyte permittivity dispersion is neglected and ε_{el} takes a frequency independent value equal to $\varepsilon_s(S,T)$, that is $\varepsilon_{el}(\omega = 0)$ in Eq. 2.39.

Looking at Fig. 5.41 we not that AC diffusion currents (curves with triangles up and triangles down) tend to decrease the capacitance of the bare system without particles tends to be almost independent of the salt concentration for frequencies above the electrolyte cut-off frequency f_c defined in Sec. 3.1.1.3 ($f_c \approx 15$ MHz at 5 mM and $f_c \approx 1.5$ GHz at 500 mM, see also Fig. 3.9). Note that, differently from the results in [3], C_0 is not exactly

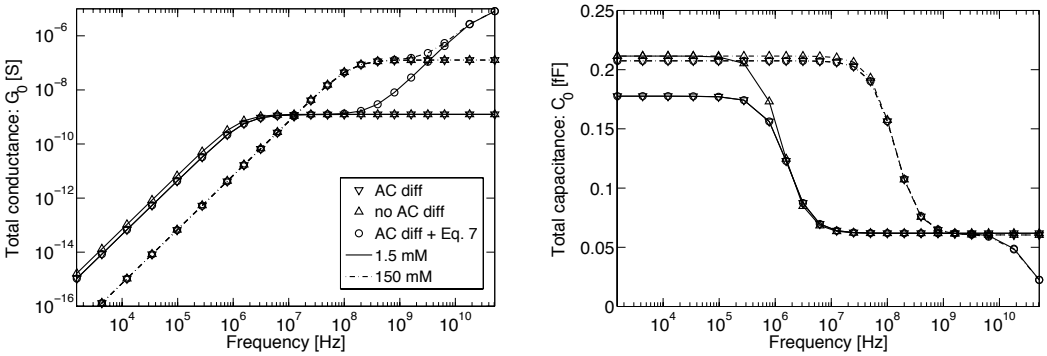

(a) (b)

Fig 5.41: Total admittance between the electrodes of the model system in Fig. 5.40 without biomolecules. The curves are computed either neglecting AC diffusion currents and the electrolyte permittivity dispersion (upward triangles), or accounting only for the AC diffusion currents (downward triangles) or accounting for both (circles) at different salt concentrations.

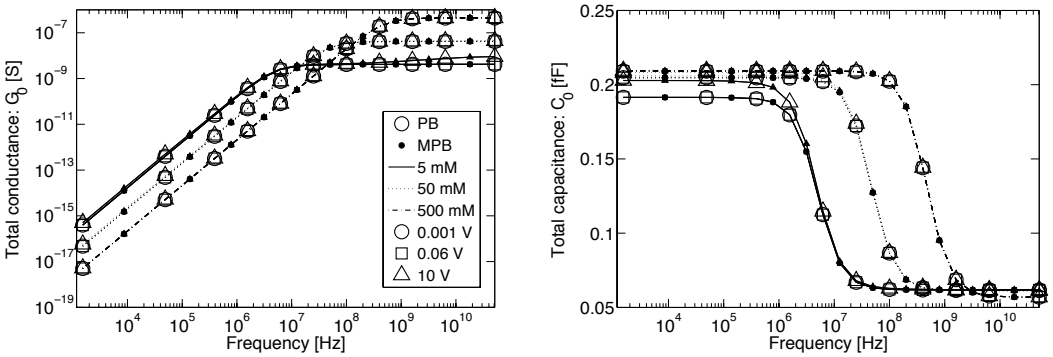

(a) (b)

Fig 5.42: Total admittance between the electrodes of the model system in Fig. 5.40 without biomolecules. The curves are computed either neglecting (PB - empty symbols) or taking into account (MPB - filled symbols) steric effects but neglecting the electrolyte permittivity dispersion for different DC voltage and salt concentrations. The ionic radius is $a = 0.25$ nm.

independent of salt concentration because the electrolyte permittivity has a small decrease for increasing salinity [48] (barely detectable in Fig. 5.41b) at and above $f \approx 10$ GHz, not accounted for in [3]. The effect is of limited practical relevance though. We also see that, at high frequency, the curves computed with the two models match perfectly, but at low frequency there is an important difference; in particular, in the new model the capacitance at low frequency depends on the salt concentration (triangles down, Fig. 5.41b), while it does not when AC diffusion currents are neglected (triangles up). The discrepancy can be explained observing that, neglecting the AC diffusion currents, there is no AC double layer on the electrodes. This means that the capacitance at low frequency C_L is given just by the SAM capacitance C_{SAM}, which doesn't depend on the salt concentration. On the other hand, if the AC double layer is present, C_L is given by the series of C_{SAM} and the double layer capacitance C_{DL} depends on the salt concentration; therefore also C_L depends on the salt concentration. Note that the dependency of ε_{el} on the salinity is so small that the effects are completely negligible at low frequencies.
When we account also for the electrolyte permittivity dispersion versus frequency, we note

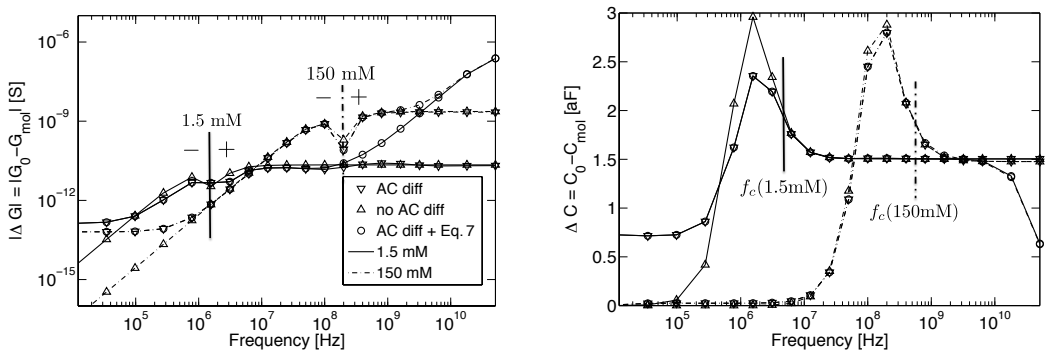

Fig 5.43: Admittance variation due to a neutral spherical biomolecule of 30 nm radius attached to the SAM. The curves are computed either neglecting AC diffusion currents and the electrolyte permittivity dispersion (upward triangles), or accounting only for the AC diffusion currents (downward triangles) or accounting for both (circles) for different salt concentrations. ΔG is negative at low frequencies and positive at high frequencies, with the sign reversal at f_c.

that nothing changes at low frequency, while at frequency above $f_{el} = 1/2\pi\tau_1 \approx 25$ GHz as defined in Eq. 2.39 (τ_1 depends weakly on the salt concentration), the dispersion effect becomes important; in particular the imaginary part of the permittivity causes a rise in the conductance G_0, while the lowering of the real part reduces the overall capacitance C_0. Compared to the capacitance, the conductance seems to be influenced by the permittivity dispersion at lower frequencies because of the logarithmic scale.

Steric effects To analyze the steric effects (see also Sec. 2.3.2), we consider simulations which include the AC diffusion currents but not the electrolyte permittivity dispersion, as already discussed. We calculated the total admittance between the electrodes as a function of the salt concentration and of the applied DC voltage (Fig. 5.42). The total conductance and capacitance are essentially independent of the applied bias in the explored conditions. Note that most of the voltage drop is across the SAM layer. The results (Fig. 5.42, filled symbols) suggest that steric effects are of limited importance in these cases, as in Sec. 2.3.2 ($a_{ions} = 0.25$ nm as appropriate for Na^+ and Cl^- [96]).
In order to explain this evidence, we follow the arguments made in [56] and we define the critical potential difference with respect to the bulk V_c at which steric effects become important as:

$$V_c = -\frac{k_B T}{Zq} \ln(n_0^\infty a_{ions}^3)\,. \tag{5.9}$$

In the worst case considered $n_0^\infty a_{ions}^3 = 0.47\%$, which corresponds to $V_c = 0.14$ V. Because of the very different thickness and permittivity of the SAM and of the bulk electrolyte, even a DC voltage as high as $V_{0B} - V_{ref} = 10$ V results in a potential at the SAM/electrolyte interface of only about 0.05 V, sufficiently smaller than V_c. Remembering also that the AC analysis is performed in the small signal approximation, it is certainly true that even accounting for the extra AC potential V_c can never be reached in the explored cases. This justifies also our choice of neglecting the steric effects in the AC analysis.

5.6.2 Response due to a neutral spherical biomolecule

We employed our solver to investigate the biosensor response to the presence of a biomolecule in the system (Fig. 5.43). Unless otherwise stated, the biomolecule is assumed to be a

spherical dielectric region touching the SAM surface, and with a frequency independent relative permittivity of 2.3 and a radius of 30 nm. Such an idealized biomolecule can be representative of a big protein cluster or a small virus [97, 95]. The change in admittance $\Delta Y = Y_0 - Y_{mol}$ is reported in Fig. 5.43. The same procedure of adding the effects one by one as in Fig. 5.41 was followed.
Looking first at the effect of AC diffusion currents only (triangles up and down in Fig. 5.43), we see that at low frequency they change remarkably the nature of the biosensor signals $\Delta G = \Re(\Delta Y)$ and $\Delta C = \Im(\Delta Y/\omega)$. We also see that at low frequency the biomolecule has a large effect on the capacitance at low salt concentrations, while at high frequencies it doesn't. This can be explained noting that, at 1.5 mM, the low-frequency screening length is sufficiently large to let the biomolecule interact with the double layer on the SAM/electrolyte interface, therefore leading to a stronger response compared to the case where the screening length is much smaller (i.e. 150 mM). We observe also that the frequency dependence is strongly affected by the salt concentration and ΔC tends to a constant, independent of the salt concentration, only when f is much larger than the electrolyte cut-off frequency $f_c \approx 450$ MHz at 150 mM.
This behaviour can be explained noting that, at low frequency, Y tends to be purely capacitive and the overall capacitance is given just by the series of the SAM capacitance with the double-layer capacitance. For this reason, changing the bulk electrolyte properties (with the addition of the biomolecule) doesn't give an appreciable effect. On the other hand at high frequency the effect of the biomolecule is purely dielectric and is due to the substitution of a portion of the electrolyte volume with a biomolecule of low permittivity. This explains why ΔC doesn't depend on the salt concentration at high frequency.
We note also that, at the cut-off frequency, there is a dip in $|\Delta G|$, which is the signature of a sign reversal. In fact, ΔG is negative at low frequencies and positive at high frequencies. The positive sign of ΔG at high frequency derives from the fact that we are replacing a conductive region with a dielectric (the biomolecule). At low frequency, on the other hand, the effect of the double layer perturbation are prominent, therefore the sign is reversed.

If we account also for the electrolyte permittivity dispersion, we can make similar statements to the case of the total admittance. Because this effect lowers the total capacitance and rises the total conductance, it is reasonable to expect ΔC and ΔG to have the same behaviour, and this is indeed what we observe in Fig. 5.43. So we can conclude that, in order to achieve the highest sensitivity and to be independent of the parameters it is desirable to work at frequencies around f_c but sufficiently lower than the permittivity cut-off frequency f_{el}. These requirements identify a frequency range between 300 MHz and 10 GHz at physiological salt concentration and between 3 MHz and 10 GHz at low salt concentration.

5.6.3 Response due to a charged spherical biomolecule

Having understood the importance of AC diffusion currents and of the complex permittivity of the electrolyte, we now investigate a more complicated but realistic case. In all the following simulations we have included both AC diffusion currents and the permittivity dispersion. Steric effects have been neglected since they are negligible in the considered systems.

We reconsider the biosensor response to the presence of a spherical biomolecule in the system as in Fig. 5.43, employing Eq. 2.39 for the electrolyte permittivity, but now adding a constant surface charge of $\pm$ 0.01 C/m^2 on the biomolecule, as expected given

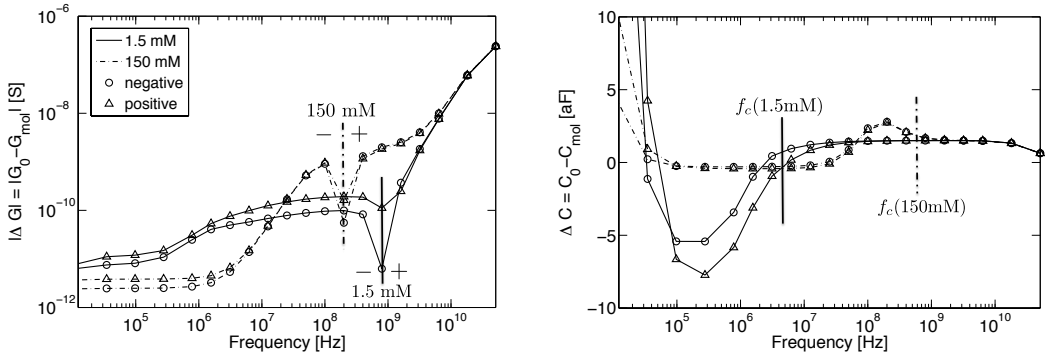

Fig 5.44: Admittance variation due to a uniformly charged spherical biomolecule of 30 nm radius with surface charge density of $\pm$ 0.01 C/m^2 attached to the SAM.

the typical protein dimension [88]. A more precise and quantitative estimation of a particular biomolecule's surface charge would necessarily need reliable experimental data or sophisticated Monte-Carlo measurements as in [98].
Also in this case of a charged particle ΔC tends to a constant, independent of the salt concentration, when the frequency is greater than f_c but sufficiently lower than f_{el} (Fig. 5.44). Interestingly, at high salt concentrations the change in admittance becomes almost insensitive to the charge on the biomolecule, while at low concentrations the charge has an important effect. More details on the impact of biomolecule charges on the response will be given in Sec. 5.8 in the discussion of DNA detection.

We also note that, in all the considered cases, for such a small nanoparticle ΔC is very tiny, giving rise to the need of employing high performance integrated charge detection systems [91]. This in turn suggests the need to exploit nanoelectrode arrays to increase the overall signal level [33].

5.7 Nanoelectrode response to small spherical particles

In this section we investigate in more detail the biosensor response due to the same spherical dielectric particle of 10 nm radius (representative of a big protein [88], $\varepsilon = 2.6\varepsilon_0$) of Fig. 5.35, and a metallic particle of same size and conductivity $\sigma = 6.3\times10^7$ S/m. Again, an array of 5×3 electrodes is considered inside a 1.8μm $\times$ 3.6μm rectangular domain. The particle is located above the central working electrode WE and the electrolyte is composed of KCl in water with concentration $n^\infty = 10$ mM. All other simulation parameters are listed in Tab. 5.4.

Fig. 5.45 shows the real part of the simulated potential profile in the absence of particles with an AC potential of 1 mV applied at the central row of electrodes. This is a small value for realistic systems, but since we are solving a linear problem ΔY does not depend on the AC modulation voltage. We observe that the electrolyte potential takes a value in-between the WE and CE potentials, as already observed in Sec. 5.3. As shown already a few times in this thesis, we note the broader penetration of the electric field at high frequency (Fig. 5.45b), which implies the ability of the system to detect analytes beyond the limitation due to static electrolyte screening.

Fig. 5.46 reports ΔC while changing the vertical (d_z) and horizontal (d_h) distance of the particle from the electrode and the DC bias applied to the central row. As expected, at high frequency the DC bias has no influence on ΔC and the response is not limited by the electrolyte screening, thus demonstrating the key advantage of the AC sensing principle. We also observe that, as expected, DC biases of opposite sign compared to the

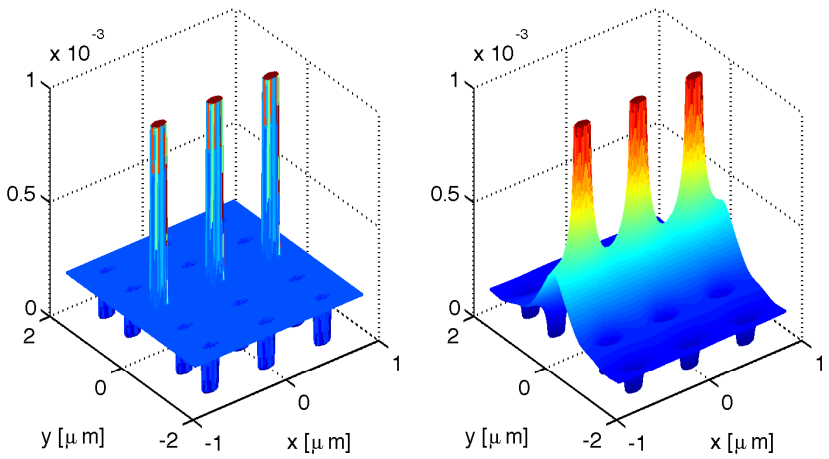

(a) 12 kHz **(b)** 1.6 GHz

Fig 5.45: Real part of the AC potential profile in the electrodes plane ($z = 0$) of a nanoelectrode array at 12 kHz (a) and 1.6 GHz (b). At high frequency (b) screening by the electrolyte is overcome, and the electric field penetrates into the system. These simulations are performed without the biomolecule.

bulk potential do not affect the AC response. This result indirectly confirms the validity of the model implementation and the accuracy of the solution in presence of DC bias. We finally note that the biosensor response increases when the particle is on the edge of the electrode, as predicted by Eq. 3.116, since the electric field at the particle location is enhanced by fringing effects.

5.8 Detection of DNA strands and hybridization

Gene sequencing is an especially relevant field of application for nanoelectronic biosensors, where the main target is to detect selectively the presence of DNA or PNA strands. Fig. 5.47 illustrates the internal structure of DNA and PNA molecules. The most stricking difference is that the latter backbone is composed of repeating N-(2-aminoethyl)-glycine units linked by peptide bonds, unlike the deoxyribose that composes DNA.
In this section we use the 2D Poisson-Boltzmann and Poisson-Nernst-Planck solver presented in [1] and ENBIOS to study the AC behaviour of nanoelectrode capacitive biosensors for DNA detection. Most of the results have been reported in [10]. A preliminary account neglecting 3D and orientation effects was given in [9].

Although the DNA/PNA strand is small compared to the electrode, in the 3D simulations a large domain of 3×5 electrodes is considered to capture the slowly decaying AC potential profile at high frequency; we have verified that adding more electrodes would not change our results. As usual, we assume a biasing scheme where rows of ideally polarizable (gold) electrodes are simultaneously biased and the current is measured at each terminal, as in the real system [33]. The Self Assembled Monolayers (SAM) employed to functionalize the electrode surface [99] are described as a compact dielectric layer with parameters as in Tab. 5.6. This is consistent with the findings in [100, 101] for dense high quality thiol-based films as those used in DNA detection.

As discussed in Sec. 2.3.2, the Poisson-Boltzmann equation is strongly non-linear and it is valid until the onset of steric effects. This is equivalent to saying that the potential drop

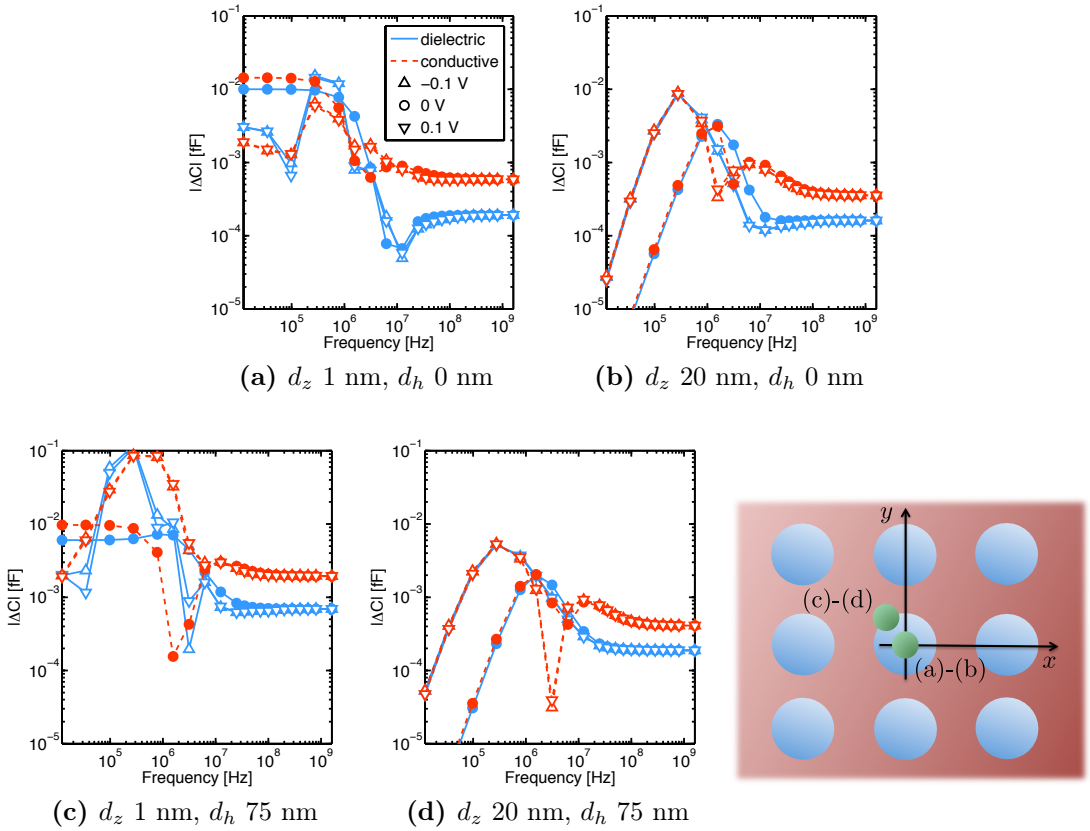

Fig 5.46: Nanoelectrode array - Change in capacitance at the central electrode (WE) due to a particle of 10nm radius with the center on top of the electrode (a-b) or on the edge of the electrode in a direction with an angle of $3\pi/4$ with respect to the x axis (c-d), see the sketch above. The particle is either attached to the electrode (a-c) or elevated by 20 nm (b-d). The DC bias is applied to the central row (x direction) and the reference potential in the bulk of the electrolyte V_{ref} is always 0 V. The salt concentration is 10 mM.

across the diffuse layer reaches the critical value [102] V_c as in Eq. 5.9. We have verified that for a typical ionic radius $a_{ions} = 0.25$ nm, even at the highest salt concentrations we never come too close to this limit, mainly because most of the potential drops across the low dielectric constant SAM ($\varepsilon_{SAM} \approx 2$ - 3 [99, 100, 101]), and consequently the surface charge density at the electrolyte/SAM interface is not so high as to invalidate the strong dilution assumptions behind the Poisson-Boltzmann model. Note that, as shown also in [103], it is possible to build very compact SAM, therefore confirming our choice to model it as an ideal uniform layer.

5.8.1 DNA / PNA model

Consistently with the results in [40], we use a simple model for the double strand DNA (dsDNA) and PNA (dsPNA), i.e. a cylindrical dielectric region of dielectric permittivity $\varepsilon_d = 2.5\varepsilon_0$, radius $r_{ds} = 1.25$ nm and height $h_{mol} = 13.2$ nm, corresponding to 40 bases. In the 2D case the cylinder stands upright along the z direction and is centered at radial coordinate $\rho = 0$. A constant volume charge density equal to the nominal value of 2 electron charges (-2q) per base pair is initially attributed to the dsDNA rod. In wet conditions however, the effective dsDNA charge per base is typically smaller than -2q per base pair and changes with the ion concentration [104], as reported in Tab. 5.5. The

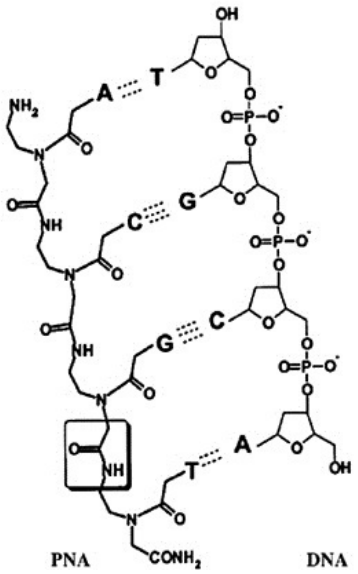

Fig 5.47: Internal structure of DNA and PNA molecules.

Molecule	150 mM	390 mM	1 M
ssDNA	0.80	0.86	0.89
dsDNA	1.3	1.5	1.6
ssPNA-ssDNA	0.85	0.91	0.93

Table 5.5: Effective number of electron charges per base (ssDNA) or base pairs (dsDNA and ssPNA-ssDNA) calculated with the model of [104]. The values for ssDNA differ from those in [9] because of the different single strand radius.

(much weaker) pH dependence of the strand charge was instead neglected because, as suggested by the results in Sec. 5.6 and confirmed in the following, the exact charge value is not critical for the high frequency capacitance response. The charge density of dsPNA is zero [105] over a wide range of pH and salt concentrations.

As for the single strand DNA (ssDNA) and ssPNA, the nominal charge per base pair is halved compared to the respective double strands and, furthermore, we considered two possible choices:

1. the ssDNA and ssPNA retain the ε and r values of the dsDNA and dsPNA;

2. the ssDNA and ssPNA parameters are the same as above but the radius is $r_{ss} = r_{ds}/\sqrt{2}$ so that the ssXNA rod (where X stands for either D or P) has half volume as the dsXNA one.

The second model differs from the one of [9] since here we assume that the displaced electrolyte volume (and not the radius) doubles when passing from single to double strand molecules. The r_{ss} and r_{ds} values we have chosen are consistent, but not exactly equal, to the ones in [104] (0.7 nm and 1 nm respectively), and, in the case of the second model above, they essentially respect the same r_{ss}/r_{ds} ratio. This small discrepancy does not affect the general conclusions of our work, whose main purpose is to provide insight on the impedance response and its trends, but not strictly quantitative values. In fact, the choice of optimum r_{ss} and r_{ds} values requires a careful comparison with reliable experiments which are not yet available (to the best of our knowledge) or sophisticated molecular dynamics simulations [40], and goes beyond the scope of the present work.

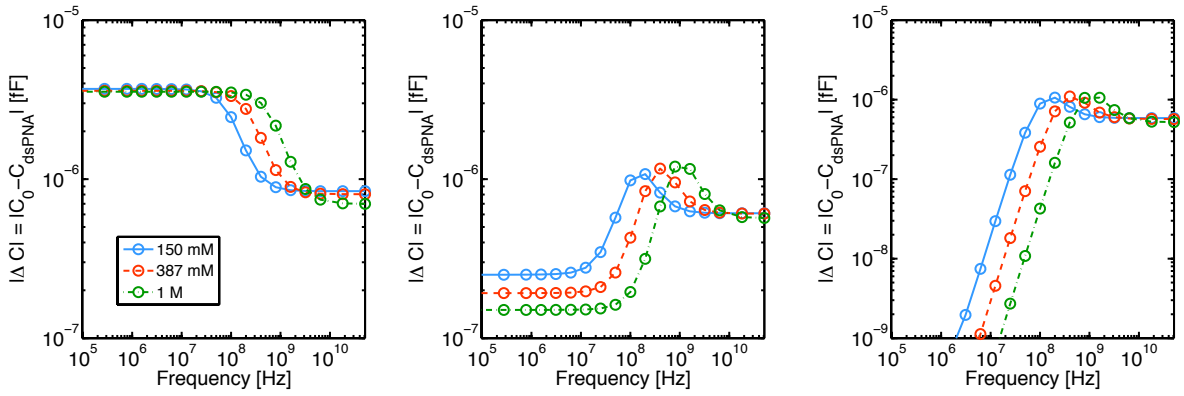

(a) $d_z = 0$ nm **(b)** $d_z = \lambda_D/2$ **(c)** $d_z = h_{mol}$

Fig 5.48: Change in nanoelectrode capacitance between the case when a dsPNA molecule is introduced in the system at a distance $d_z = 0$ (a), $d_z = \lambda_D/2$ (b) and $d_z = h_{mol}$ (c) between the bottom part of the biomolecule and the SAM. λ_D is the Debye length.

Parameter	Symbol	Value	Units
Bottom electr. DC pot.	V_{0B}	0.05	[V]
Top electr. DC pot.	V_{0T}	0	[V]
Bulk potential	V_{ref}	0	[V]
System radius	ρ_{max}	91	[nm]
System height	z_{max}	200	[nm]
Electrode radius	r_{el}	75	[nm]
Pitch in the x direction	p_x	600	[nm]
Pitch in the y direction	p_x	890	[nm]
SAM thickness	h_{SAM}	2.5	[nm]
Mobility of K^+ [52]	μ_1	4.75×10^{11}	[m/Ns]
Mobility of Cl^- [52]	μ_2	4.937×10^{11}	[m/Ns]
Temperature	T	307.66	[K]
SAM permittivity	ε_{SAM}	$2.3\varepsilon_0$	[F/m]
DNA-PNA permittivity	ε_d	$2.5\varepsilon_0$	[F/m]

Table 5.6: Parameters used in the 2D and 3D simulations.

5.8.2 Simulations

In all simulations, if not otherwise stated, we have used the parameters listed in Tab. 5.6. The electrolyte is a KCl solution in water; however, using NaCl would not change our results significantly (as evident comparing these calculations to the ones reported in [9]).

5.8.2.1 ΔC due to dsXNA and hybridization

As previously done in several sections of this thesis, we interpret the admittance $Y(f)$ between the electrodes with an equivalent circuit consisting of the parallel connection of a conductance $G(f)$ and a capacitance $C(f)$, $Y(f) = G(f) + j\omega C(f)$. Since we are interested in capacitive biosensors, in the following we concentrate on $C(f)$.

In this section we initially calculate the change in capacitance ΔC between the case where no molecule is present (C_0, reference condition) and the one where a biomolecule is inserted in the system, that is $\Delta C = C_0 - C_{dsXNA}$. Fig. 5.48 shows ΔC due to a dsPNA (which is an uncharged biomolecule) versus the distance from the SAM/electrolyte interface. As expected, because of static Debye screening, at low frequencies ΔC rapidly drops to zero when the dsPNA moves away from the SAM (compare Fig. 5.48 a,b and c)

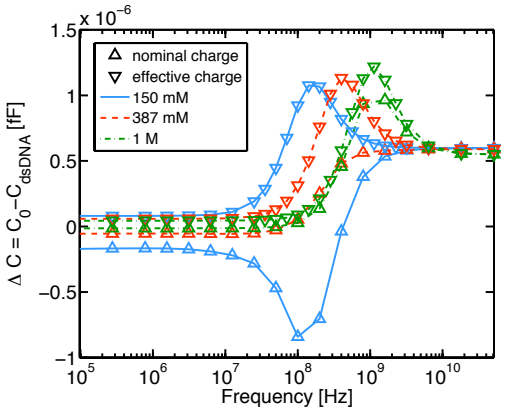

Fig 5.49: Change in nanoelectrode capacitance with and without biomolecule at a distance λ_D from the SAM. The biomolecule is dsDNA with either -2q per base pair (triangles upward) or the effective charge from Tab. 5.5 (triangles downward).

so that the response is very sensitive to the actual biomolecule height above the electrode. On the contrary, at high frequency ΔC is almost independent of the distance from the SAM, d_z. This is because above the electrolyte's dielectric relaxation cut-off frequency ($f_c = \sigma_{el}/(2\pi\varepsilon_{el} \approx 350$ MHz at 100 mM) the dominant effect causing the capacitance change is the replacement of some volume of the high permittivity electrolyte with a molecule of much smaller permittivity. We also note that in proximity of the electrolyte's dielectric relaxation cut-off frequency ($f_c = 0.47$, 1.3, 3.9 GHz at $n^\infty = 150$, 387 and 1000 mM respectively) the capacitive response ΔC is always close to the maximum so that f_c can be regarded as a nearly optimum detection condition. A more accurate estimate of the frequency of peak response was given in Sec. 3.1.1.4.

If we now consider charged DNA strands, we observe similar qualitative trends (Fig. 5.49, triangles upward) but, because the charge and the substitution of electrolyte's volume with the biomolecule give ΔC of opposite sign, a few sign changes appear in Fig. 5.49 which were not previously present. This can be regarded as an interesting signature of the presence of charges. Interestingly, these sign changes closely resemble the ones seen in Sec. 3.3.5, indicating that also in this case they are most likely due to a balance between the diffusion and ohmic terms in the PNP equation. Also in this case ΔC at low frequency is much smaller than at high frequency.

The correction from the nominal to the effective charge has quite a strong impact on ΔC at low frequency (compare triangles upward and downward in Fig. 5.49), essentially due to the strong non-linearity of the equilibrium Boltzmann distribution. Note however, that in the high frequency limit ΔC is insensitive to the biomolecule charge, and therefore to charge fluctuations as well. This is another potential advantage of high-frequency compared to low-frequency sensor operation.

Having discussed the main trends of the ΔC spectra, we investigate next the position and orientation effects. To this purpose, the charges on the molecules will always be those from Tab. 5.5.

5.8.2.2 ΔC position effects

So far we have always calculated ΔC as the change in capacitance between the case without biomolecule and the case when a biomolecule is present. In actual DNA sensors, however, the sensing process occurs via hybridization of a pre-existing layer of DNA or

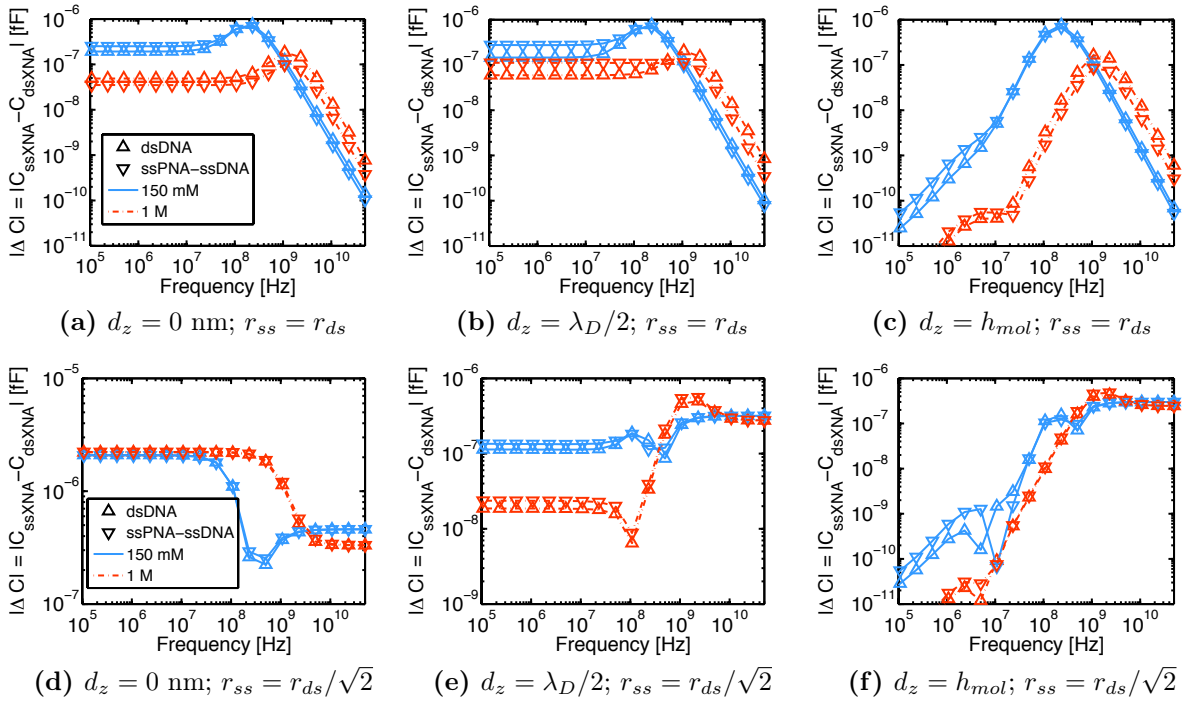

(a) $d_z = 0$ nm; $r_{ss} = r_{ds}$ **(b)** $d_z = \lambda_D/2$; $r_{ss} = r_{ds}$ **(c)** $d_z = h_{mol}$; $r_{ss} = r_{ds}$

(d) $d_z = 0$ nm; $r_{ss} = r_{ds}/\sqrt{2}$ **(e)** $d_z = \lambda_D/2$; $r_{ss} = r_{ds}/\sqrt{2}$ **(f)** $d_z = h_{mol}$; $r_{ss} = r_{ds}/\sqrt{2}$

Fig 5.50: Absolute value of the change in capacitance due to the ssPNA-ssDNA or dsDNA hybridization for the different models and at different heights of the molecule from the SAM. The sharp cusps at intermediate frequencies are caused by sign changes.

PNA attached to the SAM by complementary DNA strands in solution. Therefore, it is more interesting to calculate ΔC as the change in admittance between the case when a ssDNA or ssPNA strand is initially present and the case when a dsDNA or a ssPNA-ssDNA complex are present, that is $\Delta C = C_{ssXNA} - C_{dsXNA}$.
To this purpose, two idealized cases have been considered as explained in Sec. 5.8.1: $r_{ss} = r_{ds}$ and $r_{ss} = r_{ds}/\sqrt{2}$.

Fig. 5.50 reports the change in capacitance due to the formation of a ssPNA-ssDNA complex from a ssPNA (triangles down) and of a dsDNA from a ssDNA (triangles up). As we see, the ΔC spectrum is sensitive to the model used. In particular, according to the first model where single and double strands have the same diameter (Figs. 5.50a, b, c), ΔC is very low at high frequency because the effect of volume substitution is absent and features like the charge per base have modest effect on the response (as already shown in Fig. 5.49). At low frequency the ΔC values predicted by the two models are in the same order of magnitude, indicating that in this case the change of the charge effect is comparable to the volume substitution. We again note the sign changes in ΔC, as discussed for Fig. 5.49.

Fig. 5.51 takes a different perspective on these data, showing ΔC at a fixed low (50 kHz) and high frequency (500 MHz) and large salt concentration (1 M) as a function of the distance from the SAM. As expected, $|\Delta C|$ is larger when the molecule is close to the SAM and drops much faster with distance at low frequency. It is also larger at high frequency if we assume a radius change during hybridization (dashed lines). The sign of ΔC at high frequency depends on the choice made to model the ssXNA, confirming that the effects of the charge and the dielectric constant (volume change) go in opposite directions. The experimentally observed sign change [75] suggests that when a compact layer of hybridized DNA forms on the electrode, the dielectric effect is dominant, but more accurate studies are necessary to clarify this behaviour. The comparison carried out

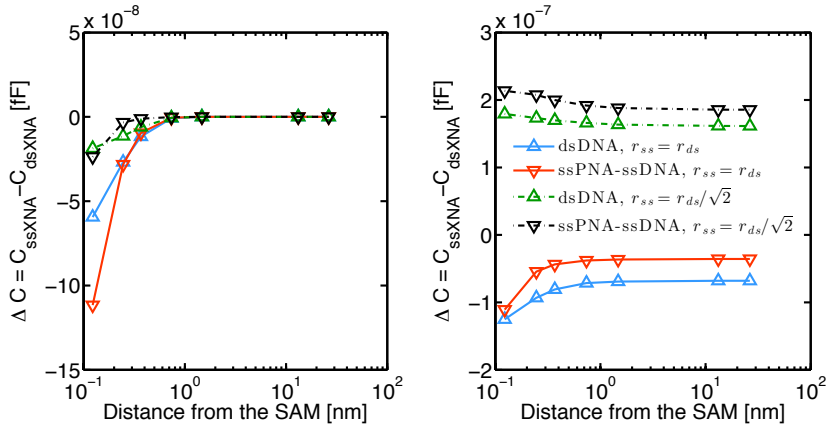

(a) 50 kHz **(b)** 500 MHz

Fig 5.51: 2D simulation of the ΔC due to the ssPNA-ssDNA (triangles downward) or dsDNA (triangles upward) hybridization at 50 kHz (left) and 500 MHz (right) and 1 M. $r_{ss} = r_{ds}$ (solid lines); $r_{ss} = r_{ds}/\sqrt{2}$ (solid lines).

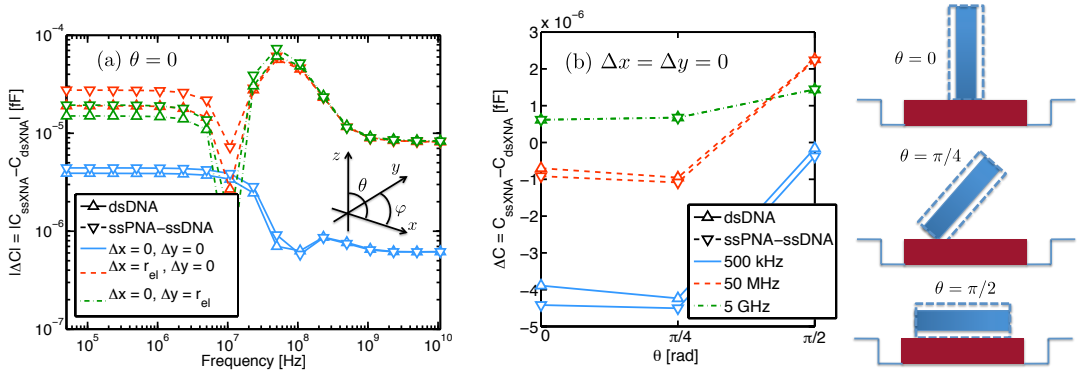

Fig 5.52: 3D simulation of the ΔC due to the ssPNA-ssDNA (triangles downward) or dsDNA (triangles upward) hybridization. The data are reported either at a fixed orientation (a) or at a fixed position in the x-y plane (b), and the salt concentration is 150 mM. The dsXNA (dashed rectangles) is modeled as a cylinder concentric to the ssXNA (filled rectangles), as sketched in the figure.

in this section highlights the potential of physical models to elucidate some of the signal transduction mechanisms. Unfortunately, to the best of our knowledge there is still too limited experimental data gathered on well-defined repeatable and reliable conditions to allow for extensive comparisons with experiments.
We also note that, since the frequency is high, there is almost no screening of the AC field and thus ΔC remains large even for DNA/PNA strands at large distance from the SAM which is a clear advantage in terms of biomolecule detection. We finally note that, in this high frequency regime, using ssPNA as a probe molecule instead of ssDNA (compare triangles up to triangles down) gives little advantage in terms of signal strength.

5.8.2.3 ΔC orientation effects

We now consider a realistic 3D system where the unperturbed (without biomolecules) field distribution is non-uniform. To this purpose, we have employed the full 3D CVFEM solver ENBIOS and simulated the biosensor array [33], with the parameters listed in Tab.

5.6. Fig. 5.52 shows ΔC due to the formation of a ssPNA-ssDNA complex from a ssPNA and of a dsDNA from a ssDNA, using a radius of $r_{ds}/\sqrt{2}$ for the single stranded molecule. The double strand molecules are always attached to the SAM (i.e., $d_z = 0$), have either the axis oriented in the z direction ($\theta = 0$) or tilted at $\theta = \pi/4$ and $\theta = \pi/2$ with respect to it, while the angle with respect to the x axis is always $\varphi = 0$ (see the sketches in Fig. 5.52). The midpoint of the strand is located either at the center of the working electrode ($\Delta x = \Delta y = 0$) or on its edge in the x or y direction, $(\Delta x;\, \Delta y) = (r_{el};0)$ or $(0;r_{el})$. Since the interelectrode distance is not the same in the x and y directions, these two cases are expected to give a different ΔC. A difference is also expected because of the row-wise AC excitation of the electrodes.

We immediately note (Fig. 5.52a) that ΔC for the molecule in the center of the electrode is very similar to the one reported in Fig. 5.50d, as expected since the electric field in this region is fairly uniform and therefore the 2D simulation is a reasonably accurate representation of the more realistic 3D system. On the other hand, we note that ΔC at both low and high frequency increases by approximately an order of magnitude when the particle is on the edge of the electrode, due to the locally high value of the fringing electric field. The non-uniformity of the field gives also rise to a different shape of the curves, and a maximum appears when the particle lies at the edge; this suggest the existence of optimum detection conditions within non uniform fields and the possibility to optimize the $\tilde{E}_0/\tilde{V}_0$ ratio for optimum sensitivity (see the model in Sec. 3.3.6). We also note that the slight asymmetry of the array does not have a great impact on ΔC for a z-oriented molecule ($\theta = 0$, compare red and green curves in Fig. 5.52a). Fig. 5.52b shows that the orientation is instead important at low frequency for a molecule in the center of the electrode. We explain this observation noting that when the molecule is horizontal ($\theta = \pi/2$), the ssXNA is slightly detached from the SAM. The very small elevation ($d_z = 0.4$ nm) is sufficient to change considerably the response at low frequency, as evident also from Fig. 5.50. As expected, it still holds that in all cases ΔC at high frequency is independent on the charge and frequency and it has a weaker dependence on position and orientation.

5.9 Summary

In this chapter we have studied the response of a nanoelectrode array biosensor to spherical microparticles my means of simulations and compared the results with measurements mostly carried out at the University of Twente by the group of Prof. S. Lemay (Sec. 5.3). The agreement we found between simulations and measurements is excellent, essentially without fitting parameters. This is a remarkable confirmation of the adequacy of the chosen model for the problem at hand. *Our study demonstrated the fact that high frequency measurements can indeed probe particles beyond the static screening length. In addition, we have shown that the nanoelectrode array is capable of probing the particle's material; namely, to discriminate between dielectric and conductive particles. Simulations based on the models of Chap. 2 confirmed their usefulness for the extraction of quantitative information on the analytes from the measurement data.*

In Sec. 5.4 we have validated, by means of simulations, an analytical model for the admittance change at a nanoelectrode due to a small spherical particle. The model is not directly comparable to results in Sec. 5.3 because of the assumptions made on the particle and system dimensions, but nevertheless provides extremely useful physical insight. Notably, the model predicts the response to be proportional to the particle volume and complex conductivity and to the magnitude of the electric field in the location of

the particle. This model suggests a wide range of possibilities for the engineering of nanoelectrode biosensors. In particular it is shown that there is no advantage in having a non-uniform field over the particle volume, but it is advantageous if small particles are located at positions with high AC field.

The simulations above allowed us to test the performance of ENBIOS for the analysis of realistic complex systems. The results motivated the proposition of an original simulation scheme (Sec. 5.5) to greatly reduce the computational burden due to the fine meshing of Electrical Double Layers by replacing them with circuit lumped elements.

We have also explored the nanoelectrode biosensor response due to small spherical particles, which can represent big proteins or viruses (Secs. 5.7-5.6), and to DNA molecules (Sec. 5.8), including orientation effects. We found that, unless the strand adheres to the electrode, modest changes in capacitance should be expected. These simulations confirmed once more the potential advantage of high frequency operation, namely:

- the ability to overcome of the static screening and the independence of the response on salt concentration;
- the very good theoretical predictability of the response, even in the presence of non-idealities such as surface charges;
- the insensitivity to hardly controllable parameters such as free charges;
- the additivity of the response with respect to the number of particles, at least for a small number of them;
- the identification of optimum detection frequencies and critical cut-off frequencies;
- a greater freedom to engineer the biosensor, in order to take advantage of the fact that the region sensitive to the analyte is not limited to the sensor surface.

As a final remark, note that for one small biomolecule $\Delta C \approx 1$ zF, i.e., it is close to the lowest detection limits experimentally demonstrated so far [92]. This observation entails that it might be difficult but not impossible to reach single-molecule detection with current or scaled versions of nanoelectrode arrays such as the one in [33].

Chapter 6

Nanowire pH-sensors and bio-sensors

Nanowire (NW) devices, in particular Silicon NWs (SiNW) are of great interest in both nanoelectronics and nanotechnology. In the field of biosensors, the roughly 1D nature of the NWs is beneficial to achieve short settling time, due to considerations on the geometry of diffusion from the bulk electrolyte to the sensor device [106]. SiNWs operated in subthreshold regime can also offer a high sensitivity, although at the expense of increased noise [31]. Two main applications have recently emerged for SiNW sensors: Ion Sensitive FET (ISFET) and BioFET.
Since their introduction in 1970 [27], ISFETs have found their major application as pH sensors. The physical transduction mechanism is provided by the build up of the site-binding charge (see Sec. 2.1.1.1). It is only recently that ISFETs have found broader applications in the biosensor industry [19], but the implementation still relies on the pH sensing.

Attempts have also been made to use SiNWs as biosensors, but the issue of static Debye screening, already discussed in Chaps. 3-5, has so far prevented a major success of these devices [107]. Silicon nanowire ISFETs have been recently studied, as for instance in [31, 93, 34, 108].

In the previous chapters we have seen that the Debye screening limit is overcome when operating the sensing element in the AC high frequency regime. In this chapter, we will explore this concept for SiNWs considering both pH sensor and biosensor applications.

6.1 Nanowire pH sensors

This section presents the work on SiNWs for pH sensing developed in collaboration with CEA/LETI laboratories in Grenoble (Dr. Thomas Ernst), which fabricated the SiNWs, and CLSE/EPFL laboratory in Lausanne (Prof. Carlotta Guiducci), which developed the microfluidic and the measurement protocols. The experimental setup and measurement protocols we started with are described in [108]. Here we report for convenience a few essential informations as well as the specific improvements made to perform AC measurements.

Devices The SiNWs are fabricated from Silicon-on-Insulator (SOI) wafers. The wafers feature a 200 nm top silicon layer on a 400 nm thick SiO_2 insulating bulk oxide (BOX). The silicon top layer is first thinned down by several steps of silicon thermal oxidation/deoxidation to $t_{Si} = 50$ nm, where the t_{Si} corresponds to the nominal height of the SiNWs. The NWs are patterned using deep ultraviolet (DUV) or e-beam lithography and etched by reactive ion etching (RIE). The SiNWs body is covered by a high quality SiO_2

gate oxide grown by thermal dry oxidation while the rest of the chip is passivated by a multilayered insulator.
The fabricated chip features 75 SiNWs with different widths and lengths and nominal thickness of either 50 or 25 nm. Different chips with various doping and oxide thickness are available. In this thesis we always used the devices denoted as p05 and p07, whose characteristics are summarized in Tab. 6.1. Note that, because of the doping configuration, the p05 devices work in accumulation and the p07 in inversion. These chips always feature silicized contacts. Most of the work presented here will be done on 5B02 devices, which have nominal length 500 nm and width 80 nm.

The SiNW chip is coupled with a microfluidic module that employs custom made Ag/AgCl reference electrodes (REs) and allows subsequent injections of different solutions into sub 5 μl microchannels. Ag/AgCl pseudo-RE were obtained starting from pure silver by chemical anodization in chlorine ions solutions (e.g., KCl) or by plasma treatments in chlorine chambers. In our setup, silver L-shaped tubes are anodized in 0.1 M KCl solution, in order to obtain a 5 μm thick AgCl metal salt layer. These tubes are inserted into a microfluidic chip, serving both as REs and as inlet/outlet of the system. The microchannels are realized with a chemical resistant double-coated tape (3M 9086), patterned by laser micromachining. The height of the channels is defined by the thickness of the tape (190 μm). A Polymethyl methacrylate (PMMA) cap is placed on top to seal the channels and the inlet and outlet tubes inserted. A sealing polymer is used to avoid fluid leakages from the inlet/outlet. During measurements, the solutions are fluxed by means of an external syringe pump (Harvard Apparatus). Particular care is needed to avoid the formation of air bubbles. The SiNWs can be operated either by the solid-state back gate and/or by the liquid fluid gate. Fig. 6.1 reports the chip photograph, together with the microfluidics.

Differently from almost all previous studies (except [79, 109], to our knowledge) and coherently with all the previous work shown in this thesis, we measure the SiNWs in

	p05 - $n^+/n/n^+$ resistor	p07 - pMOSFET
Source/Drain doping	n-type, 10^{20} cm^{-3}	p-type, 10^{20} cm^{-3}
Channel doping	n-type, 10^{16} cm^{-3}	n-type, 10^{16} cm^{-3}
Nanowire oxide thickness	3 nm	8.5 nm
Nanowire width	$80 \div 150$ nm	$80 \div 150$ nm
Nanowire length	$500 \div 2375$ nm	$500 \div 2375$ nm

Table 6.1: Parameters of the CEA/LETI SiNWs chips and devices used in this thesis.

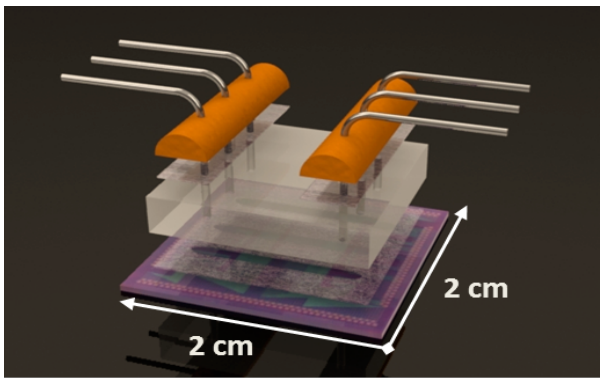

Fig 6.1: Photograph of the silicon nanowire chip and of the microfluidics. The picture is reproduced from [108].

the AC domain. To this purpose we use an Agilent 4294A impedance analyzer, which is connected to drain (high input) and source (low input). The back and fluid gate are instead biased via a semiconductor parameter analyzer (Agilent 4156C). With this configuration the measured admittance is then given by the measured AC source current divided by the applied AC drain voltage $Y_{exp} = \tilde{I}_S/\tilde{V}_D$. In order to achieve a reasonable signal to noise ratio, if not otherwise specified, the magnitude of the AC voltage applied to the high potential is 100 mV. Note that, although the instrument can reach measurement frequency up to 100 MHz, in practice because of the off-chip parasitics the maximum measurement frequency was limited in the range between 40 Hz and 1 MHz, since, as we will see in the following, the response starts to be dominated by the parasitics already at $\sim$ 300 kHz. This bandwidth, however limited, is still much larger than that in [109] and comparable to those in [75, 79].
The open and short compensations are always performed as suggested by the instrument manual. In some measurements we also use a very large device to run an additional load compensation; however, the only difference we could observe between the cases with and without the load compensation occurs in the range where the response is dominated by the parasites.

6.1.1 Measurements of pH ladders

As usual in the study of ISFETs for pH sensing, in this section we show experimental pH ladders. We start with a solution of known pH and gradually increase (or decrease) the pH value to reach the final value, while continuously running measurements, where at each time step we acquire an entire AC admittance spectrum in the 40 Hz $\div$ 1 MHz frequency range.
The solutions are made of KCl dissolved in milliQ water, while the pH has been adjusted by adding strong acid (HCl) or base (KOH). These solutions range from pH = 3 to pH = 8, with steps of one pH unit. The final pH value has been controlled with a commercial pH meter. The target salt concentration for all solutions is 100 mM; however the addition of acid or base do not guarantee a precisely constant salt concentration for all solutions.

We have also prepared solutions with a controlled target salt concentration of 0.15

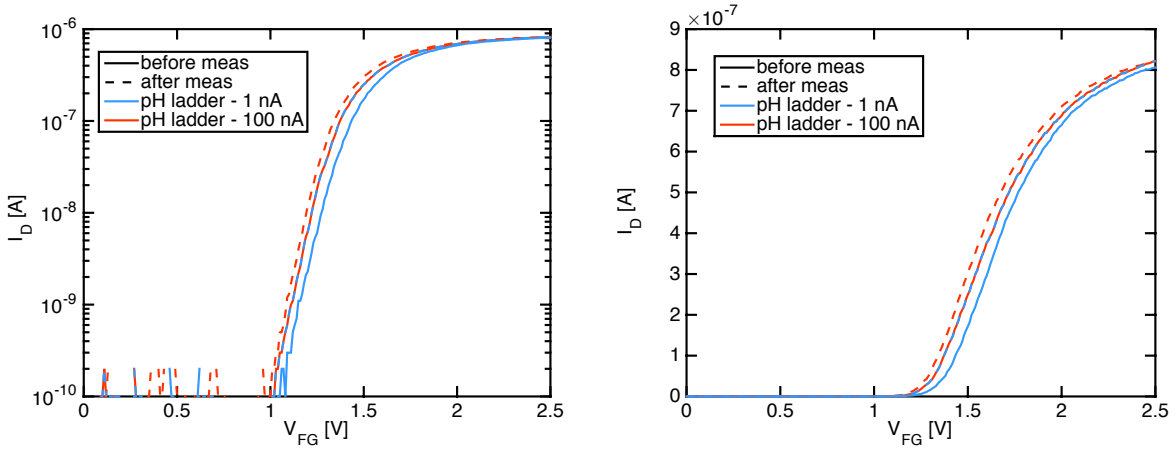

(a) logarithmic **(b)** linear

Fig 6.2: $I_{DS}(V_{FG})$ curves (in DC), before and after one pH ladder at 1 nA and one other at 100 nA on the 5A02 device ($W = 80$ nm, $L = 500$ nm) in chip number 20 of the p05 type ($n^+/n/n^+$ resistor), either in logarithmic or linear scale. $V_{DS} = 100$ mV.

mM ranging from pH = 5 to pH = 8, with steps of one pH unit. Since in this latter case the solution is not buffered and has a very low salt content, it is very sensitive to changes in pH due to the absorption of CO_2 from the air, resulting in a not very well-controlled pH.

6.1.1.1 $n^+/n/n^+$ resistor

The n-type devices used in this section (5A02 and 5B02) both belong to chip number 20 of the p05 type. They have equal nominal dimensions (width 80 nm, length 500 nm)

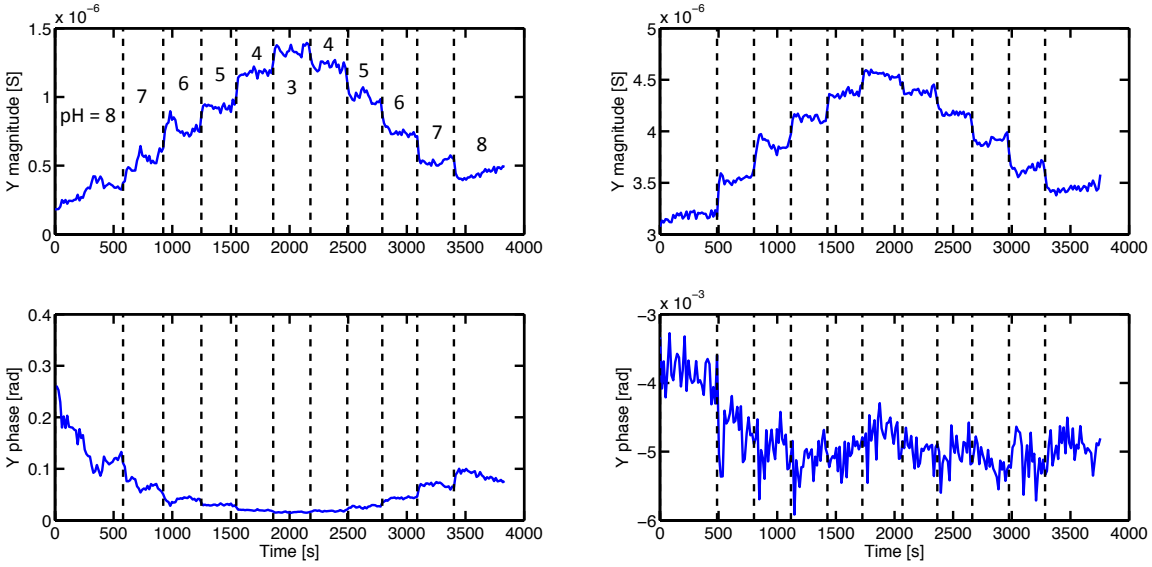

(a) 20 kHz, $I_{DS} = 1$ nA

(b) 20 kHz, $I_{DS} = 100$ nA

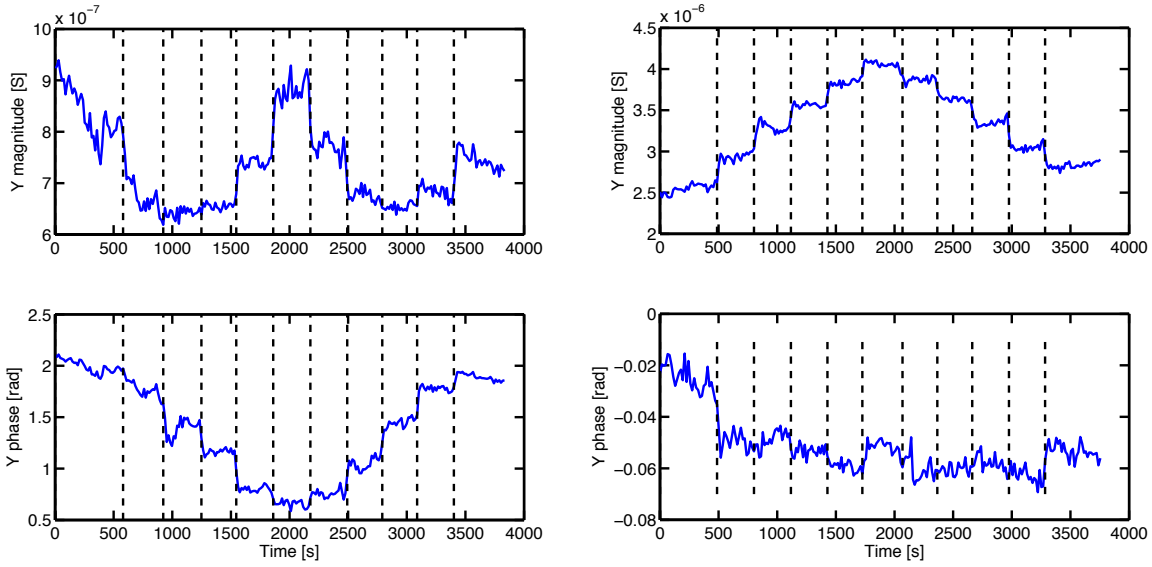

(c) 200 kHz, $I_{DS} = 1$ nA

(d) 200 kHz, $I_{DS} = 100$ nA

Fig 6.3: pH ladder on the 5A02 device ($W = 80$ nm, $L = 500$ nm) in chip number 20 of the p05 type ($n^+/n/n^+$ resistor) at a few bias points and frequencies. The injections go from pH 8 to pH 3 and then again up to pH 8.

but are located in different parts of the chip. p05 devices have a thin gate oxide (3 nm). We have performed $I_{DS}(V_{FG})$ measurements in DC before and after each pH ladder to check the device stability and choose the bias points (above and below threshold). Since all the pH ladders start from pH 8, this is the pH at which the $I_{DS}(V_{FG})$ curves are measured. Therefore, throughout the whole section, $I_{DS} = x$ nA denotes a $I_{DS}(V_{FG})$ curve measured at pH = 8 before the pH ladder at $V_{DS} = 100$ mV. In a few cases the admittance Y is reported not as magnitude and phase but as conductance and capacitance ($Y_{exp} = G_{exp} + j\omega C_{exp}$). Measurements in this section were always made after short/open and load compensation with the on-chip 5A00 calibration resistor of 55 kΩ.

Fig. 6.2 reports the $I_{DS}(V_{GS})$ curves in DC at $V_{DS} = 100$ mV measured before and after each pH ladder. The threshold voltage $V_T \approx 1.2$ V does not shift appreciably after the measurements, meaning that the characteristics are fairly stable. Note that at $I_{DS} = 100$ nA the bias point is slightly above threshold at the considered pH (i.e., pH = 8), but it will result well above threshold for the other pH values, since the curves shift to the left for decreasing pH.

Fig. 6.3 shows magnitude and phase of Y_{exp} versus time while stepping the pH of injected solutions from pH = 8 to pH = 3 and then back to pH = 8 in steps of one unit of pH. The curves are shown for different DC current (1 nA and 100 nA) and frequency. We immediately note a drift in the characteristics, especially at pH = 8, as also observed previously in the literature [108, 110]. Consistently with Fig. 6.4, we also observe a higher conductance sensitivity S_G below threshold. Finally, we note that at low frequency (20 kHz) and above threshold the pH ladder is visible in the Y_{exp} magnitude but not clearly in its phase, while at high frequency and below threshold the opposite occurs. In contrast, in the other regimes the pH ladder is visible when looking at both magnitude and phase. As a general remark, all the pH ladders are fairly noisy, possibly because of RTN noise, especially at threshold. Another possible source of variability and drift is the very thin gate oxide, which can be easily penetrated by ions. Finally, also the reference electrodes may contribute to the drift.

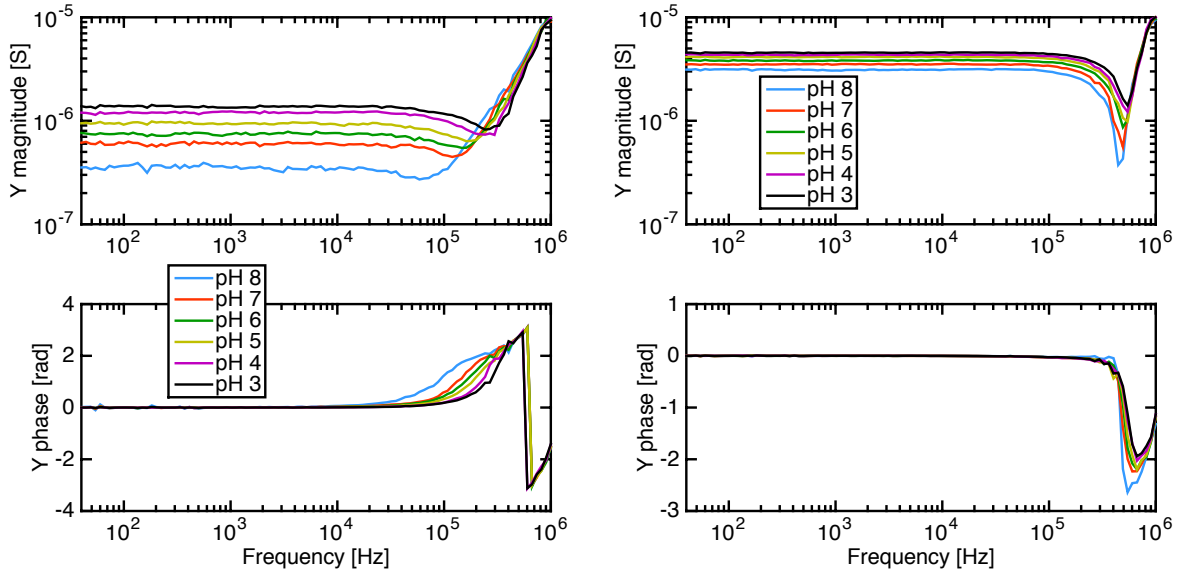

(a) $I_{DS} = 1$ nA **(b)** $I_{DS} = 100$ nA

Fig 6.4: AC admittance spectra on the 5A02 device ($W = 80$ nm, $L = 500$ nm) in chip number 20 of the p05 type ($n^+/n/n^+$ resistor) at different pHs.

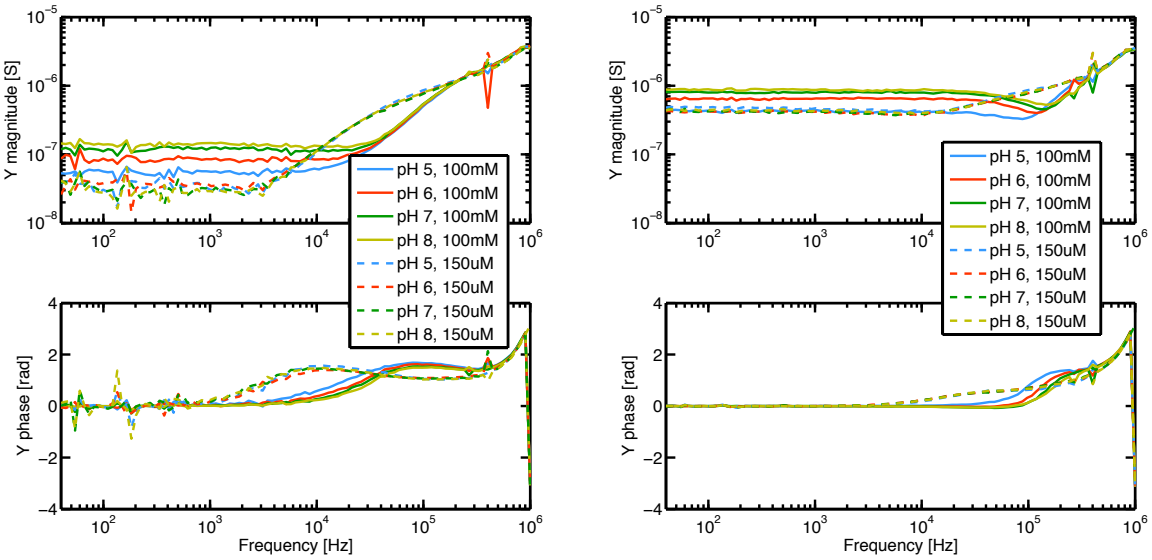

(a) $I_{DS} = 1$ nA **(b)** $I_{DS} = 10$ nA

Fig 6.5: AC admittance spectra on the 5B02 device ($W = 80$ nm, $L = 500$ nm) in chip number 20 of the p05 type ($n^+/n/n^+$ resistor) at different pHs and salt concentration. Load compensation on the parasitic resistance and inductance.

Fig. 6.4 shows the Y_{exp} spectra varying the pH. We immediately notice that, for frequencies above ~ 300 kHz, all the curves fall one on top of the other, which means that the response is dominated by the parasitics. We also note that, as expected because this is an n-type device and the site-binding charge becomes more negative increasing the pH, the conductance $G_{exp} = \Re(Y_{exp})$ at low frequency increases with pH. In addition, since at $I_{DS} = 1$ nA we are below threshold, the sensitivity in conductance $S_G = \Delta G_{exp}/G_{exp}$ for varying pH is larger than at $I_{DS} = 100$ nA (above threshold). We finally see that the phase of Y_{exp} changes with the pH.

The cut-off frequency f_c at 100 mM is $\simeq 300$ MHz (Chap. 3, Eq. 3.27), and thus our measurement frequency range is too narrow to capture the effects due to the AC de-screening. In an attempt to put in evidence AC descreening effects as those reported in Chap. 5 for the nanoelectrode system, we therefore decided to use the solutions with salt concentration 0.15 mM, and compare the results to the ones at 100 mM. Fig. 6.5 shows such a comparison for the spectra of Y_{exp} and varying the pH. Now we observe a clear effect of the salt concentration on the response in the range between 3 and 200 kHz. This is likely due to a difference in the double layer capacitance at the oxide/electrolyte interface. We will discuss this point in more detail in the following.

6.1.1.2 *p*MOSFET

This section reports measurements similar to the previous ones, but on the 3dots chip of p07 type (*p*MOSFET), always on the 5B02 device (width 80 nm, length 500 nm). These devices are *p*-doped (as opposed to the *n*-doped p05 ones) in the source and drain regions and the same (low) *n* doping in the nanowire. In addition, they have a thicker gate oxide (8.5 nm), which is more resistant to contamination and salt penetration.

The pH ladders start from pH = 5 and reach pH = 8 and then goes back to pH = 5,

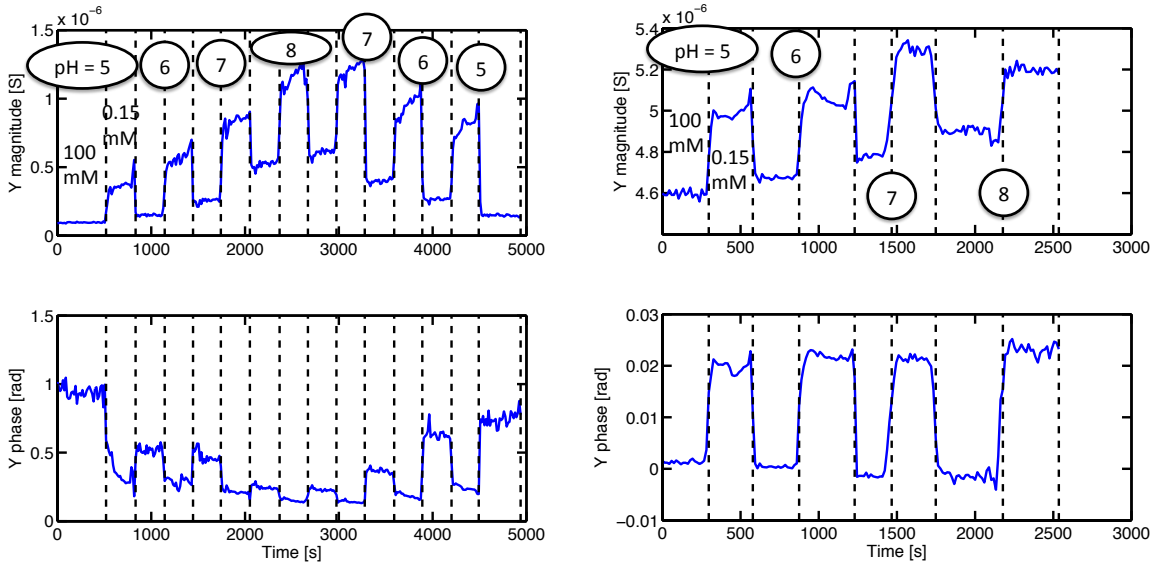

(a) 20 kHz, $I_{DS} = 10$ nA

(b) 20 kHz, $I_{DS} = 100$ nA

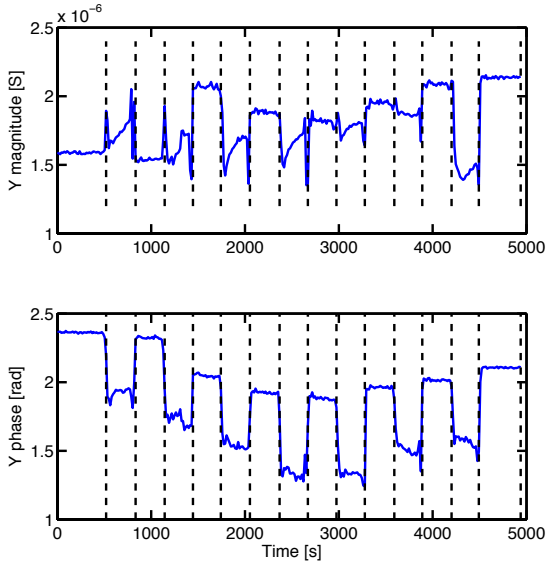

(c) 200 kHz, $I_{DS} = 10$ nA

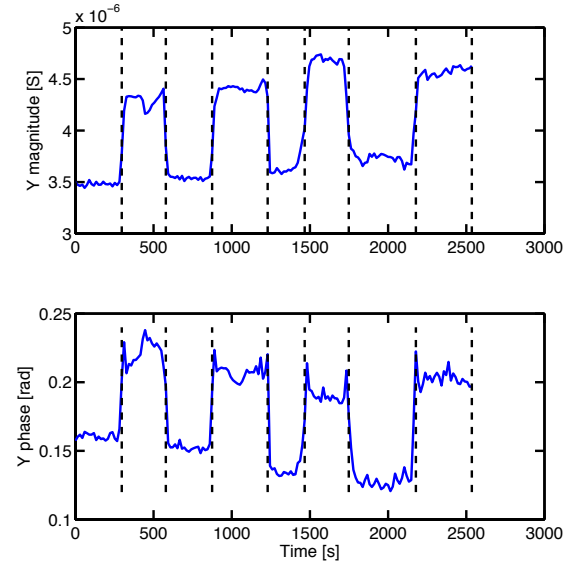

(d) 200 kHz, $I_{DS} = 100$ nA

Fig 6.6: pH ladder on the 5B02 device ($W = 80$ nm, $L = 500$ nm) in chip 3dots of the p07 type (*p*MOSFET). The injections go from pH = 5 to pH = 8 and then again up to pH = 5 for the case at $I_{DS} = 10$ nA, and just from pH = 5 to pH = 8 at $I_{DS} = 100$ nA. In all cases, at each pH step the measurement is done first at the salt concentration 100 mM and then at 150 μM. Load compensation on the parasitic resistance of the 5B00 large device.

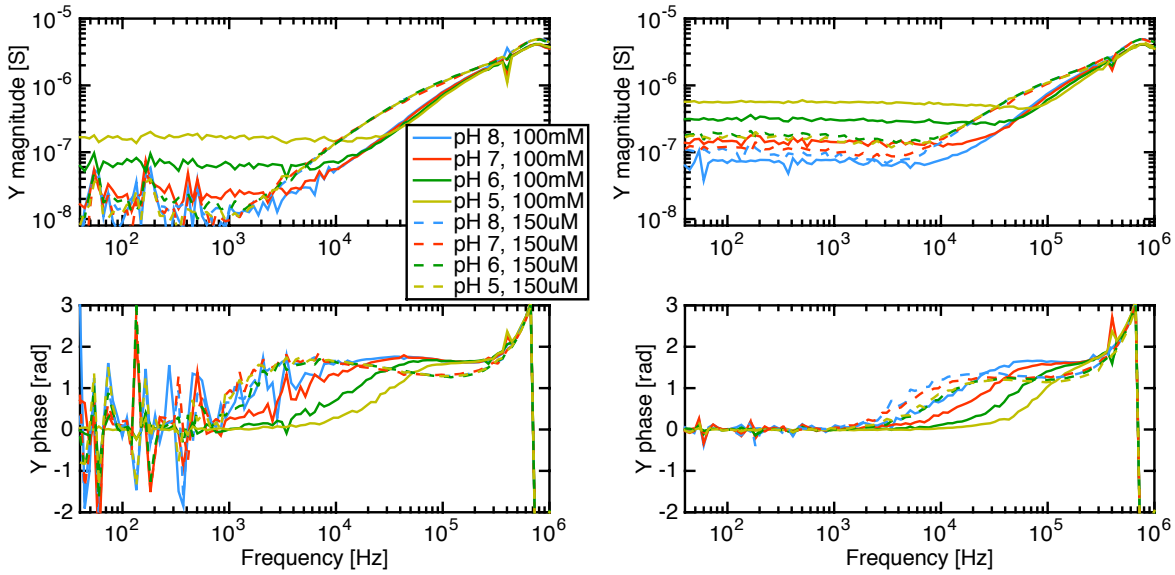

(a) $I_{DS} = 1$ nA **(b)** $I_{DS} = 10$ nA

Fig 6.7: AC admittance spectra on the 5B02 device ($W = 80$ nm, $L = 500$ nm) in chip 3dots of the p07 type (pMOSFET) at different pHs and salt concentration. Load compensation accounts for both the parasitic resistance and inductance of the calibration resistor.

therefore the admittance first increases and then decreases with time, as in the previous section. The first pH step is done at salt concentration 100 mM, then the 0.15 mM at the same pH is injected, afterwards the following pH at 100 mM is used and so on. In this way the static $I_{DS}(V_{FG})$ curves (always done at $V_{DS} = 100$ mV) are measured at the same pH = 5 and salt concentration 100 mM.
In the first measurements (Fig. 6.6) we have applied the load compensation with a 65 kΩ calibration resistor (5B00 device). In all subsequent measurements we compensated for both the resistance and the inductance of the calibration device. We concluded that the inclusion of the inductance compensation does not change the admittance in the range where the response is not dominated by the parasitics, i.e. below ≈ 300 MHz (not shown).

Fig. 6.6 shows the pH ladders measured alternating the solutions at 100 mM and 0.15 mM salt concentration, for two polarizations, one below ($I_{DS} = 10$ nA) and one above threshold ($I_{DS} = 100$ nA). We immediately note the lower stability of the solutions at 150 μM, which is evident from the drift and the presence of peaks in the response. Regarding the frequency and polarization dependencies, all the considerations that we made for Fig. 6.3 still hold.

Fig. 6.7 shows similar measurement, where the load compensation is active both on the parasitic resistance and inductance. We immediately note that, regardless of the different oxide thickness with respect to p05 devices, the results are qualitatively similar to the ones in Fig. 6.5. In particular we see that at 100 mM and before the onset of parasitics the admittance exhibit only one zero, while at 0.15 mM the first zero is shifted to lower frequency and there is an additional pole at higher frequency. Once again, the salt concentration has an impact on the response in the range between ∼ 3 and 300 kHz.

Fig. 6.8 shows the corresponding pH ladders, with pH range between 5 and 8 and using only the solutions with salt concentration 100 mM. Once again, regarding the frequency and polarization dependencies, all considerations in the previous section still hold. In particular, a drift in the characteristics is present, which depends on pH. In addition, at

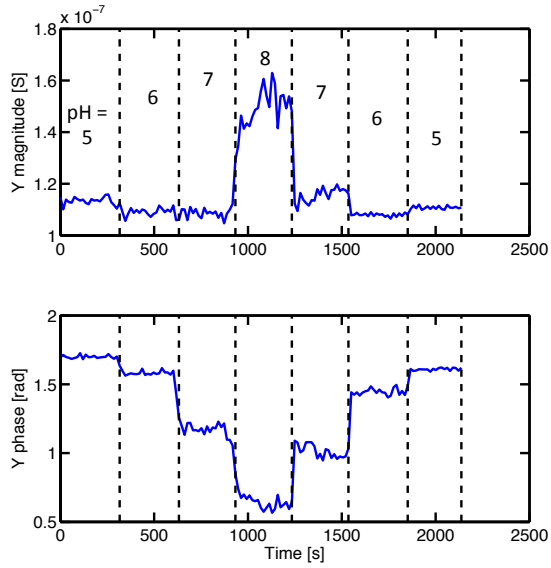

(a) 20 kHz, $I_{DS} = 1$ nA

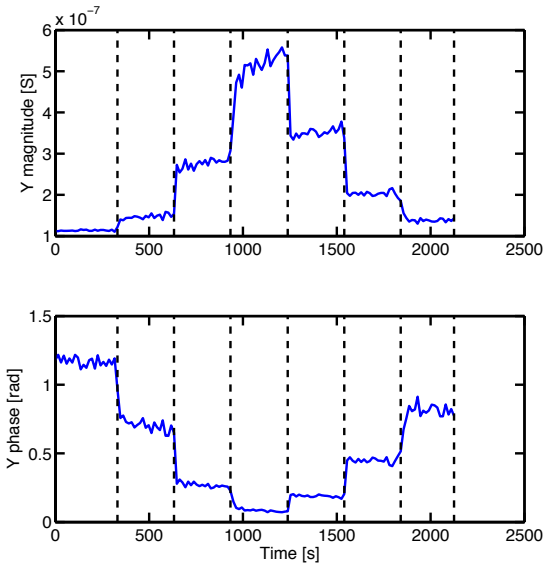

(b) 20 kHz, $I_{DS} = 10$ nA

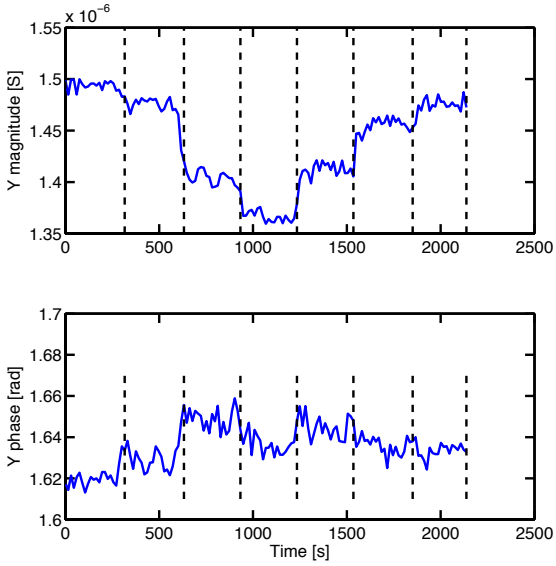

(c) 200 kHz, $I_{DS} = 1$ nA

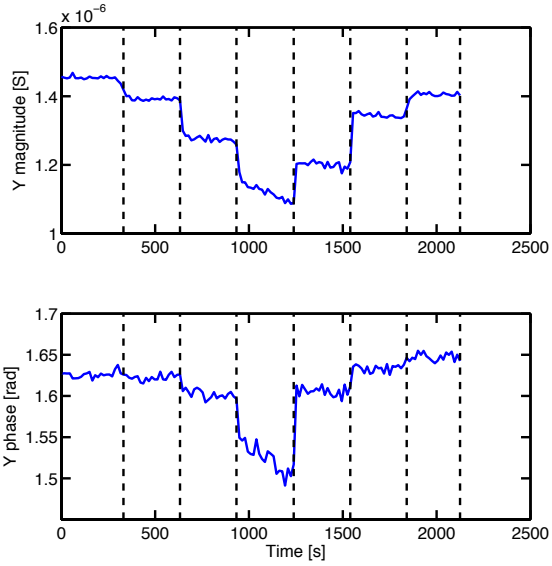

(d) 200 kHz, $I_{DS} = 10$ nA

Fig 6.8: pH ladder on the 5B02 device ($W = 80$ nm, $L = 500$ nm) in chip 3dots of the p07 type (pMOSFET). The injections go from pH = 5 to pH = 8 and then again up to pH = 5. Solutions at salt concentration 100 mM. Load compensation on the parasitic resistance and inductance.

low frequency (20 kHz) and at higher DC current the pH ladder is visible in the Y_{exp} magnitude but not clearly in its phase, while at high frequency and low DC current the opposite occurs. In contrast, in the other regimes the pH ladder is visible when looking at both magnitude and phase.

6.1.2 Experimental admittance spectra versus salt concentration

Figs. 6.5-6.7 unambiguously show a remarkable sensitivity of the admittance to salt concentration in the intermediate range between $\sim$ 3 and 300 kHz. We therefore want to analyze this aspect in more detail, disregarding for the moment the pH dependencies. In fact, provided that the H^+ (or OH^-) concentrations are much smaller than the salt concentration, changing the pH only causes a threshold shift, as evident from the previous results (Figs. 6.5-6.7) and coherently with the literature [27].

In this section we then show additional measurements on p05 and p07 chips varying the salt concentration. To this purpose, we prepared 5 solutions of KCl in MilliQ water with concentrations from 100 μM to 1 M. The measured pHs are reported in Tab. 6.2, with a measurement error of $\pm$0.1 pH. Note that these pHs, as well as those reported in previous sections, deviate from the theoretical value of pH = 7 due to the absorption of CO_2 from the air, which is then transformed into a weak acid in solution (H_2CO_3). However we verified that during our measurements they did not vary from the values in Tab. 6.2 of more than 0.1 pH.

KCl concentration	**pH**
100 μM	6
1 mM	5.9
10 mM	5.85
100 mM	5.75
1 M	5.65

Table 6.2: pHs of the KCl solutions.

6.1.2.1 *p*MOSFET

We reconsider the 3dots chip of p07 type (*p*MOSFET) and the 5B02 device (width 80 nm, length 500 nm). In the following, we skip the load compensation, since it does not affect the results in the frequency range of interest.
Fig. 6.9 shows the admittance spectra for a few salt concentration, polarization and oscillator level V_{AC} (i.e., the AC potential applied at the high electrode). As expected, changing the oscillator level from 10 mV to 100 mV does not appreciably change the response, but it lowers down considerably the noise. In addition in graphs (b) and (c), we now clearly see the effect of salt concentration on the admittance in the intermediate frequency range.
Fig. 6.10 shows the $I_{DS}(V_{GS})$ curves measured before and after the acquisition of the AC spectra. We see that the AC measurements do not introduce perturbation in the DC curves, thus providing reassuring indications on the meaningfulness of the data. Moreover, we observe a shift of the curves of about 50 mV per salt concentration decade, likely due to a concentration dependent offset of the reference electrode voltage. The 100 μM and 1 mM solutions provide similar results, possibly due either to the contamination between different solutions or to the presence of relatively large quantities of H_2CO_3.

6.1.2.2 $n^+/n/n^+$ resistor

We have repeated the measurements of previous section also on the number 20 chip of p05 type ($n^+/n/n^+$ resistor) and the 5B02 device (width 80 nm, length 500 nm), featuring a much thinner oxide. At first we have used the usual 5B02 device, and then we have

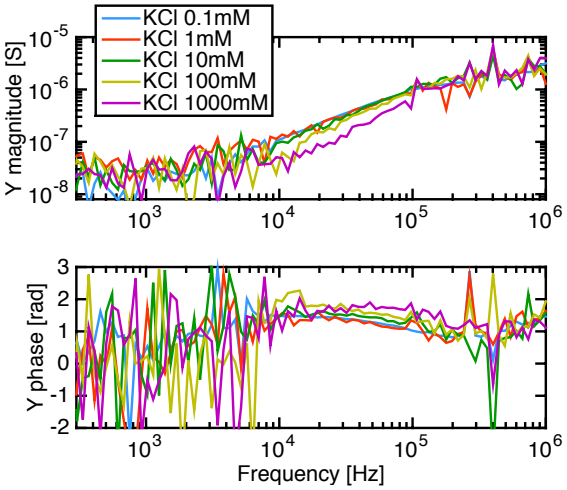

(a) $V_{AC} = 10$ mV, $I_{DS} = 10$ nA

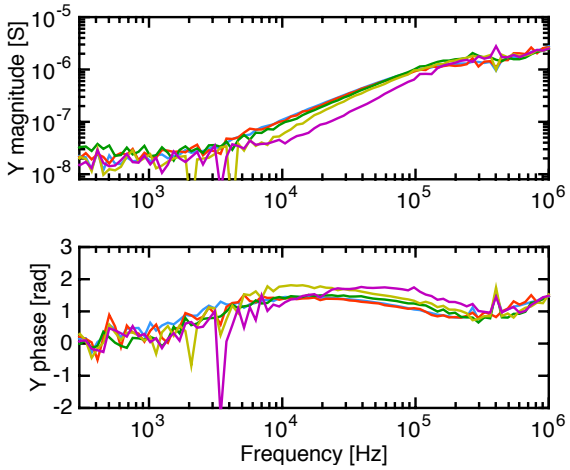

(b) $V_{AC} = 50$ mV, $I_{DS} = 10$ nA

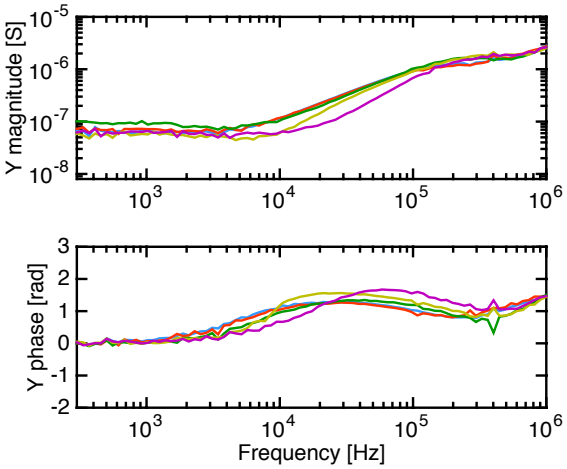

(c) $V_{AC} = 100$ mV, $I_{DS} = 10$ nA

Fig 6.9: AC admittance spectra on the 5B02 device ($W = 80$ nm, $L = 500$ nm) in chip 3dots of the p07 type (pMOSFET) varying salt concentration and AC oscillator level. No load compensation, bandwith 5.

changed the length and width of the device by measuring two 4A devices (4A07: width 80 nm, 4A10: width 150 nm), all with length 2375 nm, see Tab. 6.3. These measurements are done with a simple open/short compensation and an AC oscillator level of 100 mV, unless otherwise specified.

Fig. 6.11 (a) and (c) shows similar results to Fig. 6.9 (b) and (c), confirms that doping, working regime (accumulation or inversion) and oxide thickness do not have a strong impact on the shape of the AC response spectra. Here we also show the admittance Y_{exp} as $Y_{exp} = G_{exp} + j\omega C_{exp}$, that is, using a parallel conductor/capacitor model. These plots reveal that the difference between the admittance spectra in the intermediate frequency

	5A02 and 5B02	4A07	4A10
Nanowire width W	80 nm	80 nm	150 nm
Nanowire length L	500 nm	2375 nm	2375 nm

Table 6.3: Measured devices on the CEA/LETI SiNWs chips used in this thesis.

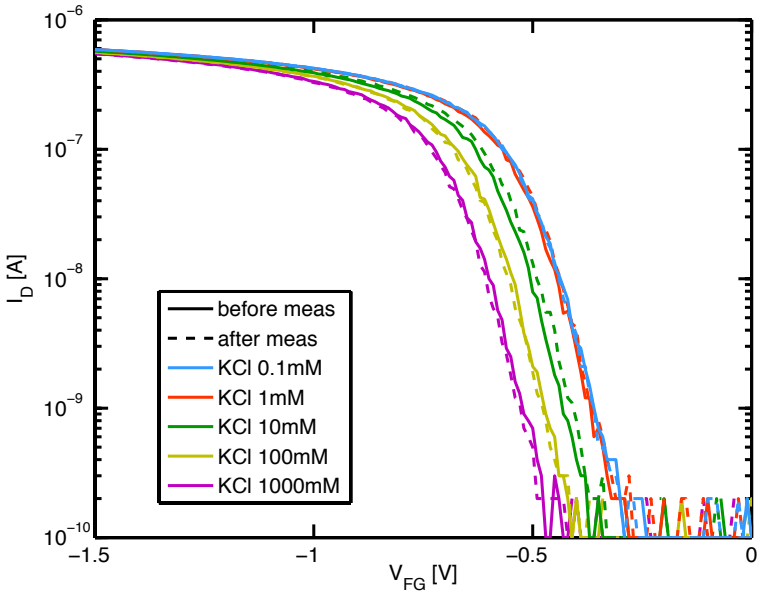

Fig 6.10: $I_{DS}(V_{FG})$ curves on the 5B02 device ($W = 80$ nm, $L = 500$ nm) in chip 3dots of the p07 type (pMOSFET) varying salt concentration. $V_{DS} = 100$ mV.

range is mainly due to a decrease of the capacitance with salt concentration.
This behaviour is totally unexpected, since the theoretical models for the double layer capacitance (see Sec. 3.1.1.2) predict an increase with salt concentration. The $I_{DS}(V_{GS})$ curves measured before and after the AC characterization (Fig. 6.12) reveal the same behaviour as for the p07 chip. Namely, we observe a shift of the curves of about 50 mV per salt concentration decade, likely due to a concentration dependent offset of the reference electrode voltage.

We then performed similar measurements, but changing the device, in order to test the effect of the nanowire length and width. Fig. 6.13 reports the admittance spectra for the 4A07 and 4A10 devices (see Tab. 6.3) varying the salt concentration and bias. These devices are affected by the salt concentration in the same way as the 5B02 one, as evident also from the $I_{DS}(V_{GS})$ curves (Fig. 6.14). The qualitative trends agree with the ones for the 5B02 device, but some quantitative differences are visible.
This point is worth being investigated in detail, however for time constraints it is left for future work.

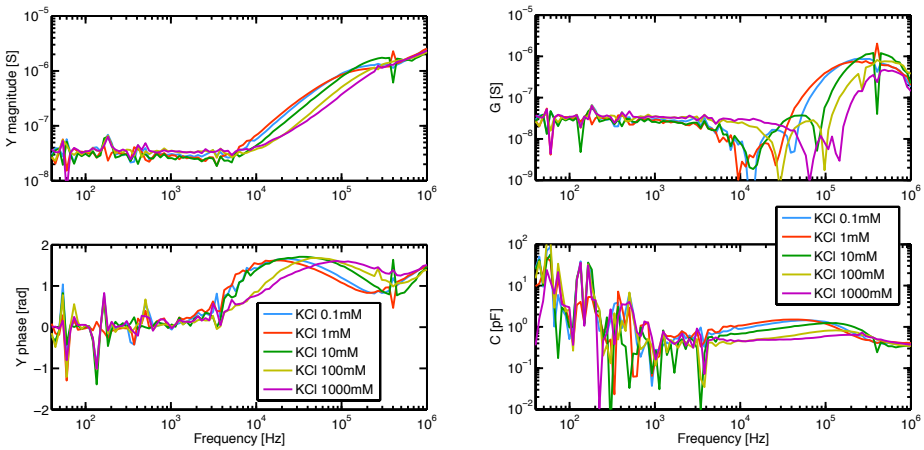

(a) $I_{DS} = 1$ nA **(b)** $I_{DS} = 1$ nA

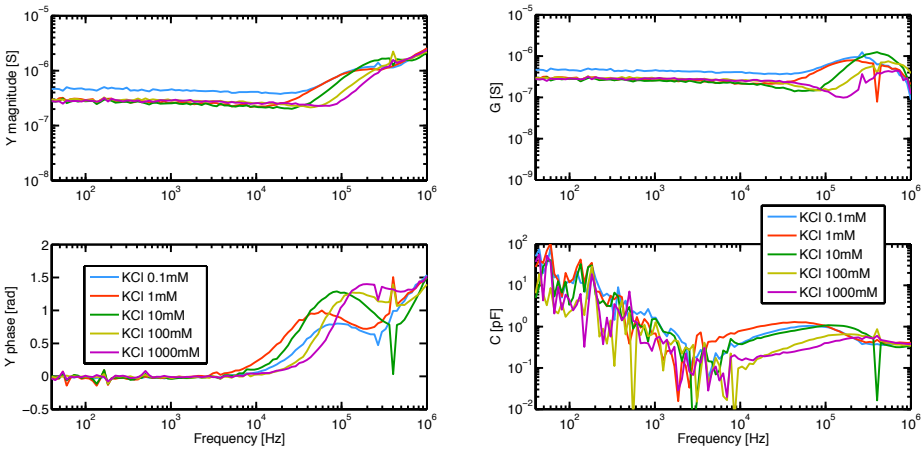

(c) $I_{DS} = 10$ nA **(d)** $I_{DS} = 10$ nA

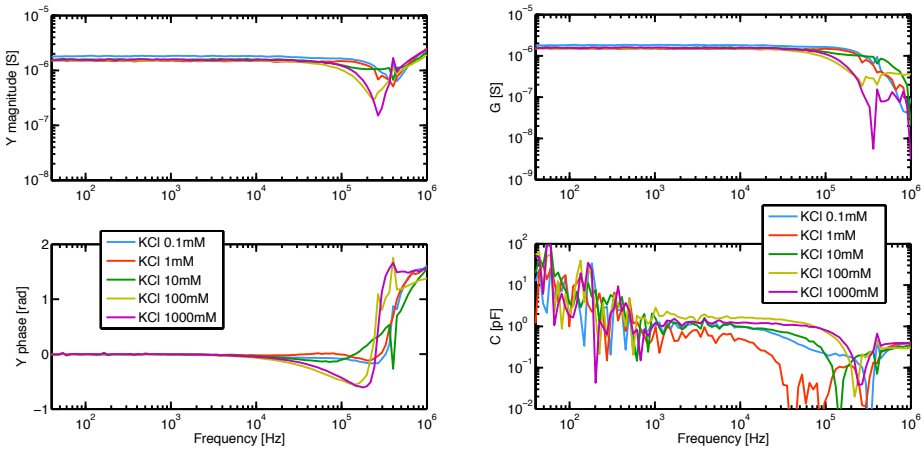

(e) $I_{DS} = 100$ nA **(f)** $I_{DS} = 100$ nA

Fig 6.11: AC admittance spectra on the 5B02 device ($W = 80$ nm, $L = 500$ nm) in chip number 20 of the p05 type ($n^+/n/n^+$ resistor) versus frequency, salt concentration and bias. The admittance is presented as magnitude and phase (left plots) or conductance and capacitance (right plots). Simple open/short compensations, $V_{AC} = 100$ mV.

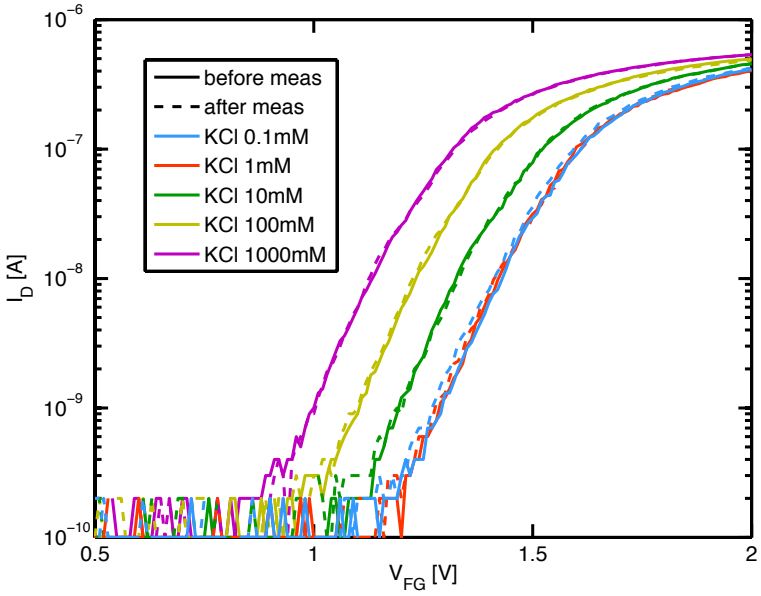

Fig 6.12: $I_{DS}(V_{FG})$ curves on the 5B02 device ($W = 80$ nm, $L = 500$ nm) in chip number 20 of the p05 type ($n^+/n/n^+$ resistor) varying salt concentration. $V_{DS} = 100$ mV.

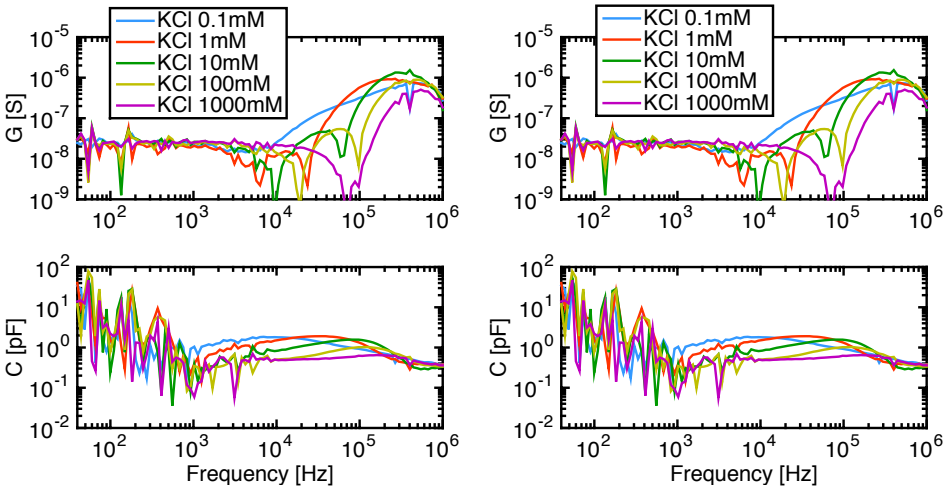

(a) 4A07 ($W = 80$ nm), $I_{DS} = 1$ nA **(b)** 4A10 ($W = 150$ nm), $I_{DS} = 1$ nA

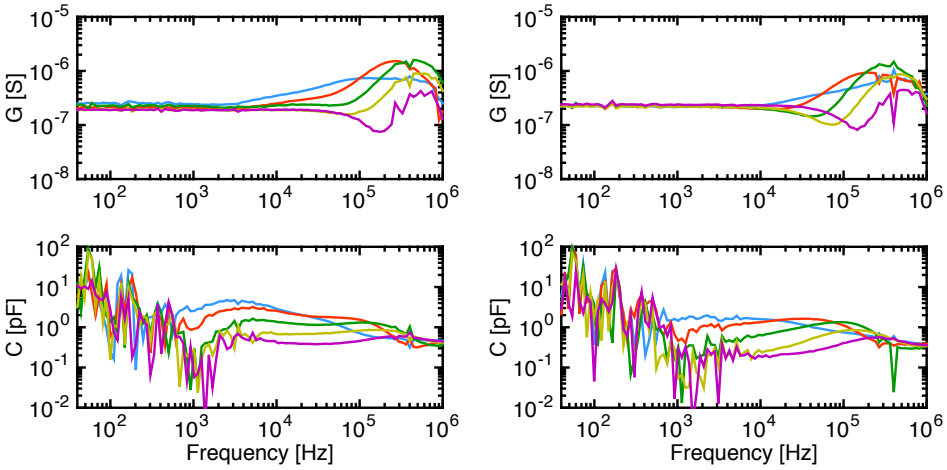

(c) 4A07 ($W = 80$ nm), $I_{DS} = 10$ nA **(d)** 4A10 ($W = 150$ nm), $I_{DS} = 10$ nA

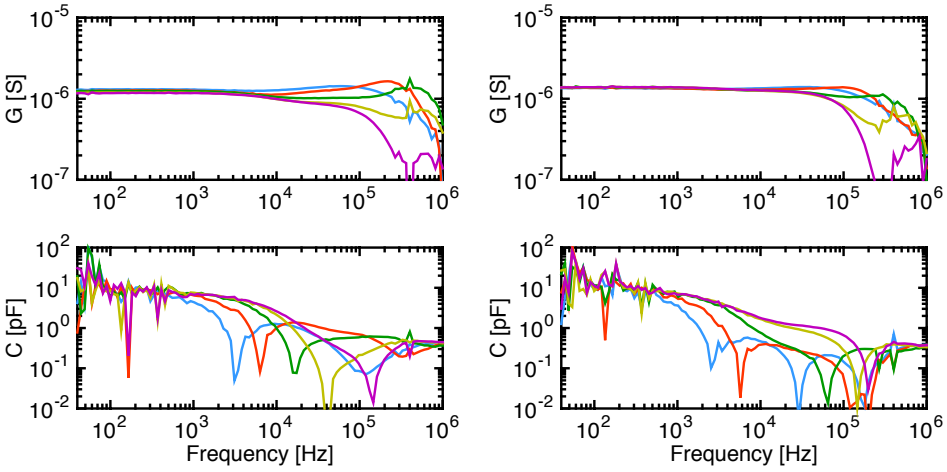

(e) 4A07 ($W = 80$ nm), $I_{DS} = 100$ nA **(f)** 4A10 ($W = 150$ nm), $I_{DS} = 100$ nA

Fig 6.13: AC admittance spectra on the 4A devices ($W = 80$ or 150 nm, $L = 2375$ nm) in chip number 20 of the p05 type ($n^+/n/n^+$ resistor) for different salt concentration, bias and device width. Simple short/open compensation.

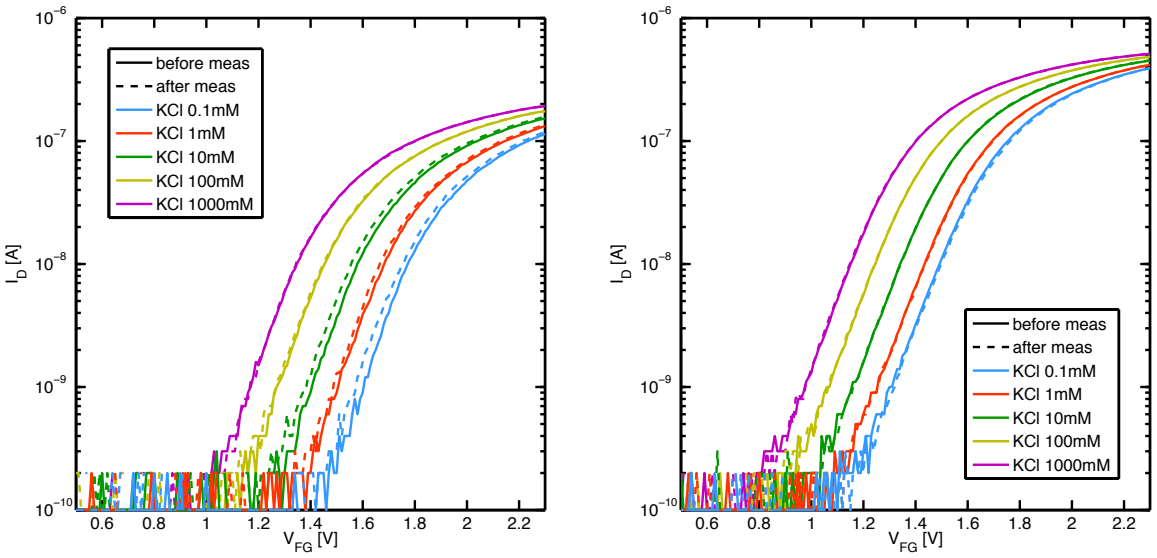

(a) 4A07 ($W = 80$ nm, $L = 2375$ nm) **(b)** 4A10 ($W = 150$ nm, $L = 2375$ nm)

Fig 6.14: $I_{DS}(V_{FG})$ curves on the 4A devices ($W = 80$ or 150 nm, $L = 2375$ nm) in chip number 20 of the p05 type ($n^+/n/n^+$ resistor) varying salt concentration. $V_{DS} = 100$ mV.

6.2 Comparison with simulations

In order to interpret the experimental findings, we compare the measurements with simulations performed with ENBIOS. To this purpose, nanowires with the same geometry as the experimental samples have been simulated to derive the behaviour of the intrinsic device. Unfortunately, real devices are affected by large parasitics, which dominate the measured response starting from a low frequency ($\approx$ 300 kHz), often much smaller than the electrolyte cut-off frequency f_c (see Sec. 3.1.1.3).

As a first step for the identification of a model for the parasitics, in Sec. 6.2.1 we derive and verify on simulations a lumped element circuit of the "intrinsic" NW (i.e., the NW without the effect of parasitics) and whose elements are physically based. Then, in Sec. 6.2.2 we derive a circuit model for the parasitics and use it in combination with the intrinsic NW equivalent circuit to compare simulations and measurements.

6.2.1 Lumped element circuit for nanowire in electrolyte

In order to determine the most appropriate circuit topology for a physically based lumped element model of the nanowire in electrolyte environment, we initially simulated with ENBIOS the intrinsic part of nanowires with the same geometry as the experimental samples (see Tab. 6.3). Remind that we defined the source admittance as $Y_{exp} = \tilde{I}_S/\tilde{V}_D$, where $\tilde{I}_S$ is the AC current measured at the source and $\tilde{V}_D$ the AC drain voltage (while all other terminals are grounded). We retain the same definition also in simulations, and consistently calculate a simulated Y_{sim}. Note that, using this definition, Y_{sim} and Y_{exp} are not admittances of two-terminal devices (although they have measure units of Siemens), since the NW device is not a bipole but has a fluid gate and a back gate terminal as well. In the following we will critically analyse this point in more detail.
Fig. 6.15 shows the simulated admittance spectra of 5B02 $n^+/n/n^+$ devices with the parameters in Tab. 6.4 in KCl electrolyte. The $Y_{sim} = G + j\omega C$ is represented by the parallel RC model. The polarizations correspond to different points on the $I_D(V_{FG})$ curves at $V_{DS} = 100$ mV. We immediately note the presence of a cut-off frequency at approximately 1, 10 and 100 MHz which depends on the salt concentration and coincides with the usual electrolyte's dielectric relaxation cut-off frequency f_c. As expected, at constant current the oxide thickness has a modest effect only above threshold (graph c).

In order to understand how the different parts of the system affect the response, we search for a lumped element circuit model of the device in the AC small signal regime. We tested a few circuits and the simplest topology we could find that reproduces the real and imaginary parts of Y_{sim} over a wide frequency range is the one of Fig. 6.16, where we joined together the terminals for the back and the fluid gate, since they are

Parameter	Symbol	Value	Units	Ref.
Nanowire length	L_{NW}	500	[nm]	
Nanowire width	W_{NW}	80	[nm]	
Nanowire height	h_{NW}	30	[nm]	
Nanowire oxide thickness	t_{ox}	3 and 8.5	[nm]	
Contacts height	h_{SD}	60	[nm]	
Temperature	T	298.16	[K]	
n doping	n	10^{22}	[m^{-3}]	
n^+ doping	n^+	10^{25}	[m^{-3}]	

Table 6.4: Parameters used in the simulations (unless otherwise stated).

both AC grounded. Here R_1 aims to represents the wire resistance, C_2 the series of the oxide and EDL capacitance, C_3 and R_3 the bulk electrolyte and the substrate capacitance and resistance and C_4 a source to drain capacitive coupling via the electrolyte and the substrate. This physical interpretation will be critically re-examined later in more detail. We emphasize that this model was not only derived from physical considerations, but mostly because it was the simplest we could find that could reproduce the surprising decrease of the capacitance for increasing salt concentration observed in previous section. From the model in Fig. 6.16 we immediately note that the NW can be represented as a

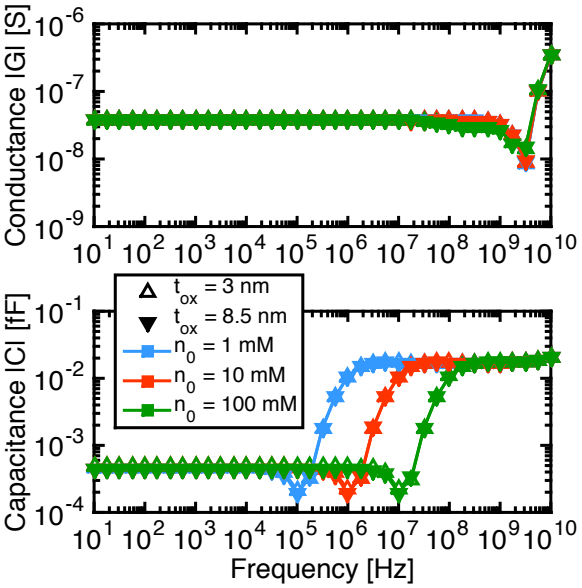

(a) $I_D = 1$ nA

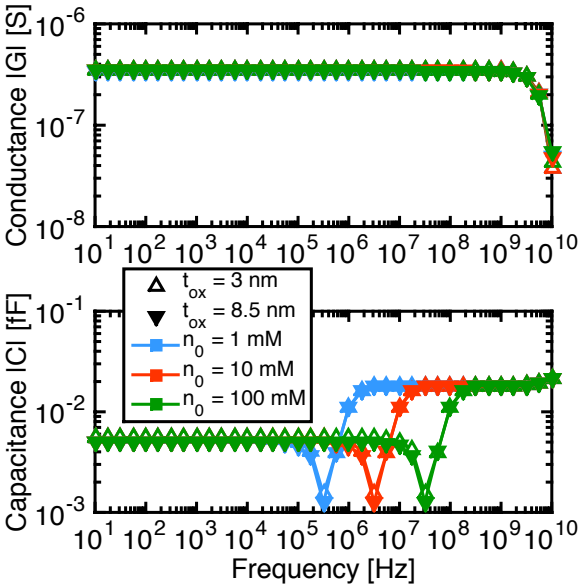

(b) $I_D = 10$ nA

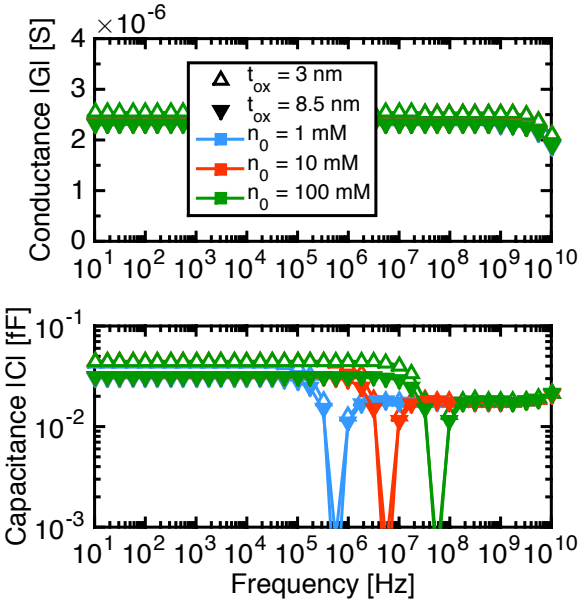

(c) $I_D = 100$ nA

Fig 6.15: Nanowire source admittance spectra at different bias points, corresponding to depletion and accumulation on the $I_D(V_{FG})$ curves at $V_{DS} = 100$ mV. Note the steady increase of conductance for increasing current. The dips in the capacitance correspond to sign changes. Here and in the following n_0 is the salt concentration in the bulk of the electrolyte.

2-port with admittance matrix:

$$\mathbf{Y} = \begin{bmatrix} Y_{DD} & Y_{DS} \\ Y_{DS} & Y_{SS} \end{bmatrix} \tag{6.1}$$

where the currents at the drain and source contacts are:

$$\begin{bmatrix} \tilde{I}_D \\ \tilde{I}_S \end{bmatrix} = \mathbf{Y} \begin{bmatrix} \tilde{V}_D \\ \tilde{V}_S \end{bmatrix} \tag{6.2}$$

With this definition it is immediate to see that $Y_{sim} = \tilde{I}_S/\tilde{V}_D = Y_{DS}$, since we always keep $\tilde{V}_S = 0$.
It is natural at this point to evaluate how well can the model of Fig. 6.16 (which we call 2R3C model) fit to the simulation data for the intrinsic device. Fig. 6.17 shows the comparison between simulations and the model. All parameters, except for R_1, which is directly extracted from the low frequency conductance, are simultaneously fitted using a least-square optimizer. The relative deviations:

$$\epsilon_R = \frac{\Re\{Y_{sim} - Y_{fit}\}}{\Re\{Y_{sim}\}}, \qquad \epsilon_I = \frac{\Im\{Y_{sim} - Y_{fit}\}}{\Im\{Y_{sim}\}} \tag{6.3}$$

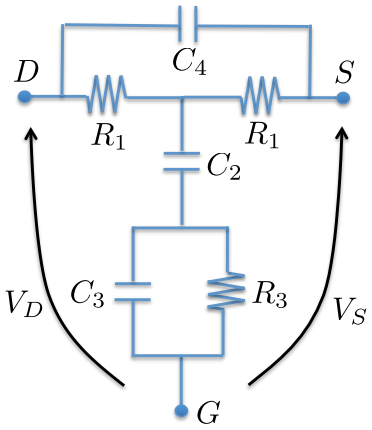

Fig 6.16: Nanowire system equivalent circuit 2R3C.

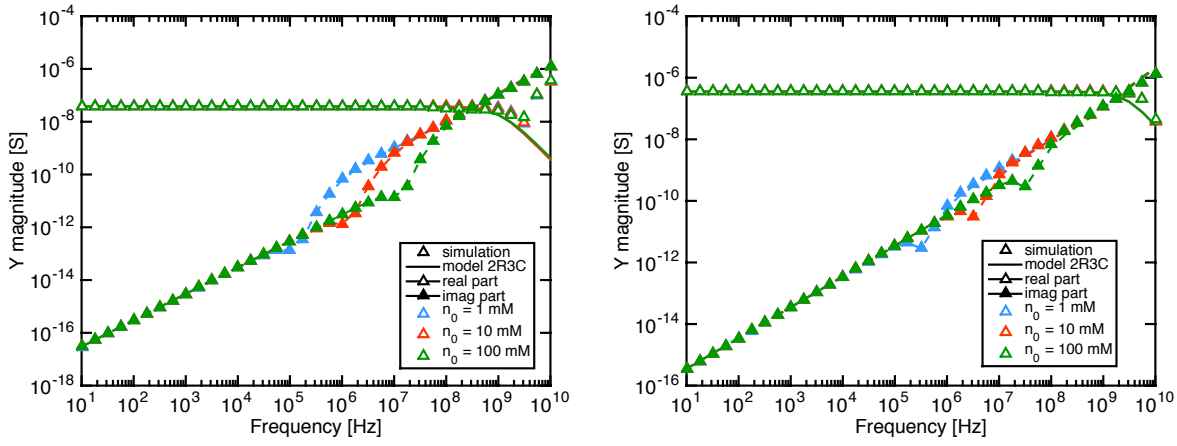

(a) $I_D = 1$ nA **(b)** $I_D = 10$ nA

Fig 6.17: Nanowire source admittance spectra and corresponding fit to the 2R3C model at different polarizations, corresponding to different points on the $I_D(V_{FG})$ curves at $V_{DS} = 100$ mV. $t_{ox} = 3$ nm.

obtained by this unconstrained fit are chosen as error functions in order to well reproduce not only the magnitude of Y but the real and imaginary parts separately. The circuit elements are reported in Fig. 6.18 for the devices with $t_{ox} = 3$ nm (left plots) and 8.5 nm (right plots). We immediately recognize that G_3 is directly proportional to salt concentration in all cases (top plots), suggesting the idea that it represents the bulk electrolyte conductivity, as originally thought. All the other elements do not depend on n_0 and this is surprising in view of the fact that C_2 should include the effect of the concentration dependent EDL capacitance. Furthermore, looking at the dependence on the DC bias (bottom plots), expressed as a function of the DC resistance R_1, we note that all the capacitive elements have non-trivial and not easy to interpret dependences. Since the blind fitting procedure does not seem to yield physically based results for the capacitances, in the next section we then devise a different procedure to identify the physical origin of these circuit elements and to extract physically based values.

6.2.1.1 Extraction of circuit elements

To attribute a physical meaning to the circuit elements and extract physically meaningful values, we use a two-step procedure. The idea behind it is that, since the real part is

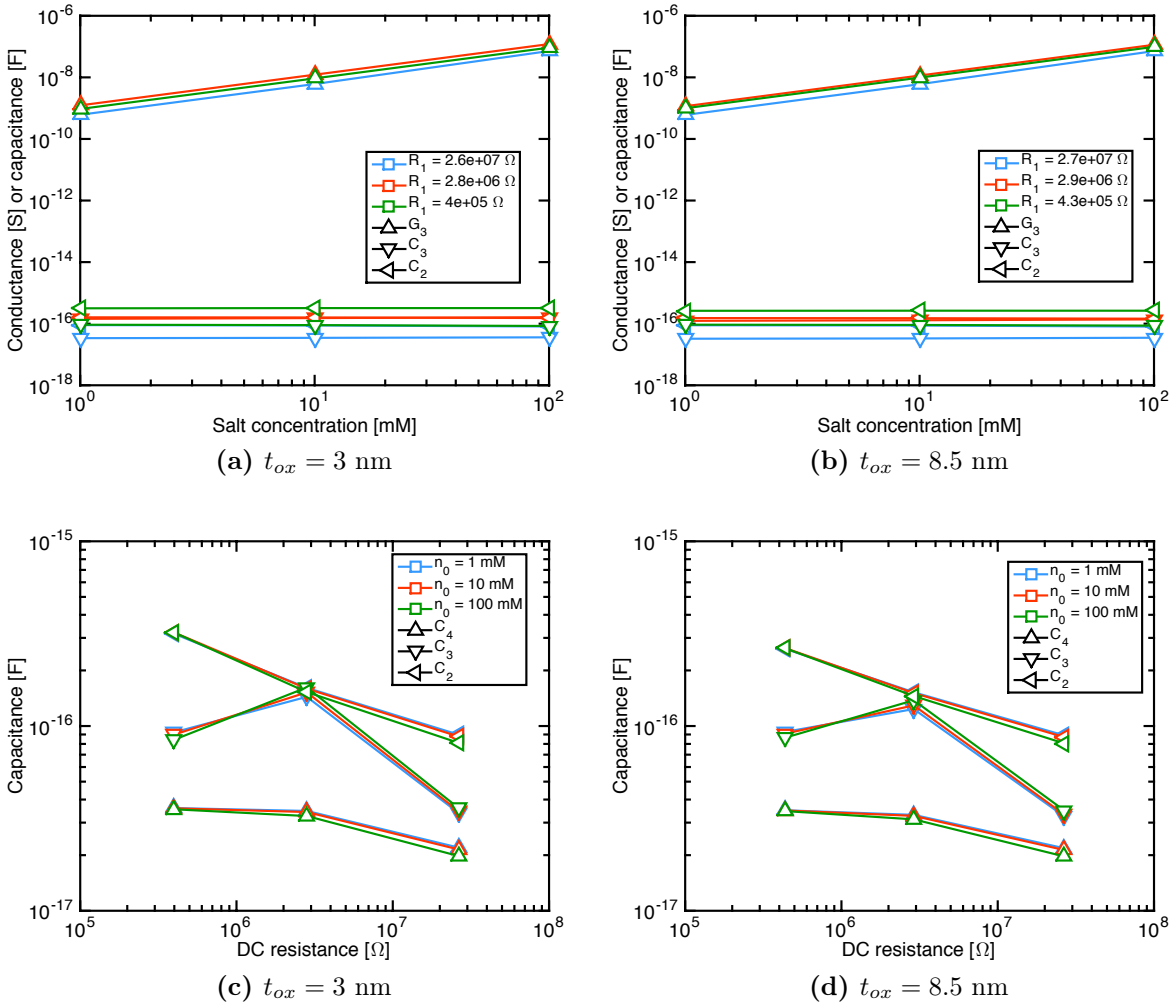

(a) $t_{ox} = 3$ nm **(b)** $t_{ox} = 8.5$ nm

(c) $t_{ox} = 3$ nm **(d)** $t_{ox} = 8.5$ nm

Fig 6.18: Circuit elements of the 2R3C model derived by unconstrained fitting the simulated admittance spectra.

so much larger than the imaginary part over most of the frequency spectrum (see, e.g., Fig. 6.17) a global fitting procedure will be inaccurate in extracting the tiny capacitances responsible for the appearance of the small imaginary part of Y_{sim}. The procedure has the following steps:

1. we fix the resistance R_1 to the value of the nanowire resistance at very low frequency;

2. we derive all the lumped circuit elements from the simulated NW admittance spectrum, as in the previous section;

3. we then assume, consistently with previous results (Fig. 6.18), that G_3 represents the bulk electrolyte conductance, and therefore it should not depend on the bias. Accordingly, we fix G_3 to the value obtained from the previous fitting at a particular DC bias, which is chosen in subthreshold since the large NW resistance make the result very sensitive to the electrolyte;

4. we fix $C_3 = \dfrac{G_3}{\xi}$, where ξ is the electrolyte's dielectric relaxation cut-off frequency;

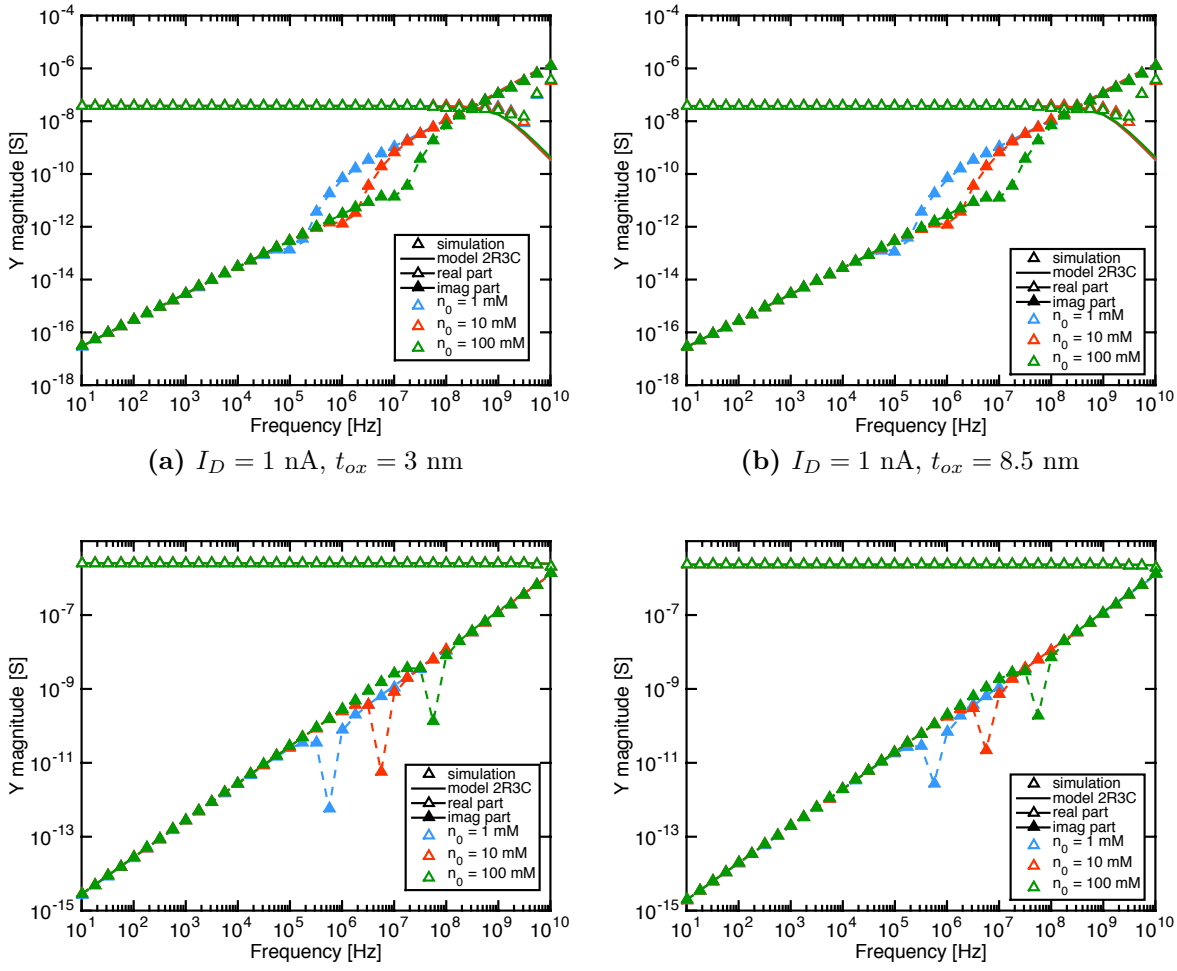

(a) $I_D = 1$ nA, $t_{ox} = 3$ nm

(b) $I_D = 1$ nA, $t_{ox} = 8.5$ nm

(c) $I_D = 100$ nA, $t_{ox} = 3$ nm

(d) $I_D = 100$ nA, $t_{ox} = 8.5$ nm

Fig 6.19: Nanowire source admittance spectra and corresponding fit to the 2R3C model (second fit only on C_2 and C_4) at different oxide thickness and polarizations, corresponding to different points on the $I_D(V_{FG})$ curves at $V_{DS} = 100$ mV.

5. we re-fit C_2 and C_4 of the 2R3C model, using as initial guess the values derived from the previous fitting.

This new extraction procedure yields an excellent agreement between the 2R3C model and numerical simulations, essentially indistinguishable from the previous one (compare Figs. 6.17 and 6.19). In particular, the model nicely reproduces the existence of a frequency interval where the imaginary part decreases for increasing salt concentration, definitely an unusual effect. Also, the sign changes and the frequency of the zero are nicely reproduced. Figs. 6.20 - 6.21 show the lumped element values versus concentration n_0 and drain current. We see that by imposing a bias and concentration independent C_3 (as it is expected to be based on the physical consideration that it should represent the bulk electrolyte and substrate capacitances) we obtain that also C_4 is essentially bias independent. The following physical interpretation appears then natural:

- R_1: nanowire resistance;
- C_2: series of accumulation, oxide and double-layer capacitances;
- G_3 and C_3: bulk electrolyte conductance and capacitance;
- C_4: capacitance between source and drain.

In particular, if we concentrate on C_2 (see Fig. 6.21), we immediately recognize the typical bias dependence of accumulation and oxide capacitances in series of MOSFET devices. The concentration dependence of the EDL capacitance is visible only at large DC bias. Indeed, we estimated the oxide capacitance with a simple 1D approximation, i.e. considering the three edges of the nanowires as if they were planar surfaces with no fringing effects. This estimation gives $C_{ox} = 1.15$ fF for $t_{ox} = 3$ nm and $C_{ox} = 0.41$ fF for $t_{ox} = 8.5$ nm, which is reasonable if we look at the asymptotic values of C_2 for increasing V_{FG}. In addition to the MOSFET accumulation capacitance we observe an effect of the salt concentration at high DC bias, where the double layer capacitance C_{DL} (assumed real and frequency independent since its anomalous frequency behaviour is not relevant in this case) is not any longer so much larger than the series of the oxide and accumulation capacitances and can be estimated in the same way as for C_{ox}, but using as thickness the Debye length λ_D. This estimation gives $C_{DL} = 6.9$ fF at 1 mM and $C_{DL} = 69$ fF at 100 mM, thus supporting our hypothesis.

6.2.2 Parasitics and simulation comparisons

Having derived a physically based circuit model for the intrinsic nanowire in electrolyte environment which reproduces accurately the simulations, we can now move to the comparison with experimental results. As discussed in Sec. 6.1, the available nanowires have very large parasitics, which result in a cut-off frequency of about 300 kHz, which is very low compared to f_c at 1 - 100 mM. In order to compare simulations to measurements, we then need to include the parasitics in the model.
Fig. 6.22 shows the chosen topology for the network of external parasitic elements, where the inner rectangle (**W**) denotes the intrinsic NW, which we will represent with the equivalent circuit of Fig. 6.16. In the fitting procedure used to extract the parasitic lumped element values we decided to freeze the intrinsic NW circuit elements to the values extracted with the two-steps procedure above (except for R_1 which is adjusted to the measured DC conductance value); thus, we fit only the parasitics. We already derived the value of the

parasitic series resistance R_S in Sec. 6.1 from the measurements of the very large 5B00 devices and they are:

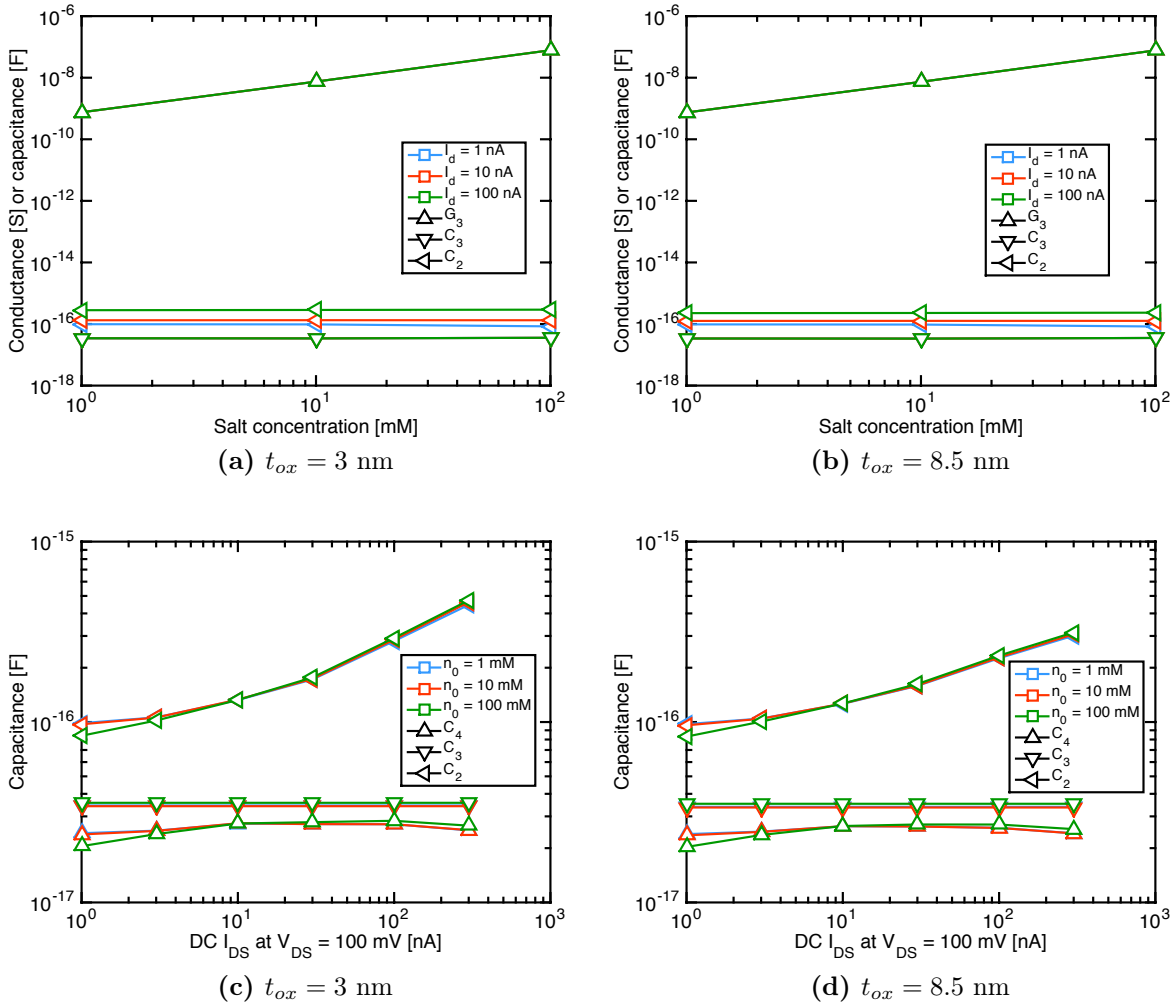

(a) $t_{ox} = 3$ nm **(b)** $t_{ox} = 8.5$ nm

(c) $t_{ox} = 3$ nm **(d)** $t_{ox} = 8.5$ nm

Fig 6.20: Circuit elements of the 2R3C model derived by the constrained, two-steps fitting of the simulated admittance spectra. Note the constant C_3 (by construction) and C_4.

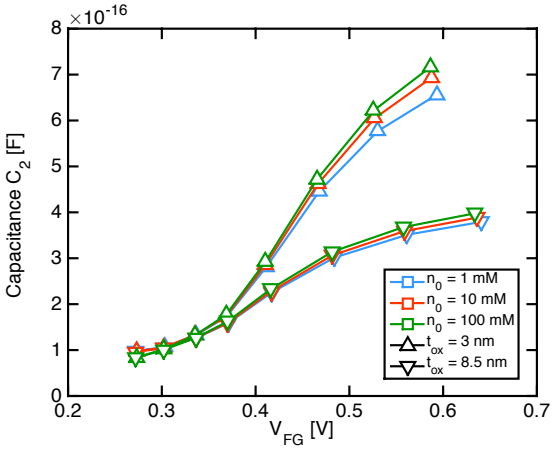

Fig 6.21: Capacitance C_2 of the 2R3C model derived by the constrained, two-steps fitting the of simulated admittance spectra. The estimation of the oxide capacitance C_{ox} by means of simple 1D models give $C_{ox} = 1.15$ fF for $t_{ox} = 3$ nm and $C_{ox} = 0.41$ fF for $t_{ox} = 8.5$ nm.

- $R_S \simeq 55$ kΩ in p05 chips ($n^+/n/n^+$ resistors);

- $R_S \simeq 65$ kΩ in p07 chips (pMOSFETs).

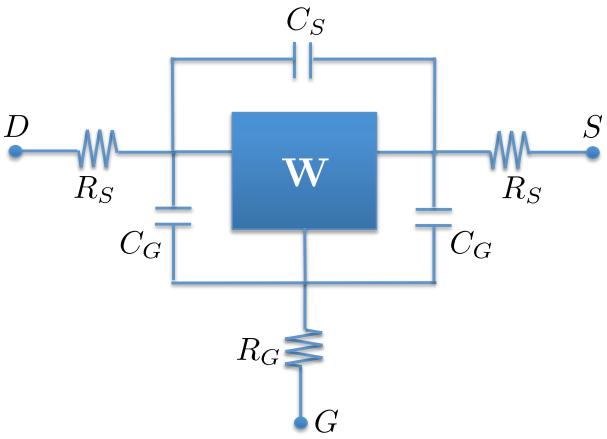

Fig 6.22: Equivalent circuit of the nanowire system with parasitics.

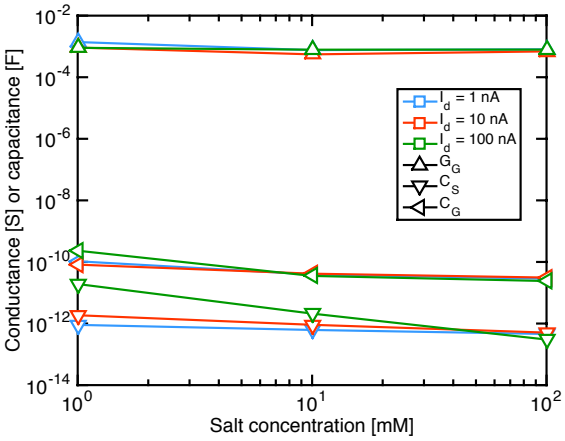

(a) p05, 5B02

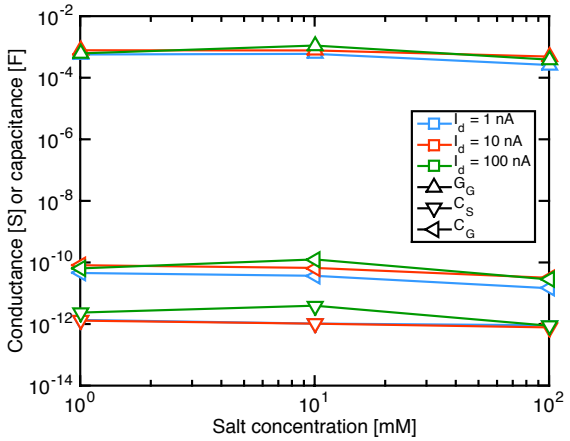

(b) p07, 5B02(1)

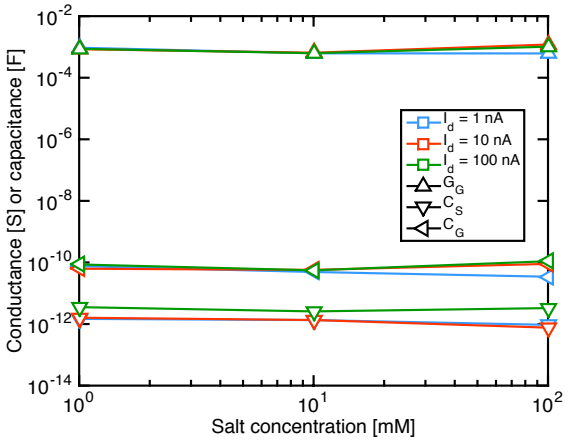

(c) p07, 5B02(2)

Fig 6.23: Parasitic elements of the circuit model of Fig. 6.22, using for **W** the 2R3C circuit (Fig. 6.16a) with parameters extracted from numerical simulations via the constrained two-steps fitting procedure. (a): $n^+/n/n^+$ resistors in p05 chips; (b): pMOSFETs in p07 chips.

For the sake of a rapid analysis of many devices, and despite the different doping species in p05 and p07 chips, we used the same simulated data of $n^+/n/n^+$ resistors for both resistor and pMOSFET analysis. This choice is justified noting that all admittance spectra are measured at fixed points on the $I_D(V_{FG})$ curves, that is either in subthreshold or immediately above threshold. In these conditions, the admittance spectra are influenced by the doping only via the slightly different mobilities between electrons and holes. The fitting was based only on the data points that lie above the noise level (see for instance Fig. 6.24), which is around 10^{-8} S.

Fig. 6.23 shows the measured admittance spectra and the fits with the circuit model of Fig. 6.22. The fitting is satisfactory in almost all cases, especially in view of the fact that the parameters of the intrinsic NW are taken directly from the simulations and from the DC conductance value.
Fig. 6.24 reports the extracted values of the parasitics as a function of salt concentration. It is difficult to identify clear trends in the elements' dependency on salt concentration and on DC bias.

These considerations support our statement that the measured admittance in our setup is dominated by the on-chip parasitics (the off-chip ones are in principle calibrated out by the initial instrument calibration procedure). In order to confirm this finding, we performed similar measurements as before on devices with very narrow nominal width and negligible current at any DC bias. Using SEM measurements on similar chips we verified that the nanowires were indeed not present in these chips, probably due to a non well-controlled etching process.
Fig. 6.25 shows the admittance spectra of these "absent" devices in p05 and p07 chips at various DC bias and salt concentration. We see no clear dependence on V_{FG} of any parasitic element. We also immediately recognize that the only qualitative difference between the curves in Fig. 6.24 and the ones of Fig. 6.25 is in the conductance at low frequency. This statement is confirmed from the data of Fig. 6.26, where the measurements on nanowires are directly compared to the measurements in absence of devices. These observations lead us to conclude that these devices's response are unfortunately too much dominated by parasitics to be able to observe the intrinsic NW behaviour predicted by simulations in any parameter except the DC conductance. A similar conclusion regarding the importance of parasitics is reported for instance in [78]. This stress out once more the importance of having integrated platforms like [33], to be able to reduce the effect of parasitics and to do on-chip calibrations.

In all these measurements, however, we have noted that the capacitance in the intermediate frequency range has a dependence on salt concentration which is opposite to our expectations based on the physical models of Chap. 2. To elucidate this point, we have performed additional measurements with an improved setup featuring a lock-in amplifier. The discussion and validation of this setup is still ongoing, but we show some preliminary result here.
Fig. 6.27 shows the admittance measured with the new setup between the source and fluid gate terminals, keeping the drain and the back gate floating. We immediately see that, in this case the capacitance increases with salt concentration, as expected from the theory and oppositely to all other measurements in this section. This observation leads us to conclude that the anomalous frequency behaviour may be due to the combination of two effects:

1. the source admittance that we measured is not a real admittance, but an element of the 2-port admittance matrix of the system;

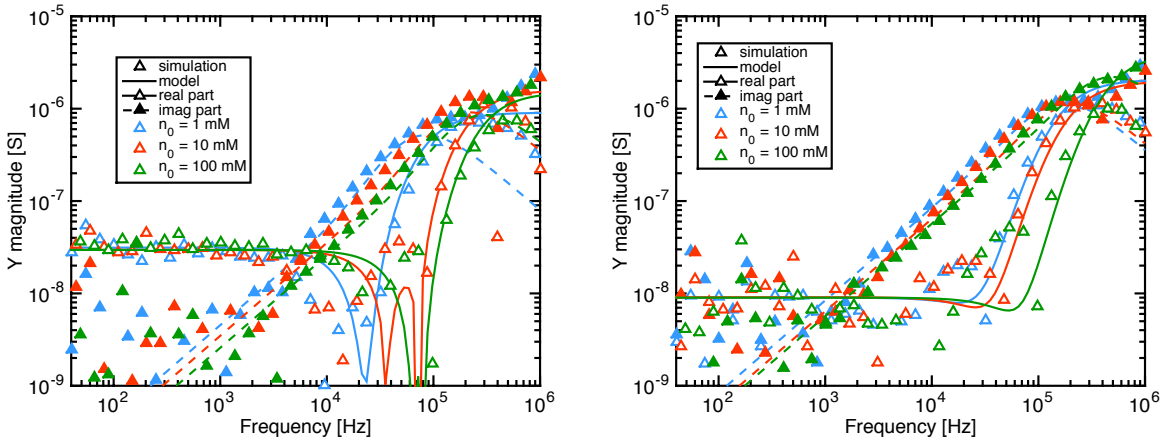

(a) p05, 5B02, $I_D = 1$ nA **(b)** p07, 5B02(1), $I_D = 1$ nA

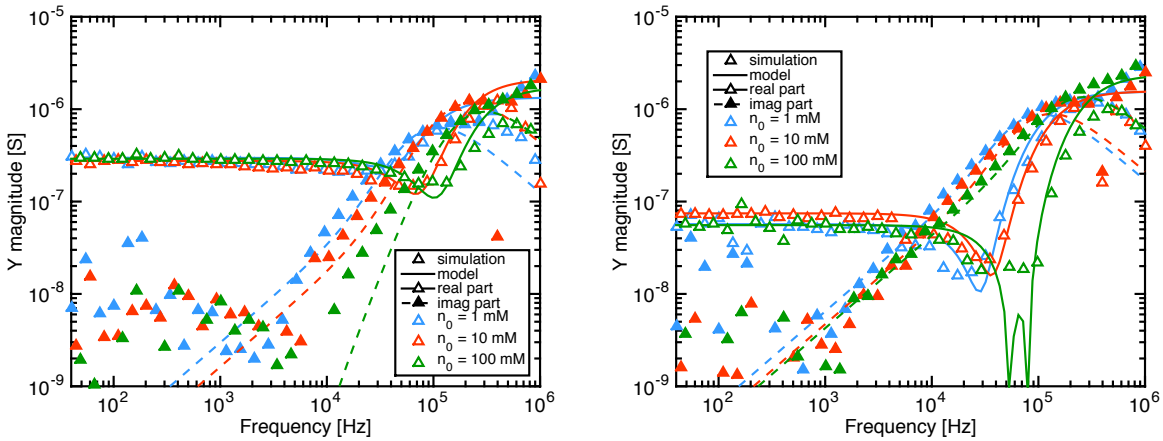

(c) p05, 5B02, $I_D = 10$ nA **(d)** p07, 5B02(1), $I_D = 10$ nA

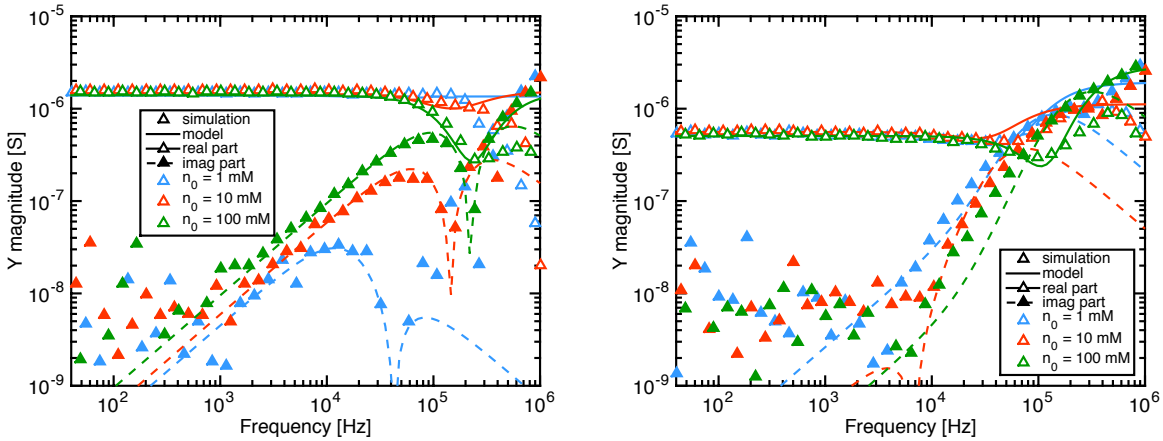

(e) p05, 5B02, $I_D = 100$ nA **(f)** p07, 5B02(1), $I_D = 100$ nA

Fig 6.24: Comparison between the measurements on p05 (left) and p07 (right) devices and the model of Fig. 6.22 fitted to the data at fixed polarization and varying the salt concentration. The intrinsic nanowire **W** is modelled with the 2R3C circuit of Fig. 6.16, with the parameters taken directly from the simulations.

2. also in simulations (for instance Fig. 6.17) there are intermediate frequency ranges where the capacitance changes and is apparently decreasing with salt concentra-

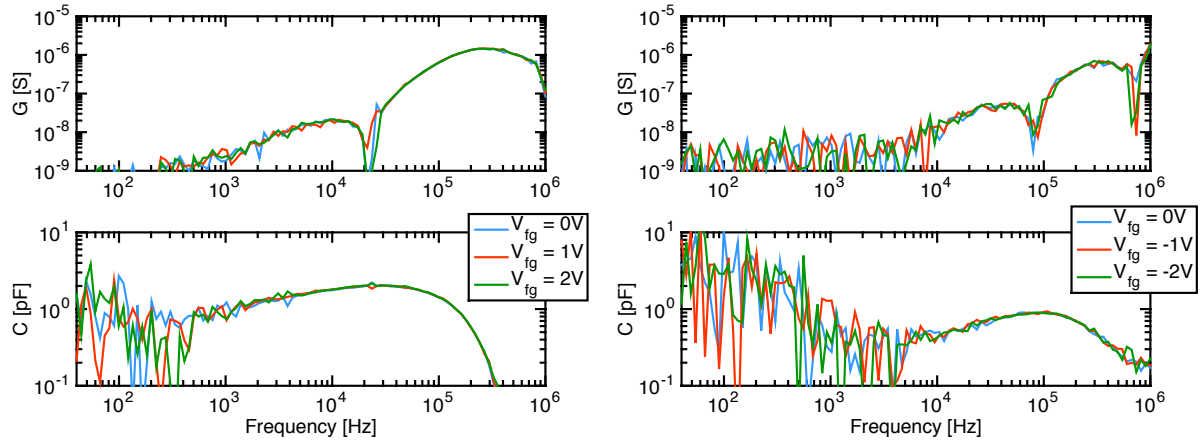

(a) p05, $n_0 = 1$ mM **(b)** p07, $n_0 = 100$ mM

Fig 6.25: Measurements with no nanowires in p05 and p07 chips, showing that the admittance does not depend on the DC bias. This supports the statement that in this case the devices are absent.

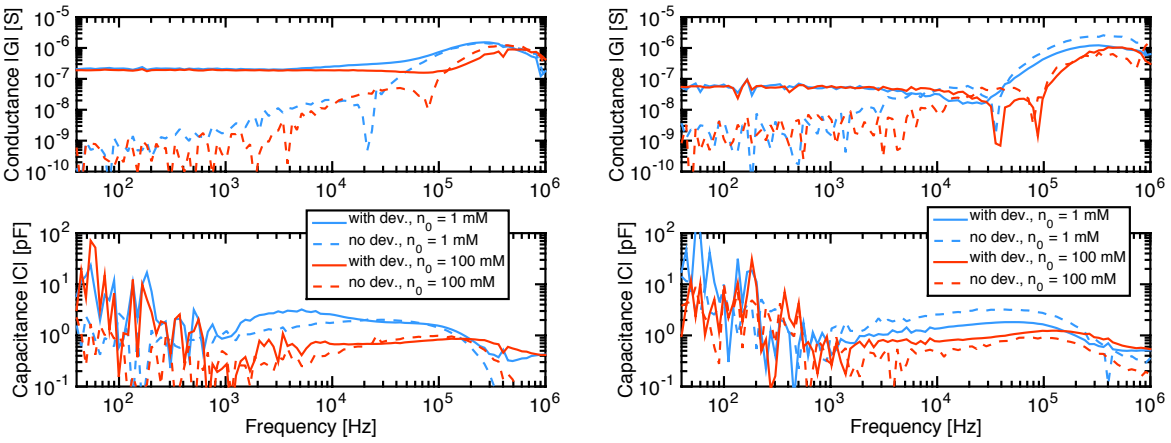

(a) p05 **(b)** p07

Fig 6.26: Comparison between measurements on nanowires (at $I_{DS} = 10$ nA) and measurements in absence of nanowires. We immediately see that the parasitics are dominating the response, with the only exception of the DC resistance.

tion; since in the measurement we could only look at a very small portion of the spectrum, we may as well be in an intermediate frequency range. Note also that the fact that the lower cut-off frequency in the simulations is much larger than in the measurements is coherent with this view, since this frequency is very sensitive to the exact geometry. Since in simulations we only include the intrinsic nanowire, the parasitics present in the real system not surprisingly can provide lower cut-off frequencies.

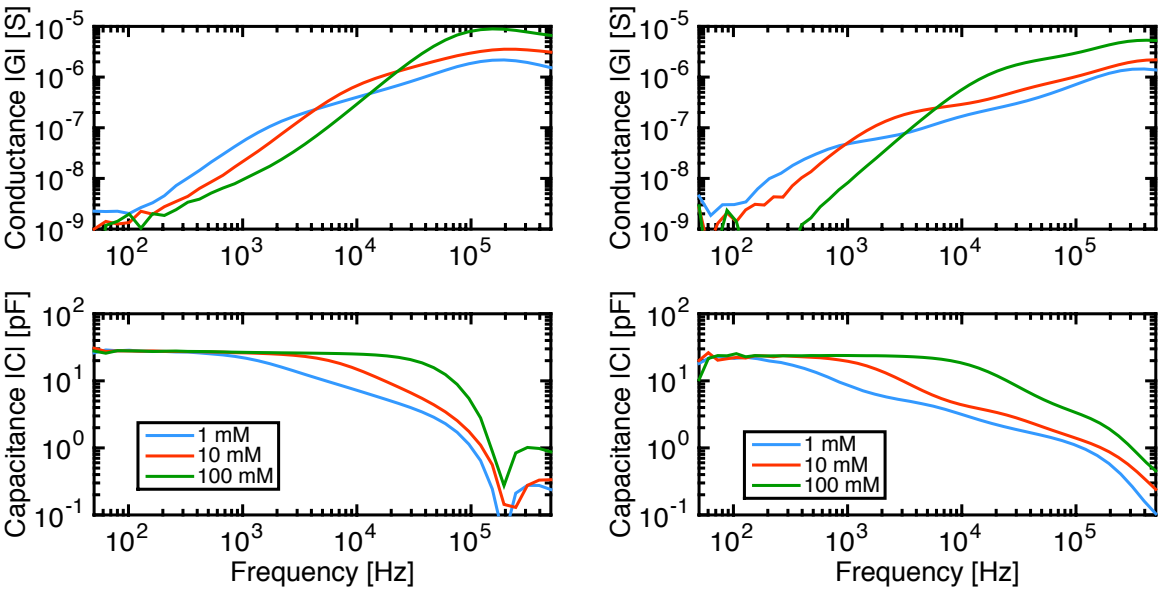

(a) p05 **(b)** p07

Fig 6.27: Measurements of the admittance between fluid gate and source with drain and back gate floating on 5B02 nanowires. The measurement setup is different from the other measurements of this section and features a lock-in amplifier. Note the capacitance increase for increasing salt concentration.

6.3 Nanowire biosensors

Nanowire Bio-FETs (NWs) have been investigated recently (e.g. for DNA and proteins detection [111, 112, 113]) because of the expected enhanced sensitivity, also due to the geometry of the diffusion process [31, 114].
As mentioned several times in this thesis, Bio-FETs that detect changes of the DC conductance, G, threshold voltage, V_T, or drain current, I_D, induced by the biomolecule charge suffer severe limitations due to static screening beyond the Debye length λ_D ($\sim$1nm at physiological salt concentration $\approx$100 mM, see Fig. 3.3) [107]. The analytical and numerical models developed in Chaps. 3-4 and the experiments in [79, 77] suggest that AC operation may lead to overcome this limit, to improve the sensitivity and the measurement stability, thus disclosing a wide range of industry-relevant applications.
While low frequency AC impedimetric sensors are well established in electrochemical measurements [76, 75], few authors addressed NW Bio-FET AC operation [79, 109]. Specifically, models are missing to explore working frequencies up to or above the electrolyte dielectric-relaxation cut-off frequency, $f_c = \sigma_{el}/2\pi\varepsilon_{el} \approx 300$ MHz@100mM, which is feasible in integrated CMOS technology.
In this section, we investigate theoretically the AC small signal operation of nanowire sensors up to frequency above f_c by means of full three-dimensional simulations of NW Bio-FETs in electrolyte environment with ENBIOS. The analysis aims at serving as physically sound and transparent foundation for the development of compact models of nanowires in electrolyte environment.

6.3.1 Models and devices

We study n^+nn^+ and p^+pp^+ SOI NWs (Fig. 5.20) with the default parameters given in Tab. 6.5, unless otherwise specified. Compared to the CEA/LETI devices, here we consider NWs with thicker gate oxide (20 nm), as necessary in practice to eliminate spurious gate leakage and ion contamination. We assume a KCl electrolyte, but qualitative results are independent of the buffer. A compact Self Assembled Monolayer (SAM), either

Parameter	**Symbol**	**Value**	**Units**	**Ref.**
Nanowire length	L	500	[nm]	
Nanowire width	W	60	[nm]	
Nanowire height	h	60	[nm]	
Oxide thicknesses	t_{ox}, t_{box}	20, 400	[nm]	
SAM thickness	t_{SAM}	2.5	[nm]	
Contacts height	h_{SD}	60	[nm]	
Temperature	T	298.16	[K]	
n and p dopings	n, p	10^{22}	[m^{-3}]	
n^+ and p^+ dopings	n^+, p^+	10^{25}	[m^{-3}]	
Mobility of K^+	μ_1	$4.755 \cdot 10^{11}$	[m/Ns]	[52]
Mobility of Cl^-	μ_2	$5.052 \cdot 10^{11}$	[m/Ns]	[52]
SAM permittivity	ε_p	$2.5\varepsilon_0$	[F/m]	[97]
Biomolecule radius	r_p	10	[nm]	[88]
Biomolecule permittivity	ε_p	$2.6\varepsilon_0$	[F/m]	[97]

Table 6.5: Parameters used in the simulations. The nanowire dimensions are those of the reference device.

directly bound to the gate dielectric or to a 20 nm thin intermediate gold layer (not shown in Fig. 6.28) is assumed to functionalize the NW [99]. The SAM is treated as an ideal interface-charge-free dielectric [99] capable of suppressing the surface pH sensitivity, consistently with [110]. As shown also in [103], it is possible to build very compact SAM, therefore confirming our choice to model it as an ideal uniform layer. Biomolecules are modelled as dielectric spheres [97, 88], with $r_p = 10$ nm (i.e., a big protein, [88] and an optional surface charge of ± 5 mC/m^2, as expected from the data in [88]; qualitatively similar results were obtained for different particle radius, charge and shape. A more precise and quantitative estimation of a particular biomolecule's surface charge would necessarily need reliable experimental data or sophisticated Monte-Carlo measurements as in [98]. We also do not consider the noise and fluctuations associated with the binding/unbinding of the biomolecules on the surface, which has been extensively described in [115]. We consider $n^\infty = 1$ mM and 100 mM bulk ion concentration, and three particle elevations above the SAM at each salt concentration: $d_z \simeq 2\lambda_D$, $d_z \simeq \lambda_D/4$, and $d_z = 0$ nm (see sketch in Fig. 6.28), where λ_D is taken at the corresponding n^∞ value.

6.3.2 Numerical simulations of nanowires

In this section a large number of nanowire simulations is presented. On the one hand we aim at understanding the response of the nanowire to AC signals and biomolecules; on the other hand those simulations constitute a database for the development of physically based equivalent circuit models, as shown in Sec. 6.2.

Fig. 6.29 (right) reports the nanowire $I_{DS}(V_{FG})$ curves in wet environment. As we have seen also in this chapter, a site-binding charge at the dielectric/electrolyte interface (SBC) gives a rigid pH dependent threshold shift in absence of biomolecules. In presence of biomolecules however, as shown in Fig. 6.30, the SBC reduces, sometimes remarkably, the nanowire sensitivity to charged biomolecules, and increases the response to neutral biomolecules. We note however that the response to neutral biomolecules in presence of SBC is qualitatively similar (although numerically lower) to the response to charged biomolecules in absence of SBC. For this reason and in the spirit of a worst case appraisal of possible advantages of AC operation the SBC is not included in the following calcu-

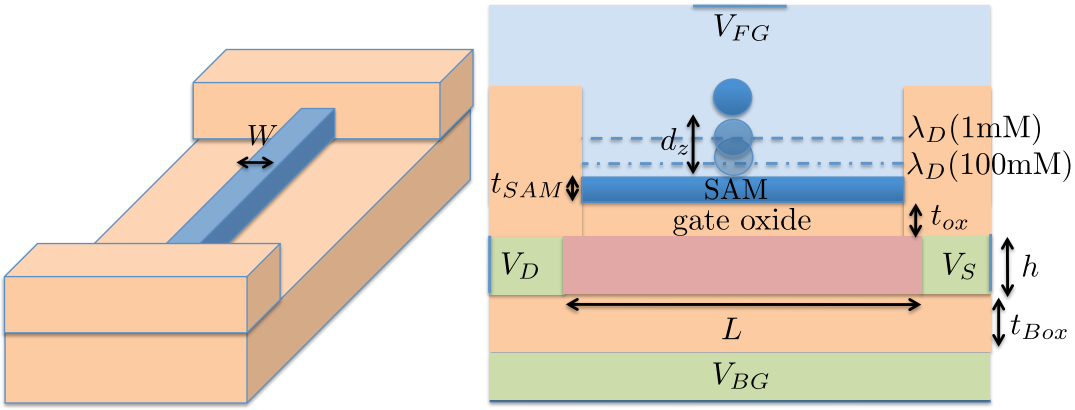

Fig 6.28: 3D and 2D views of the simulated nanowire biosensor with indication of the considered biomolecule positions w.r.t. λ_D. The electrolyte is biased at V_{FG} by an ideal Faradaic reference electrode. The AC voltage $\tilde{V}_D$ is applied at the drain with all other terminals grounded. If explicitly mentioned, a 20 nm thick gold layer (not shown) is deposited above the dielectric to facilitate adhesion of the SAM.

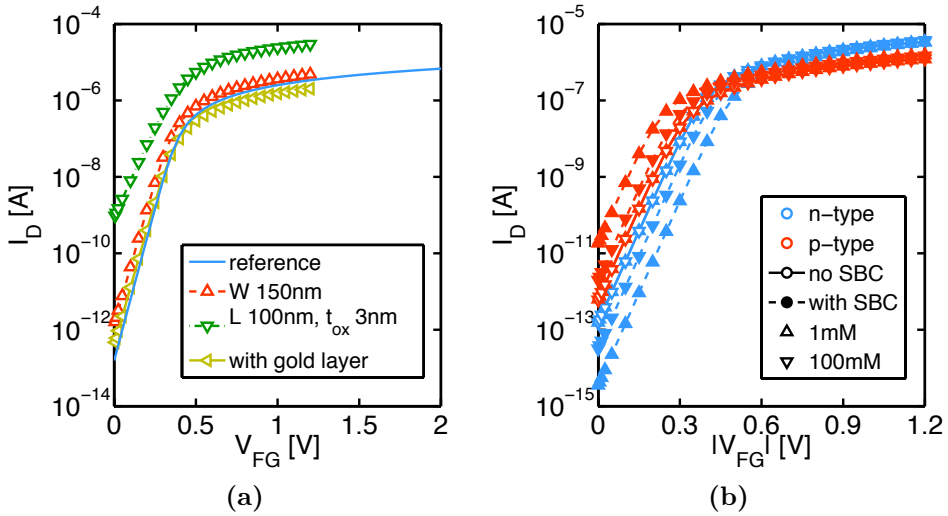

Fig 6.29: $I_D(V_{FG})$ characteristic of n^+nn^+ (blue) and p^+pp^+ (red) nanowires with different geometry (left) and charge models (right). V_{DS}=50 mV. Note the rigid shift of the curves for different site-binding charge (SBC) values, which proves the correct implementation of the SBC in ENBIOS.

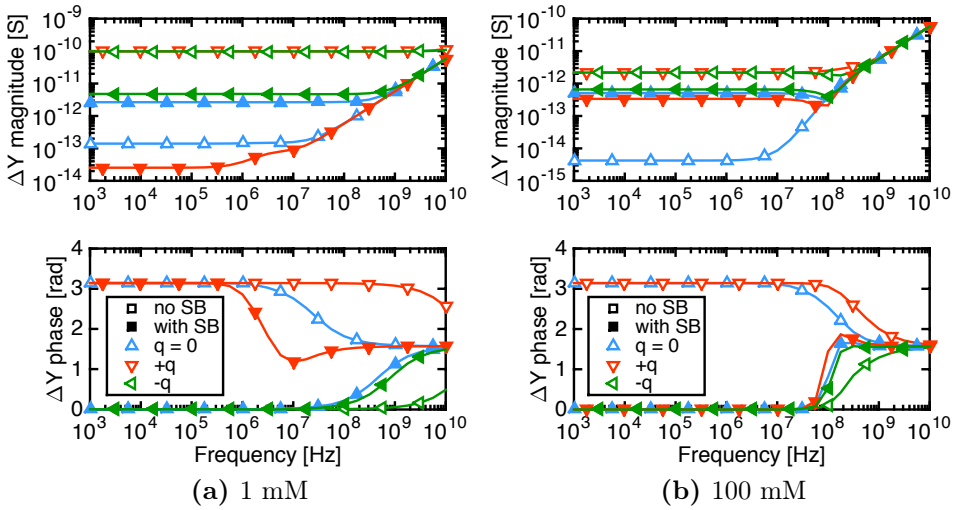

Fig 6.30: Change in source trans-admittance $\Delta Y = \Delta\tilde{I}_S/\tilde{V}_D$ due to the introduction of one neutral (blue), positive (red) and negative (green) particle at $d_z = 0$ centred on the reference nanowire, either including or neglecting SB charges. The bias point is in the subthreshold regime. Note that the SBC decreases the sensitivity to charged biomolecules, but increases it for neutral ones.

lations. This approach is also consistent with [110] if the SAM surface has suppressed sensitivity to pH and the nanowire operates at the isoelectric point. Since gold layers are sometimes used to favour adhesion of the SAM to the sample, the presence of a thin Au layer is also considered in some calculations.

Fig. 6.29, left shows that the current-voltage curves of a few devices with different geometry calculated by ENBIOS scale as expected with W and L until the onset of short channel effects. The graph demonstrates ENBIOS ability to trace the whole $I-V$ characteristic from subthreshold to inversion/accumulation regimes. In the following we examine either

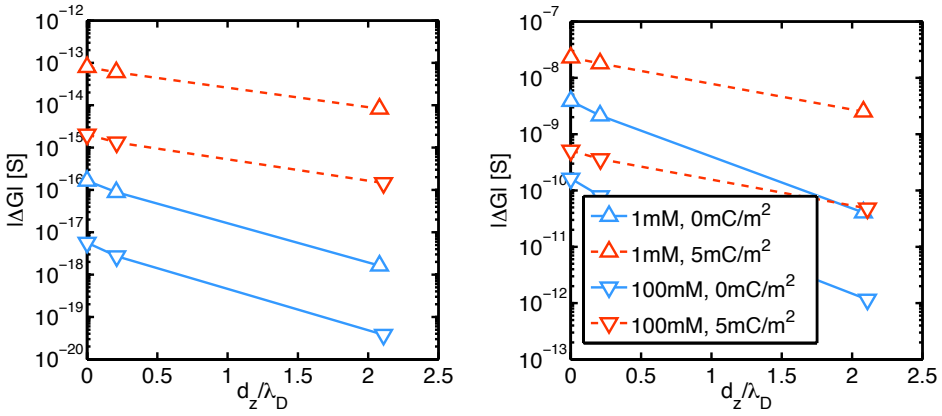

(a) V_{FG}=0 V **(b)** V_{FG}=2 V

Fig 6.31: DC conductance change ΔG versus normalized particle distance from the SAM for the reference n^+nn^+ nanowire in depletion (left) and accumulation (right). Note the dramatic drop for increasing d_z/λ_D and n^∞ and decreasing charge ($\lambda_D \simeq$1 nm at 100 mM and $\simeq$ 10 nm at 1 mM). V_{DS} = 50mV.

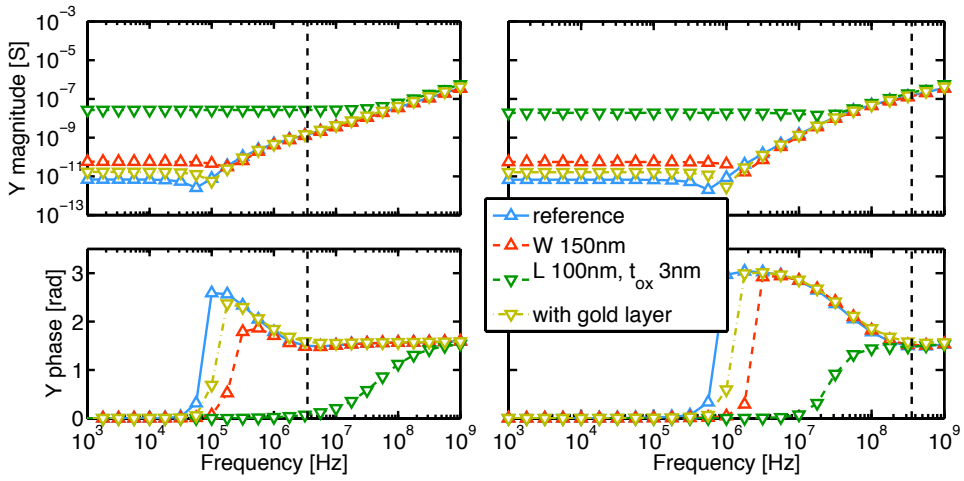

(a) n-type NW, 1 mM **(b)** n-type NW, 100 mM

Fig 6.32: Source admittance $Y = \tilde{I}_S/\tilde{V}_D$, varying the geometry, salt concentration and doping type in depletion (V_{FG}=0 V). Note the capacitive behaviour in AC for $f > f_c$. $f_c \approx$ 3.5 MHz@1 mM; $f_c \approx$ 350 MHz @100mM (dashed vertical lines).

two fixed bias points, representative of depletion and accumulation conditions in long devices ($|V_{FG}|$ = 0 V and 2 V, respectively), or two points at a fixed distance from the threshold voltage V_T, defined as the voltage for I_{DS} = 100 nA on the $I-V$ characteristic (V_{FG} = 0.19 V at V_T − 200 mV and V_{FG} = 0.89 V at V_T + 500 mV in the cases shown here).

Fig. 6.31 reports the change in DC conductivity due to the presence of one particle, at the center of the channel ΔG, vs. normalized particle distance from the SAM, d_z/λ_D, and clearly illustrates the main issue with DC detection techniques; namely: the rapid drop of $|\Delta G|$ for increasing d_z and n^∞.

Figs. 6.32-6.33 show the calculated nanowire source trans-admittance spectra $Y(f) = \tilde{I}_S/\tilde{V}_D$. As expected, in the absence of SBC the only difference between $n-$ and $p-$type NWs is the value of the DC conductance G, that scales according to the asymmetric carrier

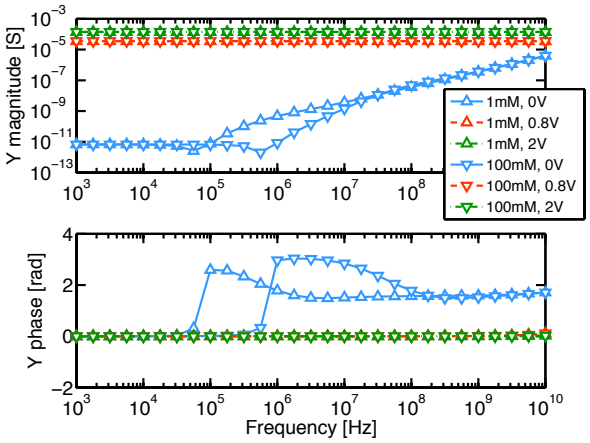

(a) n^+nn^+ nanowire

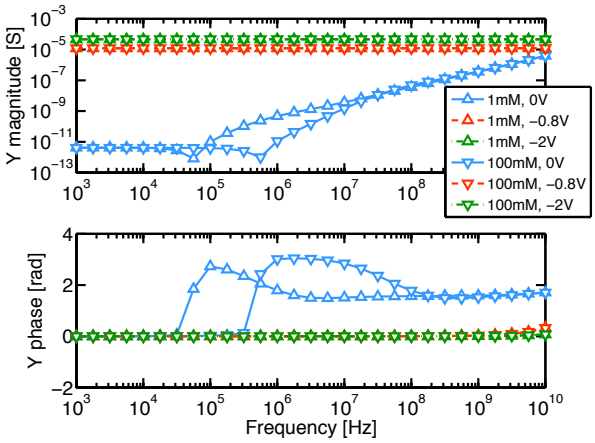

(b) p^+pp^+ nanowire

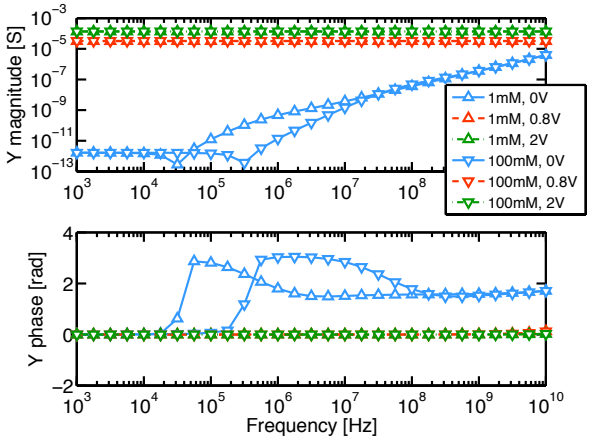

(c) n^+pn^+ nanowire

Fig 6.33: As in Fig. 6.32 for the reference nanowire varying doping, salt concentration and DC bias.

mobility. The channel conductance is small for $V_{FG} < V_T$ and the electrolyte capacitance dominates $Y(f)$ for $f > f_c$, as clearly visible from the increase of $|Y|$ with frequency and the phase approaching $\pi/2$. We also note that, similarly to the frequency f_s in Sec. 3.1.1.3, a first cut-off frequency $f_1 < f_c$ exists, which also depends on salt concentration and gives a sudden increase in the Y phase. On the contrary, G is large above threshold, yielding an essentially constant $Y(f)$ regardless of n^∞.
Fig. 6.34 shows also the admittances $Y_{BG} = \tilde{I}_{BG}/\tilde{V}_D$ and $Y_{FG} = \tilde{I}_{FG}/\tilde{V}_D$ calculated at the back and fluid gates respectively. We note that, as expected, above threshold $|Y| \gg [Y_{BG}, Y_{FG}]$, that, is the current flows almost exclusively in the nanowire. On the other hand, below threshold the current flows appreciably (in some cases even predominantly) towards the gates.

To explore the potential of high frequency operation, we examine the change in source trans-admittance ΔY due to the introduction of one biomolecule at 1 kHz, representative of existing impedimetric sensing techniques, at 1MHz and at 1 GHz, respectively comparable and higher than f_c. Above f_c the ions do not respond to the AC signal and consequently become ineffective in screening the analyte. Fig. 6.35 reports ΔY for one biomolecule attached to the SAM. ΔY for charged biomolecules is never smaller than for neutral ones; at high frequency in depletion $|\Delta Y|$ tends to be insensitive to the charge

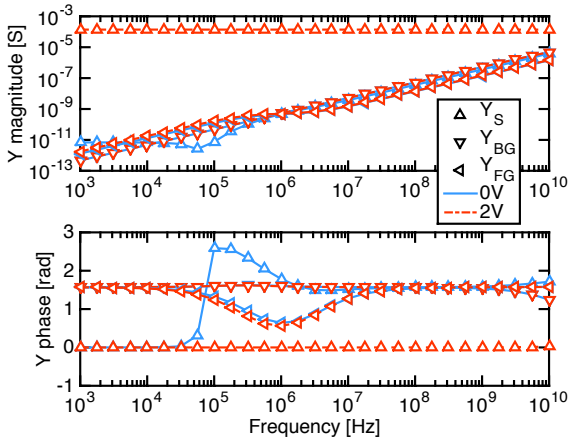

(a) n^+nn^+ nanowire, 1mM

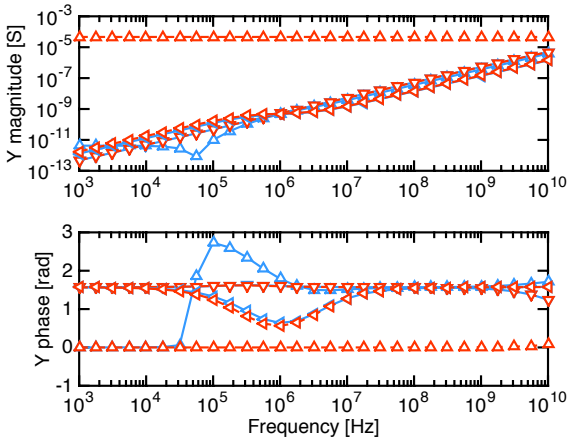

(b) p^+pp^+ nanowire, 1mM

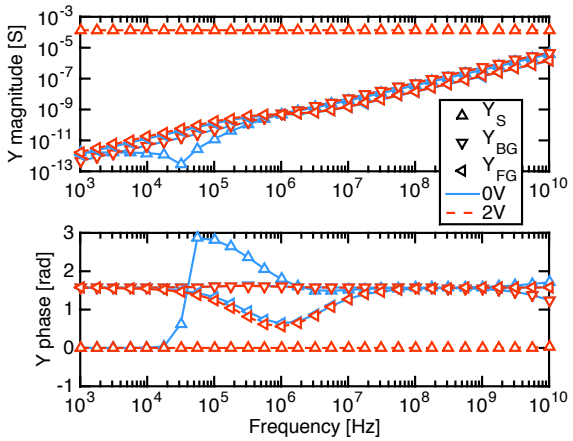

(c) n^+pn^+ nanowire, 1mM

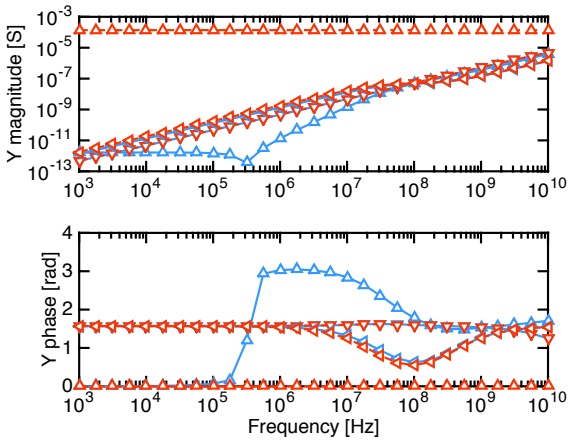

(d) n^+pn^+ nanowire, 100mM

Fig 6.34: Source $Y = \tilde{I}_S/\tilde{V}_D$, back gate $Y_{BG} = \tilde{I}_{BG}/\tilde{V}_D$ and fluid gate $Y_{FG} = \tilde{I}_{FG}/\tilde{V}_D$ admittances, where $\tilde{V}_D$ is the drain small-signal voltage, for different dopings, salt concentrations and DC biases. $V_{FG} = 0$ V $< V_T$ and $V_{FG} = 2$ V $> V_T$.

sign while the phase is opposite. This result is consistent with those reported for charge biomolecules and DNA strands in Secs. 5.6-5.8 and suggests the potential of AC operation to provide less drift and more stable response than DC techniques, essentially because of the reduced surface AC field. Therefore, in the following we focus on n-type NWs and on positive charges only. The same data of Fig. 6.35 are shown in Fig. 6.36 in terms of admittance $Y = G + j\omega C$. We see that the change in capacitance ΔC at high frequency is constant, independent of the biomolecule charge and very weakly dependent on the DC bias.

Fig. 6.37 shows ΔG (top) and ΔC (bottom) in depletion versus d_z/λ_D and n^∞ for neutral (left) and charged (right) particles. As d_z increases above λ_D, the particle exits the static surface electrical double layer (see sketch in Fig. 5.20), whose thickness $\approx \lambda_D$ is set by n^∞ ($\lambda_D \simeq 1$ nm at 100 mM and $\simeq 10$ nm at 1 mM). Consequently, at 1 kHz the signal decays rapidly for increasing d_z, similarly to the DC case (Fig. 6.31), whereas at high frequency ΔG and ΔC are almost unaffected by d_z and n^∞, which means that the NW can detect analytes beyond the Debye screening limit. Fig. 6.38 reports similar results at V_{FG}=2 V. ΔG is now large and independent of f but still rapidly decaying with d_z; in contrast, ΔC at high frequency is independent of d_z and n^∞ for both charged and

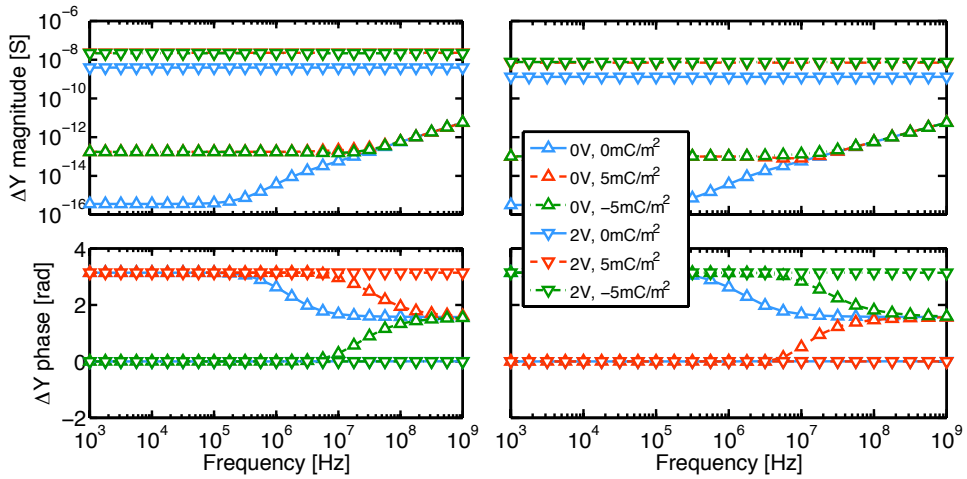

(a) n^+nn^+ NW, $|V_{FG}|$= 0 and 2 V **(b)** p^+pp^+ NW, $|V_{FG}|$= 0 and 2 V

Fig 6.35: Change in source admittance ΔY due to the introduction of one neutral (blue), positive (red) and negative (green) particle at $d_z = 0$ centred on the reference nanowire, at 1 mM salt concentration. The absence of site-binding charge results in symmetric response to positive and negative charges.

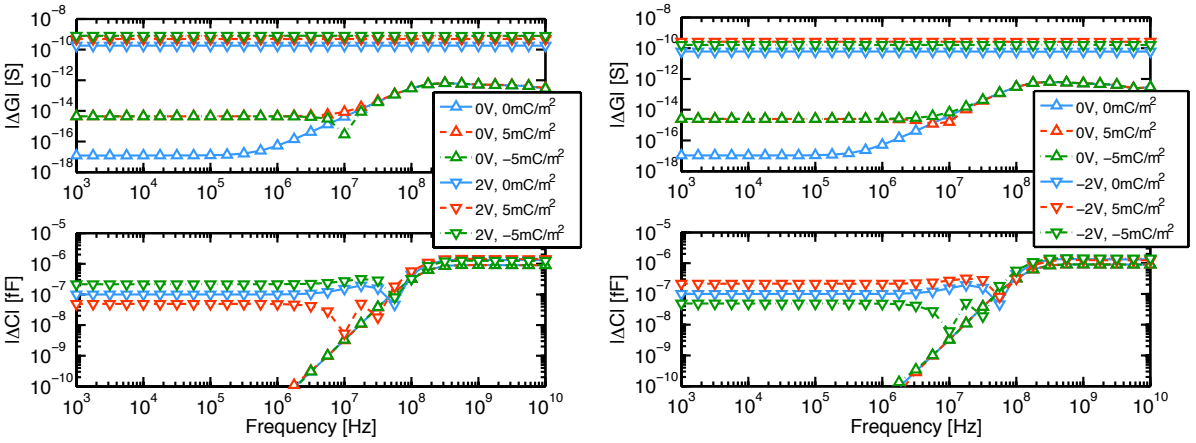

(a) n^+nn^+ NW, $|V_{FG}|$= 0 and 2 V **(b)** p^+pp^+ NW, $|V_{FG}|$= 0 and 2 V

Fig 6.36: Same as Fig. 6.35 but representing the admittance change as $\Delta Y = \Delta G + j\omega\Delta C$.

neutral particles.

Note that again $\Delta C \approx 1$ zF, i.e., it is close to the lowest detection limits experimentally demonstrated so far [92]. Therefore it appears that single biomolecule detection is hardly reachable with this type of device design. Fig. 6.39 shows that, consistently with the DC results of [31], in the examined NWs the AC response to the introduction of k biomolecules $\Delta Y = \Delta G_k + j\omega\Delta C_k$ scales linearly with k for small k values, regardless of frequency, bias and n^∞. Consequently, our one-particle results are also representative of more realistic conditions where a large number of biomolecules is captured for a measurable response.

For practical sensor design, not only the absolute but also the relative response is important, since it sets the ADC resolution. In this spirit, Fig. 6.40 reports the high frequency conductance and capacitance sensitivities, $S_G = \Delta G/G_0$ and $S_C = \Delta C/C_0$, respectively, for a particle distance beyond the static screening limit ($d_z \simeq 2\lambda_D$). We observe that $S_C > S_G$ at high frequency and for neutral particles, underlying another

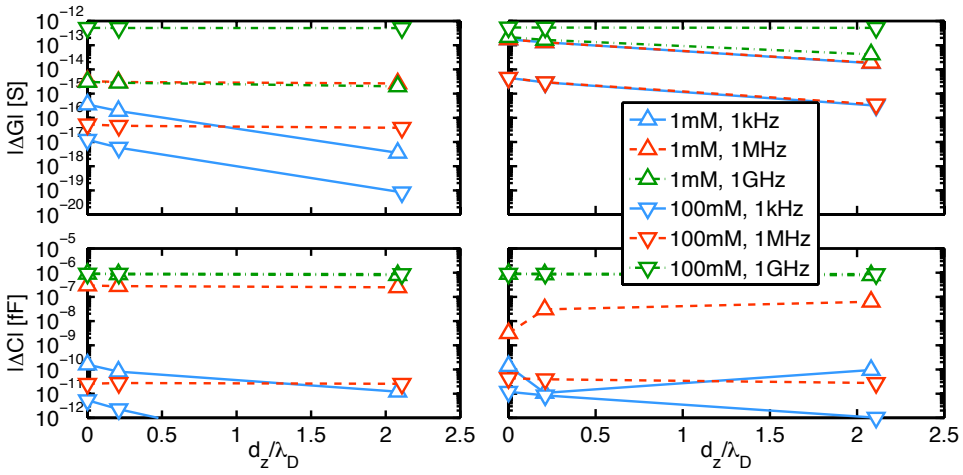

(a) 0 mC/m^2, V_{FG}=0 V **(b)** 5 mC/m^2, V_{FG}=0 V

Fig 6.37: ΔG (top) and ΔC (bottom) in depletion due to one neutral (a) and positively charged (b) particle located at a few d_z above the SAM for $f = 1$ kHz $\ll f_c$ (blue); $f = 1$MHz $\approx f_c$@1mM $\ll f_c$@100mM (red); $f = 1$GHz $\gg f_c$@100mM (green). Reference n^+nn^+ nanowire at V_{FG}=0 V. The responses increase and becomes flatter as f increases.

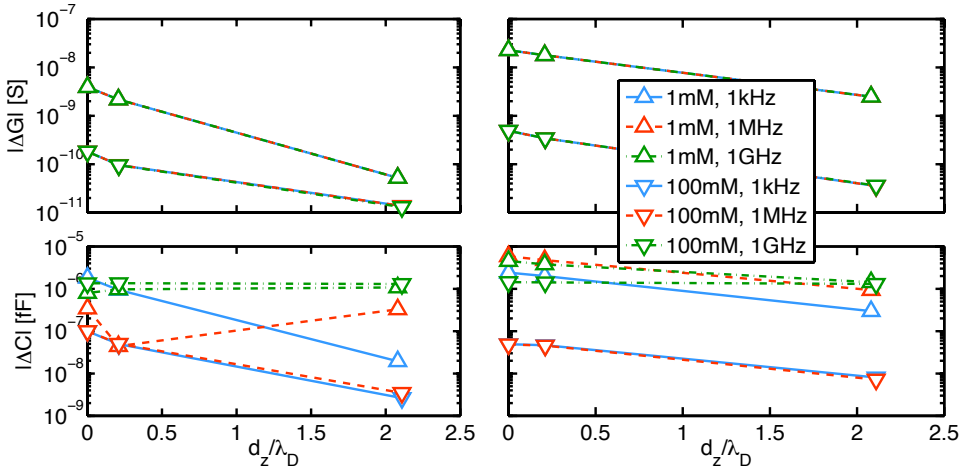

(a) 0 mC/m^2, V_{FG}=2 V **(b)** 5 mC/m^2, V_{FG}=2 V

Fig 6.38: Same as Fig. 6.37 for V_{FG}=2 V (accumulation). The capacitance response increases and becomes flatter as f increases.

advantage of the use of high detection frequency. Note that S_C increases with frequency until it becomes independent of salt concentration and charge, whereas S_G is large only for charged particles at low salt concentration.

According to [31, 79, 106], the DC conductance sensitivity scales as $-\log(n^\infty)$ for large electrolyte voltage drop and low Bio-FET channel charge, and as $1/\sqrt{n^\infty}$ for small voltage drop. We thus decided to investigate the scaling of the high frequency response. As a first step, we verified that in both DC and AC small signal regimes our device works in presence of a small electrolyte voltage drop. If a large voltage drop were present, non-linearity and steric effects would dominate the response leading to a scaling of the type $-\log(n^\infty)$ [31].

Fig. 6.41a shows the behaviour of S_G in the DC regime. The best fit of the simulation

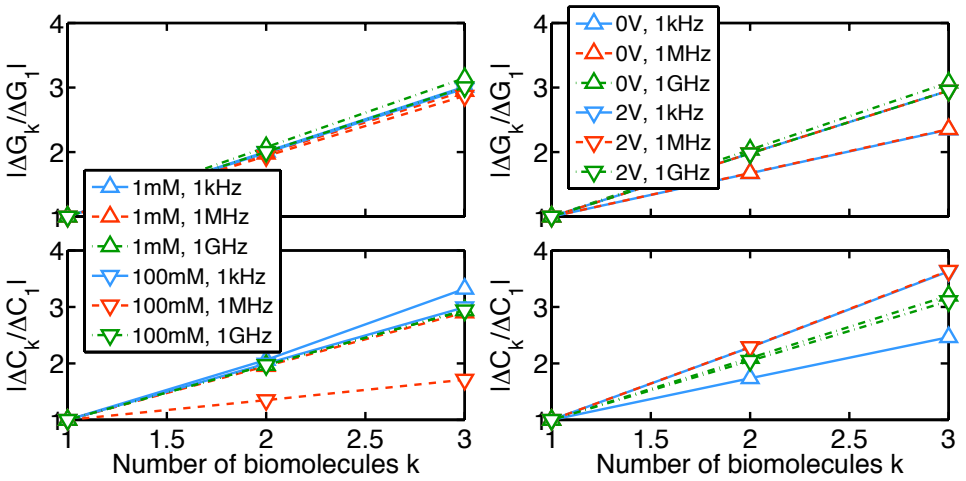

(a) V_{FG}=0 V, 0 mC/m^2, L dir. **(b)** n^{∞}=100 mM, 5 mC/m^2, W dir.

Fig 6.39: $\Delta Y_k/\Delta Y_1$ versus number of particles, k, for the reference n^+nn^+ nanowire. Particles are attached to the SAM (d_z=0 nm) and located at different positions in the W or L directions. Note the proportionality to the number of molecules at all frequencies, as predicted in [31] for small voltage conditions.

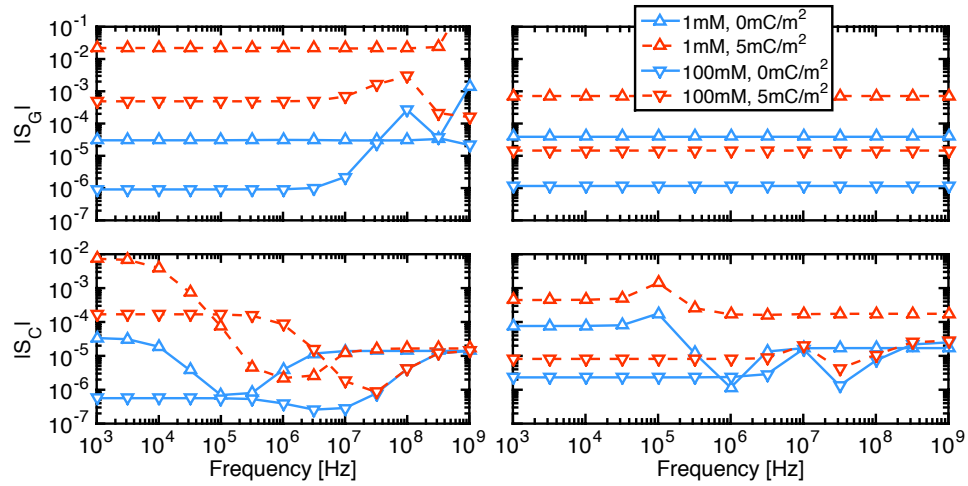

(a) $V_{FG} = 0.19$ V **(b)** $V_{FG} = 0.89$ V

Fig 6.40: Conductance sensitivity, $S_G = |\Delta G/G_0|$, and capacitance sensitivity $S_C = |\Delta C/C_0|$, to one neutral (blue) and charged (red) particle for $d_z = 0$ nm.

results is obtained with a $1/(n^{\infty})^{3/4}$ line. To illustrate the corresponding behaviour in AC regime Fig. 6.41b reports S_G and S_C=$\Delta C/C_0$ for both depletion and accumulation bias points. Fig. 6.41b refers to 1kHz and suggests again a $1/(n^{\infty})^{3/4}$ scaling trend for a small single molecule as in the explored case study. Interestingly, S_C at 1kHz (bottom graph) obeys a similar law. Fig. 6.42 reports similar results at a few frequencies: below f_s (1 kHz), in between f_s and f_c (1 MHz) and above f_c (1 GHz). For $f > f_c$ S_C is essentially insensitive to n^{∞} and particle charge q (green curves). Note that achieving such a high f is not strictly necessary since at physiological salt concentration f_c is only about 350 MHz. If the signal frequency is lowered (e.g., 1 MHz), a non-trivial dependency of S_C vs. n^{∞} is found, essentially due to the interaction of the particle and NW double layers. This complex behaviour is a further obstacle to a simple interpretation of detection

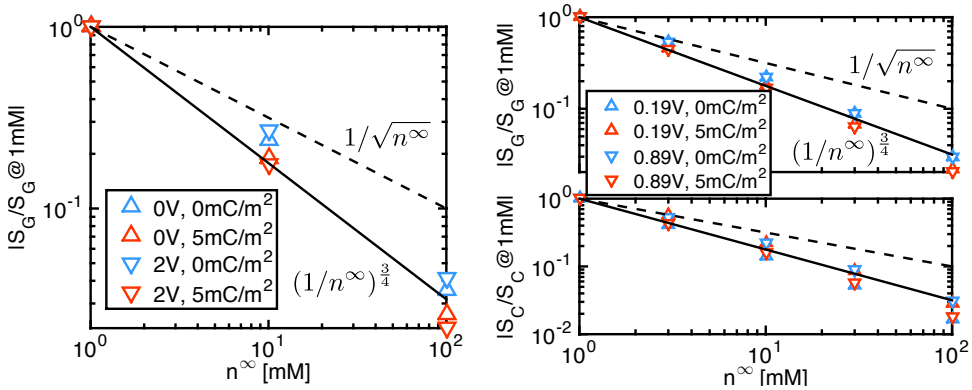

(a) DC **(b)** AC at f=1 kHz

Fig 6.41: Normalized conductance sensitivity, S_G, and capacitance sensitivity, S_C, versus salt concentration, n^∞ in depletion and accumulation. a) DC case where the dashed lines are fits to the simulations (symbols) assuming a dependence of the type $1/\sqrt{n^\infty}$, as reported in [106]. b) same as (a) for AC conditions and 1 kHz frequency in depletion and accumulation. $d_z = 0$nm, $r_p = 10$ nm.

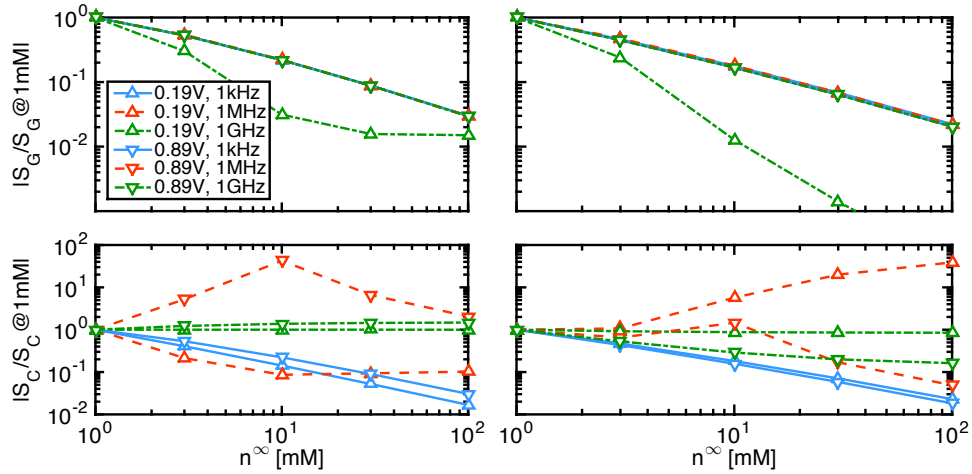

(a) 0 mC/m^2 **(b)** 5 mC/m^2

Fig 6.42: Same as in Fig. 6.41.b, but varying the frequency and the charge on the biomolecule. Note the remarkably flat conductance and capacitance sensitivities for $f \geq f_c$ (red and green lines). The low frequency response, as expected, drops rapidly for increasing n^∞. $d_z = 0$nm, $r_p = 10$ nm.

experiments, thus supporting the choice of exploring the very high frequency range.

6.4 Summary

In this chapter we have studied nanowire-based pH- and bio-sensors operated in the AC regime. We have performed the measurements in collaboration with CEA/LETI (dr. Thomas Ernst) and EPFL (prof. Carlotta Guiducci). In Sec. 6.1 we have reported pH ladder measurements which show that, depending on the chosen frequency of operation, the pH effect may be visible in the magnitude of the admittance, in its phase or in both. This observation opens a new and largely unexplored set of possibilities for the design of pH sensors.
We have also investigated the effect of the salt concentration on the nanowire trans-admittance $\tilde{I}_S/\tilde{V}_D$, and we have proven that in our samples it has an effect in the frequency range between a few kHz and few hundred of kHz. We have unexpectedly found that the nanowire trans-capacitance in this intermediate frequency range decreases with salt concentration, while intuitively one would expect it to increase.

Sec. 6.2 develops an accurate lumped element circuit model for the real and imaginary parts of the NW trans-admittance and a corresponding parameter identification procedure from simulations. The model reveals the existence of an intermediate frequency range where the trans-capacitance of the intrinsic NW decreases for increasing frequency. Furthermore, Sec. 6.2 reports the comparison between our measurements and simulation results obtained with ENBIOS. The agreement is very good if we consider the presence of the parasitics, that also exist in the real system. Unfortunately, the same parasitics hide the response of all NW parameters except the DC conductance. Additional work has to be done in this area to reach a complete and detailed understanding of the results and to benchmark the performance against competitor sensing schemes.

Finally, in Sec. 6.3 we have investigated by means of ENBIOS simulations the response of a nanowire biosensors to small spherical particles, representative of large proteins. We have proven that, also for this sensing device (and not just for nanoelectrodes), working at high frequency can increase the response by overcoming the screening and reducing the sensitivity to the exact position of the particle, to its charge and to the salt concentration. The magnitude of the response to a single biomolecule is comparable to the lowest detection limits experimentally proven to date. This is a promising finding in view of the goal to achieve single molecule detection, but more work will be necessary in the future to explore noise level and signal to noise ratio limitations.

Chapter 7

Conclusions and outlook

In this work we have developed compact analytical models and complex numerical simulation tools to study nanoelectronic biosensors. Simulation results were compared to pioneering experimental findings by the group of Prof. Lemay University of Twente and to measurements on nanowires fabricated at CEA/LETI. Most of the work focused on high frequency impedimetric techniques based on nanoelectrodes and nanowires. For this class of sensors we interpret the admittance spectra and their changes due to various types of biomolecules. The key steps of our research and most relevant findings can be summarized as follows (in order of exposition).

Chap. 2 provides a general overview of the model equations to describe in the continuum multi-ion electrolyte, insulator and semiconductor materials in DC and AC small signal regimes. In particular, in DC conditions (Sec. 2.1) the adopted model equations are the Poisson-Nernst-Planck (PNP, also known as Poisson-Drift-Diffusion) equations. In small signal AC conditions (Sec. 2.2) the model is given by the linearized Poisson-Nernst-Planck equations. In both the DC and AC regimes we impose a combination of Neumann (zero outer flux) and Dirichlet boundary conditions to describe ideally polarizable and Faradaic electrodes.
We have also investigated a few physical mechanisms possibly responsible of localized or global deviations of the electrolyte electrical properties from the PNP equations. Among these, the site-binding reactions at the dielectric/electrolyte surface, the electrolyte permittivity dependence on temperature, salt concentration and frequency (Sec. 2.3.1) and the so called steric effects (i.e., the compact layer of ions that forms at charged interfaces, Sec. 2.3.2). Careful implementation of refined model equations allowed us to identify the range of conditions where these effects become important, and to conclude that, in many instances relevant for biosensor simulation, a simple but effective way to alleviate substantially the model inaccuracy is to mimic the compact Stern layer by introducing a thin dielectric layer on the interfaces with the electrolyte. The dielectric constant in this layer, which is reduced with respect to the electrolyte due to surface polarization, can be estimated *a priori*, as we have shown that its dependence on the surface electric field is not so large to be of practical relevance in typical operating conditions.

In Chap. 3 we derive original analytical models for the AC small signal regime in electrode/dielectric/electrolyte systems either in 1D cartesian (Sec. 3.1) or 1D and 2D spherical (Sec. 3.3) coordinates. The electrodes are always assumed ideally polarizable, which is a desirable property for impedimetric sensors, sometimes difficult to achieve in real systems. In all cases we have shown the formation of the Electrical Double Layer (EDL) at the electrodes at low frequency and the existence of different length scales of the ion concentration. The EDL prevents the electric field to penetrate into the bulk of

Parameter	Symbol	Expression
Debye screening length	λ_D	$= \sqrt{\frac{\varepsilon_{el} k_B T}{2q^2 n_0}}$
Angular cut-off frequency	ξ	$= \frac{2q^2 \mu n_0}{\varepsilon_{el}} = \frac{\sigma_{el}}{\varepsilon_{el}} = \frac{1}{\tau} = 2\pi f_c$
First cut-off frequency (1D cartesian)	f_s	$\simeq \frac{\xi}{\pi} \frac{\lambda_D}{L}$
AC inverse screening length	κ	$= \sqrt{\frac{\xi + j\omega}{D}} = \frac{1}{\lambda_D}\sqrt{1 + j\omega\tau}$
Double layer admittance	y_{DL}	$\propto j\omega\varepsilon_{el}\kappa$

Table 7.1: Summary of the most relevant electrolyte parameters derived in the AC models of Secs. 3.1-3.3.

the system, thus impeding to probe analytes at large distance. The classical model for the EDL adequately fits the numerical results, but we demonstrated that an ω^p dependence of the EDL capacitance vs. frequency (with fractional p values) has to be expected, because of the dispersive behaviour of the EDL even for a perfectly flat surface, regardless of the electrode's surface roughness. Therefore the EDL cannot be represented simply by conventional capacitances and resistances, nor the representation is unique. We have also shown that a first cut-off frequency f_s exists, above which the electric field begins to penetrate into the electrolyte, and that above a second cut-off frequency f_c (the electrolyte's dielectric relaxation cut-off frequency) the EDLs disappear and the response of the system is purely dielectric. We have noted that f_s is geometry-dependent; the f_c, instead, is solely dependent on the electrolyte conductive and dielectric properties.
By comparing results in 1D cartesian and 2D spherical coordinates we could show that some relevant parameters (summarized in Tab. 7.1) have a general applicability regardless of the system geometry.
In particular, the electrolyte dielectric relaxation cut-off frequency f_c is a general property of all the considered systems, regardless of the geometry and of the properties of the electrodes surface. In contrast, we have seen that the first cut-off frequency f_s is also affected by the physical details of the electrodes. In real biosensor systems this could be an issue, since on the electrodes surface electrochemical phenomena and deviations from simple theory may occur, leading to a not well-controlled nor easy to interpret behaviour in the frequency range between f_s and f_c.

In Chap. 4 we develop and validate the full 3D numerical simulator ENBIOS for nanoelectronic biosensors. ENBIOS relies on the models described in Chap. 2, which have been solved on general 3D unstructured tetrahedral grids using for the first time the Control Volume Finite Element Method. Care has been given to calculate accurately the currents at the electrodes in order to retain the method's global conservation property, hence the accuracy on current calculation, that is mandatory to compute the tiny admittance changes due to the introduction of small molecules in the domain. We have also discussed in detail the methods for the calculation of surface and volume integrals, with respect to accuracy and computational speed. In fact, the presence of highly non linear (exponential) terms poses unique and critical accuracy problems in the evaluation of these integrals.
The implementation has been validated against the analytical models described in Chap. 3. A comparison with the standard Galerkin Finite Element Method shows that CVFEM offers an advantage, especially for coarse grids. This in turn entails the possibility to use

CVFEM with less refined grids than GFEM, a highly desirable property when meshing the thin electrical double layer.
We have also shown a procedure to describe electrolytes by means of a commercial TCAD for semiconductor devices (Sentaurus Device, which does not natively support the electrolyte environment, Sec. 4.6). Despite the successful results, the inherent limitations of TCAD prevent this approach to be widely applicable to all classes of biosensors. This further justifies our need of developing an ad-hoc simulator like ENBIOS.

In Chap. 5 we study the response of a nanoelectrode array biosensor to spherical microparticles and compare the simulation results with measurements mostly carried out at the University of Twente by the group of prof. S. Lemay (Sec. 5.3). The agreement between simulations and measurements is excellent, essentially without fitting parameters. This is a remarkable confirmation of the adequacy of the chosen model for the problem at hand. *Our study has confirmed by theory and experiment that high frequency measurements can indeed probe particles beyond the static screening length. In addition, we have shown that the nanoelectrode array is capable of discriminating between dielectric and conductive particles. These remarkable findings open a new scenario in the field of nanoelectronic biosensors.* Simulations confirmed their usefulness for the extraction of quantitative information on the analytes from the measurements.
In Sec. 5.4 we have validated, by means of simulations, an analytical model for the frequency dependent admittance change at a nanoelectrode due to a small spherical particle. The model provides extremely useful physical insight and predicts a response proportional to the particle volume and complex conductivity and to the magnitude of the electric field in the location of the particle normalized to the applied voltage. Remarkably the model also predicts a sign change of ΔG and ΔC for conductive particles, due to a balance between drift and diffusion current components. This model suggests a large number of possibilities for the engineering of nanoelectrode biosensors, but unfortunately, limitations of present hardware did not allow us to verify experimentally the prediction of a sign change in the response.
The simulations allowed us to test the performance of ENBIOS for the analysis of realistic complex systems. The results motivated the proposition of an original simulation scheme (Sec. 5.5) to greatly reduce the computational burden due to the fine meshing of Electrical Double Layers by replacing them with circuit lumped elements.
We have also explored the nanoelectrode biosensor response to small spherical particles, which can represent large globular proteins or viruses (Secs. 5.7-5.6), and to DNA molecules (Sec. 5.8), including orientation effects. We found that, unless the strand or particle adheres to the electrode, modest changes in capacitance should be expected as a result of orientation, mostly at low frequency. These simulations confirmed once more the potential advantage of high frequency operation, namely:

1. the ability to overcome the static screening and the independence of the response of salt concentration;

2. the very good theoretical predictability of the response, even in the presence of non-idealities such as surface charges;

3. the insensitivity to hardly controllable parameters such as free charges;

4. the additivity of the response with respect to the number of particles, at least for a small number of them;

5. a greater freedom to engineer the biosensor, in order to take advantage of the fact that the region sensitive to the analyte is not limited to the sensor surface;

6. the identification of optimum detection frequencies and critical cut-off frequencies.

This thesis led us to unambiguously clarify what should exactly be considered as high-frequency range. We have concluded that the electrolyte dielectric relaxation cut-off frequency f_c is a general property of all the considered biosensor systems, regardless of geometry and condition of the electrodes' surface. The frequency f_c is high (≈ 300 MHz) at physiological salt concentration compared to state of the art impedance spectroscopy systems [84] but not unreachable for integrated CMOS nanoelectronic circuits where parasitics can be reduced. Working above f_c gives the benefits 1.-5. above.
The static Debye screening is partly overcome also above the cut-off frequency f_s, which is typically much lower than f_c and, furthermore, geometry dependent; hence, device design dependent. In fact, in the field of impedance spectroscopy it is common to work up to frequency in the neighbourhood of f_s [84], at least at low salt concentration. We have however demonstrated that f_s is remarkably dependent on the geometry and on the physical details of the electrodes surface compared to the electrolyte properties, in particular, on the product between the double layer capacitance and the bulk electrolyte resistance. In real biosensor systems this could be an issue, since electrochemical phenomena at the electrodes' surface and deviations from simple theory may occur, leading to a not well-controlled behaviour in the frequency range between f_s and f_c where the admittance changes the most versus frequency. Furthermore, benefits 1.-4. in the above list do not hold in this regime.

In Chap. 6 we study nanowire-based pH- and bio-sensors operated in the AC regime. We have performed measurements on real devices in collaboration with CEA/LETI (dr. Thomas Ernst) and EPFL (prof. Carlotta Guiducci). Due to large parasitics, however, we could not explore the intrinsic NW behaviour above approximately 100 kHz, which is much larger frequency than in many EIS systems but not large enough to overcome f_c at high salt concentration. We also carried out pH ladder measurements (Sec. 6.1) which show that, depending on the chosen frequency, the pH effect may be visible in the magnitude of the admittance, in its phase or in both. Also this observation opens a new and largely unexplored set of possibilities for the design of pH sensors.
The salt concentration affects the nanowire admittance in the frequency range between a few kHz and few hundreds of kHz. We have unexpectedly found that the nanowire trans-capacitance in this intermediate frequency range decreases with salt concentration, while the gate-source capacitance increases as predicted by all the models in Chap. 3. Since the same behaviour is found in identical structures without nanowire, we conclude that this anomaly should be attributed to the parasitics. In particular, the anomalous frequency behaviour may be due to the combination of two effects:

1. the source admittance that we measured is not a real admittance, but an element of the 2-port admittance matrix of the system;

2. also in simulations (for instance Fig. 6.17) there are intermediate frequency ranges where the capacitance is apparently decreasing with increasing salt concentration; since in the measurement we could only look at a very small portion of the spectrum, we may as well be in this intermediate frequency range.

An accurate lumped element circuit model and extraction procedure has been developed for the intrinsic NW based on simulations (Sec. 6.2). The comparison between our measurements and ENBIOS simulations (Sec. 6.2) is very good if we consider the presence of parasitics, that exist also in the real system. Additional work has to be done in this area to reach a complete and detailed understanding of the results and to benchmark the

performance of high-frequency nanowire sensing against competitor sensing schemes. For the latter step, consideration of layout constraints and parasitics of a realistic detector seems a mandatory step to this end.
Finally, we have investigated by means of simulation the response of a nanowire to small spherical particles, representative of large globular proteins (Sec. 6.3). We have again observed that a high frequency signal can provide distinct advantages in order: 1) to increase the response by overcoming the screening; 2) to be very weakly dependent on the exact position of the particle, on its charge and on salt concentration. The magnitude of the response to a single biomolecule is comparable to the lowest detection limits experimentally proven to date. This is a promising finding in view of the goal to achieve single molecule detection, but more work will be necessary in the future to explore how this threshold compares to noise level and signal to noise ratio limitations.

As an indication for future work, we briefly underline that nanoelectronic biosensors are likely to be on the edge of widespread diffusion in several new fields of application. The development of quantitative analytical tools based on general purpose, customizable integrated devices heavily relies upon the ability to improve our understanding of the transduction chain via modelling and simulation, and on the demonstration of a robust transduction principle suited to deliver signals with large signal to noise ratio in the variable and unstable environments where biomolecules are contained. In this respect, integrated electronic biosensor platforms, and in particular micro- and nanoelectrode impedimetric arrays, can provide all the required parallelism, compensation, and calibration hardware and software to obtain reliable data with sufficient statistics.
A brief and incomplete list of problems which have not been adequately addressed with reference to high-frequency impedance spectroscopy in general and nanoelectrode sensors in particular is the following:

- Scaling laws of nanoelectrode biosensor, verified by means of simulation.
- Simulations with a realistic description of complex biomolecules, including charge effects.
- Statistical and noise analysis of nanoelectrode response to multiple randomly distributed molecules.
- Non-linear analysis with arbitrary time-domain signal.
- Modelling of surface dipoles and surface chemical reactions in AC regime for technologically relevant materials.
- Study of non planar nanoelectrode geometries and surface roughness.
- Accurate compact models with and without biomolecules to assist the design of readout circuits.

Bibliography

Papers of the author

[1] F. Pittino, L. Selmi, and F. Widdershoven. "Numerical and analytical models to investigate the AC high-frequency response of nanoelectrode/SAM/electrolyte capacitive sensing elements". In: *Solid-State Electronics* 88.0 (2013), pp. 82 –88. ISSN: 0038-1101. DOI: http://dx.doi.org/10.1016/j.sse.2013.04.016. URL: http://www.sciencedirect.com/science/article/pii/S0038110113001780.

[2] F. Pittino, P. Scarbolo, F. Widdershoven, and L. Selmi. "Derivation and numerical verification of a compact analytical model for the AC admittance response of nanoelectrodes, suitable for optimization of electronic nanobiosensors". In: *IEEE Transactions on Nanotechnology* (submitted).

[3] F. Pittino, F. Widdershoven, and L. Selmi. "Efficient DC and AC simulation of nanoelectrode-nanoparticle interactions in capacitive biosensors". In: *Proceedings of the International Conference on Ultimate Integration on Silicon (ULIS)*. 2012, pp. 189–193.

[4] F. Pittino and L. Selmi. "Use and comparative assessment of the CVFEM method for Poisson-Boltzmann and Poisson-Nernst-Planck three dimensional simulations of impedimetric nano-biosensors operated in the DC and AC small signal regimes". In: *Computational Methods in Applied Mechanics and Engineering* (278 2014), pp. 902–923. DOI: 10.1016/j.cma.2014.06.00. URL: http://dx.doi.org/10.1016/j.cma.2014.06.00.

[5] P. Palestri, R. Sette, F. Pittino, F. Saccon, D. Esseni, and L. Selmi. "Simulation of nano-biosensors based on conventional TCAD". In: *Proceedings of the International Conference on Ultimate Integration on Silicon (ULIS)*. 2013, pp. 77–80. DOI: 10.1109/ULIS.2013.6523495.

[6] F. Pittino, P. Palestri, P. Scarbolo, D. Esseni, and L. Selmi. "Models for the use of commercial TCAD in the analysis of silicon-based integrated biosensors". In: *Solid-State Electronics* 98.0 (2014). Selected Papers from ULIS 2013 Conference, pp. 63 –69. ISSN: 0038-1101. DOI: http://dx.doi.org/10.1016/j.sse.2014.04.011. URL: http://www.sciencedirect.com/science/article/pii/S0038110114000598.

[7] A. Bandiziol, P. Palestri, F. Pittino, D. Esseni, and L. Selmi. "A TCAD-based Methodology to Model the Site-Binding Charge at ISFET/Electrolyte Interfaces". In: *IEEE Transactions on Electron Devices* (submitted).

[8] F. Pittino and L. Selmi. "A technique to model the AC response of diffuse layers at electrode/electrolyte interfaces and to efficiently simulate impedimetric biosensor arrays for many analyte configurations". In: *Proceedings of the International Conference on Simulation of Semiconductor Processes and Devices (SISPAD)*. 2014, pp. 353–356.

[9] F. Pittino, F. Passerini, P. Palestri, L. Selmi, and F. Widdershoven. "On the response of nanoelectrode capacitive biosensors to DNA and PNA strands". In: *Proc. Int. Workshop on Advances in Sensors and Interfaces*. 2013, pp. 40–45.

[10] F. Pittino, F. Passerini, L. Selmi, and F. Widdershoven. "Numerical simulation of the position and orientation effects on the impedance response of nanoelectrode array biosensors to DNA and PNA strands". In: *Microelectronics Journal* 45.12 (2014), pp. 1695 –1700. ISSN: 0026-2692. DOI: http://dx.doi.org/10.1016/j.mejo.2014.09.011. URL: http://www.sciencedirect.com/science/article/pii/S0026269214002778.

[11] P. Palestri, M. Mouis, A. Afzalian, L. Selmi, F. Pittino, D. Flandre, and G. Ghibaudo. "Sensitivity of Silicon Nanowire Biochemical Sensors". In: *Beyond-CMOS Nanodevices 1*. John Wiley & Sons, Inc., 2014, pp. 43–63. ISBN: 9781118984772. DOI: 10.1002/9781118984772.ch3. URL: http://dx.doi.org/10.1002/9781118984772.ch3.

[12] C. Laborde, F. Pittino, H. A. Verhoeven, S. G. Lemay, L. Selmi, M. A. Jongsma, and F. Widdershoven. "Real-time imaging of microparticles and living cells with CMOS nanocapacitor arrays". In: *Nature Nanotechnology* (submitted).

[13] F. Pittino and L. Selmi. "Improved sensitivity of nanowire bio-FETs operated at high-frequency: a simulation study". In: *Proceedings of the International Conference on Nanotechnology (IEEE Nano 2015)*. 2015.

[14] P. Scarbolo, E. Accastelli, F. Pittino, T. Ernst, C. Guiducci, and L. Selmi. "Characterization and modelling of differential sensitivity of nanoribbon-based pH-sensors". In: *Proceedings of the International Conference on Solid-State Sensors, Actuators and Microsystems (Transducers)*. 2015.

References

[15] J. Höller, V. Tsiatsis, C. Mulligan, S. Karnouskos, S. Avesand, and D. Boyle. *From Machine-to-Machine to the Internet of Things: Introduction to a New Age of Intelligence*. Elsevier, 2014. URL: http://store.elsevier.com/product.jsp?isbn=9780124076846.

[16] R. Sarpeshkar. *Ultra low power bioelectronics: fundamentals, biomedical applications, and bio-inspired systems*. Cambridge University Press, 2010. ISBN: 9780521857277. URL: http://bks6.books.google.co.ug/books?id=eYPBAyDRjOUC.

[17] P. Kozma, F. Kehl, E. Ehrentreich-Förster, C. Stamm, and F. F. Bier. "Integrated planar optical waveguide interferometer biosensors: A comparative review". In: *Biosensors and Bioelectronics* 58.0 (2014), pp. 287–307. ISSN: 0956-5663. DOI: http://dx.doi.org/10.1016/j.bios.2014.02.049. URL: http://www.sciencedirect.com/science/article/pii/S0956566314001377.

[18] N. S. Oliver, C. Toumazou, A. E. G. Cass, and D. G. Johnston. "Glucose sensors: a review of current and emerging technology". In: *Diabetic Medicine* 26.3 (2009), pp. 197–210. ISSN: 1464-5491. DOI: 10.1111/j.1464-5491.2008.02642.x. URL: http://dx.doi.org/10.1111/j.1464-5491.2008.02642.x.

[19] N. Rusk. "Torrents of sequence". In: *Nature Methods* 8 (2011). DOI: 10.1038/nmeth.f.330. URL: http://dx.doi.org/10.1038/nmeth.f.330.

[20] C. Toumazou, L. M. Shepherd, S. C. Reed, G. I. Chen, A. Patel, D. M. Garner, C.-J. A. Wang, C.-P. Ou, K. Amin-Desai, P. Athanasiou, et al. "Simultaneous DNA amplification and detection using a pH-sensing semiconductor system". In: *Nature methods* 10.7 (2013), pp. 641–646.

[21] M. E. J. Obien, K. Deligkaris, T. Bullmann, D. J. Bakkum, and U. Frey. "Revealing neuronal function through microelectrode array recordings". In: *Frontiers in Neuroscience* 8.423 (2014). DOI: 10.3389/fnins.2014.00423.

[22] T. Vo-Dinh and B. Cullum. "Biosensors and biochips: advances in biological and medical diagnostics". In: *Fresenius J Anal Chem* 366.6-7 (2000), pp. 540–551. URL: http://www.ncbi.nlm.nih.gov/entrez/query.fcgi?cmd=Retrieve&db=PubMed&dopt=Citation&list_uids=11225766.

[23] S. M. Borisov and O. S. Wolfbeis. "Optical Biosensors". In: *Chemical Reviews* 108.2 (2008), pp. 423–461. DOI: 10.1021/cr068105t. URL: http://dx.doi.org/10.1021/cr068105t.

[24] X. Fan, I. M. White, S. I. Shopova, H. Zhu, J. D. Suter, and Y. Sun. "Sensitive optical biosensors for unlabeled targets: A review". In: *Analytica Chimica Acta* 620.1-2 (2008), pp. 8–26. ISSN: 0003-2670. DOI: http://dx.doi.org/10.1016/j.aca.2008.05.022. URL: http://www.sciencedirect.com/science/article/pii/S0003267008009343.

[25] A. Jain and M. A. Alam. In: Springer, 2013. Chap. Physics of Nonlinear MEMS Biosensors.

[26] J. Wang. "Electrochemical Glucose Biosensors". In: *Chemical Reviews* 108.2 (2008), pp. 814–825. DOI: 10.1021/cr068123a. URL: http://dx.doi.org/10.1021/cr068123a.

[27] P. Bergveld. "Development of an Ion-Sensitive Solid-State Device for Neurophysiological Measurements". In: *Biomedical Engineering, IEEE Transactions on* BME-17.1 (1970), pp. 70–71. ISSN: 0018-9294.

[28] A. Matsumoto and Y. Miyahara. "Current and Emerging Challenges of Field Effect Transistor Based Bio-sensing". In: *Nanoscale* 5 (2013), pp. 10702–10718.

[29] E. Stern, J. Klemic, D. Routenberg, P. Wyrembak, D. Turner-Evans, D. LaVan, T. Fahmy, and M. Reed. "Label-free immunodetection with CMOS-compatible semiconducting nanowires". In: *Nature* 445 (2007), pp. 519–522. DOI: 10.1038/nature05498.

[30] N. Couniot, A. Afzalian, N. van Overstraeten-Schlögel, L. Francis, and D. Flandre. "Capacitive biosensing of bacterial cells: Analytical model and numerical simulations". In: *Sensors and Actuators B: Chemical* 211.0 (2015), pp. 428–438. ISSN: 0925-4005. DOI: http://dx.doi.org/10.1016/j.snb.2015.01.108. URL: http://www.sciencedirect.com/science/article/pii/S0925400515001355.

[31] P. R. Nair and M. A. Alam. “Screening-Limited Response of NanoBiosensors”. In: *Nano Letters* 8.5 (2008), pp. 1281–1285. DOI: 10.1021/nl072593i. eprint: http://pubs.acs.org/doi/pdf/10.1021/nl072593i.

[32] C. Berggren, B. Bjarnason, and G. Johansson. “Capacitive Biosensors”. In: *Electroanalysis* 13.3 (2001), pp. 173–180. URL: http://doi.wiley.com/10.1002/1521-4109%28200103%2913%3A3%3C173%3A%3AAID-ELAN173%3E3.0.CO%3B2-B.

[33] F. Widdershoven et al. “CMOS Biosensor Platform”. In: *Proceedings IEDM* (2010), pp. 816–819.

[34] S. Baumgartner, C. Heitzinger, A. Vacic, and M. A. Reed. “Predictive simulations and optimization of nanowire field-effect PSA sensors including screening”. In: *Nanotechnology* 24.22 (2013), p. 225503. URL: http://stacks.iop.org/0957-4484/24/i=22/a=225503.

[35] *Synopsys Sentaurus Device simulator user manual*. Synopsis Inc. 2013.

[36] A. J. Bard and L. R. Faulkner. *Electrochemical Methods: Fundamentals and Applications*. Second. John Wiley & Sons, 2001.

[37] Y. Liu and R. W. Dutton. “Effects of charge screening and surface properties on signal transduction in field effect nanowire biosensors”. In: *Journal of Applied Physics* 106.1, 014701 (2009), pp. –. DOI: http://dx.doi.org/10.1063/1.3156657. URL: http://scitation.aip.org/content/aip/journal/jap/106/1/10.1063/1.3156657.

[38] S. Baumgartner and C. Heitzinger. “Existence and local uniqueness for 3d self-consistent multiscale models of field-effect sensors”. In: *Commun. Math. Sci* 10.2 (2012), pp. 693–716.

[39] F. Fogolari and A. Brigo and H. Molinari. “The Poisson-Boltzmann equation for biomolecular electrostatics: a tool for structural biology”. In: *Jou. of Molecular Recognition* 15 (2002), pp. 377–392.

[40] J. C. G. Montoro and J. L. F. Abascal. “Ionic distribution around simple DNA models. I. Cylindrically averaged properties”. In: *The Journal of Chemical Physics* 103.18 (1995), pp. 8273–8284.

[41] A. Konrad and M. Graovac. “The finite element modeling of conductors and floating potentials”. In: *Magnetics, IEEE Transactions on* 32.5 (1996), pp. 4329–4331. ISSN: 0018-9464. DOI: 10.1109/20.538859.

[42] D. E. Yates, S. Levine, and T. W. Healy. “Site-binding model of the electrical double layer at the oxide/water interface”. In: *J. Chem. Soc., Faraday Trans. 1* 70 (0 1974), pp. 1807–1818. DOI: 10.1039/F19747001807. URL: http://dx.doi.org/10.1039/F19747001807.

[43] S. Martinoia, G. Massobrio, and M. Grattarola. “An ISFET model for CAD applications”. In: *Sensors and Actuators B: Chemical* 8.3 (1992), pp. 261 –265. ISSN: 0925-4005. DOI: http://dx.doi.org/10.1016/0925-4005(92)85029-V. URL: http://www.sciencedirect.com/science/article/pii/092540059285029V.

[44] A. Tarasov, M. Wipf, R. L. Stoop, K. Bedner, W. Fu, V. A. Guzenko, O. Knopfmacher, M. Calame, and C. Schönenberger. “Understanding the Electrolyte Background for Biochemical Sensing with Ion-Sensitive Field-Effect Transistors”. In: *ACS Nano* 6.10 (2012). PMID: 23016890, pp. 9291–9298. DOI: 10.1021/nn303795r. eprint: http://dx.doi.org/10.1021/nn303795r. URL: http://dx.doi.org/10.1021/nn303795r.

[45] G. Barbero, A. Alexe-Ionescu, and I Lelidis. "Significance of small voltage in impedance spectroscopy measurements on electrolytic cells". In: *Journal of applied physics* 98.11 (2005), p. 113703.

[46] E. Salm, C. D. Guevara, P. Dak, B. R. Dorvel, B. Reddy, M. A. Alam, and R. Bashir. "Ultralocalized thermal reactions in subnanoliter droplets-in-air". In: *Proceedings of the National Academy of Sciences* 110.9 (2013), pp. 3310–3315. DOI: 10.1073/pnas.1219639110. eprint: http://www.pnas.org/content/110/9/3310.full.pdf. URL: http://www.pnas.org/content/110/9/3310.abstract.

[47] P. Woias, L. Meixner, D. Amandi, and M. Schönberger. "Modelling the short-time response of ISFET sensors". In: *Sensors and Actuators B: Chemical* 24.1-3 (1995), pp. 211 –217. ISSN: 0925-4005. DOI: http://dx.doi.org/10.1016/0925-4005(95)85045-7. URL: http://www.sciencedirect.com/science/article/pii/0925400595850457.

[48] A. P. Stogryn, H. T. Bull, K. Rubayi, and S. Iravanchy. "The microwave dielectric properties of sea and fresh water". In: *GenCorp Aerojet, Tech. Rep.* 1995.

[49] T. Meissner and F. Wentz. "The complex dielectric constant of pure and sea water from microwave satellite observations". In: *Geoscience and Remote Sensing, IEEE Transactions on* 42.9 (2004), pp. 1836–1849. ISSN: 0196-2892. DOI: 10.1109/TGRS.2004.831888.

[50] R. Somaraju and J. Trumpf. "Frequency, Temperature and Salinity Variation of the Permittivity of Seawater". In: *IEEE Transactions on Antennas and Propagation* 54.11 (2006), pp. 3441–3448. ISSN: 0018-926X. DOI: 10.1109/TAP.2006.884290.

[51] E. Lewis. "The practical salinity scale 1978 and its antecedents". In: *Oceanic Engineering, IEEE Journal of* 5.1 (1980), pp. 3–8. ISSN: 0364-9059. DOI: 10.1109/JOE.1980.1145448.

[52] J. Speight, ed. *Lange's Handbook of Chemistry*. 15th. McGraw-Hill, 1999.

[53] I. Borukhov, D. Andelman, and H. Orland. "Adsorption of large ions from an electrolyte solution: a modified Poisson-Boltzmann equation". In: *Electrochimica Acta* 46.2-3 (2000), pp. 221–229. ISSN: 0013-4686. DOI: 10.1016/S0013-4686(00)00576-4. URL: http://www.sciencedirect.com/science/article/pii/S0013468600005764.

[54] E. Gongadze and A. Iglic. "Decrease of permittivity of an electrolyte solution near a charged surface due to saturation and excluded volume effects". In: *Bioelectrochemistry* 87.0 (2012). International Symposium on Bioelectrochemistry and Bioenergetics, 21st BES 2011, pp. 199 –203. ISSN: 1567-5394. DOI: http://dx.doi.org/10.1016/j.bioelechem.2011.12.001. URL: http://www.sciencedirect.com/science/article/pii/S1567539411002015.

[55] R. van Hal, J. Eijkel, and P. Bergveld. "A general model to describe the electrostatic potential at electrolyte oxide interfaces". In: *Advances in Colloid and Interface Science* 69.1-3 (1996), pp. 31 –62. ISSN: 0001-8686. DOI: http://dx.doi.org/10.1016/S0001-8686(96)00307-7. URL: http://www.sciencedirect.com/science/article/pii/S0001868696003077.

[56] M. S. Kilic, M. Z. Bazant, and A. Ajdari. "Steric effects in the dynamics of electrolytes at large applied voltages. II. Modified Poisson-Nernst-Planck equations". In: *Phys. Rev. E* 75 (2 2007), p. 021503. DOI: 10.1103/PhysRevE.75.021503. URL: http://link.aps.org/doi/10.1103/PhysRevE.75.021503.

[57] C. W. Outhwaite, L. B. Bhuiyan, and S. Levine. “Theory of the electric double layer using a modified Poisson-Boltzmann equation”. In: *J. Chem. Soc., Faraday Trans. 2* 76 (0 1980), pp. 1388–1408. DOI: 10.1039/F29807601388. URL: http://dx.doi.org/10.1039/F29807601388.

[58] C. Heitzinger, Y. Liu, N. J. Mauser, C. Ringhofer, and R. W. Dutton. “Calculation of Fluctuations in Boundary Layers of Nanowire Field-Effect Biosensors”. In: *Journal of Computational and Theoretical Nanoscience* 7.12 (2010). DOI: doi:10.1166/jctn.2010.1644. URL: http://www.ingentaconnect.com/content/asp/jctn/2010/00000007/00000012/art00011.

[59] B. Eisenberg, Y. Hyon, and C. Liu. “A mathematical model for the hard sphere repulsion in ionic solutions”. In: *Communications in Mathematical Sciences* 9.2 (2011), pp. 459–475.

[60] J. Chen, B. McGaughy, D Sylvester, and C. Hu. “An on-chip, attofarad interconnect charge-based capacitance measurement (CBCM) technique”. In: *Proceedings IEDM*. 1996, pp. 69–72. DOI: 10.1109/IEDM.1996.553124.

[61] *Comsol website*.

[62] O. Zienkiewicz, R. Taylor, and J. Zhu. *The Finite Element Method: Its Basis and Fundamentals*. Elsevier Science, 2005. ISBN: 9780080472775.

[63] M. J. Martinez. “Comparison of Galerkin and control volume finite element for advection-diffusion problems”. In: *International Journal for Numerical Methods in Fluids* 50.3 (2006), pp. 347–376. ISSN: 1097-0363. DOI: 10.1002/fld.1060. URL: http://dx.doi.org/10.1002/fld.1060.

[64] R. E. Bank and D. J. Rose. “Some Error Estimates for the Box Method”. English. In: *SIAM Journal on Numerical Analysis* 24.4 (1987), pp. 777–787. ISSN: 00361429. URL: http://www.jstor.org/stable/2157588.

[65] T. Apostol. *Calculus*. Vol. 1. Blaisdell Publishing Company, 1962.

[66] M. Abramowitz and I. A. Stegun. *Handbook of Mathematical Functions with Formulas, Graphs, and Mathematical Tables*. ninth Dover printing, tenth GPO printing. New York: Dover, 1964.

[67] A. Quarteroni. *Modellistica Numerica per Problemi Differenziali*. 3rd. Springer Italia, 2006.

[68] M. Piller and E. Stalio. “Development of a mixed control volume - Finite element method for the advection diffusion-equation with spectral convergence”. In: *Computers & Fluids* 40.1 (2011), pp. 269 –279. ISSN: 0045-7930. DOI: http://dx.doi.org/10.1016/j.compfluid.2010.09.026. URL: http://www.sciencedirect.com/science/article/pii/S0045793010002549.

[69] *Matlab documentation*. The MathWorks, Inc. 2013.

[70] J. Schöberl. *Netgen documentation*. ver. 4.3. 2003. URL: http://www.hpfem.jku.at/netgen/.

[71] K. Levenberg. “A method for the solution of certain problems in least squares”. In: *Quart. Applied Math.* 2 (1944), pp. 164–168.

[72] Z. Cai. “On the finite volume element method”. English. In: *Numerische Mathematik* 58.1 (1990), pp. 713–735. ISSN: 0029-599X. DOI: 10.1007/BF01385651. URL: http://dx.doi.org/10.1007/BF01385651.

[73] I.-Y. Chung, H. Jang, J. Lee, H. Moon, S. M. Seo, and D. H. Kim. "Simulation study on discrete charge effects of SiNW biosensors according to bound target position using a 3D TCAD simulator". In: *Nanotechnology* 23.6 (2012), p. 065202. URL: http://stacks.iop.org/0957-4484/23/i=6/a=065202.

[74] M. M. Kohonen, M. E. Karaman, and R. M. Pashley. "Debye Length in Multivalent Electrolyte Solutions". In: *Langmuir* 16.13 (2000), pp. 5749–5753. DOI: 10.1021/la991621c. eprint: http://dx.doi.org/10.1021/la991621c. URL: http://dx.doi.org/10.1021/la991621c.

[75] A. Manickam, A. Chevalier, M. McDermott, A. Ellington, and A. Hassibi. "A CMOS Electrochemical Impedance Spectroscopy (EIS) Biosensor Array". In: *Biomedical Circuits and Systems, IEEE Transactions on* 4.6 (2010), pp. 379–390. ISSN: 1932-4545. DOI: 10.1109/TBCAS.2010.2081669.

[76] C. C. Wong, C. Drews, Y. Chen, T. S. Pui, S. Arya, R. Weerasekera, and A. Rahman. "CMOS based high density micro array platform for electrochemical detection and enumeration of cells". In: *Proceedings IEDM*. 2013, pp. 14.2.1–14.2.4. DOI: 10.1109/IEDM.2013.6724628.

[77] N. Couniot, T. Vanzieleghem, J. Rasson, N. V. Overstraeten-Schlögel, O. Poncelet, J. Mahillon, L. Francis, and D. Flandre. "Lytic enzymes as selectivity means for label-free, microfluidic and impedimetric detection of whole-cell bacteria using ALD-Al_2O_3 passivated microelectrodes". In: *Biosensors & bioelectronics* (2014). DOI: 10.1016/j.bios.2014.07.084.

[78] P. Dak, A. Ebrahimi, and M. A. Alam. "Non-faradaic impedance characterization of an evaporating droplet for microfluidic and biosensing applications". In: *Lab Chip* 14 (14 2014), pp. 2469–2479. DOI: 10.1039/C4LC00193A. URL: http://dx.doi.org/10.1039/C4LC00193A.

[79] G. S. Kulkarni and Z. Zhong. "Detection beyond the Debye Screening Length in a High-Frequency Nanoelectronic Biosensor". In: *Nano Letters* 12.2 (2012), pp. 719–723. DOI: 10.1021/nl203666a. eprint: http://pubs.acs.org/doi/pdf/10.1021/nl203666a. URL: http://pubs.acs.org/doi/abs/10.1021/nl203666a.

[80] J.-M. Woo, S. H. Kim, H. Chun, S. J. Kim, J. Ahn, and Y. J. Park. "Modulation of molecular hybridization and charge screening in a carbon nanotube network channel using the electrical pulse method". In: *Lab Chip* 13 (18 2013), pp. 3755–3763. DOI: 10.1039/C3LC50524C. URL: http://dx.doi.org/10.1039/C3LC50524C.

[81] I. Giaever and C. Keese. "A morphological biosensor for mammalian cells". In: *Nature* 366 (1993), pp. 591–592.

[82] Y. Cui, Q. Wei, H. Park, and C. M. Lieber. "Nanowire Nanosensors for Highly Sensitive and Selective Detection of Biological and Chemical Species". In: *Science* 293.5533 (2001), pp. 1289–1292. DOI: 10.1126/science.1062711. eprint: http://www.sciencemag.org/content/293/5533/1289.full.pdf. URL: http://www.sciencemag.org/content/293/5533/1289.abstract.

[83] F. Patolsky, B. P. Timko, G. Yu, Y. Fang, A. B. Greytak, G. Zheng, and C. M. Lieber. "Detection, Stimulation, and Inhibition of Neuronal Signals with High-Density Nanowire Transistor Arrays". In: *Science* 313.5790 (2006), pp. 1100–1104. DOI: 10.1126/science.1128640. eprint: http://www.sciencemag.org/content/313/5790/1100.full.pdf. URL: http://www.sciencemag.org/content/313/5790/1100.abstract.

[84] A. Lasia. *Electrochemical Impedance Spectroscopy and its Applications*. Springer, 2014.

[85] J. Daniels and N. Pourmand. "Label-Free Impedance Biosensors: Opportunities and Challenges". In: *Electroanalysis* 19.12 (2007), pp. 1239–1257. DOI: doi:10.1002/elan.200603855.

[86] C. Fung, P. Cheung, and W. Ko. "A Generalized Theory of an Electrolyte-Insulator-Semiconductor Field-Effect Transistor". In: *IEEE Transactions on Electron Devices* 33.1 (1986), pp. 8–18.

[87] P. Barabash, R. Cobbold, and W. Wlodarski. "Analysis of the Threshold Voltage and Its Temperature Dependence in Electrolyte-Insulator- Semiconductor Field-Effect Transistors (EISFET's)". In: *IEEE Transactions on Electron Devices* (1987), pp. 1271–1282.

[88] H. P. Erickson. "Size and Shape of Protein Molecules at the Nanometer Level Determined by Sedimentation, Gel Filtration, and Electron Microscopy". English. In: *Biological Procedures Online* 11.1 (2009), pp. 32–51. DOI: 10.1007/s12575-009-9008-x. URL: http://dx.doi.org/10.1007/s12575-009-9008-x.

[89] W. Hale. *The HarperCollins Dictionary Of Biology*. HarperCollins, 1991.

[90] E. Gongadze, U. van Rienen, and A. Iglic. "Generalized Stern models of the electric double layer considering the spatial variation of permittvity and finite size of ions in saturation regime". In: *Cellular and Molecular Biology Letters* 16 (2011), pp. 576–594.

[91] S. Polonsky, P. Solomon, J. Liao, L. Medina, and M. Ketchen. "Front-End-Of-Line Quadrature-Clocked Voltage-Dependent Capacitance Measurement". In: *Proc. IEEE Int. Conf. on Microelectronic Test Structures*. 2011, pp. 4–7.

[92] M. Carminati, G. Ferrari, F. Guagliardo, and M. Sampietro. "ZeptoFarad capacitance detection with a miniaturized CMOS current front-end for nanoscale sensors". In: *Sensors and Actuators A: Physical* 172.1 (2011), pp. 117 –123. ISSN: 0924-4247. DOI: http://dx.doi.org/10.1016/j.sna.2011.02.052. URL: http://www.sciencedirect.com/science/article/pii/S0924424711001257.

[93] S. Baumgartner and C. Heitzinger. "A one-level FETI method for the drift-diffusion-Poisson system with discontinuities at an interface". In: *J. Comp. Phys.* 243 (2013), pp. 74 –86. ISSN: 0021-9991. DOI: http://dx.doi.org/10.1016/j.jcp.2013.02.043.

[94] J. Rollins and J. Choma. "Mixed-mode PISCES-SPICE coupled circuit and device solver". In: *Computer-Aided Design of Integrated Circuits and Systems, IEEE Transactions on* 7.8 (1988), pp. 862–867. ISSN: 0278-0070. DOI: 10.1109/43.3217.

[95] R. E. F. Matthews. "A classification of virus groups based on the size of the particle in relation to genome size". In: *J. Gen. Virol.* (1975), pp. 135–149.

[96] Y. Marcus. "Ionic radii in aqueous solutions". In: *Chemical Reviews* 88.8 (1988), pp. 1475–1498. DOI: 10.1021/cr00090a003. eprint: http://pubs.acs.org/doi/pdf/10.1021/cr00090a003. URL: http://pubs.acs.org/doi/abs/10.1021/cr00090a003.

[97] T. Simonson and C. Brooks. "Charge Screening and the Dielectric Constant of Proteins: Insights from Molecular Dynamics". In: *J. Amer. Chem. Soc.* 118.35 (1996), pp. 8452–8458. DOI: 10.1021/ja960884f. eprint: http://pubs.acs.org/doi/pdf/10.1021/ja960884f.

[98] A. Bulyha and C. Heitzinger. "An algorithm for three-dimensional Monte-Carlo simulation of charge distribution at biofunctionalized surfaces". In: *Nanoscale* 3 (4 2011), pp. 1608–1617. DOI: 10.1039/C0NR00791A. URL: http://dx.doi.org/10.1039/C0NR00791A.

[99] R. Janek, W. Fawcett, and A. Ulman. "Impedance Spectroscopy of Self Assembled Monolayers on Au(111): Evidence for complex double-layer structure in aqueous NaClO4 at the potential of zero charge". In: *J. Phys. Chem. B* 101.42 (1997), pp. 8550–8558.

[100] M. A. Rampi, O. J. A. Schueller, and G. M. Whitesides. "Alkanethiol self-assembled monolayers as the dielectric of capacitors with nanoscale thickness". In: *Applied Physics Letters* 72.14 (2004), p. 1781.

[101] A. Tlili, A. Abdelghani, S. Hleli, and M. A. Maaref. "Electrical Characterization of a Thiol SAM on Gold as a First Step for the Fabrication of Immunosensors based on a Quartz Crystal Microbalance". In: *Sensors* 4 (2004), pp. 105–114.

[102] M. S. Kilic, M. Z. Bazant, and A. Ajdari. "Steric effects in the dynamics of electrolytes at large applied voltages. I. Double-layer charging". In: *Phys. Rev. E* 75 (2 2007), p. 021502. DOI: 10.1103/PhysRevE.75.021502. URL: http://link.aps.org/doi/10.1103/PhysRevE.75.021502.

[103] M. Punzet, D. Baurecht, F. Varga, H. Karlic, and C. Heitzinger. "Determination of surface concentrations of individual molecule-layers used in nanoscale biosensors by in situ ATR-FTIR spectroscopy". In: *Nanoscale* 4 (7 2012), pp. 2431–2438. DOI: 10.1039/C2NR12038K. URL: http://dx.doi.org/10.1039/C2NR12038K.

[104] M. Aubouy, E. Trizac, and L. Bocquet. "Effective charge versus bare charge: an analytical estimate for colloids in the infinite dilution limit". In: *Journal of Physics A: Mathematical and General* 36.22 (2003), p. 5835. URL: http://stacks.iop.org/0305-4470/36/i=22/a=302.

[105] P. Wittung, P. E. Nielsen, O. Buchardt, M. Egholm, and B. Norden. "DNA-like double helix formed by peptide nucleic acid". In: *Nature* 368 (6471 1995), pp. 561–563. DOI: 10.1038/368561a0.

[106] M. A. Alam. *Principles of Electronic Nanobiosensors*. Nanohub web course. 2013.

[107] A. Matsumoto and Y. Miyahara. "Current and emerging challenges of field effect transistor based bio-sensing". In: *Nanoscale* 5 (2013), pp. 10702 –10718. DOI: 10.1039/c3nr02703a.

[108] E. Accastelli, G. Cappi, J. Buckley, T. Ernst, and C. Guiducci. "Comparison between front- and back-gating of Silicon Nanoribbons in real-time sensing experiments". In: *Nanotechnology (IEEE-NANO), 2013 13th IEEE Conference on*. 2013, pp. 517–520. DOI: 10.1109/NANO.2013.6721024.

[109] M. Rossi, M. Bennati, M. Lombardini, P. Ashburn, H. Morgan, E. Sangiorgi, and M. Tartagni. "Hybrid System for Complex AC Sensing of Nanowires". In: *Proc. ULIS*. 2014.

[110] M. Wipf, R. L. Stoop, A. Tarasov, K. Bedner, W. Fu, I. A. Wright, C. J. Martin, E. C. Constable, M. Calame, and C. Schönenberger. "Selective Sodium Sensing with Gold-Coated Silicon Nanowire Field-Effect Transistors in a Differential Setup". In: *ACS Nano* 7.7 (2013), pp. 5978–5983. DOI: 10.1021/nn401678u. eprint: http://pubs.acs.org/doi/pdf/10.1021/nn401678u.

[111] M. Reed. “CMOS Biosensor Devices and Applications”. In: *Proceedings IEDM*. 2013, pp. 208–211.

[112] G. Wenga, E. Jacques, A. Salaün, R. Rogel, L. Pichon, and F. Geneste. “Step-gate polysilicon nanowires field effect transistor compatible with CMOS technology for label-free DNA biosensor”. In: *Biosensors and Bioelelectronics* 40.1 (2013), pp. 141 –146. ISSN: 0956-5663. DOI: http://dx.doi.org/10.1016/j.bios.2012.07.001.

[113] S. Baumgartner, M. Vasicek, A. Bulyha, and C. Heitzinger. “Optimization of nanowire DNA sensor sensitivity using self-consistent simulation”. In: *Nanotechnology* 22.42 (2011), p. 425503. URL: http://stacks.iop.org/0957-4484/22/i=42/a=425503.

[114] C. Guiducci, E. Accastelli, and F. Spiga. “Digital approaches in electronic biochips”. In: *Proceedings IEDM*. 2013, pp. 204–207.

[115] G. Tulzer and C. Heitzinger. “Fluctuations due to association and dissociation processes at nanowire-biosensor surfaces and their optimal design”. In: *Nanotechnology* 26.2 (2015), p. 025502. URL: http://stacks.iop.org/0957-4484/26/i=2/a=025502.